论文集

INFATS PROCEEDINGS

The 11th International Forum of Automotive Traffic Safety

November 13-14th, 2014,Chongqing,China

INFATS PROCEEDINGS

The 11th International Forum of Automotive Traffic Safety

• November 13-14, 2014 Chongqing, China •

INFATS Secretariat
State Key Laboratory of Advanced Design and Manufacturing for
Vehicle Body, Hunan University
410082 Changsha, P.R.China
Tel: +86-731 88823603 Fax: +86-731 88822051
E-mail: INFATS@vip.163.com Website: http://infats.hnu.cn

ORGANIZING COMMITTEE

Chairman:
ZHONG Zhihua, ZHAO Hang, REN Xiaochang

Co-Chairman:
YANG Jikuang

Organizer
State Key Laboratory of Advanced Design and Manufacturing for Vehicle Body Hunan University

LOCAL ORGANIZING COMMITTEE

Chairman:
LI Kaiguo, China Automotive Engineering Research Institute Co., Ltd

Co-Chairman:
LI Wei, Chongqing Changan Automobile Co., Ltd
ZHOU Lin, The Third Military Medical University

Secretary-General
XIE Fei, China Automotive Engineering Research Institute Co., Ltd

Deputy Secretary-General
ZHAO Hui, Chongqing Changan Automobile Co., Ltd, State Key Laboratory of Vehicle NVH and Safety Technology
YIN Zhiyong, The Third Military Medical University, Chongqing Key Laboratory of Vehicle Crash/Bio-impact and traffic safety
DENG Zhaoxiang, China Automotive Engineering Research Institute Co., Ltd, State Key Laboratory of Vehicle NVH and Safety Technology

Local organization:
State Key Laboratory of Vehicle NVH and Safety Technology
Chongqing Key Laboratory of Vehicle Crash /Bio-impact and traffic safety
China Automotive Engineering Research Institute Co., Ltd.
Chongqing Changan Automobile Co., Ltd
The Third Military Medical University

Co- organization:
Chongqing Automobile Collaborative Innovation Center

ACADEMIC COMMITTEE

Chairman: *ZHONG Zhihua, WANG Zhengguo, GUO Konghui, LI Jun*
Co-Chairman: *YANG Jikuang*

Members(in alphabetic order):
ANDERSON Robert, Adelaide University, Australia
CESARI Dominique, IFSTTAR, France
Clive CHIRWA, University of Bolton, UK
CHEN Chaozhuo, Chery Automobile Engineering Institute
CHEN Keming， China Automotive Engineering Research Institute Co., Ltd
CAO Libo, Hunan University
FILDES Brian, Monash University, Australia
GUO Konghui, Jilin University, Hunan University
GU Lei，Beijing Automotive Technology Center
GONCAL Tejera，IDIADA，Spain
HOU Fei, Pan Asia Technical Automotive Center (PATAC), Shanghai.
HUANG Hongwu, Xiamen University of Technology
HAN Xu, Hunan University
HU Yuanzhi，Chongqing University of Technology
JIN Xianlong, Shanghai Jiao Tong University
KAN Steve, The George Washington University, USA
KAJZER Janusz, Kabimec Consulting, Sweden/Hunan University
LIN Zhongqin, Shanghai Jiao Tong University
LI Sanhong, National Automobile Quality Supervision Test Center (Xiangfan)
LI Guangyao, Hunan University
LOVSUND Per, Chalmers University of Technology, Sweden
MCLEAN Jack, Adelaide University, Australia
MIZUNO Koji, Nagoya University, Japan
MASAO Nagai，Japan Automotive Research Institute，Japan
OTTE Dietmar, Medical University Hannover, Germany
RUAN Jesse, FORD Motor Company, USA
SHEN Haidong, Pan Asia Technical Automotive Center (PATAC), Shanghai.
SVENSSON Mats, Chalmers University of Technology, Sweden
WANG Zhengguo, Third Military Medical University
WILLINGER Remy, Strasbourg University, France
WISMANS Jac, SAFETEQ, The Netherlands/Chalmers University of Technology
WAN Xinming，China Automotive Engineering Research Institute Co., Ltd
YANG Jikuang, Hunan University/ Chalmers University of Technology
YANG King H., Wayne State University, USA /Hunan University
YIN Zhiyong, Third Military Medical University
TEO Ee-Chon, Nanyang Technological University, Singapore
ZHONG Zhihua, Hunan University
ZHOU Qing, Tsinghua University
ZHU Xichan, Tongji University
ZHAO Hui, Changan Automotive Engineering Academy

Acknowledgement

The INFATS2014 Conference was sponsored by:

The Ministry of Education of P.R. China
中华人民共和国教育部

State Administration of Foreign Experts Affairs, the P.R of China
中华人民共和国国家外国专家局
State Key Laboratory of Advanced Design and Manufacturing for

Vehicle Body, Hunan University
湖南大学汽车车身先进设计和制造国家重点实验室
State Key Laboratory of Vehicle NVH and Safety Technology
汽车振动噪声和安全技术国家重点实验室
Chongqing Key Laboratory of Vehicle Crash/Bio-impact and traffic safety
车辆/生物碰撞安全重庆市市级重点实验室
China Automotive Engineering Research Institute Co., Ltd.
中国汽车工程研究院股份有限公司
Chongqing Changan Automobile Co., Ltd
重庆长安汽车股份有限公司
The Third Military Medical University
第三军医大学
Chongqing Automobile Collaborative Innovation Center
重庆自主品牌汽车协同创新中心
Humanetics Innovative Solutions, Inc.
首美安全系统设备商贸（上海）有限公司
MESSRING Systembau MSG Gmbh
Shanghai Hengstar Technology Co., Ltd.
上海恒士达科技有限公司

Table of Contents

SESSION I: Road vehicle accident

Session S1-1: Motorized-two-wheelers and pedestrian accident

ATS.2014.101 **Influence Parameter and Accident Factors in comparing Light and Heavy Motorized-two-wheelers** 1
Otte, D., Jänsch, M., Wiese, B.

ATS.2014.102 **A Study on Vehicle-Electric Bicycle Impact Accidents Reconstruction Based on the Uncertainty Theory** 18
LI Li,TU Xiang, LI Pingfei, LIU Youbao

ATS.2014.103 **Study on Pedestrian's Head Injury in Accidents Using a Biomechanical Simulation Model** 24
Lv Xiaojiang, Ma Zhengwei, Sun lizhi, Chen Jiqing, Zhou Dayong, Liu Weiguo

ATS.2014.104 **A study of Lower Limb serious injuries based on passenger car field accident data analysis in Germany** 32
Bingyu Wang, Jikuang Yang, Dietmar Otte, Xiaoqing Jiang, Yong Peng

ATS.2014.105 **The study about airbag error function during the cars and electric bikes collision** 41
PengWei, QiZhiNan,ZengBiQiang, GuoLanShen

Session S1-2: Road vehicle accident

ATS.2014.106 **Epidemiological Analysis on Road Traffic Injuries in Shanghai from 2005 to 2013** 47
JIANG Bang-shui, CHEN Jun-yi, PAN Shu-ming, WANG Hong-yan

ATS.2014.107 **Multiple Analysis of Heavy Vehicle Accident based on Real-life Cases** 54
Wenchao Liu, Zhiqiang Zhou

ATS.2014.108 **Study on validity of airbags to car with crash barrier of highway** 58
WangDe, ZhaoXiDa,ZengBiQiang

ATS.2014.109 **Research on the national standard of the rear underrun protection devices of truck in China** 64
Feng Wenxuan , Wang Honyan, Xiao Lingyun , Hu Wenhao , Chen Junyi

ATS.2014.110 **Occupant Injury Analysis in Traffic Accident Based on the Coupling of PC-Crash and MADYMO** 74
Qiang CHEN, Bing DAI

ATS.2014.111 **Traffic Accidents Involving Child Passengers Travelling on Powered Two-Wheel Vehicles** 82
Eloi BOIX, Adrià FERRER, Juan José ALBA, Sergi FERRIS, José A. AZPEITIA

SESSION II: Vehicle crashworthiness

Session 2-1:Small overlap impact and vehicle crash safety

ATS.2014.201 **Crashworthiness analysis of real small overlap impact (SOI) accidents in Spain and comparison to SOI tests** 91
Xavier Da SILVA, Adrià FERRER

ATS.2014.202 **Vehicle Body Engineering Approach of Some SUV for Small Overlap** 100
Derek Wu Chun-Tao, Zhang Kai, Yang Ling-Jun, Liu Zhen-Hai, Chen Xian-Ling

ATS.2014.203 **The simulation and analysis on electric vehicle's front impact** 108
CUI Shujuan,CHEN Keming,CAO youqiang,DONG hongliang

ATS.2014.204 **Real Solutions for Safety in L7e Vehicles** 115
Eloi BOIX, Aritz ESNAOLA, Óscar CISNEROS, Juan José ALBA, Massimiliano AVALLE, Alessandro SCATTINA, Pawel JARCZEWSKI, Ewa WYSGA

ATS.2014.205 **Study of Quasi-static Mechanical Properties of Vehicle Power Lithium Battery and Failure Criteria** 122
Binghe Liu,Jun Xu

ATS.2014.206 **Analysis of Front Impact Safety on FSAE Racing Car** 129
Xulai PENG, Fan LI

ATS.2014.207 **Coupling Low-Speed and Pedestrian Collisions to Design an Adaptive Car Bumper Energy Absorber** 136
Yu Chuanhui, Mo Fuhao, Xiao Zhi,Peng Yong, Du Min, Li Fan

ATS.2014.208 **Comparative Analysis of Performance and Criteria for Crash Cushions in U.S. and EU** 143
Chun-juan SHI, Wei WANG, Ming ZHONG, Ze-you PENG, Lan YANG

ATS.2014.209 **Analysis of Structure Dynamic Characteristics of ATV Frame with Engine** 149
Fang Ye, a, Zhongming Xu, Xicheng Zhai

Session 2-2: Lightweight structure design and crashworthiness

ATS.2014.210 **Crash performances comparison and selection of bumper beam with different lightweight methods** 154
Zhang Jingwen ,Fan Tiqiang ,Zhao Qingjiang ,Li Yang

ATS.2014.211 **Optimization Design For Crashworthiness Of Bumper Based On Linear And S-Type Function TRB** 162
Liu Hongbin,Xiao Zhi,Li Suwen

ATS.2014.212 **Research on CAE Model Updating Method for Robust Design Optimization and its Application to Vehicle Weight Reduction** 170
ZHAN Zhenfei , YANG Junqi , SHU Yajing, ZHENG Ling ,FU Yan ,YANG Ren-Jye

ATS.2014.213 **基于ENCAP侧面柱碰的门槛梁、车门防撞杆优化设计** 180
王彬花 ， 范体强 ， 赵清江， 李阳

ATS.2014.214 **Numerical Simulation Analysis and Test of Standing Wave Border Speed about Radial Tire** 187
Wang Qiang， Shi Yuhuan， Zhang Na

ATS.2014.215 **A Method Study on the Optimal Ground Clearance of Truck Under-run Protector** 193
Yan Lei, Chen Qiang, Sun Zhendong, Lin Miao

ATS.2014.216 **Minibus low constraint system to cope with the new regulations frontal crash** 200
Zhou Yinge， Duan Zhichun， Cui Taisong， Zhao Hui

ATS.2014.217 **Research on The Method of Optimizing Brackets in IP Based on Chinese Rule GB11552-2009** 205
Liao Gaojian, Chen Xianqing , Dian Bo， Shao Jinhua

SESSION III-1: Occupant protection

Session S3-1-1: Occupant behavior and protective effectiveness

ATS.2014.301 **A preliminary study on the protective efficiency of the child restraint system in school bus** 209
HAN Yong, Zhou Shui-ting, Zhuang Shu-ji, XIE Jing-ping, Koji Miuzno

ATS.2014.302 **Research on the Factors of the Consistency of Child Restraint System Sled Test** 220
YANG Lang, ZHU Xichan, DONG Liping, MA Zhixiong， Zhang Shaowei

ATS.2014.303 **Optimized Design of the Airbag Parameters for OOP Children Based on LS-OPT** 228
Fei Jing , Bai Zhonghao, Chen Keming

ATS.2014.304 **Optimization Research on Restraint System Development for Female Driver** 238
Li Hongyun, Lu Shuang, Han Feifei, Li Guo, Cao Huan

ATS.2014.305 **Research the effects of seat belt wearing position on HIII 5th female dummy's chest characteristics** 251
Ma Weijie, Duan Bingxu, Bai Peng, Li Xiangrong

ATS.2014.306 **Effect of rotation of passenger compartment on occupant behavior in car impacts** 258
Yiwei CHEN, Hiroki IWANAKA, Daisuke ITO, Koji MIZUNO and Yong Han

ATS.2014.307 **Development and Validation a Finite Element Model of the Thigh of a Chinese 50th Percentile Male** 269
Guan-Jun Zhang, Long-Liang Wang, Xian-Ping Du, Yue-Qun Hu

ATS.2014.308 **Braking Effects on Occupant Kinematics and Injury during the Full Frontal Impact simulation using Human Model** 278
Chengyue JIANG, Xi LIU, Yuanzhi HU,Shugang XIE, Hongyun LI

ATS.2014.309 **Model Development of Grid Points Meshing in Pedestrian Headform Protection Simulation Based on HyperMesh** 284
Zhao Rutao, Zhu Xichan, Dong Liping, Zheng Zudan, Wu Bin, Song Yalan, Ma Zhixiong

ATS.2014.310 **Research on the Protective Effect of New Front Safety Seat in the Car Frontal Collision and Emergency Braking** 293
Ge Ruhai, Hong Liang

SESSION III-2: Injury Biomechnics

Session S3-2-1: Injury Biomechanics

ATS.2014.311 **Abdominal Impact Study on Pediatric Cadaveric Subjects** 303
Jun Ouyang, Qingan Zhu, Zeyu Li, Chang Liu, Shizhen Zhong

ATS.2014.312 **Evaluation of Mass-based Scaling Law for Brain Injury Criteria: A Preliminary Study** 311
Lihai REN, Daniel BAUMGARTNER, Jikuang YANG, Narayan YOGANANDAN,Brain D STEMPER

ATS.2014.313 **Simulation Analysis of Impact to Occupant Head Based on Head Impact Regulation FMVSS 201U** 319
Du Tianya, Chen Jiqing , Huang Wei, Ma Zhengwei

ATS.2014.314 **Development and Validation of a Human Neck Muscles FE Model in Low-speed Vehicle Collisions** 326
Cao Yingchun， Li Fan， Hu Wei， Su Sicheng

ATS.2014.315 **Study of anatomical differences between six-year-old child and adult based on CT images** 334
LV Wen-le, RUAN Shi-jie, LI Hai-yan, WANG Chun-xiang, CUI Shi-hai

ATS.2014.316 **Development of a FE Model of Lower Extremity for Chinese Pedestrians** 343
Lan Fengchong, Huang Wei, Chen Jiqing, Wu Kai

ATS.2014.317 **Impact Simulation of a Child Head and the Engine Hood** 352
CUI Shi-hai LI Xiang-nan LI Hai-Yan ZHAO Wei RUAN Shi-jie

ATS.2014.318 **Numerical analysis of compressive neck injuries due to vertical loading applied through the head** 357
Haibin CHEN, Liying ZHANG, Jing ZHANG, Shuo TANG, Li HE, Jihong ZHOU

ATS.2014.319 **Finite element analysis of human thoracic injury criteria in side impact** 363
Fang WANG, Jikuang YANG , Yong HAN, Guibing LI , Xiaoqing JIANG

SESSION IV: Active safety technology and V2x

Session S4-1 : Active safety

ATS.2014.401 **Control Strategy of Regenerative/Electro-Mechanical Hybrid Braking System for Hybrid Electric Vehicle Based on Urban Driving Cycle** 370
Zhen WEI, John XU, Dunant HALIM

ATS.2014.402 **A safety impact benefit assessment of Autonomous Emergency Braking Systems based on real traffic scenarios** 379
He Jun, Zhu Xichan

ATS.2014.403 **Summarization of Typical Scenarios of Adaptive Cruise Control Based on Natural Drive Condition** 387
Gu Rongrong, Zhu Xichan

ATS.2014.404 **Study on the influence of the driving behavior when vehicle collision avoidance** 394
Huang Jiang， Li Hong

SESSION V: Crash test and Measuring techniques

Session S5-1 : Crash test dummies and measurement technology

ATS.2014.501 **Comparative Study between the WorldSID and the EuroSID II in Static Impact Tests** 404
Maria de ODRIOZOLA, Adrià FERRER , Ignacio LÁZARO

ATS.2014.502 **Comparison of Current ATDs with China's Adult Population in Anthropometry** 412
Kai ZHANG, Lingbo YAN, Xin LV, Libo CAO

ATS.2014.503 **Comparative Analysis of the Biological Simulation of Pedestrian FLEX-PLI and TRL-LFI** 417
Wang Kun， Li Haibin， Wang Yang

ATS.2014.504 **Research on Lumbar Calibration of 50th Crash Dummy** 425
Li XIANGRONG, Wang KAI, Duan BINGXU, Xie MINGHAO

ATS.2014.505 **Optimization of Two-dimensional Measurement Equipment in Vehicle Crash Test** 431
ZHU cui-ping, ZHAO you-mei, MA de-ren,

ATS.2014.506 **A study on the effect of changes in side impact protocol of 2015 Euro NCAP** 435
Liu Xilong, Dong Liping, Zhu Xichan, Ye Wentao, Huang Xuan

ATS.2014.507 **Research on Validation Metrics for Multiple Dynamic Responses Comparison** 444
Zhenfei ZHAN, Junqi YANG , Ling ZHENG, Yajing SHU， Yan FU, Ren-Jye YANG, Saeed Barbat

ATS.2014.508 **Research On The AE-MDB And Vehicle Front Stiffness** 451
Li XIANGRONG, Ma WEIJIE, Zhu HAITAO

Proceedings of the 11th International Forum of Automotive Traffic Safety, 2014, pp 1- 17
No. ATS.2014.101

Influence Parameter and Accident Factors in Comparing Light and Heavy Motorized-Two-Wheelers

Otte, Dietmar[1], Jänsch, M.[1], Wiese, B.[2]

[1]*Accident Research Unit, Hannover Medical School, Carl-Neuberg-Str. 1, D-30625 Hannover, Germany*

[2] *Biometric Institute, Hannover Medical School, Carl-Neuberg-Str. 1, D-30625 Hannover, Germany*

Email: otte.dietmar@mh-hannover.de

Abstract: This study will describe the injury frequency and injuries in detail for motorcycle drivers on German roads involved in traffic accidents and comparing the analysis with the whole group of all kinds of motorized two-wheelers. The study is based on accident sampling by GIDAS (German In-Depth-Accident Study). The current situation on injury frequencies on different body areas and the severity of such injuries are well documented and compared to previous time frames. Also the characteristics of the accident causes are analyzed on the basis of a special coding system ACAS (Accident Causation Analysis System) showing human factors responsible for the accident occurrence. For the present study 3.083 accidents with 3.144 motorized two wheeler riders are given as representative distribution for the German situation, based on a statistical random selection of accident documentations and weighting procedure. Two-thirds of all motorized two-wheeler suffered from minor injuries MAIS 1 and 10% received severe injuries MAIS 3+. The trend of the last decades is shown a positive decrease of numbers in fatalities and severely injured riders. Nearly 50% of the riders used protective clothes while 98% wear helmets. The impact location and load levels are discussed regarding an optimization of the safety level on the motorcycle and demands to the rider on protective equipment. Over 70% of the riders had contributed to the emergence of the accident with a human failure and in less than 2% of the cases a technical defect of the motorcycle was a contributing factor for causing the accident. Over 10% of the motorcycle riders had caused an accident due to an influence from the traffic environment or weather. This study will show that also demands to the drivers of motorcycles are needed to get further reduction in accident events.

Keywords: Injury Severity, Accident Causation, Human factors, Effectiveness of helmet and protective clothes

1 Introduction and objectives

Road users without a protective outer shell are called "Vulnerable Road User". This includes pedestrians, cyclists and motorized two-wheeler users (powered two wheelers PTW). The latter are categorized by the German Federal Highway Research Institute (BASt) and the EU vehicle classification into “Kleinkrafträder” (EU-class L1e, <45km/h, <50ccm) and motorcycles (L3e, L4e >50ccm, >45 km/h). The so called “Kleinkrafträder” include cycles (<50ccm, <45 km/h), Mopeds and Mofas(<25 km/h) and Light Mofas (<30ccm, <0.5KW, <20km/h).The motorcycles can be divided into motorcycles (>50ccm, > 45 km/h),light motorcycles (<125ccm, <11KW) and heavy so called “standard” motorcycles (>125ccm, >11KW).

Due to the different types of PTW and their different use driving and motion behavior on public roads are different. There are also different requirements for limits of speed arising from the motor vehicle authorities within these groups. The protection existing for users of these PTW is not fundamentally different, as there are helmets and protective

clothing available. However the usage behavior is different riders of motorcycles almost generally use full face helmets protecting the whole head and often use protective clothing to protect the whole body also with special protectors. For scooters and mopeds however rarely a full face helmet is used, but more often half-shell helmets and open-face helmets. Protective clothes is also found in different frequencies depending on the type of PTW and special protectors inside the clothing are found almost exclusively among the riders of motorcycles (however also in rather low frequency of use).

The accidents which occur are often a reflection of driving performance, handling and traffic participation, while riders of PTW involved in accidents are found in almost all age groups. While crashed motorcyclists are quite often characterized by more mature ages, light motorcycles and scooters are mainly used by the younger generation. Age plays a part in the causes of accidents but also the results of suffering injuries as the biomechanical load limits of the elderly compared to the younger people are significantly reduced. The injury severity however is particularly influenced by the different masses of the colliding accident partners and thus by the loads transmitted to the body by the collision. Therefore the severity of the accident and the resulting injuries are different in the various groups of PTW.

It is currently estimated that there are about 30 million motorized two-wheelers in Europe, and a market for Europe is currently indicated to about 2.5 million two-wheelers annually [1]. Here, a heavy increase was observed in the years after 2005(with only 2.0 million units). The trend of mopeds (<50ccm) and scooters is now declining to about 1 million annually, in contrast the registrations of motorcycles (> 50ccm)however is increasing by +3% to 1.5 million. Particularly in Asia motorized two-wheelers add to the overall picture of traffic. In India, for example, 69% of all motorized vehicles are motorized two-wheelers and 27% of all road deaths are among the group of riders of motorized two-wheelers. In Thailand it is estimated that 70-90% of road deaths and about 60% in Malaysia are from the group of riders of motorized two-wheelers. In many so-called "low and middle income countries PTW are among the increasing means of transport. Consequently, it is not surprising that also many people of this road user group die in traffic. This is not the case in western countries, although there also many people are injured or killed every year by using these types of PTW. In the European Union about 40,000 people are killed in traffic each year [2] of which in 2006 6,200 riders of PTW in the EU 25 countries lost their lives. These represent 16% of all traffic fatalities, while they only represent 2% of the total mileage driven. The risk to be killed is classified 18 times higher than with car drivers. It has been postulated that Norway, Switzerland, Denmark and Finland are the least dangerous countries for motorized two-wheelers, while the central and eastern Europe are represented as the most dangerous regions.

PTW users are particularly vulnerable as a result of the higher driving speeds collisions with heavier vehicles such as cars and trucks lead to high energy conversions. The use of protection such as helmet and protective clothing is common in many countries, but it is registered that in view of different temperatures from north to south the usage frequency varies. Similarly, half-shell and open-face helmets are used more frequently in southern countries. In Germany in 2008 97% of the drivers of PTW were wearing a helmet, only 51% wore additional protective clothing, 19% wore full protective clothing [3]. It can be explained by the relatively high usage rate of protection gear that the injury situation on the road for motorcyclists now compared to previous years turns out positively. In 2009 651 killed motorcyclists were counted in Germany, about 18% less than 4 years ago [4].The number of killed moped users on the other hand, remained constant (at about 100 fatalities per year), which also applies to the number of injured.

As technical causes, given the high technical quality of vehicle engineering and road design, hardly come into appearance for the occurrence of accidents and also as vehicles are continuously optimized in terms of safety, human causes may be stated as the main source for the occurrence of accidents. Especially to reduce the number of injuries and

fatalities even further in the future the reduction of the absolute number of accidents is also required. Past studies revealed that the motorcyclist involved is obviously less culpable for the accident than the drivers of cars or trucks with which he collided. The neglecting of the right of way of the PTW by other road users is currently one of the most common causes of accidents [5]. According to the Association of insurance companies in situations where the motorcyclist was injured the car drivers often were to be blamed for the occurrence of the accident [6].

The present study will clarify the extent to which the accident and injury situation has changed for the group of riders of PTW and which measures to increase safety must be sought in the future. For this it is effective to use the continuously carried out on-scene accident research in Hannover and Dresden (GIDAS) for analyzing the accident-structure. The study aims to analyze the structural characteristics of the different types of road users based on detailed documented traffic accidents and thereby identify injury priorities and mechanisms in connection with the used protective equipment such as a helmet and protective clothing. Furthermore accident causation factors and characteristics therefore should be identified.

2 Basis of the study

As part of GIDAS about 2,000 traffic accidents involving personal injury are documented annually by scientific teams in Hanover and Dresden. The reconstruction of the driving and collision velocities as well as the detailed documentation of the sustained injuries is recognized through the comprehensive collection of information [7, 8]. By means of a new coding system of accident causation factors (ACAS Accident Causation Analysis System) accident-relevant situations can be worked out and prophylactic measures can be defined [9,10]. The injuries are recorded based on the AIS [11] and injury severities using the usual definition according to MAIS (maximum single-AIS on all registered injuries) are compared to the technical framework. For the determination of the collision and driving speeds, the traces of the accident scene are documented in a scaled drawing using 3D laser technology and the crash collision analysis is conducted by the simulation software PC-Crash [12]. Based on the documentation of traffic accidents by statistically representative sampling methods and by an annually renewed matching of the data, the accident data in GIDAS can be regarded as representative for Germany [13].

The analysis of the statistically weighted data set was made as descriptive statistics. Therefore unknown parameters in the data set were not included, so that hereby the presented tables and graphs may display different numbers of n.

To display the current accident and injury situations of road users the official statistics of traffic accidents in a country is to be look at. From this, the total number of traffic accidents with injured motorcyclists in terms of the number of killed, seriously injured and slightly injured can be determined. However the exact course of the accident and the circumstances leading to the injury, especially the exact injury patterns of motorcyclists is not known from the data of the official statistics. In order to implement measures to increase road safety for motorcyclists, it is necessary to carry out further detailed surveys that are done in a comprehensive and detailed analysis, including reconstruction of the accident on the example of the Accident Research Unit Hanover. The on scene accident research provides detailed information about vehicle damage for the two-wheeler as well as for the collision partner's cars and trucks. Access to the injured is allowed and thus the detailed knowledge of injuries, including consideration of X-rays and insight into the medical documentation is available, hence the impact and injury kinematics of the riders of two-wheelers as well as the mechanics of injury can be determined. Essential characteristics of an evaluation of the trauma development are the technical accident circumstances such as impact speed and relative speed between the vehicles involved. These can be

reconstructed with the use of traces on the roadway and the points of rest of vehicles and people involved using mechanical principles. Interviews of accident participants also provide information about the accident development, situational actions of the drivers involved and failures in the driving task. Such a comprehensive accident research is continuously conducted in Germany as part of the GIDAS project (German In-Depth Accident Study) by the Federal Highway Research Institute and the Research Association for Automotive Technology FAT since 1999. Two teams, one each in the regions of Hannover and Dresden annually document 2000 traffic accidents involving personal injury[8] based on a statistical sampling method [13].

3 Data structure of the study

For the present study GIDAS data from the years 1999-2011 (n=24,013) were analyzed and from this accidents with motorized two-wheelers (n=3,474) were selected. After excluding cases with unknown information such as cases without riders, and cases in which important parameters were unknown such as injury information, head injury, wearing of safety helmet, a total of 2,864 riders of powered two-wheelers including 1,406 motorcyclists remained for the analysis (Figure.1). These 2 groups are compared within this study. On the one hand this study will display the injury situation of motorcyclists compared to the group of all PTW; on the other hand aspects of passive safety (injury and injury severity and their distributions) and active safety (causation and avoidance strategies) will be analyzed as a snapshot of the current accident situation. For the latter a subsample of the years 2008-2012 was chosen as for this data a special classification of accident causes (ACAS Accident Causation Analysis System) was started in the investigation at Hannover Medical School. This is a special coding system of human, vehicle and environmental causation factors collected from interviews and accident descriptions [9].

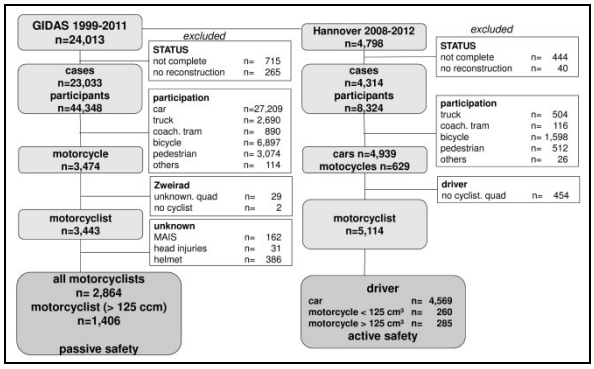

Figure.1 Sample Frame of the Study for GIDAS Database (left: passive safety, right: active safety)

4 Injury situations of motorcyclists

The analysis is conducted for the different types of motorized two wheelers PTW according to the categories valid in Germany. There are 4 major categories summarized in the group of "all motorized two-wheelers":

1. "**Mofa**": maximum speed of 25 km/h , in this study referred to as **moped25**
2. "**Mokick**": engine displacement of up to 50ccm and a maximum speed of 45 km/h, in this study referred to as **moped**
3. "**Kleinkraftrad**": with an engine displacement of up to 125ccm in this study referred to as **group of light motorcycle**

4. "Motorrad": with an engine displacement of over 125ccm, in this study referred to as **Group of (heavy) motorcycle**

The injuries are classified by the Abbreviated Injury Scale (AIS) in 6 degrees of severity AIS 0 uninjured, AIS 1 minor, AIS 2 moderate and AIS 3 severe up to AIS 6 (AIS 3+)[11,14]. 57.3% of all motorcyclists suffered from minor injuries MAIS 1, 25.6% had an injury severity of MAIS 2 and 11.9% of motorcyclist suffered from serious injuries of MAIS 3+. Only a comparison with other road users allows an assessment to what extent the proportion of the severely injured is of importance for the whole accident situation. For this purpose, belted car occupants were considered (data source GIDAS 2013, accidents of 2000-2012, n = 21,668), for which a proportion of the severely injured occupants MAIS 3+ results in 1.8%.This shows that motorcycling has a 6.6-times higher risk to suffering serious injuries.

Figure.2 shows that the proportion of the severely injured riders varies for different types of motorized two-wheelers. Thus, the smallest proportion of severe injuries MAIS 3+ can be observed for moped25 riders with 3.3%. The groups of mopeds have a proportion of 7.5%, the group of light motorcycles has a proportion of 8.8% and the group of heavy motorcycles has a portion of 16.3% severely injured riders.

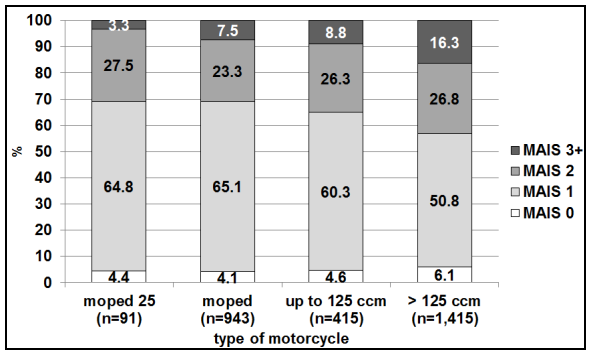

Figure.2 Maximum injury severity grades for motorcyclists of different two-wheeler-groups (100% each group)

The relevant parameter for the injury severity apparently is the impact speed which is resulted by the relative velocity between the colliding vehicles in which the collision angle comes into account. 80% of the relative speeds for the motorcyclists are below 60km/h. Compared to this 80% of the relative speeds of the total group of powered two-wheelers are found to be at 50km/h which means that motorcycle accidents are obviously characterized by a higher speed of the motorcycle itself.

A higher injury severity can also be detected at higher engine displacement. Thus 15.8% of the riders of motorcycles with an engine displacement over 750ccm were severely injured MAIS 3 +, whereas only 7.7% of the moped riders (up to 50ccm) and 8.9% of riders with PTW in the 51 to 125ccm displacement class. However the analysis shows that the curb weight of the vehicle has no influence on the injury severity.

That the riders of bigger motorcycles have a higher incidence of severe injuries can also be seen when analyzing different classes of engine power of the PTWs. While 15% of the riders of PTWs with an engine power of 50-75 kW are severely injured this share rises to 25% for riders of PTWs with an engine power greater than 75 kW. Consequently the proportion of severe injuries is also influenced by the power to weight ratio (mass/kW) of the vehicle (Figure.3). This is visible especially for light-weight motorcycles with high power (0-3 kg/kW) where the share of severely injured (MAIS 3+) riders is about twice as high as for the other power weight classes.

An influence of injury severity for different age groups of motorcyclists, however, is not visible. From the sample

of cases a weak trend towards higher injury severity may be seen for over 60 year olds a certainty however cannot be given due to the small number of people in the sample.

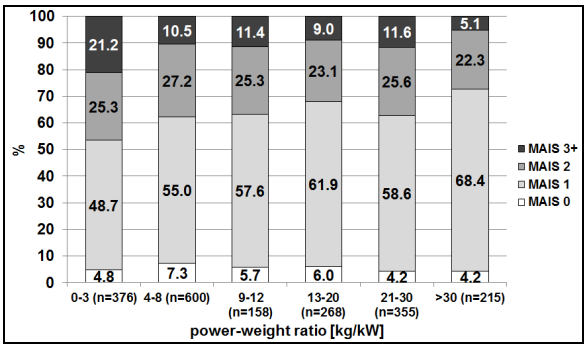

Figure.3 Maximum injury severity grade and power to weight ratio (100% each group)

5 Accident types

The classification of accident situations can be done on the basis of a classification system using 7 accident types which is also used in official accident statistics [15]. Here the conflict situation which led to the accident immediately before collision is considered. It turns out that riders of PTW are mostly involved in accidents which occurred due to a conflict between a turning in or crossing road user without priority and a vehicle with priority at crossings with 26.5%.Accidents involving pedestrians (cutting across the roadway) are rare at only 2.4%, as well as accidents with stationary traffic at 5.2%. The proportion of severely injured riders is relatively constant for almost all types of accidents (10-15%), yet a high proportion of moderate injuries MAIS 2 can be seen in driving accidents and "turning off accidents" due to a conflict between a turning off road user and a road user coming from the same direction or the opposite direction.

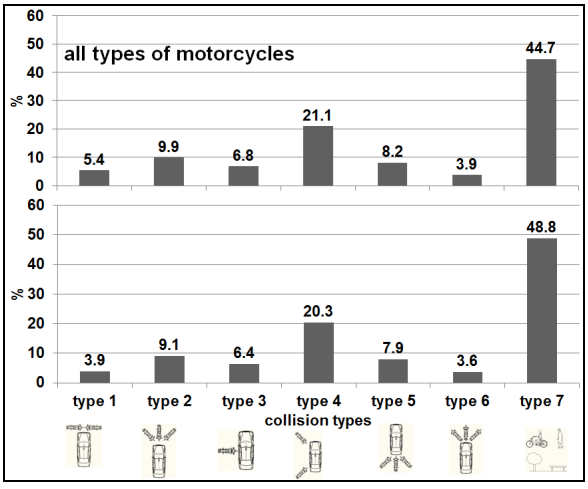

Figure.4 Collision configurations (types) of all motorcycles (n=2,848) and motorcycles > 125ccm (n=1,406), 100% all persons in each diagram

Form from the conflict situations (accident types) between the parties different collision constellations result between motorcycle and opponent, which are scientifically classified by collision types. Here 7 collision types were established based on a former study of the authors [16] which are scientifically widely recognized and often found in literature.

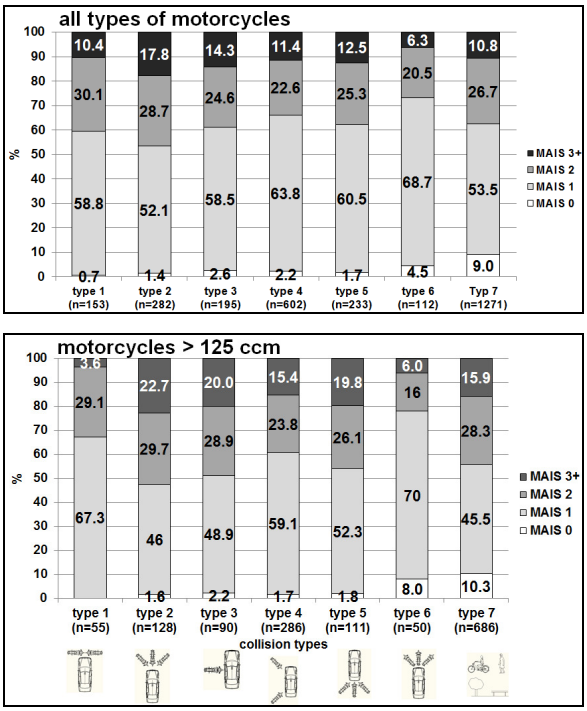

Figure.5 Collision configurations (types) of all motorcycles (n=2,848) and motorcycles > 125ccm (n=1,406) and maximum injury severity grade of motorcyclist (100% each group of collision types)

For PTW in general, the oblique collision frontally into the side of a vehicle (type 4 with 21.1%) and the single vehicle accident with impact with objects (type 7 with 44.7%) are the most common collision types (seeFigure.5). Also for motorcyclists (> 125cm) these two collision configurations are most common (20.3% respective 48.8%). The most severe types of collisions turn out to be the types 2,3,4,5 and 7. The most severe collisions are found in type 2 where the PTW collides into the front of the collision opponent at an oblique angle as well as the impact of the PTW practically perpendicular into the side of the car in the area of the compartment. These provide a particular exposure to head injuries, often associated with trauma to the entire body

6 Influence of a safety helmet on the severity of injury

To determine the effectiveness of a safety helmet in the accident situation of riders of PTW, 2 groups were formed, riders with safety helmet (n = 2,725) and riders without helmet (n = 139) – see Figure.6. The ratio of the number of cases shows the high usage rate of safety helmets, which in Germany is found to be at 99% according to studies of the Federal Highway Research Institute (BAST, 2009). When considering the injury severity by AIS, a significantly lower proportion of severe head injuries AIS 3+ is found with riders that had used the helmet (3.4%) versus riders that had not used the helmet (4.3%). Also, the injury severity of AIS 2 (moderate) shows up much less with helmet use with 9%, compared to 11.5% of cases without a helmet. Even AIS 1 injuries are less frequent at 7.6% with the protective helmet compared to 11.5% without the helmet.

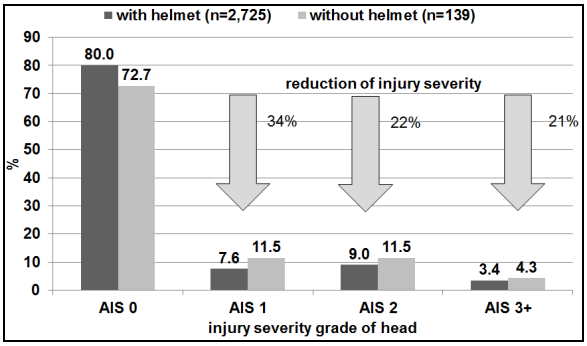

Figure.6 Injury severity grade head with and without use of helmet (100% each group of persons – with and without helmet)

Thus, the protective effect of the helmet is clearly visible, which leads to the effect that there are a higher proportion of uninjured riders with helmet (80%) than without helmet (72.7%). This is particularly evident, when considering the overall injury severity MAIS of all riders with a helmet where serious injuries often occur at the total body, while the head is not or less seriously injured due to the helmet. This is particularly important for patients hospitalized as poly trauma victims (per definition more than 3 injured body regions with AIS 3+ each), so that with the absence of severe head injuries, the chances of survival can be improved with a helmet.

The following reduction of injury severity with the use of a helmet can be deduced from the study:

AIS 1 minus 34%

AIS 2 minus 22%

AIS 3+ minus 21%

This high level of protection provided by a motorcycle helmet can also be found when considering the injury-frequency of different body regions (Figure.7). Motorcyclists (PTW > 125ccm) only had head injuries in 19.9% of the cases, while the injuries to other body regions were more frequently observed.

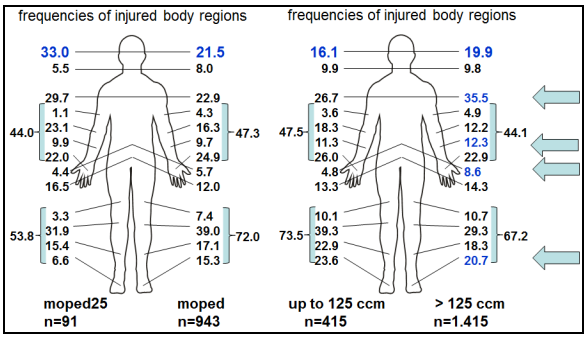

Figure.7 Frequencies of injured body regions of motorcyclists for different types of motorcycles (100% all persons each group)

Arm injuries were present at 44.1% of the injured motorcyclists (> 125ccm) and leg injuries were present at 67.2% of motorcyclists. Particularly common are also chest injuries with 35.5%. Especially thoracic injuries have the higher percentages with riders of motorcycles (> 125ccm) than with riders of other types of PTW. Here obviously the combination of the used protection, such as protective clothing and with special impact energy absorption zones seems to be the reason for the differences between the different types of PTW[17].In contrast with the exception of the helmet which is used by nearly all riders of PTW, protective clothing is rarely found within the other types of PTW[18].

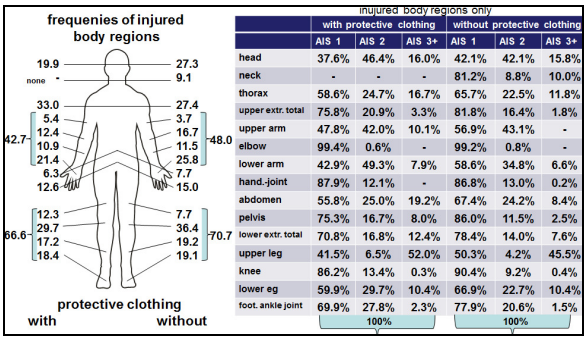

injured body regions only

	with protective clothing			without protective clothing		
	AIS 1	AIS 2	AIS 3+	AIS 1	AIS 2	AIS 3+
head	37.6%	46.4%	16.0%	42.1%	42.1%	15.8%
neck	-	-	-	81.2%	8.8%	10.0%
thorax	58.6%	24.7%	16.7%	65.7%	22.5%	11.8%
upper extr. total	75.8%	20.9%	3.3%	81.8%	16.4%	1.8%
upper arm	47.8%	42.0%	10.1%	56.9%	43.1%	-
elbow	99.4%	0.6%	-	99.2%	0.8%	-
lower arm	42.9%	49.3%	7.9%	58.6%	34.8%	6.6%
hand.-joint	87.9%	12.1%	-	86.8%	13.0%	0.2%
abdomen	55.8%	25.0%	19.2%	67.4%	24.2%	8.4%
pelvis	75.3%	16.7%	8.0%	86.0%	11.5%	2.5%
lower extr. total	70.8%	16.8%	12.4%	78.4%	14.0%	7.6%
upper leg	41.5%	6.5%	52.0%	50.3%	4.2%	45.5%
knee	86.2%	13.4%	0.3%	90.4%	9.2%	0.4%
lower eg	59.9%	29.7%	10.4%	66.9%	22.7%	10.4%
foot. ankle joint	69.9%	27.8%	2.3%	77.9%	20.6%	1.5%
	100%			100%		

Figure.8 Frequencies of injured body areas with and without protective clothing related to the injury severity grades AIS (100 % all injured body areas)

In the scope of this study an attempt was made to determine the effectiveness of the use of protective clothes (Figure.8). For this purpose, riders were considered with and without protective clothes. An analysis based on all persons included in the study (100%) was conducted analyzing at which body regions the rider was wearing protective clothes and which injury severity grade according to AIS were found there by percentage frequency. Unfortunately no clear result regarding the effectiveness could be seen here.

It is remarkable however that the identified percentages for AIS 1 injuries without the use of protective clothes are higher for almost all body regions. This could be an indication of the existing effectiveness of protective clothing for riders of PTW.

7 Development of Safety for motorcyclists and PTW based on the Injury Outcome in traffic Accidents

The safety level can be detected in looking to the injury severity in traffic accidents at different time positions. Here GIDAS can be used for such overview regarding the fact that in-depth-investigation carried out at the Medical University Hannover since 1985 by using the same methodology of accident sampling. It can be seen in Figures 9 and 10 that the proportion of severe injury grades MAIS 3+ are reduced with the factor of nearly 3 from the years 1985-93 to 2003-11 for users of PTW. There could be seen a reduction of severely injured motorcyclists of nearly 50% over the time period of more than 20 years.

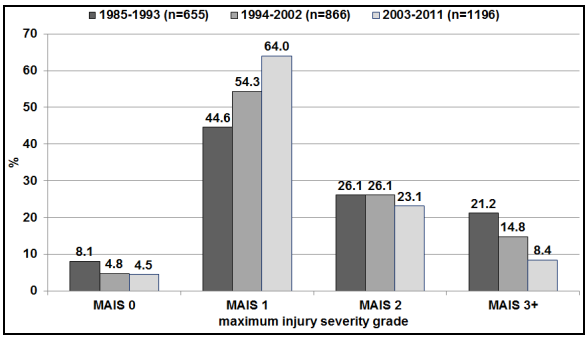

Figure.9 Frequency of injury severity grades MAIS of all motorcyclists related to different year groups (100% all persons each year period)

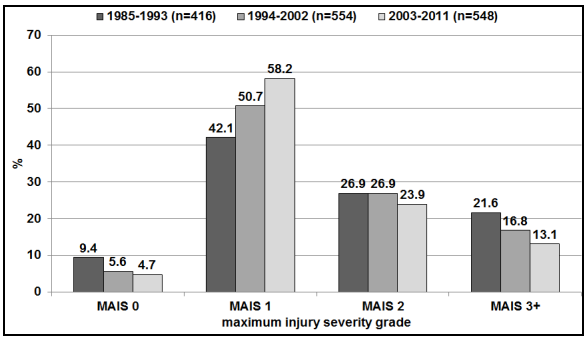

Figure.10 Frequency of injury severity grades MAIS of all motorcyclists on motorcycles with > 125ccm only related to different year groups (100% all persons each year period)

7 Causes of accidents

A look into the German national statistics shows that road users depending of the age do not cause accidents at the same rate. This is revealed when comparing the amount of accidents causers of an age group with the amount of road users at that age group which did not caused an accident (Figure.11).

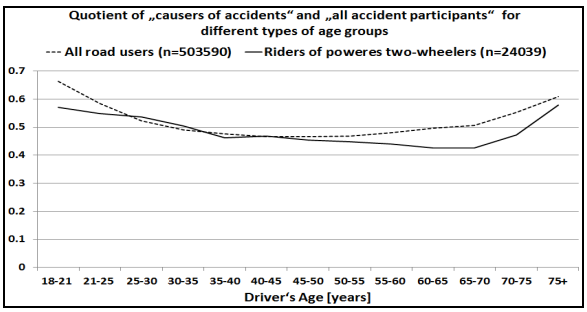

Figure.11 German national statistics 2010: Quotient of causers of accidents and all accident participants for different age groups, comparing riders of PTW with all road users.

The graph shows the quotient of accident causers to all accident participants comparing riders of PTW to all road users. Thus for example young road users (aged 18-21) in 66% of the cases the main causation leads to the driver of the PTW when involved in an accident. For the group of all road users the risk of causing an accident decreases with the age and with gaining more experience over the years to about 47% for road users aged between 40 and 60. However this risk begins to rise for road users over 60 years of age to a point where the group of the over 75 year old again have a risk of causing the accident which with over 60% has nearly reached that of young novice road users. Interestingly this graph has a visible deviation for the riders of PTW: On one hand the young riders of PTW are less likely to be the causer of an accident (57%) than young road users not using a PTW (66%). On the other hand elderly riders of PTW of ages between 60 and 70 when in an accident only have a risk of 43% to be the causer of that accident while other road users at that age when in an accident in 50% of the cases have caused the accident. So elderly motorcycle riders seem to be more cautious in traffic and cause less often accidents than other types of road users at that age. It is assumed that more mentally and physically fit seniors use PTW.

For the prevention of accidents with VRU above all the knowledge of the causes of the accidents is of special importance. Thus the need for in-depth accident causation data in accident research led to the development of a special

tool for the collection and coding of such data called ACAS (Accident Causation Analysis System), which was developed based on the GIDAS methodology and presented at international conferences in 2006 and 2009 [10,19]. In ACAS causation factors of traffic accidents which contributed to the emergence of the accident are collected for each accident participant. According to the ACAS methodology the factors are divided in to three different groups: Human factors (group 1), factors from the vehicle technology (group 2) and factors from the driving environment and/or from the infrastructure (group 3). Figure.12 displays the distribution of causation factors on the three groups, comparing causes of motorcycle riders (light and heavy motorcycles depending on the engine displacement) with the causes of car drivers.

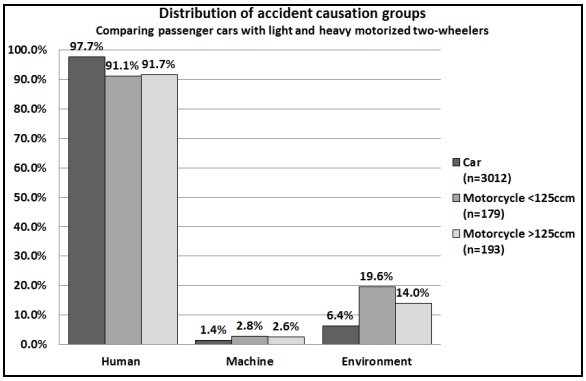

Figure.12 Distribution of accident causation factors on the three groups of the ACAS system, comparing heavy (>125ccm) and light motorcycles (<125ccm) with cars (100% each vehicle type).

For all types of road users the vast majority of causation factors are related to human failures (over 90%) thus the focus of this analysis is on this group of causes. Technical failures of the vehicle in general rarely contribute to the emergence of accident with fewer than 3% of the cases. The fact that here motorcycles have higher rates of causes in this group was not further analyzed but can be explained by the effect of a vehicle failure (e.g. blown tire) which may lead to an accident more frequently with motorcycles than with cars. A higher influence on the accident causes and a more significant difference between cars and motorcycles can be seen in the group of factors from the environment. While only 6.4% of the accidents caused by cars had a contributing factor from the environment some 14% respectively over 19% of the accidents caused by motorcycles had a contributing factor from the environment. The reason here is that riders of PTW are even more dependent on the continuous traction between tires and road. However environmental conditions like rain or a poor condition of the road surface have a strong influence on the traction. As seen in Figure.12 human factors yield over 90% of the causes of traffic accidents. The core of the ACAS system therefore is based on the analysis of these human factors, which is achieved by describing the human participation factors - and failures of these - in a chronological sequence from the perception to a concrete action/operation.

Composition of 4-digit-code on accident-causation-factors. In road traffic accidents causes for all fields of interaction can be expected: (1) Human causes, (2) causes from the range of the technology of the vehicle and (3) causes from the range of the infrastructure and/or the environment (so called 3 different groups), given the first number of the causation code, accordingly with all human causation factors in group 1. Each of the three fields of interaction is subdivided into specific categories of causation factors, as seen exemplarily for group 1 in Figure.13igure.13.

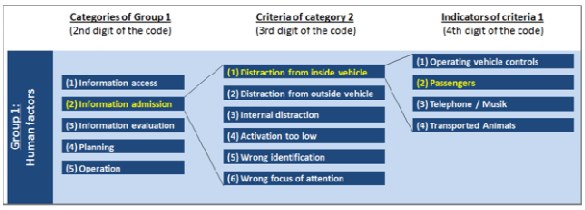

Figure.13 Composition of the ACAS-code – here exemplarily for the Group 1 (human factors)

These categories are described by the 2nd number of the causation code. Each category is further subdivided into characteristic influence criteria (3rd number of the code), which represent the most frequent factors, which led to an accident. Only in the human causation factor group 1 each influence criteria can be further specified by specific indicators (4th number of the code). In the group of the vehicle technical defects of accident influences can be stated.

Example: If someone were distracted by a conversation with a passenger, and thus did not recognize important traffic information, the code of this cause would be:

1 – 2 – 01 – 3 Code

Explanation: The accident cause is from the group of human causation factors (first number = 1); Not recognizing something is a failure in the category of the information admission (second number = 2); The influence criterion here is a distraction from inside the vehicle (third number of the code = 1); The distraction in the vehicle occurred due to a passenger (fourth number of the code = 3)

For the present study the frequency-distribution of human causation factors on the five categories was analyzed again comparing the situation of riders of light (<125ccm) and heavy (>125ccm) motorcycles with the situation of car drivers (Figure.14).

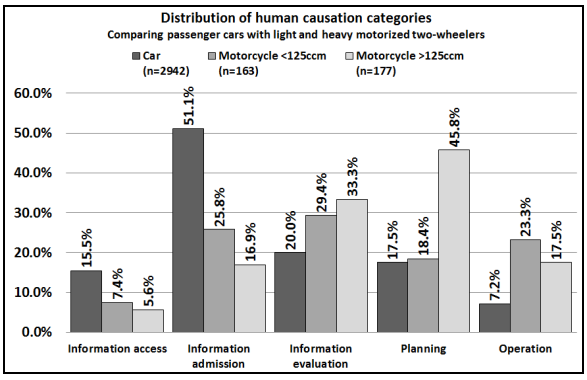

Figure.14 Frequency distribution of human causation factors on the 5 categories of human failures. Comparison of heavy (>125ccm) and light motorcycles (<125ccm) with cars (100% each vehicle type)

When looking at the **first category (Information access)** it becomes obvious that car drivers (15.5%) more frequently had a problem with the information access than the riders of powered two-wheelers (7.4% respectively 5.6%). The analysis of the codes of this category revealed that failures of car drivers are mostly related to factors like hidden Information (e.g. crash opponent) by buildings, vegetation or other vehicles on the one hand and information masking and subsequently poor visibility e.g. due to heavy rain on the other hand. Both effects are less common with riders of PTW as they generally have a higher seating position and thus a better overview and less frequently ride during bad weather.

In **category 2 (Information admission)** again car drivers more frequently have problems than the riders of PTW. In over 50% of the cases car drivers had a failure of acquiring the relevant information which contributed to the emergence of the accident (PTW only 25.8% respectively 16.9%). A further analysis revealed that drivers of cars are more often distracted and have a wrong focus of attention than the riders of PTW. This seems quite plausible as riders of PTW have less sources of distraction like passengers or in car electronics.

The **third category (Information evaluation)** consists of failures concerning misjudgments and misinterpretations. Riders of PTWs (29.4% respectively 33.3%) more often have failures in this category than car drivers (20%). Looking into these causation factors reveals that the high frequency among the PTWs is often related to a misjudgment of the own vehicle (in about 20% of the cases). Typical factors here are a misjudgment of the vehicle behavior (dynamics and stability) as well as a misjudgment of the own speed. Major differences between light and heavy Motorcycles are not evident in this group.

Failures from the **category 4 (Planning of an action)** are twice as likely with the riders of PTWs as with car drivers. Interestingly, here the level of the light motorcycles (<125ccm) is about that of the cars (both approx. 18%). The increased proportion of planning errors (over 45%) is solely related to the riders of heavy motorcycles and here only due to the subcategory of "intentional traffic violations" (in over 40% of the cases). The analysis of the distribution of the intentional violations of heavy motorcycles (> 125ccm) shows that this is mainly a matter of excessive speed (in over 2/3rds of the cases of intentional violations).

Failures from **category 5 (Operation)** are significantly more frequent with riders of PTWs (23.3% respectively 17.5%) than with car drivers (only 7.2%). Both types "mix up- or operation errors" as well "reaction errors" are common with PTW riders. The handling of PTWs in general is more difficult than that of cars. Especially when it comes to braking with PTWs this can be a cause of an accident: While it is difficult to cause an accident due to wrong braking with cars this is still well possible with motorcycles as an over braking and blocking of the front wheel mostly results in a crash. These cases can are still common in real life accidents while ABS for PTWs is not as widespread as for cars.

To answer the question whether the types of human causes have an influence on the injury situation, the causation factors of riders of PTWs were correlated with the injury severity. Therefore in a first step the injury severity distribution for different types of human causation categories was analyzed for all types of PTWs (Figure.15). Accidents caused due to an information admission failure (e.g. the rider misses to see a relevant road user due to a wrong focus of attention) have visibly caused higher shares of moderate injuries (MAIS 2) to the rider with 36.2% and of severe injuries (MAIS 3+) with 11.6% than the accidents caused due to other human failures. A possible explanation here is that with accidents caused by Information admission failures the relevant information often possibly was not seen at all or very late which leaves no or very little time for a possible avoidance maneuver like braking. On the other hand accidents based on an information admission failure imply that the relevant information was seen in time, but was just misinterpreted/falsely estimated which may have left time to begin an avoidance maneuver.

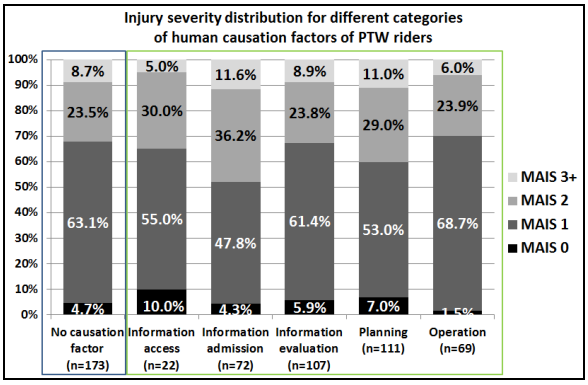

Figure.15 Injury severity distribution for different types of human causation categories from riders of PTWs (100% each category of causation factor)

When looking at the group of riders of motorcycles with an engine displacement of over 125ccm (Figure.16) the correlation between the accident causes and the injury severity shows a very similar qualitative characteristic. While accidents caused by an information admission failure again have high rates of moderate injuries (MAIS 2) with 50% and of severe injuries (MAIS 3+) with over 10%, no significant differences between the other causation categories can be identified due to the low number of cases. As expected the shares of severe injuries are visibly higher with riders of motorcycles than with riders of all types of PTWs.

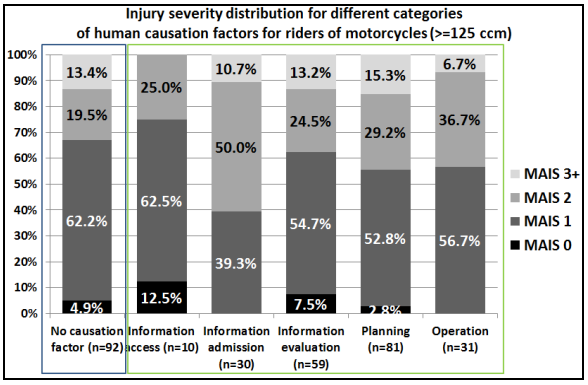

Figure.16 Injury severity distribution for different types of human causation categories for riders of motorcycles with an engine displacement of over 125ccm (100% each category of causation factor)

8 Significance of several accident parameters for injury severity

An ordinal logistic regression was performed to examine the influence of both the causes of accidents as well as other parameters. In addition to the causes of accidents the type of powered two-wheeler, crash weight, age, relative velocity and the annual mileage were included.

Here, a separate category was created for "unknown" annual mileage to not exclude those cases in the analysis. The significant p-values are highlighted in yellow.

It turns out that in addition to age, relative speed, crash weight and type of powered two-wheeler the human causation categories “information access” and “information admission” have a significant impact on the injury severity, while the relative velocity has a highly significant impact.

Table 1: Statistical analysis of effects of several accident parameters for the injury severity grade MAIS

Effect	DF	Wald	Pr>ChiSq（Chi-Square）
Relative velocity	1	50.9341	<.0001
Age	1	8.8486	0.0029
Crash weight	1	3.9641	0.0465
Annual mileage	8	7.4723	0.4866
Information access	1	4.5625	0.0327
Information admission	1	6.2102	0.0127
Information evaluation	1	0.0822	0.7743
Planning	1	0.0369	0.8477
Operation	1	0.3300	0.5657
Type of powered two-wheeler	1	4.9166	0.0266

9 Discussion and conclusion

The study of accidents of powered two-wheelers in comparison to the group of motorcycles showed that the injury situation of both groups improved steadily over the past few years. Still, a share of 8.4% of severely injured and most severely injured (MAIS 3+) riders in the group all PTWs and correspondingly 13.1% in the group of motorcyclists is registered. With a high proportion of slightly injured (MAIS 1) of 60 to 65%, a high level of safety is achieved on the road. Wearing the motorcycle helmet here proves especially beneficial to the resulting injury frequency and injury severity of a person, as with motorcyclists only 19.9% suffered head injuries. Motorcyclists are well protected by the helmet; the study reveals an effectiveness of the helmet usage in relation to a reduction of head injuries AIS 1 to minus 34% and AIS 2 to minus 22% and severe head injuries AIS 3+ to minus 21%.

The study could also determine the protective effect of protective clothing, however not with the expected significance. Here influences of different materials, the different use of protective clothing for different body regions and the sometimes very low use of protective clothing result in an undetectable effect in the statistical sample.

Since the distributions of the relative velocities of the considered groups of motorcycles and other PTW not very much different from each other, the collision constellations define the outcome of injury in relation to the collision types only a little. The most serious consequences occur when the rider's body collides relative to the chassis of the collision partner. Cars thus only represent a particular danger at accidents at crossings with the possibility of the rider to hit the passenger compartment, with trucks almost all collisions against front, side or rear are equally dangerous. Here the study revealed a high proportion of oblique collisions of two wheelers against the vehicle side with both cars and trucks (collision type 4 with about 21%). Particularly among motorcyclists this type as well as the perpendicular frontal crash against the side of the vehicle (type 3) showed a high proportion of severely injured MAIS 3+. Relatively common are single-vehicle crashes of motorcyclists with about 45%. This also includes those collisions where another two-wheeler or a pedestrian were involved. Severe injuries AIS 3+ are particularly often in association with a high risk of bone

injuries of the cervical spine and the lower extremities. Leg injuries in future require special attention as they are often accompanied with long treatment durations and long-term consequences [20]. One useful solution is seen here in the usage of protective clothing with protectors and the use of padded machines whose injury protection effectiveness in combination with the development of special leg protectors have been shown to be useful in previous publications [21].

To be able to further improve the injury situation of motorized two-wheeler in the future, accident analyzes in the scope of on-scene surveys are still important to gain detailed knowledge about injury patterns, the kinematics and injury mechanisms. In addition, however, it is especially important to avoid accidents at the beginning of the development. This can be achieved through adequate measures concerning the road layout, measures at the PTW and also measures concerning the attitude and behavior of drivers of PTW.

Attention must be turned towards the causes of the accidents and their relationships to human, machine and the environment to be able to postulate measures for the prevention of accidents in addition to the injury prevention.

The application of causation analysis tools ACAS (Accident Causation Analysis System) showed that riders of powered two-wheelers do have a characteristic distribution of cause factors when compared to drivers of cars. Even though there is a higher influence of environmental factors on the causes of accident from riders of PTW than on car drivers, the focus still lies on the human factors for both groups (over 91% for riders of PTW, 97.7% for car drivers). The human factors in ACAS are divided into 5 categories of possible failures. Here the analysis revealed that riders of PTWs had frequent failures in the Information evaluation which are often related to a misjudgment of the behavior or speed of the own vehicle (in about 20% of the cases). Furthermore riders of powered two wheelers have a high incidence of accident causes from the subcategory of intentional breach of rules. While riders of light motorcycles (<125ccm) are at the same level as car drivers with about 18% of causation factors, the riders have motorcycles (≥ 125ccm) have an incidence of over 40% from this subcategory which is mostly related to excessive driving speed. Another source of accident causes which is specifically high with PTW when compared to cars are operation failures (23.3% for light motorcycles, 17.5% for motorcycles but only 7.2% for cars) as the handling of a PTW in general is more difficult than that of cars. As a result wrong braking or over braking with PTW does lead to accidents as ABS for PTW is not as widespread as for cars.

A correlation between the causation factors of riders of PTW with the injury severity revealed that the category of human failure had no significant influence on the injury severity distribution with one exception: Accidents caused by a failure of information admission (e.g. the rider misses to see a relevant road user due to a wrong focus of attention) of the rider of a PTW resulted in visibly higher shares of MAIS 2 had MAIS3+ injuries than failures from the other categories.

Acknowledgement

For the present study, accident data from GIDAS (German In-Depth Accident Study) was used. GIDAS, the largest in-depth accident study in Germany, is funded by the Federal Highway Research Institute (BASt) and the German Research Association for Automotive Technology (FAT), a department of the VDA (German Association of the Automotive Industry). Use of the data is restricted to the participants of the project. Further information can be found at http://www.gidas.org.or ordered at otte.dietmar@mh-hannover.de

References

[1] ACEM, *The European PTW market in 2007*, 2007

[2] ETSC, Countdown to 2010, only two more years to act, Road Safety Report, ETSC, 2008

[3] BASt, *Gurte, Kindersitze, Helme und Schutzkleidung 2008*, Wissenschaftliche Informationen der Bundesanstalt für Straßenwesen, Info 05/09, Bergisch-Gladbach, 2009

[4] DeStatis, Statistisches Bundesamt – *Verkehrsunfälle*, www.destatis.de, 2010

[5] IFZ, *Sicherheit - Umwelt - Zukunft V*, Tagungsband der 5. Internationalen Motorradkonferenz, Institut für Zweiradsicherheit, 2004

[6] Sporner, *A.; Langwieder, K. Polauke, J.:Risk of Leg injuries of motorcyclists-present situation and countermeasures*, 12th ESV Conf. Göteborg Sweden, 1989

[7] Otte, D., Krettek, C., Brunner, H., Zwipp, H.: *Scientific Approach and Methodology of a New In-Depth-Investigation Study in Germany so called GIDAS*, ESV Conference, Japan, 2003

[8] Brühning E., Otte D., Pastor C.*: 30 Jahre wissenschaftliche Erhebungen am Unfallort für mehr Verkehrssicherheit*, Zeitschrift für Verkehrssicherheit 51, 175-181, 2005

[9] Otte D., Pund, B., Jänsch, M.: *A New Approach of Accident Causation Analysis by Seven Steps with ACASS*, Paper Number 09-0245 ESV Conference Stuttgart 2009

[10] Pund, B., Otte, D., Jänsch, M. (2007): *Systematic of Analysis of Human Accident Causation – Seven Steps Methodology.* In: Reports on the ESAR-Conference on 1st/2nd September 2006 at Hannover Medical School, Berichte der BundesanstaltfürStraßenwesen, Heft F 61

[11] AAAM, Association for the Advancement of Automotive Medicine: *The Abbreviated Injury Scale - Revision 98*, Morton Grove, Illinois (USA) (1998)

[12] Otte, D.*: 3-D Laser systems for scaled accident sketches and documentation of the traces after traffic accidents as basis of biomechanical analysis*, Ircobi Conference, 435-438,2005

[13] Pfeiffer, M., Schmidt, J.: *Statistical and Methodological Foundations of the GIDAS Accident Survey System*, 2nd ESAR Conference, Hannover, 2006

[14] Otte, D.: *Injury Scaling: from lesion assessment to passive safety improvement*, Vortrag Round Table, Institute of Legal Medicine, University of Verona, Juni 1995

[15] GDV, Gesamtverband der deutschen Versicherungswirtschaft (GDV), Institut für Straßenverkehr (ISK), *Der Unfalltypenkatalog*, Köln, 1998

[16] Otte, D., Willeke, H., Chinn, B., Doyle, D., Schuller, E.: *Impact Mechanisms of Helmet Protected Heads in Motorcycle Accidents - Accidental Study of COST 327*, Institut für Zweiradsicherheit e. V., Tagungsband der 2. Internationalen Motorradkonferenz, 1998, 83-109

[17] Otte, D.:*Welchen Beitrag kann Schutzkleidung zur passive Sicherheit des Motorradfahrers leisten*, VDI-Berichte 657, 281-303, 1987

[18] Otte, D.; Felten, G.: *Requirements on chin protection in full face helmets for motorcyclists*, Forschungsbericht IFZ Nr. 7, 229-264, 1991

[19] Otte, D.; Pund, B.; Jänsch, M.*; Unfallursachen-Analyse ACASS für Erhebungen am Unfallort - Seven-Steps-Methode*, Zeitschrift für Verkehrssicherheit, 55. Jahrgang, G 12441 F, ISSN 0044-4654, Heft 3, *2009*

[20] Kalbe, P.; Suren, E. G.; Otte, D.: *Trauma Assessment of Injuries and their Consequences in Accidents with Two-Wheelers*, Proc. 6th IRCOBI-Conference, Salon de Provence (France), 1981

Proceedings of the 11th International Forum of Automotive Traffic Safety, 2014, pp 18- 23
No. ATS.2014.102

A Study on Vehicle-Electric Bicycle Impact Accidents Reconstruction Based on the Uncertainty Theory

LI Li[1], TU Xiang[1,2], LI Pingfei[3], LIU Youbao[1]

1College of Mechanical and Vehicle Engineering, Hunan University, Changsha,China,410082
2College of Automotive, Guangdong Mechanical and Electrical College ,Guangzhou,China,510515
3 College of Transportation and Automotive Engineering,Xihua University, Chengdu,China,610039
Email: jqy_ll@hnu.edu.cn

Abstract: Car-electric bicycle impact accident is very complex, the study of accident reconstruction involves many uncertain factors. This paper applied the uncertainty theory to the speed calculation of car-electric bicycle impact accident reconstruction, introduced the computer simulation analysis software PC-Crash and the simulation of accident reconstruction, and then got comprehensive analysis method to improve the accuracy of the car-electric bicycle impact accident reconstruction. Moreover, a real accident case was used to verify the feasibility of the methods.

Keywords: Electric-bicycle, Accident Reconstruction, Uncertainty Theory, Computer Simulation

基于不确定度理论的汽车-电动自行车碰撞事故再现研究

李莉[1]，涂祥[1,2]，李平飞[3]，刘优宝[1]

[1]湖南大学机械与运载工程学院，410082，长沙，中国
[2]广东机电职业技术学院汽车学院，510515，广州，中国
[3]西华大学交通与汽车工程学院，610039，成都，中国
Email: jqy_ll@hnu.edu.cn

摘 要：汽车与电动自行车碰撞事故非常复杂，对其进行事故再现研究牵涉到较多的不确定因素。本文将不确定度理论应用于汽车-电动自行车碰撞事故再现车速计算；引入计算机仿真分析软件 PC-Crash 进行事故再现研究，从而得到可以提高汽车-电动自行车碰撞事故再现准确性的综合分析方法。并以一起真实事故为例，验证了本文方法的适用性。

关键词：电动自行车；事故再现；不确定度理论；计算机仿真

1 引言

目前，我国电动自行车保有量快速增长，道路上汽车与电动自行车碰撞事故急剧增加。事故再现可以使整个事故的发生过程在时间和空间上得以重现，从而科学地解释事故发生的原因，明确事故各方当事人应负的责任，方便交通事故责任认定和保险理赔[1]。在交通事故再现中，由于受输入参数的限制，事故再现结果与真实值可能不相符，从而影响事故再现的准确性。为此，本文将不确定度理论和计算机仿真分析软件 PC-Crash 引入汽车-电动自行车碰撞事故再现研究，探讨提高事故再现准确性的方法。

2 不确定度理论及其评定方法

德国物理学家海森堡在 1927 年最早提出“不确定度”概念[2]， 测量不确定度是测量结果不确定的程度，用以表征被测量的真值在某个量值范围的一个估计。不确定度评定的一般流程如图 1 所示[3]。

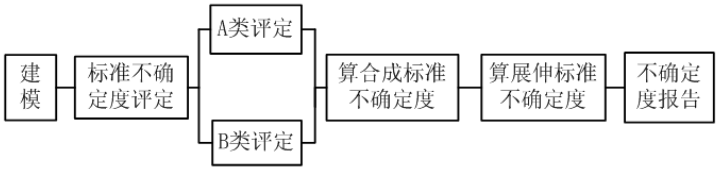

Figure.1 The flowchart of uncertainty evaluate

图 1 不确定度评定流程图

2.1 标准不确定度评定

被测量 Y 常取决于 n 个其他无关输入量 $X_i(i=1,2,\cdots,n)$，即：$Y=f(X_1,\ X_2,\ X_3,\cdots,\ X_n)$ (1)

由输入量 X_i 的最佳值 x_i 可得 Y 的最佳值 y，即测量结果：$y=f(x_1,\ x_2,\ x_3,\cdots,\ x_n)$ (2)

故测量结果 y 的标准不确定度 u_y 由每个输入量 x_i 的不确定度 $u(x_i)$ 决定，标准不确定度评定分为 A 类评定和 B 类评定[3]。A 类评定是在数理统计基础上，获取一系列的观测量的标准差 σ，通常使用贝塞尔法。对 X_i 作 n_i 次等精度的相互独立测量，得到测量序列 x_{i1}，x_{i2}，x_{i3},…，x_{in}，则其最佳值为平均值为：

$$x_i=\frac{1}{n}\sum_k x_{ik}=\frac{1}{n}(x_{i1}+x_{i2}+x_{i3}+\cdots+x_{in}) \tag{3}$$

X_i 的标准不确定度为：$$u(x_i)=\sigma(x_i)=\sqrt{\frac{1}{n(n-1)}\sum_k(x_{ik}-x_i)^2} \tag{4}$$

B 类评定基于信任度的先验分布，以概率论原理为基础，通过分析测量列分布特征获取标准差。标准不确定度 $u(x_i)$ 由 x_i 的变化范围 a_i 除以包含因子 k_i，即：$$u(x_i)=\frac{a_i}{k_i} \tag{5}$$

对于正态分布，包含因子 k 由正态分布置信概率表查询相应置信水准 p 获得，一般取包含因子 k=2~3；反正弦分布 $k=\sqrt{2}$，均匀分布 $k=\sqrt{3}$，梯形分布与三角分布 $k=\sqrt{6}$。

其中，x_i 的相对标准不确定度为：$$u'(x_i)=\frac{u(x_i)}{|x_i|} \tag{6}$$

2.2 合成标准不确定度评定

若被测量值 Y 的估计值 y 由 n 个测量值 x_1，x_2,…，x_n 的函数决定，x_i 变化单位量时引起 y 的变化值，称为不确定传播系数，记为：$$c_i=\frac{\partial f}{\partial x_i} \tag{7}$$

则由 x_i 引起被测量 y 的标准不确定度分量为：$$u_i(y)=|c_i|u(x_i)=\left|\frac{\partial f}{\partial x_i}\right|u(x_i) \tag{8}$$

由误差合成理论，每个输入量都将带入一个不确定因素，则该函数在这些因素共同影响下的合成不确定度为：$$u_c(y)=\sqrt{\sum_{i=1}^{n}\left(\frac{\partial y}{\partial x_i}\right)^2(u_{xi})^2+2\sum_{1\le i<j}^{n}\frac{\partial y}{\partial x_i}\frac{\partial y}{\partial x_j}\rho_{ij}u_{xi}u_{xj}}=\sqrt{\sum_{i=1}^{n}u_i^2+2\sum_{1\le i<j}^{n}\rho_{ij}u_iu_j} \tag{9}$$

ρ_{ij} 为任意两个测量值 x_i 与 x_j 的相关系数，若 x_i、x_j 的不确定度相互独立，则 $\rho_{ij}=0$。

则相对合成标准不确定度分量为：$$u'(y_i)=|c_i|u'(x_i)\frac{x_i}{y} \tag{10}$$

其相对合成标准不确定度为：

$$u'(y)=\sqrt{\sum_{i=1}^{n}u'(y_i)^2}=\sqrt{\sum_{i=1}^{n}\left(c_i u'(x_i)\frac{x_i}{y}\right)^2} \tag{11}$$

2.3 展伸不确定度评定

在实际交通事故、商业和工业等领域应用中，常需提供一个不确定度测度，以给出测量结果区间，合理赋予被测量值分布的大部分可望含于其中，这一不确定度测度称为展伸不确定度，又称扩展不确定度。

展伸不确定度 U 由合成标准不确定度 $u_c(y)$ 乘以包含因子 k，即：$U=ku_c(y)$ (12)

则函数 Y 的值可以表示为：$Y=y\pm U$ (13)

若是通过相对不确定度计算，则相对展伸不确定度为：$U'=ku'(y)$ (14)

则可得函数 Y 的最终取值范围，即不确定度报告：$Y=y\pm yU'$ (15)

3 不确定度理论在事故再现中的应用

在交通事故的鉴定中，汽车车速计算的基本思路是：事故数据采集→建立事故碰撞过程模型→汽车车速计算→车速结果验证。在这个过程中，不确定度理论可以应用到建模前的参数输入过程以及建模后结果部分的精度分析[4]，以此提高参数和结果的可靠性与准确性。

3.1 真实事故案例信息

本事故发生于某月某日晚上 20 时许，事故地点位于长沙县泉塘街道办事处漓湘东路三景国际路段，事发当天为下雨天，事故路段为沥青路面，限速 $60\,km/h$。一辆轿车由西往东行驶，一辆电动自行车由东往南行驶，由于汽车大致行驶在道路中央，加上天色昏暗，汽车驾驶员判断失误，所以在碰撞前轿车并未采取制动措施；而电动自行车当时准备转向三景国际方向，所以在道路上是逆向行驶，在汽车的前照灯灯光照射下，电动自行车骑车人误判交通状况，也没能及时靠边避让行驶，从而造成汽车和电动自行车正面碰撞，造成电动自行车驾驶员严重受伤，送往医院抢救。如图 2 所示原始事故现场草图，图 3 是汽车和电动自行车损坏图。

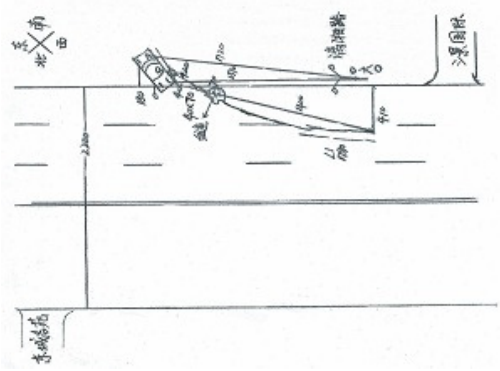

Figure.2 The original scene of the accident

图 2 原始事故现场图

Figure.3 The damage of automobile and electric bicycle

图 3 汽车和电动自行车损坏图

该事故造成汽车前保险杠右端和右前翼子板距地高 300~800mm 处损坏变形，右前翼子板变形，右大灯内板和右转向灯损坏，前挡风玻璃右下角损坏，中心离地高 1000mm；电动自行车前叉距地面高 700mm 处弯曲变形，右脚踏损坏，坐凳、蓄电池脱落，方向把扭曲变形。

3.2 车速理论计算及不确定度评定

(1)汽车速度理论计算

根据汽车碰撞后至停止位置留下的制动印迹可以计算出汽车在碰撞后的瞬间车速[5]，可以将汽车碰撞后的

制动印迹长度与汽车轮胎和地面的摩擦系数两个参数作为不确定因子加以分析研究。由于事发夜晚，事故现场环境不利于事故数据的采集，所以事故处理人员采集到的地面刹车印迹长度存在较大的不确定性，根据实测汽车在碰撞后制动滑移距离，可以取 $L=18.2\sim19.2\text{m}$，即 $L=18.70\pm0.50\text{m}$；事发地段为沥青路面，而且路面条件较好，结合路面与轮胎的新旧程度，可以取 $\mu=0.6\sim0.7$，即 $\mu=0.65\pm0.05$；重力加速度取值 $g=9.81\,m/s^2$。

根据滑行拖印公式可得汽车碰撞后瞬间的速度为：

$$v_1=\sqrt{2\mu gL}=\sqrt{2\times0.65\times9.81\times18.7}\approx15.44\,m/s=55.59\,km/h$$

(2)车速不确定度评定

利用汽车刹车印迹计算时影响车速的不确定因子，制动印迹长度 L 与汽车轮胎和地面的摩擦系数 μ，对应的包含因子 $k_1=2$，则其标准不确定度为：

$$u(\mu)=\frac{a_1}{k_1}=\frac{0.05}{2}=0.025$$

$$u(L)=\frac{a_2}{k_2}=\frac{0.5}{2}=0.25$$

其相对标准不确定度为：

$$u'(\mu)=\frac{u(\mu)}{\mu}=\frac{0.025}{0.65}=0.0385$$

$$u'(L)=\frac{u(L)}{L}=\frac{0.25}{18.7}=0.0134$$

两个参数的不确定传播系数为：

$$c_u=\frac{\partial f(L,\ \mu)}{\partial\mu}=\frac{\partial v}{\partial\mu}=\sqrt{\frac{gL}{2\mu}}=\sqrt{\frac{9.81\times18.7}{2\times0.65}}=11.8791$$

$$c_L=\frac{\partial f(L,\ \mu)}{\partial L}=\frac{\partial v}{\partial L}=\sqrt{\frac{gu}{2L}}=\sqrt{\frac{9.81\times0.65}{2\times18.7}}=0.4129$$

则相对标准不确定度分量为：

$$u'(v_u)=|c_u|u'(\mu)\frac{\mu}{v}=|11.8791|\times0.0385\times\frac{0.65}{15.44}=0.0193$$

$$u'(v_L)=|c_L|u'(L)\frac{L}{v}=|0.4129|\times0.0134\times\frac{18.45}{15.44}=0.0066$$

不确定参数的不确定度评定结果如表 1 所示[6]。

Table 1. Evaluation results of uncertainty

表 1 不确定度评定结果

参数	变化范围 a_i	包含因子 k	标准不确定度 $u(x_i)$	相对标准不确定度 $u'(x_i)$	不确定传播系数 c_i	相对标准不确定度分量 $u'(v_i)$
μ	0.05	2	0.025	0.0385	11.8791	0.0193
L	0.5	2	0.25	0.0134	0.4129	0.0066

则汽车碰撞后瞬间车速的相对扩展不确定度为：

$$U'=ku'(v)=2\times2.04\%=4.08\%$$

由相对扩展不确定度可得出不确定度报告，即汽车制动前车速取值范围：

$$V=v\pm vU'=(15.44\pm15.44\times4.08\%)\,m/s=(55.59\pm2.27)\,km/h=53.32\sim57.86\,km/h$$

综合以上分析可知，当取置信概率 p=95.4%时, 汽车制动前车速取值范围为 53.32~57.86 km/h。

3.3 事故再现计算机仿真分析

利用计算机仿真分析软件 PC-Crash 对该事故进行模拟仿真，以验证不确定度理论计算车速的有效性。

(l)建立模型：根据事故信息建立道路模型和车辆模型。该事故中轿车为哈飞路宝，厂牌型号为松花江 HFJ7；电动自行车为鹰王牌电动自行车。

(2)仿真模拟：计算机仿真模型建立完成后，设定车辆位置和运动学参数，然后反复调试汽车和电动自行车整碰撞点、碰撞部位、碰撞角度、摩擦锥面、制动强度、转向角度、碰撞速度等参数，直至模拟车辆运动轨迹（痕迹）和停止位置姿态与事故现场勘验情况基本吻合。仿真模拟过程中汽车、电动自行车与骑车人相对位置如图 4 所示。

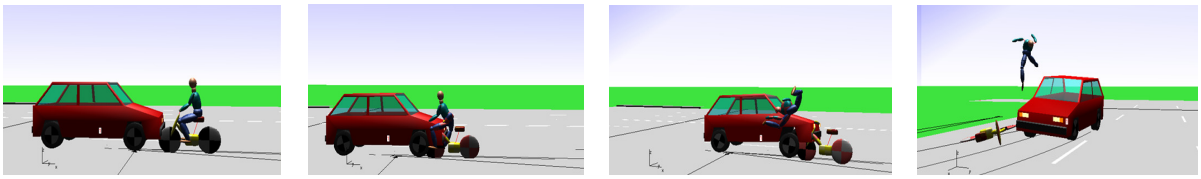

（a）t=0 s　　（b）t=0.049 s　　(c) t=0.147 s　　(d) t=0.6s

Figure.4 The relative position of the Automobile, electric bicycle and rider model

图 4 仿真模拟汽车、电动自行车与骑车人相对位置

(3)仿真模拟结果：运用 PC-Crash 软件仿真事故再现，得到汽车、电动自行车与骑车人的运动情况和最终停止位置，经过反复调试，当哈飞路宝轿车车速为 58 km/h，电动自行车速度为 15 km/h 时，最终停止位置如图 5 所示；计算得到骑车人身体有关部位的力和加速度的数据，如图 6 所示。

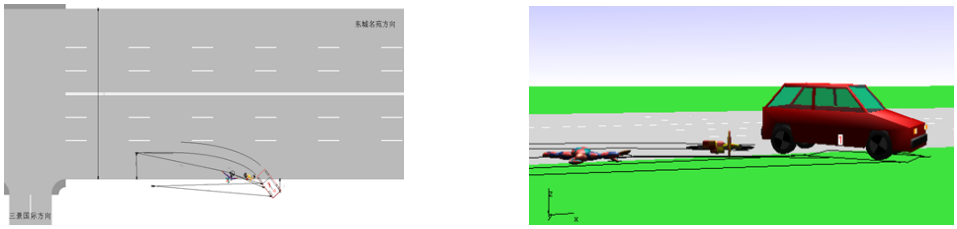

(a) Stop position 2 d figure　　(b) Stop position 3d figure

(a) 停止位置 2D 图　　**(b) 停止位置 3D 图**

Figure.5 The final position of Automobile, electric bicycle and rider

图 5 汽车、电动自行车与骑车人最终停止位置

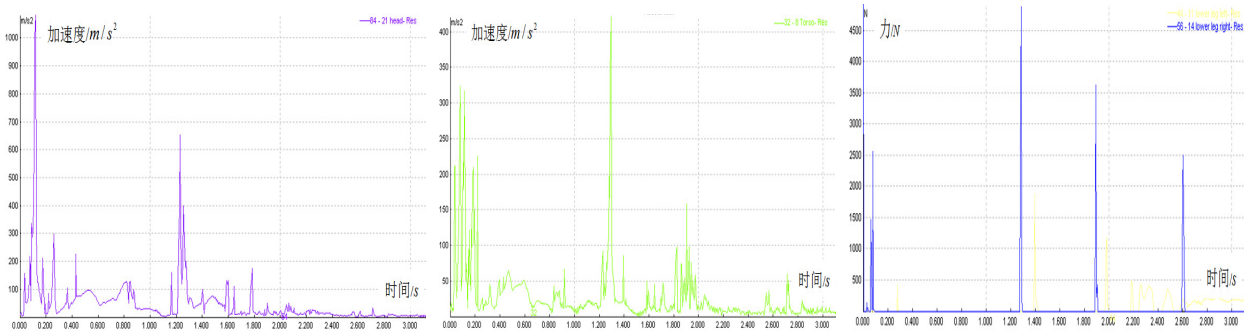

Curve:cyclists head synthetic acceleration　　Curve:cyclists chest synthetic acceleration　　Curve:cyclists crus shear force

骑车人头部合成加速度曲线　　**骑车人胸部合成加速度曲线**　　**骑车人小腿剪切合力曲线**

Figure.6 Curve: cyclists parts of the body force and acceleration

图 6 骑车人身体部位受力和加速度曲线图

(4)计算机仿真骑车人损伤分析：由图 6 可以看出，电动自行车骑车人头部合成加速度峰值出现在 0.120s 时，其值为 1083.38 m/s^2；胸部合成加速度最大值出现在 1.294s，其值为 406.41 m/s^2；骑车人右侧小腿受到剪切合

力最大值出现在 1.284s，其值为 4551.74N；左侧小腿剪切合力最大值出现在 1.395s，其值为 1764.57N。即骑车人头部冲击汽车右侧挡风玻璃，导致汽车前挡风玻璃右下角损坏时，对骑车人头部的冲击最大，而骑车人身体与地面发生碰撞时，骑车人胸部和小腿受到的冲击最大。根据电动自行车骑车人头部受到的最大冲击时的合成加速度曲线，计算得到骑车人头部 HIC 值为 1106.94，高于标准中规定的 1000 的极限值，所以电动自行车骑车人颅脑受到损伤；而胸部持续 3ms 最大加速度值为 41.4g，低于 60g 的上限，对人体胸腔器官伤害不是很大；左侧小腿受到剪切力小于小腿骨折最大剪切力 4.7±1.2kN，而右侧小腿则位于上限值附近，可能骨折或严重受伤。计算机仿真中骑车人损伤情况和实际事故中骑车人损伤情况相符，这也证明应用计算机仿真分析方法进行事故再现研究的可行性和有效性。

3.4 事故再现结果

哈飞路宝轿车在碰撞电动自行车前的瞬时车速，计算机仿真分析结果与传统理论计算得到的车速相对误差区间为 0.24%~8.07%。由此可以证明利用不确定度理论可以有效提高车速计算的准确度。综合理论计算和计算机仿真分析，最终可以认定哈飞路宝汽车在碰撞前的车速为 $56\,km/h$，而发生事故路段限速 $60\,km/h$，所以该起事故中哈飞路宝轿车并未超速。

4 结论

本文综合运用基于不确定度理论的传统理论车速计算方法与计算机仿真分析方法，针对真实汽车-电动自行车碰撞事故案例进行事故再现研究，并详细分析了电动自行车骑车人损伤情况，从而验证以上建立的车速计算分析流程的可行性，提高了汽车-电动自行车碰撞事故再现的准确性。

致谢

本论文研究工作得到了“汽车测控与安全”四川省重点实验室开放基金“SZJJ2013-026”项目资助，特此表示诚挚的感谢！

参考文献

[1] Xu Hongguo, He Biao. Reconstruction and analysis of traffic accident [M]. Beijing:Police Education Press, 1996.
许洪国,何彪.道路交通事故分析与再现[M].北京:警官教育出版社,1996.

[2] Liu Zhimin,The uncertainty and its practice[M]. Beijing:Standards Press of China ,2000.
刘智敏.不确定度及其实践[M].北京:中国标准出版社,2000.

[3] National Quality Technology Supervision Bureau Metrology Department,Guide of evaluation and Expression of Uncertainty in Measurement[M].Beijing:China Metrology Publishing House , 2000.
国家质量技术监督局计量司.测量不确定度评定与表示指南[M].北京:中国计量出版社,2000.

[4] Yuan Quan,Zhang Gaoqiang, Guo Rui, Research Evolution on the Theory Methods of Vehicle-speed Analysis of Traffic Accidents[J]. Journal of Transportation Engineering and Information, 2009,7(2):21~27.

[5] Yang Zhaoyang, Traffic accidents mechanics appraisal tutorial[M]. Nanning: Guangxi Science and Technology Press,2002.
阳兆祥.交通事故力学鉴定教程[M].南宁:广西科学技术出版社,2002.

[6] Xue Dawei,Bai Zhu,Sun Yunxia,Evaluation method of traffic accident velocity based on uncertainty[J].Journal of Heilongjiang Institute of Technology, 2009,23(4):36~40.

[7] Wang Yan, Liu Bohan, Xu Jun, Li Yibing,Simulation of Cyclist Injury in Vehicle to Electric-Bicycle Accident Based on PC-Crash [A]. Hunan University, China.INFATS Proceedings of the 9th International Forum of Automotive Traffic Safety[C].Hunan University, China:,2011:7.

Proceedings of the 11th International Forum of Automotive Traffic Safety, 2014, pp 24- 31
No. ATS.2014.103

Study on Pedestrian's Head Injury in Accidents Using a Biomechanical Simulation Model

Lv Xiaojiang[1,3], Ma Zhengwei[2], Sun lizhi1[3], Chen Jiqing[2], Zhou Dayong[1,3], Liu Weiguo[1,3]

1Geely Automobile Institute, Hangzhou 311228, Zhejiang, China;
2 School of Mechanical & Automotive Engineering, South China University of Technology, Guangzhou 510641, Guangdong, China;
3 Zhejiang Key Laboratory of Automobile Safety Technology, Hangzhou 311228, Zhejiang, China

Abstract: This study was aimed to the head injury of Chinese pedestrians in accidents. According to the results of multi-body dynamics (MBD) analysis on vehicle and pedestrian, the process of a vehicle-pedestrian crash accident was reconstructed and four kinds of analysis cases were obtained. Based on these data, the pedestrian's injury of head skull, brain was analyzed utilizing a head bio-mechanical model of the 50th percentile Chinese male. Results show that during the collision of the same target, because the skull collision position is different, the skull damage also is different. The collision position located frontal and temporal bone have fracture risk. For head injury, as the collision position is different, there are different risk for contusion and laceration of brain and concussion of brain.

1 Introduction

Head injury is one of the most common injury types that lead to serious injury or death in traffic accidents. According to the statistics released by World Health Organization (WHO), the death of vulnerable road users accounts for 50% of all deaths in traffic accidents and that of pedestrians accounts for 22% in it [1]. Considering the mixed traffic conditions in China, the injury factor is larger to pedestrians. The statistics of WHO showed 689,996 Chinese pedestrians died in 2010, which accounted for 25% of all traffic deaths [2]. So it's of great significance to study pedestrians' injury in China.

2 Traffic accident reconstructions

For the multi-body dynamics analysis, a 50 percentile male dummy of pedestrian in Madymo software was utilized. Table 1 lists the basic parameters of the model [3]. According to available data in the literature, the pedestrian stride is set to 63.7 cm [4].

Table1 Pedestrian dummy basic parameters

parameter	value
Stand height	1.74m
Sit height	0.92m
Shoulder breadth	0.47m
Knee height	0.54m
weight	75.7kg

The vehicle model's parameters, such as the geometry and stiffness, were defined using those in a Geely SUV model. The contact friction coefficient between the vehicle and pedestrian was set as 0.2, while those of the

vehicle-ground and the pedestrian-ground were defined as 0.67 and 0.8 respectively. Base on the traffic accident data, the vehicle's speed was set to 40 km/h. Figure 1 shows the MBD analysis of the vehicle and pedestrian.

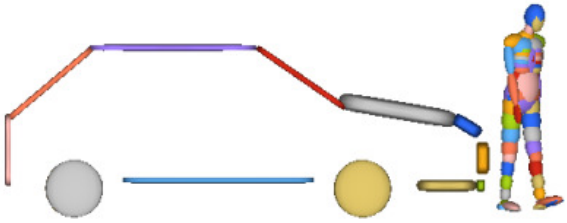

Figure 1 multi-body dynamics analysis model

The calculation of pedestrian's movement was divided into 8 kinds of cases according to the crossing angle between the pedestrian and vehicle. Table 2 shows the simulation results in these cases. From table 2, it could be observed that different crossing angles between the vehicle and pedestrian lead to different collision positions of the pedestrian's head. In the crossing angle of + 90° and 135°, the frontal bone contacted with the vehicle front end during the impact. In the crossing angle of 120 ° and -90 °, the parietal bone contact with the vehicle front end during the impact. In the crossing angle of 60 ° and 105 °, the occipital bone contact with the vehicle front end during the impact. In the crossing angle of 45 ° and 75 °, the temporal bone contact with the vehicle front end during the impact.

Table 2 Pedestrian movement in different crossing Angle

Crossing Angle	Pedestrian movement		
	0 s	0.2 s	0.4 s
45°	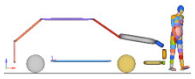	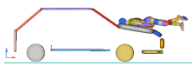	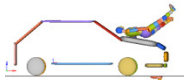
60°	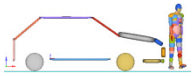	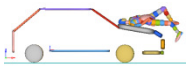	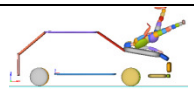
75°	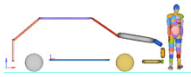	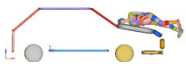	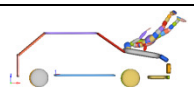
+90°	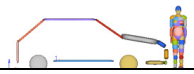	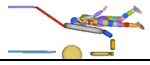	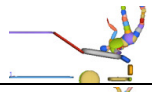
135°	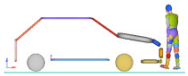	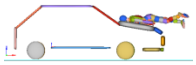	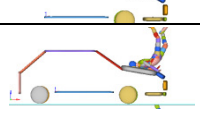
120°	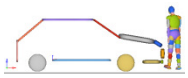	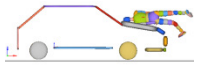	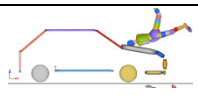
105°	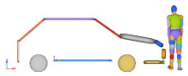	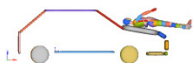	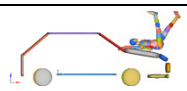
-90°	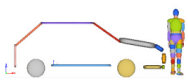	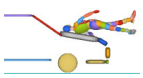	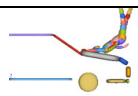

3 Model development

3.1 Head model development

In this study, the head biomechanical model was developed by the South China University of Technology. Model geometry was derived from the computed tomography (CT) image data of a volunteer representing the 50th percentile Chinese male. It was created using reverse engineering in CAD and pre-processing technology in finite element method (FEM). The head model developed is shown in Figure 2[5]. It weights 4.08 Kg and contains details of the head, such as the scalp, skull, facial bone, falx, brain curtain, cerebellum sickle, pia mater, cerebrospinal fluid, brain, cerebellum and brain stem.

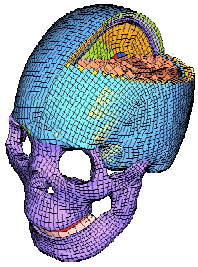

Figure 2. Biomechanical finite element model of the head

The geometric dimensions in the head model correlated with those of 50th percentile Chinese male [6]. The model was validated against the Post Mortem Human Subjects (PMHS) test by Nahum (1976) [7]. Figure 3 shows the simulation set-up based on the test conditions. In the simulation, an impactor of 5.59 kg impacted the forehead at s speed of 6.3m/s.

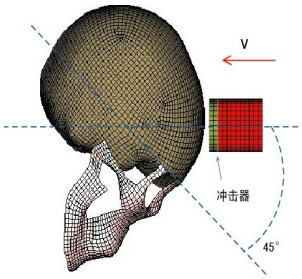

Figure 3. Simulation set-up against the test of Nahum

Figure 4 shows the comparison of the simulation and test results.(The solid line is the test curve, the dotted line is the simulation curve.) From the figures, it can be observed that the simulation curves agree well with those of the test, which indicates that the model developed can be used to accurately predict the head injury of real human body.

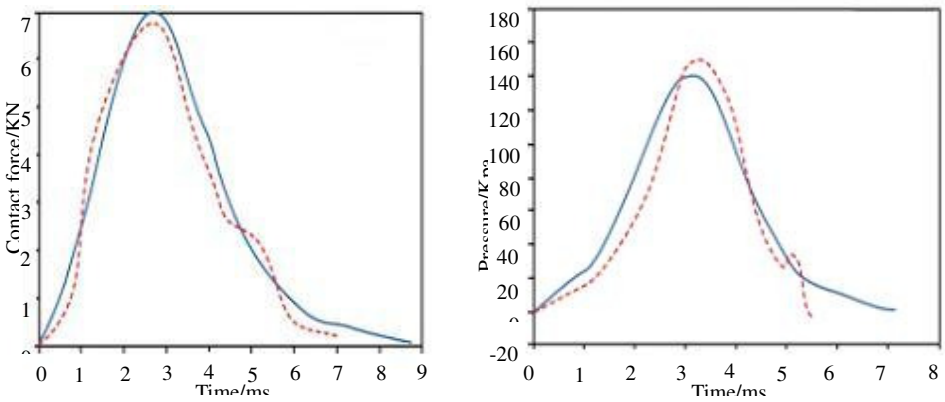

(a) head contact force curve of frontal impact test **(b) intracranial pressure curve of front impact position**

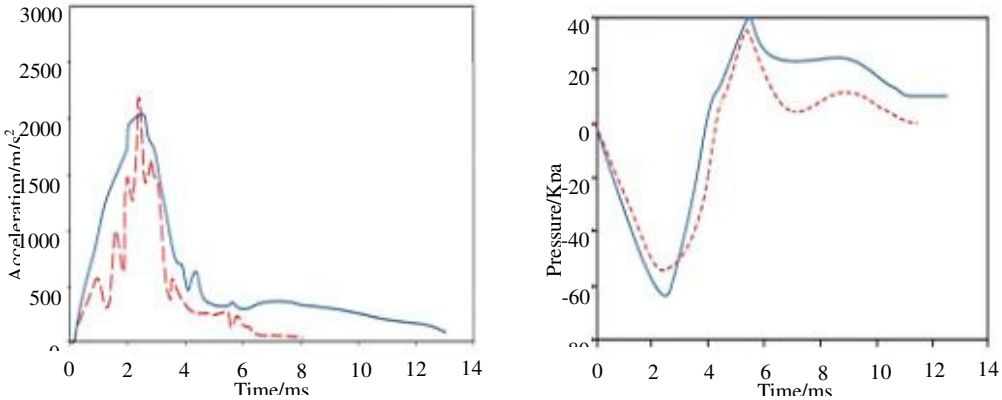

(c) Head acceleration curve of centroid **(d) Occipital cerebral fossa pressure curve**

Figure 4. Test of Nahum and simulation comparison

3.2 Vehicle Model development

Figure 5 shows the finite element (FE) model of the vehicle's front end. It contains about 1,107,982 nodes and 1,115,218 elements. The basic element size is 5×5mm.

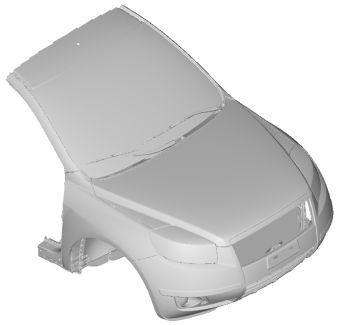

Figure 5. Finite element model of front-end vehicle

4 Injury Study on Pedestrian head

4.1 Analysis cases

With a launch angle of 65°, four cases of simulations were performed with different impact zones, as shown in table 3. The impact velocity was 40km/h and the model calculation time was 20 ms. The pedestrian's gait and its relative position with respect to the vehicle would result in the collision area of the head on vehicle hood. The four cases' analysis program below was made based on them.

Table 3. Analysis cases

Case	Schematic view	Collision zone
1	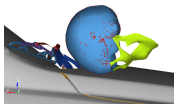	Frontal bone
2	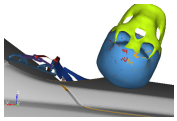	Parietal bone
3	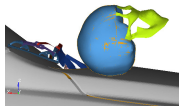	Occipital bone
4	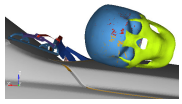	Temporal bone

4.2 Skull injury analysis

The main types of skull injury are facial soft tissue injury, as well as the fractures of the facial bone and skull. Skull fractures include depressed fracture and linear fracture. The pedestrian's skull fracture has something to do with the impact point and contact area of skull. When the collision area is small, skull depressed fracture occurs due to the stress concentration, the energy absorption by the small collision area. When the collision area is large, the energy spreads easily on the head, and a wide linear fracture is generated at the position away from the point of impact [8]. The limits of the skull fracture tolerance in different parts are shown in table 4[9~10].

Table 4. Different parts of the skull fracture tolerance limits

Area	Contact force peak	Conclusions from
Frontal bone	3.6~9.0	Hodgson and Thomas.1968
Cheekbones	0.5~2.9	Nahum etc.1971
Temporal bone	5.0~12.5	Allsop etc.1991
Occipital bone	6.4	SAE.1980
Parietal bone	6.8~9.4	Chen Xingwu etc.2005
Maxillary bone	2.0~4.2	Nyquist etc.1986

Figure 6 shows the skull contact force - time curves in the four cases. It could be observed that the overall trends of the curves ser similar. Their peak values difference was small. But the curve of case 4 occurred a large shock near 5 ms. The reasons might be that the facial bone contacting with the vehicle hood absorbed parts of the collision energy. In case1, the maximum contact force was 5.9 kN, which indicated a risk of frontal bone fracture. In case 2, the maximum contact force was 5.8 KN, below the limit of parietal bone destruction. In case 3, the maximum contact force was also 5.8 kN, blow the limit of occipital bone destruction. In case 4, the maximum contact force was 5.9 kN. There was a risk of temporal bone fracture. From the analyses above, it can be concluded that different collision location in skull will lead to different injury. The collisions on the frontal bone and temporal bone have greater risks of fracture owing to their low tolerance limit.

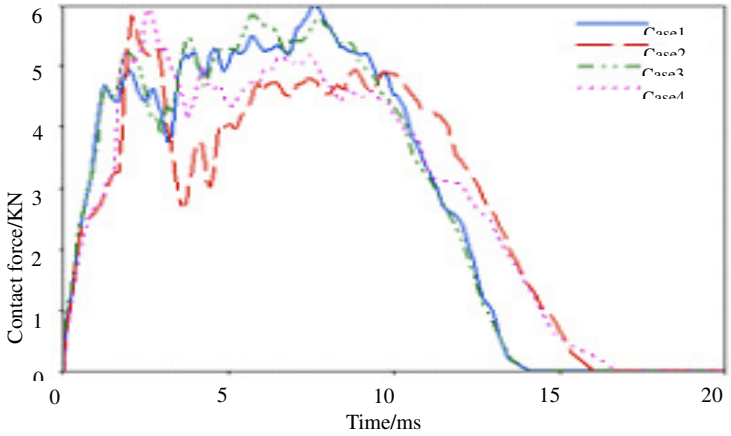

Figure 6. Skull contact force - time curve

4.3 Brain injury analysis

Brain injury can be divided into centralized brain injury and diffuse brain injury. Centralized brain injury includes the injuries, such as epidural hematoma, subdural hematoma, subarachnoid hemorrhage, intracerebral hematoma and brain contusion. Diffuse brain injury included brain concussion and diffuse axonal injury. Brain injury in a car accident was mainly caused by the dynamic loads. Head collision can result in the skull deformation and the stress wave transmitted within the brain. The inertial movement of the inner brain will cause positive pressure in the impact side and negative pressure in the other side, thereby forming a pressure gradient in the brain. Intracranial compression can lead to locally concentrated brain injury, such as the cerebral contusion [11]. Studies have shown that the translational acceleration in the head will cause concentrated brain injury, while the rotational acceleration will lead to diffuse brain injury [12~13].

4.3.1 Brain pressure analysis

Ward et al. noted that when the intracranial pressure went beyond 235 kPa and the tensile stress reached -186kPa, a serious brain injury would appeared. But the intracranial pressure between the 173-235kPa would only lead to moderate brain injury[14]. Figure 7 shows the intracranial press distribution in 4 cases. In case 1, the frontal bone impacted on the vehicle hood. A positive pressure appeared on the lateral frontal, while a negative one on the occipital. The maximum pressure in the frontal position was 209.1 kPa and the corresponding tensile stress was -187.8 kPa, which indicated a risk of brain contusion. In case 2, the parietal bone contacted with the vehicle front-end. The positive pressure on the collision side was 221.5 kPa, while the negative pressure on the contralateral side was 202.3 kPa. There was a risk of brain contusion at this time. The case3 Occipital bone collision with vehicle front-end, occipital lobe showed a positive pressure of 165.5kPa, the maximum pressure does not exceed the limits given literature, so brain

contusion appears less likely. The case4 temporal bone collision with the vehicle front-end, the collision side of the right temporal lobe showed a positive pressure, collision contralateral left temporal lobe showed a negative pressure, but the maximum pressure does not appear in the collision and collision contralateral side, which appear in the lower part of the right temporal lobe, close to the irregular parts of the pressure value reaches 344.9kPa, there is a serious risk of cerebral contusion.

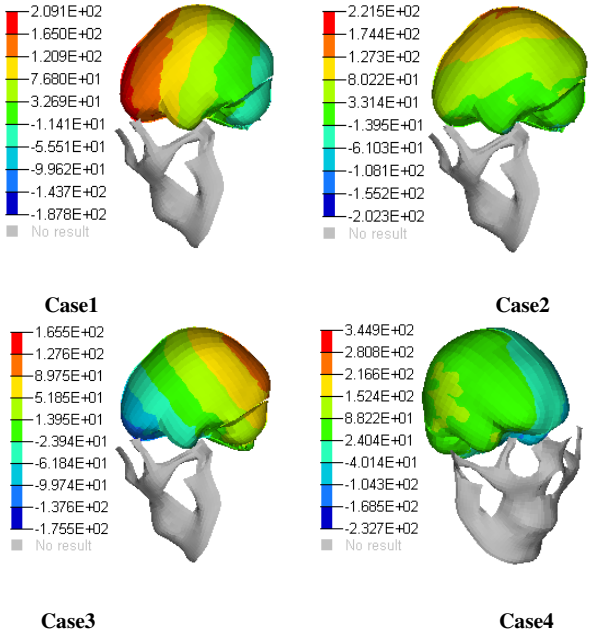

Figure 7. Intracranial pressure distribution /kPa

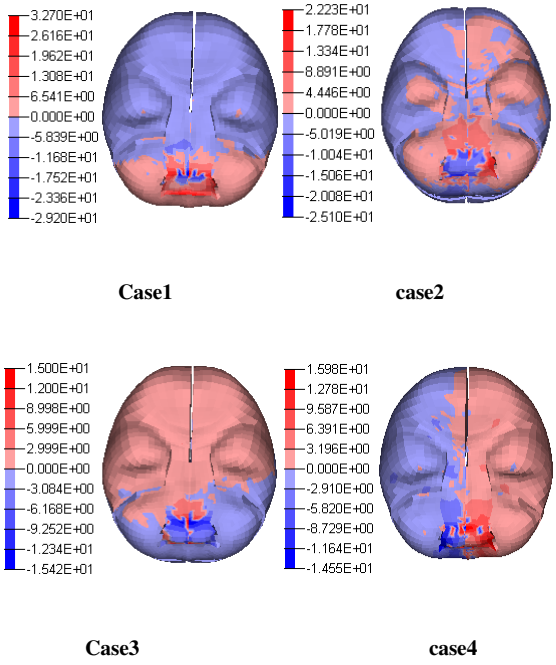

Figure 8. Schematic of intracranial stress /kPa

4.3.2 Brain stress analysis

Figure 8 shows the intracranial stress distribution in 4 cases. Willinger et al. pointed out that when the intracranial

stress reached 15-20kPa, it would cause a slight concussion. When the intracranial stress exceeded 38kPa, it would lead to serious brain concussion. In case 1 and case 2, the intracranial maximum stress was 32.7kPa and 25.1kPa respectively. Both of them exceeded the injury tolerance limits, and there was a risk of serious concussion. In case 3 and case 4, the intracranial stresses stayed within the injury tolerance limits, which mean a injury of slight concussion.

5 Conclusions

(1) When skull different locations at the same target point collision, the frontal and temporal bone have greater fractures risk because there is a lower tolerance limits.

(2) At the same initial conditions, the temporal bone collision with the front of the vehicle there is a serious risk of cerebral contusion; frontal and parietal bone collision with the front of the vehicle there is a more serious concussion risk.

Acknowledgements

This study was funded by Zhejiang Key Laboratory of Automobile Safety Technology and Geely Automobile Institute (Fund ID 2011E10002). The authors would like to acknowledge their constant supports.

References

[1] World Health Organization. Global Status Report on Road Safety 2013: Supporting a Decade of Action[R]. Switzerland: World Health Organization, 2013.

[2] World Health Organization. Estimated road traffic death rate 2010[E]. (2013-7-18). http://gamapserver.who.int/gho/interactive_charts/road_safety/road_traffic_deaths2/atlas.html.

[3] TASS. MADYMO Human Models Manual Release 7.3[R].Netherland: TNO, 2010.

[4] Li dewei, Han baoming. Pedestrian traffic[M]. Beijing: People's traffic press, 2011.

[5] Cai Zhihua, Lan Fengchong, Chen Jiqing, et al. Construction and Validation of the Assessment Model for Human Head Injury in Vehicle Traffic Accident[J]. Automotive Engineering, 2012, 34(9): 782-786.

[6] GB/T2428-1998. Head-face dimensions of adults[S]. Bei Jing: General Administration of Quality Supervision, Inspection and Quarantine of the People's Republic of China, 1998.

[7] Nahum A, Simth M D. An experimental model for closed head impact injury[C]. In: Proc of 20th Stapp Car Crash Conference. Dearborn: Society of Automotive Engineers, 1976, 785-814.

[8] Xu Wei. A Study of Head Biomechanical Response and Injury Mechanisms in Vehicle Traffic Accidents[D]. Chang Sha: Hunan University, 2007.

[9] Jikuang Yang. Review of injury biomechanics in car-pedestrian collisions[J]. Int. J. Vehicle safety, 2005, 1: 100-117.

[10] Chen Xingwu, Wang Huijun, Zhao Weidong, et al. Biomechanical study on the impact tests conducted on human head with hammer[J]. Chinese Journal of Clinical Anatomy, 2005, 23(3): 298-302.

[11] Shi Lei. Study on Human Head Biomechanical Response and Simulation in Vehicle Collisions[D]. Guang Zhou: South China University of Technology, 2011.

[12] Lissner H, Lebow M and Evans F. Experimental studies on the relation between acceleration and intracranial pressure changes in man[J]. Surgery, Gynecology and Obstetrics, 1960, 18(1): 58-60.

[13] Gennarelli T, Thibault L and Ommaya A. Pathophysiologic responses to rotational and translational accelerations of the head[C]. In: Proc of 15th Stapp Car Crash Conference. Detroit, USA: Society of Automotive Engineers, 1972, 296-308.

[14] Ward C and Thompson R. The development of a detailed finite element brain model[C]. In: Proc of 19th Stapp Car Crash Conference. San Diego: Society of Automotive Engineers, 1975, 641-674.

Proceedings of the 11th International Forum of Automotive Traffic Safety, 2014, pp 32-40
No. ATS.2014.104

A Study of Lower Limb Serious Injuries Based on Passenger Car Field Accident Data Analysis in Germany

Bingyu Wang[1, 3], Jikuang Yang[1, 2], Dietmar Otte[3], Xiaoqing Jiang[1], Yong Peng[4]

1 Research Center of Vehicle and Traffic Safety (VTS), State key Laboratory of Advanced Design Manufacturing for Vehicle Body, Hunan University, Changsha, 410082, P.RChina

2 Department of Applied Mechanics, Chalmers University of Technology, Gothenburg, 41296, Sweden

3 Accident Research Unit, Medical University of Hannover, Hannover, 30625, Germany

4 Key Laboratory of Traffic Safety on Track of Ministry of Education, School of Traffic & Transportation Engineering, Central South University, Changsha, 410075, China

E-mail:wangyu1986w@sina.com

Abstract: In the non-fatal vehicle–pedestrian accidents, lower extremity injuries are the most common injury patterns. In order to investigate the lower extremity injury risks using real world accident data, a subsample of 371 cases with pedestrian lower extremity AIS1+ injuries from GIDAS database, were used to conduct statistical analysis. Furthermore, the logistic regression models of the risks for lower extremity AIS2+ injuries and tibia/fibula fractures were developed by means of vehicle impact speed and pedestrian ages. The results revealed that impact speed and age were the two statistically significant predictors for pedestrians sustaining lower extremity AIS2+injuries and tibia/fibula fractures. In the selected sample, the lower extremity AIS2+ injury risk is 50% probability at impact speed of 46.3km/h. The tibia/fibula fracture injury risks are 50% and 20% at impact speed of 64.6km/h and 42.6km/h, respectively. Risk of injury increases with increasing of impact speed as well as does age was also found according to the data analysis.
Keywords: pedestrian traffic accident; lower extremity AIS2+ injuries; tibia/fibula fractures, logistic regression model; impact speed

1. Introduction

As vulnerable road users, pedestrians are injured or even killed frequently in vehicle traffic accidents due to lack of outer protective equipments [1]. According to the report of European Commission, in 2012 about 6004 pedestrians were killed, accounting for 20% of all fatalities in the traffic accidents [2]. In China, the number reached to 16,381, taking up about 25% of all causalities in the traffic accidents [3]. Therefore, it is necessary to conduct detail statistic analysis on the real-world accidents to mitigate pedestrian injuries.

Statistic analysis of traffic accidents indicated that head and lower extremity were the most frequently injured body regions [4]. In the past decades, most statistic analysis concern on the pedestrian fatal and severe injury risks, which means that head injuries were comprehensively investigated [5-8]. These studies provided important reference value for the formulation of pedestrian protection regulations. However, only few studies of real-world pedestrian accident focused on lower extremity injury risks. Only Klinich and Schneider[9] conducted detail statistical analysis on pedestrian lower extremity injuries, the relationships between lower limb injuries and the factors related to them were analyzed as well. However, the cases used for this research were collected from July 1994 to December 1998. It is not certain whether the results can be used for current studies due to the changes of passenger car front structure and the body structure of pedestrian. Following, Matsui[10]found knee ligament injury occurred at lower impact velocity and long

bone fractures happened at high impact speed after analyzing 62 pedestrian cases. Nevertheless, the number of sample was small, which leading the study results were not persuasive.

Since recent publications did not include a detailed analysis of pedestrian lower extremity injuries, an analysis of the GIDAS database was performed in current study with a focus on lower extremity injuries.

2. Methodology and materials

2.1 Data and sampling criteria

The data of accident database of GIDAS (German in-Depth Accident Study) were employed in the present study. In the frame of GIDAS, teams in Hannover and Dresden annually document approximately 2000 traffic accidents [11]. The collected cases in the GIDAS database contain very detailed information about pedestrian victims on age, gender, height/weight, injuries, speed determination and details of the accident cars as well as the accident scene issues [12]. The injuries were classified according to the AIS (Abbreviated Injury Scale).

In order to emphasis on the analysis of lower extremity injuries in GIDAS, the following sampling criteria were employed: (1) only cases with lower extremity injuries AIS1+ (2) only bonnet-type front ends of passenger cars, meaning vans and SUVs are excluded; (3) only pedestrians who are taller than 150cm; (4) the impact speed can be determined and speed is lower than 80km/h; (5) collision configurations involving only the 2:00-4:00 o'clock and 8:00-10:00 o'clock clock system(indicated in Fig.1). The final database consists of 373 crashes, of which 139 sustained lower extremity AIS2+ injuries.

2.2 Speed determination

Klinich and Schneider [9] reported that impact speed and age were the most common predictors of lower extremity injuries to different lower extremity regions. Vehicle impact speed refers to the speed at the time of the car colliding with the pedestrian in the accident. Age is very easy to get from the identify cards. However, the determination of car impact speed is not so easy. Usually, the following three methods were used to confirm the impact speed.

The first method used in the situation with clearly skid marks available on the accident scene. The impact speed v (km/h) can be estimated by using the mathematic formula:

$$v = 3.6 \times \sqrt{2\mu g L} \qquad (1)$$

where μ is the fiction coefficient, which is assessed by regarding the road conditions(wet/dry) and kind of road material as well as vehicle tire type; g is the gravity acceleration; and L is the length (m) of skid mark in accident scene[8].

However, most of the modern cars equipped with Anti-Brake System (ABS), which make it difficult to collect the clear skid marks. In this circumstance, Otte[13]developed a formula to a estimate car impact speed using throw distance.

$$v = \sqrt{2aw} \qquad (2)$$

in this formula, w is the throw distance of pedestrian, meaning the distance from first impact point between the car and pedestrian and rest position of the pedestrian; a the average deceleration of the pedestrian and the value is recommended to be 7.1m/s^2.

If the above two methods are not available to estimate the impact speed, then accident reconstruction software PC-Crash will be used to reconstruct the accident and determine the car impact speed.

Following, based on the subsample, multiple logistic regression models were generated to evaluate the risks of lower

extremity injury and tibia/fibula fracture considering age and impact velocity as two variables.

3. Results

3.1 Data analysis of whole sample

At first, the curb weight of accident vehicle was analyzed. Approximately 56% of vehicles had a curb weight from 1000 to 1300kg, about 23% ranged from 1300 to 1600kg, and only 4.5% were more than 1600kg.

As shown in Figure.2, approximate 95% of pedestrians were moving when the pedestrian suffering lower extremity injuries. Only 4.5% of pedestrians were stand still or in other statures at the collision time.

Fig.1. Impact configurations recorded in clock system in GIDAS

(the black arrows represent the vehicular impact direction relative to pedestrian)

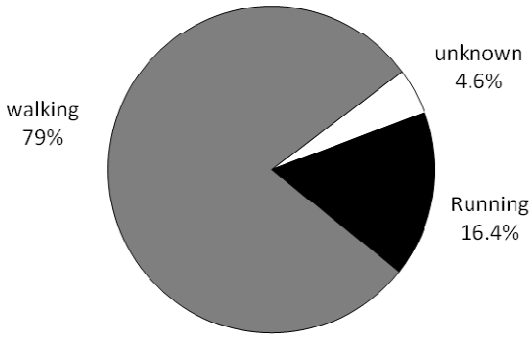

Fig.2. Pedestrian statures at the impact point

3.2 Data analysis of lower limb AIS2+ injuries

Lower extremity AIS2+ injuries included femur fracture, tibia/fibula fracture, knee fracture and ankle /foot fracture. In GIDAS, the fractures to the fibular malleolus were included in the ankle /foot category, and fractures to the tibial plateau as well as tibia and femur condyles were included in the knee fracture category. Knee soft-tissue injuries were grouped separately from the knee fracture injuries. Figure.3 shows the distribution of all AIS2+ lower extremity injuries in the GIDA database. These results show that fractures to the knee are most frequent, followed by leg and ankle/foot injuries.

Pedestrians over age 60 have a disproportionately high frequency of lower limb AIS2+ injuries, especially in the femur injuries and ankle/foot injuries (seen in Fig.3). The number of femur fractures in current study is very small, causing no youth sustained femur fractures.

Table.1 reveals that lower limb AIS2+injuries frequently happened when the impact speed at the range of 20-50km/h. The main lower limb AIS2+ injuries at the impact speed lower than 20km/h is the knee injuries; the main injury pattern may be ligament injuries. On the other hand, the main injuries at impact speed of around 40km/h were tibia/fibula fractures and knee fractures. When the impact speed was more than 50km/h, tibia/fibula fractures were the main lower limb AIS2+ injuries.

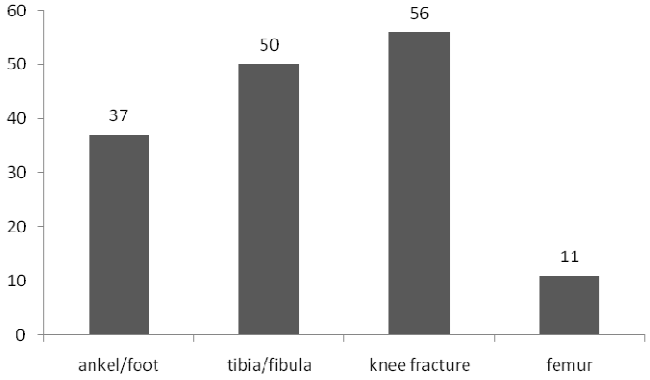

Fig.3. Distribution of lower extremity AIS2+ injuries by body region

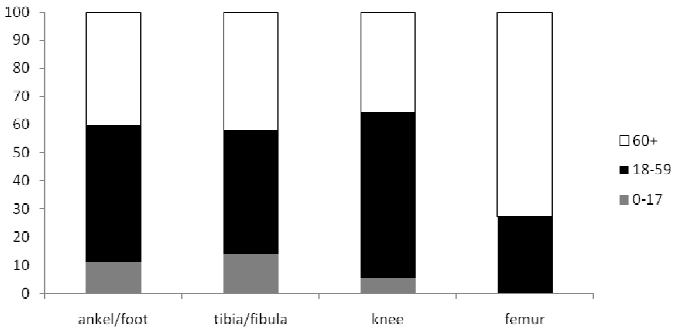

Fig.4. Lower extremities in the GIDAS database by age group and body region

Table.1. Speed distributions of Lower extremity AIS2+ injuries

Impact Speed	AIS2+				Cases
	ankle/foot	tibia/fibula	knee	femur	
0-10	1	0	8	1	10
11-20	7	2	14	0	23
21-30	9	10	9	3	26
31-40	6	16	17	2	36
41-50	10	8	6	2	26
51-60	2	6	2	2	10
61-70	1	5	0	1	5
71-80	1	3	0	0	3
sum	37	50	56	11	139

3.3 Effect of impact speed on lower limb AIS2+injury and tibia/fibula fracture risks

In current study, the logistic regression models were employed to study the lower extremity AIS2+ injury and

tibia/fibula fracture risks in terms of impact speed and pedestrian age since the outcome variable is binary(0 or 1)and the predictor variables are continuous, categorical, or both. At first, single logistic regression model was used to estimate the correlation between vehicle impact speed and the lower limb AIS 2+ injury and tibia/fibula fracture risks. The corresponding function P(v) is expressed as:

$$P(v) = 1/(1+e^{(\alpha-\beta v)}) \qquad (3)$$

where α is the intercept and β is the coefficient of the regression function. Both parameters can be determined via maximum likelihood method [14]. Goodness-of-fit of the statistical model was examined by means of chi-square $\chi^2$and significance level p. If the value of p is lower than 0.05, the examined variable has a statistically significant relationship with the lower extremity AIS2+ and tibia/fibula fracture risks.

Table.2 lists the values ofα,β, χ^2 and p of the regression model. The logistic regression plots for observed injury risks and vehicle impact velocity are presented in Fig. 5and Fig. 6. The 50% probability of lower extremity AIS2+ injuries correspond to vehicle impact speed of 46.3km/h. On the other hand, the 20% and 50% probability of tibia/fibula fracture are 42.6 and 64.6 km/h, respectively.

Table.2. Results from logistic regression analyses

Outcome variable	α	β	χ2	p
Lower limb AIS2+ injuries	1.482	0.032	20.722	0.000
Tibia/fibula fractures	4.076	0.063	40.173	0.000

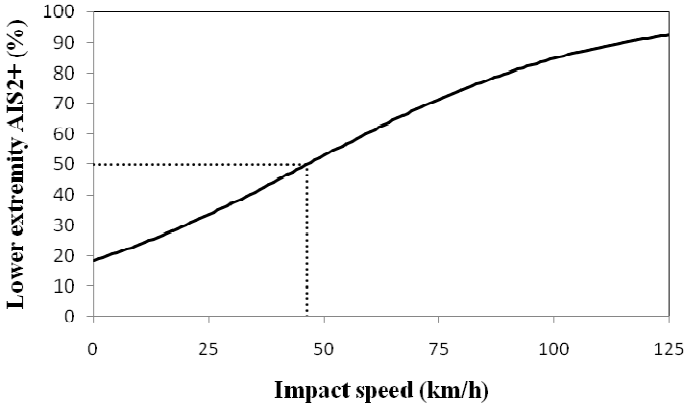

Fig. 5 Lower limb AIS2+ injury risk as function of impact speed

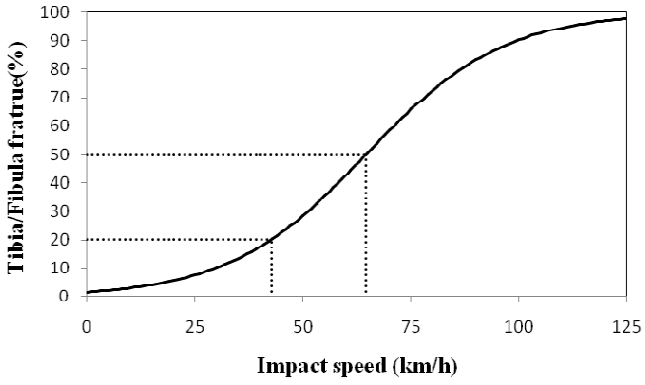

Fig.6. Tibia/fibula injury risk as function of impact speed

3.4 Correlation between lower extremity AIS2+ injury risks and age

According to statistical analysis of pedestrian accidents [9, 15], impact speed and pedestrian age was a predictive factor for lower extremity AIS2+ injury and Tibia/Fibula fracture. To get a better understanding of the distribution of variables such as pedestrian age and impact speed, corresponding descriptive statistics were employed and presented in table. In the table3-5, it can be seen clearly that the mean impact speed and pedestrian age for the whole sample are 29.8km/h and 41.11 years, respectively. However, in the lower limb AIS2+ injuries subset and tibia/fibula fractures group, the corresponding parameters are 34.52km/h and 49.11 years as well as 42.96km/h and 49.34 years, respectively. Therefore, the impact speed can be considered as the most predictive factor influencing lower extremity AIS2+ injuries and tibia/fibula fractures. As for the factor of age, the effect of this parameter should be conducted using more depth investigation.

Table.3 Descriptive statics of the lower limb AIS1+ injuries (N=371)

Parameters	N	Mean	Median	S.D.	Min	Max
Impact speed(km/h)	371	29.8	30	15.72	3	80
Age(years)	371	41.11	36	23.89	7	94
Height(cm)	139	168.4	169	8.67	152	189
Weight(kg)	136	67.05	67	15.08	37	130

Table.4 Descriptive statics of the lower limb AIS2+ injuries (N=139)

Parameters	N	Mean	Median	S.D.	Min	Max
Impact speed(km/h)	139	34.52	35	16.4	5	80
Age(years)	371	49.11	51	23.47	10	94
Height(cm)	371	168.8	168	8.59	152	189
Weight(kg)	367	68.46	69	14.02	37	120

Table.5 Descriptive statics of tibia/fibula fractures (N=50)

Parameters	N	Mean	Median	S.D.	Min	Max
Impact speed(km/h)	50	42.96	40	15.5	13	80
Age(years)	50	49.34	51.5	24.65	11	92
Height(cm)	50	168.7	170	8.58	152	186
Weight(kg)	47	67.77	70	13.40	37	92

Based on the selected sample cases from GIDAS, the multiple logistic regression models for probability of lower limb AIS2+ injuries and tibia/fibula fractures were developed using age and impact speed as two independent variables at a confidence level of 95%. The multiple logistic regression models can be expressed as the following function:

$$P(v, y) = 1/(1 + e^{(\alpha - \beta v - \omega y)}) \qquad (4)$$

where v is the impact speed, y is the pedestrian age, and α,β,and ω are coefficients to be estimated by the method of maximum likelihood[14]. The results of multiple regression analyses are presented in Table.6. It can be found that p-Value in both models are lower than 0.05.Therefore, vehicle impact speed and pedestrian age are two significant predictors for lower limb AIS2+ injury and tibia/fibula fracture risks.

Figure.7 shows the probability of AIS2+ lower extremity injuries by impact speed and pedestrian age. Curves are shown for 15-year-old, 45-year old, and 65-year-old pedestrians in Fig.7. The 50% probability of injury is at 64 km/ h for a 15-yearold, 42.7 km/h for a 45-year-old and 28.5 km/h for a 65-year-old.

Table.6. Results from multiple logistic regression analyses

Outcomes	Variables	Estimate	Standard error	p-Value
Lower limb AIS2+ injury risk	Intercept	α=2.62	-	-
	Impact speed	β=0.035	0.005	0.000
	Age	ω=0.025	0.007	0.000
Tibia/fibula fracture risk	Intercept	α=4.918	-	-
	Impact speed	β=0.064	0.011	0.000
	Age	ω=0.018	0.007	0.007

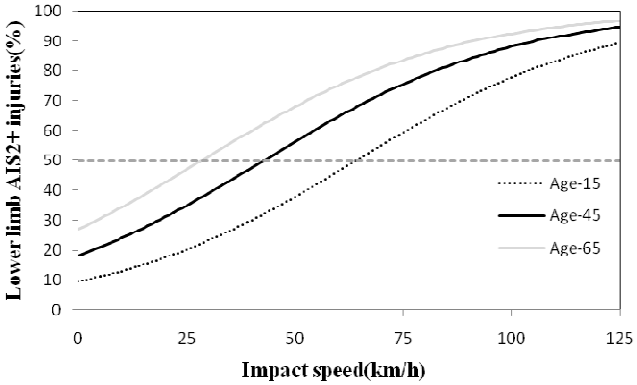

Fig.7. Probability of lower extremity AIS2+ injury risk by impact speed and pedestrian age.

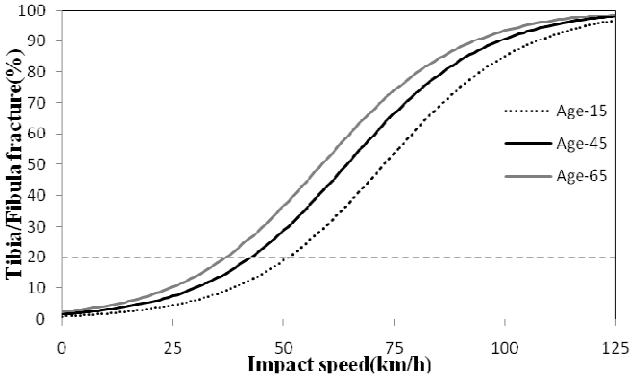

Fig.8. Probability of tibia/fibula fracture risk by impact speed and pedestrian age.

The same curves were made to assess the tibia/fibula fracture risks by considering impact speed and age, as shown in Fig.8. The 20% probability of injury is at 51 km/ h for a 15-year-old, 42.5 km/h for a 45-year-old and 37 km/h for a 65-year-old.

4. Discussion

In current study, a subsample of 371 pedestrian cases with lower extremity injuries from GIDAS database was used to perform general epidemiologic analysis. In order to corresponding to the boundary condition setup of European pedestrian protection regulation [16], only the cases with lateral impact and standard passenger cars were chosen. According to the analysis, most pedestrian with lower extremity injuries were impact when they were moving.

In the distribution of lower limb AIS2+ injuries by body, fractures to the knee are found to be the most frequent, followed by lowerleg and ankle/foot injuries. There are some differences from the study on of Mizuno [4], the reason

may be that the condyle fractures and tibia plateau fractures were categorized into knee fractures. According to the Fig.4, compared with adult and youth persons, the elder pedestrians are more easily to sustain long bone fractures. The reason may be the long bones become weaker with the increasing of age.

Table.1 shows that when the impact speed lower than 20km/h, the main lower limb AIS2+injury pattern is knee injuries, this may be the avulsion or laceration of knee ligaments. When the impact speed is about 40km/h, condyle or tibial plateau fractures may be the may knee AIS2+ injuries. Tibia/fibula fracture is the main lower extremity AIS2+ injury pattern when the impact speed is more than 40km/h.

A single logistic regression approach is employed to evaluate the relationship of impact speed to lower extremity AIS2+ injury and tibia/fibula fracture risks. Based on the statistical results, the urban city speed limit should be considered according to the occurrence of accident frequency. In current study the speed is suggested lower than 42.6km/h to protect lower extremity.

As is presented in the Fig.5 and Fig 7, even in the very low impact speed, lower extremity still sustain high probability of lower extremity AIS2+ injuries. Furthermore, the multiple logistic regression analyses were conducted to estimate the probability of lower limb AIS2+ injuries and tibia/fibula fractures by considering impact speed and age. The result shows that impact speed and age are two significant predictors for lower limb AIS2+ injury and tibia/fibula fracture risks. The probability of injury increases with increasing of impact speed, so does with age. This finding remains us that pedestrian age should not be ignored when the lower limb protection regulation is developed.

Good understanding of traffic accidents is very important for the development of protection regulation and the design of safety countermeasures. Although detailed analyses have been done in current study, more parameters related to lower limb injuries should be considered. For example, the correlation between car front structure parameters and lower limb injuries should be considered in the following investigation. The influence of one kind of lower limb injury on the other kinds of limb injury should be considered as well.

5. Conclusion

Based on the in-depth traffic accident investigation data from GIDAS, logistic regression analyses were performed to investigate the pedestrian lower extremity AIS2+ injuries and tibia/fibula fractures in terms of impact speed and pedestrian age. The statistical data indicate that most pedestrian were in motion when the collisions occurred. The results of logistic regression analyses show that impact speed and age are the statically significant predictors for lower extremity AIS2+ injuries and tibia/fibula fractures. The probability of injury increases with increasing of impact speed, so does with age. It is can be found that the 50% probability of lower extremity AIS2+injuries is at 64 km/ h for a 15-yearold, 42.7 km/h for a 45-year-old and 28.5 km/h for a 65-year-old. As for the tibia/fibula fracture risk, 20% probability of it occurred at 51 km/ h for a 15-year-old, 42.5 km/h for a 45-year-old and 37 km/h for a 65-year-old.

Acknowledge

This study was sponsored by China Scholarship Council (CSC), and supported by Accident Research Unit of Medical University of Hannover.

References

[1] Otte D, Jänsch M, Haasper C. Injury protection and accident causation parameters for vulnerable road users based on German In-Depth Accident Study GIDAS. Accident Analysis and Prevention, 2012. 44: 149-153.

[2] Pace JF, Tormo MT, Sanmartin J, et al. Traffic Safety Basic Facts 2012: Pedestrians, European Road Safety Observatory.http://ec.europa.eu/transport/road_safety/pdf/statistics/dacota/bfs2012_dacota-intras-pedestrians.pdf.

[3] Statistics of Road Traffic Accidents in PR of China (2013). Traffic Administration Bureau of China, Ministry of Public Security, Beijing.

[4] Mizuno Y, Summary of IHRA pedestrian safety WG activities (2005)－proposed test methods to evaluate pedestrian protection offered by passenger cars, SAE paper, No: 05-0138.

[5] Cuerden R, Richards D, Hill J. Pedestrians and their survivability at different impact speeds. In: Proceedings of the 20th International Technical Conference on the Enhanced Safety of Vehicles, Lyon, France, Paper No. 07-0440.

[6] Oh C, Kang Y.S, Kim W. Development of probabilistic pedestrian fatality model for characterizing pedestrian - vehicle collision. Accident Analysis and Prevention. 2008, 40 (3): 935 - 942.

[7] Rosen E, Sander U. Pedestrian fatality risk as a function of car impact speed. Accident Analysis and Prevention.2009, 41(3): 536-542.

[8] Kong CY, Yang JK, Logistic regression analysis of pedestrian casualty risk in passenger vehicle collisions in China, Accident Analysis and Prevention. 2010, 42(4):987–993.

[9] Klinich K.D, Schneider L. Biomechanics of pedestrian injuries related to lower extremity injury assessment tools: a review of the literature and analysis of pedestrian crash database. University of Michigan Transportation Research Institute Report No. UMTRI-2003-25. Sponsored by the Alliance of Automobile Manufacturers.

[11] Otte, D., Krettek, C., Brunner, H., Zwipp, H., 2003. Scientific Approach and Methodology of a New In-Depth-Investigation Study in Germany so called GIDAS. ESV Conference, Japan.

[12] Yang, J.K., Otte, D., 2007. A comparison study on vehicle traffic accident and injuries of vulnerable road users in China and Germany. SAE paper Number 07-0417.

[13] Otte, D., 2004. Use of Throw Distances of Pedestrians and Bicyclists as Part of a Scientific Accident Reconstruction Method. SAE paper Number 01-1216.

[14] Dobson A.J. An Introduction to Generalized Linear Models. Chapman &Hall/CRC. 2002.

[15] Zhang GJ, Cao L.B, Hu J, et al. A Field Data Analysis of Risk Factors Affecting the Injury Risks in Vehicle-to-Pedestrian Crashes. Proceeding of 52th Annals of Advances in Automotive Medicine Conference. SanDiego, 2008:199-213.

[16] European New Car Assessment Programme, Assessment Protocol ___ Pedestrian Protection.2009, Version 5.0.

[17] MacKenzie E.J, Burgess A.R, McAndrew M.P, et al. Patient-Oriented Functional Outcome after Unilateral Lower Extremity Fracture. Journal of Orthopedic Trauma. 1993, 7:393-401

Proceedings of the 11th International Forum of Automotive Traffic Safety, 2014, pp 41-46
No. ATS.2014.105

The Study about Airbag Error Function during the Cars and Electric Bikes Collision

Peng Wei[1], Qi ZhiNan[1], Zeng BiQiang[2], Guo LanShen[1]
[1]*School of Mechanical Engineering ,HeBei University of Technology,TianJin,300130*
[2]*Automotive Engineering Research Institute ,China Automotive Technology and Research Center,TianJin,300399*

Abstract: According to CIDAS statistical results show that cars and electric bikes occurred a higher probability of collision conditions in road traffic collision in China. Based on the investigation of CIDAS , this article simulates and reconstructes the process of cars and electric bicycles collisions by LS-DYNA. It is not noly studing the response of the structure of the cars during the collision process of electric bicycles and cars, also analysing the causes of airbag error function during the collision process of electric bicycle refered to the automobile safety reted condition. Then this article puts forward feasible technical means to avoiding airbag error function during the ACU calibration.

Keywords: Collision; Electric bikes; Vehicle safety calibration; Airbag error function

汽车与电动自行车碰撞事故中气囊误作用研究

彭伟[1,2]，祁志楠[1,2]，曾必强[2]，郭兰申[1]
1 河北工业大学机械工程学院，天津，300130，pengwei1989@gmail.com
2 中国汽车技术研究中心工程研究院，天津，300399

摘　要：根据 CIDAS 统计结果显示汽车与电动自行车碰撞是中国道路交通事故发生概率较高的碰撞工况，也是气囊误作用情况高发的碰撞工况。本文基于 CIDAS 调查案例，通过 LS-DYNA 仿真软件对电动自行车与汽车碰撞过程进行了模拟再现。研究了轿车与电动自行车碰撞过程中轿车结构响应规律，参照轿车安全标定工况对与电动自行车碰撞过程中气囊误作用原因进行了分析，对 ACU 标定中避免气囊误作用提出了可行的技术手段。

关键词：碰撞；电动自行车；车辆安全标定；气囊误作用

1　引言

我国是人口大国，电动自行车也是我国居民短途出行的绝大部分选择方式。根据 CIDAS 统计结果显示汽车与电动自行车碰撞是中国道路交通事故发生概率较高的碰撞工况，也是气囊误作用情况高发的碰撞工况。为了更好的降低交通事故中人员于财产的损失，降低和消除今后该工况下气囊误作用的概率。本文基于 LS_DYNA 模拟再现典型交通事故场景，提取碰撞过程中车辆响应的共性规律。为将来将该工况纳入新车安全开发标定工况中提供参考。

2　气囊工作原理

汽车安全气囊的基本思想是：在一次碰撞发生后、二次碰撞前，迅速在乘员和汽车内部结构之间打开一个充满气体的袋子，让乘员扑在气囊上。通过气囊的排气节流阻尼吸收乘员的动能，使猛烈的二次碰撞得以缓冲，以达到保护乘员的目的。安全气囊主要由传感器，控制器，气体发生器和气囊组成[1]。

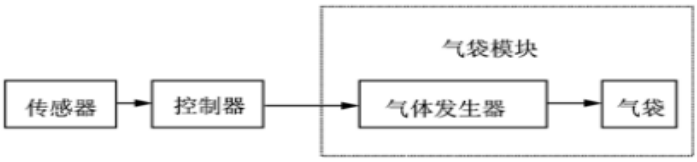

图 1　安全气囊组成

安全气囊匹配试验一般包括实车碰撞试验和行驶误作用试验两大部分，在试验完成后，采集数据，处理数据，将各种数据进行汇总、分析，由专业技术人员进行起爆标定并刷入安全气囊 ECU；之后再做验证试验，验证气囊在各种碰撞当中对乘员的保护作用、气囊起爆程序是否正常等，并且对碰撞当中的乘员伤害进行优化等[2]。

3　典型交通事故及模拟

图 1、图 2 是由中国交通事故深入研究项目（CIDAS）提供的典型的两种交通事故。

图 2　交通事故一正面碰撞

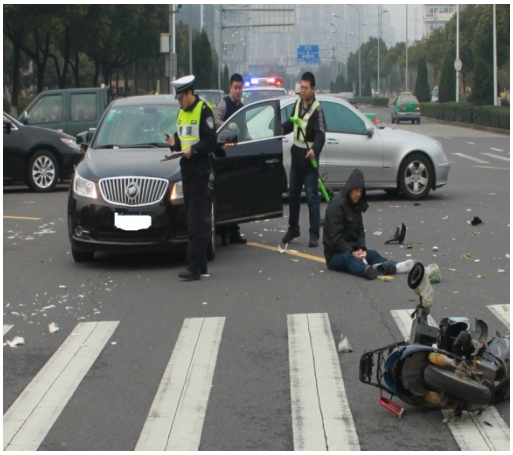

图 3　交通事故二左前方碰撞

为了在不同的交通事故中更好的模拟出现场情况，在基于 LS-DYNA 的模拟仿真中，根据以上两种交通事故的现场图并结合我国的实际情况，分别赋予假人 80kg，电动自行车 55kg，轿车 1400kg。为了更好的研究轿车与电动自行碰撞事故中气囊的误作用，作者特别将交通事故一、二，分别设定不同的速度。并且与汽车在 21km/h100%正面刚性墙碰撞、30km/h，30°斜角刚性墙碰撞、32km/h 正面柱碰等作为对比参考。

表 1　各个交通事故模型设定速度

	事故一	事故二	对比试验
1	20km/h	20km/h	21km/h,100%正面刚性墙碰撞
2	40km/h	40km/h	30km/h，30°斜角刚性墙碰撞
3	60km/h	60km/h	30km/h，正面柱碰

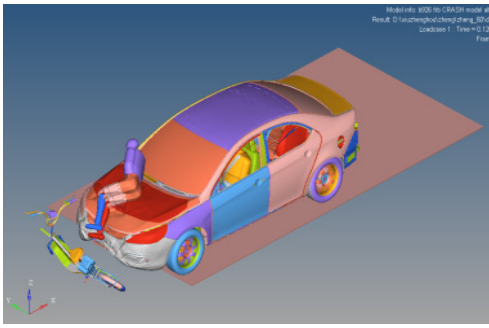

图 4　事故一模拟

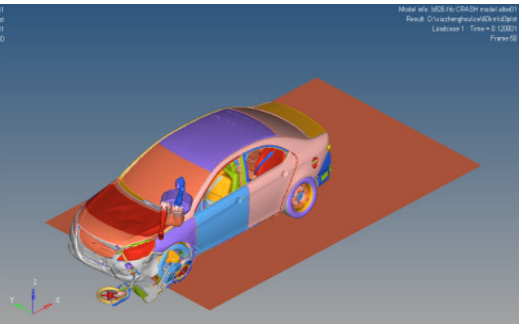

图 5　事故二模拟

4　车身碰撞响应分析

当汽车发生碰撞事故时，安全气囊控制系统检测到冲击力（减速度）超过设定值时，安全气囊 ECU 立即接通充气元件中的电爆管电路，点燃电爆管内的点火介质，火焰引燃点火药粉和气体发生剂，产生大量气体。在 30ms 的时间内即将气囊充气,使气囊急剧膨胀，冲破转向盘上装饰盖板鼓向驾驶员和乘员，使驾驶员和乘员的头部和胸部压在充满气体的气囊上，缓冲对驾驶员和乘员的冲击，随后又将气囊中的气体放出。

气囊的点爆与车辆 ACU 传感器测得的数值有关，所以在模拟仿真中测出车身碰撞响应规律，可以用该规律来研究车辆与自行车相撞过程中 ACU 误作用原因。

4.1　相关 ACU 标定试验

选用合适的标定工况对 ACU 进行标定是 ACU 在车辆碰撞过程中能否正常给气囊发出合理响应信号的前提和依据。经分析在 ACU 标定工况与汽车正面与电动自行车碰撞较为密切的标定工况有正面刚性壁碰撞、30 度斜角刚性壁碰撞、正面刚性柱碰撞，如下图所示。

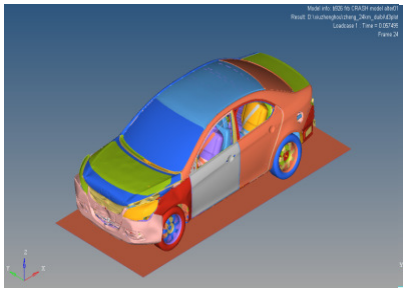

图 6　21km/h100%正面刚性墙碰撞

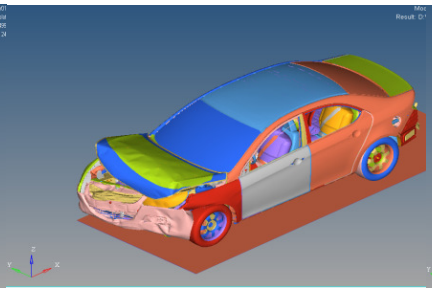

图 7 30km/h30°斜角刚性墙碰撞

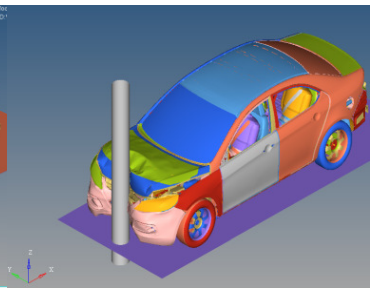

图 8　30km/h 正面柱碰

在以上三个标定工况中我们分别提取在不同对比试验下的车辆的前保中间加速度、左前前纵梁加速度、右前前纵梁加速度、B 柱左侧加速度来进行分析，如下图所示。

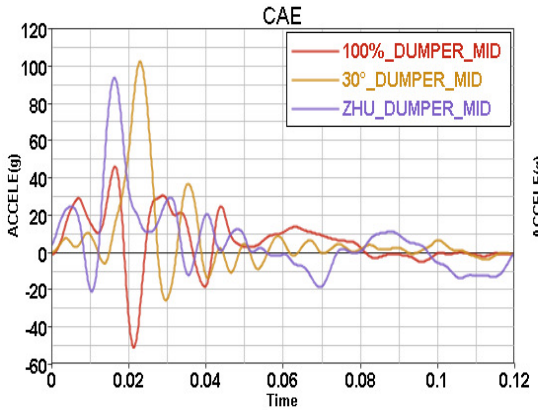

图 9　前保中间加速度

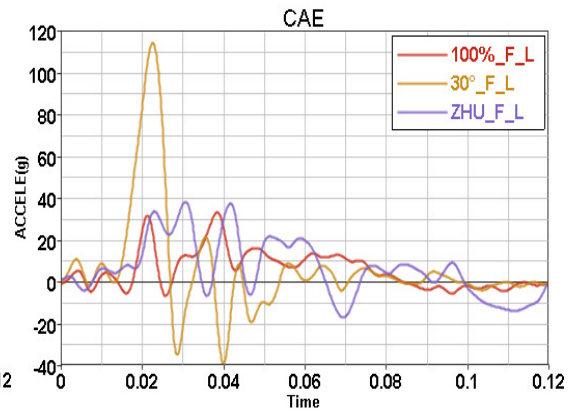

图 10　左前前纵梁加速度

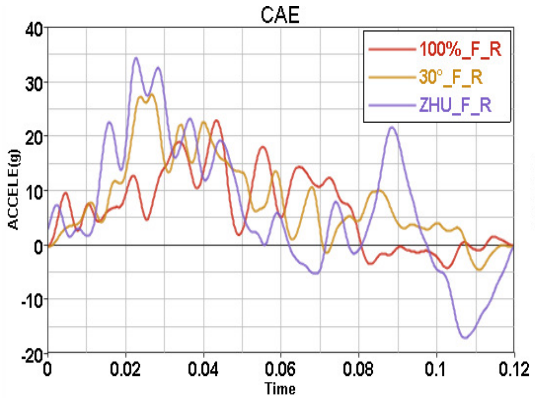

图 11　右前前纵梁加速度

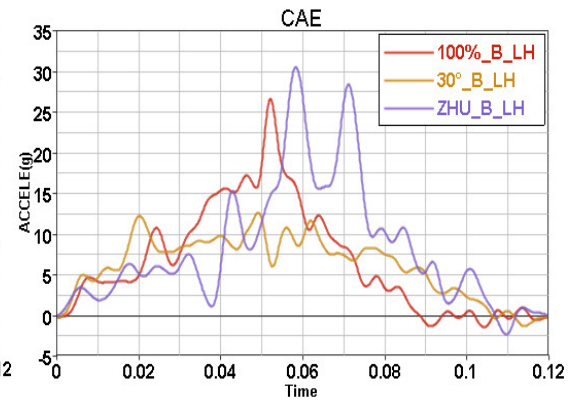

图 12　B 柱左侧加速度

从图可见，在以上三个标定工况碰撞响应加速度曲线中 20ms 左右均出现了较高的峰值，根据 ACU 响应规律判断该响应峰值可作为 ACU 点火信号所对应的碰撞特征信号。从图中可见前保中部及前纵梁左右侧加速度信号峰值均在 20ms 左右的碰撞前期，而左侧 B 柱加速度信号在 20ms 以后继续增大直至 60ms 左右。表 2 为以上四个位置在碰撞 20ms 左右过载值。

表 2 对比试验 20ms 各个构件最大加速度

	正面刚性墙碰撞	斜角刚性墙撞	正面柱碰
前保中间	48g	100g	90g
左前前纵梁	30g	110g	30g
右前前纵梁	12g	20g	12g
B 柱左侧	7g	12g	7g

由表 2 可见在碰撞 20ms 左右车辆前保-前纵梁-B 柱三个位置从前往后加速度迅速衰减，前保加速度值约为纵梁加速度值的 2-5 倍，纵梁加速度约为 B 柱加速度 2-5 倍。

4.2 交通事故一（正前方）模拟分析

分别提取模拟交通事故一中不同碰撞速度下车辆前保中间加速度、左前前纵梁加速度、右前前纵梁加速度、B 柱左侧加速度。如下图所示。

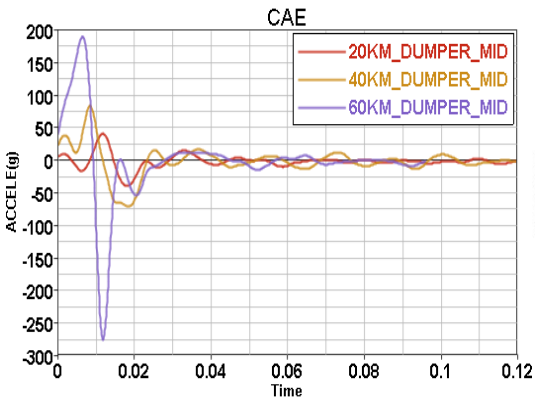

图 13　前保中间加速度

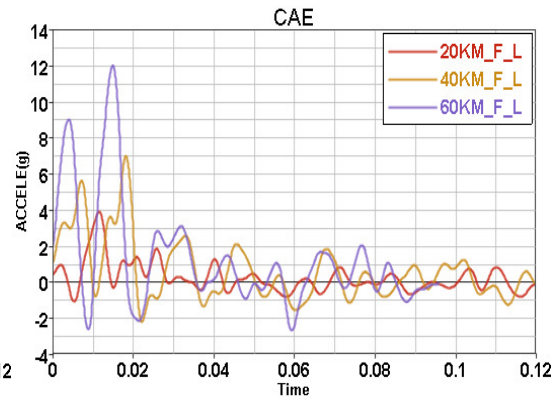

图 14　左前前纵梁加速度

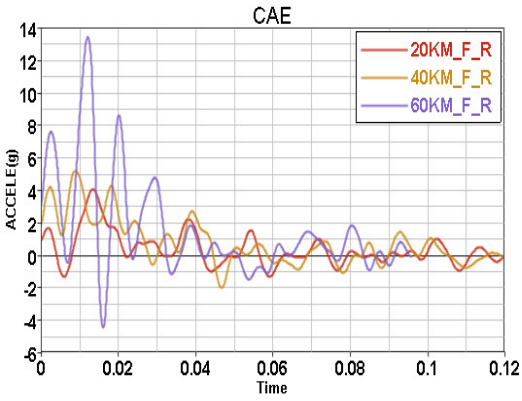

图 15　右前前纵梁加速度

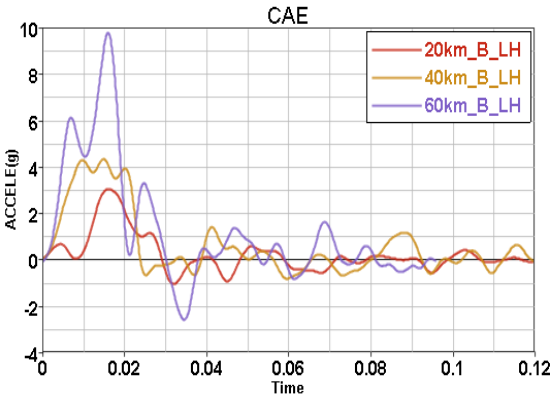

图 16　B 柱左侧加速度

由图可见与电动自行车碰撞车身碰撞加速度集中在 20ms 以前，且加速度峰值与上述三个 ACU 标定工况 20ms 左右加速度峰值相当。所以由此可见汽车与电动自行车碰撞较容易造成 ACU 误判而导致气囊起爆。

由上图 13-图 16 还可见在碰撞中前保-前纵梁-B 柱三个位置测得加速度值仍然呈逐级衰减趋势，但以表 2 所示三个标定工况中加速度衰减趋势对比可知，汽车与电动自行车发生碰撞时从前保到前纵梁的加速度衰减较标定工况更为迅速，前纵梁到 B 柱的加速度衰减较标定工况缓慢。前保驾驶度约为前纵梁加速度的 10 倍，前纵梁加速度约为 B 柱加速度的 1-1.5 倍。

4.3 交通事故二（斜前方）模拟分析

分别提取模拟交通事故二中不同碰撞速度下车辆前保中间加速度、左前前纵梁加速度、右前前纵梁加速度、B 柱左侧加速度。如下图所示。

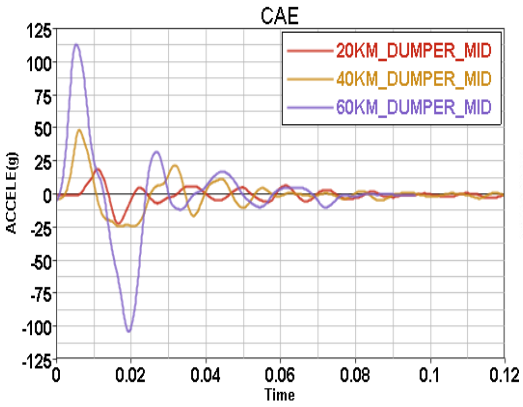

图 17　前保中间加速度

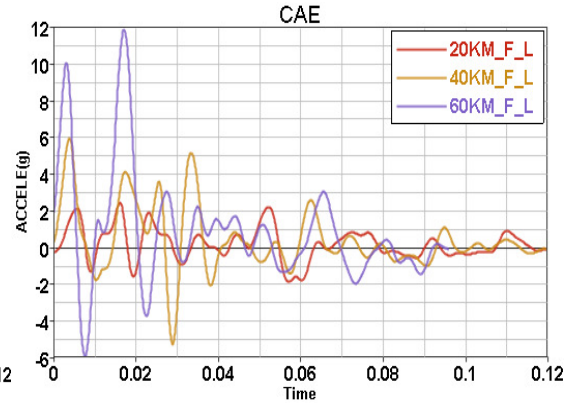

图 18　左前前纵梁加速度

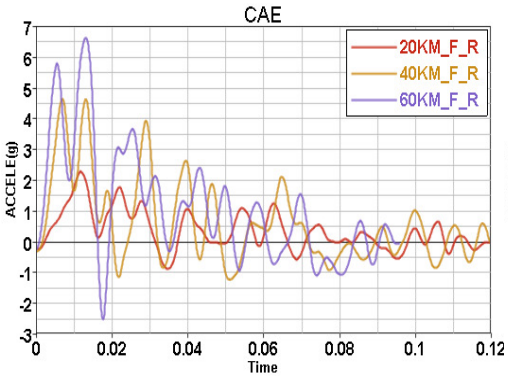

图 19　右前前纵梁加速度

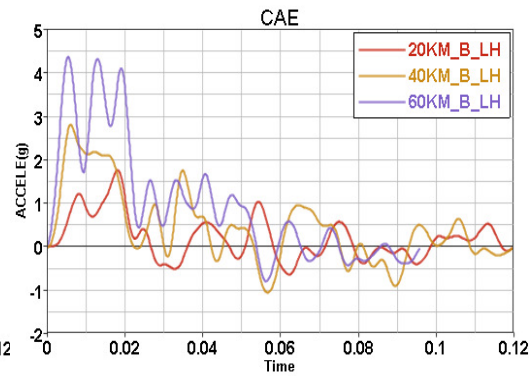

图 20　B 柱左侧加速度

由图可见电动自行车与车身斜前方发生碰撞时车身响应规律与电动自行车与车身正前方发生碰撞时响应规律完全一致。其 20ms 前加速度信号强度与标定信号相当，可能导致气囊误作用。在碰撞中前保到前纵梁加速度衰减较标定工况更为迅速。

5　结论

本文以 CIDAS 汽车与电动自行车碰撞事故为基础，对汽车与电动自行车碰撞事故特征进行深入的响应分析可以得到以下三点结论。

1、电动自行车与汽车碰撞事故中，碰撞轿车车身 ACU 传感器测量位置加速度强度可达 ACU 标定强度，较容易出现气囊误作用。

2、轿车与电动自行车碰撞中，车身前保加速度最大，加速度从前保到前纵梁传递过程衰减较标定工况更快，前纵梁与 B 柱间碰撞加速度衰减较标定工况慢。

3、电动自行车与轿车侧前方碰撞同与轿车正前方碰撞有相同的响应规律。

通过以上研究可知，由于信号强度和响应规律的相似性汽车与电动自行车发生碰撞中较容易发出气囊误作用。但增加 ACU 传感器检测位置，完善 ACU 内部对前保、前纵梁、B 柱（乘员舱）三个位置碰撞加速度的对比分析能力，ACU 可以区分与电动自行车的碰撞，避免气囊发生误作用。

参考文献

[1] 唐波. 中国汽车安全气囊标准制定的探讨. 《汽车与配件》技术与应用，2012，32：13-15
[2] 张金换，杜汇良，马春生等. 汽车碰撞安全性设计[M]. 北京：清华大学出版社，2010.2

Proceedings of the 11th International Forum of Automotive Traffic Safety, 2014, pp 47-53
No. ATS.2014.106

Epidemiological Analysis on Road Traffic Injuries in Shanghai from 2005 to 2013

JIANG Bang-shui[1], CHEN Jun-yi[1], PAN Shu-ming[2], WANG Hong-yan[1]

[1]*College of Automobile Engineering, Tongji University, Shanghai, 201804, China*

[2]*Xinhuan Hospital Affiliated to Medical School of Shanghai Jiaotong University, Shanghai, 200092, China*

E-mail：why-sos@vip.sina.com

Abstract:

Background： As the number of motor vehicles and the mobile population rises constantly in Shanghai, the biggest city in China, there is a sharp increase in the number of roads, vehicles as well as the traffic flow and the road traffic accidents increase accordingly. Meanwhile, the injury rate and mortality due to road traffic accidents both remain at a high level.

Objective: By investigate the epidemiological characteristics of the road traffic trauma (RTT) in Jiading District, Shanghai from 2005 to 2013 to provide a reference for improving the safety of the driver and passenger.

Method and Material: Descriptive methods and chi-square analysis were used to analyze the characteristics of the 1136 traffic accidents, which happened from 2005 to June 2013 in Jiading District of Shanghai, collected by Shanghai United Road Traffic Safety Scientific Research Center.

Results: The injury rate in females was about 26% higher than that in male. The difference between the rates were statistical significant (=126.53, P<0.01). From 2005 to 2012, the mortality increased at first and then decreased. The injury rate had the same trend. The highest injury rate (57%) was observed in May. The highest injury rate and death rate occurred from 3 o'clock to 5 o'clock. As for collision types, the injury rate (=1002.23, P<0.01) and the mortality (=133.38, P<0.01) were statistical significant. The injury rate and mortality in the young under the age of 10 and the old over 60 were higher than that in other age groups. With the increase of driving experience, the number of people involved in traffic accident, including the injured and the dead was in decline. Common segments witnessed the largest number of deaths. In the traffic accidents, head was the most serious injured position.

Conclusion： With epidemiological analysis of road traffic injured, preventive measures should be developed for the population with high risk of traffic injuries, the accident-prone time and the accident black spot to ultimately control and minimize the harmfulness of traffic injuries.

Key words: Road traffic accident injury, Injury rate, Mortality, Epidemiology

上海市 2005-2013 年道路交通事故伤流行病学分析

蒋邦水 1，陈君毅 1，潘曙明 2，王宏雁 1

[1]*同济大学汽车学院，201804，上海，中国*

[2]*上海交通大学医学院附属新华医院，200092，上海，中国*

E-mail：why-sos@vip.sina.com

摘　要:

研究背景：上海是中国最大的城市，随着机动车数量和流动人口的不断增加，道路、车辆及交通流量均有大幅增加，道路交通事故也随之增多，与此同时，上海的道路交通事故伤害的受伤率和死亡率均维持在较高的水平。

目的：探讨上海市 2005-2013 年道路交通事故伤流行病学特征，为改善驾乘人员的安全提供科学依据。

方法和材料：调取上海联合道路交通安全科学研究中心从 2005 年至 2013 年 6 月在上海市嘉定区所采集的 1136 起交通事故数据，采用描述性方法和卡方检验分析事故特征。

结果：女性比男性受伤率高约 26%，受伤率差异有统计学意义（=126.53，P<0.01）；从 2005 年至 2012 年死亡率呈现出先增大后减少的趋势，受伤率也呈现同一趋势，5 月受伤率（57%）最大，每日 3-5 时是受伤率及死亡率均最高的时段；在碰撞类型方面，受伤率(=1002.23，P<0.01）和死亡率（=133.38，P<0.01）具有明显的统计学意义；10 岁以下人员和 60 岁以上的老人比其他年龄段人员受伤率和死亡率均较高；随着驾龄的增加，事故人数、受伤人数及死亡人数均呈下降趋势；普通路段的死亡人数最多；在交通事故中，头部是受伤最为严重的部位。

结论：通过对道路交通伤患者的流行病学分析，针对交通伤患者高发人群和事故易发时间、路段制定相应的措施，最大程度控制和预防交通事故伤的危害。

关键词：交通事故伤　受伤率　死亡率　流行病学

道路交通事故伤已成为全球严重的公共卫生问题[1]，有关专家预测，到 2020 年道路交通伤将成为全球疾病和伤害负担的第三位原因[2]。中国是世界上交通事故死亡人数最多的国家之一，交通受伤和死亡人数居高不下。因此，本文对上海联合道路交通事故科学研究中心采集的 2005-2013 年道路交通事故进行上海市流行病学分析，以期发现上海市交通事故伤的特点及分布规律，为降低道路交通事故的受伤率和死亡率提供科学依据。

1 数据与方法

1.1 数据来源

本文研究数据来源于上海联合道路交通事故科学研究中心，从 2005 年至 2013 年 6 月份在上海市嘉定区所采集到的 1136 起交通事故，涉及人数为 3238 人。

1.2 研究内容及分析方法

事故信息中包含上海市交通事故交通伤发生的事故类型、时间、道路类型，伤亡人员的性别、年龄、受伤部位。描述性分析交通伤伤亡人群分布特点，包括性别、时间和年龄分布。本文研究的事故类型包括正面碰撞、侧面碰撞、追尾事故、两轮车事故及行人事故。根据简明损伤定级标准（Abbreviated Injury Scale，AIS）-90 版评分将受伤部位分为头部、面部、颈部、胸部、腹部、脊柱、上肢、下肢和体表共 9 个部位。并按 AIS-ISS 法对受伤部位受伤程度进行评分，AIS=1 轻度、AIS=2 中度、AIS=3 较严重、AIS=4 严重、AIS=5 危重、AIS=6 致死性。

1.3 统计学分析

数据分析和处理应用 Excel 2010 和 SPSS 21.0 统计软件，计数资料采用例数和百分数进行描述，死亡率和受伤率比较采用检验，P<0.05 为差异有统计学意义。

2 事故流行病学特点

2.1 性别分布

上海联合道路交通事故科学研究中心采集的 2005 年至 2013 年 6 月份交通事故中，共涉及 3238 人。其中男 2470 例（76.28%），女 564 例（17.42%），性别信息不详 204 例（6.30%）。在受伤情况已知的男性（2439 例）和女性（555 例）中，女性比男性受伤率高约 26%，见表 1。受伤率差异有统计学意义（=126.53，P<0.01），死亡率与性别没有明显的关系（=0.17，P>0.05）。

Table 1. Gender Distribution of the Traffic Injurers

表 1. 交通伤患者性别分布情况

性别	总例数	受伤例数(比例)	死亡例数（比例）
男	2439	1056 (43.30%)	286 (27.08%)
女	555	387 (69.73%)	109 (28.17%)

2.2 年龄分布

在受伤人数中，20-29 岁、30-39 岁人数最多，分别为 382 例（27.82%）、352 例（25.64%）。随着年龄的增加，受伤率呈现先增大后减少再增大的趋势，且具有明显的统计学意义（=149.57，P<0.01），10 岁以下人员和 60 岁以上的老人受伤率较高；死亡率差异有统计学意义（=118.67，P<0.01），随着年龄的增加呈现出先减少后增加的趋势，70 岁以上的老人死亡率超过 80%。

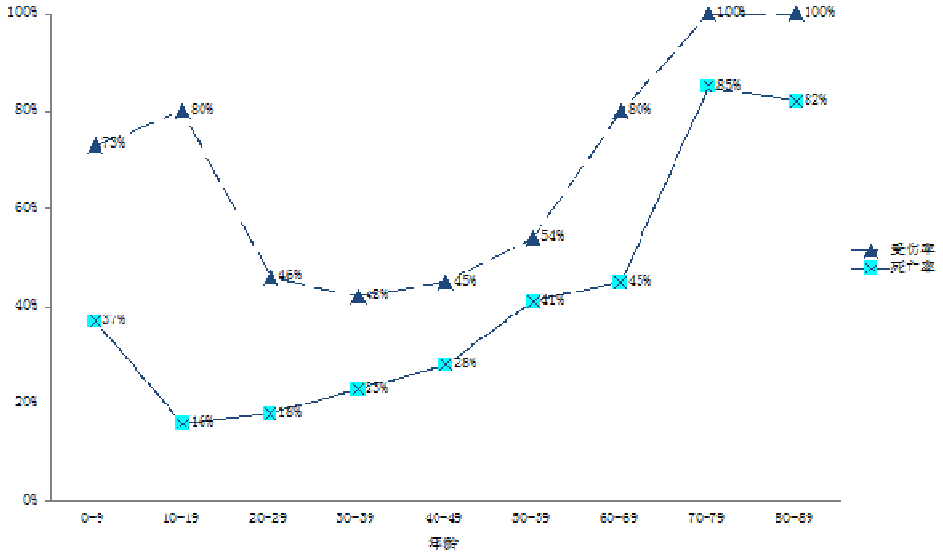

Figure 1. Injury Rate & Mortality of the Casualties with the Age

图 1. 交通伤患者受伤率和死亡率与年龄的趋势图

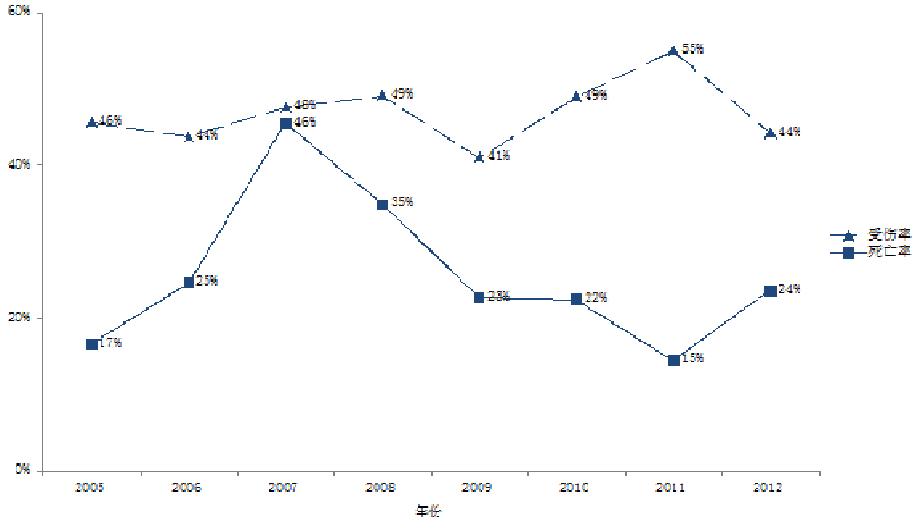

Figure2. 2005-2012 Trend Figure of Injury Rate and Mortality of the Casualties

图 2. 2005-2012 年交通伤患者受伤率和死亡率趋势图

2.3 驾龄分布

新驾驶员事故发率及伤亡人数均较高，驾龄在 0-4 年事故人数为 431 人，致 18 人死亡和 122 人受伤，随着驾龄的增加，事故人数、受伤人数及死亡人数均呈下降趋势。

2.4 受伤部位分布

在图 3 的交通伤患者身体部位受伤程度分析中，头部 AIS3+的比例最高，说明交通事故中，头部是受伤最为严重的部位。按 AIS3+对各受伤部位进行排序：头部（50.3%）、胸部（29.7%）、下肢（18.7%）、腹部（14.7%）、脊柱（8.6%）、体表（3.1%）、面部（2%）、上肢（1.9%)、颈部(0)。

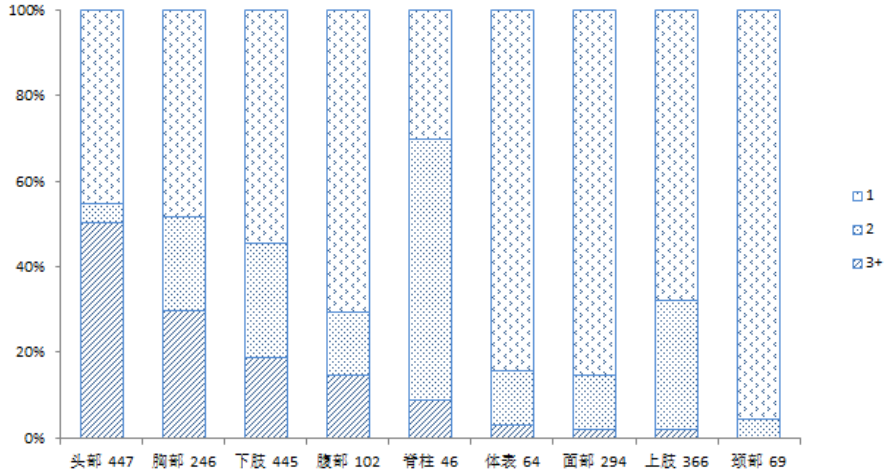

Figure 3. Levels of Injured Position in Traffic Accidents

图 3 交通伤患者身体各部位受伤程度

2.5 事故类型分布

在各事故类型中，正面碰撞和侧面碰撞涉及人数最多，分别为 1551 例、1352 例；造成死亡人数最多的事故为侧面碰撞和两轮车事故，分别为 318 例、172 例。在碰撞类型方面，受伤率和死亡率具有明显的统计学意义，卡方检验分别为=1002.23，P<0.01 和=133.38，P<0.01。

Table 2. Distribution of Injurers in Traffic Accidents

表 2. 交通伤患者事故类型分布情况

类型	总例数	受伤例数(比例)	死亡例数（比例）
正面碰撞	1551	462 (29.79%)	73 (15.80%)
侧面碰撞	1353	948 (70.12%)	318 (33.54%)
追尾事故	245	72 (29.39%)	8 (11.11%)
两轮车	479	456 (95.20%)	172 (37.72%)
行人	124	124 (100%)	78 (62.90%)

2.6 时间分布

2.6.1 年份分布特点

从 2005 年至 2012 年，受伤率整体呈现出缓慢增加的趋势（=19.84，P<0.01）；死亡率变化较为明显(=79.49，P<0.01)，呈现出先增大后减少的趋势，在 2007 年死亡率最高（46%）。

2.6.2 月份分布特点

受伤率呈现出先增加后减少的趋势，且在各个月份具有统计学意义（=22.29，P<0.05），在 5 月受伤率（57%）最大，其次为 8、9 月份。死亡率在各个月份变化不大，差异无统计学意义（=4.329， P>0.05）。

2.6.3 每日分布特点

3-5 时是受伤率及死亡率最高的时刻，受伤率为 54%，受伤率在各个时间段内没有较明显的变化（=8.196，P>0.05）；死亡率也是在 3-5 时最高，为 40%，明显多于 12-14 时的死亡率 18% （=4.137，P<0.05）。

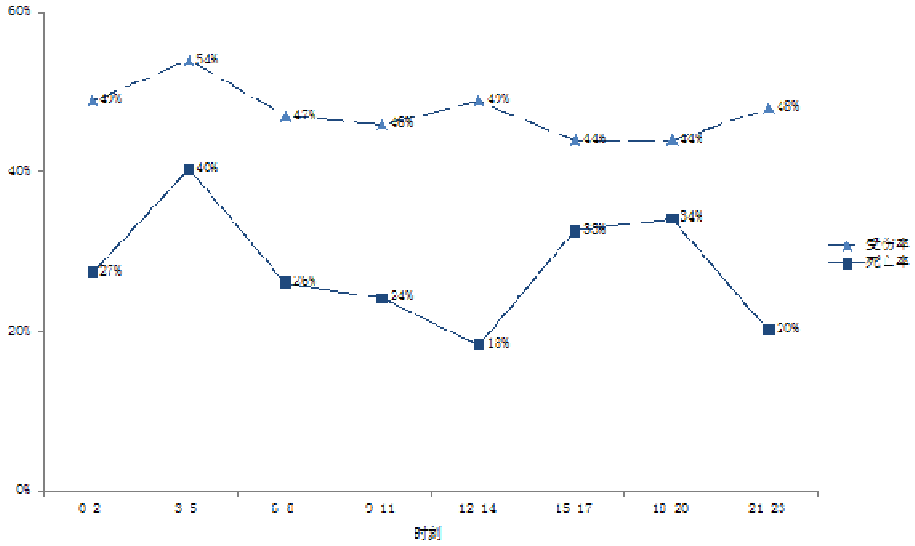

Figure 4. Injury Rate & Mortality of the Casualties with the Time

图 4 交通伤患者受伤率和死亡率与时刻的趋势图

2.7 路口路段分布

在四枝分叉口路段事故人数及受伤人数最多，分别为 1343 例、640 例，普通路段死亡人数最多，为 156 例。

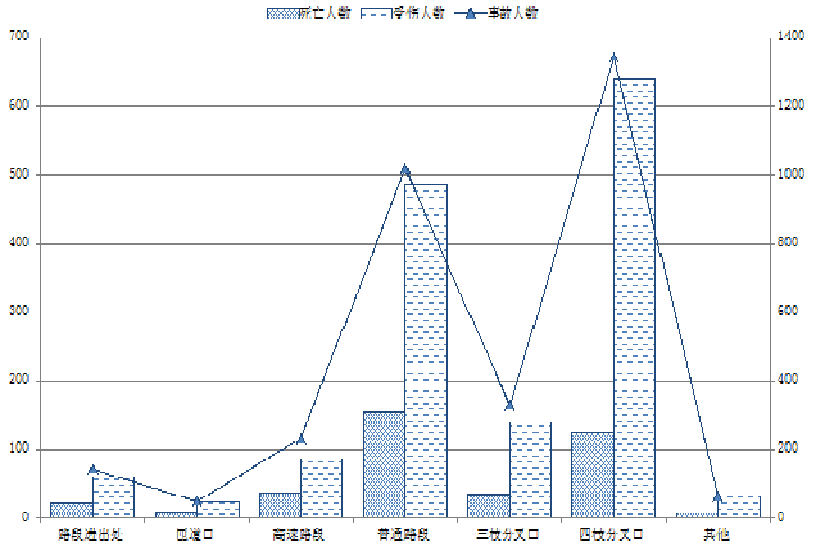

注：图中死亡人数及受伤人数为左侧坐标，事故人数为右侧坐标

Figure 5. Relation between Injuries and Intersections

图 5 路口路段与伤亡情况关系

3 讨论

男性受伤人数是女性的 2.6 倍，这可能与男性社会活动较多有较大关系，但女性的受伤率多于男性 26%，在交通方式的选择中，女性选择非机动车和步行比男性多，这两者的比例高出约 18.7%，在交通事故中，非机动车和步行人员的受伤比例较大，故女性较男性受伤率高。

头部和颈椎的损伤是造成儿童永久性损伤的主要部位[3]，0-9 岁儿童重伤及死亡情况交通工具多为车内和两轮车，车内无儿童安全座椅使用案例出现，可以看出人们在日常的出行中对儿童的保护意识不足。死亡率随着年龄的增加呈现出先减少后增加的趋势，这与国内相关研究基本一致[4]。70 岁以上老人多选择步行和两轮车，重伤及死亡占总数的 84.2%，因老年人在遇到事故时的应变能力和反应能力比青年人要低，且老年人受伤后恢复能力差，使得老年人受伤率及死亡率均最高。

随着驾龄的增加，驾驶员的经验丰富且安全意识较高，我国以机非混合交通方式为主，驾龄较长 的驾驶员心里较为稳定，事故发生时能够采取有效的避让措施，使得发生事故的危险性减少[5]，并且驾龄较长的驾驶员违反交通规则的动机较小[6]，故受伤人数及死亡人数随着驾龄的增加而逐渐减少。

侧面碰撞和正面碰撞涉及人数最多，说明这两种碰撞类型是交通事故最为常见的两种事故类型。侧面碰撞与正面和追尾碰撞相比，碰撞吸能最小，驾驶室侧面侵入量过大，是造成人员伤害的主要原因。相关研究结果显示，摩托车交通事故因头部受伤导致的交通事故死亡远远高于其他部位受伤所导致的死亡[7]，颅脑损伤是导致电动自行车和自行人员死亡或重伤的主要原因[8]，本研究结果与此类似，两轮车人员头部是受伤率最高的部位，也是伤情最为严重的部位，是造成两轮车人员死亡的主要原因。两轮车人员头盔使用率较低[9]，上海联合道路交通安全科学研究中心采集到的数据显示，两轮车人员头盔使用率仅为 11.07%，两轮车人员头部容易与发动机罩、挡风玻璃、地面发生撞击，未佩戴头盔会造成较大的伤害。戴头盔可以明显降低两轮车人员受伤的严重程度和死亡率，并且大幅度降低与此类撞车有关的卫生保健费用[10]。

每日受伤率死亡率最高的为 3-5 时，此时间段驾驶员易疲劳，且光线较暗，事故发生率较多，并且此时间段大中型货车、工程车、拖挂车事故约占 47.5%；15-20 时死亡率较高，行人及两轮车事故较多，此时间段为交通高峰，人员活动较为频繁。

四枝分叉口路段发生事故的主要原因是违反交通信号灯、未确保安全车距，这与驾驶员、行人、两轮车人员不按规定信号灯通行有很大的关系。普通路段机动车撞非机动车、行人事故最多，分别为 214 例、177 例，这可能与非机动车人员及行人随意横穿马路有很大关系。

综上所述，在对道路交通事故伤流行病学特征分析的基础上，医疗部门应加强与交管部门的合作，针对交通伤患者高发人群和事故易发时间、路段制定相应的措施，做好交通事故伤的预防工作。同时我们应借鉴发达国家的道路交通管理经验，加大监管力度，加强交通参与者交通安全教育，最大程度控制和预防交通事故伤的危害。

致谢

本论文是在王宏雁导师的悉心指导下完成的。导师渊博的专业知识、严谨的治学态度，精益求精的工作作风，诲人不倦的高尚师德，对我影响深远。在这里我要感谢我的导师对我的悉心培养。

同时我要感谢陈君毅博士对本文修改做出的精心指导，感谢潘曙明教授就交通事故伤分析给予我的莫大帮助，帮助我解决疑难问题。是他们在我写作过程中给了我们巨大的帮助与鼓励，使我能够顺利完成本篇论文，在此表示衷心的感激。

参考文献

[1] WANG Zhengguo. Current Situation and Future of Road Traff Injury [J]. Journal of Trauma Surgery, 2011, 13(3): p. 193-196.

王正国. 道路交通伤的现状和未来 [J]. 创伤外科杂志，2011，13（3）：193-196.

[2] Peden M, Scurfield R, Sleet D, et al. World report on road traffic injury prevention [M]. Geneva: World Health Organization, 2004: 3, 5, 39, 82.

[3] Bohman, K., et al. Long-term medical consequences for child occupants 0 to 12 years injured in car crashes [J]. Traffic Injury Prevention, 2014, 15(4): p. 370-378.

[4] QIU Jun, Analysis on Causes, Features and Trend of Road Traffic Crashes and Traffic Injuries in China [D]. Chongqing: Third Military Medical University, 2009.

邱俊. 中国交通事故和交通伤成因、特点与趋势研究 [D]. 重庆：第三军医大学, 2009.

[5] Allan F. Williams. Views of U.S. drivers about driving safety [J]. Journal of Safety Research, 2003, 3(5): p. 491-494.

[6] Yagil D. Gender and age-related differences in attitudes toward traffic laws and traffic violations [J]. Transportation Research Part F: Traffic Psychology and Behavior, 1998, 1(2): p. 123-135.

[7] YU Chunjun, WANG Changjun. Interrelated Studies on Safety Helmet and Traffic Accidents Involving Motorcycles [J]. Journal of Safety Science and Technology, 2009, 5(2): p. 76-80.

俞春俊，王长君. 摩托车头盔与摩托车交通事故的相关研究[J]. 中国安全生产科学技术. 2009, 5(2):76-80.

[8] Hu F, Lv D, Zhu J, et al. Related risk factors for injury severity of e-bike and bicycle crashes in Hefei [J]. Traffic Injury Prevention, 2014, 15(3): p. 319-323.

[9] Orsi C, Ferraro O E, Montomoli C, et al. Alcohol consumption, helmet use and head trauma in cycling collisions in Germany [J]. Accident Analysis & Prevention, 2014.

[10] WHO. Helmet use saves lives. URL:http:// www.who.int/mediacentre/news/releases/2006/pr44/en/

Proceedings of the 11th International Forum of Automotive Traffic Safety, 2014, pp 54-57
No. ATS.2014.108

Multiple Analysis of Heavy Vehicle Accident Based on Real-life Cases

Wenchao Liu, Zhiqiang Zhou
Road Traffic Safety Research Center of the Public Security Ministry, Beijing, China, 100062
E-mail: liuwenchao03@163.com

Abstract: This study chose 17 real-life heavy vehicle accidents from 2010-2013 which take more than 10 deaths on average as data base to analyze sorts of basic reasons including roll stability, mass breakpoint and driving behavior when unexpected occurs. The result shows that it's not just the stable roll angle value but also the test process which could play a crucial role on roll stability of heavy vehicles. The breakpoint model of mass and dimension works efficiently for over-loaded influence calculation, especially for lorries. The accident rates of the fleets where defensive driving training has applied decrease by more than thirty percent. Consequently it suggests to test the stable roll angle with the most uneven center of gravity and set the breakpoint schedule for mass and dimension of heavy vehicles. Defensive driving education and training also play a significant role in vehicle accident prevention.

Keywords: heavy vehicle accident, roll stability, mass breakpoint, defensive driving

1 Introduction

Each year there are tens of thousands of people dead in road traffic accidents, which include far more injuries. Among all the fatal accidents with all sorts of vehicles, the heavy vehicle accidents often take conspicuously more death and injuries on average. According to the annual road traffic accident reports of recent years, most of the heavy vehicle accidents involved incorrect emergency response, vehicle rollover and foundational defection such as brake system, transmission shaft etc[1]. Multiple analysis of heavy vehicle accidents should consider both the human and vehicle factors related to the tragedy, which includes stable roll angle, mass breakpoint and space cushion driving in this study.

2 Method and Material

2.1 Real-life Heavy Vehicle Accidents

This study chose 17 real-life heavy vehicle accidents from 2010-2013 which take more than 10 deaths on average as data base to analyze sorts of basic reasons including roll stability, mass breakpoint and driving behavior when unexpected occurs. All of these accidents had something to do with passenger vehicles, middle-size or large, or both. Through the 17 accidents chosen to be analyzed for causes, there are 9 cases with rollover movement during the collisions occurred, and 15cases in which the drivers made incorrect decisions before the just moment the beginnings. On the other hand, it's important to figure out that almost thirty percent (5 cases) of all the chosen accidents had something to do with foundational defection such as brake system, transmission shaft etc. Based on drawings of scene for road traffic accident[2] and accident reports, this study chose roll stability, mass breakpoint and driving behavior as multiple causes of heavy vehicle collision analysis and reconstruction.

2.2 Driving Simulation Analysis and Real Vehicle Detection

Comparing with the counterpart of the U.S. transportation department, it's found that almost all the pivotal data and regulations of vehicle product standards including stable roll angle are detected and measured through static test process. Considering that most of passenger vehicles involved in fatal accidents lost control of themselves during the process of collisions, set the contrast test of even and uneven loaded situations to measure the stable roll angle. Discuss the model of breakpoints of mass and dimension[3] from the state of New South Wales, Australia, which could be taken for developing our own breakpoint model as a reference. Finally take the defensive driving as active safety technology of drivers facing the straight risk of all sorts. Introduce defensive driving education and training[4] to the local fleets in Shanxi and Hebei provinces, evaluate the difference of the traffic violation and collision rate before and after the introduction.

3 Results

3.1 Limit Gauging of Stable Roll Angle

Contrast tests are set for measuring the difference of stable roll angle of passenger vehicles with all the passengers and load even and uneven distributed. According to the regulation of safety specifications for vehicles operating on roads[5], the stable roll angle of passenger vehicle's both sides should be more than 28° , which is tested with the full and complete passengers and empty cargo loaded. Considering that all the passengers or loads of moving vehicles could be distributed extremely uneven at the most dangerous moment before the rollover occurs, it's significant to set the stable roll angle test with all the passengers and cargo on the same side. With the same large passenger vehicle loaded differently in the stable roll angle tests for five times, the results show that extremely uneven loaded situation could be 3-4° different from traditional test situation as table 1.

Table 1 stable roll angle test

No.	even loaded left	uneven loaded left	even loaded right	uneven loaded right
1	29.8°	27.1°	29.2°	26.8°
2	29.9°	27.2°	29.4°	26.9°
3	29.6°	26.9°	29.4°	27.0°
4	29.4°	26.7°	29.1°	26.6°
5	29.5°	26.6°	29.2°	26.8°

The rollover movement of passenger vehicle is formed from stable roll angel, lateral centrifugal acceleration and coefficient of road adhesion[6]. When the stable roll angel is smaller than lateral centrifugal acceleration, the vehicle would roll over rather than slip away. Comparing with the extremely uneven loaded situation during the real collisions, the traditional test process of stable roll angle is not sufficient for sure.

3.2 Breakpoint Model of Overloaded Vehicles

Every vehicle has its own dimension and loading requirements, which should not be broken for any bit. However, most countries with such laws and regulations barely have the measurable risk relationship between overload and foundational defections. In the state of New South Wales, Australia, there is the breakpoint model of overloaded vehicles as table 2.

Table 2 breakpoint risk level of overloaded vehicle

vehicle types	legal axle weight limit (t)	risk category break points (t)		
		minor	substantial	severe
rigid 2 axle truck	6.0 (1st axle)	6.2	⩾6.3	⩾7.2
	9.0 (2nd axle)	9.4	⩾9.5	⩾10.8
rigid 3 axle truck	6.0 (1st axle)	6.2	⩾6.3	⩾7.2
	16.5 (2nd and 3rd axles)	17.3	⩾17.4	⩾19.8
rigid 4 axle truck	27.5 (gross)	28.8	⩾28.9	⩾33.0
articulated 4 axle truck	6.0 (1st axle)	6.2	⩾6.3	⩾7.2
	9.0 (2nd axle)	9.4	⩾9.5	⩾10.8
	16.5 (3rd and 4th axles)	17.3	⩾17.4	⩾19.8
articulated 5 axle truck	6.0 (1st axle)	6.2	⩾6.3	⩾7.2
	16.5 (2nd and 3rd axles)	17.3	⩾17.4	⩾19.8
	16.5 (4th and 5th axles)	17.3	⩾17.4	⩾19.8
articulated 6 axle truck	6.0 (1st axle)	6.2	⩾6.3	⩾7.2
	16.5 (2nd and 3rd axles)	17.3	⩾17.4	⩾19.8
	20.0 (4th, 5th and 6th axles)	20.9	⩾21.0	⩾24.0

Breakpoint risk level model of overloaded vehicles describes concrete load with risk level on every axle of the goods transportation vehicles, which could inform the drivers and operators of the correct disadvantage of overloading instead of traditional methods such as "illegal" or "dangerous". On the other hand, breakpoint risk level model suggests reliable basis for legal punishments of overloading.

3.3 Defensive Driving Simulation Experiment

Defensive driving behavior, sometimes under the name of space cushion driving in the United States or Australia, has come to use for more than sixty years, which was originally put out from Harold Smith in the United States. Defensive driving highlights the advantage of eyes and brain rather than the hands and feet when before the wheel. There are five key points[7] such as "aim high in steering", "get the big picture", "keep your eyes moving", "leave yourself an out" and "make sure they see you". By setting and taking 20 drivers involved in driving simulation experiment and real vehicle driving in the traffic environment for more than two years, it's delighted to tell the distinct characters of driving behavior before and after the education and training. Taking the original amount of traffic violation as the targeted objective, it measured the average amount of each driver during every six months and found that almost all the drivers declined their traffic violation behavior by contrast as table 3.

Table 3 traffic violation rate of each driver

No.	original	0-6 months	7-12 months	13-18 months
1	16	15	9	5
2	15	15	11	7
3	11	12	8	4
4	15	13	10	7
……				
20	12	12	9	4

According to the instructors of defensive driving, most of the drivers were unwilling to accept the concept at first, and few could comply with the suggestions literally. Things got better from the second 6 months, during which period most drivers' traffic violation behaviors began to decline. On the other hand, both fleets in Shanxi and Hebei provinces which took the defensive driving courses showed remarkable drop in the accident rate year by year.

4 Conclusions

The dynamical stable roll angle plays the most significant role on roll stability of moving vehicles, which often exists with all the passengers or loads distributed unevenly at the most dangerous moment before the rollover occurs. It's important to test the stable roll angle in extreme cases with the most uneven center of gravity.

Axle breakpoint does not only depend on the gross weight but also relate to the axle load distribution. Setting the breakpoint schedule for mass and dimension of various types of heavy vehicles makes it more reasonable for the loader or manger to keep the shipping suitable.

Defensive driving education and training focus on space cushion concepts and skills, which help keeping the drivers away from potential hazards of traffic environment, not just reaction to emergency. Active safety system of drivers themselves usually works much better than that of all the other objects including vehicles and road traffic facilities.

References

[1] The Public Security Ministry of Peoples Republic of China. The road traffic accident report of 2013 [J]. Beijing: Traffic Management Research Institute of Ministry of Public Security , 2014. (in Chinese)

[2] The Public Security Ministry of Peoples Republic of China. GA49-2009, Public security industry standard of the People's Republic of China—The drawing of scene for road traffic accident [S]. Beijing：China Standards Press, 2009. (in Chinese)

[3] NSW road and maritime service. Heavy Vehicle Driver Handbook [M]. Sydney：NSW Government, 2011. (in English)

[4] Smith System®. The Smith 5 Keys Handbook [M]. Arlington：Smith System®, 2013. (in English)

[5] Traffic Management Research Institute of Ministry of Public Security etc. GB 7258-2012 [S]. Beijing：Standards Press of China, 2012: 12.

[6] Cao Libo,Yan Lingbo. Overview of Rollover Associated Safety Studies and Tests [J]. Chinese Journal of Automotive Engineering, 2002, 2(4): 236—237. (in Chinese)

[7] Smith System®. Arrive Alive Safety Meeting Series [M]. Arlington：Smith System®, 2014. (in English)

Proceedings of the 11th International Forum of Automotive Traffic Safety, 2014, pp 58-63
No. ATS.2014.109

A Study on Validity of Airbags to Car with Crash Barrier of Highway

Wang De[1], ZhaoXiDa[1],ZengBiQiang[2]
[1] School of Mechanical Engineering ,HeBei University of Technology,TianJin,300130,
[2] Automotive Engineering Research Institute ,China Automotive Technology and Research Center,TianJin,300399
Email:wangde2013@126.com

Abstract：In this paper, CIDAS traffic accident investigation results of SUV vehicle collision guardrail of highway based on airbag failure phenomena are studied by computer simulation, collision model reproduces the process of structural response in the vehicle collision, the airbag sensor may focus on the ACU response law position of airbag failure reasons of acceleration, the collision has carried on the discussion and the analysis, proposed can reduce the optimization methods ACU system collision airbag failure in SUV and highway guardrail.
Keyword：accident highway guardrail　effective airbag　　new car safety demarcate

汽车与高速公路护栏碰撞中气囊有效性研究

王德[1,2]，赵希达[1,2]，曾必强[2]
[1] 河北工业大学机械工程学院，天津，300130，
[2] 中国汽车技术研究中心工程研究院，天津，300399
Email: wangde2013@126.com

摘　要:本文基于 CIDAS 交通事故调查结果对 SUV 车型碰撞高速公路护栏气囊失效现象进行了研究，通过计算机仿真碰撞模型再现了碰撞中车辆结构响应过程，重点研究了气囊 ACU 传感器可能位置加速度响应规律，对碰撞中气囊失效原因进行了探讨和分析，提出了可以降低 SUV 与高速公路护栏碰撞中气囊失效的 ACU 系统优化方法。
关键字：交通事故　高速公路护栏　气囊有效性　车辆安全标定

1 研究背景

伴随着汽车保有量的不断增加以及行驶速度的不断提高，全世界每天都会发生大量的车祸，而根据 CIDAS（中国交通事故深入调查）统计结果显示在中国车辆与道路交通条件下，汽车与高速公路护栏碰撞时由于安全气囊的误作用造成人员伤亡概率较高，对人们的出行安全造成了很大的威胁。

Figure 1.1 Highway guardrail car collision

图 1.1 汽车碰撞高速公路护栏

安全气囊在车辆发生碰撞时能够起到缓冲作用，在车辆碰撞高速公路护栏事故中，由于车速较大，所以气囊的有效展开显得尤为重要，但是国家没有统一的标准对气囊的相关生产和设计标准进行规定。气囊生产商和制造商就会以气囊未爆开是因为碰撞角度和速度问题，为了驾驶员不会被气囊爆开而伤害为理由进行抗辩，而消费者则会以自己的伤害是因为气囊未爆开而造成的。这方面的诉讼案件数量在过去的几年中，出现了较大规模的增长。由于没有相应的国家标准和事故车辆的气囊鉴定标准，所以很难划清责任问题，在裁定相应的责任事故中，也遇到了相当大的困难。所以，中国急需对车辆碰撞高速护栏后气囊是否有效打开的情况进行标定，进一步推动气囊乃至整个汽车行业的发展，从而使得汽车安全性发展迈上新的台阶。提高新车安全标定方案对该工况的有效覆盖率[3]。

2 安全气囊工作原理

安全气囊的工作原理是当汽车发生碰撞后迅速展开，在乘员和汽车构件之间形成一个充满气体的气垫，使乘员因惯性而移动时扑在这个气垫上，从而吸收碰撞能量，以减轻乘员的伤害程度。

安全气囊系统一般由传感器、电子控单元、气体发生器、气囊等组成，通常气体发生器和气囊等做在一起构成气囊模块。图 2.1 为安全气囊的原理图。

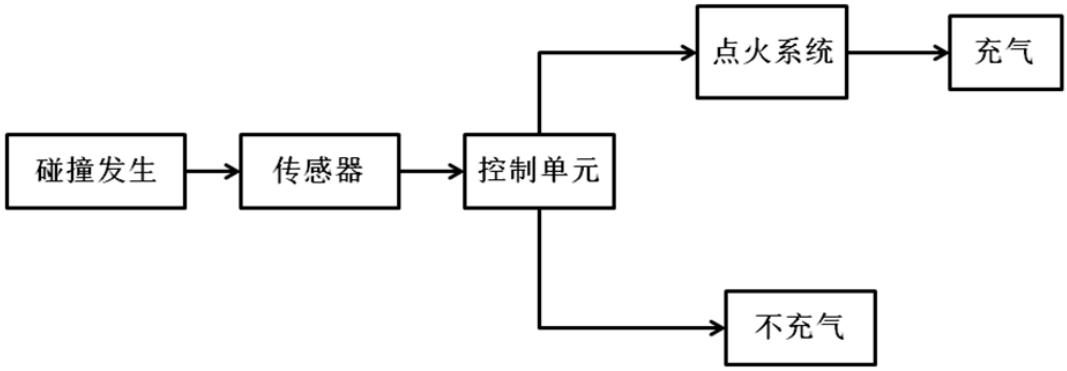

Figure 2.1 The principle diagram of the airbag

图 2.1 安全气囊原理图

安全气囊的展开与否，主要是受气囊的电子控制单元（airbag control unit）控制，该控制单元和传感器相连，通过对传感器采集的数据进行分析，计算，从而判断气囊是否展开。这时候控制算法就显得尤为重要了，

其中主流上有以下几种控制算法：

加速度峰值法，速度变化量法，加速度梯度法，功率导数法，在气囊标定过程中，控制的方法非常灵活，为了辨别，标定，有时同一款车可以同时运行几种控制方法。

不同的控制算法有其独有的特点和效果。加速度峰值法中，加速度传感器单元的工作就是采集实时的车辆加速度信号，算法简单有效。因此在本次仿真模拟汽车碰撞高速公路护栏的标定过程中我们采用加速度峰值法，判断安全气囊的有效性，通过测试汽车的不同位置加速度的响应情况判断安全气囊是否展开。

3 相似碰撞标定工况分析

对于一个正面的安全气囊开发，参考相关资料，可以定义基本的标定试验如下：

20km/h 零度刚性碰撞壁碰撞，气囊不点爆。

25km/h 零度刚性碰撞壁碰撞，气囊可能点爆。

50km/h 刚性壁碰撞

56km/h 40％偏正碰撞

30km/h 30 度刚性壁碰撞

30km/h 中心柱撞

粗糙路面与误用实验等

为针对目前与高速公路护栏碰撞交通事故中气囊时常不被点爆的问题进行研究，通过碰撞工况相似性分析选定 25km/h 正面刚性壁碰撞、30km/h 右 30 度角刚性壁碰撞、30km/h 正面中心柱碰撞三个工况为高速公路护栏碰撞研究对比标定工况[1]。采用 CAE 有限元仿真，模拟某 SUV 轿车分别与高速公路护栏碰撞和在以上三个标定工况中的碰撞过程。通过与高速公路护栏碰撞中车身响应规律与以上标定工况中车身响应规律进行对比研究，探讨事故中气囊失效的原因及其解决方法。

4 气囊有效性分析

4.1 仿真

高速公路上汽车与护栏碰撞是一个复杂的过程，它受司机乘员，整备质量，整车结构等许多因素的影响。本次仿真我们结合 CIDAS 统计得到的汽车与高速公路护栏碰撞事故的典型特征和碰撞冲击方式，通过 CAE 仿真再现的方式对有代表性的某 SUV 碰撞事故进行模拟，由于事故调查中碰撞再现误差的原因，本文模拟过程采用了 3 种碰撞工况如下表所示。

Table 4.1.1 Different working conditions

表 4.1.1 不同工况

	碰撞速度	碰撞角度
工况 1	100km/h	20°
工况 2	85km/h	30°
工况 3	70km/h	30°

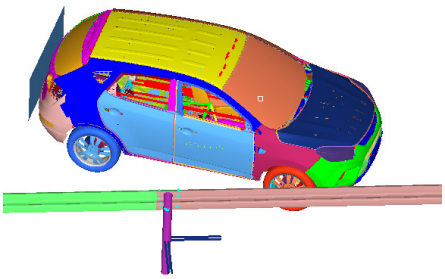

Figure 4.1.1 CAE model

图 4.1.1 CAE 模型

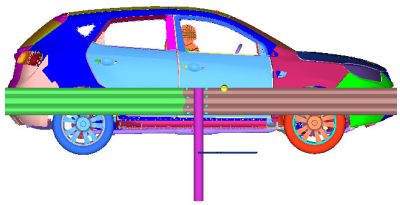

Figure 4.1.2 Vehicle and barrier height contrast diagram

图 4.1.2 车辆与护栏高度位置对比示意图

如上图为车辆与高速公路护栏位置关系对比图，从图中可见 SUV 重心位置要位于护栏上方。

由于左右 B 柱下端，中央通道 ECU 处加速度和前保险杠中间加速度值能反映车的整体响应情况，其为加装 ACU 传感器的主要位置，根据车的响应情况，通过加速度峰值法，观察其是否达到阈值，来判断气囊是否打开。由此我们通过汽车与高速公路波形护栏碰撞的计算机仿真，测试得到左右 B 柱下端，中央通道 ECU 处加速度反应情况，由于仿真模型是撞击的汽车的右部分，所以我们同时分析了右吸能盒附近汽车的加速度响应曲线。

4.2 不同工况撞高速公路护栏响应对比分析

下图为表 4.1.1 所示三个工况汽车碰撞高速公路护栏过程中主要部位加速度响应情况。

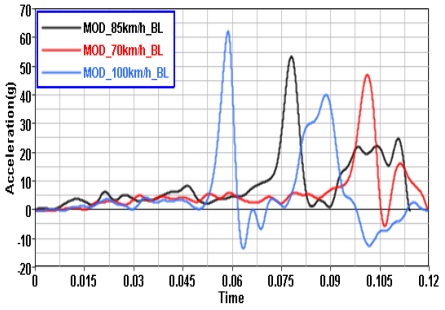

Figure4.2.1 The left B pillar lower end of acceleration

图 4.2.1 左侧 B 柱下端加速度

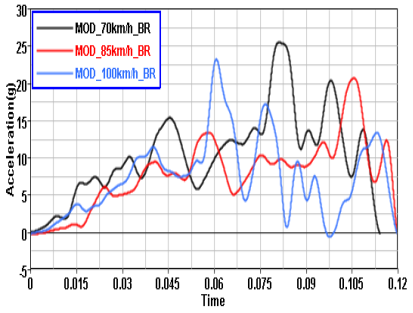

Figure 4.2.2 The right side of B pillar acceleration

图 4.2.2 右侧 B 柱下端加速度

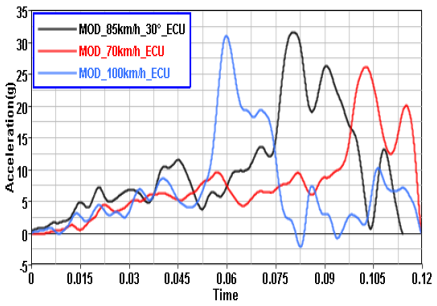

Figure4.2.3 The control ECU acceleration

图 4.2.3 中控道 ECU 处加速度

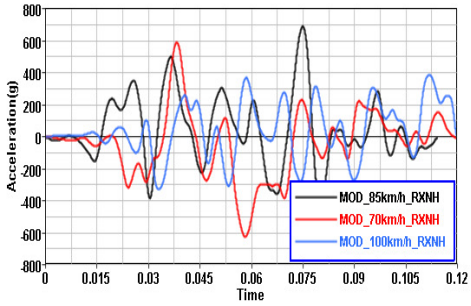

Figure4.2.4The right energy absorption box acceleration

图 4.2.4 右吸能盒加速度

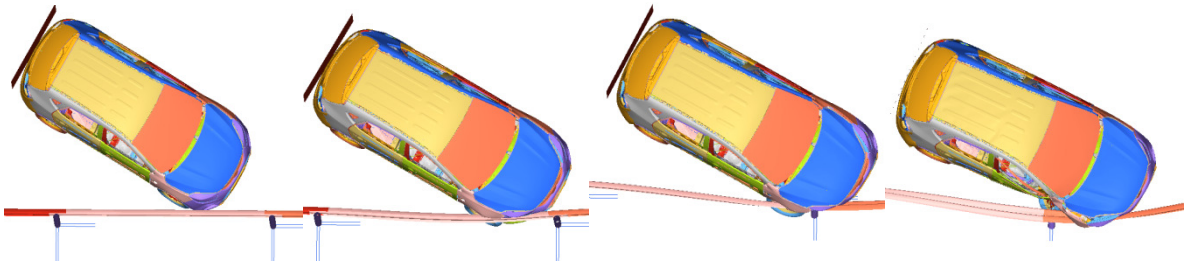

Figure 4.2.5 Mode 2 the vehicle and guardrail collision diagram(0ms 25ms 50ms 100ms)

图 4.2.5 工况 2 中车辆与护栏碰撞示意图（0ms、25ms、50ms、100ms）

由图可见三个工况碰撞所得车身响应规律趋势基本一致。车辆与高速公路护栏波纹板发生碰撞过程中车辆沿波纹板向前滑动，碰撞前期车辆乘员舱加速度值总体不高，当滑到与护栏立柱发生碰撞时车身乘员舱加速度将会发生较大的上升。在碰撞过程中总体趋势为碰撞侧加速度要高于非碰撞侧加速度，车辆中间加速度位于碰撞侧与非碰撞侧加速度之间。相对碰撞速度，车辆与护栏的碰撞较低对车身加速度的影响更为敏感。尤其是前方吸能盒位置。如果碰撞夹角较小碰撞侧吸能盒位置在碰撞前期碰撞加速度同样较小。

4.3 碰撞高速公路护栏与标定工况车身响应对比

在以上三个高速公路护栏碰撞工况中选定工况 2 与三个标定工况中车身响应情况对比如下所示。

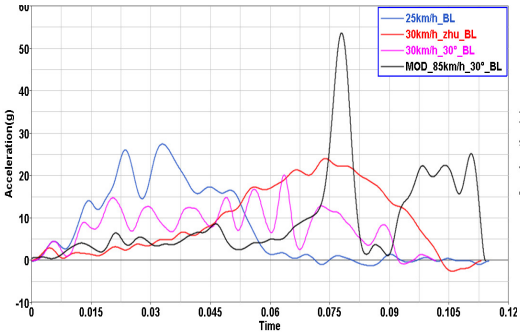

Figure4.3.1 The left B pillar lower end of acceleration

图 4.3.1 左侧 B 柱下端加速度

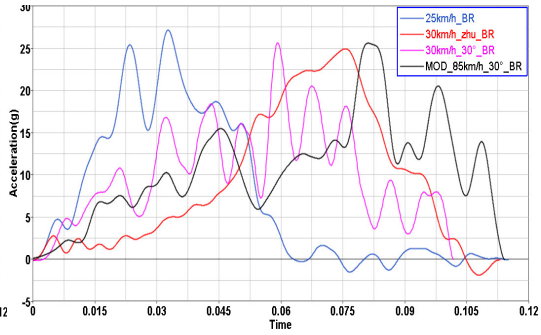

Figure 4.3.2 The right side of B pillar acceleration

4.3.2 右侧 B 柱下端加速度

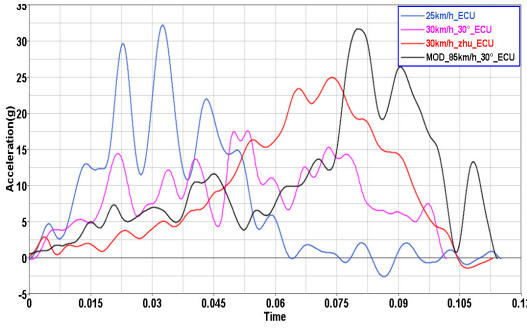

Figure4.3.3 The control ECU acceleration

图 4.3.3 中控道 ECU 处加速度

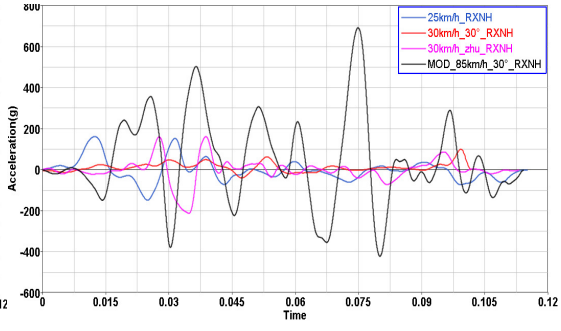

Figure4.3.4The right energy absorption box acceleration

4.3.4 右吸能盒加速度

由图可见在车辆与护栏碰撞前期车身乘员舱加速度值总体较标定工况低，但吸能盒加速度值较标定工况高。

5 结论

通过以上三种与高速公路护栏碰撞工况车身响应规律的仿真分析，及车辆与护栏碰撞响应规律与标定工况响应规律的对比可知，车辆与高速公路护栏碰撞导致气囊不能起爆的原因有：

1、车辆与高速公路护栏碰撞过程中，乘员舱加速度值在碰撞初期较低，如果没有撞到护栏立柱在整个碰撞过程中加速度上升斜率较缓，导致不能满足 ACU 起爆气囊所要求的阈值条件。

2、由于车辆与高速公路护栏碰撞过程中对车辆前端的损坏较大，在碰撞中造成部件破坏，导致 ACU 线缆系统已经被破坏，在车辆撞击护栏立柱出现较大加速峰值也不能起爆气囊。

3、车辆与高速公路护栏碰撞过程中，重心较高车辆有可能越过护栏发生翻滚而不能起爆气囊。

通过以上研究还可知道在车辆前端加装 ACU 外围传感器是避免与高速公路护栏碰撞气囊起爆失效的有效途径。

参考文献

[1] Xigong LIU. Domestic automobile airbag system troubleshooting practical handbook [M]. Beijing: mechanical industry publishing house, 2007.
刘希恭 . 国产汽车安全气囊系统故障检修实用手册［M］. 北京： 机械工业出版社，2007.

[2] Jinhuan ZHANG,Huiliang DU,Chunsheng MA. Automobile collision safety design. Tsinghua university press, 2010.2
张金换 杜汇良 马春生等著. 汽车碰撞安全性设计. 清华大学出版社 2010.2

［3］Liangyou MA. The car safety electronic control technology [J]. Electrical/electronic, 2003
麻友良.汽车安全电子控制技术[J] 汽车电器.2003

Proceedings of the 11th International Forum of Automotive Traffic Safety, 2014, pp 64-73
No. ATS.2014.110

Research on the National Standard of the Rear Underrun Protection Devices of Truck in China

Feng Wenxuan [1], Wang Honyan [1], Xiao Lingyun [2], Hu Wenhao [2], Chen Junyi [1]
[1]*Tongji University, Shanghai, China, 201804*
[2]*China National Institute of Standardization, Beijing, 100101*
Email: fwxjlutju@163.com, why-sos@vip.sina.com

Abstract: In all kinds of traffic accidents in China, the under-run crash accident between the car and heavy truck is often a fatal accident, due to the lack of high-quality rear underrun protection of the heavy truck, resulting in the high death and injury rate of the people in the car that rear a truck. In this paper, through the research and analysis on the relevant standard and regulations of rear underrun protection devices, combined with the accident investigation statistics and experiment of rear underrun protection devices, the suggestion of the standard modification is put forward.

Keywords: Rear underrun protection devices Accident investigation Standard modification Multi point simultaneously loading

我国货车后下部防护要求的标准研究

冯文轩 [1]，王宏雁 [1]，肖凌云 [2]，胡文浩 [2]，陈君毅 [1]
1 同济大学，上海，中国，201804
2 中国标准化研究院，北京，中国，100101
Email: fwxjlutju@163.com, why-sos@vip.sina.com

摘　要: 在我国各类交通事故中，由于道路上行驶的许多货车没有良好的后下部防护装置，造成乘用车追尾货车时，追尾的乘用车车内驾驶员和乘员伤亡的比例非常高，属于致死率非常高的恶性事故之一。本文通过对后下部防护要求的相关标准及法规的分析研究，并结合事故调查统计数据和后下部防护装置试验，提出我国标准中可以完善的地方及修改意见。

关键词: 后下部防护要求；事故调查；多点同时加载；标准修改

1 引言

轿车追尾大型货车的事故是十分严重的交通事故形态之一[1]。2001 年国家出台了 GB11567.2-2001[2]《汽车和挂车后下部防护要求》，对货车后下部防护装置的强度做出明确要求。但是在交通事故深度调查中却发现[3]，非常多的货车后下部防护装置强度不足或者没有安装后下部防护装置，导致在碰撞过程中轿车钻入货箱底部，此时轿车的前保险杠及纵梁一般不参与碰撞，正面气囊有可能不点爆。由于轿车内乘员的坐高与货车车厢底板高度相当[4]，碰撞过程中乘员头部就极有可能直接撞击货车车厢，导致严重伤亡。即使正面气囊弹出，由于轿车和货车的碰撞相容性[5]，轿车 A 柱和挡风玻璃也抵挡不了货车车厢的侵入，前排驾驶员和乘客也会因生存空间的丧失而伤亡。

2 事故调查与标准分析

自 2011 年 11 月起，国家质检总局缺陷产品管理中心先后联合国内 6 地 7 家机构开展车辆事故深度调查，启动国家车辆事故深度调查体系（National Automobile Accident In-Depth Investigation System,即 NAIS）。NAIS 借鉴了汽车工业发达国家成熟的车辆事故深度调查的做法，专注于死亡事故和车辆安全。

截止 2014 年 6 月，NAIS 采集了 95 起乘用车追尾货车的交通事故，事故共造成 134 人死亡，103 人受伤。从事故的深度分析中发现，大多数事故货车的后下部防护装置强度不足，严重变形，在发生碰撞时没有提供有效的保护作用，防止钻碰发生，如图 1 所示。

Figure 1 Accident scene
图 1 事故图片

根据实际事故调查分析，轿车追尾货车事故中主要有以下三种形态：

1、货车后下部防护装置碰撞宽度达全宽的 85%以上，且后下部防护装置双侧悬臂发生碰撞变形，这类碰撞定义为 100%重叠率碰撞。

2、货车后下部防护装置碰撞宽度约占全宽的 75%（50%、30%），且只有一侧悬臂碰撞变形，这类碰撞定义为 75%（50%、30%）重碰撞。

3、货车后下部防护装置的两侧悬臂均无碰撞变形，这类碰撞定义为小角度碰撞。

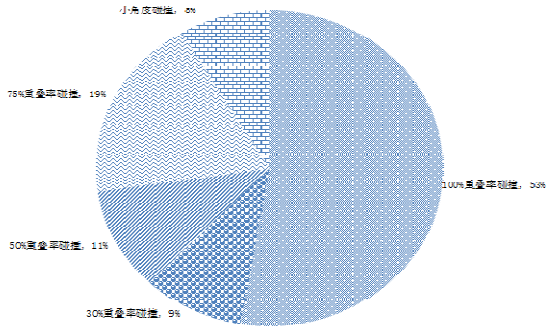

Figure 2. Analysis of Collision type（N=95）
图 2 碰撞类型分析（N=95）

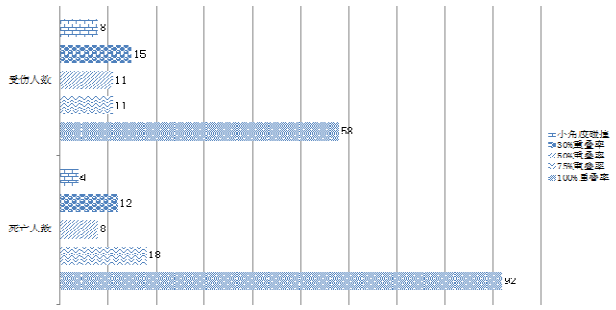

Figure 3. Analysis of injury

图 3 伤情分析

从图 2 和图 3 可发现，100%重叠率碰撞事故数量最多，占 53%，死亡人数和受伤人数亦最多（涉及到驾驶员、副驾驶员）。75%、50%和 30%重叠率事故数占比 39%，主要是事故时驾驶员紧急转向对某一侧人员造成严重伤害。小角度碰撞的事故较少，占比 8%。

载货车后下部防护装置强度不足，没有起到应有的作用，一是产品本身质量的问题，另一方面是国家标准对后下部防护装置试验载荷过低以及试验工况与实际交通事故的工况差异造成的问题。

Table 1. Regulation of the experiment load of different country

表 1. 各国标准对试验载荷的规定

法规	P1	P2	P3
GB11567.2-2001（国标）	**25KN** 或相当于车辆最大总质量 **12.5%** 的水平载荷（取两者较小者）	**25KN** 或相当于车辆最大总质量**12.5%**的水平载荷（取两者较小者）	**100KN** 或相当于车辆最大总质量 **50%** 的水平载荷（取两者较小者）
ECE R58[6]（欧标）	**50KN** 或相当于车辆最大总质量 **25%** 的水平载荷（取两者较小者）	**50KN** 或相当于车辆最大总质量 **25%** 的水平载荷（取两者较小者）	**100KN** 或相当于车辆最大总质量 **50%** 的水平载荷（取两者较小者）
FMVSS223[7]	**50KN**	**50KN**	**100KN**

对比中外相关标准（表 1）可见，欧标在进行三点加载时，加载力为车辆总质量的 1/4（车重大于 20 吨时，加载力仅为 50KN）；而国标仅为车辆总质量的 1/8（且车重大于 20 吨时，加载力仅为 25KN），国标的加载力没有欧标要求高；而美标的要求更为严格，三点加载时的加载力为 50KN，两点加载为 100KN。由此可见，国标对静态加载载荷的要求过低，因此造成企业根据国标设计生产的后下部防护装置强度相对较低，实际发生交通事故时对轿车的保护能力有限。

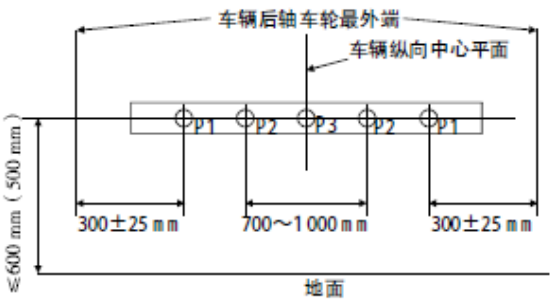

Figure 4. Position of the loading point
图 4 加载点位置

国标中规定的货车后下部防护装置静态加载试验方法是采用单点加载方式，分别对五个加载点进行静态加载（见图 4）。这种试验方法与在追尾碰撞事故中的实际受力工况（不同重叠率的碰撞）存在很大的差异，单点加载方式不符合实际钻入追尾碰撞事故过程的载荷特征和事故形态。此外，移动壁障方式的追尾碰撞动态测试试验，因费用较高，目前我国货车生产厂家基本都没有采用它来验证后下部防护装置的性能。因此，现行的 GB11567.2-2001 标准在静态加载方式和实施移动壁障追尾碰撞试验两方面必须做出改进。

3 后下部防护装置静态试验研究

在研究中分别采用国标、欧标以及多点同时加载(非标准试验)的方式进行货车后下部防护装置的静态试验。

3.1 试验准备

试验采用自主开发的货车后下部防护装置强度检测设备进行，该设备可进行整车测试或独立的零部件测试，不仅可满足国标中规定的单点加载要求，也具备更接近实际工况的两点、三点和五点同时加载测试的能力，如图 5 所示。

Figure 5. Test equipment
图 5 试验设备

试验用独立零部件进行，为连接试验设备及后下部防护装置，设计了多套工装，工装方案与后下部防护装置实际安装到车上的连接部件相同，如图 66 所示。

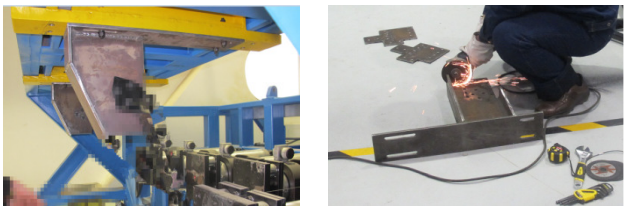

Figure 6. Tooling
图 6 工装

3.2 试验结果

3.2.1 某车型后下部防护装置三点加载试验（国标）

按照国标要求，对后下部防护装置左侧进行单点加载试验，加载力为车重的 1/8。

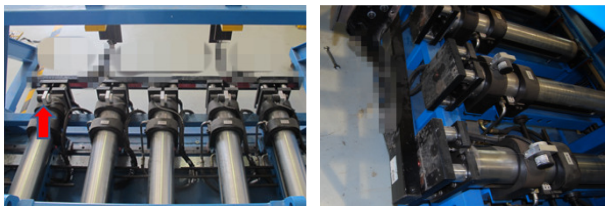

Figure 7. Experiment scene (GB)
图 7 试验图片(GB)

试验后，后下部防护装置基本没有变形。

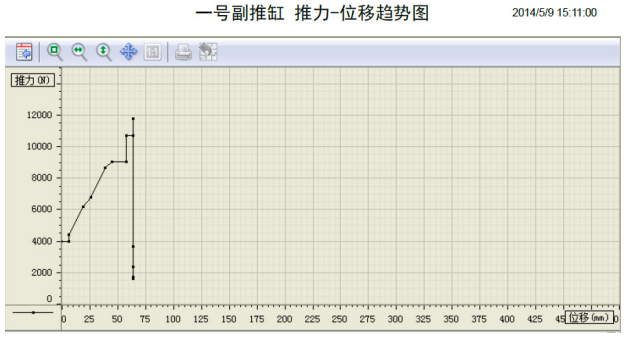

Figure 8. Experiment curve (GB)
图 8 试验曲线(GB)

按 GB11567.2—2001 规定，在做三点加载试验时，后下部防护装置应承受 10.9KN（1/8 车辆最大总质量，8890kg）的力，后下部防护装置的变形量不大于 400mm 为合格。试验时，该车后下部防护装置在承受大约 12KN 的力时，最终变形量为 65mm。根据国标判断该后下部防护装置强度合格。

3.2.2 某车型后下部防护装置三点加载试验（欧标）

按照欧标要求，对后下部防护装置右侧进行单点加载试验，加载力为车重的 1/4。

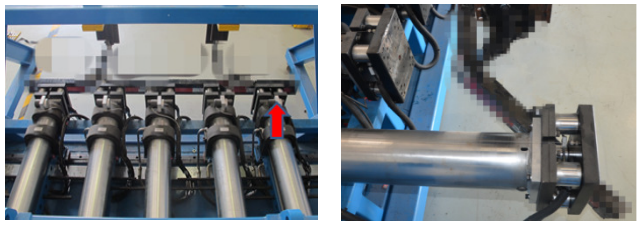

Figure 9. Experiment scene (ECE)

图 9 试验图片(ECE)

试验后，后下部防护装置发生了明显变形。

Figure 10. Experiment curve (ECE)

图 10 试验曲线(ECE)

按 ECE R58 规定，在做三点加载试验时，后下部防护装置应承受 21.8KN（1/4 车辆最大总质量，8890kg）的力，后下部防护装置的变形量不大于 400mm 为合格。试验时，该车后下部防护装置在承受大约 15.5KN 的力后达到屈服极限，最终变形量为 400mm。按照欧标判定该后下部防护装置强度不合格。

德国汽车俱乐部 ADAC 通过实车碰撞（车速 56km/h，75%重叠率碰撞）验证后下部防护装置的有效性。试验表明，后下部防护装置无法抵挡高于 56km/h 车速轿车的钻入，如图 11 所示，并且碰撞力峰值达到了 450kN，远远大于 GB11567.2—2001 中静态加载载荷的要求。

Figure 11. Experiment scene (ADAC)

图 11 试验图片(ADAC)

由此可见，国标对于货车后下防护栏的强度要求过低，主要原因是加载力要求仅为货车最大总质量的 1/8。根据实际交通事故调查和实车试验，按照这样强度要求生产的合格的后下部防护装置，在事故中也不能阻止快速行驶的轿车的钻入。所以，国标中的加载力需要有所提高。

3.2.3 某车型后下部防护装置多点同时加载试验（非标准试验）

目前多点同时加载试验在各国标准中均没有提及，在此进行初步的探究和试验。

（1）三点同时加载试验（每点加载力为车重的 1/4）

Figure 12. Experiment scene (three point simultaneously loading)

图 12 试验图片（三点同时加载）

试验后，后下部防护装置右侧和中部发生了明显变形。

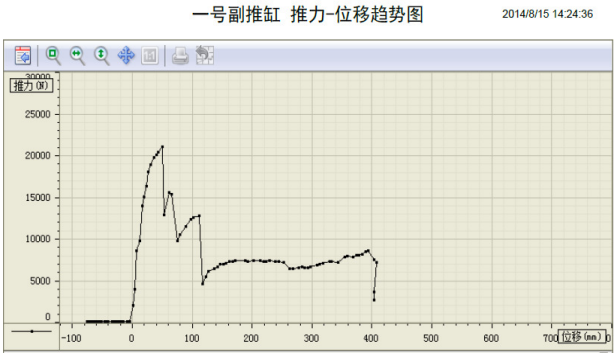

Figure 13. Experiment curve (three point simultaneously loading)

图 13 试验曲线（三点同时加载）

试验结果表明，后下部防护装置一侧变形量达到 400mm，支臂与横梁连接处断裂（见图 144），超过现行国标要求。

Figure 14. (Scene of local damage)

图 14 局部损坏图

（2）五点同时加载试验（加载力总和为 1.75 倍车重）

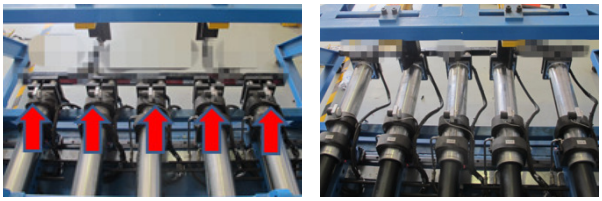

Figure15. Experiment scene (five point simultaneously loading)
图 15 试验图片（五点同时加载）

试验后，后下部防护装置整体后移。

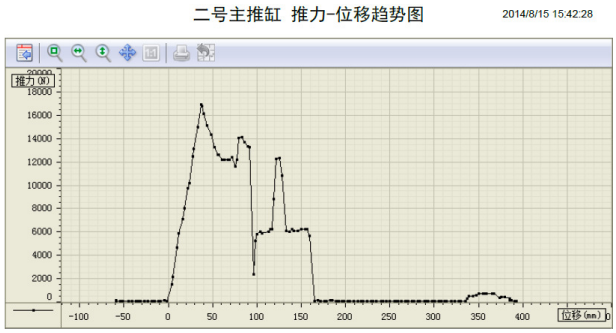

Figure 16. Experiment curve (five point simultaneously loading)
图 16 试验曲线（五点同时加载）

后下部防护装置五个加载点（其余 4 个加载点曲线与上图类似，不再赘述）最终变形量均达到 400mm，后下部防护装置左右侧连接工装的螺栓先后断裂（如图 17 所示），连接强度过低导致后下部防护装置整体后移，失去防护能力。

Figure 17. Bolt failure
图 17 螺栓剪断

3.3 试验小结

1) 从图 8 和图 10 可以发现，满足国标要求的后下部防护装置不能满足欧标要求。
2) 在进行五点同时加载试验时，后下部防护装置结构基本没有损坏，但是后下部防护装置与工装连接处的连接螺栓断裂失效，导致后下部防护装置整体后移，失去防护能力。
3) 将图 10 和图 13 进行对比分析可以发现，进行多点同时加载时，后下部防护装置变形的速度较快（曲线的斜率可以明显看出），当变形量达 40mm 左右达到了屈服极限，而单点加载则到了大约 75mm 才

到屈服极限。多点同时加载时后下部防护装置更快地失效。

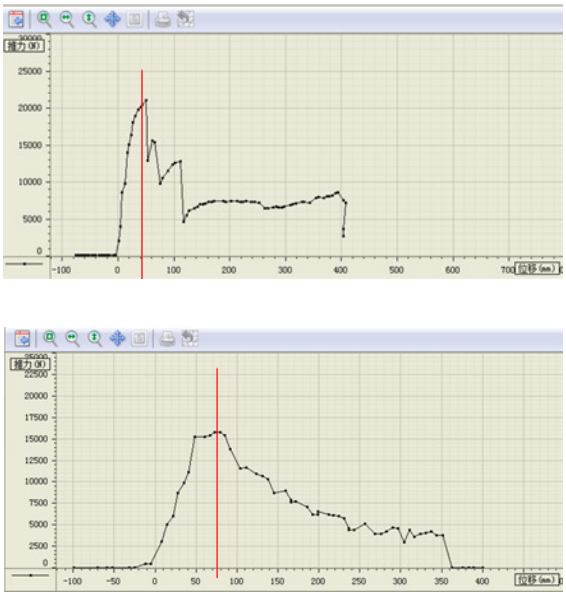

Figure 18. Comparison of experiment curve
图 18 试验曲线对比

4) 在试验过程中还发现，，GB11567.2—2001 规定，进行两点加载时，加载位置 P2 点（如图 4 所示）是由制造商自行确定的。大多数情况下，后防护栏的支臂在标准规定的两个加载点之间。为通过认证，制造商一般会选择最靠近支臂的位置进行加载，此位置强度最大。导致货车后下防护栏的整体强度并未真正满足要求。因此，GB11567.2—2001 标准附录 A 中的 A3.1.1 条款需要完善，应明确规定加载点位置。

4 国标修改讨论

1) 货车后下部防护装置的静态加载试验中，是否应将单点加载方式改为多点同时加载。因为试验表明，多点同时加载对后下部防护装置的要求更高，不仅需要装置本身有足够的结构强度，还需要装置与汽车车架连接处有足够的连接强度；并且多点同时加载的方式与实际追尾事故时后下部防护装置的碰撞受力工况更为接近。
2) 静态加载试验时，加载力是否应参考欧标及美标要求，予以增大。因为试验表明，满足国标要求的后下部防护装置不能满足欧标要求，更不可能满足美标要求，而实际交通事故深度研究的结果表明，追尾车速与欧美相当，所以，加载力的提高，强化后下部防护装置的强度要求是很有必要的。
3) GB11567.2—2001 标准附录 A 中的 A3.1.1 条款中，进行两点加载时是否应该将“作用点的具体位置由制造商给定”这样的规定，修改成有可操作性的指定位置，使得在考核后下部防护装置的真正强度时，选择的是最薄弱点进行试验，从严要求后下部防护装置的强度。

致 谢 (Acknowledgement)

在事故调查时，国家车辆事故深度调查体系（NAIS）和上海联合道路交通安全科学研究中心(SHUFO)提供了有力的数据和技术支持，使我可以顺利地进行交通事故分析。在进行后下部防护装置试验时，国家质检总局缺陷产品管理中心(DPAC)提供了有力的设备和技术支持，使我得以利用中心自主开发的设备和购

买的后下部防护装置进行多次有效的试验。在此，我向我的指导老师、NAIS、SHUFO 和 DPAC 的同事们表示最诚挚的谢意！

参考文献 (References)

[1] Zhang Yihong, Zhou Yanxuan. Analysis and Precaution Measures of Traffic Accident Caused by Rear-end Collision between Car and Truck[J]. Journal of Xihua University, Natural Science, 2006, (7).
张易红, 周廷萱. 轿车追尾碰撞货车事故分析及预防措施[J] 西华大学学报, 自然科学版, 2006, (7).

[2] GB 11567.2—2001: Requirements of vehicle and trailer's rear underrun protection[S]. Beijing: General Administration of Quality Supervision, Inspection and Quarantine of the People's Republic of China, 2001.
GB 11567.2—2001: 汽车和挂车后下部防护要求[S]. 北京: 中华人民共和国国家质量监督检验检疫总局, 2001.

[3] Cheng Yong, Zhu Xichang. Characteristics and improvement measures of vehicle passive safety of large truck[J]. Automotive Technology. 2002, (5).
程勇, 朱西产. 大型载货汽车被动安全性的特点及改进措施[J]. 汽车技术. 2002, (5).

[4] Liu Handong, Zhong Weikun. Problems and suggestions of the rear underrun protection standard of truck in China[J]. Bus tech- nology and research. 2010, 43(6).
刘翰东, 仲伟坤. 我国载货汽车后下部防护装置标准存在的问题及建议[J]. 客车技术与研究. 2010, 43(6).

[5] An Analysis on the Optimal Ground Clearance and Stiffness of Truck Under-run Protector[J]. Vehicle Engineering. 2002, 24(5).
朱西产, 程勇. 载货汽车防护装置最佳离地高度和刚度的分析[J]. 汽车工程. 2002, 24(5).

[6] Regulation No 58 of the Economic Commission for Europe of the United Nations (UN/ECE) -- Uniform provisions concerning the approval of: I. Rear underrun protective devices(RUPDs), II. Vehicles with regard to the installation of an RUPD of an approved type, III. Vehicles with regard to their rear underrun protection (RUP)) [S/OL]. Geneva, Switzer-land: UN ECE, 2008 [2008- 09- 10]. http:// www.unece.org/trans/main/wp29/wp29regs41- 60.html.

[7] 49 CFR 571.203 Rear impact guards [S/OL]. Washington, D.C: the UnitedStates Government Printing Office web site, 2009. http://www.access.gpo.gov/nara/cfr/waisidx_09/49cfr571_09.html.National Highway Traffic Safety Administration, Department Of Transportation, USA.

Proceedings of the 11th International Forum of Automotive Traffic Safety, 2014, pp 74-81
No. ATS.2014.111

Occupant Injury Analysis in Traffic Accident Based on the Coupling of PC-Crash and MADYMO

Qiang CHEN, Bing DAI
China Automobile Technology & Research Center, Beijing,China,100176
Email: daibing@catarc.ac.cn

Abstract: The study chose a typical car-to-car accident in CIDAS database and made its reconstruction simulation by using PC-Crash and MADYMO. Firstly, the initial impact velocity, yaw velocity and other information which were defined as initial boundary conditions of MADYMO were obtained by using PC-Crash program. Then the vehicle model, restraints system model (seat belts and airbag) and occupant model were modeled by MADYMO. According to output of physical injury parameters from MADYMO reconstruction, evaluation of driver injury risks was conducted based on human injury tolerances according to Euro-NCAP. The methods advanced provide a way of evaluating and analyzing the protective effect of vehicle to occupants in real accident, simultaneously, occupant injuries in accident can be studied by using the way presented in this thesis.
Keywords: Traffic Accident, Accident Reconstruction, Injury Analysis

1 Introduction

The injury caused by vehicle traffic accidents has been a common challenge globally. The statistics of World Health Organization (WHO) show that nearly 1.2 million people were killed in traffic accidents every year. As the rate of car ownership continues to increase in China and the road traffic and the speed of automobile are gradually improved, the total amount of motor traffic accidents as well as the consequent casualties and property damage have been particularly severe in recent years. The traffic accidents in developing countries like China account for 90% of the total traffic accidents in the world each year[1]. Experts speculate that if no effective measures are taken in time, the total casualties caused by traffic accidents will increase by about 65% worldwide as of 2020.

In terms of accident patterns, the car-to-car accident can be divided into different types including front impact accident, side impact accident and rear-end accident. National Highway Traffic Safety Administration (NHTSA) investigated the car accident types in major developed countries and regions such as United States, European countries and Japan, and the statistics indicated that the car accident pattern that caused the most casualties among the frequent car-to-car accidents was car-to-car front impact accident.

2 Methods and data

2.1 Accident description

The accident case studied in this thesis was selected from CIDAS database.

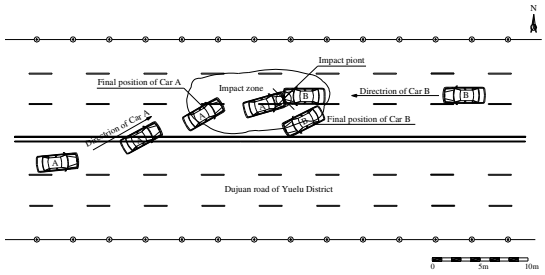

Figure 1 Sketch of car-to car accident

Figure1 shows the sketch of the car-to-car accident. When the accident occurred, Car A was travelling across the double yellow lines against the direction of traffic from west to east, while Car B was running on the right lane in accordance with the traffic rule. Car A had no chance of avoiding Car B, and the two cars smashed straight into the right front of each other. In the accident, the front parts of the two cars were damaged and the head of the driver in Car A was injured.

2.2 Accident reconstruction

The vehicle model database of PC-Crash was used to create the simulation model of car-to-car accident. On this basis, the parameters of the two cars like geometry and quality were set in combination with the practical situation of the accident. Based on the optimized reconstruction simulation, the travel speed of Car A and Car B at the moment when they collided were 46km/h and 67km/h, respectively.

In the accident, the Car A involving occupant injury was selected as the target car model. The translational acceleration in x-axis and y-axis at the center of mass and the time history of the rotation angle around the z-axis (i.e. the yaw θ) were extracted from the PC-Crash results. Since the momentum/impulse method was used in the PC-Crash reconstruction to assume that the exchange of impact occurred within an infinitesimal time step and the impact only acted on the collision center, the impact impulse of the two cars cannot be output directly. Based on the theory of average acceleration proposed by H Steffan et al[2]. and the method "using equivalent acceleration impulse to replace collision impact" proposed by Shen Jie et al[3]. were applied for parameter passing between PC-Crash and MADYMO. Based on the relationship between "impact velocity and impact duration" summarized by Liu Xueshu, et al[6]. appropriate exchange time of impact was selected according to engineering experience as shown in Table 1.

Table 1 Impact velocity and impact duration

Impact velocity (km/h)	60	70	80	120
Consumed time (ms)	80	70	50	40

The moment when the two cars reached the maximum deformation (0.120s) was selected as the moment of impact exchange. The time interval from initial collision to maximum deformation was set at 45ms. Since the PC-Crash collision center (i.e. the midpoint of contact plane when the two cars reached the maximum deformation) was defined as the position where the cars approximately reached the half impact impulse, 0.120s was regarded as the symmetric center of rectangular wave of equivalent acceleration impulse. The time window of the rectangular wave was 90ms (the interval from 0.075s to 0.165s). The time for momentum transfer was used to equalize the impact effect of the two cars.

The time interval of momentum transfer t was set as 90ms according to engineering experience. The components of momentum transfer on the x-axis and y-axis of the inertial coordinate system were calculated. The value of rectangular wave of equivalent impulse was then obtained based on the formula of impulse equation (1).

$$a_x = \frac{I_x}{mt}, \quad a_y = \frac{I_y}{mt} \quad (1)$$

Figure 2 shows the translational acceleration of center of mass of the target car A relative to the inertial coordinate system in the case that the impact effect was considered. In the figure, the value of the curve before 0.075s was the acceleration before collision. After 0.075s, the rectangular wave of impulse was added, and the time window of rectangular wave was 90ms. After 0.165s, the rectangular impact wave ended.

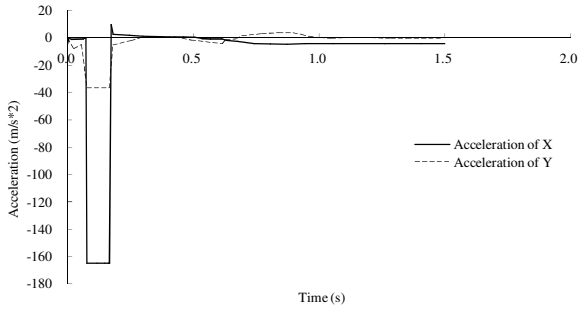

Figure 2 Acceleration curve at the center of mass of Car A

In the multibody dynamics simulation of MADYMO, ball joints are usually used to describe the yawing motion of the research object, and the Euler quaternion including q0, q1, q2 and q3 is used to represent the change of relative angles of ball joints. Based on Euler's laws, an attitude of rigid body can be realized through rotating by a limited angle θ once around a specific axis in the space (unit vector u). The rotation angle around the z-axis was defined as the car's yaw θ. Figure 3 shows the time history curve of the rotation angle of the target car's center of mass around the z-axis.

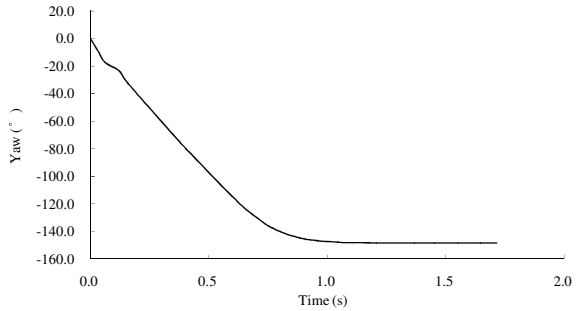

Figure 3 Time history of yaw of Car A's center of mass

Since the yaw's rotation axis of the research object was parallel to the z-axis of the fixed coordinate system in the space, the unit vector u could be represented as $u(0,0,1)$. Figure 4 shows the time history curve of yaw represented by Euler quaternion. Therefore, the initial boundary conditions including the acceleration of the car's center of mass and the time history of yaw which were input in the multibody dynamics simulation of MADYMO were obtained.

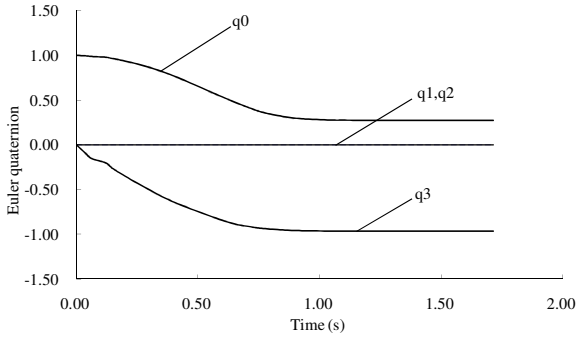

Figure 4 Time history of yaw represented by Euler quaternion

2.3 Modeling of restraint system

The devices that protect occupants in car crash are called occupant restraint system. In this thesis, based on the accident reconstruction in PC-crash, the driver-side MADYMO restraint system was modeled.

Since the equivalent impulse was added between 0.075s and 0.165s and the driver injury mainly occurred during this period, the driver's response during the 120ms time interval from 0.060s to 0.180s was selected for analysis.

The preliminary simulation of dummy positioning and safety belt should be conducted before collision simulation, because there was initial contact force between seat and dummy as well as between safety belt and dummy in the restraint system model. Figure 5 shows the initial positioning state of the driver dummy on seat after the preliminary simulation was completed.

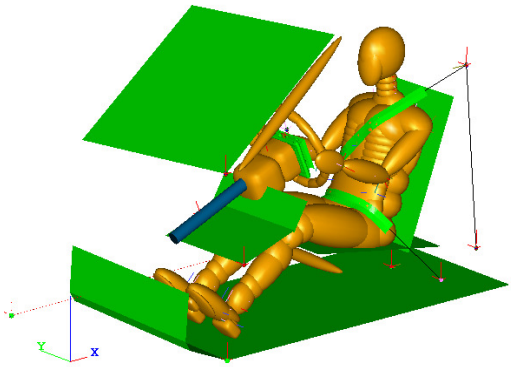

Figure 5 Initial positioning state of driver dummy after the preliminary simulation

The acceleration curve of Car A's center of mass and the yaw velocity response obtained in PC-Crash simulation reconstruction were adopted as the initial boundary conditions for driver injury reconstruction in MADYMO. In addition, a gravity field along the negative direction of the z-axis should be exerted on the restriction system.

3 Results and discussions

3.1 Discussions for risk of injury

The research on risk of injury is to simulate the overall dynamic response of human body during collision and evaluate the calculated physical damage of all parts of human body according to the corresponding injury criteria.

The Euro-NCAP damage indicator and the Abbreviated Injury Scale (AIS) were used to assess the driver's

risk of injury. The evaluation criteria for injuries of head, chest, lower limbs and neck are the main evaluation criteria in front impact.

Figure 6 shows the driver's dynamic response during collision. Based on the acceleration of Car A in PC-Crash accident reconstruction, the collision process of the two cars basically ended at 150ms. Therefore, in the reconstruction analysis of the driver's risk of injury, 0~150ms was selected as the time history of the driver's dynamic response in consideration of the car body's acceleration and yaw velocity.

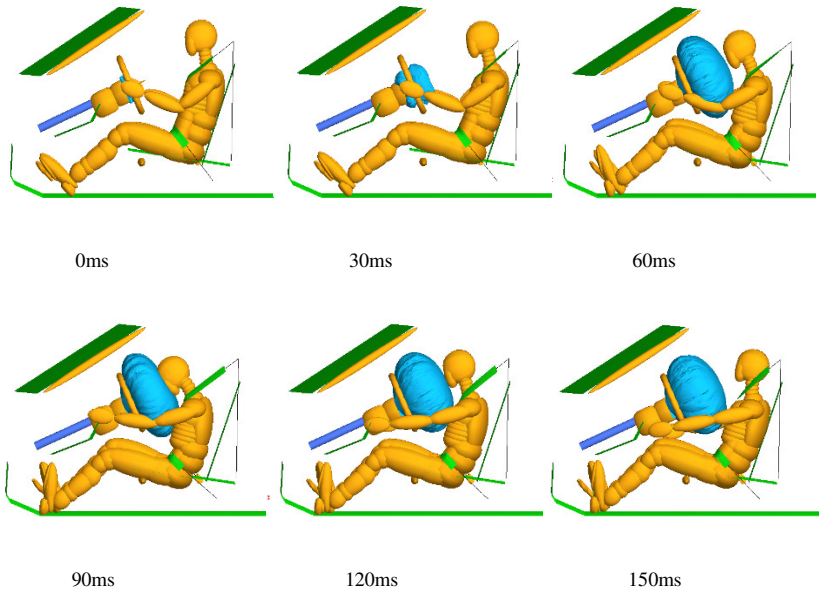

Figure 6 Driver's dynamic response during collision (t=150ms)

Figure 7 shows the time history of resultant acceleration of the driver's head; Figure 8 shows the time history of resultant acceleration of the driver's chest; Figure 9 shows the time history of deformation of the driver's chest. Based on the driver's dynamic response process and the response time history of the driver's head and chest during collision, the driver's risk of injury can be analyzed in three stages:

(1) The first stage (0-60ms). Since 10ms, the forward acceleration acted on the driver's head and chest. Due to the restriction of safety belt on the chest, there was a large difference between the motions of chest and head, and the acceleration of the chest increased more rapidly than the head. At 85ms, the acceleration of the chest reached its peak - 29.70g, and the compression of the chest also reached its peak - 26.6mm.

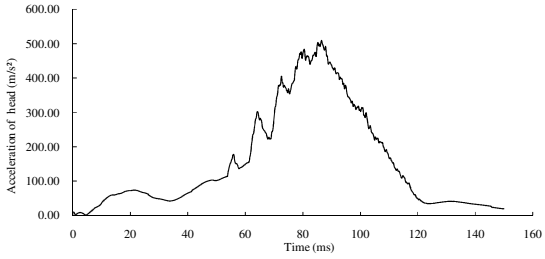

Figure 7 Time history of resultant acceleration of the driver's head

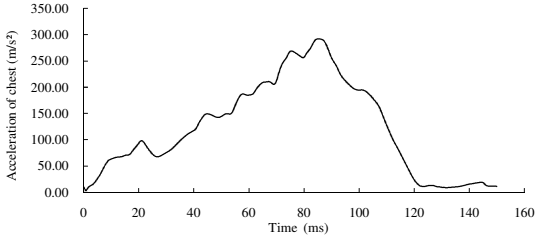

Figure 8 Time history of resultant acceleration of the driver's chest

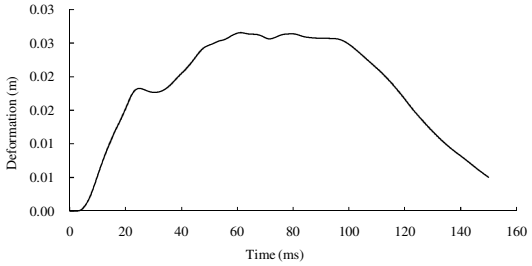

Figure 9 Time history of deformation of the driver's chest

(2) The second stage (60-120ms), in which the airbag contacted with the driver's head. At 60ms, the airbag was completely expanded. Based on the dynamic response process, the driver's head did not collide with the steering wheel due to the protection of the airbag. At 90ms around, the driver moved forward to the farthest position in the front, the peak of the head's acceleration was about 52g, and the head's HIC36 value was 351.33.

(3) The third stage (120-150ms), in which the driver was in the state of spring-back. At 150ms around, the protection from airbag and safety belt tended to be over.

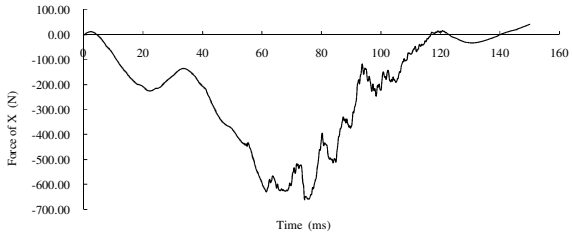

Figure 10 Time history of load on the driver's neck in the x-axis

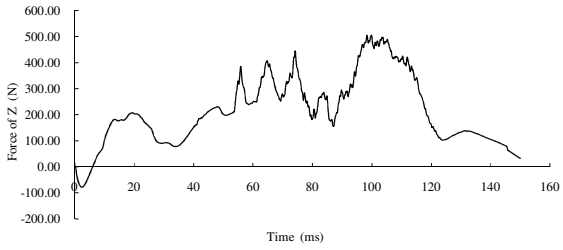

Figure 11 Time history of bending moment on the driver's neck around the y-axis

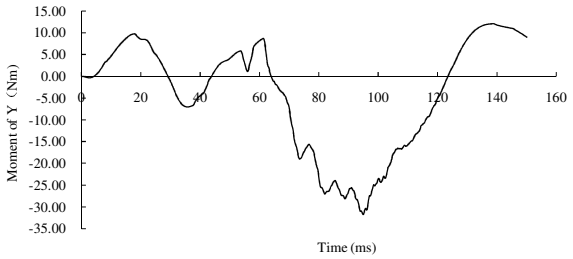

Figure 12 Time history of load on the driver's neck in the z-axis

During collision, the load and bending moment on the driver's neck are shown in Figure 10-12. Figure 10 shows the time history of load on the driver's neck in the x-axis; Figure 11 shows the time history of bending moment on the driver's neck around the y-axis; Figure 12 shows the time history of load on the driver's neck in the z-axis. Due to the restriction from airbag, the bending moment formed by the inertia of head and neck was restricted. Therefore, the time when the neck's stretch bending moment reached its peak was close to the head's acceleration phase. At 95ms around, the neck's bending moment reached its peak - 31.74Nm.

3.2 Analysis results of risk of injury

Based on the tolerance limits to injuries of all parts of human body in Euro-NCAP test requirements, the reconstruction results of injury of risk were assessed. In this case, the driver's HIC value was 351.33, lower than the value in regulations (1000), indicating the probability that the head may have the risk of injury at AIS3 or above was lower than 5%. The results suggested the risk that the head was injured in the accident was very low, which was consistent with the information in the driver's medical record and the head's injury level (AIS1) collected in the hospital where the driver was treated.

Table 2 Output of dummy's injury parameters

Injured part	Injury parameters	Injury value (peak)	Standard value in Euro-NCAP
Head	HIC36	351.33	1000
Neck	Positive shearing force on neck Fx (kN)	0.14	3.1
	Negative shearing force on neck Fx (kN)	0.93	3.1
	Tension of neck Fz (kN)	0.51	3.3
	Stretch bending moment of neck My (Nm)	31.74	57
Chest	Resultant acceleration (g) of chest at 3ms	29.4	38
	Amount of compression of chest RDC (mm)	26.6	50
	Viscosity index VC (m/s)	0.092	1.0
Lower limbs	Compressive force of thigh (kN)	1.13	3.8
	Tibia index (TI)	0.6	1.3
	Compressive force of shank (kN)	0.51	8.0

The VC value of the chest's maximum deformation was 26.6mm, lower than the specified 50mm in regulations; the chest's viscosity index was 0.092m/s, lower than the specified 1.0m/s in regulations. In addition, the injuries on the neck, thigh and shank were all lower than the corresponding injury index in regulations, indicating the risk of injury on these parts was relatively low. In motor traffic accidents, the risk of the occupant's

injury was greatly affected by the intrusion of the car body's deformation [9]. In the research, the cab was not deformed largely, so the space for the driver's survival was guaranteed. Based on the above analysis, the driver's injury in the accident was classified as mild injury (AIS1). The research results were consistent with relevant medical reports.

Table 2 lists the main injury values of all parts of the driver dummy and the standard values in Euro-NCAP.

4 Conclusions

(1) The dynamic parameters before, during and after the two cars collided were output through the accident reconstruction in PC-Crash. The reliability was verified based on the final parking positions and motion trails of the two cars.

(2) The equivalent impact impulse was adopted to obtain the impact impulse and yawing motion parameter of the car body, which were regarded as the initial input boundary conditions for reconstructing the risk of injury in MADYMO.

(3) The reconstruction model of the driver's risk of injury was set up in MADYMO. On this basis, biomechanics-related parameters of the driver's injury were calculated and the risk of injury was analyzed. The result analysis indicates that the coupled simulation and reconstruction method based on PC-Crash and MADYMO can better reproduce the driver's dynamic response process during collision. Meanwhile, it is able to provide an accurate prediction for the injured parts of driver in traffic accidents.

References

[1] PEDEN M, et al. Word Report on Road Traffic Injury Prevention. Geneva,Word Health Organization, 2004: 1-5.

[2] H. Steffan and B. C. Geigl. A New Approach to Occupant Simulation Through the Coupling of PC-Crash and MADYMO. SAE Paper, No. 1999-01-0444

[3] H. Steffan, A. Moser and B. C. Geigl. Validation of the Coupled PC–CRASH -MADYMO Occupant Simulation Model. SAE Paper, No. 2000-01-0471

[4] SHEN Jie,JIN Xian-long, Guo Lei, ZHANG Xiao-yun.The Accident Reconstruction based on Occupant Kinematics. Journal of Shanghai Jiaotong University,2006.40(6):p.963-967

[5] YangX ingmei, Yang Jikuang, LiHongjian, Hao Yumin,A Study on Child Occupant Accident Reconstruction,Automo tive Engineering,2009.31(12):525-528

[6] Liu Xueshu,Song Zhen huang,Yu Chang ji.Study on Basic Principle of Vehicle Crash[J].Tianjin Automobile,2004(3):p.22-25

[7] Mertz, H. Anthropomorphic test devices. Accidental Injury - Biomechanics and Prevention, Chapter 4. Ed. Alan Nahum and John Melvin. Pub. Springer-Verlag 1993

[8] MEYER E G and HAUT R C. The Effect of Impact Angle on Knee Tolerance to Rigid Impacts. Stapp Car Crash Journal. 2003.47: p.1-19

[9] KIRKISH S L, BEGEMAN P C and PARAVASTHU N S. Proposed Provisional Reference Values for the Humerus for Evaluation of Injury Potential. SAE Paper, No. 962416

Proceedings of the 11th International Forum of Automotive Traffic Safety, 2014, pp 82- 90
No. ATS.2014.112

Traffic Accidents Involving Child Passengers Travelling on Powered Two-Wheel Vehicles

Eloi BOIX[1], Adrià FERRER[1], Juan José ALBA[2], Sergi FERRIS[3], José A. AZPEITIA[4]
[1]*Applus+ IDIADA, L'Albornar – PO Box 20, E-43710 Santa Oliva, Tarragona (SPAIN)*
[2] *Universidad de ZaragozaC/Mariano Esquillor s/n, E-50018 Zaragoza (SPAIN)*
[3]*SafeDsign, Avinguda Catalunya 6, E-43830 Torrededembarra, Tarragona (SPAIN)*
[4]*Babyauto, C/Amezti 3 bajo, E-20800 Zarautz, Guipuzcoa (SPAIN)*
Email: eboix@idiada.com, jjalba@unizar.es, sergiferris@safedsign.eu, josean@babyauto.com

Abstract: Over recent years motorcycle sales have increased significantly. At the same time, they are by far the most dangerous means of transport. Two groups (children and elderly people) are especially vulnerable due to their physical weakness with regard to the impact, reflexes and reaction to the accident, etc. The European Commission is not aware of any specific national standard in the Member States, apart from requiring helmet use by motorcycle drivers and passengers.

The KID-SHELL project aims to design and develop a protection system addressed to children who are travelling as Powered Two-Wheel passengers. A study to analyze the state of the art of the main characteristics of the motorcycles traffic accidents where passengers between 6 and 13 years old are involved was carried out. Taking into account the traffic accidents data, a test protocol based on biomechanical references was defined in the second phase.

Keywords: Motorcycle, Children, Protection system, Accidents, Test Protocol

1 Introduction

Over recent years motorcycle sales have increased significantly. The number of motorcycles throughout the European Union increased from 16 million to more than 22 million between 2001 and 2008 [1].

Taking all powered two-wheeled motor vehicles (PTW's) into account, in 2008 approximately 33 million vehicles were registered. At the same time, motorcycles are by far the most dangerous means of transport. In 2008, according to CARE database 5,126 fatalities amongst motorcyclists (EU-24), accounted for 14% of the total 37,234 road traffic fatalities in these 24 Member States. According to CARE, two-wheeled motor vehicles account for just 2% of all road vehicles, underlining the potential risk for motorcyclists on Europe's roads.

Among PTW users, two groups (children and elderly people) are especially vulnerable due to their physical weakness with regard to the impact, reflexes and reaction to the accident. 36 children under 14 years old on PTW's were killed on Europe's roads in 2010 [2].

The European Commission is not aware of any specific national standard in the Member States, apart from requiring helmet use by motorcycle drivers and passengers.

2 PTW Accidents

In 2011, 83,027 traffic accidents with casualties were reported in Spain with 2,060 fatalities, 11,347 severe injuries and 104,280 slight injuries. These figures suppose a decrease of 16.8% of fatalities and 5.4% of severe injuries with respect to the previous year [3].

The same year, 19,093 motorcycles and 8,527 mopeds were being driven in Spain. From those, 348 motorcycles and 71 mopeds were involved in fatal accidents.

2.1 Mopeds

In urban accidents involving mopeds, 12,87% of the casualties (7,284) were passengers. 10,82% were fatalities, 9,93% were severe injuries and 13,34% were slight injuries.

The youngest injured people due to an urban accident were between 6 and 9 years old: three slightly injured children. 1 fatality, 7 severely injured and 12 slightly injured were between 10 and 14 years old.

Statistics show the youngest casualty occurred at 1 year old (one case), but also 2 cases between 2 and 5 years old and 9 slight injuries between 6 and 9 years old. 43 slight injuries and 3 severe injuries occurred between 10 and 14 years old. The most usual moped accident is a collision against other vehicle in urban environment (65,18%).

2.2 Motorcycles

In Spain, on rural roads, 8,71% of the severely injured and 11,39% of the slightly injured were passengers. In urban roads, 9,09% of the casualties were motorcycle passengers (13,584), 4,12% of them were fatalities, 7,09% severe injuries and 9,34% slight injuries.

One casualty occurred between 2 and 5 years old on rural roads. However, 5 casualties (one severely injured) occurred between 6 and 9 years old and 10 casualties (one severely injured) occurred between 10 and 14 years old. Children represent between 6% and 10% of motorcycle passengers in the urban environment in Spain. Child casualties in urban areas show alarming statistics: 2 severely and 1 slightly injured between 0 and 1 year old and 23 injured between 6 and 9 years old.

According to statistics, collisions against other vehicles are the most usual accidents in urban accidents. On the other hand, rollovers and run-off-road collisions are the most frequent on rural roads [4].

3 Aspects to be considered in a PTW accident

Although the aspects to be considered in the event of an accident are not always clearly identified, some concepts can change the consequence of each accident and should be taken into account:

- Recognition of accident scenario
- Actions of the passenger
- Kind of accident

3.1 Recognition of accident scenario

The rider should be able to determine the risk of falling off or crashing against another vehicle and the probabilities that given scenarios could occur by positioning himself/herself in a defensive way in order to protect his/her body.

However, in most crashes, the passenger does not perceive the danger in the very first moments of the accident. This situation is of particular concern if the passenger is a child due to their smaller height.

3.2 Actions of the passenger

The reaction of the passenger in the event of a PTW accident may change the severity of the injuries of the PTW occupants. The most frequent situations in which the passenger is involved are as follows:

- In some accidents, the passenger uses the body of the driver as a shield to be protected.
- The passenger is ejected and his/her initial path is guided by the back of the driver, which acts as a springboard.
- The driver partially impacts the passenger while they are sliding after they have fallen down.

- The passenger could partially impact the driver and injure him/her.
- The passenger could change the path of the driver.

3.3 Kind of accident

One of the most important issues in the event of a PTW accident is whether the occupants fell before the first impact and whether they had been positioned in a defensive way or started to decelerate due to the friction against the ground. To analyze the injury mechanism, the fall before the impact needs to be considered.

The event of a PTW accident is divided in 3 phases:

- Conflict situation: the action which causes the accident.
- Initial contact: the PTW occupants slide on the ground with or without subsequent collision.
- Engagement and disengagement, sliding or projections between the occupants or the occupants and the motorcycle.

The road and mainly the environment conditions are decisive in most PTW accidents. The obstacles that the occupants impact in the path and their protection elements (helmet, gloves, etc.) should also be taken into account.

On the other hand, the main direction and the force of the impact are used to assess the severity of both the accident and the injuries of the occupants. The most severe PTW accident is the frontal impact against another vehicle because the energies of both vehicles are added. The most common and severe PTW accidents are as follows:

- Leaving the road: Normally located in curved paths. Over-confidence in adherence, inadequate speed, lack of uniformity and regularity of the road surface, gaps in the transverse coefficient of friction of the road are usually the main causes. Four possible scenarios may be generated in straight paths:
  - Maneuver to avoid a collision
  - Distraction
  - Glare
  - Drowsiness
- Frontal impact: Three scenarios may cause this kind of impact:
  - Invasion of the opposite direction lane
  - Loss of control of the motorcycle and invasion of the opposite direction lane
  - Overtaking maneuvers
- Side impact: It mainly happens in joining lanes or in T-junctions or crossroads.
- Collision against an obstacle: The driver loses the control of the motorcycle after avoiding the obstacle or he/she was not able to avoid the obstacle.
- Rear-end collision: Different speeds between 2 vehicles which were driving in the same direction. This scenario happens particularly in traffic lights zones in the amber phase and with stop and yield traffic signals.
- Side scraping collision: It normally happens in the event of a motorcycle overtaking.
- Road accident without damage in the PTW vehicle: The passenger normally falls because of the acceleration because he/she is not gripping enough.

4 The problem of children as motorcycle passengers

In Spain, people older than 12 years old can travel (but not drive) by motorcycle if fulfil the conditions as follows:

- They use a certified helmet.
- They travel astride.
- The feet are located on the side footrests.
- They seat on the corresponding seat behind the driver.

People older than 7 years old can travel (but not drive) by motorcycle if fulfil the conditions as follows:

- The motorcycle is driven by his/her father, mother, guardian or adults who authorize them.
- They use a certified helmet.
- The points of the previous paragraph are fulfilled.

Weakness: The use of a certified helmet of child size is not mandatory for children older than 12 years, so they can use any type of certified helmet. Moreover, the use of another active or passive safety element by children is not mandatory either.

4.1 General aspects of child arm strength

From the physiological point of view, strength is understood to be the ability a muscle has to produce tension when activated.

The passenger's ability to hold on to the motorcycle supports to coordinate and equilibrate the action of the forces associated with moving is of great importance. The analysis of the needs must consider the following:

1. Strength is developed throughout childhood.
2. Muscle contraction speed in children is lower than in adults.
3. Child bone structure is more elastic due to lower calcification causing a lower resistance to pressure and shear forces.

As a general rule, motorcycle hanging supports are allocated in such a way that they are ergonomically more efficient for deceleration than for accelerating manoeuvres. This is often balanced by the fitting of a back rest as shown in Figure 1 below.

Figure 1. Motorcycle with hanging support and backrest.

As can be observed in Figure 3, the child has little options to increase the balance on the motorcycle and poor equipment. This picture is a perfect example of the non-usage of the hanging support (1) and the currently used method (2).

Figure 2. Motorcycle lacking support for passenger balance

Figure 2 shows an example of the lack of a support structure for the passenger. In this case, deceleration can cause impact against the rider and acceleration falling from the vehicle. However, the foot support may compensate the problem in the acceleration cases.

Figure 3. Example of non-usage of the provided hanging systems

4.2 Motorcyclists accidents in the city of Barcelona

Barcelona is the European city with the highest rate of PTW's per inhabitant. The flexibility in terms of mobility that this type of vehicle provides added to the favourable climate makes this vehicle one of the preferred options by the citizens of Barcelona. The Public Health Agency of Barcelona (Agència de Salut Pública de Barcelona, ASPB) has, since 1997, managed accident data of seven hospitals of the city (Hospital Clinic, Dos de Maig, Hospital de l'Esperança, Hospital del Mar, Hospital Sant Joan de Déu, Hospital Sant Pau and Hospital de la Vall d'Hebron). They cover about 85% of the city's traffic emergencies.

An analysis of data of motorcycle and moped accidents occurred between 1997 and 2011 in which children between 7 and 12 years old were involved was carried out. During the period of the study, 184 children (107 males and 77 females) were identified and met the selection criteria. So, the sample consisted of 184 cases. It is observed that the number of cases increases according to the age and the year of the study. This may be due to an increasing use of

motorcycles as transportation means by this group and because the coding of the vehicle is improving; therefore more cases can be identified.

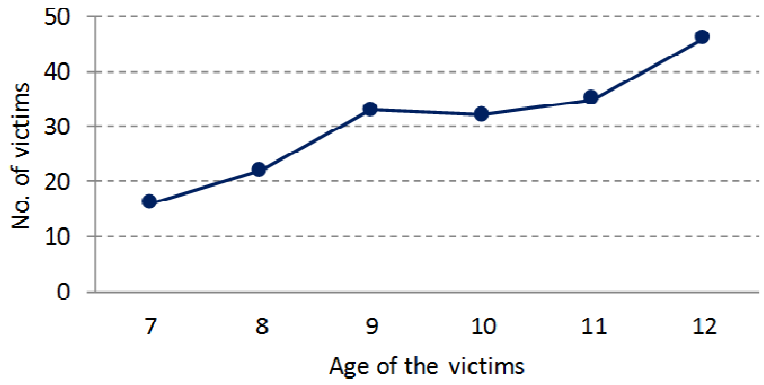

Figure 4. Casualties between 7 and 12 years old according to age

Figure 5. Casualties between 7 and 12 years old according to year

If the injuries are classified according to the Maximum Abbreviated Injury Score (MAIS), 74.1% are slight and only 1.7% are severe. The fact that the accidents occurred in an urban area means that impact velocities are lower than if they were produced on rural roads, so the consequences are not as severe.

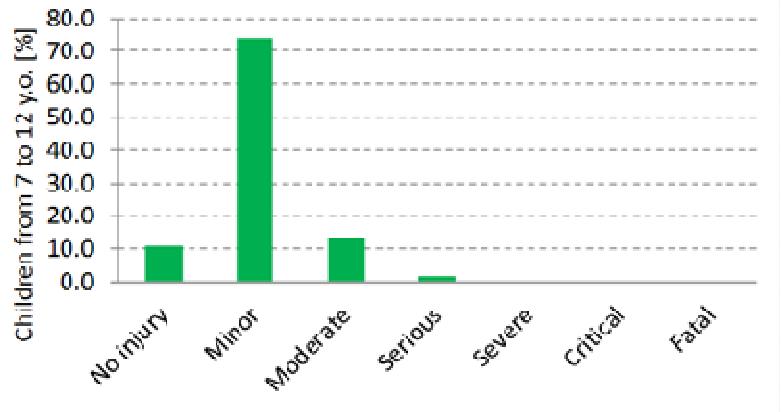

Figure 6. Casualties between 7 and 12 years old according to the MAIS

If the type of injury is analyzed, the most usual injuries are contusions (66.7%) followed by fractures (11,1%).

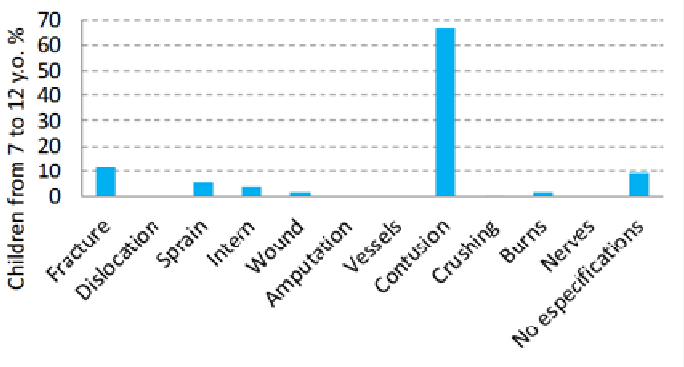

Figure 7. Type of injuries of children between 7 and 12 years old

According to body regions, extremities are the zones where most of the injuries occur (18.6% upper and 34.1% lower) followed by the head.

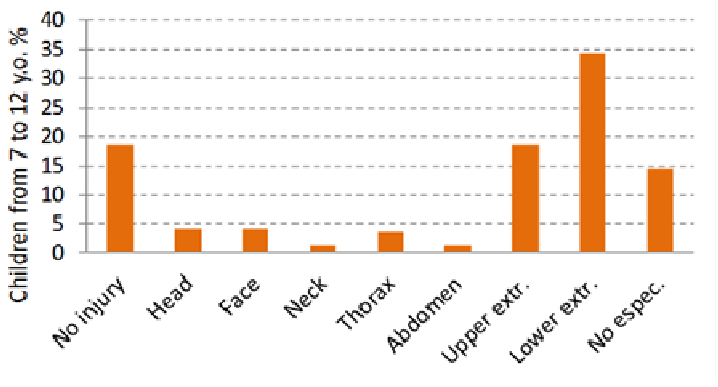

Figure 8. Body region where injuries occur of children between 7 and 12 years old

If injuries in other body regions are analyzed, 1.3% of the strains are produced in the neck, the same percentage results in the chest and 0.6% in the abdomen. 2.6% of the contusions occur in the chest and 0.6% in the abdomen. Although these kinds of injuries are less usual, they are especially important as they can seriously jeopardise different vital areas.

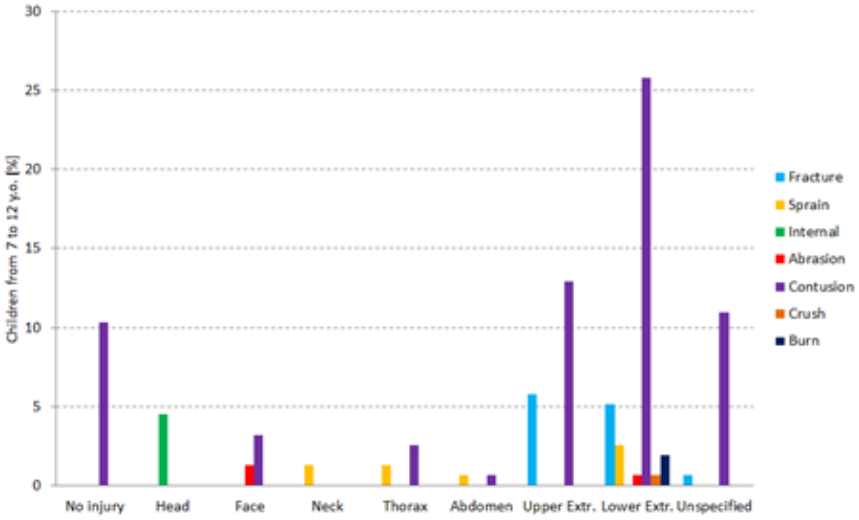

Figure 9. Body region where injuries occur of children between 7 and 12 years old according the kind of injury

In the case of injuries which do not occur in the extremities, each injury in each body region was classified according to the Barell matrix.

Table 1. Body regions (no extremities) according to the Barell matrix

Grouped Body Region	Body Region According to Barell	Type of Injury	n
Neck	Head/Face/Neck/Unsp	Contusion	5
	Cervical VCI	Sprains and Strains	3
Thorax	Chest (Thorax)	Contusion	1
		Sprains and Strains	1
	Trunk	Contusion	3
	Torso	Contusion	1
		Sprains and Strains	2
Abdomen	Abdomen	Contusion	6
	Trunk	Contusion	1

In the case of upper extremities, injured regions were classified according to the Barell matrix because they could be reduced depending on the area of the arm where they occurred.

Table 2. Injuries occurred in upper extremities according to the Barell matrix

Grouped Body Region	Body Region According to Barell	Type of Injury	n
Upper Extremities	Shoulder and Upper Arm	Fracture	2
		Contusion	2
	Forearm and Elbow	Fracture	4
		Internal	2
		Contusion	12
	Wrist, Hand and Fingers	Fracture	4
		Internal	1
		Contusion	8

2 fractures and 2 contusions occurred in shoulders and upper arms regions [5].

4.3 Testing protocol of back protection systems in PTW passengers

Based on the statistics data shown in the previous stage of the project, a testing protocol of back protection systems in PTW passengers was defined. The aim of this protocol is to compare the consequences in the zone of the back due to a PTW accident if the passenger wears a safety device or not.

The testing system consisted of one impactor and a dummy which represented the scenario where the passenger impacts against the floor with his/her back after a PTW collision. The impactor was a flat and rigid sheet and acted as the floor. The child was represented by a P-series dummy.

To achieve not only a repeatable but also a feasible test layout, the dummy will be lying down and will receive the impact from the floor.

The dummy will be impacted at an impact speed representative of PTW urban accident scenarios. The impactor's dimensions have to be bigger than the ones from the dummy. Several load cells will be placed under the dummy in order to register the transmission of the forces from the back area to the chest zone.

The tests will be carried out according to different impact angles and points to assess the areas of protection of the back device.

Finally, the results will be assessed in order to know if the safety device meets the established biomechanical limits.

5 Conclusions

The aim of this study is to know the state of the art of the main characteristics of the motorcycles traffic accidents where passengers between 6 and 13 years old are involved.

In the city of Barcelona, an analysis of data of motorcycle and moped accidents which occurred between 1997 and 2011 in which children between 7 and 12 years old were involved was carried out. Most of the injuries in children due to motorcycle accidents were slight and the most common kinds of injuries were not only contusions but also fractures. On the other hand, the body areas most frequently damaged were the extremities and the head.

People who want to transport children between these ages by motorcycle cannot find protective clothing and assume risks which they try to compensate for by decreasing the speed or adopting more cautious behavior.

Children often wear wrongly-sized helmets and rarely incorporate any additional safety clothing such as protective gloves or a jacket. One of the reasons for the lack of the use of safety clothes by children is that many families cannot afford the cost of providing the child with a special kit when he/she is growing up. Some manufacturers have tried to solve this issue by developing a grip system between the driver and the passenger. However, this product could even lead to similar trajectories between the two bodies in a fall scenario and, as a consequence, a partial risk of crushing (risk to both bodies).

A feasible partial solution could be to design and develop a device to protect the neck, shoulders, back and chest of the child in an impact scenario against abrasion and perforation. This solution would involve three key factors:

- Ergonomics: The system should be adapted to the shape of the child's back and should allow his/her mobility.
- Adjustment to child height and weight: The same system should protect a child in the period between 7 and 12 years old. The physical evolution of the child should be taken into account.
- Grip: The system should add different points of effective grip with ergonomically designed handles suitable for the pressure capabilities of child hands.

Taking into account the traffic accident data, a test protocol based on biomechanical references was defined in the second phase of the project to assess child protection systems in shoulder and back areas.

References

[1] Association des Constructeurs Européens de Motocycles. Annual report 2010 (2011).

[2] KfV (Austria), NTUA (Greece), SWOV (The Netherlands), TRL (United Kingdom), INTRAS-UVEG (Spain), IFSTTAR (France)：Annual Statistical Report 2012, DaCoTA, Building the European Road Safety Observatory, Workpackage 3, Deliverable No: D 3.9, p.49-50 (2012).

[3] Dirección General de Tráfico：Anuario estadístico de accidentes 2011, p.5, 9-11 (2011)..

[4] Instituto de Seguridad Vial del Motociclista：Análisis de riesgos de usuarios pasajeros de motocicletas, p.5-8 (2013).

[5] Catherine Pérez, E. Santamariña-Rubio：Persones lesionades per trànsit ateses a serveis d'urgències a Barcelona 1997-2012 (2013).

Proceedings of the 11th International Forum of Automotive Traffic Safety, 2014, pp 91- 99
No. ATS.2014.201

Crashworthiness Analysis of Real Small Overlap Impact (SOI) Accidents in Spain and Comparison to SOI Tests

Xavier Da SILVA[1], Adrià FERRER [1]
[1]*Applus+ IDIADA, L'Albornar – PO Box 20, Santa Oliva, Spain, E-43710*
Email: xavier.dasilva@idiada.com, adria.ferrer@idiada.com

Abstract:
Background: Recent studies identified new trends in frontal accident configurations, i.e. small overlap.
Objective: This emerging type of crash represent a higher injury risk for the occupants compared to other frontal crashes due to the small interaction of the structural energy absorption elements.
Method and Material: In response to this new accident reality, IIHS introduced a new type of crash test to evaluate crashworthiness: the Small Overlap Impact (SOI) test.
Results: The purpose of this study is to analyze the accident trend in Spain to study the changes in the overlap in frontal crashes and identify crashworthiness similarities between an SOI crash test and a real crash.

Keywords: Accident Analysis, IIHS, Crashworthiness, Small Overlap Impact (SOI).

1 Introduction

Over the last 30 years, the consumer test programs enhanced the development of crashworthiness in cars and, with lower impact, light trucks. These initiatives caused a positive response in the automakers which developed several innovative countermeasures significantly increasing the safety level of their vehicles [1].

Although, frontal impacts is the most common crash test configuration, these type of accidents still represent the largest proportion of crashes with serious and fatal outcomes in terms of occupant injury [2] and several factors were identified that are thought to contribute to fatalities of restraint occupants in newer vehicles [3,4]. For this reason IIHS performed a study on frontal crashes of good rated vehicles resulting in serious or fatal injuries[4] as despite that consumer programs are a significant contributing factor of the increase in vehicle safety, a lack of further progress incentives was identified in 2009[5].

Additionally, accident studies indicate that Small Overlap Impacts (SOI) account for a significant percentage of frontal crashes [6, 7]. SOI are frontal crashes in which the impact forces do not engage the interaction of the rails in charge of energy absorption (Figure 1).

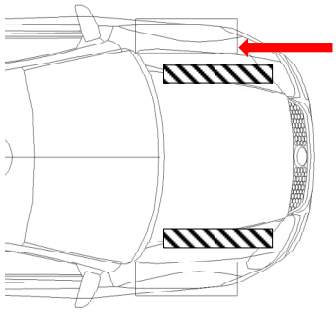

Figure 1. Example of force intrusion outside the long members

This type of crash is at least as severe as other frontal crashes. Some authors consider that the countermeasures designed for frontal crashes with more overlap may not be effective for SOI [2] as this impact configuration is not only frequent but also pose greater injury risk [7]. However, other studies observed that the injury risk is similar for other frontal crashes [1].

2 Test configurations

As a result, the Small Overlap Impact test was introduced in 2012 by the IIHS as a consumer assessment test aiming to increase the crashworthiness of vehicles in this new impact situation that was not tested previously.

In the SOI test, a vehicle is propelled at 64.4 km/h towards a rigid barrier. The test vehicle is aligned with the rigid barrier with a 25 ± 1 percent overlap between the vehicle's frontend width and the right edge of the barrier's surface. The test configuration is shown in Figure 2.

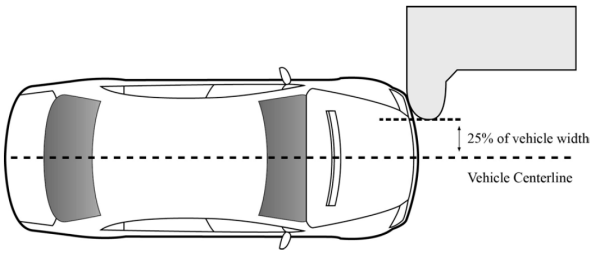

Figure 2. Small Overlap Impact Test configuration. Source:9

The side of the barrier is set back from the radius to prevent secondary contacts with the vehicle.

3 Implications of SOI test to vehicle design

Crush zones of newer vehicles manage crash energy to reduce forces on the occupant compartment but main structures are concentrated in the middle 50 percent of the front end. Small overlap frontal crashes primarily affect a vehicle's outer edges, which are not well protected by the crush zone structures.

Real accident analysis enables to determine the most common injuries occurred in these types of crashes and the main structural parts involved. The injuries can be divided in upper (head and chest) and lower (pelvis and legs) body regions [7].

3.1 Upper body region

The upper body region is the second area with the highest percentage in AIS 3+ injuries (42% for chest and 20% for head) in small overlap crashes [10]. This crash configuration frequently produce lateral motion increasing injury risk from contacts with outboard components such as A-Pillar and door [4]. This is due to the fact that this lateral motion causes oblique kinematics to the occupant influencing to the interaction with the restraint systems significantly reducing its performance.

However, there are other identified factors related to the restraint systems interaction such as steering wheel intrusion, seat belt characteristics and the airbags design [7]. The interaction of these factors is shown in Figure 4.

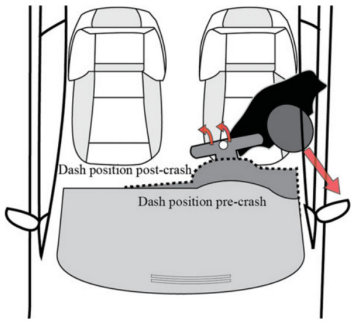

Figure 3. Interaction between the dummy lateral displacement and the dashboard intrusion. Source (7)

The oblique motion is also identified in SOI tests. As the occupant in real crashes, this crash configuration causes the Hybrid III dummy to move laterally and therefore increase the risk of head impact against the A-Pillar and steering column. In fact, in testing environment is frequent that, the most critical aspect in head and chest injury prevention is the poor interaction with the restraint systems.

However, it is know that the forward head excursion of the Hybrid III dummy it is usually undervalued due to dummy kinematics [11] for this reason, it is possible that in test cases the head contacts is being underestimated.

Additionally, the impact with the stiffest vehicle structures leave to a severe acceleration pulse and the restraint system must dissipate a lot of energy. This energy causes an increase of upper body region injury risk.

New restraint systems improvements are needed to prevent the abovementioned occupant excursion and lateral movements.

3.2 Lower body region

The most injured body region in SOI crash conditions is the knee-thigh-hip (KTH) (including pelvis). In fact, the percentage of AIS 3+ injuries in KTH is more than 70% [10] making the lower body region the most critical area in SOI.

The lateral motion of the dummy not only affects the overall performance in the upper body region but also has a negative influence in the lower part of the dummy. The dummy lateral displacement causes that the knee impact zone is not the expected in other frontal impacts. Therefore, the knee impacts in a stiffer zone increase the KTH injury risk.

Additionally, tibia and foot injuries account for AIS 2+ injuries in 36% of cases [10]. These injuries are commonly caused by the lower Instrument Panel (IP), footrest and brake pedal. In this lower area the barrier hits the wheel impacting against the wheel house and firewall. The crashworthiness of this area is very important to prevent intrusions in the lower structures. It is necessary to reduce the intrusion to prevent injuries by creating load paths to the long members, floor, subframe, door, roof and rocker panel.

3.3 Countermeasures

As previously mentioned, SOI tend to show high levels of intrusion and there is strong relationship between intrusion and injury severity [5]. The challenges posed by the SOI in terms of energy dissipation and structural intrusion suggest that improvements have to be made in order to prevent these intrusions when the vehicles is loaded outboard of the longitudinal members [2].

In the EC FIMCAR project [12] the need for improvement was also identified. It is suggested that spreading the loads in the horizontal direction is also an important factor for addressing small overlap cases.

Literature identifies two main countermeasures to increase crashworthiness in this crash configuration. One is based on a design that enables to deflect the vehicle and avoid the full engagement [1]. The second consist in modifying the structural elements to increase energy absorption [14].

3.4 Sliding collision strategy

The main differences between sideswipe and no sideswipe crashes rely on the initial impact location and the overall performance of the deformation structures. This countermeasure aims to cause a sliding motion of the car against the barrier by increasing the stiffness of the impacted structural elements to prevent the vehicle engaging.

The interaction between the crash barrier and the wheel is highly important in the general motion of the vehicle in a SOI. Depending on the stiffness of the wheel rim and the wheel supporting elements, the vehicle can deflect the trajectory causing a sliding collision. This design avoids high intrusion values but causes a high lateral motion which is very demanding for the restraint systems. Additionally, the lateral motion can also increase the risk of knee impacts in stiffer areas increasing injury risk.

3.5 Energy absorption strategy

In contrast to the previous strategy, in this case the vehicle structure is designed to absorb the crash. As mentioned previously, the wheel crashworthiness can determine the intrusion in the lower area. For this reason an efficient design of the load paths is of high importance to prevent intrusions in the occupant compartment. Developing new structural elements to use the traditional load paths and the increase of the stiffness of the most affected areas can be useful solutions to increase the crashworthiness of new vehicles.

Additionally, to provide effective protection in SOI, the occupant compartment needs to resist crash forces that are not tempered by new designed crush-zone structures and the restraint systems must dissipate the high acceleration due the stiffness structure.

4 SOI in Europe

Currently the SOI test is only implemented in IIHS consumer tests and therefore is only applicable to vehicles sold in the US market. However, Lindquist et al. [6] identified that 34% of fatal frontal crashes occurred in Sweden were SOI. Additionally, accident data from the PENDANT EC-project [16] showed that nearly 20% of the analyzed frontal crashed corresponded to an overlap lower than 25% (Figure 5).

Additionally, results from the FIMCAR project [16] using GIDAS accident data show a higher rate of fatal outcome for lower overlap rates (Figure 6).

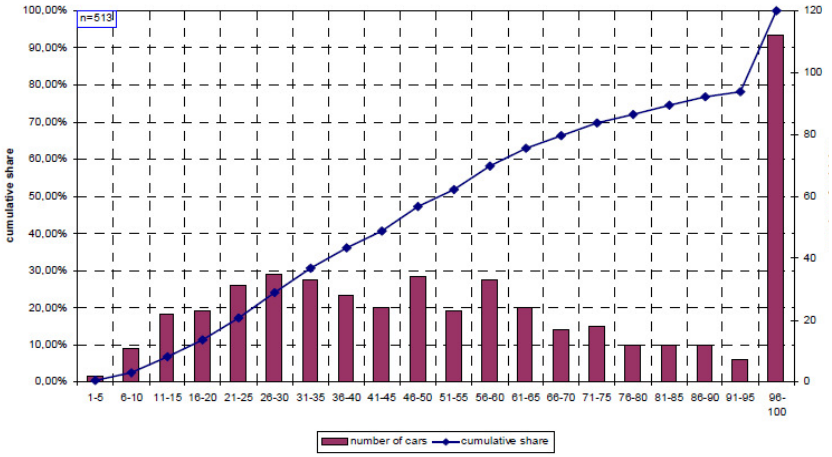

Figure 4. Level of overlap in the PENDANT cases. Source (15)

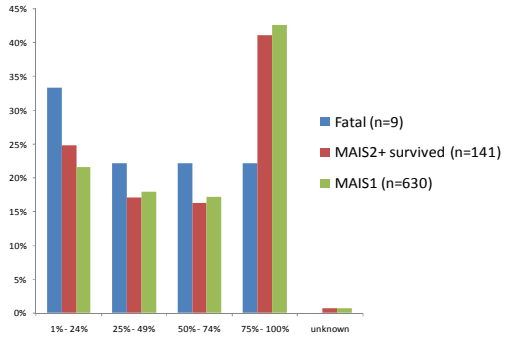

Figure 5. Outcome severity depending on the impact overlap. Source (16)

4.1 Spanish data

From publicly available Spanish accident data it is not possible to determine the frequency or risk of SOI due to the lack of injury and overlap information. However, analyzing accident records from the Spanish Traffic Administration [17] it can be observed that frontal crashes account for only 12% of total accidents but for the 38% of accidents with fatal outcome (Figure 7).

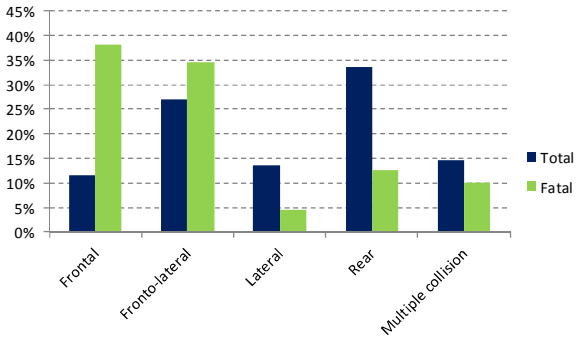

Figure 6. Crash configuration of the Spanish accidents. Source (17)

This overrepresentation indicates that further research is needed in frontal crashes in Spain and more detailed information needs to be collected to enable this research.

5 Analysis of real SOI accidents

In response of the lack of research in frontal accidents and SOI in Spain, this paper shows the result of the study of 19 frontal impacts corresponding to SOI.

5.1 Data sources and selection criteria

The Accident Investigation Team at Applus+ IDIADA gathered in-depth accident data since 1999. A total of 110 cases were made available for analysis.

The selection criterion was based on the Collision Deformation Classification (CDC) as it is a good indicator of the type of crash and extent of the deformation. However each case was individually examined through picture reports as limiting the selection to the CDC can significantly reduce the number of SOI cases[5] because when the frontal longitudinal structure is engaged it is easier to classify the crash[18] and therefore SOI can be underrepresented in CDC.

Only crashes on the left side of the vehicle were selected as all vehicles are left handled drive (LHD) and therefore the CDC codes shown in Figure 8 were selected:

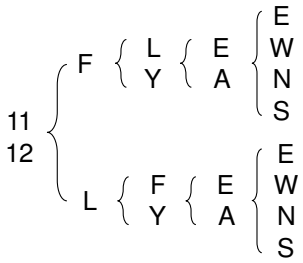

Figure 7. CDC options used for the sampling criteria

22 cases were obtained complying with the abovementioned selection criterion. However, after exhaustive analysis of the accident graphic material, 5 accidents were identified as SOI that can be well compared with the current SOI test configuration.

6 Results

The selected cases were analyzed in detail through the investigation reports and pictures. The results of this analysis are shown in this section.

First of all the different types of vehicles involved are analyzed as in laboratory crash tests, there is only one car involved and therefore there is no interaction with other structural elements from the oncoming vehicle. In the sample selected, the 70% of the vehicles are Passenger Cars (PC) which are the most testes vehicles in the IIHS SOI tests. However, there is also a 10% of Sport Utility Vehicles (SUV), Utility Vehicles (UV) and trucks (Figure 9). Although the work reflected here does not correspond to a full impaired analysis, the differences between the two involved vehicles are taken into account when analyzing the consequences of the impact.

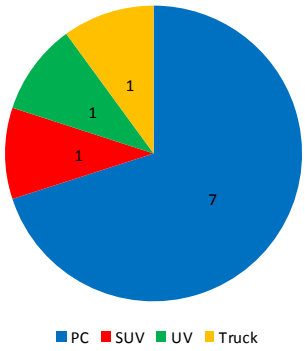

Figure 8. Distribution of the type of vehicles involved in the studied accidents

One of the most important differences between the two vehicles is the different mass. For this reason, the mass ratio was taken into account as shown in Figure 10. In four out of five cases, the mass ratio is 1±0.2 which is significantly adequate for direct comparison.

However, in the second case a mass ratio lower than 0.2 can be observed. This is due to the fact that one of the involved vehicles is the truck that was mentioned previously. The truck collided against a passenger car and therefore the difference in the mass of both vehicles is very high.

Despite this limitation, the second case was still considered for analysis as the deformation patterns that can be observed in the accident pictures show good correlation with the common patterns in crash tests. The deformation of the vehicle can be observed in Figure 11.

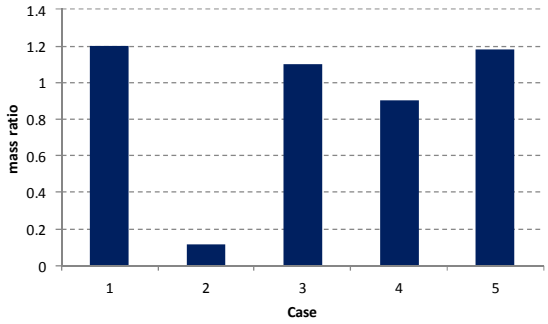

Figure 9. Mass ratio between the involved vehicles in each of the studied cases

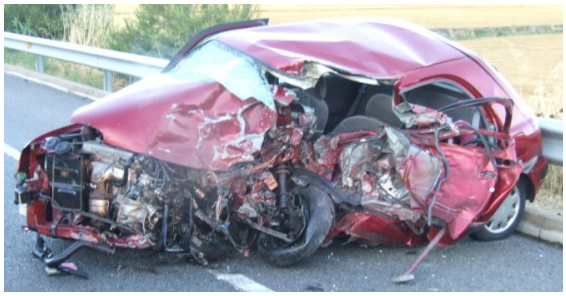

Figure 10. Final position of a vehicle involved in a SOI crash

As mentioned in the deformation patterns that are commonly observed in SOI tests, in Figure 11 it can be observed that the incoming force did not involve longitudinal structural elements causing high levels of intrusion in the driver compartment.

In all of the analyzed cases, the estimated impact speed is considerably higher than the speed in SOI tests. The calculated delta V which is commonly used to express impact severity in accident investigation are highly variable but this variability is mainly due to the second case with a very low delta V for the truck that was involved. This can be observed in Figure 12.

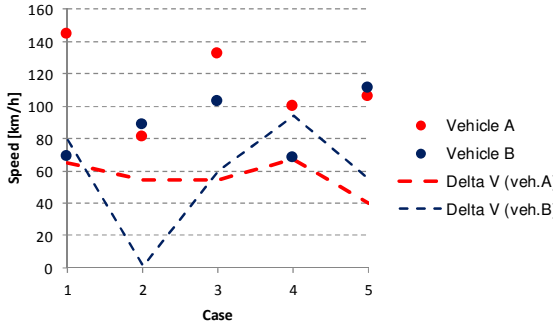

Figure 11. Impact speeds and delta V of the studied cases

Finally, concerning the injuries, all the investigated accidents had severe outcome. This is mainly due to the fact that the sampling criterion of the source database is based on fatal outcome or severe outcome for several passengers. This bias the database and therefore most of the injured passengers suffered severe injuries.

This fact can be observed in Figure 12 in which the number of MAIS 3+ injuries for the upper and lower extremities is shown. In the analyzed cases, these injuries are usually caused by the high intrusions in the vehicle due to

the impact. Additionally, lower extremities injuries is more closely related to that fact and it is also reflected in the graph of Figure 12 with an 80% of lower extremities injuries with injury severity of MAIS 3 or more.

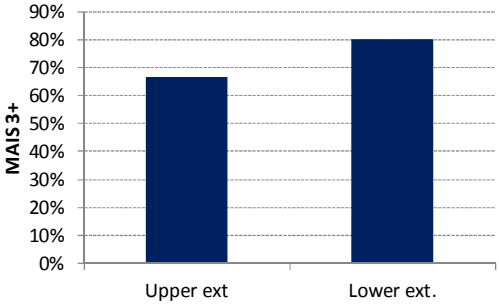

Figure 12. Level of severe injuries in the upper and lower extremities

7 Conclusions

The introduction of Small Overlap Impact tests responded to a reality observed in the United States. Some studies also show that this type of accident also occur in Europe. Additionally, these accidents are significantly frequent and pose at least the same risk than other type of frontal crashes.

The passive safety improvements achieved in the last years led to a significant reduction of fatalities in the roads. Consumer tests have been one of the main drivers for these improvements and still are by improving the current crash procedures and assessments and introducing new ones. These improvements are always connected to the accident reality or technological improvement of vehicles. This is reflected in the introduction of the SOI test in the IIHS assessment.

As abovementioned, in Europe there is also evidence of the existence of this type of accident and the extensive work carried out in the EC-funded FIMCAR project concerning frontal impact reflected that several improvements in frontal impact compatibility should be made.

However, further research must be conducted in this field to assess the suitability of the introduction of this type of crash in the European consumer assessment as the priorities must be based on cost benefit assessment and, to the knowledge of the authors; there is no research in this direction for this type of countermeasures.

Finally, with the current accident data in Spain the incidence of this type of accident nor the injury risk to the occupants cannot be assessed. Additionally, the database used for analysis is biased as it only includes a small number of cases and only with severe outcome. However, some trends such as injuries related to SOI intrusion in the occupant compartment were identified.

References

[1] Scullion, P., Morgan, R. M., Mohan, P., Kan, C. D., Shanks, K., Jin, W., & Tangirala, R. (2009). *A reexamination of the small overlap frontal crash. Association for the Advancement of Automotive Medicine.* Scientific Conference (Vol. 54, pp. 137-148).

[2] Pintar, F. A., Yoganandan, N., & Maiman, D. J. (2008). *Injury mechanisms and severity in narrow offset frontal impacts.* Association for the Advancement of Automotive Medicine. Scientific Conference (Vol. 52, pp 185-189).

[3] Brumbelow, M.L. & Zuby, D.S. (2009) *Impact and injury patterns in frontal crashes of vehicles with good ratings for frontal crash protection.* 21st International Technical Conference on the Enhanced Safety of Vehicles, paper number 09-0257.

[4] Rudd, R.W., Bean, J., Cuentas, C., Kahane, C.J., Mynatt, M. & Wiacek, C. (2009) *A study of the factors affecting fatalities of air bag and belt restrained occupants in frontal crashes*. 21st International Technical Conference on

the Enhanced Safety of Vehicles, paper number 09-0555
[5] Sherwood, C. P., Nolan, J. M., & Zuby, D. S. (2009). *Characteristics of small overlap crashes*. 21st International Technical Conference on the Enhanced Safety of Vehicles (pp. 1-7).
[6] Lindquist, M., Hall, A., & Björnstig, U. (2004). *Car structural characteristics of fatal frontal crashes in Sweden*. International journal of crashworthiness, 9(6), 587-597
[7] Sherwood, C.P. , Mueller, B.C., Nolan, J.M, Zuby, D.S. & Lund, A.K. (2013) *Development of a Frontal Small Overlap Crashworthiness Evaluation Test*. Traffic Injury Prevention, 14:sup1, S128-S135, DOI:10.1080/15389588.2013.790539
[8] Saunders, J., & Parent, D. (2013*). Repeatability of a Small Overlap and an Oblique Moving Deformable Barrier Test Procedure.* SAE International Journal of Transportation Safety, 1(2), 309-327
[9] Insurance Institute for Highway Safety (IIHS) (2012). *Small Overlap Frontal Crashworthiness Evaluation Crash Test Protocol* (version II).
[10] Rudd, R. W., Scarboro, M. & Saunders, J. (2011). *Injury analysis of real-world small overlap and oblique frontal crashes.* 22nd International Technical Conference on the Enhanced Safety of Vehicles, paper no. 11-0384.
[11] Shaw, G., Crandall, J. R., & Butcher, J. (2000). *Biofidelity evaluation of the THOR advanced frontal crash test dummy*. In Proceedings of the 2000 International IRCOBI Conference on the Biomechanics of Impact
[12] Johannsen, H., Adolph, T., Thomson, R., Edwards, M., Lázaro, I., & Versmissen, T. (2011). *FIMCAR-Frontal Impact and Compatibility Assessment Research-Strategy and first results for future frontal impact assessment.* In 22nd Enhanced Safety Vehicle Conference, paper no.11-0286
[13] Winkler, S., Bernd, F., & Willhem, B. (2001). *Sliding Collisions in Case of Frontal Crash with Small Lateral Offset*. Vehicle Safety Department/Crashsimulation, Steyr-Daimler-Puch Fahrzeutechnic.
[14] Saito, M., Gomi, T., Taguchi, Y., Yoshimoto, T., & Sugimoto, T. (2003). *Innovative body structure for the self-protection of a small car in a frontal vehicle-to-vehicle crash*.18th International Technical Conference on the Enhanced Safety of Vehicles, Nagoya, Japan, 19-22
[15] Lenard, J., (2006) PENDANT*: a European crash injury database*. 2nd Expert Symposium on Accident Research, Hannover
[16] Thompson, A., Edwards, M., Wisch, M., Adolph, T., Krusper, A., Thomson, R., & Johannsen, H. (2011). *Report detailing the analysis of national accident databases.* FP7 European Commission FIMCAR project. GA no. 234216
[17] Dirección General de Tráfico (2013). *Anuario Estadístico de Accidentes 2012*. ISSN: 1578-9446.
[18] Hill JR, Frampton RJ, Mackay M: *Appropriate Frontal Barrier Tests for Restrained Occupants*. AAAM proceedings. pp287-302, 1993

Proceedings of the 11th International Forum of Automotive Traffic Safety, 2014, pp 100- 107
No. ATS.2014.202

Vehicle Body Engineering Approach of Some SUV for Small Overlap

Derek Wu Chun-Tao, Zhang Kai, Yang Ling-Jun, Liu Zhen-Hai, Chen Xian-Ling
Great Wall Motors Co., Ltd., 071000, Baoding, China
E-mail: wuchuntao_d@hotmail.com

Abstract:

***Background*:** Small Overlap (SOL) in IIHS is aggressive for most vehicles. Most of OEMs struggled to improve the performance for SOL. The Rating of most vehicles in SOL is not reasonable, although which can rate 5 star for US-NCAP.

***Objective*:** Find feasible solutions adapted to current designed SUV to have a 'good' rating of structure assessment.

***Method and Material*:** Via Review the results of Small Overlap Oblique released by IIHS, feasible engineering solutions are concluded to have 'good' rating of structure assessment for SOL. Then it is adapted to the designed SUV. A full vehicle LS-DYNA model is generated to verify the countermeasures.

***Results*:** For most of the vehicle have 'good' rating, the following characters could be summarized: a. the vehicle pass by the rigid barrier, b. the tire will drop off the vehicle or the tire rim breaks, c. large enough curtain airbag to protect the head of occupant from impacting on hard components. the vehicle compartment deformed merely. Above key phenomena is reproduced well by the designed vehicle via employing the failure of the connections to wheel anchor and the tire rims.

***Conclusions*:** The tire dropping off or rim breaking reduce the load transferred to rocker, increase the deformable space and the deformation of vehicle body become smaller, which not only lead to 'good' rating of structure assessment, but also create the pre-condition for 'good' rating of occupant protection due to more friendly impacting pulse.

Keywords: Car body design, Crashworthiness, Small Overlap, IIHS

1 Introduction

It is known that New Car Assessment Program (NCAP) contributes a lot to improving safety performance of vehicles and which compel and encourage the OEM to dedicate in providing better protections not only to occupants but also vulnerable road users. As a reward the ratings of top vehicles will be published, which is good advertisement. It is reported that vehicles of 5 star in NCAP will have 20% more than that of vehicles with 4 star.

In 2012, IIHS in USA has released a very aggressive impacting scenario, Small Overlap, SOL[1]. The vehicle is accelerated to 40 MPH and impacts on a rigid barrier with 25% overlap, shown as figure 1.

It is totally different from the traditional frontal full width rigid wall impact and frontal offset 40% overlap barrier impact. Because that most of the vehicle designed according to the traditional impacting scenarios does neither have enough structure to consume energy nor have strong enough carbine cage to retain the loading from the rigid barrier, shown as figure 2. As a disaster, most of vehicles including top brands, such as Audi, Benz, BMW, VW, Toyota and etc., did not have a good result for SOL. To rebuild the confidence of consumers to the brands, it is must be done that their vehicle achieves a good rating or acceptable rating in SOL to have a place in IIHS as models of TSP or TSP+.

First author：Wu Chun-Tao (1981-). Dedicated in Vehicle Safety Performance Development.

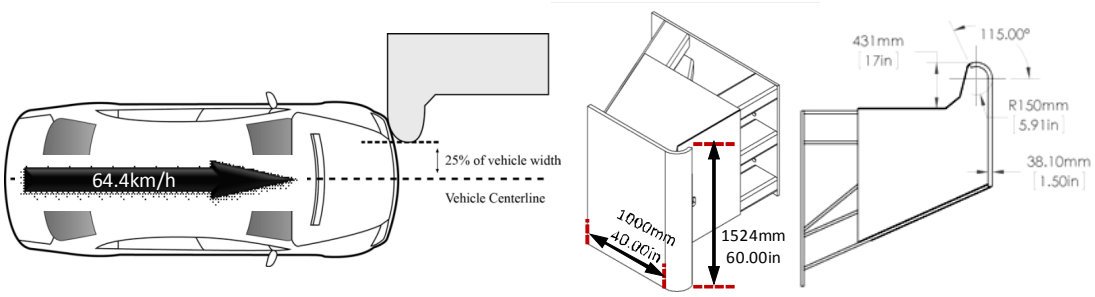

Figure 1. Impacting scenario of small Overlap

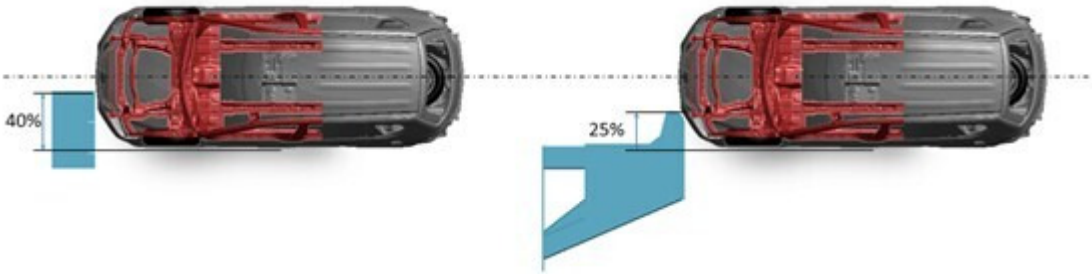

Figure 2. Vehicle Structure Overlapping with Barrier

2 Current Status and Engineering Approach

In 2012, IIHS released the first group of small overlap results in 2012, only 3 out of 33 were assessed as 'Good'. It leaded overwhelming pressure on OEMs. The safety performance of vehicles has been doubted a lot. Some of the OEMs started to complain the scenario is too aggressive and in-repeatable [2].

In 2013, the ratings of SOL are improved for most of the vehicle. Within 2014, 48 vehicles, including 9 vehicles for 2015, sold in USA could succeed 'Good' or no less than 'Acceptable' and ranked as TPS or TPS+, shown as figure 3[3].

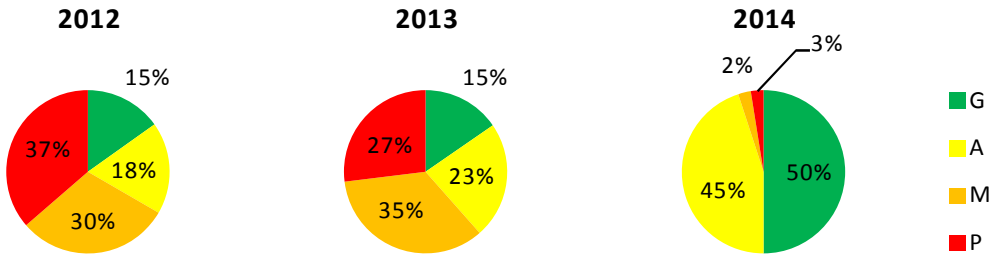

Figure 3. Small Overlap Rating Improvements by Years
(G-Good, A-Acceptable, M-Marginal, P-Poor)

After 2 years dedication work, a part of the OEMs have raped meaningful results. However, 48 vehicles ranking in TSP/TSP+ in 2014 and 2015 is about 40% of the number of TSP/TSP+ in 2013, 120 vehicles. There is a long and difficulty way for the rest vehicles to overcome.

2.1 Phenomena Observed in the released results

All the happiness is similar and the painfulness is different from each other.

According to results of small overlap in 2012, Honda Fit has the wheel disconnected from the vehicle body, which is very stiff and pushes the rocker and A-pillar deforming. It become much worse in the case of Hyundai Tucson, Toyota Camry, Honda Pilot and etc., shown as figure 4. However all of above ranked in TSP in 2012.

It can be summarized for the vehicle earned 'P' in SOL, which is called Category-A, that:

a) The wheel is attached or is not designed purposely to be disconnected from vehicle body the during the impact.
b) The rim of wheel remain undeforming, rupture or fly off the vehicle body, which will can absorb energy and reduce the loading to A-pillar and rocker.
c) The carbine of vehicle should be strong enough to minimize the deformation of vehicle body.
d) To earn 'G' as overall assessment, 'G' or 'A' for structure assessment is the precondition.

Honda Fit	BMW 3 Series	Hyundai Tucson	Toyota Camry	Honda Pilot
2012 'P'	2012 'M'	2012 'P'	2012 'P'	2012 'P'

Figure 4. Phenomena observed in vehicles with 'G' for SOL
(All the wheels disconnected with vehicle body, even rim ruptured)

According to latest results of 2014, very similar phenomena can be observed that the wheel on strut side of all vehicles have been disconnected from vehicle body and even some rim of them ruptured during the severe impact, Acura MDX, BMW 2 Series, Chevrolet Malibu for instance, shown as figure 5.

Acura MDX	BMW 2 Series	Chevrolet Malibu	Mini Cooper Countryman	Volvo XC60
2014 'G'	2014 'G'	2014 'G'	2014 'G'	2014 'G'

Figure 5. Phenomena observed in vehicles with 'G' for SOL
(All the wheels disconnected with vehicle body, even rim ruptured)

It can be summarized for the vehicle earned 'G' in SOL, which can be called Category-B, that:

e) The wheel can be removed off from the vehicle body during the impact.
f) The rim of wheel can deform, rupture or fly off the vehicle body, which will can absorb energy and reduce the loading to A-pillar and rocker.
g) The carbine of vehicle should be strong enough to minimize the deformation of vehicle body.
h) To earn 'G' as overall assessment, 'G' or 'A' for structure assessment is the precondition.

2.2 Theoretically Analysis

Kapil Butala and etc. studied the occupant injuries due to different categories of vehicle pulse based on reasonably correlated MADYMO models, shown as figure 5[4]. They concluded that the category 2 is more friendly to occupants: HIC15 50% reduced, Chest Deflection 15% reduced.

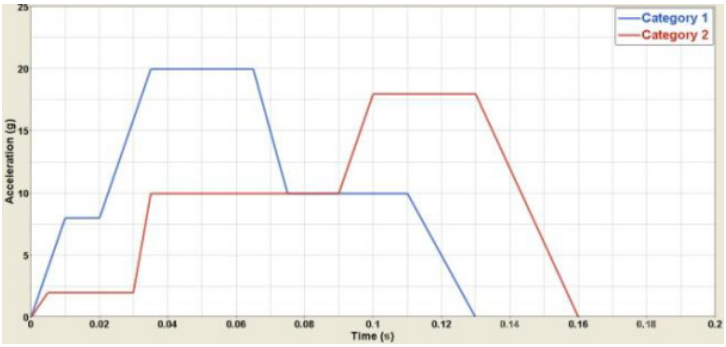

Figure 6. Simplified Acceleration versus Time Data based on Vehicle Categories[4]

Normally, the wheel rim of SUV is about 500mm. Considering the rotation and deformation, the undeformed wheel rim will take space about 450mm. Comparing with Category-A, Category-B will have additional 350mm deformation space, which result in a quite different pulse of vehicle for Category-A from that of Category-B theoretically, as shown in figure-7, if the same kinetic energy is dissipated by structural deformation. The pulse of Category-B will be much better than that of Category-A regarding to occupants protection. It will benefit the vehicle better performance in SOL wholly.

Simply, the loading to side structure will be reduced dramatically, about 40% reduced. This results in a complete different approach to earn 'G' in terms of structure performance: without weight penalty, the vehicle performs perfectly by designing realistic failure of knuckle assemble, which allows the wheel flying off.

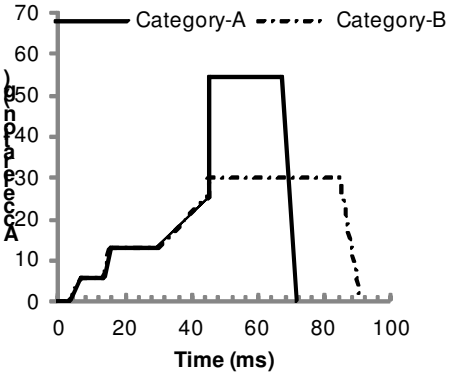

Figure 7. Vehicle impacting pulse due to failure of wheel knuckle assembly
(Category-A: vehicles without failure design; Category-B: vehicles with good failure design)

3 Engineering Approach

Based on above analysis, a SUV is designed in purpose of failure for wheel flying off from vehicle body to minimize the loading to side structure of vehicle, having a better performance and earning overall 'Good' assessment in SOL definitely.

3.1 Failures of Connections of Frontal Wheel to Knuckle Assembly

For common passenger vehicles, the frontal wheels are linked and attached to vehicle body by several connections: wheel to knuckle, knuckle to steering bar, knuckle to damping strut, knuckle to transmission shaft, and knuckle to swing bar, examples shown as figure 8.

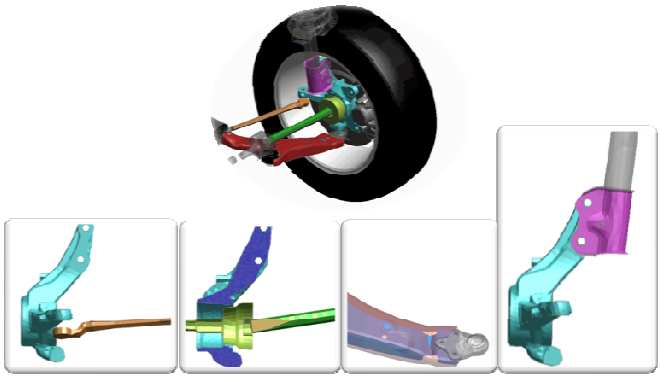

Knuckle to Steering bar | Knuckle to transmission shaft | Knuckle to Swing Bar | Knuckle to Strut

Figure 8. Connections of frontal wheels to vehicle body

If all of above connections fail or rupture during the impact, the wheel will fly off the vehicle body. Knuckle to steering bar is connected with a sphere joint, which can be disconnected if the loading to above the permit load, so does the connection between knuckle to transmission shaft and that of swing bar to knuckle. The connection of knuckle to strut may fail due to rupture of bolts or the damping bar dragged out of the sleeve, when the barrier push the tyre away from the vehicle body. In addition, Wågström studied oblique car-to-car impact by LS-Dyna Simulation in 2012[5]. The wheel rim is modeled with failure material, the tyre has ventilation and separation capabilities and the bushing is modeld with solid rubber elements representing the real structure to predict the response more accurately. Due to lacking the testing data of the connections, arbitrary time-dependent failures are set in the model.

3.2 Vehicle Response and Performance

The SUV studied has a complete and advanced structure in terms of safety. The fine designed body can earn 'Marginal' of structure assessment according the rating protocol of small overlap[6], which means body frame is advanced. With the state-of-art simulation technology, the failure of wheel connections is integrated to vehicle model successfully and the wheel can fly off from the vehicle body, shown as figure 9. The assessment of structure performance is upgraded from 'M' to 'G', shown as figure 10.

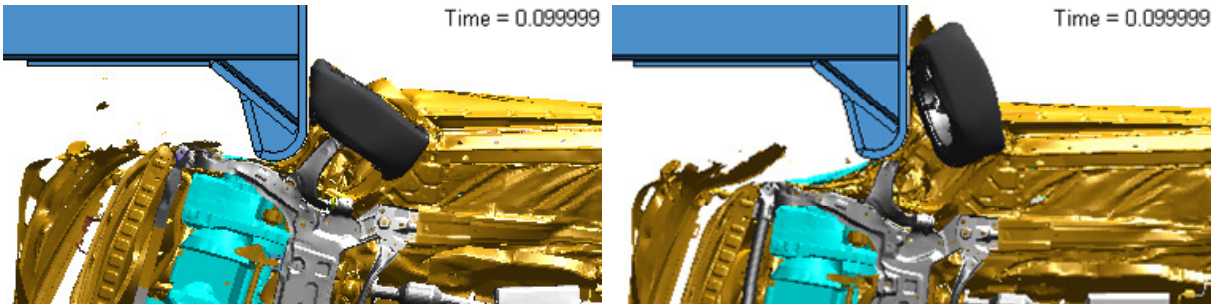

a) Without failure of wheel assembly **a) With failure of wheel assembly**

Figure 9. Comparison of vehicle deformation due to failure of wheel

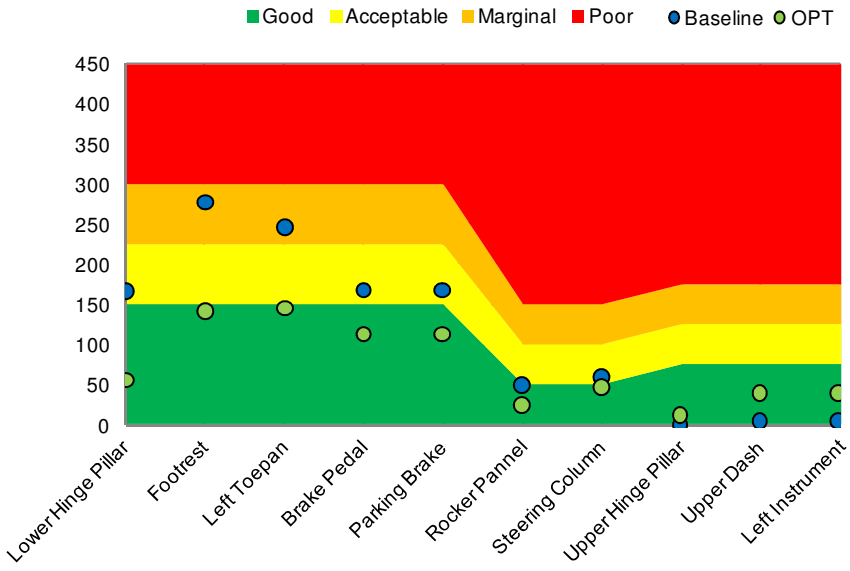

Figure 10. Comparison of structure assessment due to failure of wheel

The vehicle pulse become friendlier indeed, which has the similar trend as the prediction of theoretically analysis. Although the peak of the pulse is not improved a lot, there is some residual velocity, which means the vehicle can pass the barrier by after the impact, shown as figure 11. This lead to the total energy dissipated by vehicle body reduced by 6% and the work done by the barrier is reduced by 12%, which decrease the demand of the side structure of vehicle body.

Table 1. Comparison of Structure assessment of Some SUV due to Failure

Cases	Final Vx	Final Vy	Final KE -X	Final KE -Y	Energy Dissipated	Δ Momentum
	m/s	m/s	J	J	J	kg/m/s
Baseline	-3.17	3.23	10035	10403	299542	35.66
OPT	1.72	5.89	2947	34687	282346	20.56
Δ%	-154%	83%	-71%	233%	-6%	-42%

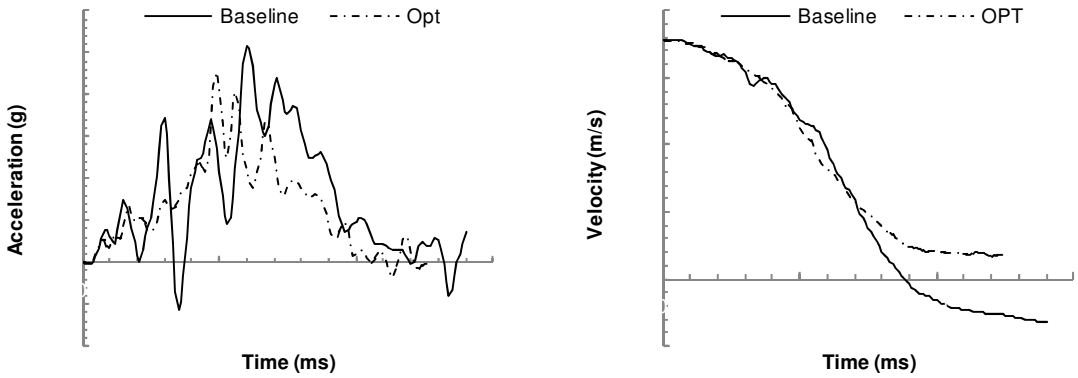

a) Vehicle deceleration vs. time

b) Vehicle velocity vs. time

Figure 11. Comparison of vehicle response due to failure of wheel

Without enhancing the vehicle body by adding reinforcement, increasing the gauge or upgrading material grades, the vehicle body can earn 'Good' assessment of structure only by considering the failure of the wheel connections, which contribute to weight reduction and worth of the full vehicle.

4 Discussions

Small overlap is a common accident scenario, which may happen by 24% in American [7], 25% in Germany [8]. Within domestic, although it is not reported officially. According to fatalities reported by WHO[9], estimated death rate of per million population is about 205 in traffic accidents. If the domestic frequency of SOL in accidents is assumed as 25%, it is estimated that 51 people per million populations will die due to small overlap in real accidents.

That is part of reason why Domestic authors investigated in SOL[10] and seek solution for full vehicle development recently[11][12] and got prepared for it.

It is can be foreseen that related regulation, standards or protocols would be released in the near future in China, considering the benefits to the consumers and harmonies of societies.

Hence, the key to vehicle structure performance for SOL will benefit the rest assessment of SOL in default, Injuries Criteria and Restraints and Dummy Kinematics. According to results released by IIHS, the vehicle having 'A' or 'G' of structure assessment will probably has 'A' or 'G' of overall assessment in 95%, 3 out of 71 vehicles, shown as figure 12.

However, it is reminded that the restraints system for SOL should have large Curtain Airbag, which interact with Driver Airbag and stably protect the head from impacting to the hard component in cabinet [11].

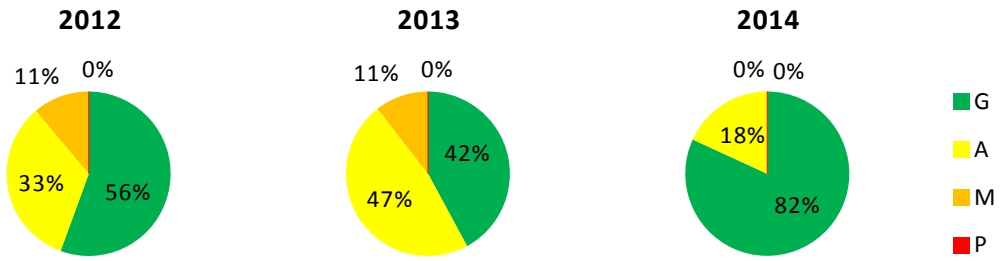

Figure 12. Vehicle rating for SOL with 'A' or 'G' of structure assessment

5 Conclusions

Small overlap is not only common (25%) in accidents but also fatal. The scenario promoted by IIHS has lead the requirement and demands of passenger vehicles for it. Although, most of traditional vehicles can not comply with it and failed to achieve a 'Good' rating. So far, it can be observed that some of the OEMs have done their best according to current results released by IIHS. There is a easier way to survived in small overlap:

1. Vehicle is designed with failure of knuckle assembly to vehicle body in purpose.
2. The side structure should be stiff enough to maintain the compartment deforming as little as possible.
3. The curtain should be large and stiff enough to interact with driver airbag and providing good protection to the head.

There is a day, when domestic vehicles rank top place of vehicle safety.

Acknowledgement

It should be thanked to assistance provided by the whole of team members of safety performance of vehicle engineering in GWM.

References

[1] Insurance Institute for Highway Safety (IIHS). Small overlap crash test protocol. http://www.highwaysafety.org.

[2] Becky C. Mueller, Christopher P. Sherwood, Joseph P. Nolan, and David S. Zuby. *Repeatability of IIHS Small Overlap Frontal Crash Tests*. Paper no. 13-0079. Proceedings of the 23th ESV International Technical Conference.

[3] Insurance Institute for Highway Safety (IIHS). Ratings. http://www.highwaysafety.org.

[4] Kapil Butala, David Gotwals, Ravi Tangirala, Kurt Shanks. Occupant Behavior in Small Front Overlap Event – A Parametric Study. Paper no. 13-0135. Proceedings of the 23th ESV International Technical Conference.

[5] Linus Wågström. LS-DYNA Simulations of oblique car-to-car frontal impacts. Proceedings of LS-DYNA Nordic Users' Forum 2012.

[6] Insurance Institute for Highway Safety (IIHS). Small overlap rating protocol. http://www.highwaysafety.org.

[7] Sherwood C P, Nolan J M, Zuby D S. Characteristics of small overlap crashes [C] Proc the 21th Int'l Tech Conf on the Enhanced Safety of Vehicles, Germany, 2009, Paper No. 09-0423.

[8] Matthias Kuehn, Thomas Hummel and Jenoe Bende. Small-Overlap Frontal Impacts Involving Passenger Cars in Germany. Proceedings of the 23th ESV International Technical Conference. Paper no. 13-0370.

[9] World Health Organization. World report on road traffic injury prevention [R]. Geneva: WHO 2012.

[10] CHEN Keming, HU Lijuan, HU Yanshu. Small-overlap frontal-impact assessments for a vehicle made in China. J Automotive Safety and Energy, 2013, Vol. 4 No. 1, 027-034.

[11] Liu Zhenhai, Qiao Leilei, Yue Guohui, Chen Xianling. Simulation Research and Optimal Analysis for Small Overlap Frontal Crashworthiness of a Real Car. Journal Automotive Safety and Energy, 2012, Vol. 3 No. 4, 339-346.

[12] Cui Dong, Xie Shugang, Yan Xiaoxiao, Hou Yanjun. The Differences Between IIHS 40% Overlap Crash and Small overlap Crash in the Requirement of Body Structure. Proceedings of 2013 China SAE Automotive Safety Conference, 2013-CNST043, 722-726.

Proceedings of the 11th International Forum of Automotive Traffic Safety, 2014, pp 108- 114
No. ATS.2014.203

The Simulation and Analysis on Electric Vehicle'S Front Impact

CUI Shujuan[1],CHEN Keming[1],CAO youqiang[2],DONG hongliang[2]
(*1.Vehicle Safety Technology and Research Center,China Automotive Engineering Research Institute Co.,Ltd,*Chongqing 400039,China
*2. NVH Research Center China Automotive Engineering Research Institute Co.,Ltd,*Chongqing 400039,China)

Abstract: The purpose of this article is to study an electric vehicle crash performance by using finite element vehicle model which is modified from traditional fuel vehicle.It was found that the modified vehicle model has worse vehicle acceleration and more firewall instrusions than those of an original fuel vehicle.The integrity of cells may not be maintained for the modified electrical vehicle.Then the optimal design scheme is reached by three rounds' optimization and design. Crash safety of the electric car can be improved significantly by adding structure between the bumper and battery and applying hot forming material to bumper frame instead of ordinary steel. By calculating, these optimizations can strengthen the crashworthiness of the vehicle effectively.
Key words: electric vehicle; crash worthiness; buffer

某电动车正面耐撞性优化分析

崔淑娟[1]，陈可明[1]，曹友强[2]，董红亮[2]
（1.中国汽车工程研究院股份有限公司 汽车安全技术研究中心，重庆 400039，中国
2.中国汽车工程研究院股份有限公司 NVH技术研究中心 重庆 400039，中国）

摘要： 本文研究的是基于传统燃油车改装的一款纯电动汽车，需要其正碰性能满足国标法规。采用有限元分析方法研究得知，改装后的基础电动车在正面碰撞过程中，B柱加速度和防火墙侵入量过大，电池的完整性差。从结构和材料两方面出发，经过三轮优化，最终确定优化设计，即在前防撞梁和前置电池之间增设缓冲吸能装置，最大程度地降低了B柱加速度和防火墙的侵入量，从而提高了该电动汽车的碰撞安全性。
关键字： 电动汽车;碰撞安全性;缓冲吸能

1 概述

为了应对能源短缺、环境污染等问题，从节能环保角度出发，对电动汽车的研究和应用越来越广泛和迫切。作为面向大众的消费品，其安全性是汽车制造商必须要面对的现实问题[1]。通常来说电动汽车的质量比传统燃油车大很多，并且储能电池等大质量块的质量要占到整车质量的 20%以上，这些大质量块通常都是刚性不易变形体，在碰撞发生时，对乘员的伤害很大。除此以外，电池前置的电动汽车在正碰中，电池很容易受到直接撞击、挤压，从而产生严重变形，导致电池壳体破裂、电池漏液甚至爆炸等问题[2]。因此，在研发电动汽车时，碰撞安全分析是非常重要的。

本文研究的电动汽车是基于传统燃油车改装的，由于加装电池组使得车辆自身重量增加，在碰撞中的能量增加，所以改装成电动汽车后其碰撞安全性需要验证[3]。本文所分析的改进后的纯电动汽车正碰性能应满足国标《GB11551-2003 乘用车正面碰撞的乘员保护》相关要求。

2 有限元模型

2.1 基础车有限元模型有效性验证

基于等效性原则，首先对原燃油基础车的有限元模型进行 50km/h 工况下正面刚性壁障碰撞仿真分析，将仿真碰撞结果与 ssssss 实车正面刚性碰撞试验结果进行对比，以验证本文模型的有效性。使用 Hypermesh 软件进行前处理，LS-DYNA 软件进行求解分析。

从整车变形来看，翼子板和发动机罩变形模式和程度接近，左侧 A 柱车门均无明显变形。对于关键吸能零部件变形对比，以左前纵梁为例，前纵梁前端均充分压溃，中段折弯部位一致，变形模式相同，如图 1 所示。另外，从图 2 的左侧 B 柱加速度值对比来看，二者趋势一致，峰值误差在一定范围内，所以认为该有限元模型真实有效，可以用于后续分析。

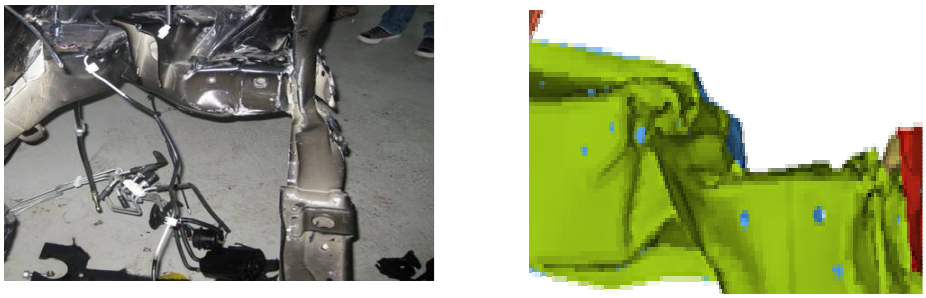

(a) 实验结果　　(b)仿真结果

图 1 正面碰撞整车前纵梁变形

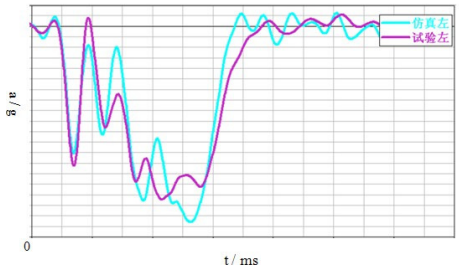

图 2 正面碰撞左侧 B 柱加速度试验仿真对比

2.2 电动汽车有限元模型建立

本文搭建了一款以轮毂电机为驱动系统的底盘平台，通过控制驱动电机的转速来控制车速，采用独立整体框架结构方式固定电池组。为充分利用车辆空间，改装后的电动汽车的动力电池分为前后两箱，分别安置在原发动机位置和车身底板下方（行李舱的位置），如图 3 所示。新增的电池在前舱占据了大量的可变形吸能空间。

模型总质量共计 1380kg，包括车辆整备质量、两个前排 50 百分位假人及燃油质量。模型以 50km/h 的速度正面碰撞刚性墙。模型中点焊采用 Beam 单元，缝焊、CO_2保护焊、铆接、螺栓连接以及铰接采用刚性连接，不考虑失效。模型中重力场的施加采用*loadbody 关键字[4]。

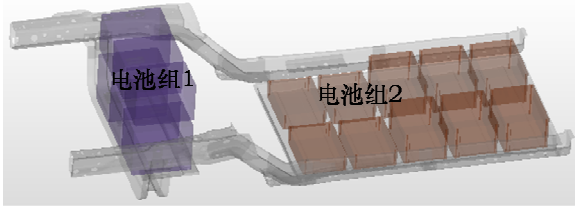

图 3 电池组位置示意

汽车碰撞过程表征了一个能量守恒、动量交换的瞬态过程，只有小部分动能以热能等其他能量形式耗散掉，因而碰撞过程中的总能量是基本保持不变的，大致应等于总内能和总动能之和。沙漏能、滑移能、质量增加均在 5%以内[5]。如图 4 所示，该仿真模型能量变化均在有效范围之内

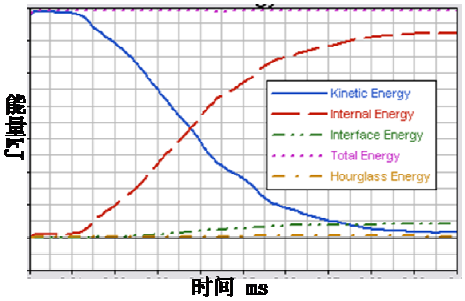

图 4 能量曲线

2.3 电动汽车仿真分析结果

电动汽车的电池组安装位置较原车发动机沿轴向靠后，与防火墙之间的距离减小，如图 5 所示。在发生碰撞后，由于电池包安装支架较弱，与前纵梁和前围板的连接都不稳定，造成电池包后端安装支架与防火墙直接接触，而电池包整体受压，向后推动防火墙，引起接触部位发生较大变形。电动车的防火墙仿真最大侵入量相较于原车有所增加，防火墙挤压变形产生褶皱，防火墙的变形将直接影响乘员舱生存空间。

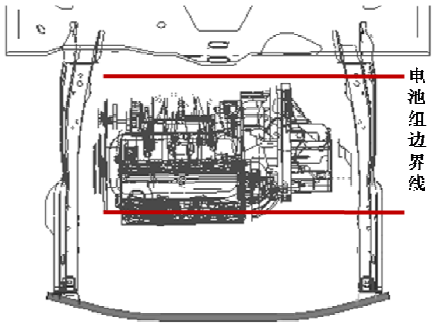

图 5 电池组在前机舱位置示意图

前纵梁变形严重，前端呈现压溃的变形模式，后端纵梁发生弯折变形，左右前纵梁变形形式基本一致，如图 6 所示。

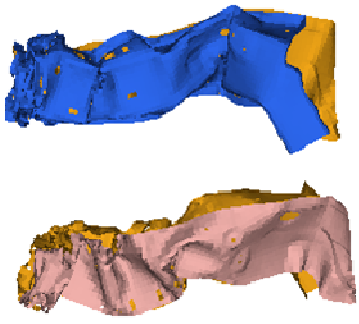

图 6 电动车前纵梁变形图

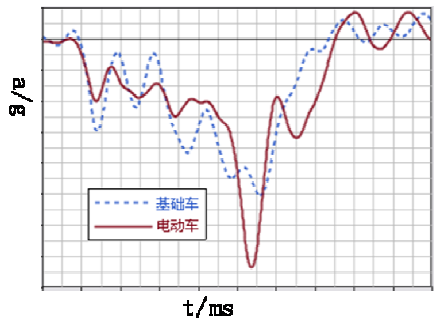

图 7 基础车与电动车左侧 B 柱加速度曲线

B 柱加速度是整车碰撞试验过程中的一个重要测试参数，它对假人头部的损伤值(HPC)具有非常重要的参考作用，是车辆耐碰撞性能的一个重要参数。纯电动车左右两侧 B 柱加速度最大值明显增大，峰值出现时刻大致和基础车相同，而且左右侧基本同时出现峰值，较原车偏大了很多，对乘员造成的伤害极大。针对加速度峰值偏大，而波形前段加速度整体偏小，表明车身前段结构吸能不足，加强车身前段结构吸能能力是下一步优化方案重点考虑的内容，降低加速度峰值是目标优化重点。

3 电动汽车设计优化仿真

3.1 设计优化方案

当电动车辆发生正面碰撞时，为保护车内乘员及电池组的安全，根据汽车碰撞损伤机理可知碰撞车辆应满足以下条件：

1） 要保证乘员足够的生存空间，即乘员舱不应发生过大的碰撞变形（包括电机、变速器等刚性部件不得侵入驾驶室）。

2） 除乘员舱以外的车体结构部分应尽可能多的变形，以尽可能的吸收撞击能量，使得作用于乘员身体上的力和加速度值不超过人体的耐受极限。

3） 电动汽车质量与同类型的燃油汽车相比一般要大，这就决定了在同样的碰撞速度下，电动汽车的吸能装置需要吸收更多的动能，从而对电动汽车的吸能装置和部件提出了更高的要求。

传统车正面碰撞的传力路径分为上中下 3 层，防撞梁、吸能盒、前纵梁、发动机舱上边梁(shotgun)、副车架为主要吸能部件。并依次向后将力分散传递至 A 柱、车门防撞梁、门槛梁，如图 8 所示。在正面碰撞中，这些部件基本可以吸收 50%的能量。

碰撞过程中，将各部分吸能区域进行划分：

$$E_0 = \frac{1}{2} m v_0^{\,2} = E_1 + E_2 + E_3 ,$$

$$E_i = \frac{1}{2} K_i \Delta D_i^{\,2} ,$$

其中：E_0为初始动能；E_1、E_2、E_3分别为前部结构、乘员舱和可变形壁障的变形量；m 为汽车质量；v_0为初始速度；$\triangle D_i$(i=1,2,3)分别为前部吸能部件平均挤压变形，乘员舱平均挤压变形，可变形壁障挤压变形；K_i(i=1,2,3)分别为 3 者等效纵向刚度[6]。

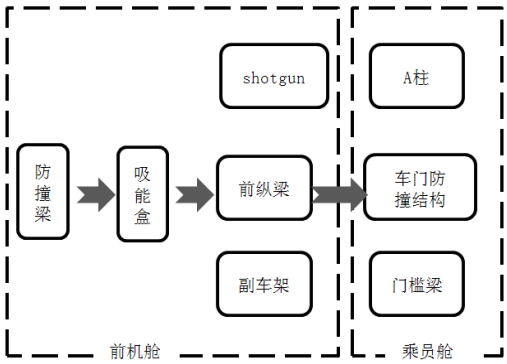

图 8 传统正面碰撞传力途径

从本文研究车体自身结构出发，并结合工程实际，通过分析可知防撞梁吸收能量较少，防撞梁和纵梁之间空间紧凑，没有安装吸能盒，对于在燃油车基础上改装的电动车对其内部空间结构的调整受限较多，而对于关键吸能零件前纵梁不能做结构改动，只能考虑在其内部增加加强件，然而，通过前期仿真验证，其对碰撞吸能效果改进不佳。所以从以下三个方向做具体修改。

a) 原车前防撞梁结构单薄，仅有上下两根圆管承担受力，其对纵向受力吸能效果不佳，修改前防撞梁结构，截面采用常见的口字形结构，并提高其材料的屈服强度。

b) 在修改后前防撞梁结构和前纵梁之间安装吸能盒。

c) 前机舱结构紧凑，通过替换原燃油车水箱散热器部分结构，在前防撞梁和电池组之间预留一部分空间以增加吸能通道（安装时需合理避让已有零件）。增加的吸能管在压溃变形过程中吸收的能量可以通过载荷-位移历程曲线的积分得到：

$$E=\int_{S_i}^{S_b} FdS = F_{mean}(S_b - S_i) = F_{mean}\Delta l$$

式中：S_b、S_i分别为吸能管的最终破坏点和起始破坏点；F_{mean}为平均载荷；Δl为有效压缩长度[7]。

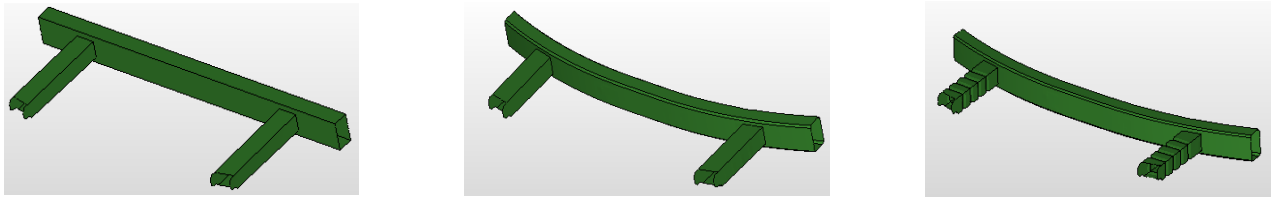

方案 1 **方案 2** **方案 3**

图 9 吸能结构设计优化过程

优化方案的参数对比见表 1

表 1 吸能结构材料参数优化过程

		方案 1	方案 2	方案 3
吸能管	厚度	1.6mm	1mm	0.7mm
	材料屈服强度	198MPa	198 MPa	129MPa
横梁	厚度	1.6mm	1.6mm	1.6mm
	材料屈服强度	198 MPa	534 MPa	534 MPa

如图 9 所示，进行了 3 轮优化。方案 1 的结构设计致使其在吸能纵向容易失稳，因此方案 2 在方案 1 的基础上将横梁改成曲面，并修改材料屈服，改变吸能管厚度，这样首先保证了横梁结构变形的稳定性，其次保证了整个吸能部件在碰撞过程中的承载力和变形次序。然而，方案 2 的结构设计中吸能管在碰撞前期发生折弯，并没有起到充分吸能的作用，因此方案 3 进一步在方案 2 的基础上在吸能管上沿碰撞方向加压溃槽，起到了很好的导向作用，并修改其材料及厚度。

3.2 仿真优化结果

通过三轮优化仿真分析，确定方案 3 为最终优化方案。该方案的主要吸能部件吸能比例之和比原电动车主要吸能部件吸能之和增加约 8.5%。增加的吸能部件有效且安全的吸收了更多的能量，如图 10 所示。

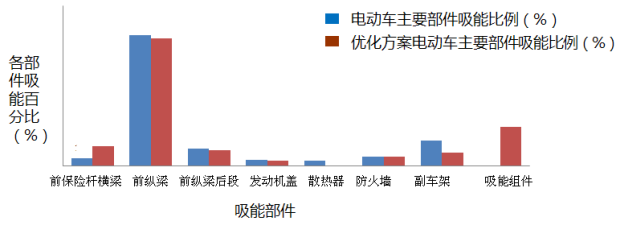

图 10 优化方案与原电动车吸收能量对比

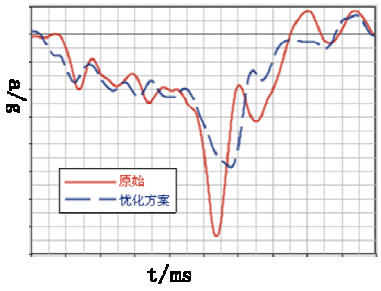

图 11 优化方案 B 柱加速度曲线

从图 11 可看出，设计优化重点目标左侧 B 柱加速度值相较于原电动车明显降低，对应乘员头部的损伤得到保护。前纵梁及吸能部件变形模式良好，充分压溃，电池组整体在碰撞纵向受到挤压，但变形量小于原电动车，车体的防火墙侵入量及 A 柱、转向管柱、踏板变形均在目标设定范围内，满足国标要求。

4 结论

本文首先根据试验结果和仿真结果的对比情况验证了仿真模型的有效性。其次分析了改装后的电动车的正面耐撞性，相比于基础燃油车，B 柱加速度，防火墙侵入量均明显增大，并且安装在前机舱的电池组发生严重挤压。根据车型结构特点，规划载荷路径分配，从结构和材料两方面出发，经过三轮优化设计，得出最优的设计方案：在防撞梁和电池之间增设吸能结构，并修改前防撞梁结构，使用热成型高强度钢材料，最大程度地降低了电池自身的加速度和防火墙的侵入量，纵梁的变形模式稳定，电池变形很小[8]。仿真计算结果表明，该方案提高了该电动汽车的碰撞安全性。

参考文献

[1] Brown S.Pyke D.Steenhof P.*Electric vehicle:the role and importance of standards in an emerging market*[J]. Energy Policy,2010,38:3797-3806.

[2] WANG Dazhi，YU Chengxiang. Frontal crashworthiness structure design of mini electric passenger cars [J]. *JAutomotive Safety and Energy*, 2010, **1**(1)：49-52. (in Chinese)
王大志，于成祥. 微型电动汽车正面碰撞结构耐撞性设计[J]. 汽车安全与节能学报，2010, **1**(1)：49-52.
[3] WANG Kai，LI Xiangrong，BAI Peng，Electrical safety of electrical vehicles in crash tests [J]. *J Automotive Safety and Energy*, 2012, **3**(1)：34-37. (in Chinese)
王凯，李向荣，白鹏. 电动汽车在碰撞试验中的电气安全[J]. 汽车安全与节能学报，2012, 3(1)：34-37.
[4] HU Yuanzhi，ZENG Biqiang，XIE Shugang. *Based on LS-DYNA and HyperWorks simulation and analysis of automotive safety* [M]. Beijing：Tsinghua University Press，2011. (in Chinese)
胡远志，曾必强,谢书港. 基于 LS-DYNA 和 HyperWorks 的汽车安全仿真与分析[M].北京：清华大学出版社，2011.
[5] JIANG Zhaojuan. *The research on several key technologies of electric vehicles crash safety*[D].Dalian university of technology, 2012.5 (in Chinese)
姜兆娟.电动汽车碰撞安全性若干关键技术研究[D].硕士学位论文：大连理工大学，2012.5
[6] CUI Shujuan，CHEN Keming. *Simulation and structure optimal analysis for small-overlap frontal-impact of a vehicle* [J]. J Automotive Safety and Energy, 2014, **5**(2)：139-144. (in Chinese)
崔淑娟，陈可明.某车型小重叠碰撞仿真及车体结构优化[J]. 汽车安全与节能学报，2014, 5(2)：139-144
[7] JIAN Xiaochun，WANG Xiao.*Simulation of crashworthiness during front impact and offset impact and vehicle body structure improvement* [J]. J Automotive Safety and Energy, 2011, **2**(3)：212-216. (in Chinese)
简晓春，王笑.正面和偏置碰撞的耐撞性仿真与车身结构改进[J]. 汽车安全与节能学报，2011, 2(3)：212-216.
[8] HOU Yongkang. *Research in simulation of electric vehicle's front collision based on ls-dyna*[D].Hefei universityof technology, 2012.5 (in Chinese)
侯永康.基于 LS-DYNA 的电动汽车正面碰撞仿真研究[D].硕士学位论文：合肥工业大学，2012.4

Proceedings of the 11th International Forum of Automotive Traffic Safety, 2014, pp 115- 121
No. ATS.2014.204

Real Solutions for Safety in L7e Vehicles

Eloi BOIX [1], Aritz ESNAOLA [2], Óscar CISNEROS[3], Juan José ALBA[4], Massimiliano AVALLE[5], Alessandro SCATTINA[5], Pawel JARCZEWSKI[6], Ewa WYSGA[7]

[1]*Applus+ IDIADA, L'Albornar – PO Box 20, Santa Oliva, Spain, E-43710*

[2] *CIDIA - Mondragón Automoción S. Coop., Uribarri Etorbidea 19, Arrasate-Mondragón, Spain, E-20500*

[3] *Centro Zaragoza, Ctra. N-232, Km.273, Pedrola, Spain, E-50690*

[4] *Universidad de Zaragoza, Mariano Esquillor s/n, Zaragoza, Spain, E-50018*

[5] *Politecnico di Torino, Corso Duca degli Abruzzi 24, Torino, Italy, 10129*

[6] *PIMOT, ul. Jagiellonska 55, Warszaw, Poland, 03-301*

[7] *BELLA, ul. Gdańska 2, Czosnów (near/Warsaw), Poland*

Email: *eboix@idiada.com*

Abstract:

***Background*:** The European Commission co-funded OPTIBODY project (Optimized Structural components and add-ons to improve passive safety in new Electric Light Trucks and Vans - ELTVs) is focused on ELTVs that are worldwide homologated as N1 and N2 vehicles and, in Europe, also include the L7e category.

***Objective*:** The OPTIBODY vehicle is based on a new structural concept for ELTVs composed of a chassis, a cabin and a number of specific add-ons. As seen in the results of the Euro NCAP tests, these vehicles have very high fatality ratios when impacting other vehicle categories.

***Results*:** To improve the safety of this kind of vehicle, its main chassis structure was designed and special attention was paid to the frontal add-on and the composite crash boxes designed for Vulnerable Road Users (VRU) and frontal impact protection.

Keywords: Quadricycles, L7e category, Passive Safety, ELTVs, Euro NCAP tests

1 Introduction

The latest trends in the automotive industry show an increase in the demand for dedicated vehicles. For this reason, more and more manufacturers have started developing and producing vehicles specifically for urban usage that are more maneuverable and practical. Although the number of EVs (Electric Vehicles) is not very significant yet, it is expected that in the 21st century they will replace vehicles relying on the internal combustion engine, especially in the Light-Duty Vehicles category [1].

In the particular case of Electric Light Trucks and Vans (ELTVs), most of them adopt the powertrain lay-out used in classic internal combustion engine vehicles and very conservative solutions and technologies are used in their development. For instance, the current EVs rely on lighter structures than internal combustion engine vehicles, which optimize energy consumption, and this partially solves the issue of operational autonomy, one of the biggest drawbacks related to this type of vehicle.

The development of electrical vehicles enables engineers to work on improving safety issues that were impossible to solve in the past. This is possible as a result of the improved structure and mainly because of the free space left after removing parts that are no longer necessary as a result of the replacement of internal combustion engines.

The main purpose of OPTIBODY is to improve the passive safety of ELTVs in order to reduce the number of fatalities and the severity of the injuries.

2 Definition of Quadricycles

2.1 European Regulation

The European Regulation classifies quadricycles in two groups according to their mass, speed and power:

L6e: light quadricycles

L7e: heavy quadricycles

2.1.1 Light Quadricycles (L6e)

Light quadricycles (L6e) are defined by Framework Directive 2002/24/EC as: "motor vehicles with four wheels whose unladen mass is not more than 350 kg, not including the mass of the batteries in case of EVs, whose maximum design speed is not more than 45 km/h, and:

whose engine cylinder capacity does not exceed 50 cm3 for spark (positive) ignition engines, or

whose maximum net power output does not exceed 4 kW in the case of other (e.g. diesel fuelled) internal combustion engines, or

whose maximum continuous rated power does not exceed 4 kW in the case of an electric motor. "

These vehicles shall fulfil the technical requirements applicable to three-wheel mopeds of L2e category unless specified differently in any of the separate Directives [2].

2.1.2 Heavy Quadricycles (L7e)

L7e are defined by Framework Directive 2002/24/EC as motor vehicles with four wheels other than those referred to (as light quadricycles), whose unladen mass is not more than 400 kg (category L7e) (550 kg for vehicles intended for carrying goods), not including the mass of batteries in the case of EVs, with a design payload not more than 200 kg (passenger) or 1000 kg (goods), and whose maximum net engine power does not exceed 15 kW. These vehicles shall be considered to be motor tricycles and shall fulfil the technical requirements applicable to motor tricycles of category L5e unless specified differently in any of the separate Directives [2].

The European Parliament and European Council passed a regulation governing market surveillance for two and three-wheeled vehicles as well as quadricycles, including environmental protection and safety measures, which will be implemented on January 1, 2016.

3 Assessment of heavy quadricyles

A New Car Assessment Program is a car safety program tasked with evaluating new automobile designs for performance against various safety threats. Its mission is to provide consumers a realistic and independent assessment of the safety performance of vehicles recently launched in the markets [3].

Euro NCAP publishes safety reports on new cars, and awards 'star ratings' based on the performance of the vehicles in a variety of crash tests, including front, side and pole impacts, and impacts with pedestrians. The top overall rating is five stars. Euro NCAP is concerned with best possible current practice and provides a continuing incentive by regularly enhancing its assessment procedures to stimulate further improvements in vehicle safety. To determine the real safety level of these kinds of vehicles, Euro NCAP has designed an L7e test protocol and assessed four different models.

3.1 Euro NCAP Test Protocol for L7e vehicles

The test protocol consists of two crash tests which represent the sorts of accidents that quadricycles might be involved in when driven on public roads.

Frontal crash:

Impact angle: 0º

Impact speed: 50 km/h

Overlap: 100%

Barrier: Deformable barrier face (300 mm)

Side crash:

Impact angle: 90º

Impact speed: 50 km/h

Barrier: ECE 95

The scoring is based primarily on dummy numbers, but penalties are given for poor performance of the structure or restraints. However, no capping is applied in the assessment. The maximum score for each test is 16 points, but no sum and no combination of score between tests is applied.

3.2 Test results

These tests are different from Euro NCAP's normal procedures and, while the results of the quadricycles can be compared with one another, they cannot be compared with the star ratings published by Euro NCAP for passenger vehicles [4].

Table 1. Specifications of the tested quadricycles.

Vehicle	Seats	Power source	Kerb weight	Maximum speed
Renault Twizy 80	2	Electric motor	474 kg	80 km/h
Tazzari Zero	2	Electric motor	542 kg	100 km/h
Club Car Villager 2+2 LSV	4	Electric motor	541 kg	35 km/h
Ligier IXO JS LINE 4 Places	4	505 cm^3 petrol	465 kg	70 km/h

Figure 13. Renault Twizy (top left), Tazzari Zero (top right), Club Car Villager (bottom left) and Ligier IXO (bottom right).

All of the quadricycles tested showed critical safety problems, although some fared better than others in the front or side impact test. The vehicles tested were type-approved and met the minimal safety requirements set by European legislation for L7e heavy quadricycles. Consumers, however, should note that quadricycles in general offer a significantly lower level of occupant protection than is offered by cars.

4 Design of the OPTIBODY vehicle

The OPTIBODY vehicle was designed taking into account both the maximum capacity of goods transportation and safety issues.

4.1 Design engineering

The frame of the vehicle was made of two aluminum main rails and a series of transverse beams welded to them (Figure 2), also made in aluminum. This solution permits reducing the weight and containing the costs compared to a standard steel solution and a normal production aluminum car body.

The rear frame is aimed at the transportation of goods and, under the floor, the battery housing. The front part is aimed at carrying the cabin, the powertrain devices and managing the energy in the case of impact. The two parts are joined together by bolts, improving the modularity of the vehicle, giving the possibility of exchanging the front cabin part with different rear equipment.

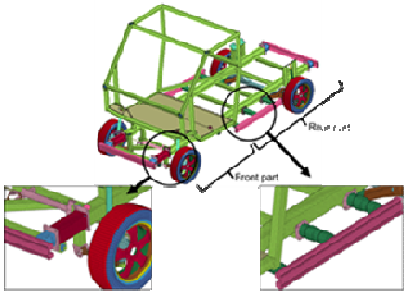

Figure 14. OPTIBODY 3D model chassis. In detail the front and side crash structures

In the rear part a series of crash boxes and a longitudinal crash beam are fixed to the main rails in order to improve the safety and to protect the batteries in case of side impact. For these two components high-strength steels are adopted to improve the energy absorption.

The front part of the vehicle is divided in two main portions. The front one, made with a stamped high-strength steel crash box and crash beam, is aimed at absorbing energy at low-speed impact (16 km/h). Behind this part, the second portion is a front rail aimed at absorbing energy in impacts at higher speed (36 km/h). Crash box, front rail and main rail are joined together with bolts in order to improve repairability. The composite crash structure is placed between the steel crash box and the aluminum longitudinal member so it is designed to be more resistant than the crash box, but softer than the longitudinal member in case of an impact.

The whole structure has been simulated to verify that there is a progressive collapse beginning from the steel crash box until the aluminum longitudinal member.

The frontal add-on will provide additional protection to the OPTIBODY vehicle occupants as well as to pedestrians in case of impact. The rounded circular shape of the add-on is designed to avoid a direct impact of the head against the cabin or the windscreen and improve the results of the impact contact with the lower extremity in case of pedestrian accident.

The final solutions are optimized to obtain the best crashworthiness behavior and consequently to maximize the energy absorption. Virtual simulations have been performed using a model of the chassis; cabin and add-ons to verify that the vehicle design fulfils the crash test requirements established at the beginning of the project. These simulations included frontal and side crash tests since they are the most common accident scenarios where the OPTIBODY vehicle is involved.

4.2 Repairability

As a part of the design of the new vehicle structure a complete analysis regarding its damageability and repairability was carried out in order to guarantee a good performance. Then, different modules of the concept were analyzed to provide the project with information related to the optimum damageability and repairability features.

Chassis: Given the weight restrictions, while maintaining the requirements of crashworthiness and safety of passengers, two main options were finally proposed. The first, a chassis completely made of aluminum beams (square profile) with inner reinforcements. The second one, a similar structure but, instead of aluminum, composites in the chassis legs were introduced. The analysis showed that it is very difficult to repair any of the options that were considered, given the complexities of reshaping them.

Cabin structure: Weight constraints mean that the use of aluminum beams cannot be excluded for the construction of the cabin structure, but the safety of the occupants can always be assured through a good sizing of the bars. A design for the joint between the cabin and the rest of vehicle which enables its full and quick replacement was essential.

Cabin panels and add-ons: Two types of materials were recommended to use both in the body panels and in the add-ons: plastics and composite materials (simple or sandwich panels).

Given the structural behavior, the following areas were distinguished:

Parts with important structural functionality: Add-ons in protection zone, cab roof and floor.

Parts with no important structural functionality: Add-ons in no-protection zone, non-structural panels of the cab.

For parts with a structural function, according to damageability and reparability criteria, the use of composite materials such as PVC sandwich panels and non-flexible thermoplastics were considered as a good option, depending on the part to be applied. For parts without structural function, the use of plastic materials with more elasticity (type PP) was considered a good alternative.

4.3 Passive safety tests

A demonstrator was integrated and the next step was to assess its performance in a crash scenario. Different tests using the integrated pilot demonstrator according to specific crash test protocols were carried out:

RCAR test

Full frontal test (25 km/h)

Full frontal test (40 km/h)

4.3.1 RCAR test

The aim of the RCAR test was to assess the damageability and the reparability of the frontal add-on of the vehicle. It consisted of a frontal impact by launching the pilot demonstrator at 15 km/h against a rigid barrier with a 40% overlap. The impact angle between the vehicle and the barrier is 10º. A 75 kg dummy was installed in the driver seat.

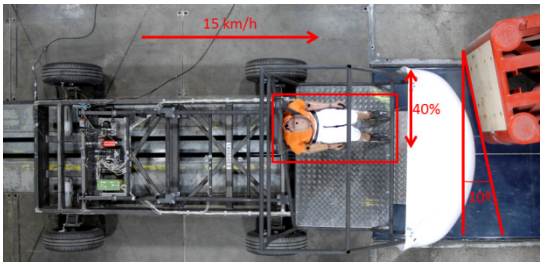

Figure 15. RCAR test settings

The real impact speed was 15.28 km/h.

Due to the collision; two cracks appeared in the frontal add-on at the area where the first contact occurred, one in the lowest frontal part and the other in the highest frontal part. Neither the crash boxes nor the front rails were

deformed. In terms of crashworthiness, the impact was not sufficiently absorbed by the crash boxes, which were too rigid, so they did not deform and the joint of the front rails had to dissipate too much energy.

After the RCAR test, repair tasks were carried out on the chassis, joints, crash boxes and front add-on.

4.3.2 Full frontal test (25 km/h)

The aim of the full frontal test was to assess the capacity of the front rails to dissipate the impact energy. It consisted of a frontal impact by launching the pilot demonstrator at 25 km/h against a rigid barrier with a 100% overlap. The impact angle between the vehicle and the barrier was 0º. A 75 kg dummy was installed in the driver seat.

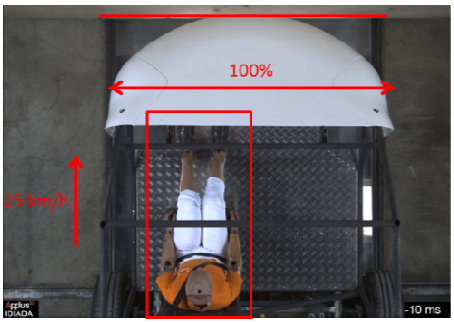

Figure 16. Full frontal test settings

The real impact speed was 25.19 km/h. Due to the collision, two cracks appeared in the frontal add-on; one located on the first impact point, in the central zone, and the other in the left area, near the joint between the upper left and the upper frontal parts. Both cracks lengthened both the upper and the lower parts. Both right and left crash boxes were deformed and joints between fibres from right front rail were separated while the left front rail remained totally without deformation. In terms of crashworthiness, the crash boxes dissipated part of the impact energy due to their total deformation, when the crash box became totally flattened the rest of the impact energy was transmitted to the front rails.

After the full frontal test (25 km/h), repair tasks were carried out on the chassis, joints and crash boxes.

4.3.3 Full frontal test (40 km/h)

The aim of the full frontal test was to assess the capacity of the front rails to dissipate the impact energy. As these elements are designed to dissipate the equivalent energy of an impact at 50 km/h of a vehicle with similar weight to an L7e vehicle, the test speed was 40 km/h in order to check that the front rails were able to dissipate the whole impact energy and that no portion was transmitted to the vehicle frame.

The test configuration is the same as in the previous test apart from the speed impact.

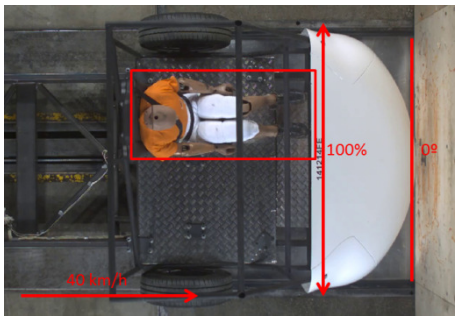

Figure 17. Full frontal test settings

The real impact speed was 40.23 km/h. Due to the high impact speed, the state of the frontal add-on after the test was more critical than the test at 25 km/h. Due to its modularity, cracks appeared in the lower part of the frontal add-on but they did not spread to the upper part. Both right and left crash boxes were compressed in the same way as in the impact at 25 km/h. The front rails dissipated the rest of the impact energy by breaking their fibres in a controlled way. In terms of crashworthiness, the crash boxes worked in the same way as in the full frontal test at 25 km/h and dissipated part of the impact energy due to their total deformation. However, the higher speed compressed the crash boxes sooner and the crash boxes were totally flattened.

5 Summary/Conclusions

The OPTIBODY has been defined as a new modular structural concept for ELTVs composed of a chassis (the key structural supporting element), a cabin and a number of specific add-ons, which will bring modularity, repairability and specific self and partner protection in case of front, rear, side impacts and rollover.

The main frame of the vehicle was designed in aluminum and was divided in two separated parts to enhance the modularity of the vehicle since it is possible to change the rear part of the vehicle (design for goods transportation) while keeping the same cabin and frontal protection structure.

Two different parts of the vehicle were designed using composites: the frontal add-on and the frontal crash boxes. The frontal add-on was focused on pedestrian protection while the crash boxes improve safety performance optimizing the energy absorption. In both cases the composites seem to be a very good replacement for classic materials used in vehicle manufacturing, such as steel and aluminum.

In the tests that were carried out to assess performance in a crash scenario, such as the RCAR test, the OPTIBODY showed a good performance both in the time invested in reparability tasks and in the costs of new materials or replacement parts. Nevertheless, in terms of crashworthiness, the crash boxes were too stiff, so they did not dissipate part of the impact energy. In the full frontal test at 25 km/h, the crash boxes worked as expected and dissipated the first part of the impact energy, but the front rails were not able to dissipate energy because they were stiffer than the vehicle chassis. Finally, in the full frontal test at 40 km/h, both crash boxes and front rails dissipated the whole impact energy in a coordinated way and the vehicle frame did not deform.

Acknowledgement

The authors would like to acknowledge the European Commission that co-funded this project through the FP7 program. The authors wish to acknowledge the Partners of the OPTIBODY consortium for their contributions. The consortium comprises: University of Zaragoza, Politecnico di Torino, PIMOT, IDIADA Automotive Technology, Centro Zaragoza, AMZ, Italdesign - Giugiaro, BELLA, SSAB and Mondragón Automoción.

References

[1] Transport, Energy and CO2, International Energy Agency. http://www.iea.org/publications/freepublications/publication/transport2009.pdf

[2] Lex EUROPA, "DIRECTIVE 2002/24/EC OF THE EUROPEAN PARLIAMENT AND OF THE COUNCIL of18 March 2002 relating to the type-approval of two or three-wheel motor vehicles and repealing Council Directive 92/61/EEC". Retrieved 2009-02-18

[3] Euro NCAP, “Euro NCAP members,” 2014. http://www.euroncap.com/members.aspx. Retrieved 2014-06-23.

[4] Euro NCAP, “Euro NCAP tests on Heavy Quadricycles,” 2014. http://www.euroncap.com/results/quadricycles.aspx#quad1 Retrieved 2014-06-23

Proceedings of the 11th International Forum of Automotive Traffic Safety, 2014, pp 122- 128
No. ATS.2014.205

Study of Quasi-static Mechanical Properties of Vehicle Power Lithium Battery and Failure Criteria

Binghe Liu[1, 2], Jun Xu [1, 2]

[1]*Department of Automotive Engineering, School of Transportation Science and Engineering, Beihang University, Beijing, China,100191*

[2] *Advanced Transportation Vehicle Research Center, Beihang University, Beijing, China,100191*

Email: junxu@buaa.edu.cn

Abstract

With the popularization of electric vehicles, vehicle battery safety has become a focus of concerns. And it has been a heated topic to find out the internal relationships between the mechanical properties and the electrochemistry of the lithium-ion batteries through basic theories. This paper builds up the finite element model of the lithium-ion battery, and the numerical simulations are calculated on the experiments of radial crashing, bending and indentation respectively. At last a failure criteria is built through unified strength theory, by the means of converting the failure of lithium-ion battery to the mechanical failure, which make theoretical basis for the judgment of the failure of lithium-ion battery.

Keywords: lithium ion battery; mechanical properties; failure criteria; unified strength theory

车用动力锂电池的准静态力学性能及失效准则研究

刘冰河 [1, 2]，许骏 [1, 2]

[1] 北京航空航天大学交通科学与工程学院汽车工程系，北京，中国，100191

[2] 北京航空航天大学先进载运工具研究中心，北京，中国，100191

Email: junxu@buaa.edu.cn

摘　要：随着电动汽车的推广与普及，车用动力电池的安全性已经成为焦点之一。电池整体机械性能与电池内部电化学之间的内在耦合已经成为锂离子电池耐撞性研究的重要障碍。本文建立了锂电池的有限元模型，对锂离子电池的径向压力实验、三点弯曲实验和压痕实验进行了数值计算。同时，将锂离子的性能失效转化为力学失效，最终通过统一强度理论建立了锂电池的力学失效准则，为锂离子电池的失效判定与研究提供了理论依据。

关键词：锂离子电池；力学性能；失效准则；统一强度理论

1 引言

随着电动汽车的日益推广与普及，车用动力电池的安全性已经成为关注焦点之一[1, 2]。目前，国内外对于锂离子电池的安全性研究主要从基础理论及工程应用两方面入手。在基础理论方面，试图通过深入探究锂电池机械性能与电池内部电化学之间的内在联系，揭示锂电池在汽车运行工况中的失效机理[3-7]；在工程应用方面则通过研究避免锂离子电池破坏的方法，提高车辆整体的安全性能[8, 9]。

Sahraei et al.[7]对方形锂电池的力学性质展开了实验与仿真；Greve 和 Fehrenbach [5]与 Sahraei et al.[6]则对圆柱型锂电池的力学性能进行实验和仿真分析，并且 Greve 和 Fehrenbach[5]借助 Mohr-Coulomb 强度准则建立了电池的失效力学模型。Wierzbicki 和 Sahraei [4]对多种锂电池做了力学实验，及有限元数值模拟，对锂离子的力学性能做了统一的研究。Lai et al.[3]对锂离子电池的代表性体积单元在不同准静态加载模式下进行了多组实验，从而对锂离子电池的代表性体积单元进行了较为深入的力学性能分析。对单个锂离子研究的基础上，Xia et al.[9]则对汽车在实际行驶过程中，锂电池组受到的力学损伤进行分析。

上述研究尚未提出精细的有限元计算模型（例如仅仅将单体电池视为一个整体等等），同时现有的强度理论无法与试验结果很好的吻合。因此，本文将在 Greve[5]的基础上重新建立更加细致的有限元模型，并通过统一强度理论对电池失效模型建立电池失效准则，进一步完善电池失效的力学模型。

2 数值计算建模与验证

本文选择 HP 602030 NCA-45 Ah/162 Wh 这款目标电池进行研究，见图 1。考虑到数值模拟计算分析的准确性，将电池分为电池盖、电池壳、电池芯与塑料薄膜等分别建模，从而获得较高质量的有限元模型。

2.1 HP 602030 NCA-45 Ah/162 Wh 锂电池模型建立

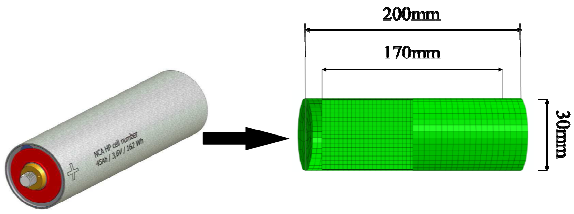

图 1. 电池的实体模型[10]与有限元模型

本文利用 Abaqus 软件建立模型。电池的基本几何参数来自于 GAIA 公司电池手册[10]，如图 2 所示。对电池盖、电池壳、电池芯以及塑料薄膜分别建模，相关建模及网格划分单元信息总结如表 1 所示。网格尺寸确定经过收敛性检验。

表 1. 标准试验系统结果数据

组成	材料	厚度 (mm)	单元类型	单元大小 (mm)	单元数量
电池盖	不锈钢	0.2	S3	8.5*8.5	61
电池壳	不锈钢	1	S4R	5*5	1520
电池芯	铜、铝等	-	C3D8R	4*4*4	8944
塑料薄膜	一种聚合物	1	S4R	3*3	3477

2.2 模型材料参数

本文选用电池的电池壳和电池盖的材料为不锈钢，杨氏模量 $E=207\ \mathrm{GPa}$,泊松比为 $\nu=0.3$ 。对于不锈钢的塑性硬化特性，选用 Swift 法则，其可靠性已经在文献[5]中得到验证。

$$R_{\mathrm{housing}}(\bar{\varepsilon}^{P})=k(\varepsilon_0+\bar{\varepsilon}^{P})^{n} \tag{1}$$

其中 $\bar{\varepsilon}^{P}$ 为材料的应变,其中 $k=0.7\ \mathrm{GPa}$， $\varepsilon_0=0.00801$ ，硬化特性指数 $n=0.1385$ 。

电池的塑料薄膜选择简单的高聚物模型进行材料建模，其杨氏模量为 $E=0.1\ \mathrm{GPa}$ ，泊松比为 $\nu=0.49$ 。

对于电池芯，根据文献[5]选取杨氏模量为 $E=1.5\ \mathrm{GPa}$,泊松比 $\nu=0.15$ 。其塑性硬化特性根据不同的模型得到了不同的硬化特性，文献[5]采用了 Greve 和 Fehrenbach 在 2012 年的模型而得到的硬化曲线为:

$$R(\bar{\varepsilon}) = 0.6 + 600(\bar{\varepsilon})^{2.7} \quad (2)$$

文献[4]中采用的不同的模型得到的硬化曲线为:

$$R(\bar{\varepsilon}) = 0.8 + 848(\bar{\varepsilon})^{2.7} \quad (3)$$

其中 $\bar{\varepsilon}$ 为材料的应变，本文选取公式（2）的硬化特性曲线。

2.3 有限元模型的验证

为了验证有限元模型的可靠性，利用已经建立的模型进行了四组准静态加载实验的数值模拟，分别为电池壳的弯曲实验，电池的径向压力实验，电池的弯曲实验，电池的压痕实验。图 2 为四组实验的有限元仿真模型。值得指出的是，在三点弯曲过程中，压头直径大小对模拟结果影响不大。

将各工况下的载荷-位移曲线与 Greve [5]的实验与数值模拟结果进行对比，图 3 为对比的载荷-位移曲线图。

由图可以看出本文的力位移曲线与文献[5]基本吻合，在径向压力实验与压痕实验的模拟中在加载位移达到 10mm 之后载荷会突然增加，这与电池材料的塑性特性相关；在三点弯曲实验中，实验在位移加载到 17mm 时载荷突然下降，然而在模拟过程中并未观察到此现象，这主要由于数值模拟并未考虑电池壳的断裂。

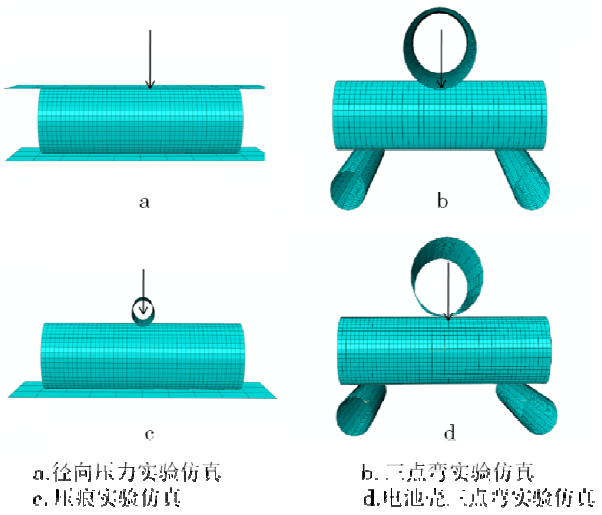

图 2. 实验有限元仿真模型

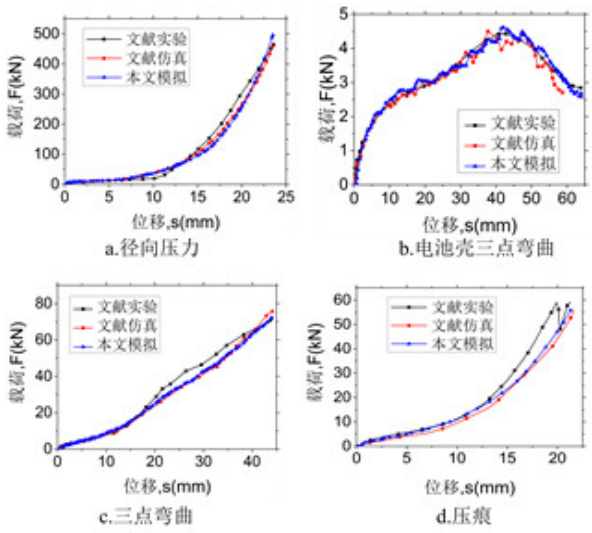

图 3.载荷-位移曲线与文献[5]的对比

图 4 为四组数值模拟在位移加载最大也就是电池失效状态时的应力云图。

可看出在径向压力实验中电池 Mises 应力的最大值在电池的中心，压痕实验的最大应力点在电池靠近压头的位置，而对三点弯曲实验，其最大应力点也位于压头附近，最大应力点有可能就是电池失效的位置，但是实际情况不尽相同：例如在三点弯曲实验中检测到的失效点就是电池的底部，而非靠近压头的部分。因此用 Mises 应力来判断电池的失效是不可靠的，本文将用其他的强度准则来建立电池失效的模型。

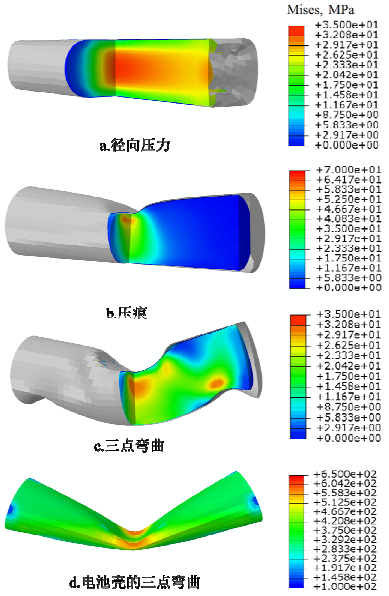

图 4. 各实验在最大加载位移时的应力云图

3 基于统一强度理论对锂电池失效模型的建立

3.1 统一强度理论的概述

统一强度理论等效应力是一系列等效应力的集合，它将各种著名的拉压同性材料和拉压异性材料的等效应力作为特例或线性逼近而包含于其中。大多数的等效应力可以从统一强度理论的等效应力中退化得出[11]，下式为统一强度理论的一般表达式：

$$\sigma_{Unified}^{eq}=\begin{cases}\sigma_1-\dfrac{\alpha}{1+b}(b\sigma_2+\sigma_3), & \sigma_2\le\dfrac{\sigma_1+\alpha\sigma_3}{1+\alpha}\\ \dfrac{1}{1+b}(\sigma_1+\mathrm{b}\sigma_2)-\alpha\sigma_3, & \sigma_2\ge\dfrac{\sigma_1+\alpha\sigma_3}{1+\alpha}\end{cases}\qquad(4)$$

其中 σ_1， σ_2， σ_3 为主应力， α 为材料拉压强度比， b 为破坏准则选择参数， $\sigma_{Unified}^{eq}$ 为统一屈服准则等效应力。

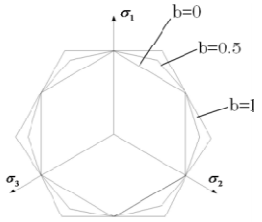

图 5. 统一极限面

统一强度理论根据 b 值的不同，选取的破坏准则不同。图 5 为统一强度理论的极限面。可以随着 b 值得增大极限面会向外扩大。当 b=0 时统一强度理论等效应力退化为 Mohr-Coulomb 等效应力；当 b=0.5 是统一强度理论等效应力退化为一个中间等效应力；当 b=1 时，统一强度理论退化为双剪等效应力。

3.2 电池失效模型的建立

文献[5]得到的电池失效位移基础上，本文对电池进行了三组模拟，分别为径向压力试验，三点弯曲试验以及压痕实验的仿真。利用有限元的方法可以直观的看到三组试验下电池的三向应力分布。

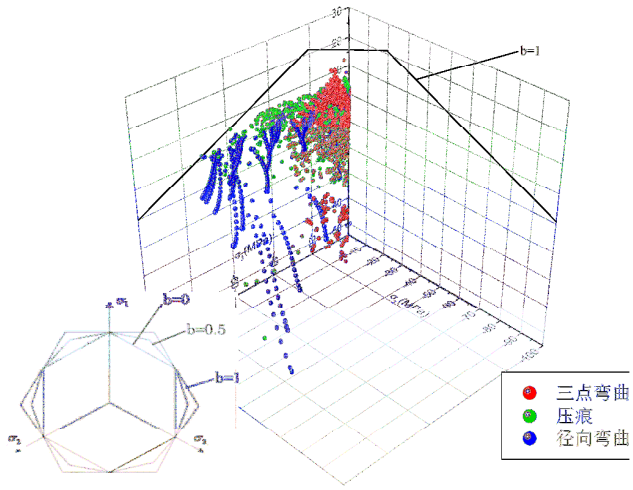

图 6 所有点主应力应力图

根据统一强度理论，锂电池在此时某些地方的应力会超出或者正好在强度的极限面上，提取出所有单元的主应力$\sigma_1,\sigma_2,\sigma_3$，如图 6 所示。在确定参数过程中，本文选取统一强度理论的上限即 b=1。为确定拉压比α 和统一屈服准则等效应力$\sigma_{Unified}^{eq}$，本文分别将三组仿真的所有点应力值带入统一强度理论公式中，在不同α 情况下三组仿真的最大值最为接近则确定，而此时最大值则为$\sigma_{Unified}^{eq}$，经过拟合拉压比$\alpha=0.215$，等效应力$\sigma_{Unified}^{eq}=16.0\ \text{MPa}$。

故，车用动力锂电池的强度失效准则为：

$$16.0\ \text{MPa}=\begin{cases}\sigma_1-0.1075(\sigma_2+\sigma_3) \\ \qquad\qquad ,\sigma_2\le 0.823\sigma_1+0.177\sigma_3 \\ 0.5(\sigma_1+\text{b}\sigma_2)-0.215\sigma_3, \\ \qquad\qquad ,\sigma_2\ge 0.823\sigma_1+0.177\sigma_3\end{cases} \tag{5}$$

图 7 为径向压力实验失效时的三向应力云图，由之前所建立的失效准则，可判定出电池的失效点位于电池中间靠两边的位置（如图 1 所示），这与 Mises 应力的最大点位置不同。

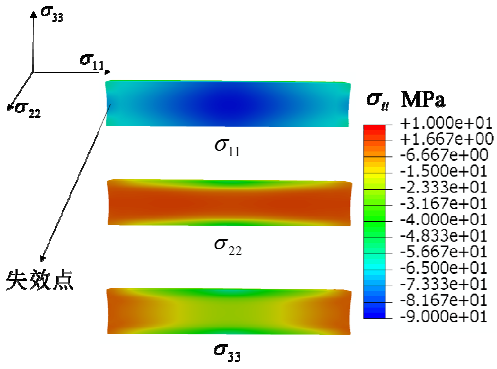

图 7 径向压力实验三向应力图

图 8 为压痕实验失效时的应力云图，同样的利用失效准则，判定电池的失效点在靠近压头的位置。

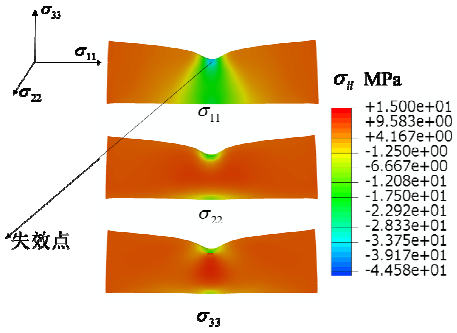

图 8 径向压力实验三向应力图

图 9 为三点弯曲实验失效时的应力云图，利用失效准则，可判定电池失效点位于电池底部。同样地，在文献[5]的实验中检测到电池的失效点与通过判定法则检测到结果相一致，可以看出建立的失效准则是可靠的。

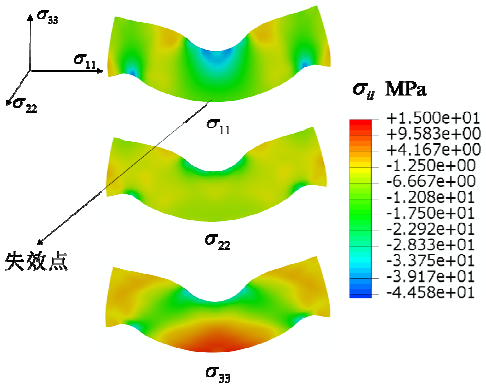

图 9 三点弯曲实验三向应力图

4 结论

本文建立了锂电池的数值模型，并对三点弯曲实验、压痕实验和径向压力实验进行了数值模拟计算，将锂电池的失效转化为力学失效，并建立了锂电池的失效准则。

锂离子电池失效与机械性能失效互相关联，在今后锂离子电池的设计及安全性能评价中考虑电池机械性能是有必要的。目前国内外对锂离子电池机械性能的研究仍然不够完善，特别是对锂离子电池的动力学性能的研究仍缺乏，这也是未来对锂离子电池机械性能研究的一个方向。

参考文献

[1] ADDIN EN.REFLIST Z. Y. L. Jinpo2.Review of vibration and shock dynamics of electric vehicles battery[J].Chinese Journal of Power Sources,2013,01:156-160.

[2] Z. Y. L. Jinpo2.Current and Development Trends of Chinese Patents in Lithium Battery[J].Journal of Intelligence,2012,31:35-40.

[3] W. J. Lai, M. Y. Ali, et al.Mechanical behavior of representative volume elements of lithium-ion battery modules under various loading conditions[J].Journal of Power Sources,2014,248:789-808.

[4] T. Wierzbicki and E. Sahraei.Homogenized mechanical properties for the jellyroll of cylindrical Lithium-ion cells[J].Journal of Power Sources,2013,241:467-476.

[5] L. Greve and C. Fehrenbach.Mechanical testing and macro-mechanical finite element simulation of the deformation, fracture, and short circuit initiation of cylindrical Lithium ion battery cells[J].Journal of Power Sources,2012,214:377-385.

[6] E. Sahraei, J. Campbell, et al.Modeling and short circuit detection of 18650 Li-ion cells under mechanical abuse conditions[J].Journal of Power Sources,2012,220:360-372.

[7] E. Sahraei, R. Hill, et al.Calibration and finite element simulation of pouch lithium-ion batteries for mechanical integrity[J].Journal of Power Sources,2012,201:307-321.

[8] J. Lamb and C. J. Orendorff.Evaluation of mechanical abuse techniques in lithium ion batteries[J].Journal of Power Sources,2014,247:189-196.

[9] Y. Xia, T. Wierzbicki, et al.Damage of cells and battery packs due to ground impact[J].Journal of Power Sources,2014,267:78-97.

[10] Handhabungshinweise für die Lithium Ionen Zelle Typ HP 602030 NCA-45 Ah/162 Wh,online available at:http://www.gaia-akku.com/fileadmin/user_upload/downloads/Handhabungshinweis_HP602030NCA-45Ah.162 Wh.pdf.

[11] Y. Maohong.New System of Strength Theory:Teory,Development and Applications[M].Xi'an Jiaotong University Press,2011.

Proceedings of the 11th International Forum of Automotive Traffic Safety, 2014, pp 129- 135
No. ATS.2014.206

Analysis of Front Impact Safety on FSAE Racing Car

Xulai PENG, Fan LI
State Key Laboratory of Advanced Design and Manufacture for Vehicle Body, Hunan University, Changsha, China
Email: slowpen712@163.com, lifandudu@163.com

Abstract
The principle of energy absorption of honeycomb used in FSAE cars was described. The finite element model of the front structure for energy absorbing was established with Hypermesh software, and submitted to the LS-DYNA computation analysis. Through the comparison of experimental and frontal rigid wall impaction, the validity of the finite element simulation model was established in this paper had been verified. The phenomenon and reasons of the front clapboard structure failure were analyzed, and some improvement measures were put forward.

Keywords: FSAE; impact attenuator; impact; honeycomb

FSAE 赛车前碰安全性分析研究

彭徐来，李凡
湖南大学汽车车身先进设计制造国家重点实验室，长沙，中国，410082
Email: slowpen712@163.com, lifandudu@163.com

摘　要：介绍了蜂窝铝的吸能原理，利用 Hypermesh 建立了前端吸能结构的有限元模型，采用 LS-DYNA 进行计算分析。通过与 FSAE 赛车前端吸能结构的正面刚性墙台车碰撞实验对照，验证了本文建立的有限元仿真模型的有效性。分析了台车实验中出现的前端吸能结构的前隔板失效撕裂现象及原因，提出了改进措施。

关键词：FSAE；前端吸能结构；碰撞；蜂窝铝模板

1 引言

FSAE 大学生方程式汽车大赛是由世界各国 SAE 主办的旨在由学生自主构思，设计和制造出符合规则的赛车来参加比赛。随着该赛事的日渐发展，基于驾驶员安全性方面的考虑越来越多地体现在各国赛事规则上。2014 年 FSAE 中国组委会规则规定：当前端缓冲安装在总重量为 300kg 的赛车上，并以 7.0m/s 的初速度与刚性障碍物发生碰撞时，整车的平均减速度不能超过 20g，最大减速度不能超过 40g，总吸收能量必须达到或超过 7350 焦耳[1]。目前国内 FSAE 赛车大部分车身使用的仍然是钢管桁架焊接组成的非承载式的车架结构。在正面碰撞中，赛车前端的吸能结构的有效皱褶变形吸能是保障赛车安全性能的关键。

2 FSAE 赛车前碰吸能结构

2.1 FSAE 赛车前碰吸能结构

FSAE 赛车发生正碰时，车身前端结构是最关键的吸能缓冲结构。前端吸能结构作为单独部件，与赛车非承载式车身进行安全连接安装在赛车前部。目前 FSAE 赛车前端吸能结构常见的吸能结构主要依靠如蜂窝铝，泡沫

基金项目：国家自然科学基金项目(51205117)，湖南省科技计划项目（2014SK3213）

铝等薄壁结构吸能材料的塑性变形来吸收能量。本文验证的是采用蜂窝铝材料的前端吸能结构。国内 FSAE 赛事规则规定[1]：

a.前端吸能结构必须安装在前隔板之前；

b.沿赛车前后方向至少长 200mm(7.8 英寸) ；

c.在前隔板之前 200mm(7.8 英寸)范围内，至少高 100mm(3.9 英寸)，宽 200mm(7.8 英寸) ；

d.碰撞时不能穿透前隔板；

e.缓冲结构和前隔板直接并且安全地连接在一起，而不是作为非承载式车身的一部分。

2.2 蜂窝铝碰撞吸能原理

蜂窝铝碰撞吸能过程是通过蜂窝铝箔的皱褶压缩将大量的动能转化为变形能。针对汽车前碰的过程，一般采用不同金属材料的薄壁吸能构件。这类薄壁构件在经受一定的轴向载荷后便会产生折叠式弹塑变形，从而消耗大量碰撞动能。蜂窝铝箔在轴向载荷作用下变形直至压溃。首先铝箔在局部最薄弱处发生弯曲变形；随着轴向载荷的增加，薄壁因挤压失稳弯曲；随后发生边缘屈服，产生塑性变形，吸收碰撞能量，元件边缘发生褶，吸能器的承载能力下降；最后塑性变形加大，边缘褶皱现象继续，外观表现为折叠，结构被压溃。

2.3 蜂窝铝有限元模型的建立

在汽车被动安全领域，蜂窝铝材料被广泛应用于汽车碰撞试验的正面偏置可变形壁障(ODB)和侧面移动可变形壁障(MDB)结构中。其一般结构如图 1 所示。但由于其变形失效形式复杂，各种有限元建模方法都兼具优缺点。目前汽车碰撞领域常用的针对蜂窝铝的建模方法有：实体单元建模;壳单元建模；离散梁单元建模等[2]。其中相对其他两种建模方式，用壳单元建立蜂窝铝模型，虽然其计算时间较长，但可以模拟较细微的变形以及非线性特性，反映动态冲击中一些不规则变形细节，从而获得较高的变形模拟精度，因此，采用壳单元建模非常适合前端吸能结构的有限元模拟。

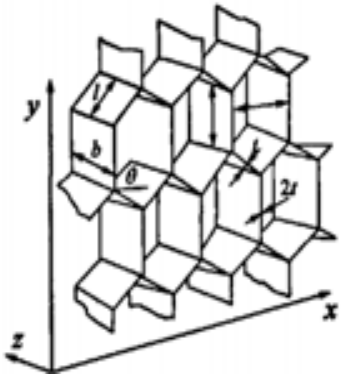

Fig1. Structure of honeycomb

图 1.蜂窝铝的结构

2.4 前端吸能结构有限元模型的建立

FSAE 赛车前端吸能结构主要由蜂窝铝吸能缓冲块，前隔板，斜撑和支架等组成。本文采用 UG 建立前端吸能结构蜂窝铝吸能缓冲块，以及由前隔板、斜撑等组成的安装车架结构的几何模型。其中蜂窝铝尺寸为 200mm×100mm×202mm。固连安装在车架前隔板上，前隔板厚度为 1mm，材料为 4130 结构合金钢，车架钢管外径为 25.4mm，壁厚为 1.6mm，材料采用 4130 结构合金钢。主要力学参数如表 1 所示。

为了节省计算资源，在仿真模型建模中，将台车整体视为刚体，忽略其局部特征，前端吸能结构连同车架部分直接固连在台车模型前端。使用 Hypermesh 对几何模型进行有限元网格划分后，共有单元 248349 个。其中前端吸能结构包括安装车架在内共有单元 242635 个，质量为 6.415Kg。台车质量为 300kg。蜂窝铝材料本构模型选取使用 LS-DYNA 中所提供的 24 号材料(PICEWISE_LINER_PLASTICITY)，一种分段线性塑性材料模型。网格单元类型为 Shell 单元。模型网格划分前处理如图 2 所示。

Table1. Mechanical parameters of materials of the main components

表 1. 主要部件材料力学参数

	密度/(t/mm^3)	弹性模量(Mpa)	泊松比	屈服强度(Mpa)
蜂窝铝	2.70x10-9	7.00x104	0.33	75
前隔板	7.89x10-9	2.20x105	0.30	290
斜撑	7.85x10-9	2.05x105	0.28	345
支架	7.85x10-9	2.05x105	0.28	345

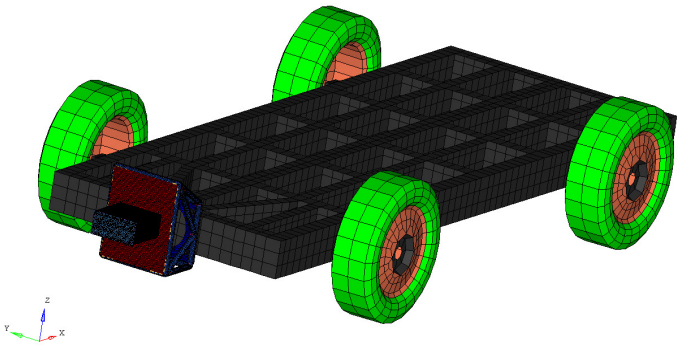

Fig2. Finite element model of frontal impact trolley

图 2. 正碰台车有限元模型

2.5 初始条件的建立

蜂窝铝吸能块结构采用 BT 壳单元模拟，其与前隔板的连接采用粘连模拟方式。前端车架钢管与钢管之间连接采用焊点固连，车架与台车的固定则采用共节点固连方式模拟。刚性墙设置在垂直于 X 轴平面距离蜂窝铝前端 1mm 处。此外定义了蜂窝铝的单面接触，蜂窝铝与前隔板的面面接触等接触方式以及针对蜂窝铝部件的沙漏控制。

3 前碰的模拟分析

台车模型以 7mm/s 的速度沿 X 轴方向，撞击刚性墙，整个碰撞仿真过程为 80ms，在四核 8G 内存的 64 位 PC 机上总求解耗时 5 小时 39 分钟。

整个碰撞过程最终质量增加控制在了 6.0x10-4kg 以内，沙漏能增加控制在 5%以内，保证了模型的可信度。总能量、动能、内能、界面滑移能以及沙漏能变化曲线如图 3 所示。

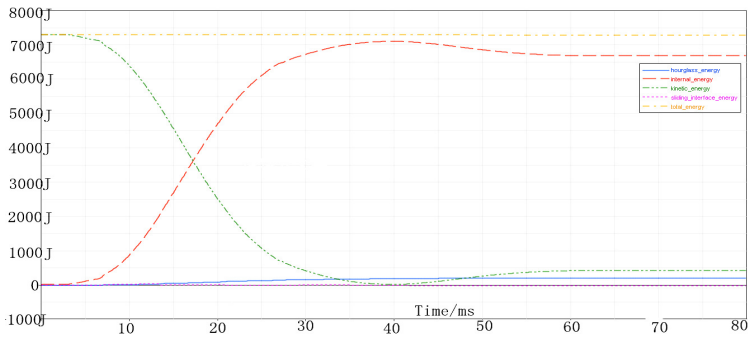

Fig.3 The energy curves

图 3 能量变化曲线

FSAE 赛车与刚性墙的前碰过程。首先蜂窝铝吸能块与刚性墙接触。蜂窝铝褶皱折叠压缩将大部分动能转化为变形能被吸收。且随着碰撞减速过程的继续，冲击速度不断减小（如图 4 所示），蜂窝铝能量吸收系数越低，蜂窝铝吸能块的吸能能力越差[3]。而与蜂窝铝吸能块粘连的前隔板所承受的冲击载荷增强，前隔板与支架焊接固连处，前隔板的剪切应力应变与拉伸应力应变增大，当增至前隔板材料的失效极限时，钢板被撕裂从车架钢管脱离，发生失效。此后，随着碰撞过程的继续，碰撞动能主要转化为前隔板后面的斜撑钢管的塑性变形能。这是 FSAE 赛车发生前碰事故蜂窝铝吸能不充分的典型情况。实际实验台车如图 4 所示。

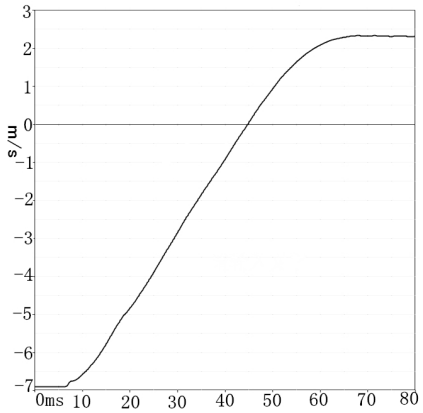

Fig4. The trolley's velocity-time curve

图 4. 台车速度-时间变化曲线

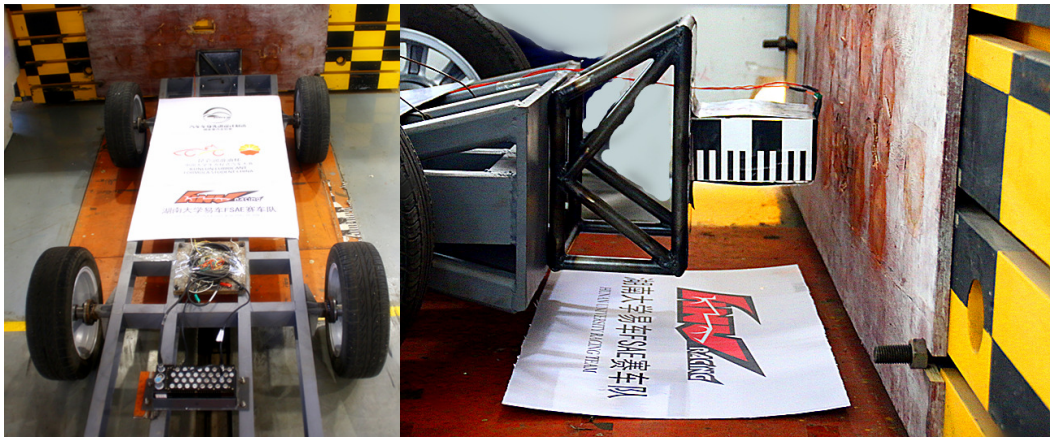

Fig5. Experimental trolley

图 5. 实验台车

3.1 前碰的减速度与应力分析

如图 6 所示，台车在前碰过程中的前 16ms，主要由蜂窝铝发生褶皱变形吸能。在此期间，加速度在 9ms-16ms 之间变化相对平缓，表面此阶段为蜂窝铝吸能块的压溃吸能阶段。在第 16ms 末，由于前隔板局部脱离固定支架发生失效，使得加速度出现较大落差，载荷转而集中到前隔板后端的斜撑上，斜撑由于局部载荷过大，出现应力集中，进而发生折弯变形.

模拟仿真的减速度曲线与台车实验减速度曲线趋势大致相似，其前隔板失效时间、加速度峰值大小都与台车实验数据基本吻合。由台车实验曲线和模拟实验曲线可知，台车碰撞过程中峰值减速度达到 21G，虽然满足法规要求的最大减速度不得超过 40G 的要求。但蜂窝铝吸能块侵入到车架的前隔板后部，前端车架发生较大变

形，说明蜂窝铝吸能块整体过硬，吸能效果不理想。

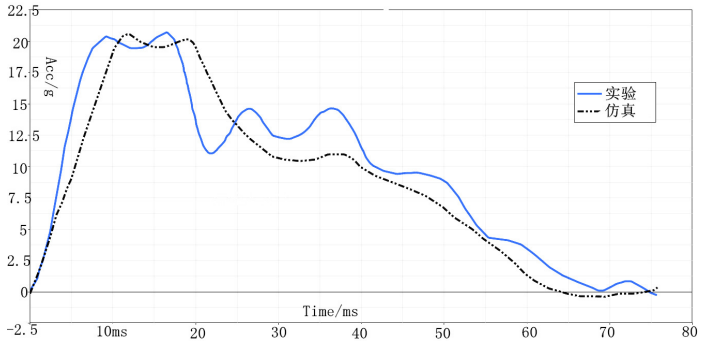

Fig6. Deceleration curve

图 6. 减速度变化曲线

进一步分析前隔板失效部分的应力分布情况，如图 7 所示。可知，在前隔板边缘布置焊缝的区域，碰撞过程中其应力分布与前隔板其他边缘区域相比始终较为集中。故前隔板与车架的焊接形式对前隔板局部撕裂失效有一定影响。可考虑采用前隔板与车架满焊改善其应力分布不均的现象。

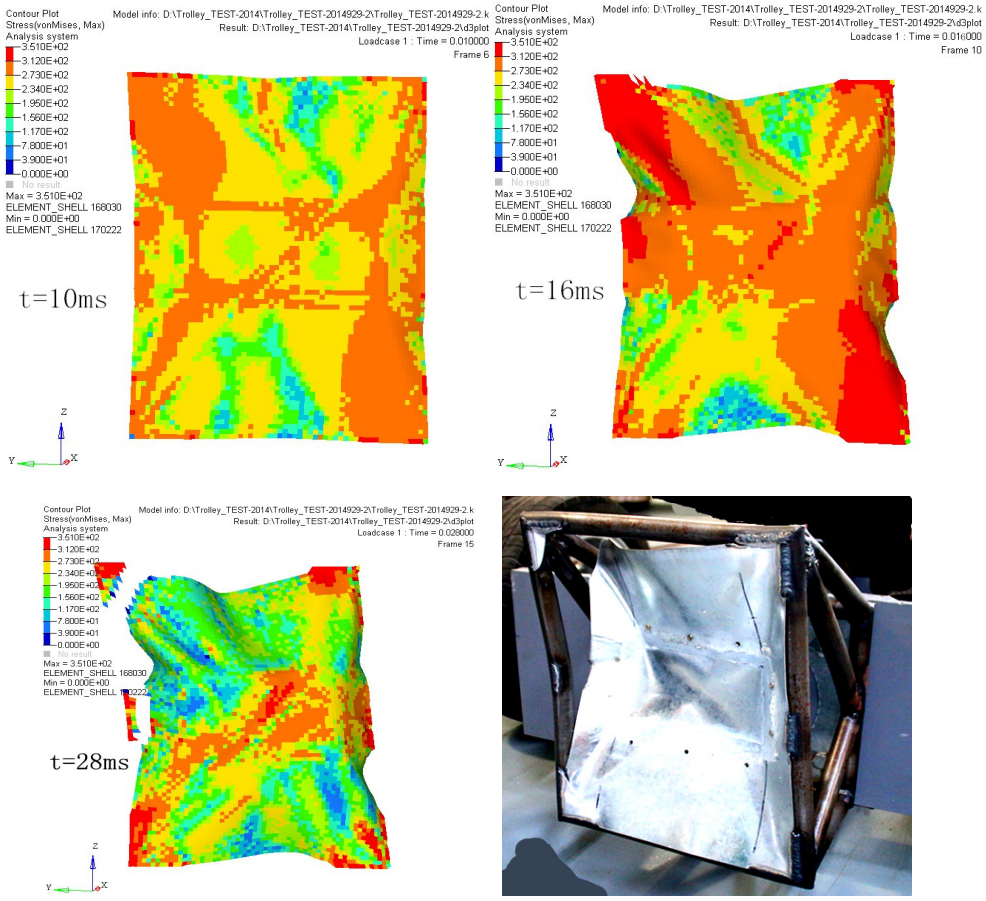

Fig7. Stress distribution at different moments

图 7. 不同时刻的前隔板应力分布

如图 8 所示，拟采用在前隔板与支架之间采用满焊方式以保证两者之间连接的可靠性。由碰撞过程结果可知，采取该方式有效避免了应力过多集中于某处焊缝连接，碰撞结束前隔板未出现撕裂失效现象。

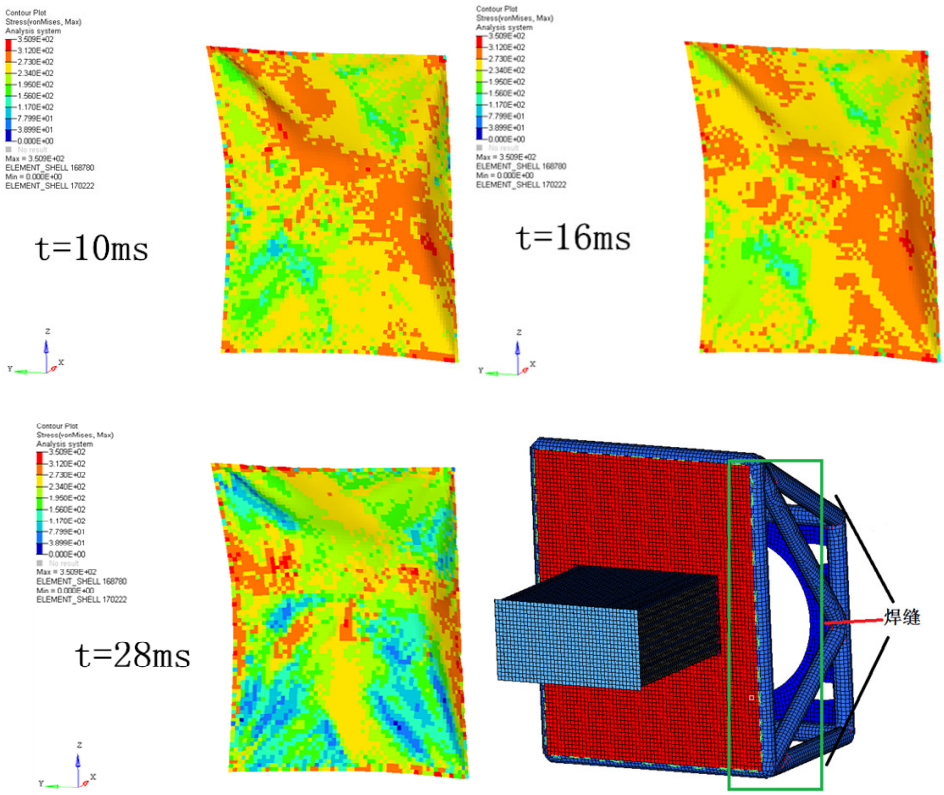

Fig8. Stress distribution under the full-welding front bulkhead

图 8. 满焊方式下前隔板应力分布

3.2 前碰的变形量分析

如图 9 所示，碰撞过程结束前后，蜂窝铝吸能块变形呈现一高一低，凹凸相差明显的形状特点，在变形量较大的一端对应粘接的是前隔板未发生失效的一侧，而变形量较小的一侧靠近前隔板失效的区域。这说明碰撞过程中蜂窝铝左右两侧产生的变形能的大小不一样，故考虑改变蜂窝铝底部的仿侵平板的材料或者厚度，提高其局部刚度，平均蜂窝铝左右两侧吸能大小，对防止出现前隔板局部能量冲击与载荷集中有帮助。

Fig9. Honeycomb structure after impact

图 9. 碰撞后的蜂窝铝吸能块结构

4 结语

基于台车实验建立起较为精确的有限元仿真分析模型，对台车试验中出现的蜂窝铝吸能块未充分溃缩吸能，而前隔板局部脱离车架的现象进行了数值模拟。通过对减速度，应力分布，变形量等分析，得出了前隔板撕裂

失效脱离车架的可能产生的原因及相应改进措施：

1.台车实验蜂窝铝整体偏硬，考虑更换偏软的蜂窝铝箔材料；

2.前隔板与车架的焊接形式，考虑前隔板与车架采取较长焊缝连接或者满焊，以增强连接的刚强度及可靠性避免出现应力集中于某几处焊缝；

3.蜂窝铝吸能块底端仿侵平板材料性能的影响，考虑改变钢板材料，或者较厚尺寸的铝板。

致　谢 (Acknowledgement)

本文完成过程中得到了湖南大学 FSAE 车队老师的支持，同时感谢李凡老师对本研究的指导。

参考文献 (References)

[1] 2014 China FSC competition rules (publicity Edition) [Z]. Beijing.SAE of China,2013.
2014 中国 FSC 大赛规则（公示版）[Z].北京.中国汽车工程协会,2013.

[2] Research of methods to develop finite element model of vehicle impact honeycomb barrier[J]. Journal of Jiamusi University: Natural Science Edition.2013,31(1)：44-47.
汽车碰撞蜂窝铝壁障有限元建模方法研究[J].佳木斯大学学报：自然科学版.2013,31(1)：44-47.

[3] Simulation of low velocity impact of aluminiurn honeycomb sandwich panels with ANSYS[J]. Mater Rev. 2102.26(4):157-160.
基于 ANSYS 的铝蜂窝夹芯板低速冲击仿真模拟研究[J].材料导报.2102.26(4):157-160.

Proceedings of the 11th International Forum of Automotive Traffic Safety, 2014, pp 136- 142
No. ATS.2014.207

Coupling Low-Speed and Pedestrian Collisions to Design an Adaptive Car Bumper Energy Absorber

Yu Chuanhui[1], Mo Fuhao [1]*, Xiao Zhi[1]*,Peng Yong[2], Du Min[1], Li Fan[1]

1.Hunan University, State Key Laboratory of Advanced Design And Manufacturing for Vehicle Body, Changsha,China, 410082

2. Key Laboratory of Traffic Safety on Track Of Ministry of Education, School of Traffic &Transportation Engineering, Central South University, Changsha,China, 410075

Email: mfuhao@gmail.com，hnuxiao@163.com

Abstract: Design of a car front bumper system needs to meet the requirements of both low speed collision and pedestrian impact. Energy absorbing structures are normally mounted between the bumper beam and fascia to meet such requirements in the current mainstream cars. This study proposes an adaptive modular bumper energy absorber. The modular X-shape energy absorbing unit can gradually improve energy absorbing ability by changing deformation modes based on the amount of impact energy. Furthermore, this type of bumper energy absorber is designed based on a car model, and its performance is evaluated and compared with traditional foam bumper absorber according to the rules of GB/T24550-2009 pedestrian protection and CMVSS215 low-speed impact. The results show that new energy absorber can deal with pedestrian and low-speed impact respectively in different deformation modes, thus it can better meet requirements for both vehicle impact conditions comparing the traditional foam bumper absorber.

Keywords: Bumper; Energy Absorber; Pedestrian Protection; Low Speed Collision

一种兼顾低速碰撞与行人保护的自适应型轿车保险杠吸能器设计

余传辉[1]，莫富灏[1]*，肖志[1]*，彭勇[2]，杜敏[1]，李凡[1]

（[1]. 湖南大学,汽车车身先进设计制造国家重点实验室，长沙 410082

[2]. 中南大学，交通运输工程学院 轨道交通安全教育部重点实验室，长沙，410075）

Email: mfuhao@gmail.com，hnuxiao@163.com

摘要：轿车前保险杠系统的设计需要同时满足行人与低速碰撞的要求。现代轿车设计中，通常通过在保险杠蒙皮和横梁之间增加吸能结构以满足此类要求。本文提出了一种模块化的自适应轿车前保险杠吸能器，其模块化X 形吸能单元可基于外部碰撞能量的大小，通过改变自身变形特征，分阶段地提升吸能能力。本文进一步以某车型为基础设计了该吸能器，并基于 GB/T24550-2009 行人保护法规和 CMVSS215 低速碰撞法规要求，利用有限元仿真分析评估了其耐撞性能，并与常用泡沫吸能器进行了对比。结果表明：不同于传统泡沫吸能结构，该吸能器在行人碰撞与低速碰撞时会产生不同的变形模式，可以更好地兼顾两种碰撞形式的防护性能。

关键字：保险杠；吸能器；行人保护；低速碰撞

1 引言

目前已经开展了很多综合考虑行人保护与低速碰撞的研究，文献[2]在低速碰撞性能较好的情况下分析了行人保护性能的不足，并设计了一种铝合金保险杠横梁以达到兼顾两种碰撞类型的目的，但并没有从设计之初就兼顾二者，因此改进后的保险杠系统虽然行人保护的性能提升了但对低速碰撞性能并未有较大的改进；文献[3]对现有轿车保险

杠系统的七个结构尺寸参数进行了多目标优化，最终得到的结果兼顾了两种性能，使两种碰撞性能均得到了提升，但其仅对原有保险杠系统进行初步优化，且并未加装吸能器，效果不够显著且不易于推广到其它车型。以上研究主要基于现有保险杠系统的结构参数进行优化，而对新结构、新材料的应用的研究较少，同时通过对保险杠吸能器的设计以兼顾行人保护与低速碰撞的研究则更少。

近年来，对于新型保险杠吸能器的研究，文献[4,5]中 Shuler 和 Mohapatra 等应用工程塑料设计的保险杠吸能器，其均采用包裹式的片状结构，主要利用突出结构的上下表面进行吸能。此类吸能器结构均过于复杂，制造难度较大，且仍采用一体化的结构；同时其结构设计并未区分不同的碰撞形式，仅考虑了行人保护的要求。因此，期待设计一种保险杠吸能器，它能根据能量吸收大小的不同，自适应地采取不同的变形模式，以分别满足行人与低速碰撞的要求。

因此，本文提出了一种新型保险杠吸能器，其安装于汽车蒙皮与保险杠横梁之间，如图 1 所示。本文在不改变轿车保险杠系统原有结构的情况下仅对保险杠吸能器进行了研究。该轿车保险杠吸能器由若干个相同的吸能单元拼装而成，压缩吸能时可产生两种不同的吸能模式，分别对应不同的碰撞形式。同时选用了性能稳定的 xenoy 合金材料，并采用了模块化的设计，便于更换，减少浪费，有利于维修。

此外，本文采用某国产车型的有限元模型（图 2），对保险杠吸能器进行了分析，并与传统泡沫型吸能器进行了对比，结果表明行人保护与低速碰撞保护性能在满足各自法规的同时均有了较大幅度的提高。

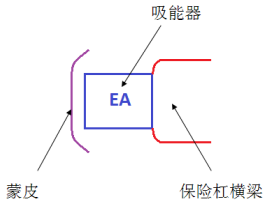

图 1 吸能器位置截面示意图

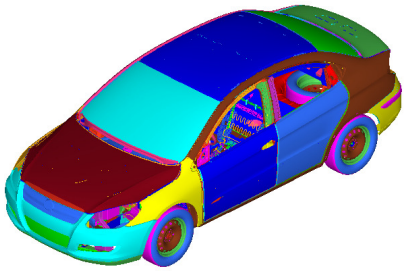

图 2 整车有限元模型

2 轿车保险杠吸能器的设计

2.1 单个吸能单元的设计

基于吸能器模块化的设计设想及参考文献[6]中对吸能器概念性设计中所采用的模块化思路，提出了一种单元拼装形式的模块化吸能器。基于单个单元包含不同吸能模式的设计设想，对比了三种不同形状吸能单元的吸能特点，最终提出了一种 X 形吸能单元，如图 3 所示。

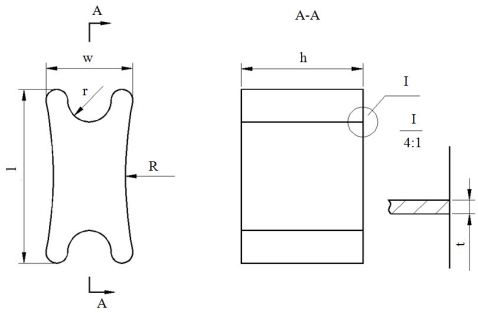

图 3 单个吸能单元

表 1 xenoy 合金材料参数

密度	弹性模量	泊松比	屈服强度
1200kg/m^3	1999.48MPa	0.3	73.8MPa

由图 1 选定车型前保险杠结构尺寸参数，选定该吸能单元长度 l=80mm，长宽比为 2：1，宽度 w=40mm，高度根据保险杠横梁高度设计 h=56mm，左右两侧边弧半径 R=180mm，上下两卡接弧半径 r=10mm。将该吸能单元进行网格划分，网格大小取 2mm，厚度 t 取 2.5mm，进行了超低速 4km/h 压缩仿真，测试吸能情况及受力情况。材料采用 xenoy 合金，材料参数如表 1 所示。

变形吸能曲线如图 4 所示，接触力曲线如图 5 所示。

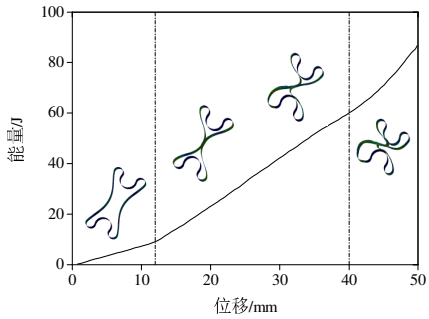

图 4 变形吸能曲线图

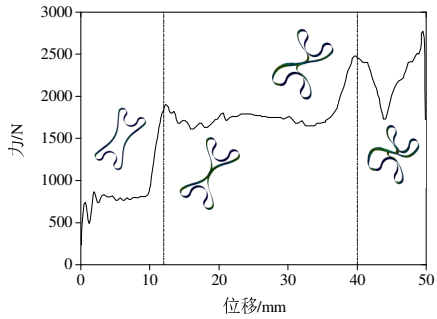

图 5 接触力-位移曲线

如图 4 可看出，X 形吸能单元的吸能曲线呈现一定的特点：0-12mm 段，单元开始压缩变形，首先达到材料的弹性极限；12-40mm 段，继续压缩，吸能单元两侧边弧接触并开始形成铰接，吸能量进一步增大；40mm 后，进一步压缩，吸能单元相互扭结在一起，形成自锁并以自锁的形式继续压缩，使吸能量达到最大。

如图 5 可看出，X 形吸能单元的力-位移曲线呈现一定的特点：即其在较小变形时产生的接触力较小，对应于图 4 中 0-12mm 的阶段，适用于行人保护；在较大变形时，由于其压缩变形形成了自锁结构，从而变形产生的接触力较大，对应于图 4 中 12-40mm 及 40mm 以后的阶段，适用于低速或较高速度碰撞中大变形下的吸能。

2.2 轿车保险杠吸能器总体设计

基于选定车型轿车前保险杠系统结构，以 1 中设计的单个吸能单元为基础，提出了一种兼顾行人保护与低速碰撞的新型保险杠吸能器（图 6）：该结构由若干个保险杠吸能单元和前后两根卡口加强梁组成。其中，加强梁与吸能单元采用卡口连接，两者通过弧形卡接结构相互耦合。加强梁的材料同样采用 xenoy 合金，厚度取 2.0mm。吸能单元的个数由行人碰撞中吸能总量 825J 以及单个单元的吸能情况初步确定为 15 个。

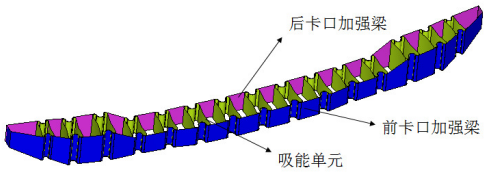

图 6 新型轿车保险杠吸能器

3 整车有限元模型有效性验证

为了确保有限元仿真的真实性，必须对整车有限元模型进行有效性验证，本文根据加速度-时间曲线对所用的整车有限元模型进行有限性验证。整车模型正碰变形后如图 7 所示，B 柱下端加速度-时间曲线如图 8 所示。

由图 8 可知，本文采用的整车有限元模型的加速度曲线和实车试验曲线具有相似的时间历程、峰值和趋势，左右两侧加速度峰值的误差均在 10%以内，因此本文认为仿真模型是有效的[7]。

（a）试验　　（b）仿真

图 7 整车正碰变形

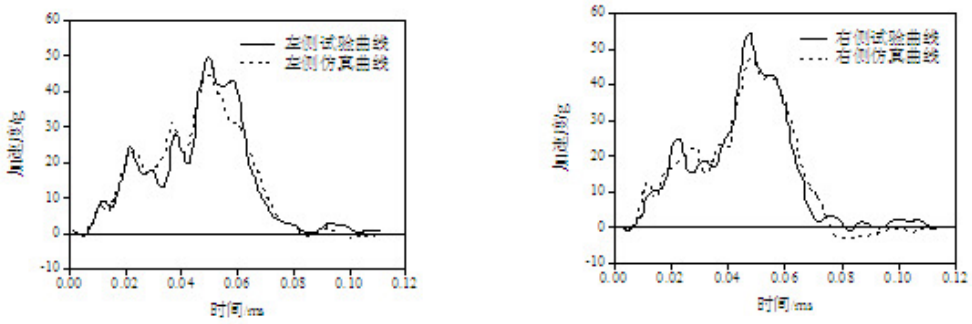

（a）左侧加速度　　（b）右侧加速度

图 8　B 柱左右两侧加速度-时间曲线对比

4 车辆行人保护性能分析

4.1 行人保护碰撞有限元模型的建立

发生行人碰撞时，行人腿部一般只会与车辆前部发生接触。因此，本文仅从整车碰撞有限元模型中截取 A 柱之前的主要单元以简化计算。模型约束 A 柱末端、门槛梁上及纵梁后端的 6 个自由度，如图 9 所示。

将所设计的吸能器几何模型用 Hypermesh 软件进行网格划分，建立有限元模型，并固定安装于保险杠横梁与蒙皮之间。同时根据 GB/T24550-2009《汽车对行人的碰撞保护》[8]中的要求选用按 EEVC 法规的要求建立的腿部冲击器模型，赋予小腿冲击器 40km/h 的初始速度碰撞保险杠部位，如图 9 所示。

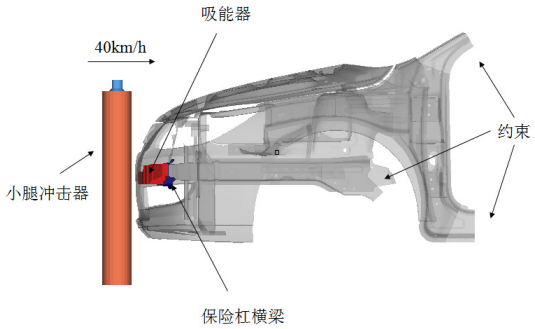

图 9 行人下肢碰撞有限元模型

4.2 仿真结果对比分析

将建立的有限元模型用 LS-DYNA 软件进行仿真分析，根据较之国内法规更为严格的 Euro-NCAP 评价体系中关于行人保护的要求（胫骨上端加速度≤150g；膝关节剪切位移≤6mm；膝关节弯曲角度≤15°）进行对比分析，对比了本文所设计的新型保险杠吸能器与传统泡沫填充式吸能器对行人下肢的保护效果，如图 10 所示。

如图 10(a)中加装新型吸能器时的胫骨加速度曲线所示，并对比试验过程可知，当小腿冲击器接触到保险杠蒙皮时，加速度曲线形成了第一个加速度峰值；X 形吸能单元开始压缩后达到弹性极限，形成了第二个加速度峰值；进一步，突破弹性极限压缩至形成明显 X 型，形成了第三个波峰。由此可以看出本文提出的新型保险杠吸能器利用自身 X 形吸能单元的结构特点，在较低冲击载荷的行人碰撞试验中自适应地采用了小变形的吸能模式（如图 11 所示），将冲击载荷均匀的分布到不同的压缩阶段，以多个波峰代替原泡沫型保险杠吸能器中的大波峰，以达到降低损伤的目的。

由图 10 可知，加装泡沫型吸能器时，小腿冲击器的胫骨加速度峰值很大，超过 210g，远没能达到 150g 的法规要求，而加装新型吸能器时，小腿冲击器的胫骨加速度峰值显著减小，达到 150g 以内，满足了法规要求；加装新型吸能器时，小腿冲击器的膝关节弯曲角度比加装泡沫型吸能器时有了较大幅度的改进；对于膝关节剪切位移，新型吸能器亦略低于泡沫型吸能器，且远小于法规限值。综上所述，新型保险杠吸能器在行人保护方面的性能较之泡沫型吸能器有了较大程度的改善，并较好的满足了法规要求。

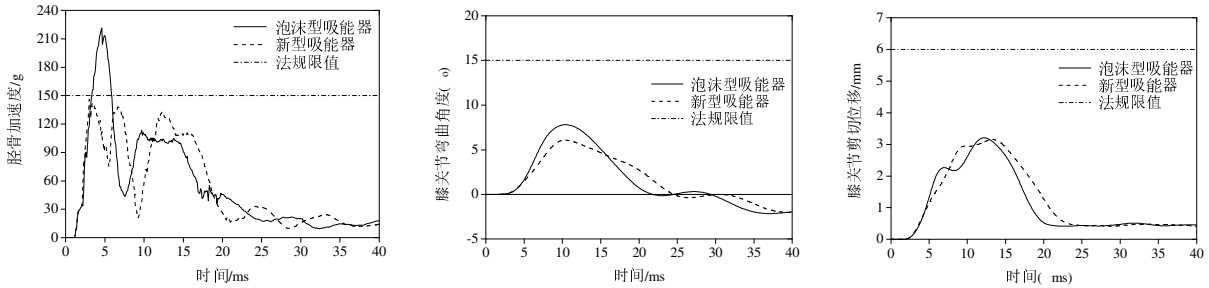

（a）胫骨加速度　　（b）膝关节弯曲角度　　（c）膝关节剪切位移

图 10 行人保护性能对比

图 11 行人下肢冲击后吸能单元的变形

5 低速碰撞性能分析

5.1 低速碰撞有限元模型的建立

为简化计算，同 3.1 节，仅取整车碰撞有限元模型中 A 柱之前的主要单元，并进行配重，同样将 3.1 节中的保险杠吸能器的有限元模型安装于保险杠横梁与蒙皮之间。在众多汽车碰撞试验法规中，选择较为严格的加拿大 CMVSS215 法规进行实验工况设置及限值选择，建立了轿车低速碰撞简化有限元模型。根据法规要求，碰撞器对中碰撞速度为 8km/h，为简化分析过程，本模型仅考虑对中碰撞的情形，如图 12 所示。

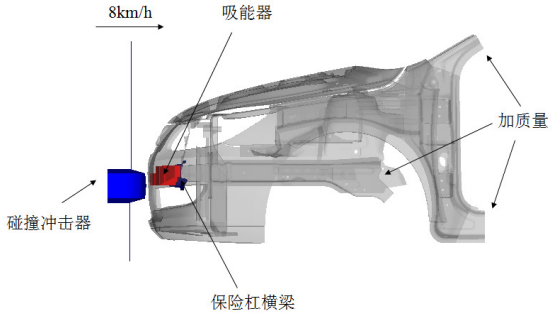

图 12 低速碰撞有限元模型

5.2 仿真结果对比分析

根据所选车型的结构尺寸参数及加拿大 CMVSS215 法规中关于对中碰撞的要求：要避免碰撞器在碰撞过程中接触到维修成本较高的零件（如发动机罩等），因此，碰撞器侵入量的最大许可位移为 165mm；保险杠横梁变形量不能超过它和车身之间间隔所决定的许可位移，因此，保险杠横梁最大变形量的最大许可值为 64mm。对比了采用新型保险杠吸能器与传统泡沫式吸能器的计算结果，如图 13 所示。

如图 13（a）中新型吸能器的保险杠侵入量曲线所示，并对比试验过程可知，当碰撞器侵入汽车保险杠系统后，X 形吸能单元处于弹性变形阶段，对比泡沫型吸能器，其保险杠变形量增大的速度明显较小；进一步，30ms 后，X 形吸能单元在较大冲击载荷的作用下突破弹性极限，两侧边弧相互接触扭结快速形成自锁结构，至 70ms 处形成峰值，此时吸能能力迅速提高；进一步压缩后，吸能量急剧增大，使曲线下降并趋于平稳。本文提出的新型保险杠吸能器利用自身 X 形吸能单元的结构特点，在较大冲击载荷的情况下，自适应地采用了大变形的吸能模式（如图 14 所示），吸收了更多的能量，使保险杠侵入量峰值大幅度降低。

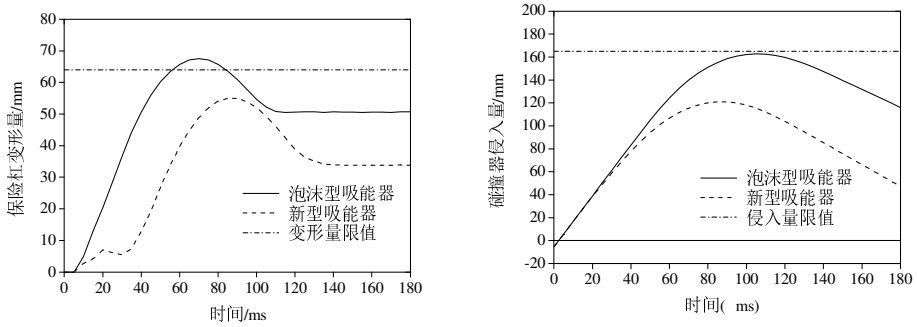

（a）保险杠变形量 **(b) 碰撞器侵入量**

图 13 轿车低速碰撞性能对比

图 14 低速碰撞中吸能单元的变形

由图 13 可知，安装传统泡沫型吸能器的保险杠侵入量不能满足法规限值的要求，采用新型保险杠吸能器后保险杠侵入量有了较大幅度的降低，满足了法规限值的要求；安装传统泡沫型吸能器的碰撞器侵入量已接近于法规限值，安装新型保险杠吸能器后碰撞器侵入量有较大程度的降低，远低于法规限值，可以满足保护维修成本较高的零件（如发动机罩等）的要求。综上所述，新型保险杠吸能器在低速碰撞上各响应参数均有不同程度的降低，可以更好地满足法规限值的要求。

6 结论

本文设计并提出了一种新型保险杠吸能器，采用了单元拼装形式的模块化设计，吸能单元采用了全新的 X 形结构，材料选用吸能性能稳定的复合材料 xenoy 合金。通过对所设计的新型保险杠吸能器行人保护及低速碰撞性能的仿真分析可知，本文提出的新型保险杠吸能器很好的利用了自身 X 形单元的结构特点，自适应地在不同的碰撞形式下采用了不同的吸能模式，尤其在当 X 形单元发生扭结后迅速提高了吸能能力，因此较之传统泡沫型吸能器而言综合性能较好，使行人保护和低速碰撞各测试参数均有了不同程度的改善，可以很好的满足相关法规的要求。综上所述，本文提出的新型轿车前保险杠吸能器改善了传统泡沫型保险杠吸能器的碰撞性能，很好的兼顾了行人保护和低速碰撞的要求。

本文所提出的新型保险杠吸能器所采用的结构尺寸仅为初步选定，相关参数优化将在后续的研究中进一步讨论。

参考文献：

[1] 熊丽君，吴璧耀. 发泡聚丙烯材料的研究生产现状[J]. 工新型材料. 2004(02)

[2] 陈杰. 综合行人下肢保护和低速碰撞的保险杠性能研究[D]. 湖南大学.2012

[3] Wenhao Mu, Jikuang Yang. *Optimization Design of Frontal Bumper System for Both Pedestrian Lower Leg Protection and Low Speed Impact Requirement* [A] INFATS Proceedings of the 10th International Forum of Automotive Traffic Safety[C]. 2012

[4] Shuler et al. Bumper System with Energy: United States, US 7163242 B2[P].2007-01-16

[5] Mohapatra et al. Bumper Assembly with Energy: United States, US 7278667 B2 [P].2007-10-09

[6] M.M. Davoodi;S.M. Sapuan and R. Yunusa. *Conceptual design of a polymer composite automotive bumper energy absorber*. Materials and Design. 2008 No.7 P1447-1452

[7] Manohar M, Panjabi, Jacek Cholewicki, eta1.Mechanism of whiplash injury.Clinical Biomechanism. 1998, 13(2):39-249

[8] GB/T24550-2009，汽车对行人的碰撞保护[S]

Proceedings of the 11th International Forum of Automotive Traffic Safety, 2014, pp 143- 148
No. ATS.2014.208

Comparative Analysis of Performance and Criteria for Crash Cushions in U.S. and EU

Chun-juan SHI[1,2,3], Wei WANG[1,2,4], Ming ZHONG[1,2,4], Ze-you PENG[1,2,4], Lan YANG[2]
[1]CCCC First Highway Consultants Co., Ltd, Xi'an 710075
[2]CCCC Civil Engineering Science & Technology Co.,Ltd. Xi'an,China, 710075
[3]Key Laboratory for Road Construction Technology & Equipment of Ministry of Education, Chang'an University , Xi'an, China, 710064
[4]Shaanxi Key Laboratory of Road Disaster Prevention, Xi'an, China, 710075
Email: scj-003@163.com

Abstract
This paper introduce and deeply comparative analyze the performance classes, impact test acceptance criteria and test methods for crash cushions in U.S. 《MASH 2009》 and EU 《EN 1317》. The difference of test methods, data acquisition and evaluation criteria in key technology and the reason for this for crash cushions are presented in this paper. By the comparative analysis of performance for crash cushions in U.S. and EU, some feasibility proposals are given, which can provide reference for the study of anti-collision pad safety evaluation and real vehicle test method in China.
Keywords: traffic engineering; specifications comparison; crash cushion; MASH 2009; EN1317

美国和欧盟防撞垫性能规范的对比分析

史春娟[1,2,3]，王　伟[1,2,4]，钟　明[1,2,4]，彭泽友[1,2,4]，杨　兰[2]
[1]中交第一公路勘察设计研究院有限公司，西安，中国，710075
[2]西安中交土木科技有限公司，西安，中国，710075
[3]长安大学道路施工技术与装备教育部重点实验室，西安，中国，710064
[4]陕西省公路交通防灾减灾重点实验室，西安，中国，710075
Email: scj-003@163.com

摘　要
对美国《MASH 2009》和欧盟《EN 1317》标准规范中防撞垫的安全性能评价标准、性能等级、试验方法和碰撞试验认可标准进行了介绍和深入的对比分析研究。主要对比了其在防撞垫试验方法、数据提取、评价验收准则等试验关键技术等方面的不同。通过总结美国和欧盟防撞垫性能规范的不同，给出了一些工作实践中的可行性建议，为国内高速公路防撞垫安全性能评价的研究和实车碰撞试验方法提供参考。

关键词：交通工程；规范对比；防撞垫；MASH 2009；EN 1317

1 引言

防撞垫是设置在岔道口、桥墩、高速公路出入口等容易发生冲撞事故处的设施，可对脱离正常行驶车道的车辆与道路上的结构物冲撞时，吸收车辆的冲击能量，降低行驶速度，从而使之停止或者改变方向，在缓冲保护结构物

基金项目：2013 年度陕西省科学技术研究发展计划社会发展攻关项目（2013k13-04-13）

的同时有效保护司乘人员、车辆和路面其他行人的安全。按照防撞垫的作用可分为导向型和拦截型两种。可导向防撞垫是指发生碰撞后，防撞垫可以改变车辆运行方向，使其回到原来车道上，表现在试验中即为可满足侧碰安全性要求。反之，设置于护栏端部，在受到车辆碰撞时不改变车辆运行方向，通过自身结构变形吸收碰撞能量，对车辆起到拦截阻碍作用，从而减轻乘员伤害程度的即为拦截型防撞垫。

目前，国内的研究学者对道路安全防护设施中的护栏研究较多，并制定了相关的设计及施工技术规范和安全性能评价标准[1,2]。而对处于重要地位的防撞垫的研究却很少，相关的技术规范和安全性能评价标准就更少了。事实上传统的护栏交通安全防护存在很多漏洞[3]。如传统的插拔式活动护栏、推拉式活动护栏、水马式活动护栏等不具备规定的防撞能力，出口三角区和收费站导流岛端部的"防撞桶"实际上仅具有警示效果，不同类型护栏的刚度过渡存在突变容易插入车体、地锚式上游端头容易造成车辆跃起并翻车，混凝土的斜坡式端头也易造成车辆跃起并翻车。因此本文将研究美国和欧盟的相关的规范和法规中关于防撞垫的部分，对其进行对比分析以期对我国后续的防撞垫的研究能有帮助。

2 防撞垫性能规范

《MASH 2009》是美国目前最新的高速公路交通安全设施安全性能评价标准[4]，是在《NCHRP Report 350》[5]的基础上做了修订更新和完善。该标准采用国际单位制，规定了质量、速度、公差等试验应用值；扩大了试验规范范围到护栏、终端、防撞垫、分离支撑结构和标杆，车载衰减器和工作区交通控制装置；规定了补充试验车型作选择来满足更高的性能等级，为不同类型的路侧安全设施定义了 6 种基础测试等级，为安全性评价定义了几种可选的测试等级；包含了为导向型安全硬件的碰撞试验的临界撞击点的选择指南；规定了更好更高等级的乘员撞击速度和加速度等级；反应了安全性能评价的最新方法和技术评价，例如可替代测试车辆和计算机仿真。

《EN 1317》是欧盟的道路约束系统法规[6]，在所有成员国强制执行的关于道路交通安全设施的完整的标准，包括 6 部分，其中《EN 1317-1》是试验方法的术语和一般准则，《EN 1317-3》是防撞垫的性能等级、碰撞试验认可标准和试验方法，《EN 1317-5》是交通安全设施耐久性和一致性评价。

3 两国规范对比研究

本文将从实验条件、试验指标允许偏差、图像记录要求以及安全评价标准这四个方面对美国和欧盟防撞垫的规范进行对比分析。

3.1 试验条件对比

表 1 是美国和欧盟防撞垫试验条件对比。除此之外《MASH 2009》中可以通过仿真程序来初步确定碰撞的临界碰撞点 CIP（目前仅用于护栏），此规范认为一个可导向防撞垫的初始碰撞点可以影响它的安全性能，车轮阻碍、车辆侵吞和装置的结构失效的可能性都取决于初始碰撞点。

Table1. Comparative of test conditions for crash cushion in America and EU

表 1. 美国和欧盟防撞垫试验条件对比

对比项\规范来源	美国《MASH 2009》	欧盟《EN 1317》
碰撞试验车型	1100C、2270P、10000S、36000T	900kg、1300kg、1500kg
碰撞速度（km/h）	50、70、80、90、100、	50、80、100、110
碰撞角度（°）	0、15、25	0、15
碰撞位置或碰撞点	正面 0°中心碰撞 正面 1/4 车身偏置碰撞 正面车头 15°碰撞 侧面车头 15°撞击防撞垫 1/2 长度位置	TC1 正面中心碰撞 TC2 正面 1/4 车身偏置碰撞 TC3 头部 15°碰撞 TC4 侧面 15°碰撞 TC5 侧面 165°碰撞。
试验等级	以速度不同划分三大等级，每级细分为 30~44 个不同类型测试，共 63 种类型	以碰撞位置不同划分 5 级，每级再以速度不同细分，共有 18 个类型。
试验类型记录	TEST 3-41：车辆类型为 2270P 以 100km/h 正碰防撞垫	TC 3.2.80：质量为 1300kg 的车辆车头偏移 15°以 80km/h 撞击防撞垫

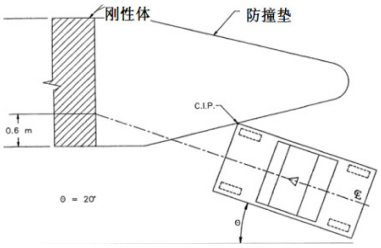

Figure 1. The CIP position when the width of crash cushion more than 1.2m

图 1. 当防撞垫宽度>1.2m 时 CIP 位置

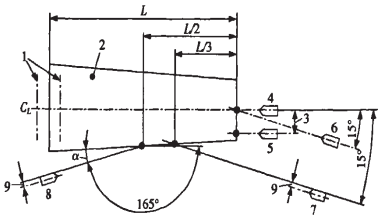

Figure 2. Impact location at different levels of EN 1317

图 2. 欧盟《EN 1317》不同等级碰撞位置图

可能的情况下，对于一个可变向装置应该选择初始碰撞点来建立一个最坏测试条件，也就是临界碰撞点，或最大可能引起试验失败的点，不管是由过多的车辆阻碍，过度侵吞或装置结构失效决定的。尽管鉴定临界碰撞点位置的研究还没做过，碰撞试验经验已经表明，对于一个狭窄的刚性体，当试验车辆的中心朝着刚体中心时，临界碰撞点在最大可能发生车辆障碍或侵吞的位置产生。对于一个宽阔的刚体这种情况，最大可能出现车轮障碍处，或当车辆重心朝着接近刚体边缘 0.6m 的点上撞击时车辆侵吞的位置，如图 1 所示。欧盟《EN 1317》规定了不同等级的碰撞位置图如图 2 所示。

3.2 试验指标允许偏差

两种规范规定的试验指标允许偏差对比见表 2。

Table2. Allowable deviation of test index

表 2. 试验指标允许偏差

性能		美国《MASH 2009》		欧盟《EN 1317》		
		1100C（小车）	2270P（皮卡）	800 kg	1300 kg	1500 kg
质量 kg	测试惯性	1100±25	2270±50	825±40	1300±65	1500±75
	假人	75	---	75	---	---
	最大压舱物	80	200	100	160	180
	总质量	1175±25	2270±50	900±40	1300±65	1500±75
尺寸 cm	轴距	230±10	335±25	---	---	---
	前悬	75±10	80±10	---	---	---
	总长	370±20	535±25	---	---	---
	车宽	135±10	165±15	135±15%	140±15%	150±15%
质心位置 cm	前轴纵向距离	80±15	140±15	90±15%	110±15%	124±15%
	车辆中心线横向偏移	---	---	7	7	8
	高于地面距离	55±5	70±5	---	---	---
碰撞速度偏差（km/h）		±4.0		±1%		
碰撞角度偏差（°）		±1.5		±1.5		

除表 2 所列的区别之外，《MASH 2009》中对碰撞试验中车辆质量、速度和角度的推荐公差用一个复合公差的限度值代表这些测试参数的组合效应，由一个碰撞严重程度 IS 来表征，式（1）为计算公式，不同试验类型的 IS 值和推荐公差如表 3 所列。

$$IS=(1/2)M(V\sin\theta)^2 \qquad (1)$$

式中：IS—碰撞严重程度（kJ）；

M—车辆的试验惯性质量（kg）；

V—碰撞速度（m/s）；

θ—碰撞角度（°）。

对非导向型的所有试验，sinθ 应设置为 1。从式（1）可知，通过调整惯性质量 M、速度 V 和角度 θ 这三个参数的任意一个均可以达到所期望的 IS 值。实际中，推荐先调整试验车辆的惯性质量，在公差范围内接近推荐的标称值。假设试验惯性质量已接近标称值，可以调整速度或角度来达到推荐的 IS 值。但是碰撞严重程度指数对角度非常敏感，因此，应调整测试速度参数来达到推荐 IS 值。

3.3 图像记录要求

美国和欧盟减震垫性能规范中都详细规定了关于数据采集的各项要求，以及相关的仪器设备和传感器的精度要求和安装使用，两者的在图像记录部分的区别是欧盟《EN 1317》中明确了图像记录的摄像机摆放位置，如图 3 所示。

《EN 1317》规定至少要放置两台高速摄像机和一台普通摄像机来记录防撞垫的性能，推荐的摄像机的流程操作包括以下：a 一台摄像机正常观测防撞垫中心线；b 顶上有一台或两台高速摄像机，放置在可以覆盖观测距离碰撞点前至少 6m 的车辆移动情况的位置处，来观测防撞垫性能；c 在车辆行驶轨迹的右侧平放一台普通摄像机；d（可选项）在碰撞点的位置安放一台高速摄像机来记录车辆的翻滚、垂直位移、穿透和碰撞后防撞垫的一系列运动。

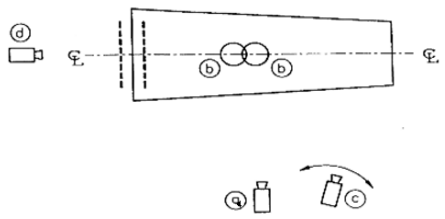

Figure 3. Placement of recording camera in EN 1317

图 3. EN 1317 记录试验的摄像机布局

3.4 安全评价标准

美国《MASH 2009》中安全评价标准给出了三个动态性能评价因素：结构充分性、乘员风险和碰撞后车辆运行轨迹。

结构充分性一般是评价的第一要素，指的是结构对于碰撞本身的要求，基于设计的预期功能，防撞垫应该通过对车辆导向，拦截车辆或允许车辆冲破装置来满足结构充分性要求。

乘员风险依据车辆总体的加速度来评价，因为它们对安全设施设计和试验车辆的外部结构设计起主要作用。乘员风险也可以由不限制的前座假人的响应来评估，评价的两个性能因素是（1）在撞击内表面时乘员部分的纵向和横向加速度部分；（2）碰撞后平均每 10ms 间隔的碰撞脉冲的车辆合成加速度的最大横向和纵向部分。尽管没有要求，试验人员应该计算和报告理论头部碰撞速度(THIV)，撞后头部减加速(PHD)，和加速度严重指数(ASI)（见表 3）。车辆轨迹风险是一种估量碰撞后车辆引起后续多车碰撞事故的轨迹的可能性的措施，由此其他车辆驾驶员遭受过度损害或者碰撞车辆的驾驶员遭受与其他固定障碍物的二次碰撞。

《EN 1317》的验收标准有：车辆撞击严重程度、车辆运行轨迹、测试车辆和防撞垫零部件的弹出、分布状况、防撞能量衰减水平、防撞垫的变形等。

防撞垫表现：防撞垫的零部件不允许穿透车辆的乘员舱，乘员舱的变形和侵入会导致驾驶员的严重损伤，这是不允许的，防撞垫上 2kg 重量的主要元件不允许完全分离，防撞垫的等级应该按照分离元件的最终位置来划分，基础件、加固物和附件的运动应该符合防撞垫的设计和实验报告，变形后的防撞垫不允许穿透障碍物的正面。

试验车辆表现：碰撞过程和之后，车辆不允许翻转，可以有适当的旋转，偏移和倾斜。测试车辆的撞后轨迹应该控制在退出线区范围内。

Table3. Severity value of vehicle collision

表 3. 车辆碰撞严重程度值

碰撞严重程度等级	指示值		
A	ASI≤1.0	试验等级为 1、2 和 3 级时 THIV≤44km/h 试验等级为 4 和 5 级时 THIV≤33km/h	PHD≤20g
B	ASI≤1.4	试验等级为 1、2 和 3 级时 THIV≤44km/h 试验等级为 4 和 5 级时 THIV≤33km/h	PHD≤20g

注：1.碰撞严重程度等级 A 为事故车辆的乘员提供了更高等级的安全性保护，推荐使用此等级；2.试验等级为 1、2 和 3 级时 THIV 的限制值更高，是因为经验表明正面碰撞可以承受更高的 THIV 值。ASI 参数中也已经考虑到承受值在正面和侧面碰撞的区别，因此 ASI 值不需要改变。

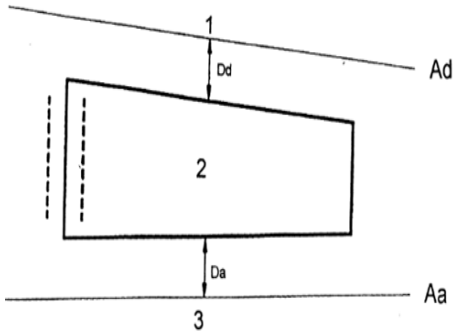

注：1 离开边线；2 防撞垫设计封闭区；3 碰撞接近边线

Figure4. Permanent deformation limit of crash cushion

图 4. 防撞垫的永久变形限制

Table 4. Permanent lateral displacement deformation region of crash cushion

表 4. 防撞垫的永久横向位移变形区域

等级	位移	
	Da(m)	Dd(m)
D1	0.5	0.5
D2	1.0	1.0
D3	2.0	2.0
D4	3.0	3.0
D5	0.5	≥0.5 试验等级 3
D6	1.0	≥1.0 试验等级 3
D7	2.0	≥2.0 试验等级 3
D8	3.0	≥3.0 试验等级 3

防撞垫横向位移：表 4 标示了有关防撞垫固定横向位移从 D1 到 D8 的 8 个等级，这个固定横向位移应该在试验报告中计算和表明。防撞垫的永久变形限制如图 4 所示。D1 到 D4 等级是依据 1，2，3，4 和 5 这五个试验等级类型进行试验的防撞垫变形应该保证在设计边线的 Da 和 Dd 内。对于等级 D5 到 D8，防撞垫应该满足与 D1 到 D4 等级相同的试验条件，除此外对于试验等级 3，防撞垫可以在退出边线一侧移动一定的距离。

4 结语

通过对美国《MASH 2009》和欧盟 EN 1317 中防撞垫部分的标准规范对比可知：美国标准对防撞垫碰撞试验等级划分比较详细，对车辆类型和所有参数的偏差值也规定的较为详细，而欧盟的碰撞试验速度更高些。

总体比较，美国的规范发展更成熟，鉴于我国高速公路防撞垫性能评价标准的空白，国内的防撞垫性能研究和此类碰撞试验可以借鉴美国的防撞垫标准规范，同时参考欧盟的一些标准，完善我国的相关标准和行业规范。

参考文献 (References)

[1] Research institute of highway ministry of transport. JTG/T F83-01-2004 The Evaluation Specification for Highway Safety Barriers[S]. Beijing: China Communications Press, 2004.
交通部公路科学研究院. JTG/T F83-01-2004 高速公路护栏安全性能评价标准[S]. 北京：人民交通出版社, 2004.

[2] Research institute of highway ministry of transport. JTG D81-2006 Guidelines for Design of Highway Safety Facilities[S]. Beijing: China Communications Press, 2006. 交通部公路科学研究院. JTG D81-2006 公路交通安全设施设计规范[S]. 北京：人民交通出版社, 2006.

[3] GE Shu-fang. Crash Cushion and It‘s application in highway[J].Journal of Highway and Transportation, 2003, 20(z1): 147-149.
葛书芳. 防撞垫及其在高速公路中的应用[J]. 公路交通科技, 2003, 20(z1): 147-149.

[4] American association of state highway and transportation officials. Manual for Assessing Safety Hardware[S]. 2009.

[5] BSI. EN 1317 European Standard Norme[S]. Edition2. British: BSI, 2007.

[6] ZHANG Gai, TAI Yong-gang. Development and study on energy absorbing crash cushions highway steerable beam[J]. Highway, 2012, (3): 174-178.
张改, 郃永刚. 吸能梁式公路可导向防撞垫开发研究[J]. 公路, 2012, (3): 174-178.

[7] ZHANG Gai, TAI Yong-gang. Development and study on new-type road crash cushions[J]. Journal of ChongQing Jiao Tong University(Naturals Science) , 2012, (3): 174-178.
张改, 郃永刚. 新型公路可导向防撞垫开发研究[J]. 重庆交通大学学报（自然科学版）, 2011, 30(5): 978-982.

[8] YAN Shu-ming. Development of new-type un-directive crash cushion[J]. Journal of Wuhan University of Technology(Transportation Science & Engineering), 2012, 36(1): 211-214.
闫书明. 新型非导向防撞垫开发[J]. 武汉理工大学学报（交通科学与工程版）, 2012, 36(1): 211-214.

[9] JIN Ming-xin. Application and test of collision cushion in road protection system—EN 1317.3 ”Collision cushiong performance levels, collision test acceptance and criteria and test methods” outline[J], Communications standardization 2007, (12): 28-30.
金明新. 道路防护系统中碰撞缓冲垫的应用和试验—EN 1317.3《碰撞缓冲垫性能等级、碰撞试验验收标准及试验方法》简述[J]. 交通标准化, 2007, (12): 28-30.

[10] YAN Shu-ming, BAI Shu-feng, LU Guo-ren. Development and research of a new type of re-direction crash cushion[J]. Journal of Beijing University of Technology, 2011, 37(8): 1162-1168.
闫书明, 白书锋, 吕国仁等. 新型可导向防撞垫开发[J]. 北京工业大学学报, 2011, 37(8): 1162-1168.

[11] YU Wen-sheng TAI Yong-gang, ZHANG Ying. research Application of re-direction crash cushion Expressway [J].Journal of China & Foreign Highway, 2013, 3: 11-16.
俞文生, 郃永刚, 张颖等. 高速公路可导向防撞垫的应用研究[J]. 中外公路，2013, 3: 11-16.

Proceedings of the 11th International Forum of Automotive Traffic Safety, 2014, pp 149- 153
No. ATS.2014.209

Analysis of Structure Dynamic Characteristics of ATV Frame with Engine

Fang Ye[1, a], Zhongming Xu[2, b], Xicheng Zhai[3, c]
[1]*Chongqing Technology and Business Institute, Chongqing 400052, China;*
[2]*Department of Mechanical Engineering of Chongqing University, Chongqing 400030, China*
[3]*Vocational Education Center of Hechuan, Chongqing 401520, China*
[a]*yef1024@163.com,* [b]*xuzm@cqu.edu.cn,* [c]*lyzxc@tom.com*

Abstract:

Background: ATV,also known as the all terrain vehicle,is often referred to as the beach car in the domestic, widely used in agriculture, military, entertainment and leisure etc, its vibration comfort has become one of the most important ATV service performance. The frame is the skeleton of ATV, the vibration characteristic analysis of the frame elastic hanging engine, has great effect on vehicle safety and vibration comfort.

Objective: The purpose of this paper is to establish finite element model of an ATV frame with engine, to analyze vehicle vibration characteristics through simulation and experiment method, to adjust ATV frame structure, and to improve the vehicle vibration comfort.

Method and Material: It is using the computer simulation method for dynamic characteristic research of ATV frame with engine, and the experimental modal analysis is competed , the result show that the calculated modes are very close to the experimental modes. So we analyze vehicle dynamic characteristics using this modal.

Results: By comparison to the computational modal and experimental modal results of ATV body, it is found the error within 10%, so the finite element model of car body is effective. Then, it's found that the ATV body's resonance is caused by vibration frequency synchronization of the excitation of the engine and ATV body.

Conclusions: This paper studied the finite element model of an ATV frame with engine, verified the validity of the model with experimental methods, and discovered that the cause of body resonance is synchronization of the excitation frequency and body frequency. So the improved scheme of the frame structure is formulated, which provides a direction and method for the improvement of the ATV ' s whole ride comfort.

Keywords: ATV; frame with engine; vibration modal; finite element analysis

ATV 车架挂发动机结构动特性分析

叶芳[1]，徐中明[2]，翟喜成[3]
1. 重庆工商职业学院，400052，重庆，中国
2. 重庆大学机械工程学院，400030，重庆，中国
3. 合川职教中心，401520，重庆，中国
E-Mail: yef1024@163.com

摘要

研究背景：ATV 又称全地形车，在国内通常被称为沙滩车，广泛应用于农业，军事，休闲娱乐等，其振动舒适性已成为 ATV 的重要使用性能之一。车架是 ATV 的骨架，分析车架弹性挂发动机的振动特性，对整车安全性和振动舒适性有较大影响。

目的：本文旨在建立某 ATV 车架挂发动机的有限元模型，通过仿真结合实验的方法进行振动特性分析，并以此指导 ATV 车架进行结构改进，改善整车振动舒适性。

方法和材料：利用解析法分析了 ATV 车架挂发动机的结构动态特性，利用实验法对该车体进行实验模态分析，通过实验和理论相结合的方法验证有限元模型的有效性，并以此模型进行车体动态特性分析。

结果：ATV 车体的计算模态和实验模态结果误差均在 10%以内，验证了车体有限元模型的有效性；进行车体动态特性分析，发现引起车体共振的原因在于激励频率与车体频率同步。

结论：论文研究了某 ATV 车架挂发动机的有限元模型，并以实验的方法验证了模型的有效性，发现引起车体共振的原因在于激励频率与车体频率同步，形成对车架结构进行改进的方案，这为整车振动舒适性的改进提供了方法和思路。

关键词：ATV，车架挂发动机，振动模态，有限元模型

1 Introduction

ATV,also known as the all terrain vehicle,applied to various fields of agriculture,forestry,animal husbandry, exploration, industrial, construction, military and so on,is the single multipurpose vehicle having the characteristics of a straddle seat, handle type steering, three or four wheel structure, large size, low pressure tires[1].

The dynamic characteristic of ATV frame elastic hanging engine largely determines vehicle vibration comfortableness and reliability. Now part of the large ATV is connected with the frame and engine using rubber mounting component. The stiffness and mass distribution is changed for this whole body, so the comfortableness is greatly influenced; it is the premise of analyzing flexible frame fatigue strength etc. The vehicle vibration characteristics were analyzed in this paper, and made some improved design for frame structure, so as to improve the comfort and safety of the ATV.

2 The dynamic characteristic analysis of ATV frame with engine

2.1 The establishment of ATV finite element model

Taking a type of 400 ATV as the research object in this article, First of all, using laser measuring instrument of three coordinate measured surface lattice model data, obtained 528698 points, created curves and surfaces models through the lattice, then imported the models into the UG NX4.0, and closed the model surface to obtain the solid model of the frame.

Considering the influence of vehicle vibration modal of the widget is very small, the car body is simplified reasonably, ignoring the engine support seat, seat supporting, front and rear suspension supporting seat and other accessories. The frame is the cage structure, which made up of some steel plate and circular tubes, so we use shell element in the MSC.NASTRAN To discrete frame structure. In order toensure the accurate model, reliability, and efficiency, we use quad4 unit almost all, the triangular element does not exceed 5%. Ignoring the effects of welding, the various components are connected together by shell unit.

After imported 3D geometrical model into Hyper mesh, the finite element model is established which contains 57636 nodes, 57104 shell unit. Because the engine quality is larger, and the rubber mount is used to connect with the frame, it is greater influence on vehicle vibration for frame elastic hanging engine. So the engine is simplified as a particle, and it is connected with frame by a rod unit [2]. The finite element model of the ATV bodies is established showing as the Fig.1, 2.

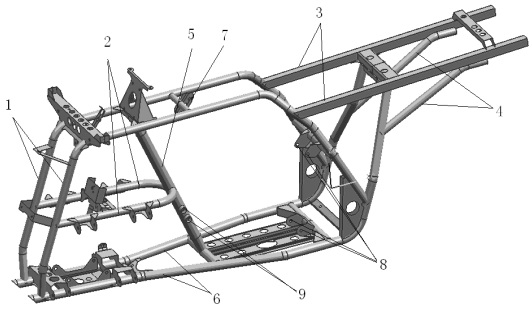

Fig 1. Geometry model of motorcycle frame

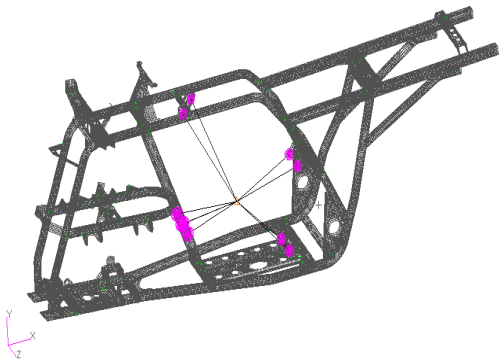

Fig 2. FEA model

2.2 The analysis of the finite element calculated mode

The major incentive for ATV is the excitation of road surface and engine excitation, road surface excitation frequency is lower, and engine excitation is mainly one order and two order inertia vibration frequency, and its speed n is generally not more than 7500rpm, so the frame frequency range we focused on can be reduced to 0~200Hz, we can calculated the first 6 order non rigid mode of the bodies, the results is shown in Table 1.

2.3 The analysis of the experimented mode

The experimental modal analysis can be used to test the calculated modal, and to improve the accuracy of the theoretical analysis. The experimental system consists of hammer, the ICP acceleration sensor, the ICP force sensor, LMS SCADAS Ⅲ data acquisition, microcomputers, LMS.TESTLAB software etc.

Using a rubber rope hanging up test-piece and choosing the hammer excitation, we can begin the test of the free modal analysis of car body. We set the 77 monitoring points in the ATV body, and choose the 71, 73 and74 point for point excitation, the other points as response point, that is MIMO, after several times of pro-experiment and consider computational modal analysis results [3]. See Fig.3, The experimental modal analysis results as shown in Table 1.

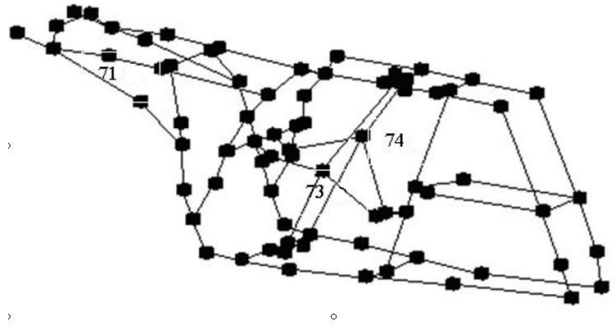

Fig 3. the testing points of ATV's body

2.4 The analysis of the modal results

By comparison to the computational modal and experimental modal results of ATV body, it is found the error within 10% except sixth order, see table 1, and the two modes are also coincident, so the finite element model of car body is effective.

This finite element model is used in vibration modal analysis of frame with engine for ATV,the results as shown in Table 1.

Table 1. the difference of body between the experimental modal analysis and the computational modal analysis

Order	Modal frequency /Hz		The relative difference
	Experimental modal	The calculating modal	
1	76.90	76.92	-0.026%
2	85.09	91.13	-7.1%
3	122.1	112.6	7.8%
4	132.2	136.4	-3.2%
5	149.7	139.9	6.5%
6	178.5	153.9	13.7%

2.5 The analysis of vehicle dynamic characteristics

In the running process, the ATV mainly gets excitation from road and engine, so the structure characteristics of frame must have mechanical properties compatible with incentive. If the inherent frequency of the vehicle coupled with the excitation frequency, ATV car will produce resonance, severe vibration, even partial destruction etc [4~5].

It can be seen from table 2, the excitation frequency of engine covering the first three order modal frequency of frame hanging engine, and the third order bending mode frequency of body is 122.1Hz, Just in this range, when the reciprocating inertia force frequency of engine synchronous the body frequency, it will cause the body resonance, The resonance speed close to the highest speed, 68.64km/h. In order to improve the ATV's vibration comfort, it is necessary to make the appropriate improvement on the structure.

Table 2. the resonance rev of the engine against body

Order	Frequency（Hz）	Revolution（r/min）	Speed（km/h）
1	76.90	4632	42.35
2	85.09	4984	46.47
3	122.1	7444	68.64
4	132.2	7828	74.65
5	149.7	8947	83.38
6	178.5	10688	98.48

3 The structure Improvement of ATV body

Method for improvement of the frame can be taken as increasing or decreasing the size of the frame in weak structure, increasing or decreasing the stiffness of the vehicle body, in order to avoid the engine working frequency caused by resonance. Due to the frame should have enough stiffness and strength to adapt to the work in the harsh environment need, it is used to increasing the size of frame structure(Increased caliber 1mm of the No1 and 6 pipe)to improve the body stiffness.

Table 3. the first six modal frequency of the body improved

Order	1	2	3	4	5	6
Frequency (Hz)	88.91	113.7	132.7	159.5	164.6	170.4

From the calculation results (see Table 3) can be seen, natural frequency of vehicle body has been improved to avoid the one order inertial force frequency of engine from 50Hz to125Hz, and Resonance frequency is avoided, the ATV body vibration comfort is improved

4 Summaries

Through the structure dynamic characteristic analysis of the ATV frame elastic hanging engine,it is found the severe vibration reasons of the car body is the body resonance caused by the engine excitation frequency cover the third order modal frequency. By increasing the size of the frame structure, improving the body stiffness, avoiding the resonance frequency, the body vibration comfortableness is improved.

Acknowledgements

In the process of paper, the author referred to lots of documents and monographs, so thanks a lot for the all of original article author, and thanks all of teachers and friends for your supports and helps.

References

[1] LMS. Theroy and background. LMS International [M]. 2002.

[2] G.S.Paddan and M.J.Griffin. *Evaluation of whole-body vibration in vehicles*. Journal of Sound and Vibration (2002) **253**(1).195-213.

[3] P. Moroney, M. Doyle, K. Mealy. *All-terrain vehicles-unstable, unsafe and unregulated A prospective study of ATV-related trauma in rural Ireland* [J]. Injury, Int. J. Care Injured, 2003, 34: 203~205.

[4] L. Dai, J. Wu. *Stability and vibrations of an all-terrain vehicle subjected to nonlinear structural deformation and resistance* [J]. Communications in Nonlinear Science and Numerical Simulation, 2007, 12: 72~82.

[5] B. REHN, I. A. BERGDAHL, C. AHLGREN et al. *Musculoskeletal symptoms among drivers of all-terrain vehicles* [J]. Journal of Sound and vibration, 2002, **253**(1): 21~29.

Proceedings of the 11th International Forum of Automotive Traffic Safety, 2014, pp 154- 161
No. ATS.2014.210

Crash performances comparison and selection of bumper beam with different lightweight methods

Zhang Jingwen[1,2] ,Fan Tiqiang[1,2] ,Zhao Qingjiang[1,2] ,Li Yang[1,2]
[1]*China Automotive Engineering Research Institute Co., Ltd. Chongqing, China, 401122*
[2]*Chongqing Automotive Lightweight Engineering Research Center. Chongqing, China, 401122*
Email:mymoneyold@163.com

Abstract: With global trends of energy saving and emission reduction, lightweight requirements of automobile and parts are become higher and higher. Bumper beam is one of major crash safety structures in the front and end of automobile, which has attracted a widespread attention in the auto parts lightweight. In this paper, the effects of bumper beam in the automobile crashes and three conditions for its performance evaluation were studied. Base on this, a normal steel bumper beam was replacement with four lightweight methods including cold stamping of high-strength steel, roll high-strength steel, hot forming steel and aluminum alloy respectively. The lightweight degree and crash performance of four lightweight methods were compared, which could provide a reference for the design of bumper beam as well as a method for bumper beam performance evaluation.

Keywords: bumper beam; lightweight; performance analysis

不同轻量化方式防撞梁的碰撞性能对比和选用

张敬文[1,2]，范体强[1,2]，赵清江[1,2]，李　阳[1,2]
[1]*中国汽车工程研究院股份有限公司，重庆，中国，401122*
[2]*重庆市汽车轻量化工程技术研究中心，重庆，中国，401122*
Email:mymoneyold@163.com

摘　要：在全球节能减排的趋势下，汽车整车及零部件的轻量化要求越来越高。防撞梁是汽车前端主要的碰撞安全结构件之一，在汽车零部件轻量化中得到了广泛关注。本文研究了防撞梁在实际整车碰撞中的作用，并分析了用于防撞梁性能评价的三种工况。采用该工况对某车型普通钢制防撞梁分别采用冷冲压高强钢、辊压成形高强钢、热成形钢以及铝合金四种轻量化方式进行替换，对比研究了四种轻量化方式的轻量化程度和零件性能，为该车型防撞的设计提供了参考，同时也为防撞梁的性能评价提供了一种方法。

关键词：防撞梁；轻量化；性能分析

1 引言

保险杠系统是大多数汽车事故中首先受到撞击的部分，它主要包括保险杠蒙皮、缓冲泡沫和防撞梁总成三个部分[1]。其中防撞梁总成作为保险杠系统中的主要碰撞安全结构件，在碰撞中发挥着极其重要的作用，其性能优劣直接影响对车身和乘员的保护效果[2]。

随着人们对汽车碰撞安全性能的要求越来越高，各国的汽车强制性法规和星级评定标准也日益严格。同时，在全球节能减排以及汽车轻量化的趋势下，国内外对防撞梁的研究重点主要集中在保证其碰撞性能的基础上实现

项目资助信息：汽车轻量化国家重点实验室筹建单位开放课题（编号：20130203）

零件的轻量化[3-4]。目前防撞梁轻量化设计主要通过使用轻量化材料、结构优化以及先进成形工艺得以实现[5-6]。但如何根据实际需要，综合考虑防撞梁的轻量化程度、生产制造因素以及碰撞性能来选择合适的轻量化方式是各大汽车厂商在防撞梁正向开发和优化设计上所面临的问题。此外，由于行业内还没有比较健全和统一的防撞梁性能评价方法，因借助于仿真软件模拟实际工况进行分析是其性能开发和改进的主要手段。本文对某车型普通钢制防撞梁分别采用高强钢、铝合金、辊压成形件以及热成形件四种轻量化方式进行替换，对比研究了四种轻量化方式的轻量化程度和零件性能，可为该车型防撞梁的轻量化设计提供一定依据。

2 防撞梁轻量化方案

2.1 方案描述

图1为原车型普通钢制防撞梁总成以及四种通过工艺验证可行的轻量化防撞梁总成的CAD模型以及相关的材料、厚度信息。其中原车型普通钢制防撞梁和高强钢防撞梁总成外形保持一致，且防撞梁由内外板通过点焊而成。其余轻量化防撞梁均为单个成形件。防撞梁总成的吸能盒均为矩形方管，并且根据实际的装车空间进行长度匹配。吸能盒前后端分别与防撞梁以及安装板通过缝合焊进行连接。

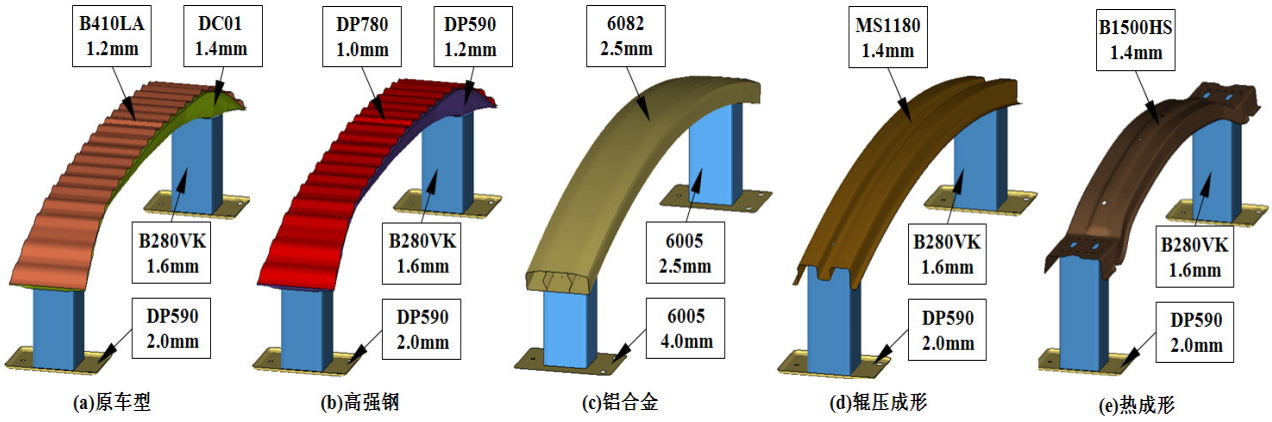

Figure 1 Lightweight program of bumper beam

图 1 防撞梁轻量化方案

2.2 轻量化程度对比

不同防撞梁总成的质量对比如表1所示。可以看出，采用高强钢方案进行替换，减重仅为9.8%。而采用其他三种轻量化方式，均可实现 15%以上的减重。其中采用辊压成形防撞梁可实现减重 18.5%，采用热成形防撞梁可实现减重 22.3%，而采用铝合金防撞梁可实现减重 26.8%。

Table 1. Mass of different bumper beam assemblies

表 1 不同防撞梁总成的质量

防撞梁总成类型	质量（kg）	相对原车型变化
原车型	5.79	—
高强钢	5.22	-9.8%
铝合金	4.24	-26.8%
辊压成形	4.72	-18.5%
热成形	4.50	-22.3%

3 防撞梁碰撞性能对比

3.1 工况研究

当汽车在正面行驶过程中，正面局部撞击到可变形障碍物，如树木、电线杆等。防撞梁的静态刚度不足便会发生折弯，并对后端汽车部件造成较大伤害，如图 2 所示。

Figure 2 Deformation of a bumper beam after local frontal crash

图 2 某车型前端局部碰撞防撞梁变形

Figure 3 Deformation of a bumper beam after low speed crash

图 3 某车型低速碰撞防撞梁变形

当汽车在停车、起步、倒车或拥堵路况等低速(通常小于 10km/h)行驶状态下，车辆前后端发生碰撞时，防撞梁良好的低速碰撞性能可以减小翼子板、散热器、发动机罩等汽车部件的损坏程度从而降低车辆的维修成本[7]，如图 3 所示。

Figure 4 Deformation of a bumper beam after frontal crash

图 4 某车型正面碰撞防撞梁变形

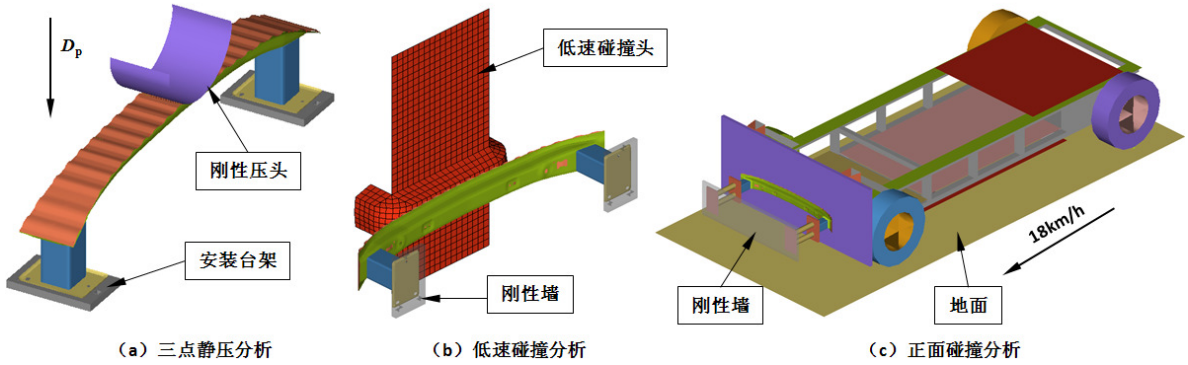

Figure 5 Simulation model of bumper beam performance analysis

图 5 防撞梁碰撞性能分析仿真模型

当汽车在中低速发生正面碰撞（10～20km/s）时，一般希望防撞梁总成可以吸收全部的碰撞能量，从而最大限度减小车身损害；当在高速正面碰撞时（通常大于 20km/h），吸能盒被完全压溃，而防撞梁提供稳定的力传导作用以保证发动机舱的连续变形[8]，如图 4 所示。

因此，根据实际的碰撞工况，防撞梁的碰撞性能主要包括静态刚度、低速碰撞性能以及正面碰撞性能三个方面。

3. 2 分析模型

根据防撞梁的碰撞性能要求建立如图 5 所示的三种仿真分析模型，包括三点静压仿真模型、低俗碰撞仿真模型以及正面碰撞仿真模型。三点静压分析时，安装板固定在安装台架上，并采用刚性压头对防撞梁中部进行恒位移加载，加载距离为 100mm[9]。防撞梁采用弹塑性材料模型，并以静态拉伸曲线作为材料的硬化曲线，如图 5（a）所示。由于仿真过程中未考虑材料的应变率硬化效应，因此加载速度设置为 1m/s 以节约计算时间。低速碰撞分析时，参考 GB17354-1998 汽车前后端保护装置的实验评价方法[10]，将防撞梁固定在刚性墙上，并采用配重为 1200kg 的低速碰撞头以 4km/h 的碰撞速度对其进行纵向中心碰撞，如图 5（b）所示。正面碰撞分析时，参考《乘用车正面碰撞的成员保护》中的实验方法[11]，将防撞梁固定在刚性墙上，并采用配重为 1000kg 的台车对其进行撞击，如图 5（c）所示。通过多次预仿真分析最终确定防撞梁正面碰撞的撞击速度为 18km/h，此时吸能盒将呈现出明显的压溃状态。在防撞梁低速碰撞和正面碰撞模型中，防撞梁采用高速拉伸曲线作为其材料的硬化模型以考虑应变率硬化效应，如图 6 所示。

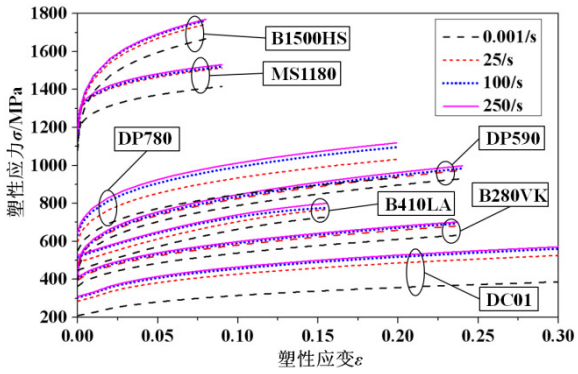

Figure 6 High speed tensile curve of different materials

图 6 不同材料的高速拉伸曲线

3.3 结果对比

3.3.1 静压分析结果

在静压过程中，一般希望防撞梁的抗压能力应不足以使吸能盒发生明显的大变形以保证防撞梁在碰撞中发挥应有的支撑作用。从图 7 中原车型及不同轻量化防撞梁的静压变形仿真结果可以看出，防撞梁中部在静压过程中均发生了折弯，而吸能盒未发生明显变形，因此防撞梁的刚度满足结构的有效性。

图 8 为原车型及轻量化防撞梁的静压力 F 随静压距离 D_P 的变形曲线。可以看出，在静压初期当 D_P 逐渐增大时，F 随之增大并达到静压力峰值 F_{max}。此时防撞梁结构稳定性遭到破坏，并发生折弯，同时 F 随 D_P 的增大而逐渐减小。当 D_P 相同时，四种轻量化防撞梁的 F 均大于原车型防撞梁，静压性能均有所提升。

表 2 和表 3 分别为轻量化防撞梁与原车型防撞的 F_{max} 和静压结构稳定距离 D_s 及对应的塑性应变 ε_s 对比。可以看出：相对于原车型防撞梁，辊压成形和热成形防撞梁的静压性能提升最为明显，其中辊压成形防撞梁的 F_{max} 和 D_s 分别提高 61.6%和 10.3%，热成形防撞梁的 F_{max} 和 D_s 分别提高 52.1%和 19.0%。高强钢防撞梁的静压性能提升效果次之，F_{max} 和 D_s 分别提高 47.9%和 6.9%。而铝合金防撞梁虽然 F_{max} 提高了 50.7%，但 D_s 却下降了 15.5%，因此静压性能提升效果最小。同时，四种轻量化防撞梁在达到静压结构稳定极限时的应变均小于各自材料的断裂应变，因此在产生 F_{max} 之前均不会发生断裂，保证了防撞梁结构的可靠性。

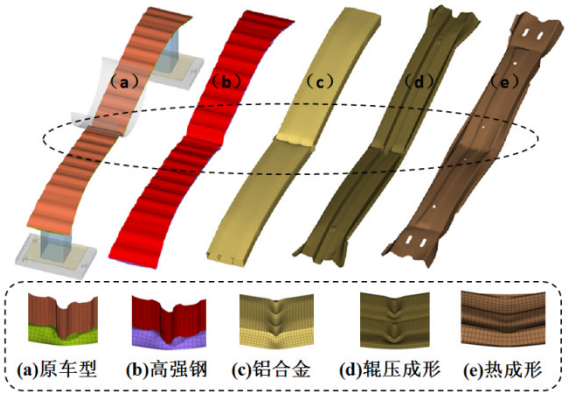

Figure 7 Deformation of different bumper beams after static press

图 7 不同防撞梁静压仿真变形结果

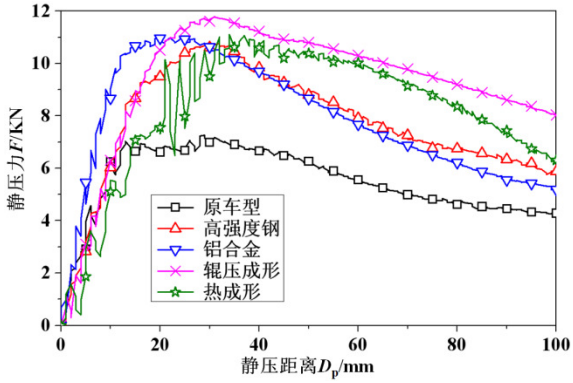

Figure 8 Static press force curve of different bumper beams

图 8 不同防撞梁的静压力曲线

3.3.2 低速碰撞分析结果

图 9 为原车型及轻量化防撞梁在低速碰撞后的位移云图对比。其中原车型和高强钢防撞梁发生了较大的塑性变形，防撞梁中部发生了明显弯曲，最大位移 D_{max} 分别为 85.3mm 和 64.0mm。铝合金防撞梁塑性变形较小，仅防撞梁中部具有塌陷的趋势，D_{max}=31.2mm。而辊压防撞梁和热成形防撞梁在低速碰撞中主要发生弹性变形，

Table 2. F_{max} of different bumper beams

表 2 不同防撞梁 F_{max} 对比

防撞梁类型	F_{max}（KN）	相对原车型变化
原车型	7.3	—
高强钢	10.8	+47.9%
铝合金	11.0	+50.7%
辊压成形	11.8	+61.6%
热成形	11.1	+52.1%

碰撞结束后防撞梁发生弹性恢复，因此外形保持完好，其中辊压防撞梁的 D_{max} 仅为 10.9mm，热成形防撞梁的 D_{max} 仅为 23.0mm。由于辊压防撞梁和热成形防撞梁的不具有明显的塑性变形，因此在发生低速碰撞后无须更换，可对车身起到良好的保护作用，并节约大量的维修成本。

Table 3. D_s and ε_s of different bumper beams

表 3 不同防撞梁 D_s 及对应的塑性应变 ε_s 对比

防撞梁类型	D_s/mm	相对原车型变化	ε_s
原车型	29.0	—	0.079
高强钢	31.0	+6.9%	0.073
铝合金	24.5	-15.5%	0.108
辊压成形	32.0	+10.3%	0.064
热成形	34.5	+19.0%	0.052

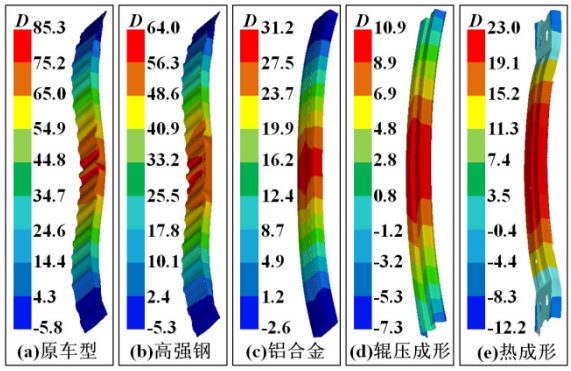

Figure 9 Displacement contours of different bumper beams after low speed crash

图 9 不同防撞梁低速碰撞后的位移云图

3.3.3 正面碰撞分析结果

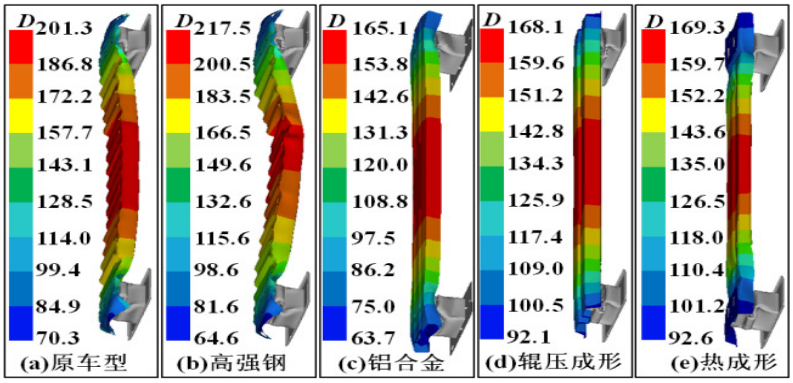

Figure 10 Displacement contours of different bumper beams when trolley speed is zero in the frontal crash

图 10 正面碰撞中台车速度为 0 时不同防撞梁的位移云图

图 10 为原车型及轻量化防撞梁在正面碰撞过程中当台车速度为 0 时的位移云图。可以看出，五种防撞梁的吸能盒均已发生明显的压溃。原车型和高强钢防撞梁中部发生明显的内侵，最大位移分别为 201.3mm 和 217.5mm，此时碰撞支反力主要由两端的吸能盒提供，防撞梁需要得到后方部件的支撑才能发挥有效的支撑作

用。铝合金、辊压成形和热成形防撞梁未发生内侵现象，防撞梁在碰撞中被压平后可将碰撞力分布到两端吸能盒及后方部件上，起到了有效的支撑作用，三种防撞梁的最大位移均在 168mm 左右。

图 11 为原车型及轻量化防撞梁在正面碰撞过程中的台车加速度曲线。其中铝合金防撞梁的加速度曲线波动幅度最大，A_{max}=17.1g，力传导稳定性相对较差。原车型、高强钢和热成形防撞梁的加速度曲线波动幅度次之，A_{max} 分别为 13.9g、13.9g 和 14.3g，力传导稳定性相对较好。而辊压成形防撞梁的加速度曲线波动幅度最小，A_{max}=12.3g，因此可以在碰撞过程中提供最为稳定的力传导作用。

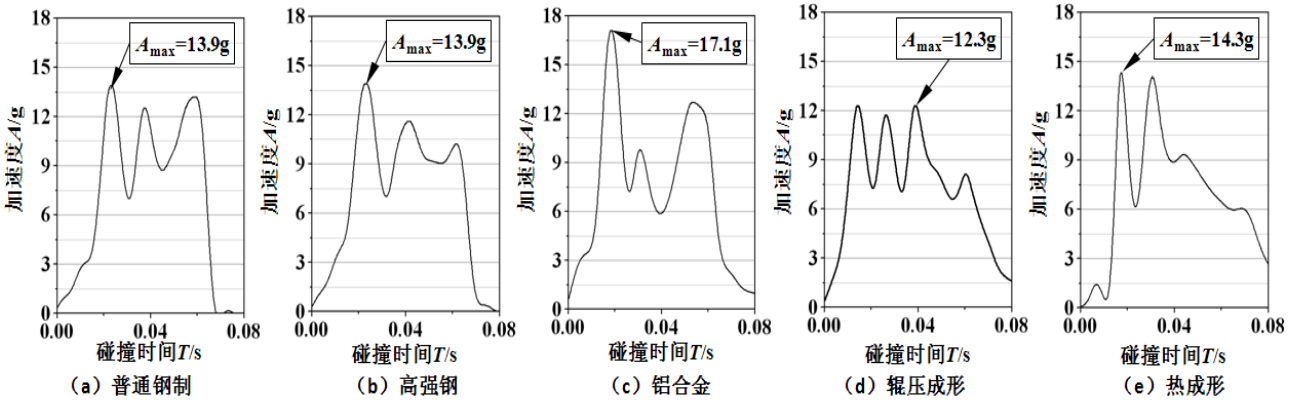

Figure 11 Acceleration curve of different bumper beams in the frontal crash

图 11 不同防撞梁在正面碰撞的台车加速度曲线

4 防撞梁选用

通过不同防撞梁的碰撞性能对比发现：四种轻量化防撞梁均能够在实现轻量化的同时保证零件性能。其中铝合金防撞梁的轻量化程度最高，但对零件碰撞性能的提升不足。冷冲压高强钢在轻量化程度和性能提升上均不具有明显优势。辊压成形和热成形钢具有较好的轻量化程度，同时也助于提升零件性能。由于该防撞梁配套车型为量产中低档乘用车，因此结合表 4 中该车型不同防撞梁的生产制造因素对比发现，辊压防撞梁在材料成本、生产成本以及生产效率上都具有比较明显的优势，可以作为参考的轻量化方式用于该车型防撞梁的后期设计。

Table 4 Manufacturing factors of different bumper beams

表 4 不同防撞梁的生产制造因素对比

因素	排序
材料成本	铝合金>热成形>辊压成形≈高强钢≈原车型
模具投入	热成形>辊压成形>铝合金>高强钢=原车型
生产成本	热成形>铝合金>高强钢≈原车型>辊压成形
生产效率	辊压成形>高强钢≈原车型>铝合金>热成形

5 结论

采用防撞梁静压、低速碰撞、正面碰撞三种简化工况可以有效的分析防撞梁在整车碰撞中的性能，可用于为防撞梁正向开发和改进设计，大幅度节约研发时间和试验成本。论文以某车型防撞梁的轻量化设计为例，对比了目前常用的四种防撞梁轻量化程度及性能提升效果，并结合防撞梁的生产制造因素为该车型防撞梁的轻量化设计提供了参考。

参考文献 (References)

[1] M.M. Davoodi, S.M. Sapuan, A. Aidy, etal. *Development process of new bumper beam for passenger car: A review*[J]. Materials and Design ,2012 , (40):304-313.

[2] Alghamdi A. *Smart frictional impact energy absorber*[J]. Int J Crashworthiness 2000,(5):169–78.

[3] Brian C, Petrinic G, Colin J. *Automotive Engineering: Lightweight, Functional, and Novel Materials* [M]. New York, Taylor &Francis Group, 2008.

[4] Zhiwen Wang.*The development of automotive lightweight technology*. Automobile Technol Mater, 2009(2):1–6.

[5] Mingtu Ma, Luxia Ma.*The application and advanced technology of the aluminium alloy in automotive lightweight*. Adv Mater Indus, 2008(9):43–50.

[6] Han Fei, Shi Lei, Xiao Hua, etal. *Development and key technologies on roll-formed automobile profiles with AHSS*[J].Journal of Plasticity Engineering, 2013,20(3):65-69.

韩飞,石磊,肖华,等. 应用先进高强钢的典型汽车零件辊压成形关键技术及开发[J].塑性工程学报, 2013,20(3):65-69.

[7] Javad Marzbanrad, Masoud Alijanpour, Mahdi Saeid Kiasat. *Design and analysis of an automotive bumper beam in low-speed frontal crashes* [J]. Thin-Walled Structures ,2009,(47):902–911.

[8] Cheng Xiusheng, Liu Weihai, Hao Yumin, etal. Optimization of a Passenger Car's Bumper Beam for Crashworthiness[J]. Automobile technology, 2011, (10):5-9.

程秀生,刘维海,郝玉敏..某轿车防撞梁结构抗撞性优化[J]. 汽车实用技术, 2011, (10):5-9.

[9] Wei Xiankun, Yang Jingjing, Mi Lin. *The quasi-static collapse research of an aluminum alloy bumper based on simulation and experiment*[J]. Journal of Chongqing University of Technology, 2013, 27(8):14-17.

魏显坤, 杨晶晶, 米林. 铝合金保险杠准静态压溃仿真与实验[J]. 重庆理工大学学报, 2013, 27(8):14-17.

[10] GB 17354-1998. Front and rear protective devices for passenger cars[S].Beijing, standards press of china, 1998.

GB 17354-1998. 汽车前后端保护装置[S].北京,中国标准出版社, 1998.

[11] GB 11551-2003. The protection of the occupants in frontal collision for passenger car[S]. Beijing, standards press of china, 2003.

GB 11551-2003. 乘用车正面碰撞的乘员保护[S].北京,中国标准出版社, 2003.

Proceedings of the 11th International Forum of Automotive Traffic Safety, 2014, pp 162-171
No. ATS.2014.211

Optimization Design for Crashworthiness of Bumper Based on Linear and S-Type Function TRB

Liu Hongbin, Xiao Zhi, Li Suwen
College of Mechanical and Vehicle Engineering, Hunan University, Changsha, China,410082,
E-mail：1023172041@qq.com

Abstract: To satisfy low-carbon economy requirement,mass reduction of a vehicle is becoming more and more important.Tailor Rolling Blanks(TRB) can significantly increase the vehicle's lightweight,safety and adaptability of structure.Based on the finite element analysis software LS-DYNA,combined with the software MATLAB,for a bumper in low-speed pole impact under 25%,40%,50% three different bias,Analysising and Comparing of linear and S-type function TRB bumper energy absorbing characteristics and influence of plate thickness on the energy absorption within and outside. And on this basis, bumper crashworthiness of multi-objective optimization design is taken.The results show that ,without increasing the mass, the Tailor Rolling Blanks(TRB) can increase the bumper energy absorption.comprehensive consideration, S-type function TRB bumper is superior to linear TRB bumper.energy absorption of the optimized S-type function TRB bumper increased about 30%.
Keywords: S-Type Function ;TRB ;Bumper ;Crashworthiness

基于线性和 S 型函数连续变截面厚度的保险杠耐撞性优化设计

刘洪斌，肖志，李素雯
湖南大学机械与运载工程学院,长沙，中国，410082
E-mail：1023172041@qq.com

摘　要: 为适应低碳经济的要求，汽车轻量化变得越来越重要。连续变截面板(TRB)对于车辆的轻量化、安全性和其结构本身的承载适应性都有显著提高。本文基于有限元分析软件 LS-DYNA，结合 MATLAB 等软件，针对某保险杠在 25%、40%、50%三种不同偏置下的低速柱碰，分析比较线性和 S 型两种不同类型的连续变截面厚度保险杠吸能特性以及保险杠内外板厚度变化对保险杠吸能的影响，并在此基础上进行保险杠耐撞性的多目标优化设计。结果表明，在不增加质量的情况下，连续变截面厚度板能有效提高保险杠的碰撞吸能。综合考虑，S 型 TRB 保险杠优于线性 TRB 保险杠。优化后的 S 型 TRB 保险杠吸能量提高了 30%左右。
关键词: S 型函数；连续变截面；保险杠；耐撞性

1 引言

汽车正面碰撞要求前部结构能够依靠自身变形来减缓碰撞时的冲击力，吸收碰撞能量以达到保护乘员的目的。保险杠是进行能量吸收的第一个重要部件，要提高保险杠的耐撞性，关键是要提高结构的能量吸收能力。目前一般采用增加板厚和内衬缓冲板来解决吸能不足的问题，但这会造成整车质量的增加，不利用当前环保和轻量化的要求[1]。

TRB 板是近年来提出具有连续变化厚度的新型板材，其在长度方向上的硬度变化比较平缓，无明显的硬度和应力波峰，具备更好的冲压成形性能。可根据部件负载情况和结构要求设计不同厚度、不同长度的组合及不

同过渡区形状与尺寸的 TRB 板，在满足安全性的前提下获得最佳减重效果[2]。现有的研究主要集中在 TRB 板和等厚板的比较以及替换，对于如何设计一个具有最佳厚度曲线的 TRB 板鲜有报道。

本文基于有限元分析软件 LS-DYNA，结合 MATLAB 等软件，在保证质量不变的情况下，针对某保险杠在 25%、40%、50%三种不同偏置下的低速柱碰，分析比较线性和 S 型两种不同类型的连续变截面厚度保险杠吸能特性以及保险杠内外板厚度变化对保险杠吸能的影响，并在此基础上通过实验设计应用 Kriging 法建立各个偏置下的代理模型，应用多目标优化算法进行连续变截面厚度保险杠耐撞性优化设计。

2 保险杠模型

2.1 初始模型和试验验证

本文所用的某保险杠模型由保险杠横梁、吸能盒构成，如图 1。横梁包括 1.2mm 厚的外板和 1mm 厚的内板；吸能盒包括 1.6mm 厚的外板和内板。保险杠横梁的弯曲半径为 1490mm，长度为 1155mm，截面外廓尺寸为 42mm×95mm, 吸能盒内侧之间的距离为 924mm。横梁的内外板均为 B410LA 材料的钢板。

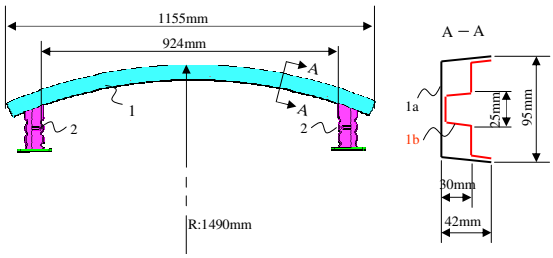

Figure 1. The geometric shapes of the bumper

图 1. 保险杠几何形状

保险杠有限元模型网格平均大小为 5×5 mm，共包含 21735 个壳单元。为了检验本文中保险杠模型的准确性，对试件进行三点压试验验证。在进行试件三点压试验时，试件与刚性平台刚性固定，压头的半径 R=152mm，压头初始位置与横梁中部位置刚好接触，如图 2。压头加载速度为 0.001m/s，若无明显破坏，则当加载距离达到 100mm 时停止。

参照试验工况，建立如图 3 仿真模型，压头与横梁之间采用自动面面接触，保险杠自身采用自动单面接触，静摩擦系数为 0.3，动摩擦系数为 0.2。由于静态求解所需时间很长，为减少计算时间，本文采取人为增加压头速度的方法减少求解时间[3]。在仿真过程中，压头的加载速度增加至 1m/s。

由静压试验和仿真分析得出的碰撞力-时间曲线如图 4，可知两条曲线变化趋势一致，峰值出现的时间也较吻合，最大误差仅 6.15%，可认为建立的保险杠有限元模型准确性较高，可用于下一步的优化设计。

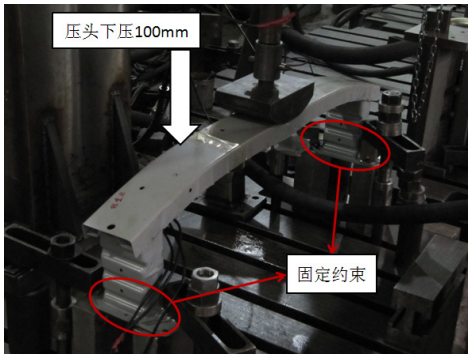

Figure 2. Three-point test of bumper specimen

图 2. 保险杠试件三点压试验

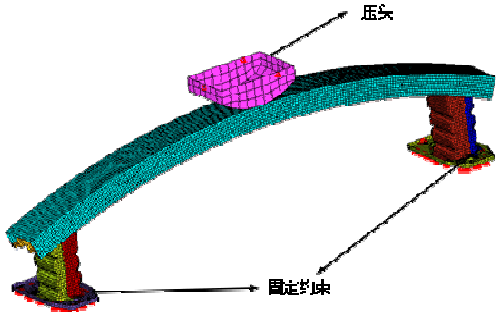

Figure 3. Simulation of three-point test of bumper specimen

图 3. 保险杠三点压试验仿真

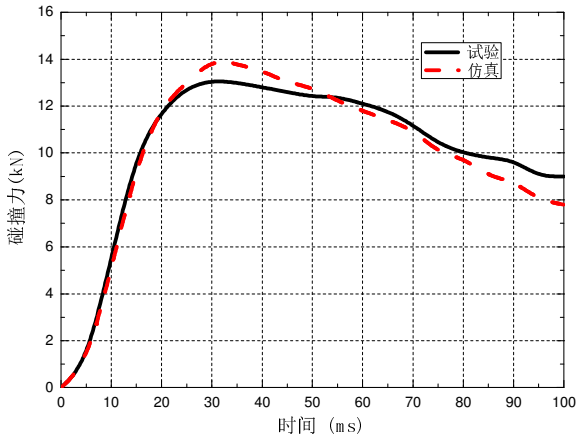

Figure 4. The collision force-time curve of three-point test and simulation

图 4. 三点压试验和仿真碰撞力-时间曲线

2.2 TRB 保险杠模型

由于采用分段等厚度截面的方法建模无法避免刚度的突变，而采用过渡单元的方法则工作量大，且不准确；采用实体单元模拟由于厚度和长度尺度相差较大需要耗费较大的计算资源，效率低。本文采用变厚度的壳单元来建立连续变截面厚度保险杠有限元模型，首先通过抽取薄板中面，根据不同类型的连续变截面厚度保险杠确定薄板截面厚度数据，将保险杠的厚度表示成随空间位置变化的函数，进而使用不等厚度壳单元来建模。

本文考虑线性和 S 型两种不同类型的连续变截面厚度保险杠，对内外板厚度在初始值的 50%范围内变化时不同类型的连续变截面厚度保险杠在三种不同偏置低速柱碰下的吸能及最大碰撞力进行分析。线性和 S 型连续变截面厚度保险杠厚度函数为：

$$\begin{cases} t=2*(t_0-a)*(|x|-0.5)+t_0 & \text{（线性）} \\ t=2*(t_0-a)/(1+e^{\wedge}(-10*(|x|-0.5))+a & \text{（S 型）} \\ x=2*s/L \end{cases} \qquad (1)$$

其中 s 是保险杠各点到保险杠中央的弧长，L 是保险杠总弧长，t_0 是原保险杠中央厚度，对于外板为 1.2mm、内板为 1.0mm，a 是连续变截面厚度保险杠中央厚度。为保证前后质量不变，各保险杠厚度均经过 $(0.5, t_0)$ 点。图 5 为保险杠外板中央厚度 a 在原厚度的 50%范围内变化时不同类型的保险杠截面厚度变化情况。

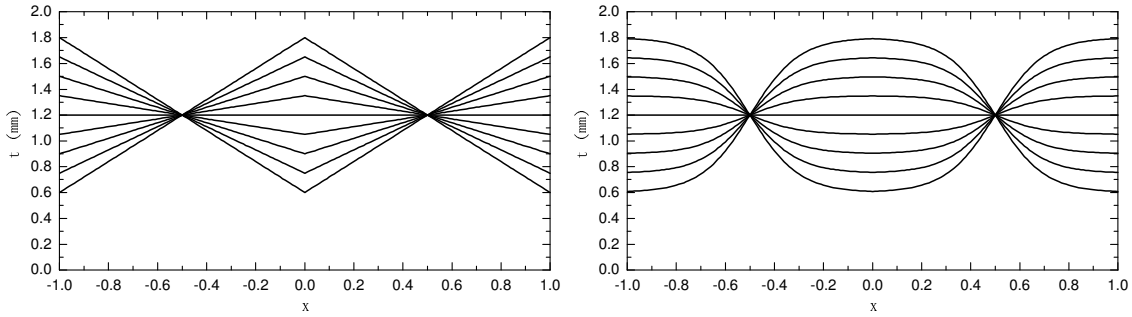

Figure 5. Section thickness of linear and S-type TRB bumper

图 5. 线性和 S 型 TRB 保险杠截面厚度变化

为实现保险杠有限元模型中厚度的连续变化，编写 MATLAB 程序将每一个单元定义为一个与 ELEMENT 同 ID 的 PART，并且引用相同 ID 的 SECTION。同样，为每一个单元定义同 ID 的 SECTION，SECTION 的四个节点厚度分别为此单元相应节点位置处的厚度函数值。这样，保险杠各处厚度就是随节点位置变化的值。建立有限元模型如图 6 所示。

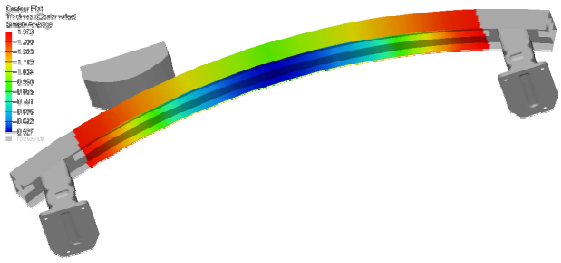

Figure 6 . Finite element model of the TRB bumper

图 6. TRB 保险杠有限元模型

3 代理模型的建立

基于前面所建立的 TRB 保险杠有限元模型针对其在 25%、40%、50%三种不同偏置下的低速柱碰，碰撞柱质量为 1100kg，速度为 15km/h。分析比较线性和 *S* 型连续变截面厚度保险杠吸能特性。

3.1 设计变量及目标

在正面碰撞耐撞性分析中，通常以结构吸能量和最大碰撞力来评价。在本文中，将保险杠吸能量 E 最大化作为优化设计目标，同时将最大碰撞力 F_{max} 最为耐撞性约束指标。过大的碰撞力容易使得乘员受到伤害[4]，在本文中要求最大碰撞力 F_{max} 不得超过 *30KN*。考虑到保险杠内外板厚度变化对保险杠吸能有一定影响，本文选取保险杠外板中央厚度 t_1、外板中央厚度 t_2 作为设计变量。为研究保险杠内外板对吸能的影响，中央厚度 t_1、t_2 在原厚度上下 50%范围内变化，如表 1 所示。

Table 1. Design variables

表 1. 设计变量

设计变量	t_1	t_2
上限	1.8	1.5
下限	0.6	0.5

3.2 仿真结果

为建立合适的代理模型需要一定数量的样本数据，采用实验设计的方法来选取样本点。拉丁超立方抽样是一种充满空间设计，在每个区间只抽样产生一个随机数，使输入组合相对均匀地填满整个实验区间，并且每个变量值仅使用 1 次，解决了传统蒙特卡罗抽样设计存在抽样次数多，数据点堆积等问题，使所得的模型能正确反映整个参数变化区域[5]。在本文中采用拉丁超立方抽样选出 20 个样本点来构造初始设计空间，得到相应的响应值，其结果如表 2。

Table 2. The samplings and responses

表 2. 采样实验点及结果

实验号	t_1	t_2	线性						S 型					
			25%		40%		50%		25%		40%		50%	
			E	F_{max}	E	F_{max}	E	F_{max}	E	F_{max}	E	F_{max}	E	F_{max}
1	0.632	1.105	1043.8	22.4	935.9	20.3	981.7	20.6	1014.5	21.5	878.8	18.2	974.3	19.7
2	0.695	1.421	980.0	22.6	1005.0	19.3	1089.0	20.1	973.6	22.1	993.5	18.5	1055.3	18.4
3	0.758	1.000	1073.3	22.4	963.0	19.8	984.6	21.3	1065.6	22.3	943.4	19.8	985.4	21.0
4	0.821	0.579	1176.7	22.4	943.2	16.9	896.9	16.9	1187.3	22.3	917.5	16.1	893.9	16.3
5	0.884	1.474	985.9	22.8	1073.6	19.7	1199.2	21.2	985.9	22.8	1095.9	20.0	1133.3	19.7
6	0.947	0.526	1189.9	22.7	977.3	17.8	936.0	17.4	1217.4	22.2	946.5	16.2	935.6	16.7
7	1.011	0.737	1146.7	22.8	1024.0	21.1	1005.4	19.7	1149.3	22.7	1017.9	20.9	1005.3	19.6
8	1.074	0.684	1160.5	22.9	1038.8	21.8	1023.0	19.7	1164.9	22.8	1035.3	21.5	1023.7	19.5
9	1.137	0.842	1124.7	23.0	1078.6	23.3	1082.8	23.7	1125.4	23.0	1078.0	23.3	1083.1	23.7
10	1.200	1.000	1090.2	22.9	1130.1	24.3	1169.4	27.0	1090.2	22.9	1129.9	24.3	1169.4	27.0
11	1.200	0.947	1101.5	22.9	1120.7	24.2	1154.4	26.5	1101.3	22.9	1120.7	24.2	1154.4	26.5
12	1.263	1.211	1047.8	22.8	1204.7	23.8	1242.9	24.3	1047.3	22.8	1203.6	23.7	1241.4	24.3
13	1.326	1.158	1059.9	22.9	1224.7	24.6	1259.9	25.1	1060.2	22.9	1225.4	24.6	1260.6	25.1
14	1.389	0.895	1118.0	23.1	1186.0	24.9	1237.5	27.7	1118.5	23.2	1187.4	24.9	1238.0	27.7
15	1.453	0.632	1177.6	23.5	1179.3	24.1	1211.4	25.6	1186.8	23.5	1180.0	23.9	1217.1	25.5
16	1.516	1.368	1028.9	23.0	1285.3	24.6	1511.6	24.9	1027.0	23.0	1300.1	24.5	1478.4	24.9
17	1.579	1.263	1047.8	23.5	1312.3	24.8	1464.2	25.3	1051.4	23.6	1325.1	24.7	1451.9	25.2
18	1.642	1.316	1041.3	23.4	1335.0	24.9	1544.9	25.3	1043.5	23.5	1361.2	24.9	1520.6	25.2
19	1.705	0.789	1150.3	24.3	1306.4	26.2	1423.3	27.8	1161.4	24.4	1353.6	27.0	1411.7	27.8
20	1.768	1.053	1094.4	24.1	1378.5	27.8	1490.2	29.4	1116.6	24.4	1445.7	28.0	1491.9	29.2

3.3 Kriging 模型

Kriging 插值法又称空间自协方差最佳插值法。它首先考虑的是空间属性在空间位置上的变异分布，确定对一个待插点值有影响的距离范围，然后用此范围内的采样点来估计待插点的属性值。该方法在数学上可对所研究的对象提供一种最佳线性无偏估计的方法。它是考虑了信息样品的形状、大小及与待估计块段相互间的空间位置等几何特征以及品位的空间结构之后，为达到线性、无偏和最小估计方差的估计，而对每一个样品赋予一定的系数，最后　进行加权平均来估计块段品位的方法,在数据点多时，其内插的结果可信度较高[6]。

利用 Kriging 插值法建立各个偏置下最大碰撞力和吸能量的代理模型。表为线性变截面厚度保险杠和 *S* 型变截面厚度保险杠不同偏置下最大碰撞力云图对比。表为线性变截面厚度保险杠和 *S* 型变截面厚度保险杠不同偏置下吸能量云图对比。

Table 3. Comparison of maximum impact force

表 3. 最大碰撞力云图对比

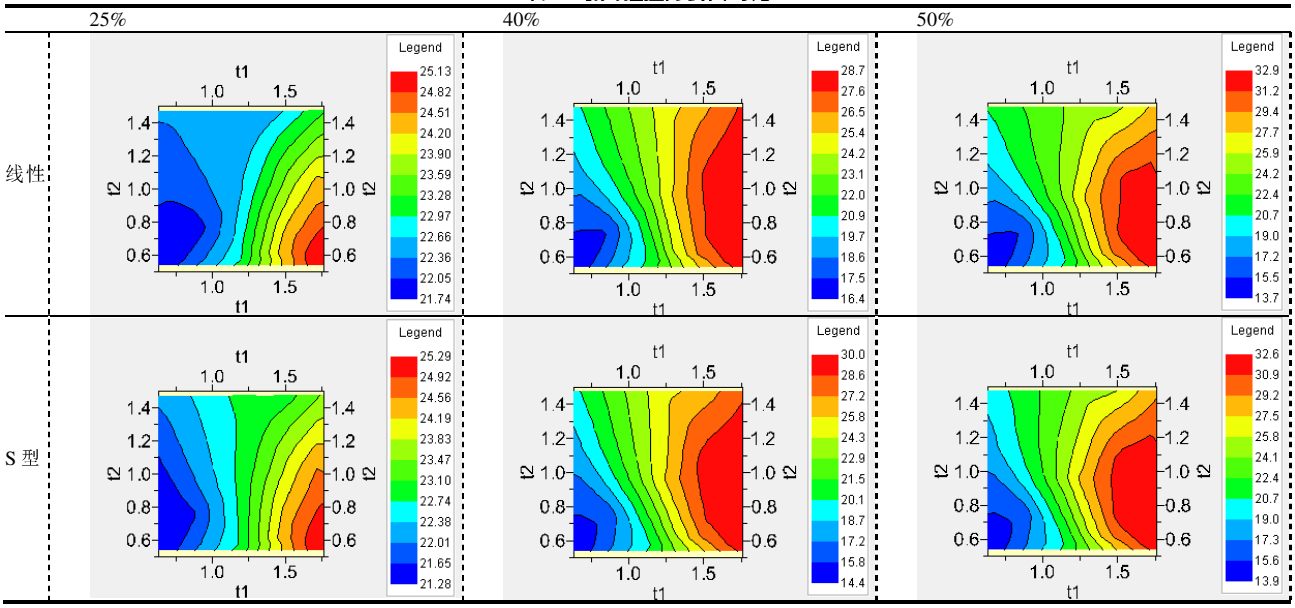

Table 4. Comparison of energy absorption

表 4. 吸能量云图对比

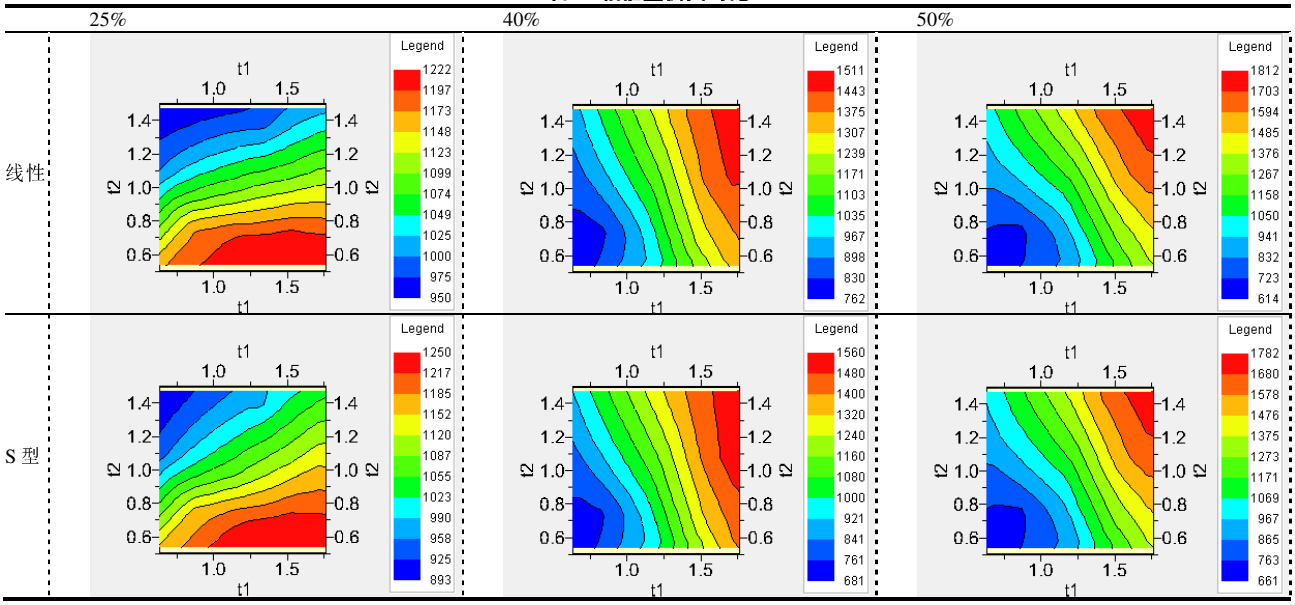

结果表明同等厚度的线性和 *S* 型函数连续变截面厚度保险杠在碰撞力和吸能量方面没有显著差异。不同偏置下，线性和 *S* 型函数连续变截面厚度保险杠的最大碰撞力和吸能变化趋势相同。同时保险杠内外板厚度对吸能和最大碰撞力的影响不一样：在 25%偏置柱碰下内板厚度对吸能有很大的影响，而在 40%,50%偏置柱碰下两者都有影响，而外板厚度影响更为明显。当外板厚度较小时最大碰撞力由外板厚度和内板厚度共同决定，当外板厚度较大时最大碰撞力则主要由外板厚度决定。

4 优化过程

4.1 优化数学模型

出于耐撞性和轻量化的考虑，本文旨在增加横梁的吸能总量和控制横梁质量；另一方面，过大的碰撞力会导致其在低速碰撞下起不到应有的保护作用[4]，甚至危害车内乘员的安全，所以碰撞力峰值也必须满足一定的约束要求。因此，TRB 保险杠优化问题可以描述如下：

$$\begin{cases} \max E(25\%，40\%，50\%)\text{s} \\ \text{s.t. } F_{\max}(25\%，40\%，50\%) \le 30kN \\ 0.6mm<t1<1.8mm \\ 0.5mm<t2<1.5mm \end{cases} \tag{2}$$

式中 E，$F_{\max}$ 分别代表保险杠总吸能量与碰撞力峰值；当横梁压缩量达到 100mm 时，取保险杠的内能之和作为保险杠总吸能量 E；取横梁压缩量达到 100mm 之前的最大碰撞力作为碰撞力峰值 $F_{\max}$。

4.2 优化结果

利用文中所建立的 Kringing 模型，使用 Isight 软件中的自动优化专家算法（Pointer）分别对线性和 S 型函数连续变截面厚度保险杠求解，得到优化结果如下表 5。

4.3 结果验证

为了进一步验证优化方案，将 TRB 保险杠厚度的优化结果代入 S 型 TRB 保险杠有限元模型中求解。有限元值和代理模型优化值对比如表 6 所示。结果表明模型误差在 10%以内，优化结果可以接受。

Table 5. Optimization value
表 5. 优化结果

	t1	t2	25%		40%		50%	
			E/J	$F_{\max}$ /KN	E/J	$F_{\max}$ /KN	E/J	$F_{\max}$ /KN
原始	1.2	1	1090.2	22.9	1130.1	24.3	1169.4	27.0
线性	1.765	1.206	1072.1	23.9	1470.8	28.3	1704.4	29.9
S 型	1.768	1.216	1105.1	24.2	1534.9	28.8	1682.9	30.0

Table 6. Comparison of FEM and model optimization value
表 6. 有限元值和代理模型优化值对比

	t1	t2	25%		40%		50%	
			E/J	$F_{\max}$ /KN	E/J	$F_{\max}$ /KN	E/J	$F_{\max}$ /KN
原始	1.2	1	1090.2	22.9	1130.1	24.3	1169.4	27.0
S 型模型值	1.768	1.216	1105.1	24.2	1534.9	28.8	1682.9	30.0
S 型有限元值			1085.3	24.7	1444.5	26.3	1549.2	26.5
模型误差 %			1.8	2.0	-5.9	-8.7	-7.9	-11.6
实际优化量 %			-0.4	7.8	27.8	8.2	32.5	-1.8

5 结论

在不增加质量的情况下，连续变截面厚度板能有效提高保险杠的碰撞吸能；同等厚度的线性和 *S* 型函数连续变截面厚度保险杠在碰撞力和吸能量方面没有显著差异。基于线性和 *S* 型 TRB 保险杠优化设计的前后板厚度基本相同，综合考虑三种不同偏置下的吸能发现 *S* 型 TRB 保险杠更均衡，对不同偏置下的吸能都有一定提高。

其中50%偏置下，最大碰撞力减少了1.8%，而吸能量提高了32.5%；40%偏置下，最大碰撞力提高了8.2%，而吸能量提高了27.8%，吸能优势明显。

参考文献（References）

[1] 范蓉, 胡平, 王洪兵, 等. 热成形高强钢车身保险杠的耐撞性研究[C].Proceedings of the 8th International Forum of Automotive Traffic Safety. 2010.Wuhu,China.

[2] 兰凤崇, 李佳光, 马芳武, 等. 连续变截面板（TRB 板）在汽车前纵梁中的应用及优化分析[J].机械设计与制造, 2014 (1): 25-28.

[3] 魏显坤, 杨晶晶, 米林. 铝合金保险杠准静态压溃仿真与试验[J].重庆理工大学学报: 自然科学版, 2013, **27**(8): 14-17.

[4] 刘子建, 张建华, 杨济匡. 碰撞生物力学基础及其应用[J].中华创伤杂志, 2001, **5**(17): 261-263.

[5] 邓乾旺, 文文. 基于拉丁超立方抽样的薄板装配误差分析 [J]. 中国机械工程, 2012, **23**(8): 947-951.

[6] 徐增密, 刘立忠, 申国哲, 等. 基于响应面和 kriging 代理模型的汽车 B 柱优化设计[J]. 汽车技术, 2012 (4): 39-43.

Proceedings of the 11th International Forum of Automotive Traffic Safety, 2014, pp 170- 178
No. ATS.2014.212

Research on CAE Model Updating Method for Robust Design Optimization and its Application to Vehicle Weight Reduction

ZHAN Zhenfei[1] , YANG Junqi[1] , SHU Yajing[1], ZHENG Ling[1] ,FU Yan[2] ,YANG Ren-Jye[2]
[1].*College of Automotive Engineering, Chongqing University, Chongqing 400044,China*
[2] *Research and Advanced Engineering, Ford Motor Company, Dearborn, MI48124, USA*
Email: zhenfeizhan@cqu.edu.cn

Abstract: Vehicle weight reduction has become one of the viable solutions to ever-growing energy and environmental crisis. In vehicle design, response surface model (RSM) is commonly used as a surrogate of the high fidelity Finite Element (FE) model to reduce the computational time and improve the efficiency of design process. However, RSM introduces additional sources of uncertainty, such as model bias, which largely affect the reliability and robustness of the prediction results. The bias of RSM need to be addressed before the model is ready for extrapolation and design optimization. The Bayesian inference based model extrapolation method which is previously proposed by the authors is further investigated , and a systematic and integrated stochastic bias corrected model extrapolation and robustness design process under uncertainty is provided. A real world NCAP frontal impact vehicle design example is used to demonstrate the validity of the proposed method.
Keywords: response surface model (RSM); robust design optimization; bayesian inference; model validation and extrapolation; vehicle body weight reduction

面向稳健性设计优化的仿真模型修正方法及其在车身轻量化中的应用

詹振飞[1*]，杨俊祺[1]，舒雅静[1]，郑玲[1]，符雁[2]，杨仁杰[2]
1 重庆大学汽车工程学院，重庆，中国，400044
2 美国福特汽车研究与先进工程中心，密西根州，美国，48121
Email: zhenfeizhan@cqu.edu.cn

摘　要：汽车轻量化作为缓解能源危机和环境污染的一个重要途径成为汽车工业的研究热点。轻量化设计不是盲目减重，而是在保证汽车安全性能的前提下最小化车重的优化设计。在结合轻量化和耐撞性的优化设计中，响应面模型作为具有较高保真度的有限元模型替代得到了广泛运用。然而响应面模型会引入模型偏差等附加的不确定性源，为了得到具有稳健性的预测结果，有必要对响应面模型进行偏差修正。本文提出了基于统计贝叶斯推断的模型外推方法，同时完整阐述了在不确定性环境下进行随机偏差修正的模型外推以及稳健性设计优化流程。通过对某 NCAP 正碰白车身仿真模型的参数优化，得到了稳健优化解。由稳健优化解与传统确定性优化结果对比可知，稳健优化结果不仅能较好满足轻量化和耐撞性设计要求，同时也使得其性能的稳健性大幅提高。

关键词：响应面模型；稳健性设计优化；贝叶斯推断；模型验证与外推；车身轻量化

1 前言

随着有限元（Finite Element, FE）技术的迅速发展及计算机性能不断提升，基于仿真的工程设计与优化成为各大汽车企业解决复杂设计问题的一种有效的工具。模型验证[1-6]是指通过比较 CAE 模型输出结果及试验结果，评估 CAE 模型在拟用途径上的有效性和准确性。成功的模型验证能明显减少在汽车设计中样机的建立和试验的投入。

在车身结构仿真设计过程中，不考虑设计变量的不确定性将直接影响车身的性能指标，使其性能不稳定，不能满足实际使用要求。考虑各种不确定性因素对产品性能参数的影响，采用稳健性设计优化方法对车身轻量

项目资助信息：国家自然科学基金(编号 51405041，50775225)资助，
自然科学类中央高校基本科研业务费资助项目 (CDJZR13110070)资助。

化参数进行设计，能够有效保证车身在实际工程应用中的整体结构性能，从而既保证产品的经济效益又确保车辆实际运行中的安全可靠。稳健性设计优化方法即通过调整设计变量使目标函数最优，同时保证设计变量在允许偏差范围内具有稳健性，一方面要确保系统的功能特性尽可能接近目标值，另一方面要尽可能减小各种干扰因素引起的功能特性波动的方差。

确定性设计优化常使最优设计逼近设计约束，几乎没有给不确定性留下空间，和确定性设计优化不同的是稳健性设计优化考虑了 CAE 模型中变量的不确定性。然而传统的稳健性设计优化一般没有考虑 CAE 模型的不确定性，即在进行稳健性设计优化之前 CAE 模型被看作是足够正确没有误差的。但是如果模型不正确且受大量的不确定性影响时，稳健性设计优化则不成功。因此，在运用稳健性设计优化前对 CAE 模型偏差进行修正是至关重要的。

然而，即使计算机运算能力不断增强，用一个完整有限元模型直接进行优化设计或稳健设计时，仿真仍然会花费大量时间。完成一个有限元模型有时会花费数小时甚至数天。为了减少开发时间，响应面模型（RSM）被广泛用来替代有限元模型。

响应面或替代模型(Response Surface、Surrogate Model)最早由 Box 和 Wilson 于 1951 年提出，是用来开发、改进、优化的数学统计方法，起初用于没有考虑噪声因素的物理实验的拟合，直到 20 世纪 80 年代 Myers 等把噪声因素引入响应面方法后才开始在结构优化领域中得到广泛应用，成为工程结构优化领域的有力工具[7]。依据近似模型所预测设计变量范围大小，可大致将其分为三大类：局部函数近似模型，全局函数近似模型与介于两者中间的中度函数近似模型[8]。

近年来多种 RSM 技术得以研究，包括径向基函数（RBF）[9]、人工神经网（ANN）、支持向量回归（SVR）以及克罗格（KRG）[10,11]。不同 RSM 技术的效率取决于不同的建模要求、可得的采样数以及物理现象自身的非线性[12,13]。无论使用哪种响应面方法，在实际 FE 模型和 RSM 之间始终会有偏差，特别是当响应面模型用于依据内插和外推的新设计预测时。这就需要对随机模型内插和外推方法进行研究，以修正 RSM 和 FE 之间的偏差并提供偏差修正后的 RSM 的预测区间。

模型更新方法不但可以量化数据不确定性的大小，而且可以进一步提高模型的预测能力，目前，该方法在模型验证或者模型标定领域取得较快发展，已成为国内外研究的前沿和热点。Kennedy 和 O’Hagan[14]最早给出了数据不确性的定义与内涵并全面阐述了近似模型模型不确定性的概念。此外，Kennedy 和 O’Hagan 指出通过优化模型参数可以减小预测模型与实际物理系统之间的误差，同时可以采用模型修正方法来提高现有预测模型的预测精度。多种统计学推理技术得以研究[15]。然而这些方法都未十分强调不确定性下的设计内插和外推的重要性。国内，相关研究目前不多见，主要有：詹振飞等[16]针对虚拟样机开发环境中不确定多元输出响应动态系统的模型验证问题，提出了基于误差统计分析、统计主元分析和贝叶斯区间假设检验的不确定性动态系统模型验证方法和流程，对某汽车正面碰撞中乘员约束保护系统的实例研究表明，该方法能有效实现虚拟样机环境下的不确定性动态系统模型验证，并进一步推导数字化仿真模型的改进。刘兴堂等[17]从系统仿真角度对模型验证和更新的概念进行了深入的阐述。考虑到这种现状，Zhan 等[26]研究了三种内插和外推方法：贝叶斯推理[27]、高斯过程建模[28]以及 Copula[29]，并使用了三种随机验证指标——面积指标、可靠度指标以及贝叶斯可信度指标——以评价所提三种方法的预测能力。

本文首先简介基于贝叶斯推理的内插和外推，随后引入稳健性设计优化方法，通过一个汽车正面碰撞实例研究所提方法的有效性，经过稳健性设计优化的 FE 仿真用来证明所得结果，最后进行探讨并得出结论。

2 基于贝叶斯推理的偏差修正

Zhan 等[26]利用贝叶斯推理和响应面模型的优点，提出了一种基于贝叶斯推理的模型内插和外推方法。该方法首先在设计空间中生成用于验证的试验设计(Design of Experiment，DOE)矩阵，随后反复进行 CAE 仿真和试验，计算出二者之间的差作为偏差分布贝叶斯推理的依据。得到先验分布后，计算预测偏差超参数的后验分布。

为了便于公式化，令 x 表示设计变量，Y_t 和 Y_m 分别代表 FE 和 RSM 模型输出。$Y_t(x)$和 $Y_m(x)$之间的关系常概括为：

$$Y_t(x) = Y_m(x) + \delta(x) + \varepsilon(x) \quad (1)$$

其中 ε 表示试验误差，δ 表示 CAE 模型的偏差。因此输出的实值，即 Y_{ture} 等于试验观察值减去试验误差，同时也等于 CAE 模型预测加上模型偏差，如式(2)所示。

$$Y_{ture}(x) = Y_t(x) - \varepsilon(x) = Y_m(x) + \delta(x) \quad (2)$$

在式(2)中，设 $\tau(x) = \delta(x) + \varepsilon(x)$。由此可见预测偏差是估计 $Y_{ture}(x)$值的重要步骤。为了方法阐述的方便，假设偏差 $\tau(x) = \delta(x) + \varepsilon(x)$ 服从已知的正态分布，如式(3)。

$$\tau(x) \sim N(\tau_\mu(x), \tau_{\delta^2}(x)) \quad (3)$$

设方差 τ_{δ^2} 已知，而均值 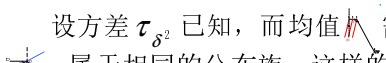 需根据已知数据得出。在贝叶斯概率理论中，后验分布 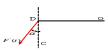 与先验分布 属于相同的分布族，这样的先验和后验分布叫做共轭分布。如正态分布族相对于正态似然函数是自共轭的。如果似然函数是正态的，选择正态先验分布可以保证后验分布也是正态的。在这里 τ_μ 的先验分布可设为：

$$\tau_{\mu 0} \sim N(\mu_0, {\sigma_0}^2) \quad (4)$$

在给出一些数据的情况下推出参数的分布是一个普遍的难题。在贝叶斯理论中，后验分布等于似然函数与先验分布 $p(\theta)$ 的乘积除以 $p(x)$ 的概率。如式(5)所示：

$$p(\theta \mid x) = \frac{p(x \mid \theta)\, p(\theta)}{\int p(x \mid \theta)\, p(\theta) d\theta} \quad (5)$$

假设先验分布为正态的共轭分布，n 表示试验观测数，则 τ_μ 后验分布可表示为：

$$\tau_{\mu 1} \sim N(\mu_1, {\sigma_1}^2) \quad (6)$$

其中 $\mu_1 = \left(\frac{\mu_0}{{\sigma_0}^2} + \frac{\sum_{i=1}^{n} x_i}{\sigma^2}\right) / \left(\frac{1}{{\sigma_0}^2} + \frac{n}{\sigma^2}\right)$，

$${\sigma_1}^2 = \left(\frac{1}{{\sigma_0}^2} + \frac{n}{\sigma^2}\right)^{-1}$$

根据试验和 CAE 数据可得每一个设计点 x 的偏差分布为：$\tau(x) \sim N(\tau_{\mu 1}(x), \tau_{\delta^2}(x))$。此方法不仅可用于共轭先验分布，也可用于非共轭。

本文为预测偏差的均值和标准差分别建立了一个响应面模型，得到 CAE 仿真结果之后便可计算得到新设计中的输出预测区间（PI）。新设计中的验证试验用以验证预测结果。如果新设计的试验结果在相应的预测区间内，则通过内插外推得到的预测就是成功的。基于所得结果，决策者可以决定接受或者拒绝预测结果。如果接受，则交付给之后流程的工程师进行优化或者稳健设计。若预测被拒绝，则会另外加入 DOE 反复此过程，直到得到好的预测结果[26]。

3 模型和数据不确定性下的稳健性设计优化

稳健性设计优化在不确定性优化设计中广泛运用，并且在设计变量不确定性下获取最可靠的设计方面有其独特优势。传统设计方法大多是确定性的，常常是将优化结果逼近设计约束的边界而未给不确定性预留空间。而稳健性设计优化考虑了 CAE 模型的可控和不可控变量的不确定性。典型的稳健性设计优化公式如式(7)所示：

Find d

$$\text{Mininize: } f(d)$$
$$\text{Subject to: } g_i(d) \le 0 \quad (i = 1,2,\ldots,k)$$
$$d^L \le d \le d^U \qquad (7)$$

其中，d 是设计变量，$f(d)$是目标函数，$g_i(d)$表示约束函数，d^LH 和d^U代表设计变量的下限和上限。

Error! Reference source not found.

大多数传统的稳健性设计优化未考虑 CAE 模型的不确定性，CAE 模型在进行稳健性设计优化之前被认为是足够准确的。如果模型不正确且受大量的不确定性影响，则稳健性设计优化不成功。因此，在进行稳健性设计优化前对模型偏差进行修正是至关重要的。图 1 展示了偏差修正响应面的稳健性设计优化流程。这个过程始于对优化设计问题的定义，随后为随机贝叶斯推理偏差模型构建 DOE。偏差模型用以修正初始 RSM 并量化来自于重复试验和 CAE 仿真的不确定性。然后使用稳健性设计优化程序寻找最优、最稳健的可靠解。再进行若干次蒙特卡罗（MC）有限元仿真得到以稳健性和灵敏度为目的的设计。如果 FE 结果和随机偏差修正后的 RSM 预测结果一致，则此过程完成，否则改善 DOE 矩阵，反复以上过程直到得到满意结果。

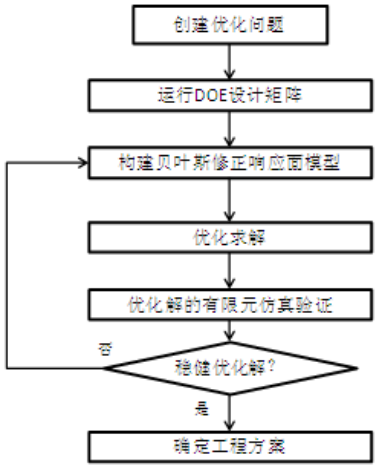

图 1　基于稳健性设计优化的随机偏差修正响应面流程

4 实例分析：汽车前部结构设计

在汽车设计实例中，对美国 NCAC(National Crash Analysis Center) [30]的 Ford Taurus 模型运用了贝叶斯推理方法。图 2 为 100%正面碰撞的试验及 CAE 模型。汽车以 56.6km/h 的仿真速度撞上刚性墙面。从试验和 CAE 结果比较可以看出 CAE 模型和试验达到合理程度的吻合。

(a)　试验　　**(b) CAE**

图 2 结构变形比较

此例在设计空间（验证域）中生成了 80 个均匀的 DOE，并在每个设计中各进行 3 次试验及 CAE 仿真。其中 65 个 DOE 样本用于构建 RSM，剩下的 15 个用于内插验证设计以研究三种内插和外推方法。如 Zhan[26]所述，基于贝叶斯推理的方法更简便、高效，调整变量更少，易应用于工程问题。贝叶斯推理修正后的 RSM 模型随后用来进行稳健性设计优化。设计目标是在满足 Chest G（CG）和 Crush Distance(CD)设计要求的前提下，通过结构优化达到质量最小化的目标。稳健性设计优化公式如下：

Find： $\mu_{x_i}=1,2,...,8$

Minimize： μ_{weight}

Subject to ： $P\{CG \le CG_{Target}\} \ge 99\%, CG_{Target}=65$

$$P\{CD \le CD_{Target}\} \ge 99\%, CD_{Target}=750$$

$$L_{x_i} \le \mu_{xi} \le U_{xi}, i=1,2,...,8$$

$$Weight = 6.012x_1 + 3.166x_2 + 2.078x_3 + 1.237x_4 + 1.463x_5 + 4.369x_6 + 3.547x_7 + 2.306x_8$$

$$CG = 84.699 - 7.7668x_6 + 0.7635x_7 - 13.133x_1 - 0.999x_2x_5 + 4.40899x_1x_6 - 0.3187x_4x_8 + 0.2922x_1x_5$$

$$CD = 922.51 - 2.5605x_6x_7 + 0.6625x_4 - 88.269x_1 + 13.929x_1^{\,2} - 1.2664x_3x_6 + 0.4711x_4x_5 - 8.2049x_2x_6 - 4.6859x_4x_8$$

其中 L_{xi} 和 U_{xi} 是设计变量的上下界，具体参考 Shi[31]以及 Zhan 等论文[27]。CG 和 CD 的设计极限分别为 65 和 750，超出则表明设计失败。本例使用了两种方法进行优化设计：一种是使用原始多项式的低保真度 CG 和 CD 响应面模型的传统稳健性设计优化，过程中只考虑设计变量的变化；另一种是使用贝叶斯推理修正偏差的模型的稳健性设计优化，不仅考虑设计变量的变化，还考虑模型的不确定性。由表 1 可以看出，传统的稳健性设计优化与基本设计相比质量更轻。稳健性设计优化模型建立如图 3 所示。

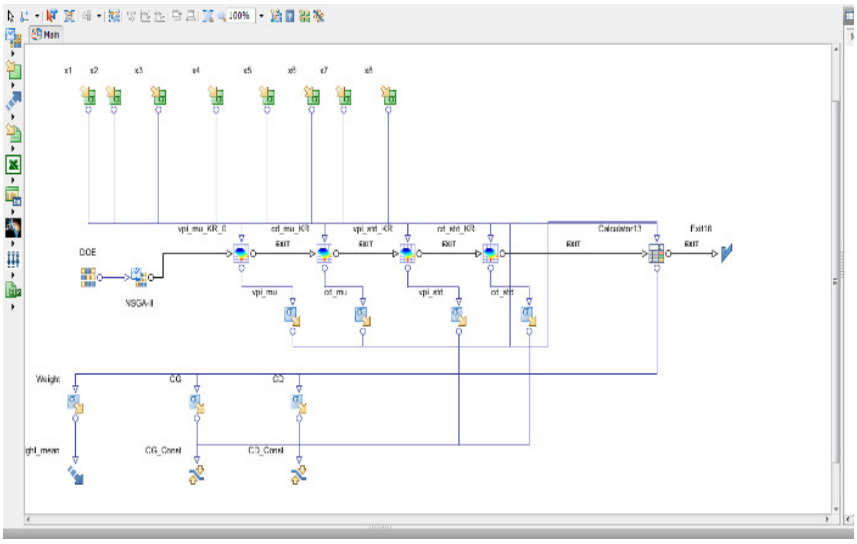

图 3 稳健性设计优化过程

表 1 稳健性设计优化(未修正偏差)与基本设计的比较

	x1	x2	x3	x4	x5	x6	x7	x8	重量
基本设计	1.90	1.91	2.51	2.40	2.55	2.55	2.25	1.50	51.97
优化设计（未修正）	1.72	1.21	1.64	3.97	1.56	1.60	1.56	3.00	44.08

为了验证解是否真的达到稳健性目标，根据传统稳健性设计优化结果的平均值生成了 10 个 MC 样本，并运行高保真度的有限元仿真，得到 CG 和 CD 相应的值。如图 4 所示，黑点代表传统稳健性设计优化解。应注意 CG 和 CD 的值是经过归一化的。明显这是一个失败的解：10 个设计中有 1 个超出了 CG 的约束范围，而 10 个设计的 CD 都在约束范围之外。此外，原始多项式的 RSM 的预测能力有限。由 MCS 得到 CG 和 CD 的概率分布与 10 个有限元仿真结果偏离过大。其中 6 个 CG 的有限元仿真以及 10 个 CD 的仿真超出了预测分布，两约束的稳健性指标都未达到 99%。

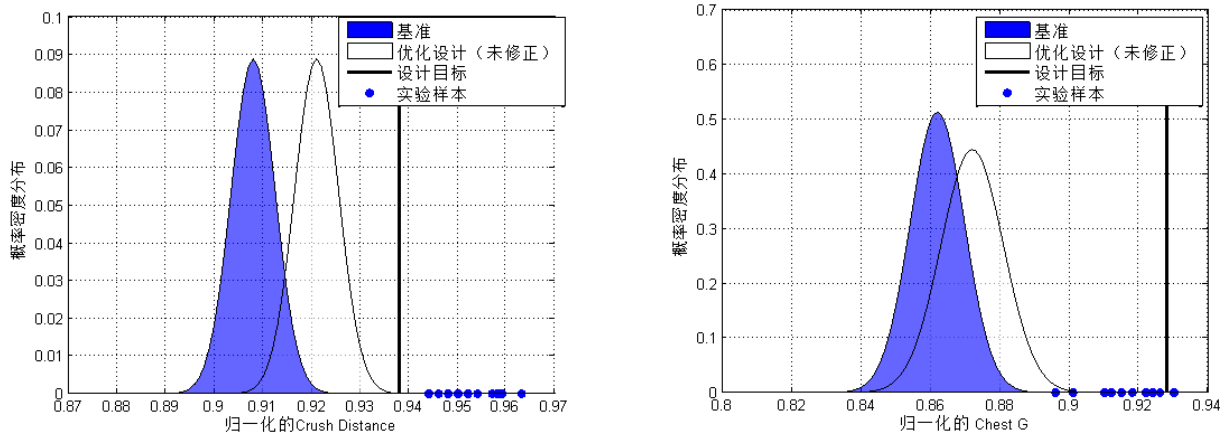

(a) 归一化的 Chest G **(b) 归一化的 Crush Distance**

图 4 稳健性设计优化（未修正偏差）的 MCS FE 验证

随后在稳健性设计优化中使用随机偏差校正的 RSM 取代原始多项式 RSM。设计优化确认流程以及参数设置如图 5、图 6 所示。两种方法得到不同的结果，如表 2 所示。传统的稳健性设计优化方法可得到较轻重量的设计，为 44.08kg。为了验证随机偏差修正的稳健性设计优化的解，另运行 10 个 FE 仿真，得到 CG 和 CD 相应的值。图 7 说明 10 个 MC 样本的 FE 仿真所得结果与随机偏差修正的 RSM 相吻合，且所有的设计都在 CG 和 CD 的正态分布中。两约束的稳健性指标均达到设计目标。本例证明了进行模型偏差验证以及不确定性下稳健性设计优化的必要性。可以看到传统低保真度的 CAE 模型的稳健性优化得到一个失败的设计。

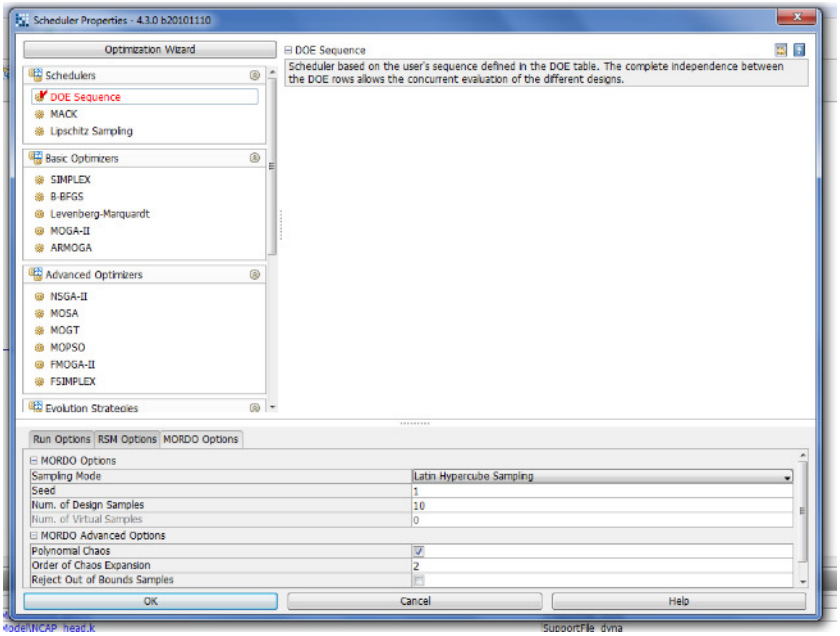

图 5　稳健性设计优化确认流程

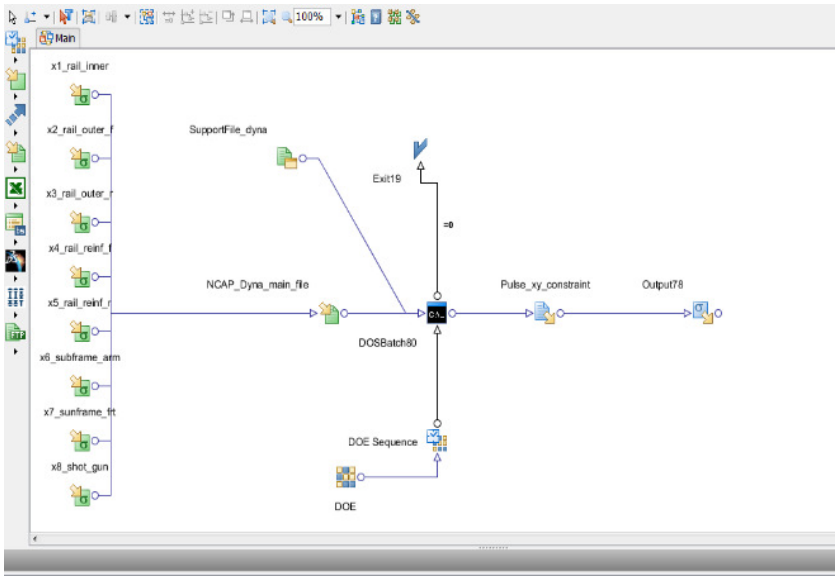

图 6　稳健性设计优化设置

表 2　未修正偏差和修正偏差的稳健性设计优化的比较

	x1	x2	x3	x4	x5	x6	x7	x8	重量
基本设计	1.90	1.91	2.51	2.40	2.55	2.55	2.25	1.5(	51.97
优化设计（未修正）	1.72	1.21	1.64	3.97	1.56	1.60	1.56	3.0(	44.08
优化设计	1.92	2.27	1.60	1.50	1.60	2.38	1.70	1.5(	46.21

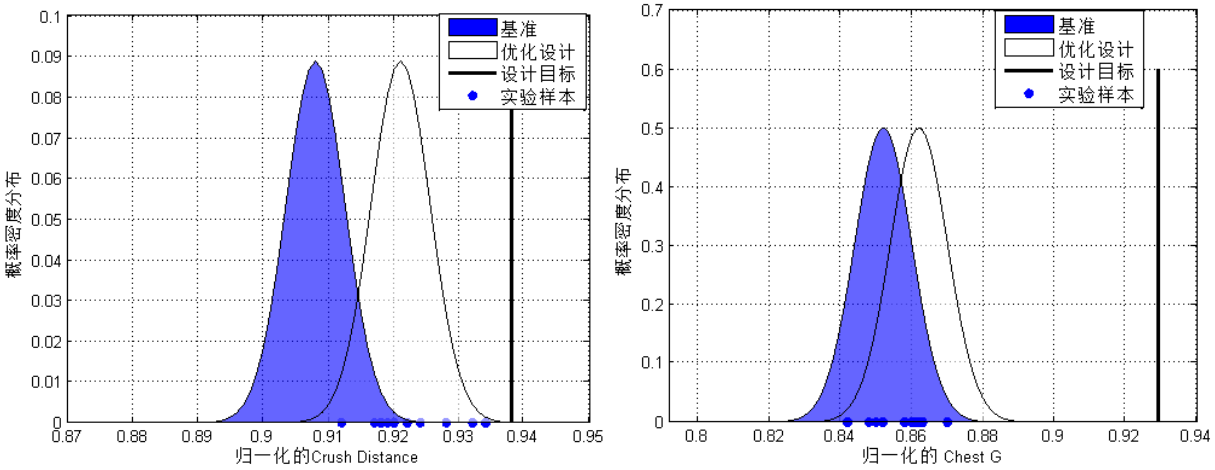

(a) 归一化的 Chest G **(b) 归一化的 Crush Distance**

图 7 偏差修正后的稳健性设计优化验证

5 结 论

本文提出了基于贝叶斯推理的模型内插和外推方法并将其运用到汽车安全设计上。介绍了一种随机偏差修正的模型外推方法以及考虑模型和参数不确定性的稳健设计方法。首先运用贝叶斯推理修正 RSM 的偏差来量化模型不确定性。然后使用改进的稳健性设计优化方法来进行设计，确保其稳健性。所提方法通过一个关于汽车轻量化的汽车安全设计问题得到阐述。在这个轻量化设计中，需满足在 CG 和 CD 上的安全性约束。模型输入的内插方法和外推方法相结合，用来验证所提出的模型偏差修正过程。经对比，改进的稳健性设计优化比起传统的稳健性设计优化能在实现轻量化的前提下得到稳健性更好的解。

参考文献

[1] Oberkampf, W. L., and Roy C. J., 2010, “Verification and Validation in Scientific Computing,” Cambridge University Press.

[2] Ferson, S., Oberkampf, W. L., and Ginzburg, L., 2008, “Model validation and predictive capability for the thermal challenge problem,” Computer Methods in Applied Mechanics and Engineering, 197, No. 29-32, pp. 2408-2430.

[3] Oberkampf, W. L., and Barone, M. F., 2006, “Measures of agreement between computation and experiment: Validation metrics,” Journal of Computational Physics, 217, No. 1, pp. 5–36.

[4] Oberkampf, W. L., and Trucano, T. G., 2008, “Verification and Validation Benchmarks,” Nuclear engineering and Design, Vol. 238, No. 3, pp.716-743.

[5] Schwer, L. E., 2007, “Validation metrics for response histories: perspectives and case studies,” Engineering with Computers, 23, No.4, pp. 295–309.

[6] FU, Y., ZHAN, Z., and YANG, R. J., 2010, “A study of model validation method for dynamic systems,” SAE 2011-01-0245, Detroit, MI, April 12-15.

[7] Khuri, A. I.,Mukhopadhyay, S. Response surface methodology[J]. Wiley Interdisciplinary Reviews: Computational Statistics, 2010, 2 (2): 128-149.

[8] 隋允康,李善坡. 结构优化中的建模方法概述[J]. 力学进展, 2008, 38 (2): 190-200.
SHUI Yunkang, LI Shanbo. Brief Review on Modeling Method in Structure Optimization[J]. Advances in Mechanics, 2008, 38(2): 190-200.

[9] Viana, F. A. C., Haftka, R. T., and Steffen, V., Jr., “Multiple Surrogates: How Cross-Validation Errors Can Help Us to Obtain the Best Predictor,” Structural and Multidisciplinary Optimization, Vol. 39, No. 4, 2009, pp. 439–457. doi:10.1007/s00158-008-0338-0

[10] Simpson TW, Peplinski JD, Koch PN, Allen JK (2001) Metamodels for computer-based engineering design: survey and recommendations. Eng Comput 17(2):129-150.

[11] WANG GG, SHAN S (2007) Review of Metamodeling Techniques in Support of Engineering Design Optimization. J Mech Design 129(4):370-380.

[12] JIN R, CHEN W, Simpson TW (2001) Comparative studies of metamodeling techniques under multiple modelling criteria. Struct Multidisc Optim 23(1):1-13.

[13] ZHANG, S., ZHU, P., CHEN, W., Arendt, P., "Concurrent treatment of parametric uncertainty and metamodeling uncertainty in robust design," Structural and multidisciplinary optimization, 2012, DOI: 10.1007/s00158-012-0805-5.

[14] Kennedy, M. C.,O'Hagan, A. Bayesian calibration of computer models. In Journal of the Royal Statistical Society: Series B (Statistical Methodology), 2001; Vol. 63, 425-464.

[15] Helton, J. C., Johnson, J. D., and Oberkampf, W. L., 2004, "An Exploration of Alternative Approaches to the Representation of Uncertainty in Model Predictions," Reliability Engineering and System Safety, 85, No. 1–3, pp. 39–71.

[16] 詹振飞,胡洁,符雁, 等. 虚拟样机环境下不确定性多元动态系统模型验证[J]. 机械工程学报, 2012,48 (5): 138-146.
ZHAN Zhenfei, HU Jie, FU Yan, etc. Bayesian Based Model Validation Method for Uncertain Multivariate Dynamic Systems under Virtual Prototype Environment[J]. Journal of Mechanical Engineering, 2012,48(5):138-146.

[17] 刘兴堂,刘力,宋坤,等. 对复杂系统建模与仿真的几点重要思考[J]. 系统仿真学报, 2007, 19 (13): 3073-3075.
LIU Xingtang, LIU Li, SONG Kun, etc. Important Considerations of Building Pattern to Complicated System[J]. Journal of System Simulation, 2007, 19(13):3037-3075.

[18] 闫明,孙志礼,杨强, 基于响应面方法的可靠性灵敏度分析方法[J].机械工程学报，2007，43（10）: 67-71.
YAN Ming, SUN Zhili, YANG Qiang, Analysis Method of Reliability Sensitivity Based on Response Surface Methods[J].Journal of Mechanical Engineering, 2007,43(10):67-71.

[19] 潘峰, 朱平,面向约束优化的改进响应面法在车身轻量化设计中的应用[J]. 机械工程学报，2011，47（10）: 82-87.
PAN Feng, ZHU Ping, Improved Response Surface Method for Constrained Optimization and Its Application to Lightweight Design of Autobody Structures[J]. Journal of Mechanical Engineering, 2011,47(10):82-87.

[20] Rebba, R., and Mahadevan, S., 2006, "Model predictive capability assessment under uncertainty," AIAA Journal, 44, No. 10, pp. 2376–2384.

[21] JIANG, X., and Mahadevan, S., 2007, "Bayesian risk-based decision method for model validation under uncertainty," Reliability Engineering and System Safety, 92, No. 6, pp. 707–718.

[22] Kim, I. Y., Kwak, B. M., (2002) Design space optimization using a numerical design continuation method. International Journal of Numerical Methods for Engineering, 53, pp. 1979–2002.

[23] CHEN, W., Baghdasaryan, L., Buranathiti, T., and Cao, J., "Model Validation via Uncertainty Propagation and Data Transformations", AIAA Journal, 42(7), 1406-1415, 2004.

[24] LI, J., Mourelatos, Z., Kokkolaras, M., Papalambros, P., and Gorsich. D., Validating designs through sequential simulation-based optimization. In Proceedings of the ASME International Design Engineering Technical Conference, 2010. Paper no. DETC2010-28431.

[25] Kakkolaras, M., Hulbert, G., Papalambros, P., Mourelatos, Z., Yang, R. J. Brudnak, M., Gorsich, D., 2011, "Towards a Comprehensive Framework for Simulation-based Vehicle Systems Design Validation", International Journal of Vehicle Design, preprint.

[26] ZHAN, Z., FU, Y., YANG, R. J., On Stochastic Model Interpolation and Extrapolation Methods for Vehicle Design, SAE International Journal of Material and Manufacturing, 6(3):517-531, 2013, doi:10.4271/2013-01-1386.

[27] ZHAN, Z., FU, Y., YANG, R. J., etc., A Bayesian Inference based Model Interpolation and Extrapolation, SAE International Journal of Material and Manufacturing, Vol. 5, No. 2, 2012-01-0223, 2012, doi:10.4271/2012-01-0223.

[28] JIANG, Z, CHEN, W, FU, Y, etc, Reliability-Based Design Optimization with Model Bias and Data Uncertainty, SAE International 2013 technical paper, 2013-01-1384, April, 2013, Detroit, USA. doi:10.4271/2013-01-1384

[29] XI, Z., FU, Y. and YANG, R., "An Ensemble Approach for Model Bias Prediction," SAE International Journal of Material and Manufacturing, 6(3):2013, doi:10.4271/2013-01-1387.

[30] National Crash Analysis Center (NCAC) , 2011, www.ncac.gwu.edu/archives/model/index.html.

[31] SHI, L., YANG, R. J., ZHU, P., "An Adaptive Response Surface Method for Crashworthiness Optimization Engineering Optimization, 2012, DOI:10.1080/03052 15X. 2012.734815.

[31] SHI, L., YANG, R. J., ZHU, P., An Adaptive Response Surface Method for Crashworthiness Optimization Engineering Optimization, 2012, DOI:10.1080/03052 15X. 2012.734815. (SCI/EI)

[32] SHI, L., YANG, R. J., Adaptive sampling-based RBDO method for vehicle crashworthiness design using Bayesian metric and stochastic sensitivity. 2013, DOI:10.1080/13588265.2013.793262 (SCI/EI)

[33] Arendt, P. D., Chen, W., and Apley, D. W., 2011, "Improving Identifiability in Model Calibration Using Multiple Responses." DETC2011-48623, Washington DC, August 28-31, 2011.

[34] Mahadevan, S., and Rebba, R., 2005, “Validation of reliability computational models using Bayes networks,” Reliability Engineering and System Safety, 87, No. 2, pp. 223–232.

Proceedings of the 11th International Forum of Automotive Traffic Safety, 2014, pp 180- 186
No. ATS.2014.213

基于 ENCAP 侧面柱碰的门槛梁、车门防撞杆优化设计

王彬花 [1,2] ，范体强 [1,2] ，赵清江 [1,2] ，李阳 [1,2]
[1] *中国汽车工程研究院股份有限公司，重庆，中国，401122*
2 重庆市汽车轻量化工程技术研究中心，重庆，中国，401122
Email: wbh260@126.com

摘 要：侧面柱碰是模拟车身横着撞击在垂直硬物比如电线杆、树木等，能严重伤害乘员，本文基于 E-NCAP 侧面柱碰撞法规，对某车型进行了侧面柱撞分析，由于对侧面柱撞影响较大的车身结构件有车门防撞杆、B 柱、车门内外板、顶棚、门槛梁等，本文重点开展了车门防撞杆和门槛梁的研究。对门槛梁进行了拓扑优化和形貌优化设计，对车门防撞杆进行了形貌优化设计，使得该车型侧面柱碰性能得到大幅度提升。

关键词：侧面柱撞，拓扑优化，形貌优化，门槛梁，防撞杆

1 引言

我国侧面碰撞法规于2006年7月开始实施，但目前对侧面碰撞的研究主要集中在车对车侧面碰撞的研究，车对柱状物体碰撞的研究很少，而且目前的蜂窝铝壁障侧面碰撞试验并不能反映来自车外柱状障碍物碰撞的威胁。侧面柱碰是模拟车身在失控时横着撞击在垂直硬物上，比如树木、电线杆等。这种碰撞在现实生活中比较常见，对成员的伤害非常大。因为电线杆这类物体几乎完全不变形，而汽车侧面却是车身结构最为薄弱的地方。在欧洲，侧面柱撞是非常被看重的测试项目，2009年E-NCAP章程将侧面柱碰撞从加分项2分改变为强制项8分，同时将侧面碰撞的16分降低到8分。随着国内人们消费观念的改变，对汽车安全越来越重视，关于侧面柱碰的汽车车身结构研究也会越来越受到关注。因此对柱碰影响较大的零件进行研究很有必要。通过对这些零件改进材料或者形状，来提高柱碰性能。

2 侧面柱碰撞仿真模型

参照E-NCAP侧面柱碰撞法规要求，试验时将车辆放置在一辆平板车上，二者相对静止不动，前排驾驶员位置放置一个EuroSID II型假人，用以测量驾驶员位置受伤害情况，刚性柱直径为254mm，刚性柱顶到碰撞车辆顶部垂直距离不小于100mm，刚性柱底到车辆门槛底部的垂直距离不小于102mm。平板车携带碰撞车辆以29km/h的速度垂直撞击刚性柱，刚性柱轴线与碰撞速度方向组成的平面通过车内部假人头部中心位置，刚性柱与车辆碰撞接触后100ms以内运载碰撞车辆的平板车不能与刚性柱和其它静止物体发生碰撞，侧面刚性柱碰撞试验图如图1所示。

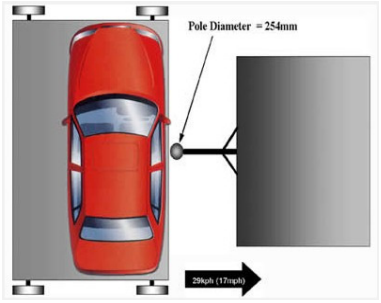

图 1 侧面刚性柱碰撞试验

本文采用的某整车模型经过了有效性和可靠性的有限元模型验证。按照ENCAP法规要求建立刚性柱，并设置整车的碰撞速度大小和方向，初始速度通过关键字*INITIAL_VELOCITY*定义，对整车模型施加Y向负方向8056mm/s的初始速度，定义整车和刚性柱之间的接触。前排座椅假人模型如图2所示，完整的侧面柱碰撞模型如图3所示。

图 2 整车侧面刚性柱碰撞假人模型

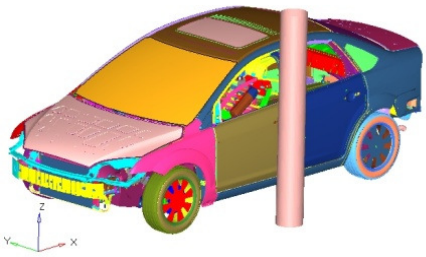

图 3 整车侧面刚性柱碰撞模型

3 仿真结果分析

3.1 模型检查

根据能量守恒定理，碰撞总能量在各个能量之间平衡的转化而保持不变。通过HyperGraph后处理平台可以获取碰撞仿真过程中的能量变化曲线，如图4所示。可以看出，各能量曲线平滑，未出现明显突变，能量转化平稳，总能量守恒。碰撞中能量占总能量的比例及模型的质量增加比如表1所示，各指标均满足要求，表明了仿真结果的有效性。

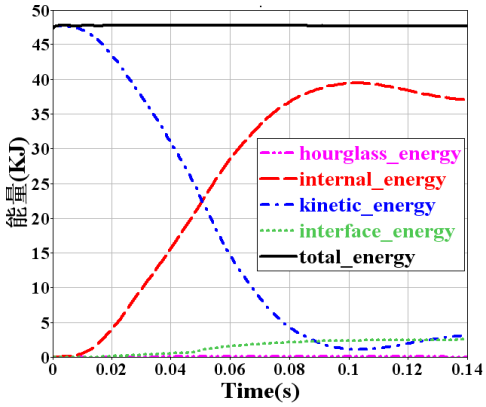

图 4 整车侧面刚柱碰撞能量曲线

表 1 能量信息

	整车侧碰	目标
沙漏能占总能量比例	0.21%	<5%
滑移能占总能量比例	4.92%	<5%
质量增加比	0.53%	<5%

3.2 侧面区域变形情况

整车柱碰的侧面区域整体变形情况以及B柱、门槛梁、车门、车门防撞杆变形情况如图5所示。

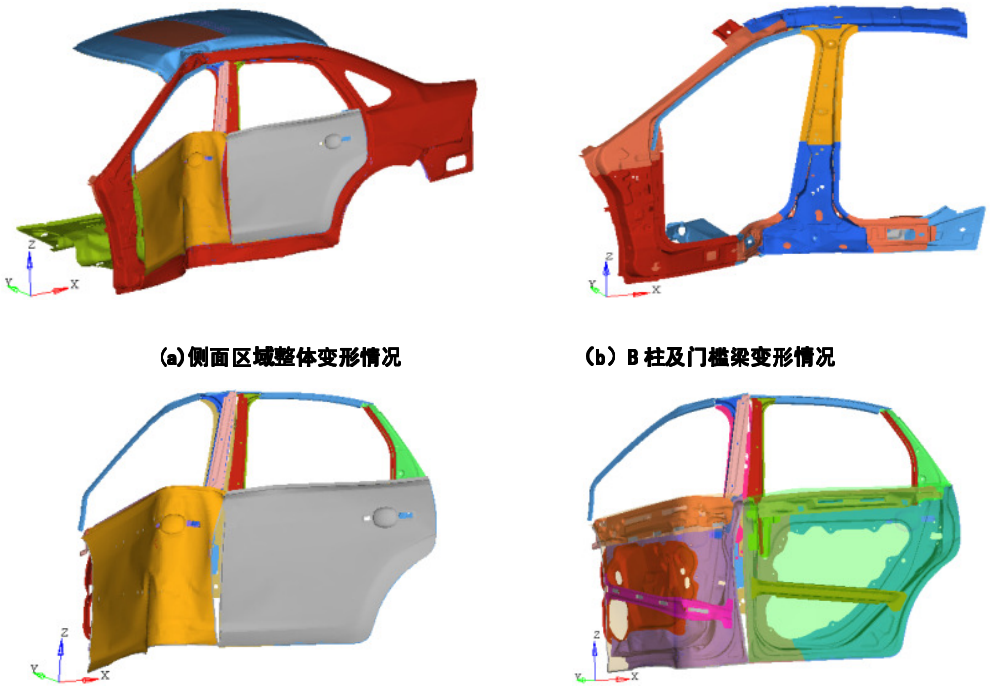

(a)侧面区域整体变形情况　　(b) B 柱及门槛梁变形情况

(c) 车门变形情况　　(d) 车门防撞杆变形情况

图 5 侧面区域变形情况示意图

从上述图中可以看出，在整车侧面柱碰过程中，车身严重变形的位置主要集中在刚性柱宽度大小的狭小区域，整个侧围结构变成“V”型，门槛梁、地板、左侧前车门及车门防撞杆发生了严重侵入变形。

3.3 侧面侵入量分析

观察分析该车型侧面柱碰的仿真动画可以看出，车门内板压溃变形严重使得驾驶员的胸部腹部受到伤害，门槛梁总成及前地板变形使得驾驶员骨盆受到挤压，由此以车门肋骨、腹部、骨盆侵入量作为评价该车型侧面柱撞性能的重要指标。通过 HyperGraph 提取各项侵入情况，车门的测量点如图 6 所示，碰撞中各个测量点的侵入量如表 2 所示。

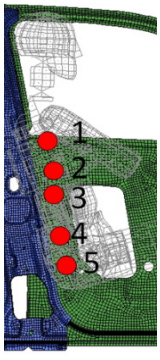

图 6 车门内板测量点

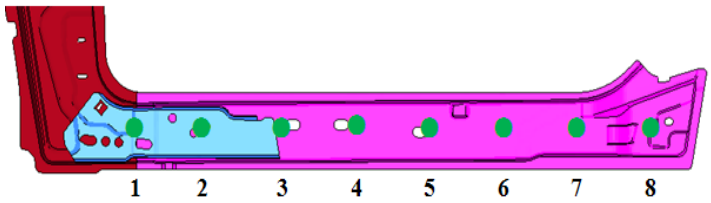

图 7 门槛测量点位置

表 2 车门变形最大侵入量

编号	测量项	最大侵入量（mm）
1	车门对应假人上肋骨	337.4
2	车门对应假人下肋骨	342.6
3	车门对应假人腹部	332.3
4	车门对应假人骨盆	303.4
5	车门对应假人 H 点	297.9

以门槛上对应的假人 R 点为中心向前或向后偏移 200mm 作为一系列测量点，各个测量点在局部坐标系下的变形如下图 7 所示，变形量如表 3 所示。

表 3 门槛测量点 Y 向最大变形量

测量点编号	1	2	3	4	5	6	7	8
最大变形量 mm	14.6	60.6	123.4	249.2	179.3	71.2	-1.1	-5.8

4 侧面结构优化

侧面柱碰撞时车身侧围结构发生很大变形，与车内乘员撞击接触导致人员受伤甚至死亡，汽车在配备安全气囊等保护装置的同时，还需改进车身结构的刚度尤其是侧围结构的刚度。本文重点开展了基于门槛梁总成以及车门防撞杆结构强度性能的结构改善与优化设计。

4.1 门槛梁总成优化改进

4.1.1 门槛梁静力学分析

门槛梁弯曲刚度不足导致在发生碰撞时压溃严重，截取门槛梁总成及侧围一部分结构，约束截面节点的所有自由度，进行弯曲刚度工况分析，约束模态分析，如图 8 所示，得出的数值作为下一步拓扑优化的参考值。

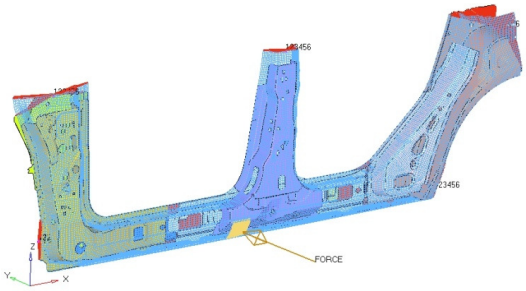

图 8 门槛梁静力学分析模型

4.1.2 门槛梁总成拓扑优化及设计

利用 OptiStruct 模块对门槛梁总成进行拓扑优化设计，设计变量为门槛梁本体与侧围板构成的空间所离散的实体 SOLID 模型，目标函数为加权应变能最小，约束为弯曲刚度工况下加载点 Y 向位移小于 1.3mm，一阶模态频率值大于基础模型的 1.2 倍即 105HZ，体积比为 0.3。得到图 9 所示的拓扑优化结果，在材料分布密度较高的位置，布置加强板（厚度设定为 1.2mm，材料的屈服强度为 330MPa），改变了门槛梁总成的截面特性。

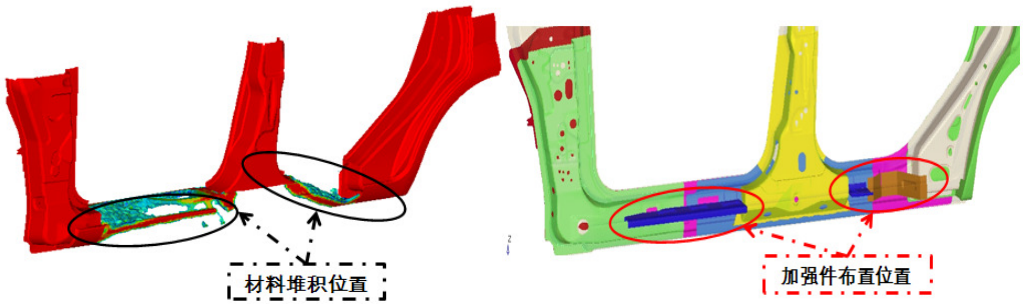

图 9 拓扑优化结果及加强件设计

4.1.3 门槛梁本体形貌优化及设计

形貌优化主要是对平板结构进行概念设计，寻找最优加强筋分布，从而提高结构刚度。对门槛梁本体进行形貌优化设计，设计变量为门槛梁本体，目标函数为加权应变能最小，约束为弯曲刚度工况下加载点的位移减小 20%，一阶模态频率值增加 20%。得到图 10 所示的形貌优化结果，按照云图以及工程经验设计加强筋，深度 6mm，角度 70°。为了便于门槛梁本体起筋，删掉一个门槛梁加强板，另一个加强板减短，如图 11 所示。

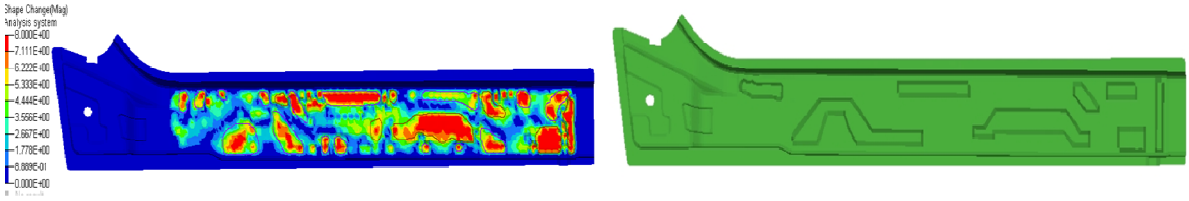

图 10 形貌优化结果及加强筋设计

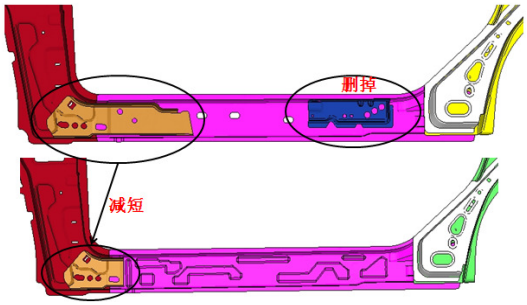

图 11 加强板修改

4.2 车门防撞杆优化改进

对车门防撞杆进行形貌优化设计，模拟侧碰撞击力的工况，如图 12 所示，加载 800N 集中力，约束连接板两端所有自由度，设计区域为红色区域，约束为加载力工况下加载点位移减小 20%，二阶模态频率增加 20%，目标为应变能最小。形貌优化结果云图如图 13 所示，按照云图及工程经验设计加强筋，深度 3mm，角度 60°

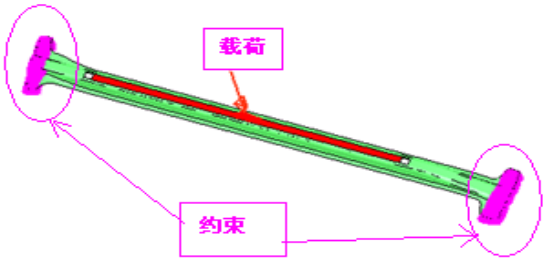

图 12 载荷及约束示意

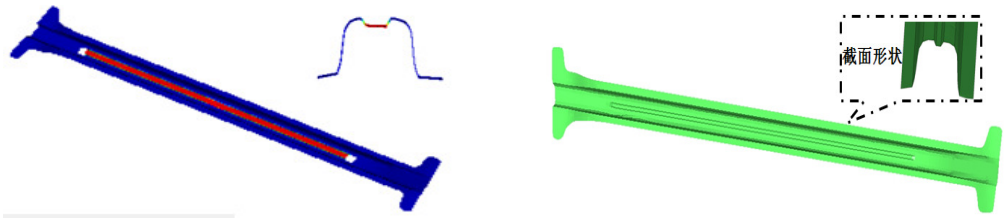

图 13 形貌优化结果及设计

4.3 材料改进

提高侧围的刚度对于车身结构变形有很大的改善，高强度钢材有高的吸能性特性，本文在结构改进的同时，对车门防撞杆和门槛梁本体进行了超高强度钢材料的应用，车门防撞杆原材料屈服强度 549MPa，门槛梁本体原材料屈服强度的 438MPa，应用的超高强度钢材料屈服强度为 936MPa。

5 优化后的柱碰性能验证

5.1 优化前后变形对比

优化前后整车柱碰最终变形情况对比如图 14 所示，侧面变形情况对比如图 15 所示。

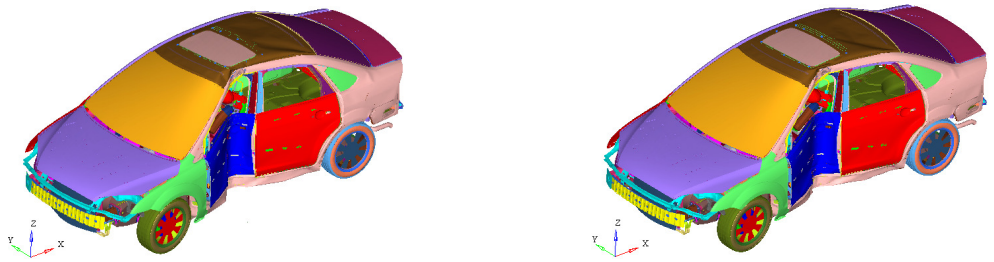

(a) 优化前　　(b) 优化后

图 14 优化前后整车柱碰最终变形图

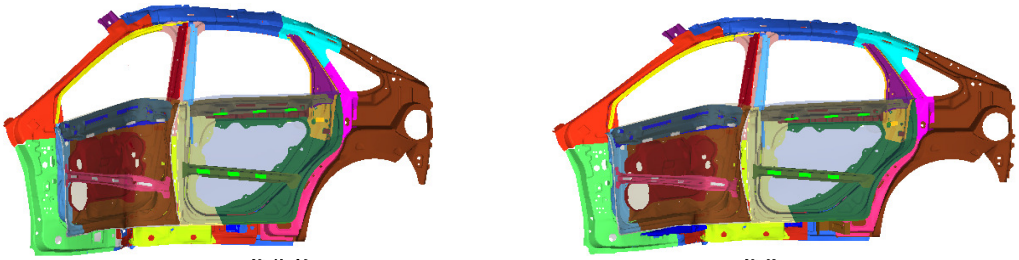

(a) 优化前　　(b) 优化后

图 15 优化前后侧面最终变形图

由变形图及变形动画可以看出，优化后的整车侧面柱碰门槛梁前端变形弯折程度较优化前减小，车门防撞杆弯折变形减小，可见该车的耐撞性能得到了有效改善。

5.2 优化前后侧面侵入量对比

参照 2.3 章节，对优化后的车门各测量点进行最大侵入量测量，优化前后各测点侵入量对比如表 4 所示，可见优化后车门各测点的侵入量明显减小，有效改善了乘员的生存空间。

表 4 优化前后车门各测量点最大侵入量对比

编号	测量项	最大侵入量（mm）		变化量
		优化前	优化后	
1	车门对应假人上肋骨	337.4	302.2	-35.2
2	车门对应假人下肋骨	342.6	307.3	-35.3
3	车门对应假人腹部	332.3	303.7	-28.6
4	车门对应假人骨盆	303.4	279.9	-23.5
5	车门对应假人 H 点	297.9	269.8	-28.1

门槛梁测量点位置参考 2.3 章节图 7 所示。优化前后的门槛梁 Y 向最大变形量对比如表 5 所示，可见优化后门槛梁各测点的最大变形量有所减小，测量点 4 和 5 在刚性柱碰撞覆盖区域，此处的最大变形量明显降低，使得压溃变形得到改善。

表 5 优化前后门槛梁 Y 向最大变形量对比

最大变形量 测量点	优化前	优化后	变化量
1	14.6	13.4	-1.2
2	60.6	59.3	-1.3
3	123.4	120.9	-2.5
4	249.2	222.3	-26.9
5	179.3	157.5	-21.8
6	71.2	66.7	-4.5
7	-1.1	4.8	5.9
8	-5.8	-7.4	-1.6

6 总结

本文根据 E-NCAP 侧面柱碰法规，对某车型进行了柱碰分析，并对影响较大的零件车门防撞杆和门槛梁进行了优化设计，使得侧面柱碰性能得到改善，为侧面柱碰结构改进提供了可行的参考依据。由于本文在只修改车门防撞杆和门槛梁的情况下使得柱碰的相关侵入量有所降低，由此可以推测，参考文中所述的优化手段对侧面结构的其他关键部件进行优化改进，应该会更加显著的改善柱碰的侵入量以及变形模式，对研究整车侧面柱碰撞抗撞性能改善有一定的参考价值和借鉴性。

参考文献

[1]汽车侧面柱碰撞的研究以及法规动态　唐波 赵晓红 北汽福田汽车工程研究院 《汽车与配件》技术与应用 2012-49
[2]轿车侧面柱碰撞结构响应与乘员损伤研究 杨济匡 覃祯员 湖南大学 《湖南大学学报》2011.1（38）
[3]侧面柱碰撞标准的发展趋势探讨 朱海涛 张振鼎 中国汽车技术研究中心 《标准解读与应用》2012.12（24）
[4] Altair Engineering. OptiStruct users manual [CP],version 5.1.

Proceedings of the 11th International Forum of Automotive Traffic Safety, 2014, pp 187- 192
No. ATS.2014.214

Numerical Simulation Analysis and Test of Standing Wave Border Speed about Radial Tire

Wang Qiang，Shi Yuhuan， Zhang Na
[1]*HeiLongjiang Institute of Technology, HarBin, China*
[2]*East University of HeiLongjiang, HarBin, China*
[3]*HeiLongjiang Institute of Technology,HarBin, China*
Email: wangqiang402@sohu.com

Abstract:

***Background*:** The standing wave phenomenon of radial tire occurs when the vehicle speed reaches a certain critical value, this phenomenon can easily result in traffic accidents.

***Objective*:** In this paper, it completed numerical simulation analysis of standing wave border speed about 195/60R15 radial tire by use of ABAQUS finite element analysis software, and determined characterization methods of standing wave border speed about radial tire, and then realized the experimental verification by use of a test system.

***Results*:** Based on these, it concludes that those measures to advance the tire pressure and reduce the tire load can increase the border speed value of standing wave effectively, which not only presents border speed indicators for the safe driving of vehicle, but also provides a scientific basis for the design and manufacture of tire that is able to resist high speed and traffic management.

Keywords: Radial Tire, Standing Wave, Border Speed,Finite Element,Numerical Simulation component

1 Introduction

With the advancement of vehicle speed, wave frequency and wave distortion of the radial tire crown surface increases and the tire standing wave phenomenon occurs when the vehicle speed reaches a certain critical point. After the standing wave happens, the thermal deformation, circumferential deformation and lateral distortion deformation of the tire increase dramatically, and the temperature of carcass rises rapidly, and the material properties decline quickly, which might cause severe puncture accidents. Early literatures that researched standing wave phenomena were more concentrated on the analytical methods, which was difficult to fully take the impact on the generation of standing wave into account and these influence factors mainly include the various parts of the tire structure and material properties and so on. In recent years, non-linear finite element technology has been widely used in tire mechanics analysis[1]. For the purpose of further improvement of traffic safety and promotion of the tire manufacturing industry, by combing ABAQUS finite element analysis software simulation with standing wave test, this paper conducts the numerical simulation analysis and test of high-speed tire standing wave. Based on these, the characterization method of the tire standing wave critical speed is determined and the critical speed indicators for vehicle safe driving are provided.

2 The standing wave critical speed of high-speed tire

Many scholars have conducted a theoretical study on the critical speed of tire standing wave[2-3].

(1) As early as 1954, Turner predicted approximately the critical velocity and it could be expressed using the following formula:

$$C = \sqrt{\frac{T}{\rho}} \tag{1}$$

Where C is the propagation velocity of wave, and it is the critical speed when the standing wave occurs; T is circumferential tension of tire and its size depends on the combination of inflation pressure and speed; ρ is density of tread material.

(2)Padovan J described the tire as the film that was supported with a damping radial spring, that is to say, the flexural rigidity of tread and longitudinal stiffness of tire weren't taken into account. Combining with the research model adopted by Padovan J, JRChoa obtained the critical speed of tires, as shown in formula(2)-(5):

Research project from HeiLongjiang Province Department of Education in 2010（N0.11551404）

$$V_C = \frac{1}{2}(-B \pm \sqrt{B^2 - 4C}) \tag{2}$$

$$B = \frac{r^2 K_r^2}{4\eta\rho^2} - \frac{r^2 C^2}{\rho} - \frac{T}{\eta\rho} \tag{3}$$

$$C = \frac{TC^I r^2}{\eta\rho^2} \tag{4}$$

$$C^I = C_r + \frac{C_5}{r^2} - \frac{2bp}{r} \tag{5}$$

Where η is the reduction rate of the centrifugal force; Kr is the radial damping of unit length; Cs is the tensile stiffness of unit length matrix; b is half of the effective width of the tread; p is the inflation pressure.

(3) The radial tire was simulated as radial and vertical spring support in the model formula of elastic base ring beam used by Zhuang Jide, that is to say, this model only took into account the radial damping of tire except the bending stiffness of tread and longitudinal stiffness of tire and advanced a more sophisticated argument and modification. The formula was expressed as:

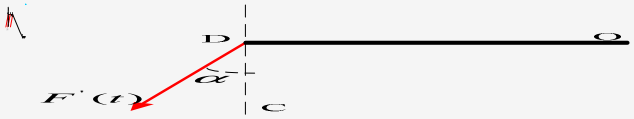

(6)

Where is the bending stiffness of tread; r is the outside radius of tire; ρ is the mass per unit length of ring beam; T is the tension of belt; C_r is the radial stiffness per unit length of tire; C_t is the longitudinal stiffness per unit length of tire; a is the wave number, $a = 2\pi/\lambda$ (λ is the wave length).

(4) Deformation and recovery of tire circumference occur repeatedly when the rotation. When vehicle travels at a high speed, the rotation speed of tire becomes faster. As deformation (wrinkles) occurred in the ground has not been recovered during the period including the time of a circle rotation and the time of contact with the ground again, the deformation wrinkles are left in the circle and tires produce standing waves. Therefore, it can be seen that standing waves occur when tire deformation is repeated, and the condition of deformation is that the tire has turned a circle in the deformation recovery time, and more exactly to say, standing waves occur when deformation superimposed with the next. Thus, when the recovery time T of tire is greater than or equal to the time t used by a circle rotation, standing waves occur. Here, fixed at an angle α, the tire deformation fully restores at the speed of V km/h[4-5].

As $v = 2V$ and $T = t$, then formula (7) is obtained, as shown:

$$t = 2\pi r / v \tag{7}$$

So formula (8) is expressed as shown:

$$V = \pi r / T \tag{8}$$

Where V is the critical speed; v is the speed of wheel rotation; r is the rolling radius; T is the recovery time.

3 Tire standing wave critical speed by use of FEM

3.1 Construction of finite element model [6]

Tread, anti-rub line and mark line were ignored when constructing the geometric model, and the contact between the tire and rim was simplified as the fixed constraint of the bead corresponding region and rim was no longer defined. And then tire and drum were assembled and the location was restricted. Finally, material behavior was super-elastic and strain potential options were Yeoh. The finite element model was shown in Figure 1.

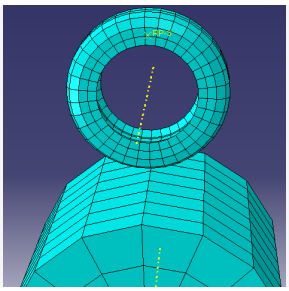

Fig.1 The finite element model

3.2 Conclusion of numerical simulation

The stress cloud figure of rotational deformation was respectively shown in figure 2,3,4 and 5 when the speed were chosen as 150km /h, 160km/h, 170km/h, 180km/h respectively. The result of strain and time was shown in figure 6 and deformation recovery time of simulation was 0.01311s.

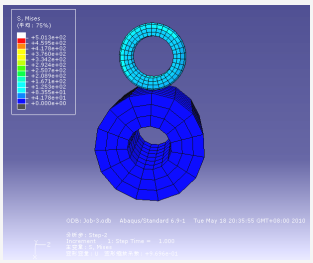

Fig.2 Deformation stress cloud figure when 150km/h

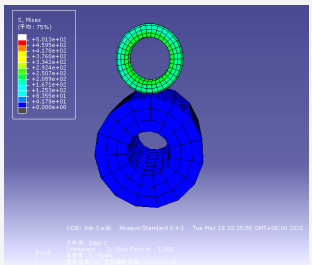

Fig.3 Deformation stress cloud figure when 160km/h

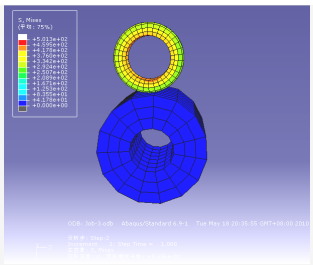

Fig.4 Deformation stress cloud figure when 170km/h

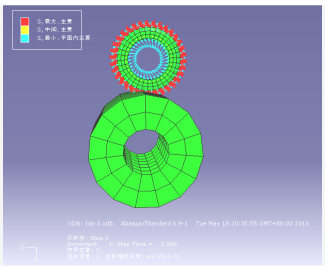

Fig.5 Deformation stress cloud figure when 180km/h

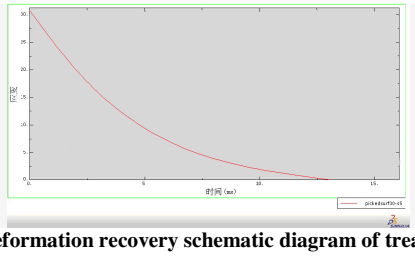

Fig.6 Deformation recovery schematic diagram of tread nodes

3.3 Calculation of the critical speed

By use of the formula (8), the result is as shown in:

$$V = \frac{\pi r}{T} = \frac{3.14 \times (0.307 - 0.0103)}{0.01311} = 255.83 km/h \quad (9)$$

4 The critical speed test and analysis of the tire standing wave

4.1 Test equipments

Test equipments mainly included a toyota corolla car (195/60 R15 radial tires), a chassis dynamometer, a high-speed camera, a desktop computer controlled by high-speed camera, a silver pen and other auxiliary devices. The test process was shown in figure7.

Fig.7 Test process

4.2 Experimental procedures

1) Marked the reference point of tire; 2) The car was fixed on the chassis dynamometer;3) High-speed camera was installed, and the camera lens was level with the tire center, and the camera direction was plumb with the tire plane; 4) The car on chassis dynamometer travelled at a constant speed and the speed range was chosen from 150 km/h to 180km / h, and the speed interval tested was 10km/h; 5) The functioning state of tire on the chassis dynamometer was obtained by camera and the radial deformation of tire was recorded at the different speed value; 6) At the same time, the deformation angle when tire being in the complete response state of elastic deformation and time were observed, and the deformation angle mentioned above was formed with the vertical direction by the complete response point connected with axis;7) Experiment data was collected using the high-speed camera; 8) the recorded images were imported into AutoCAD and calculated. Figure 8 showed the radial deformation of tire under the speed of 180km / h and the tire pressure of 1.2 MPa.

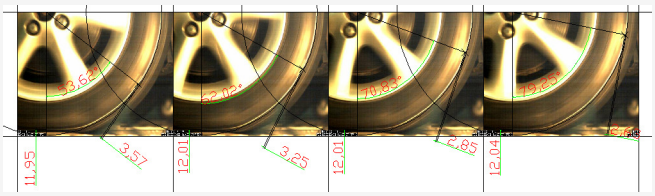

Fig.8 the radial deformation figure under the speed of 180km / h and the tire pressure of 1.2 MPa

4.3 Results analysis

The curves of the tire deformation were shown in Figure 9, 10, 11 and 12 when the vehicle speed was 150km/h, 160km/h, 170km/h and 180km/h respectively.

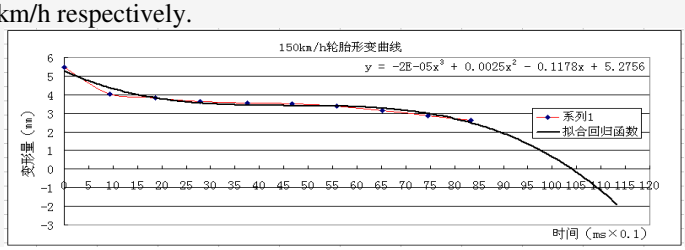

Fig.9 the tire deformation curve at the speed of 150km/h

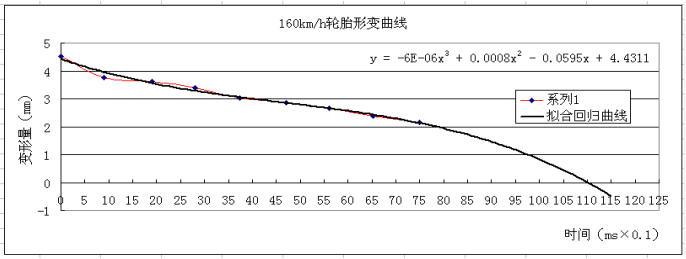

Fig10 the tire deformation curve at the speed of 160km/h

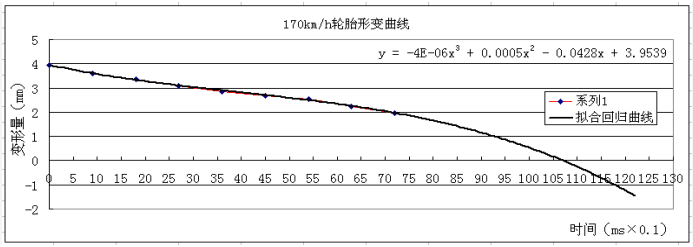

Fig.11 the tire deformation curve at the speed of 170km/h

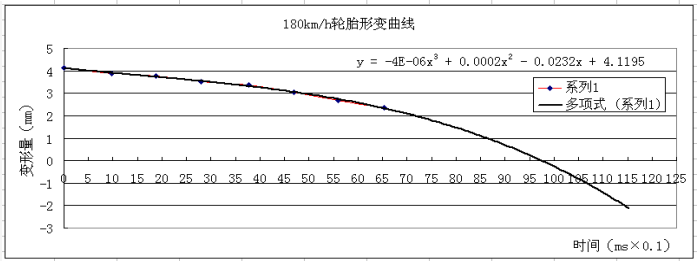

Fig.12 the tire deformation curve at the speed of 180km/h

4.4 Calculation of standing wave critical speed

It was showed from the figures obtained above that the recovery time of fitting function was T1=0.0104s, T2=0.0111s, T3=0.0108s and T4=0.0098s when the speed was 150km/h, 160km/h, 170km/h and 180km/h respectively. And then according to formula (10):

$$t = \frac{t_z}{\alpha_z - \alpha_1} \tag{10}$$

t_1=0.002049, t_2=0.002115, t_3=0.001939 and t_4=0.001861 can be concluded. And based on this, the result is expressed.

$$T_{平均} = \frac{(T_1 + t_1) + T_2 + t_2 + T_3 + +t_3 + T_4 + t_4}{4}$$

$$= \frac{0.012449 + 0.013215 + 0.012739 + 0.011661}{}$$

$$= 0.012516s$$

Where t is the previous recovery time of the No.1 point marked; t_z is the total time; α_1 is angle of the No.1 point marked; α_z is angle of the last point marked; T is recovery time from the No.1 to the last.

$$T_{average} = T = 0.012516s$$

According to the formula (8), the result was

$$V = \frac{\pi r}{T} = \frac{3.14 \times 0.2973}{0.012516} = 268.5km/h$$

which shows that the test value is slightly larger than the simulation value.

5 Conclusion

Based on the combined research results from domestic and foreign scholars, this paper made the use of ABAQUS finite element software to complete the numerical simulation of the standing wave critical speed and established the test system of critical speed. The results showed that the simulation value was consistent with the test value and the calculated value. The following conclusions are presented that firstly the critical speed of 195/60R15 radial tires is

268.5km/h under the pressure of 1.2MPa, and the load of 280KG and the outside temperature of 20℃condition; Secondly, when the load is fixed, the radial deformation can be reduced and flexible recovery time can be also shortened by advancing the pressure of tire, thereby increasing the critical speed; Thirdly, under a certain inflation pressure, the reduction of the load can help improve the critical velocity which have not linear correlations with occurrence of standing wave.

References

[1] Zhuang Jide. *Calculate vehicle ground mechanics* [M]. Beijing: Mechanical Industry Press, 2005.

[2] Zhuang Jide. *Modern vehicle tire technology* [M]. Beijing: Beijing University of Technology Press, 2001.

[3] Padovan J. *On standing waves in tires* [J]. Tire Science and Technology, 1997, 5(2).

[4] J.R.Choa, K.W.Kimb, H.S.Jeongb. *Numerical investigation of tire standing wave using 3-D patterned tire model*[J]. Science Direct, 2007(6).

[5] Aninda Chatterjee,Joseph P.Cusumano and John D.Zolock. *On contact-induced standing waves in rotating tires:experiment and theory*[J]. Journal of Sound and Vibration, 1999(5).

[6] Hong Zongyue, Wu Guizhong. *Finite element analysis of radial tire. lecture 6 finite element analysis model of radial tire* [J]. Tire Industry, 2006 (3) :187-191.

Proceedings of the 11th International Forum of Automotive Traffic Safety, 2014, pp 193- 199
No. ATS.2014.215

A Method Study on the Optimal Ground Clearance of Truck Under-run Protector

Yan Lei[1], Chen Qiang[1], Sun Zhendong[1], Lin Miao[1]
[1]China Automotive Technology & Research Center, 100176, Beijing, China
yanlei@catarc.ac.cn

Abstract *:*

Background: Rear-end collision were one of the important types of road traffic accidents with the characteristics of heavy casualties. Among the accidents, it was caused greater casualties and higher mortality in the passenger car crashes into truck accidents. According to the analysis of lots of traffic accidents, it's found that the Under-run protector has a good protective effect and can reduce casualties in this kind of accidents.

Objective: Only the analysis based on the actual accidents data was able to provide real foundation for improving the Under-run Protector. So this paper would, on the basis of actual accidents data, study the determination method of the Optimal Ground Clearance of the truck under-run protector.

Method and material: Accident data were from China In-Depth Accident Study (CIDAS). In order to study a method on the optimal ground clearance of truck under-run protector, some accidents were appropriately chosen as data samples of the passenger car crashing into truck and the passenger car participating in the accident.

Results: The relationship among the protection height difference, the crash-in depth, the head length and other parameters was analyzed, and the cumulative probability distribution was introduced into the study. Through derivation and transformation, the determination method of the optimal ground clearance was finally found out to be about 385mm.

Conclusions: This paper focused on method exploration of the automotive safety technology as well as the vehicle standard key parameters on the basis of the actual traffic accidents data, so it can also provide a reference for other key parameters to be studied.

Keywords: Truck, Passenger Car, Under-run Protector, Optimal Ground Clearance;

1 Preface

Rear-end collision were one of the important types of road traffic accidents with the characteristics of heavy casualties. Among the accidents, it was caused greater casualties and higher mortality in the passenger car crashes into truck accidents. Because the total height of the driver and passenger's sitting height and the passenger car's chassis height was almost equal to the height of the truck's chassis, the passenger car was more likely to crash into the truck's underrun part and thus the possibility of straight impact of the passenger car's driver and passenger into the truck chassis would increase, which might lead to high mortality, as was shown in Fig. 1.

According to the analysis of lots of traffic accidents, it's found that the Under-run protector has a good protective effect and can reduce casualties in this kind of accidents. The technical requirements for the Under-run protector was stated in GB 11567.2-2001"Motor vehicle and trailers-rear underrun protection requirements": the protector must have sufficient capacity to stop the rear-end vehicle and prevent it from crashing into its underrun part. As far as the protective effect was concerned, the ground clearance of Under-run Protector was one of the most important factors.

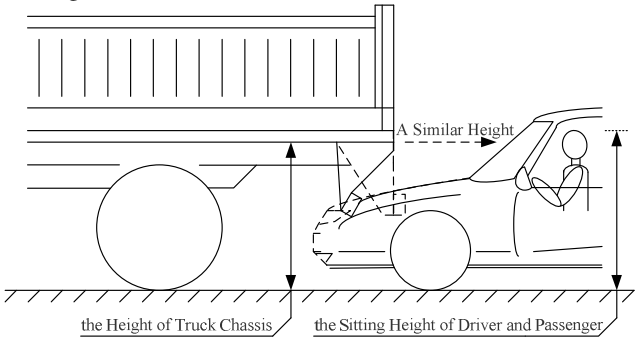

Fig. 1. Diagram of the sitting height of driver and passenger in passenger car and the height of truck chassis

In order to improve the protective effect of truck under-run protector, experts and scholars all around the world have worked on a great deal of research, but most of them were based on theoretical analysis or experimental simulation and few were based on actual traffic accidents data. However, only the analysis based on the actual accidents data was able to provide real foundation for improving the Under-run Protector. So this paper would, on the basis of actual accidents data, study the determination method of the Optimal Ground Clearance of the truck under-run protector.

2 Data

Accident data were from China In-Depth Accident Study(CIDAS). In July of 2011, the CIDAS Working Group started to conduct in-depth accident investigation in Changchun, Beijing, Weihai, Ningbo, Changsha and Foshan, and collected 1700 accidents as of June of 2014. In order to study a method on the optimal ground clearance of truck under-run protector, some accidents were appropriately chosen as data samples of the passenger car crashing into truck and the passenger car participating in the accident.

3 Research approach and model building

3.1 Determine the relationship between the protection height difference and crash-in depth

The truck's Under-run Protector were designed to protect the passenger car driver from crashing into the truck's underrun part and at the same time mitigate the car's impact. Therefore, the relationship between the depth of the car crashing into the truck's underrun part and the ground clearance of truck's Under-run Protector needs identifying and then can be used for the study on the determination method of the Optimal Ground Clearance. The depth of the car crashing into the truck's underrun part was called as "crash-in depth" in this paper.

According to the statistical analysis of the passenger car crashing into truck's tail, it's found that the passenger car's crash-in depth had something to do with the ground clearance of truck under-run protector as well as the ground clearance of the car's front protector. The difference between the ground clearance of truck's under-run protector and the ground clearance of the passenger car's front protector was called as "protection height difference" in this paper, as was shown in Fig. 2. The protection height difference was extracted as independent variable and The crash-in depth was extracted as dependent variable from the actual traffic accidents data, then fitted these data and determined their relationship. Their relation function was shown in Formula 1.

$$S = f_1(\Delta h) \qquad \ldots\ldots(1)$$

Notes: S —— crash-in depth, units are in mm;

Δh —— protection height difference, units are in mm.

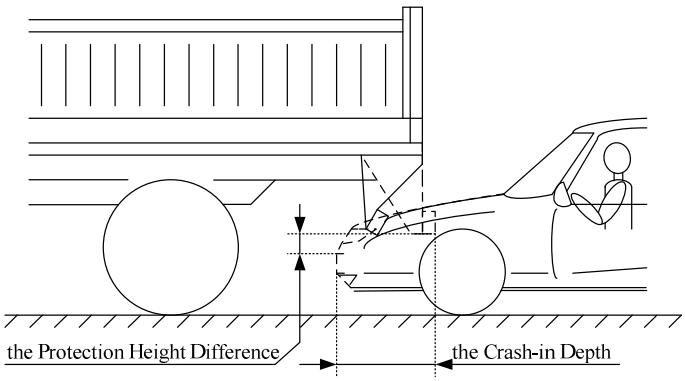

Fig. 2 Diagram of the protection height difference and crash-in depth

3.2 Determine the relationship between protection height difference and safe crash-in

The structural features of the passenger car's front part and the truck's underrun part showed that when the passenger car's crash-in depth was less than the length from the passenger car's front point to its front windshield, the driver and passengers in the passenger car were relatively safe. The length from the passenger car's front point to its front windshield was called as "head length" and in the meantime calls the above situation was called as "safe crash-in" in this paper. To determine safe crash-in proportion, the distribution of the head length should be first studied. the head

length was extract as independent variable and the cumulative probability was extract as dependent variable from the actual traffic accidents data, and then fit these data to determine the cumulative distribution. Their relation function is shown in Formula 2.

$$P_{ct} = f_2(l) \quad (2)$$

Notes: P_{ct} —— cumulative probability while head length $\le l$, $0 \le P_{ct} \le 100$, unit is %;

l —— head length of passenger car; unit: mm;

Based on the relationship between protection height difference and crash-in depth, the crash-in depth could be estimated correspondingly by the protection height difference. When the protection height difference was Δh, l> s, then it could be inferred to be safe crash-in; when l< s, then it could be inferred that it's not safe crash-in. Based on the above analysis, the relationship between protection height difference and safe crash-in could be derived combined with the relationship between protection height difference and crash-in depth and the cumulative distribution of head length.

According to Formula 1 and Formula 2, we have derived the relation function of protection height difference and safe crash-in, as was shown in Formula 3.

$$P_{aq} = f_3(\Delta h) = 100 - P_{ct} = 100 - f_2(S) = 100 - f_2(f_1(\Delta h)) \quad (3)$$

Notes: P_{aq} —— the proportion of safe crash-in when the protection height difference is Δh, $0 \le P_{aq} \le 100$, unit is %;

3.3 Determine the distribution of the protection height difference

When the truck was equipped with the same under-run protector, the protection height difference would be changed with the ground clearance of the upper edge of the passenger car's front protector. In actual traffic environment, there were many types of passenger cars that might happen to crash into truck's tail and thus the protection height difference varies a lot. As for a truck, the possible protection height difference varies with different passenger cars.

In order to determine the distribution of protection height difference, we had to at first know about the distribution of the ground clearance of the passenger car's front protector. So extract the ground clearance of the passenger car's front protector as independent variable and take the cumulative probability as dependent variable from the actual traffic accidents data, fit these data and then determine the cumulative distribution. Their relation function was shown in Formula 4.

$$P_{sb} = f_4(h_{sb}) \ldots \quad \ldots(4)$$

Notes: P_{sb} —— the cumulative probability when the ground clearance of the passenger car's front protector $\le h_{sb}$, $0 \le P_{aq} \le 100$, unit is %;

h_{sb} —— the ground clearance of the passenger car's front protector; unit: mm.

When the ground clearance of the truck's under-run protector equals *H* and the ground clearance of the passenger car's front protector which happened to crash into its tail is h_{sb}, then the protection height difference is $\Delta h = H - h_{sb}$. Above all the analysis, the distribution of protection height difference could be derived combined with $\Delta h = H - h_{sb}$ and the cumulative distribution of the ground clearance of passenger car's front protector.

According to Formula 4, we have derived the relation function of the distribution of protection height difference, as was shown in Formula 5.

$$P_{\Delta} = f_5(\Delta h) = 100 - P_{sb} = 100 - f_4(H - \Delta h) \ldots \quad \ldots(5)$$

Notes: P_{Δ} —— the proportion of the passenger cars when the ground clearance of the truck's under-run protector is H, the protection height difference between it and the truck is Δh, $0 \le P_{\Delta} \le 100$; unit: %;

3.4 Determine the relationship between the ground clearance and safe crash-in

As for a truck, the higher proportion the safe crash-in among possible passenger cars crashing into it takes, the more reasonable the ground clearance of the truck's under-run protector is. When a passenger car crashes into a truck's

tail, the protection height difference between them and the car's head length exercise influence on whether the car can crash into it safely or not and even decide the casualties in this accident.

When the ground clearance of the truck's under-run protector is H, the passenger car's proportion is P_{Δ} and the protection height difference $\leq \Delta h$. Among these passenger cars, the crash-in depth is S corresponding to the max-difference between the car and the truck. And then, we get the proportion of passenger cars with its head length over S is P_{aq}. Above all the analysis, the proportion of safe crash-in could be derived when the ground clearance of the truck's under-run protector is H and the protection height difference $\leq \Delta h$, combined with the relationship between the protection height difference and safe crash-in and the distribution of protection height difference.

According to Formula 3 and Formula 5, we have derived the proportion of safe crash-in under the above-mentioned condition, as was shown in Formula 6.

$$P_{H,\Delta h} = f_6(\Delta h) = P_{aq} \times P_{\Delta} = \left[100 - f_2\left(f_1(\Delta h)\right)\right] \times \left[100 - f_4\left(H - \Delta h\right)\right] \ldots \quad \ldots(6)$$

Notes: $P_{H,\Delta h}$ ——the proportion of passenger car's safe crash-in when the ground clearance of the truck's under-run protector is H and the protection height difference $\leq \Delta h$, $0 \leq P_{H,\Delta h} \leq 10000$, unit is ‰.

In actual traffic environment, when a truck with the ground clearance of the under-run protector H compare with all the passenger cars, we can get a minimum and maximum of protection height difference between, which provides the value range of protection height difference. $\left[\Delta h_{H\min}, \Delta h_{H\max}\right]$ is used to stand for the value range of protection height difference and then the proportion of all kinds of passenger cars' safe crash-in of the relationship between the ground clearance and safe crash-in when the ground clearance of the truck's under-run protector is H.

According to Formula 6, we have derived the relationship model of ground clearance and safe crash-in, as was shown in Formula 7.

$$P_H = f_7(H) = P_{H,\Delta h}\Big|_{\Delta h_{H\min}}^{\Delta h_{H\max}} = \left[\left(1 - f_2\left(f_1(\Delta h)\right)\right) \times \left(1 - f_4\left(H - \Delta h\right)\right)\right]\Big|_{\Delta h_{H\min}}^{\Delta h_{H\max}} \ldots \quad (7)$$

Notes: P_H ——the proportion of passenger cars that can be prevented from totally crashing into the truck's tail, when the ground clearance of the truck's under-run protector is H, $0 \leq P_H \leq 10000$; unit: ‰;

$\Delta h_{H\max}$ ——the possible maximum protection height difference, when the ground clearance of the truck's under-run protector is H;

$\Delta h_{H\min}$ ——the possible minimum protection height difference, when the ground clearance of the truck's under-run protector is H;

3.5 Determine the solution of the Optimal Ground Clearance

Owing to different values of H, then P_H is different. When P_H is the maximum value, the corresponding H is the optimal ground clearance. H is used to represent the optimal ground clearance of the truck's under-run protector and $\max(P_H)$ stands for the maximum value of the proportion of safe crash-in, then the solution of the optimal ground clearance is shown in Formula 8.

$$H_r = f_7^{-1}\left(\max(P_H)\right) \ldots \quad \ldots (8)$$

Notes: f_7^{-1} ——inverse function of the function of the proportion of safe crash-in;

$\max(P_H)$ ——the maximum value of the proportion of safe crash-in, unit is ‰;

H_r —— the Optimal Ground Clearance of the truck's under-run protector; unit: mm;

4 Data analysis

4.1 Establish a relation function of protection height difference and crash-in depth

Extract the accidents that passenger cars crashed into the truck's tail from large amounts of traffic accidents data, get data of protection height difference and crash-in depth by statistics, fit these data and then establish a relation function. The fitting figure is shown in Fig. 3 and the relation function is shown in Formula 9.

$$S = 2.7886\Delta h + 827.3818 \ldots \quad \ldots\ldots(9)$$

In actual traffic accidents, the minimum value of crash-in depth are 0 mm, accordingly the minimum value of Δh while $S \geq 0$ could be used as the actual minimum value of protection height difference. Then the actual minimum value of protection height difference could be calculated according to the above formula, $\Delta h_{\min} = -296mm$.

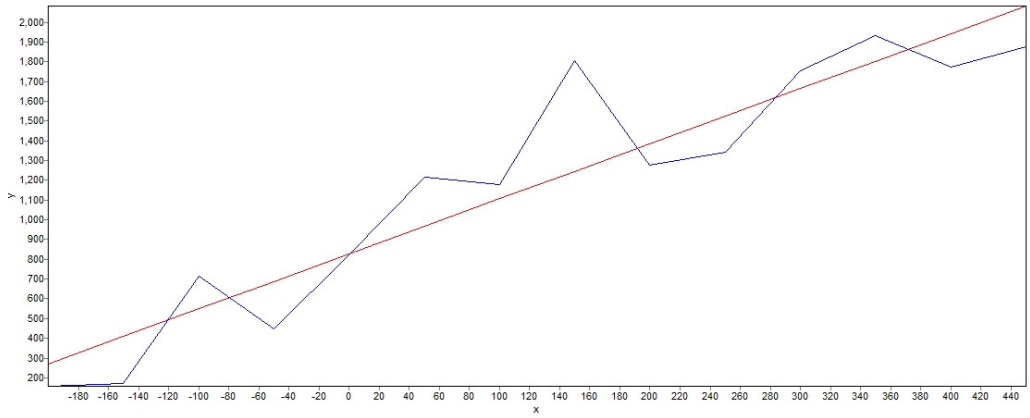

Notes: The broken line is the actual distribution map while the straight line is the fitting distribution map.

Fig. 3 Diagram of the protection height difference and crash-in depth

4.2 Establish a relation function of protection height difference and safe crash-in depth

Extract the data of head length from large amounts of traffic accidents data, fit these data and then establish a relation function as shown in Fig. 4 and Formula 10.

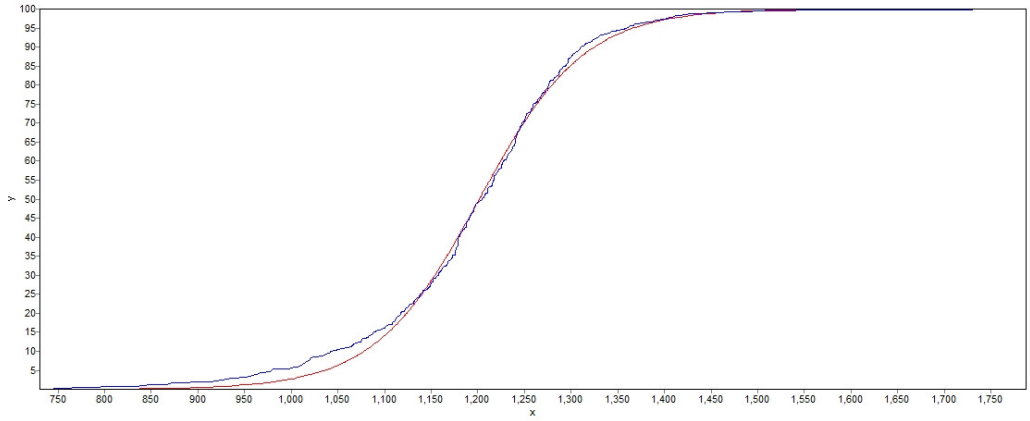

Notes: The broken line is the actual distribution map while the curve is the fitting distribution map.

Fig. 4 Cumulative probability distribution of passenger cars' head length

$$P_{ct} = \frac{100}{1 + 1943693820.6282e^{-0.01780l}} \ldots\ldots \quad \ldots (10)$$

According to Formula 9 and Formula 10, we could derive the relation function of the protection height difference and crash-in depth, as is shown in Formula 11.

$$P_{aq} = 100 - \frac{100}{1 + 780.9101e^{-0.04964\Delta h}} \cdots \quad \ldots(11)$$

4.3 Establish a distribution function of the protection height difference

Extract the data of ground clearance of the passenger car's front protector from large amounts of traffic accidents data, fit these data and then establish a relation function, as are shown in Fig. 5 and Formula 12.

$$P_{sb} = \frac{100}{1 + 179309.9533e^{-0.02124h_{sb}}} \cdots \quad \ldots\ldots(12)$$

In actual data, the minimum value of the ground clearance of passenger car's front protector is $h_{sb\cdot\min} = 320mm$.

According to Formula 12, the distribution function of the protection height difference can be derived as Formula 13.

$$P_{\Delta} = 100 - \frac{100}{1 + 179309.9533e^{-0.02124(H-\Delta h)}} \cdots \quad \ldots(13)$$

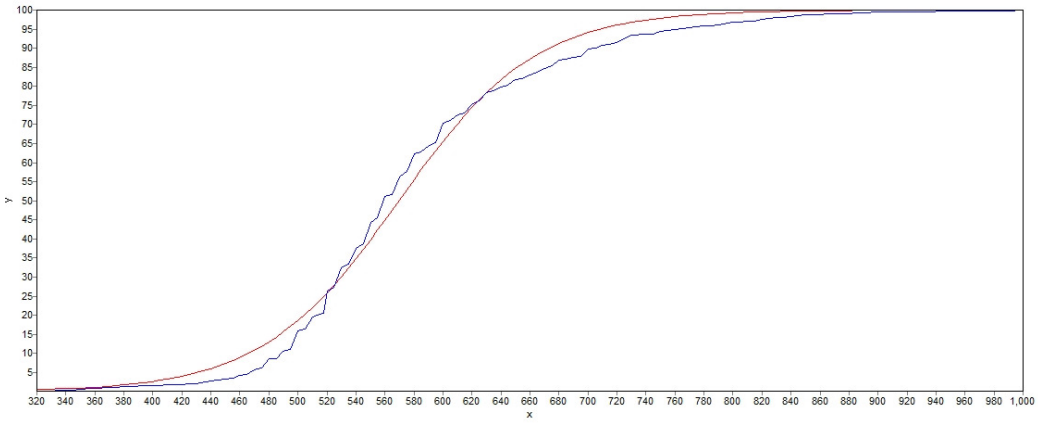

Notes: The broken line is the actual distribution map while the curve is the fitting distribution map.

Fig. 5 Cumulative probability distribution of the ground clearance of passenger car's front protector

4.4 Establish a relation function of ground clearance and safe crash-in

According to Formula 12 and Formula 13, the proportion of safe crash-in of passenger cars can be derived when the ground clearance of truck's Under-run protector is H and the protection height difference $\leqslant \Delta h$, as is shown in Formula 14.

$$P_{H,\Delta h} = \left(100 - \frac{100}{1 + 780.9101e^{-0.04964\Delta h}}\right) \times \left(100 - \frac{100}{1 + 179309.9533e^{-0.02124(H-\Delta h)}}\right) \cdots \quad (14)$$

It's known from the former text, the minimum value of the protection height difference is $\Delta h_{\min} = -296mm$ and the minimum value of the ground clearance of the upper edge of passenger car's front protector is $h_{sb\cdot\min} = 320mm$ and accordingly the value range of protection height difference is $[-296, H-320]$. Combined with Formula 14, the model of ground clearance and the proportion of safe crash-in can be derived, as is shown in Formula 15.

$$P_H = \left[\left(100 - \frac{100}{1 + 780.9101e^{-0.04964\Delta h}}\right) \times \left(100 - \frac{100}{1 + 179309.9533e^{-0.02124(H-\Delta h)}}\right)\right]\Bigg|_{\Delta h=-296}^{\Delta h=H-320} \quad \ldots..(15)$$

4.5 Solve the Optimal Ground Clearance

Draw a graph according to Formula 15, as is shown in Fig. 6.

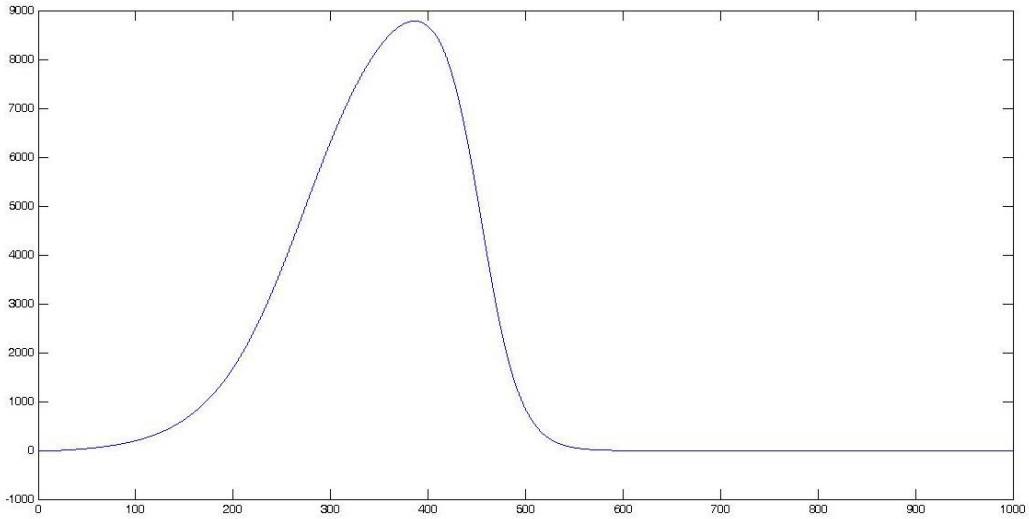

Fig. 6 Relationship graph of the ground clearance and safe crash-in

By solving this function model, we can get the maximum value $\max(P_H) = 8783.9682‰$ and the optimal solution $H_r = 385.68mm$. Therefore, the optimal ground clearance of truck's under-run protector is 385.68mm by calculation in accordance with the actual traffic accidents data.

5 Conclusions

This paper, on the basis of actual traffic accidents data and by analysis and deduction, comes up with the determination method of the optimal ground clearance of truck's under-run protector based on actual traffic accidents data. The relation function of protection height difference and crash-in depth, the relation function of protection height difference and safe crash-in, the distribution function of protection height difference and the relation function of ground clearance and safe crash-in are established in this paper based on the data analysis, and finally this function model was solved to get the optimal ground clearance of truck's under-run protector, which effectively verifies the determination method of the optimal ground clearance.

The results of this method could be provided reference to parameter revision in the GB 11567.2-2001"Motor vehicle and trailers-rear underrun protection requirements". This paper focuses on method exploration of the automotive safety technology as well as the vehicle standard key parameters on the basis of the actual traffic accidents data and this paper can also provide a reference for other key parameters to be studied.

References

[1] GB 11567.2-2001, Motor vehicle and trailers-rear underrun protection requirements[S].

[2] GB 7258-2012, Safety specifications for power-driven vehicles operating on roads[S].

[3] Zhu Xichan, Cheng Yong. *An Analysis on the Optimal Ground Clearance and Stiffness of Truck Under-run Protector*[J]. Automotive Engineering, 2001, (5).

[4] Bai Zhonghao, Ma Weijie, Cao libo, Zhang Qianbin. *Study on Car-to-Truck Rear-end Impact Experiment and Simulation Based on Accident Analysis*[J]. China Mechanical Engineering, 21(14), 2010, 7.

[5] Yu Fan, Crolla D A. *Wheelbase Preview Optimal Control for Active Vehicle Suspensions*. Chinese Journal of Mechanical Engineering, 1998, 11(2).

Proceedings of the 11th International Forum of Automotive Traffic Safety, 2014, pp 200- 204
No. ATS.2014.216

Minibus Low Constraint System to Cope with the New Regulations Frontal Crash

Zhou Yinge[1]，Duan Zhichun[2]，Cui Taisong[3]，Zhao Hui[4]
Crash Safety Department, Vehicle Development Center, Changan Motor Company,Chongqing, 400023
qyypzs@changan.com.cn

Abstract
In the 64km/h Frontal ODB analysis, The strength and structure of frontal bumper impact energy absorbing and bodywork distorting, The paper research crashworthiness and energy absorb by three different structure bumper ,and combine impact of offset deformable barrier which energy absorb and achieving structure bumper is propitious to Frontal ODB .
Keywords: offset crash; bumper;crashworthiness

几种前防撞横梁的耐撞性研究

周迎娥[1]，段志春[2]，陈贤青[3]，崔泰松[4]
汽车噪声振动和安全技术国家重点实验室，重庆，400023,
qyypzs@changan.com.cn

摘　要：在64km/h正面40%偏置碰撞工况下，前防撞横梁的结构与强度，直接影响着碰撞能量的吸收与车体的变形形式，本文通过三种不同结构前防撞横梁的简化模型，研究了其耐撞性、能量吸收占比，获得对偏置碰撞工况有利的前碰撞横梁结构。
关键词：偏置碰撞；前防撞横梁； 耐撞性

1 引言

在偏置碰撞工况中，前防撞横梁的的强度与变形形式，直接影响着碰撞能量的吸收与车体的变形形式，为了在较低材料成本下更好的吸收碰撞能量并获得较好的变形形式，本文通过三种不同结构前防撞横梁的简化模型，以一定速度模拟偏置碰撞过程，采用Ls-dyna分析软件计算，对比分析了三种不同前防撞横梁的耐撞性、能量吸收占比，获得对偏置碰撞工况有利的前碰撞横梁结构。

2 三种前防撞横梁结构及属性

2.1 有限元模型的建立

该模型主要包含刚性圆柱和前防撞横梁、支架两部分，不同部位采用不同的尺寸进行网格化分，各部件之间的焊点连接采用element_beam 单元模拟，该部分焊点未设置焊点失效，螺栓连接采用nodal_rigid_body单元模拟。

表 1 模型单元属性

模型	单元类型	单元尺寸	材料类型	单元属性
刚性圆柱	shell	10×10	MAT_020	ELFORM=2,NIP=3
前防撞横梁	shell	8×8	MAT_024	ELFORM=16,NIP=5
支架	shell	5×5	MAT_024	ELFORM=2,NIP=3

2.2 材料属性

对于CAE仿真分析来说材料参数的准确性对于结果的重要性不言而喻，本文前防撞横梁、支架所用的材料为弹塑性材料，圆柱体的材料为刚性材料，在仿真计算过程中，选用了相关的材料本构模型，并且24#材料引用真实的应力应变曲线进行处理，圆柱体、前防撞横梁、支架在准静态下的相关参数如表2：

表 2 材料参数

评价项目	密度（kg/mm3）	弹性模量(Mpa)	泊松比	屈服强度(Mpa)
刚性柱	7.85E-6	205.0	0.3	
前防撞横梁	7.85E-6	213.0	0.32	0.455

2.3 边界条件的施加

完全约束前防撞横梁支架悬空一端的自由度，约束圆刚性柱的五个自由度，只释放X 方向的移动自由度；给刚性柱施加一个初始速度10mm/ms。

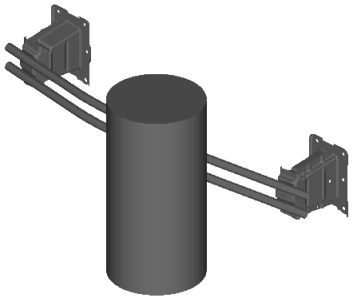

图 1 有限元分析简化模型

2.4 三种前防撞横梁的结构

图 2 第一种前防撞横梁结构

第一种前防撞横梁结构为两根直径为25mm的圆管，中间由一厚度为1.0mm、材料为DC01的钣金件连接，圆管的厚度为2.5mm、材料B340，重量5.33kg。

图 3 第二种前防撞横梁结构

第二种前防撞横梁结构为材料B340、厚度为2.5mm的钣金件，重量4.75kg。

图 4 第三种前防撞横梁结构

第三种前防撞横梁结构为材料B340、厚度为1.5mm的工字钣金梁，重量5.49。

3 三种结构前防撞横梁的耐撞性

针对三种不同结构前防撞横梁的简化模型分析结果，下面我们以前防撞横梁的耐撞性指标对比，①高比系能率（比系能率R：前防撞横梁在碰撞过程中所能吸收的最大能量E与其自身质量M的比值），②高平均载荷Fave（平均载荷Fave：前防撞横梁在受撞击变形过程中传递的平均力），③前防撞横梁在受撞击时最大动态侵入量小。

3.1 三种结构前防撞横梁评价指标对比

通过对比结果可以看出在同种材料、厚度的前提下，三种不同结构的前防撞横梁其最大动态侵入量第三种结构的前防撞横梁最小，高平均载荷、高比系能率第三种结构的前防撞横梁都大于其他两种结构类型的前防撞横梁。

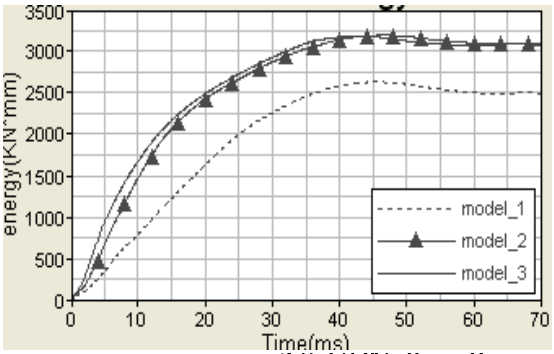

图 5 三种前防撞横梁的吸能情况

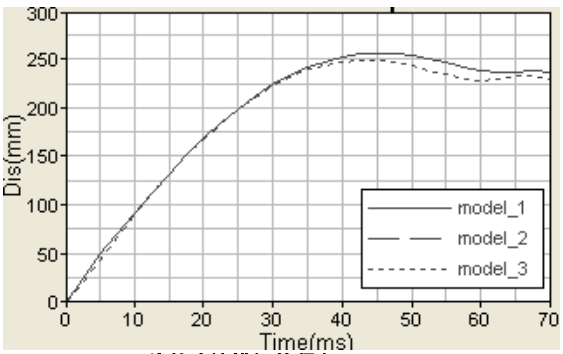

图 6 三种前防撞横梁的侵入量

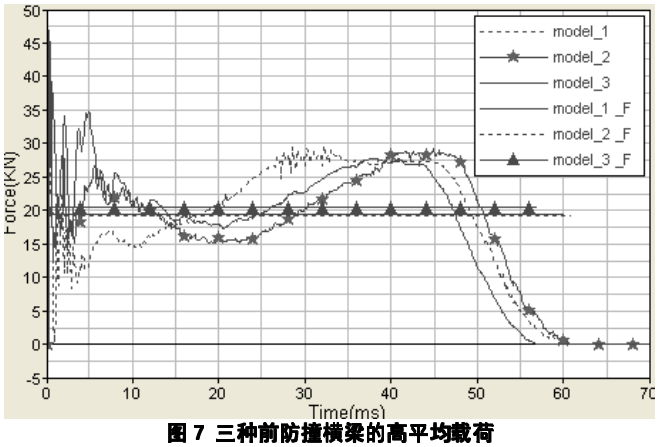

图 7 三种前防撞横梁的高平均载荷

表 1 耐撞性评价指标

评价指标	高比系能率	高平均载荷 F_{ave}	最大动态侵入量 D
第一种前防撞横梁	492.964	19.5010	256.576
第二种前防撞横梁	570.716	19.1775	256.576
第三种前防撞横梁	578.786	20.5526	248.931

4 40%偏置碰撞模型验证

本文将以某车型为例，建立64公里偏置碰撞整车模型，分析计算搭载以上三种前防撞横梁结构的偏置碰撞模型，验证这几种前防撞横梁对偏置碰撞车体加速度、前壁板侵入量等性能指标的影响，从而在设计初期选择对偏置碰撞工况有力的前碰撞横梁结构，减少后期设计阶段的设计变更及优化分析的工作量。

1） 车体减速度

仿真模型的加速度采集位置均在B柱下端，从加速度二阶方波曲线对比结果来看，在车体变形初期第三种前防撞横梁结构的模型加速度方波低于其他两种模型，在车体变形后期即纵梁中后段变形阶段三种前防撞横梁结构模型加速度方波大小差别不大。

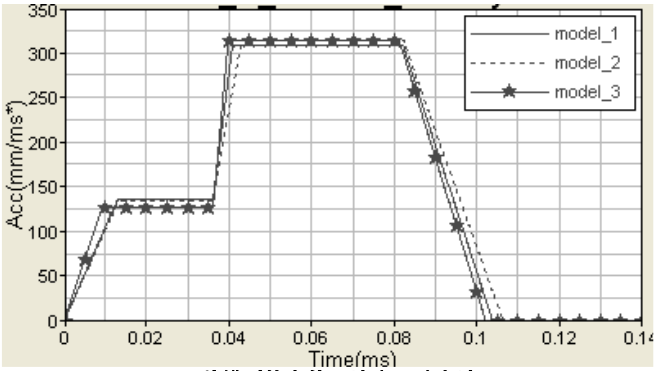

图 8 三种模型的车体加速度二阶方波曲线

2） 前壁板变形量

从三个仿真模型的前壁板侵入量可以看出，第三种前防撞横梁结构的模型前壁板侵入量最小，即乘员空间的保护最好，而第二种前防撞横梁结构模型前壁板侵入量最大。

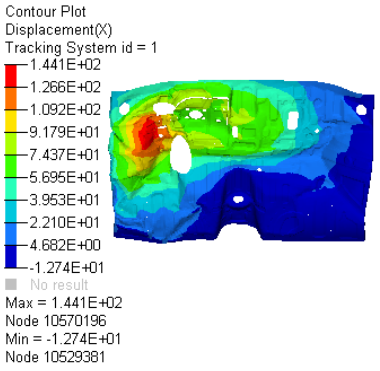

第一种前防撞横梁结构模型

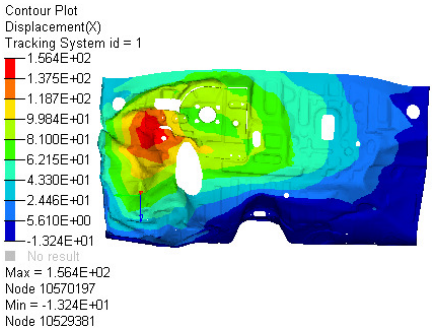

第二种前防撞横梁结构模型

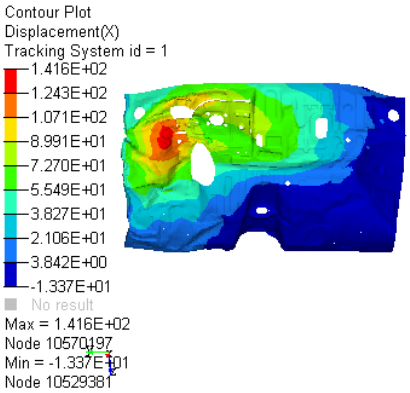

第三种前防撞横梁结构模型

图 9 三种模型的前壁板侵入量

5 结论

通过分析三种不同结构前防撞横梁的简化模型可以看出，虽然其材料、厚度一致，三种不同结构的前防撞横梁其最大动态侵入量第三种结构的前防撞横梁最小，高平均载荷、高比系能率第三种结构的前防撞横梁都大于其他两种结构类型的前防撞横梁，在64km\h正面40%偏置碰撞工况下，车体加速度二阶方波曲线总体差别不大，第三种前防撞横梁结构的模型前壁板侵入量最小，即乘员空间的保护最好，第三种结构的前防撞横梁模型在偏置碰撞工况中表现较为理想。

参考文献

[1] 王瑄，李红光等.现代汽车安全〔M〕.第一版.北京：人民交通出版社，1998,295.
[2] 《C-NCAP 管理规则（2012 年版）》.

Proceedings of the 11th International Forum of Automotive Traffic Safety, 2014, pp 205- 208
No. ATS.2014.217

Research on The Method of Optimizing Brackets in IP Based on Chinese Rule GB11552-2009

Liao Gaojian, Chen Xianqing , Dian Bo，Shao Jinhua
1.State Key Laboratory of Vehicle NVH and Safety Technology
2.Changan Auto Global R&D Centre of Changan Automobile Co Ltd

Abstract
This paper is based on a certain car which satisfies with boundaries of Chinese rule the interior fitting of passenger car (GB11552-2009),under small distortion theory, computing the main parameters of brackets absorb energy. According to the computing result optimizes the structure of brackets. Through numerical simulation, which availably reduces the 3ms acceleration.
Key words： Head Impact, 3ms Acc, Bracket

基于内凸头碰工况 IP 内部支架结构优化研究

廖高健，陈贤青，奠波，邵金华
1. 汽车噪声振动和安全技术国家重点实验室
2. 重庆长安汽车公司汽车工程研究总院

摘要:本文基于长安某款车型，在符合内凸法规 GB11552-2009 对头碰区域试验工况要求的条件下，通过把 IP 内部支架简化成力学模型，理论计算了在小变形范围内，影响支架吸能的关键参数，根据理论计算，指导优化了支架的结构形式，并且通过有限元数值分析，验证了优化后的支架结构形式能有效地降低头碰 3ms 加速度值。
关键词:头碰，3ms 加速度 ，支架

1 引言

“十五”以来，我国汽车工业持续发展，中国已经成为世界上主要的生产和消费大国，与此同时车辆的交通事故也越来越多，从而导致车内乘员受到伤害。为了加强乘员的保护，欧美日等发达国家早在 20 世纪七十年代就对汽车内部凸出物实施了强制性技术法规，我国也于 2009 年 1 月 1 日强制实施 GB11552-2009<<乘用车内部凸出物>>技术标准，其目的就是为促进我国汽车生产厂家优化和改进汽车仪表板及其安装部件设计，以减轻交通事故中乘员受到的伤害[1]。

IP 仪表板内部支架一般为金属支架，在头碰冲击过程中，往往因为其刚度较大，引起 3ms 加速度值偏大。又由于支架本身作为一个支撑部件，刚度不能太弱，因此在头碰冲击分析中，对支架本身刚度的弱化，提升的空间不大，从而给支架的优化带来一定的困扰。在头碰冲击试验中，根据 GB11552-2009 内凸法规边界条件可知，头碰冲击的总能量小于等 152.4J，引起支架的变形基本为小变形。因此根据理论计算得出支架的最优结构形式，并通过数值模拟验证，为设计提供理论指导。

2 支架吸收内能理论计算

支架在头碰冲击试验中，可以简化成如图 1 所示的力学模型，理论计算出支架吸能关键参数。其中，f(t)为 t 时刻，头碰冲击作用在支架均布力，进一步简化，假定 f(t)的合力为 F（t）作用在 OA 的中点 D。相关参数的含义如下：

l_1-OA 段的长度 ，l_2-OB 段的长度；E-杨氏模量，I-截面惯性矩；α-f(t)与 OA 垂直方向的夹角，β-OA 与 OB 的夹角.

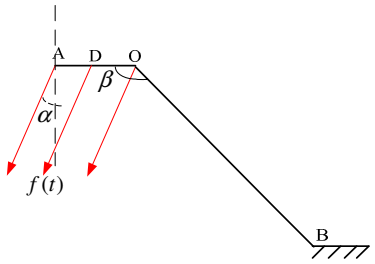

图 1 支架力学模型

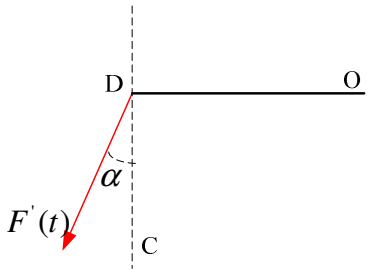

图 2 OD 段 D 点内力分析

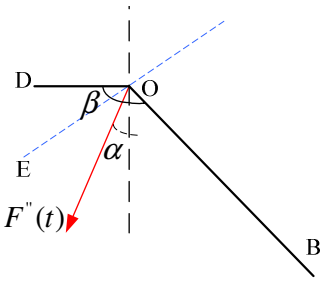

图 3 OB 段 O 点的内力分析

OA 段的受力分析，设 f(t)的合力为 F（t）作用在 OA 的中点 D，则 OD 的内力分析见图 2，因此 OD 段 D 点在其垂直方向 0-t 时间段的位移为：

$$\delta_1 = \int_0^t F'_{(t)} \cos(\alpha) dt * \frac{l_1^3}{24EI} \tag{1}$$

根据受力平衡可知，$F'(t) = F(t)$，故吸收的内能为：

$$\omega_1 = \left[\int_0^t F_{(t)} \cos(\alpha) dt \right]^2 * \frac{l_1^3}{24EI} \tag{2}$$

OB 段在 O 点的内力分析见图 3，OE 为垂直 OB 的方向，OE 与 F''(t)的夹角为$180-(\alpha+\beta)$，因此 OB 段在 O 点，沿 OB 的垂直方向 OE 在 0-t 时间段的位移为：

$$\delta_2 = \int_0^t F''_{(t)} \cos[180-(\alpha+\beta)] dt * \frac{l_2^3}{3EI} \tag{3}$$

根据受力平衡可知，$F''(t) = F(t)$，又因为 OB 段与 OD 段为刚性连接，因此 D 点在 OE 方向的位移也为δ_2，故其吸收的内能为：

$$\omega_2 = \left\{ \int_0^t F_{(t)} \cos[180-(\alpha+\beta)] dt \right\}^2 * \frac{l_2^3}{3EI} \tag{4}$$

整个支架 AOB 吸收的内能为：$\omega = \omega_1 + \omega_2$，因为$l_2$远远大于$l_1$，因此支架 AOB 吸收的内能主要为$\omega_2$，由于$F(t)$是一定的，若要支架吸收能力最大，需求$Max\left\{\cos\left[180-(\alpha+\beta)\right]\right\}^2$的值。因此当$\alpha+\beta=180$，$\cos\left[180-(\alpha+\beta)\right]=1$，$\omega_2$最大。所以，在小变形范围内，设计支架（受压）的吸能时，因尽量让$\alpha+\beta$角度接近 180 度。

3 内凸头碰冲击支架的优化

3.1 工况介绍

A 点为座椅 R 点坐标值，见下图 4，首先确定摆臂 OA 在空间的位置，即与 XY、XZ 平面的夹角，因此头型模型的空间位置也确定了。试验中，实际测量时头型运动方向与摆臂 OA 垂直，速度$V=24.1km/h$，试验时头型运动方向为与撞击相切直线的垂直方向，$V'=V*\cos\varphi$。

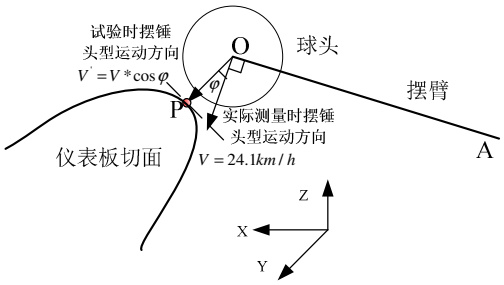

图 4　球头冲击工况介绍

3.2　有限元分析优化

如图 5 所示，建立了头碰冲击有限元模型，球头冲击点位于出风口下端，内部存在 DVD 支架，球头冲击的方向按照 2.1 工况介绍确定，初速度$V'=21.4km/h$。有限元 Base 模型材料见下表 1，Case 模型与 Base 模型材料及厚度一致，只是 DVD 支架在 Base 模型基础上进行了结构的优化见图 6。

表 1　材料牌号

材料类型	材料牌号
塑料材料	PP_EPDM
塑料材料	PP_TD20
金属材料	DC01

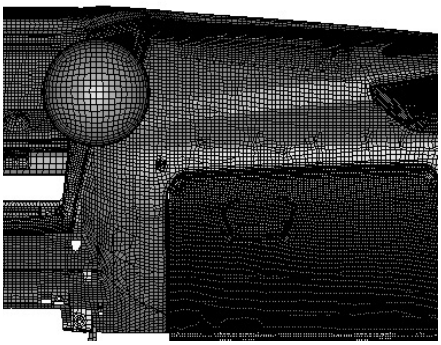

图 5　头碰冲击局部有限元模型

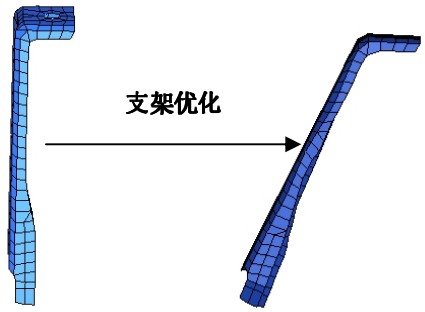

图 6　支架优化

Base 及 Case 模型 DVD 支架及周围布置与头碰模型关系见图 7。

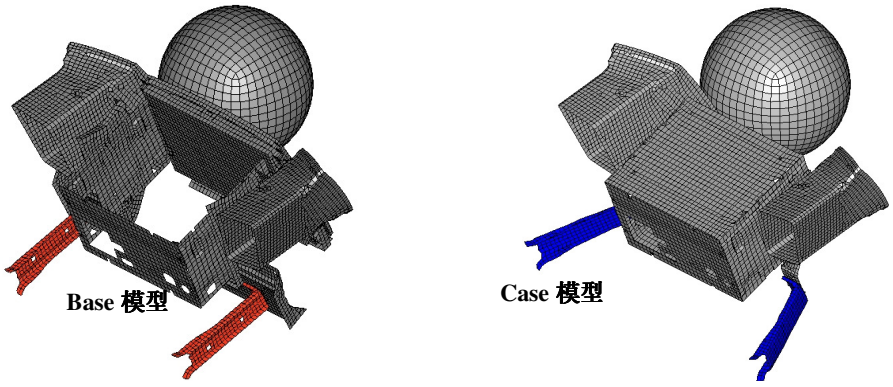

图 7　DVD 支架及周围关键件与头碰位置

假设DVD支架的受力方向为头碰冲击的方向，根据图1支架的简化力学模型，可以得到Base及Case模型α，β角。再根据公式（4），可以计算出$\{\cos[180-(\alpha+\beta)]\}^2$见表 2，它越大，越有利与支架的吸能，从而降低头碰3ms加速度值。

表 2　DVD 支架各参数值

工况 / 数值	Base 模型	Case 模型
α（度）	57.5	57.5
β（度）	90.0	114.2
$\{\cos[180-(\alpha+\beta)]\}^2$	0.71	0.98

Base模型及Case模型计算得到的3ms加速度值见图8、9，Base模型3ms加速度为70.1g，优化支架后Case模型3ms加速度为67.30g.因此优化支架后3ms加速度值降低了2.85g。

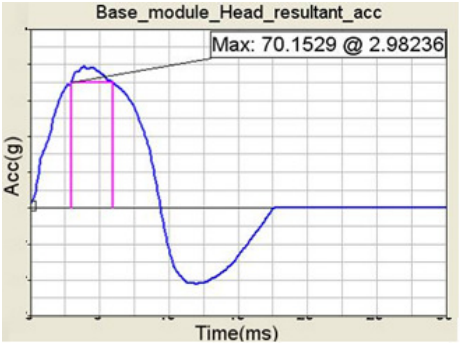

图 8　Base 模型 3ms 加速度值

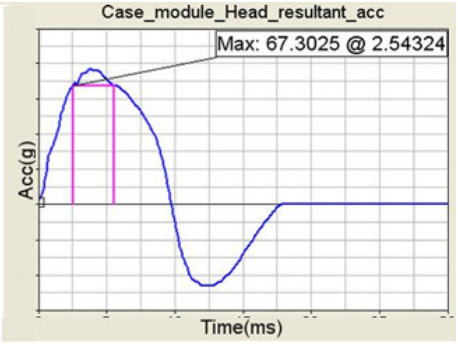

图 9　Case 模型 3ms 加速度值

4　结论

本文通过理论计算，得到在小变形范围内，支架吸收的内能与支架本身夹角及受力方向的关系，从而通过数值分析优化支架结构形式，在不弱化支架厚度的前提下，优化后的的支架结构形式在本文的工况中，3 ms 加速度值降低了 2.85g。因此可以得出，这种优化支架的方法，能够有效地降低内凸法规头碰工况中 3ms 加速度值，同时也保证了支架的强度，为 IP 内部支架的设计与布置满足内凸法规，提高对乘员的保护提供了一种有效的理论方法。

参考文献

[1]张明君，张德明．黄传义.轿车内部凸出物试验方法．汽车工程师，2010 年，3 期：42-46.

[2]《乘用车内部凸出物》（GB11552-2009）

Proceedings of the 11th International Forum of Automotive Traffic Safety, 2014, pp 209- 219
No. ATS.2014.301

A Preliminary Study on the Protective Efficiency of the Child Restraint System in School Bus

HAN Yong[1], Zhou Shui-ting[1], Zhuang Shu-ji[1], XIE Jing-ping[1], Koji Miuzno[2]
1.School of Mechanical and Automobile Engineering, Xiamen University of Technology, Xiamen, China, 361024
2.Department of Mechanical Science and Engineering, Nagoya University, Nagoya ,Japan,464-8601
Email: yonghan@xmut.edu.cn, kmizuno@mech.nagoya-u.ac.jp

Abstract: The child restraint system has an important role for children occupant injury protection in school bus. To evaluate the protective efficiency of child seat belt system for child occupants in front crash accidents , this paper establishes a school bus 6-year-old school children seat restraint system simulation model under a front crash. The paper comparatively analyses the child occupants' head, thorax dynamic responses and injury physical parameters under four conditions, which are without using seat belts, using two-point seat belt, using three-point seat belt and using five-point seat belt. Additionally, this paper also comparatively analyses the 6-year-old child occupants' head, thorax dynamic responses and injury physical parameters of three-point seat belt under three conditions, which are using adult seat belt, using the seat belt with shoulder straps at the bottom of the arm, using the seat belt correctly. The results show that using the three-point belt correctly can help to reduce the injury risk of head and chest. The study results demonstrate the child occupant restraint system effect well in the child occupant protection a vehicle collision, and it can serve as a further improvement of child occupant restraint system of reference.

Keywords: seatbelt; seat; dummy; restraint system; frontal impact

校车儿童约束系统防护效率初步研究

韩勇 [1]，周水庭 [1]，庄首吉 [1]，谢金萍 [1]，水野幸治 [2]
1. 厦门理工学院，厦门，中国，361000
2. 名古屋大学，名古屋，日本，464-8603
Email: yonghan@xmut.edu.cn, kmizuno@mech.nagoya-u.ac.jp

摘　要：在校车碰撞事故中，校车儿童座椅及安全带防护效率对对儿童保护有着重要影响。为了评估校车在正面碰撞事故中座椅安全带系统对儿童乘员损伤防护效率，本文使用混 III 6 岁儿童机械假人有限元模型建立了校车正面碰撞学龄儿童座椅约束系统数值仿真有限元模型。分析儿童乘员在校车正面碰撞中无安全带约束、使用两点式、三点式和五点式安全带约束条件下的动力学响应和头、胸部的损伤物理参数；分析了儿童使用三点式安全带的三种佩戴方式（正确使用、成人式安全带、肩带侧滑）的的头部加速度、头部前倾位移量和胸部加速度等物理损伤参数。结果表明在正面碰撞事故中，使用三点式安全带更有利于儿童乘员保护；正确使用三点式安全带可以减轻头、胸部损伤风险。本文研究结果验证了儿童乘员约束系统在校车碰撞事故中对儿童乘员的防护作用，同时可以作为进一步改进校车儿童乘员约束系统的参考依据。

关键词：安全带；座椅；假人；约束系统；正面碰撞

1 引言

根据《2011 年全国教育事业发展统计公报》，我国有在园幼儿（3-6 岁）近 3424 万人[1]。统计数字显示每年我国有超过 1.85 万名 14 岁以下儿童死于道路交通事故,儿童因交通事故的死亡率是欧洲的 2.5 倍,美国的 2.6 倍[2]。交通事故已经成为我国儿童意外死亡中仅次于溺水死亡的第二大原因,在所有儿童死亡原因中排名第六[3]。特别是 2011 年几起恶性校车事故，造成社会广泛关注和争论，其争论的焦点之一就是校车的安全性能和儿童乘员的防护。欧美日等发达国家对儿童乘员保护已有专门的法规要求并已实施，我国在儿童乘员安全方面的研究起步较晚，虽新版强制性国家标准《专用校车安全技术条件》(GB24407—2012)和《专用校车学生座椅系统及其车辆固定件的强度》(GB24406—2012)已正式发布并实

施，但是对安全带约束系统的研究文献较少。有研究表明，碰撞过程中儿童假人的行为取决于约束系统的类型[4]。本文采用有限元方法，建立了校车前碰撞 6 岁学龄儿童座椅约束系统仿真模型。对比分析儿童在无安全带、使用两点式、三点式和五点式安全带条件下的儿童的运动学响应及头、胸部损伤物理参数。为提高校车儿童保护提供参考依据。

2 材料与方法

2.1 儿童座椅有限元模型的建立

儿童座椅有限元模型是根据某校车厂家提供的儿童座椅，进行实物测量和逆向工程，建立了座椅的三维几何数据后进行网格划分而成。模型由座椅骨架、支撑架、坐垫泡沫、靠背泡沫组成，节点数为82531个，单元数为97428个（如图1）。骨架采用Q235号材料，坐垫和靠背采用低密度泡沫材料，应力-应变曲线由试验测得，如图2所示[5]。儿童约束系统安全带采用体单元模拟带扣，一维安全带单元和二维安全带单元模拟安全带和织带，模型材料如表1所示。

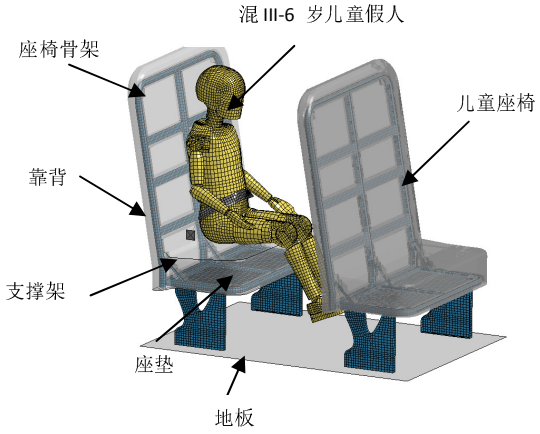

Figure 1.The finite element simulation model of child seat

图 1.儿童座椅有限元仿真模型

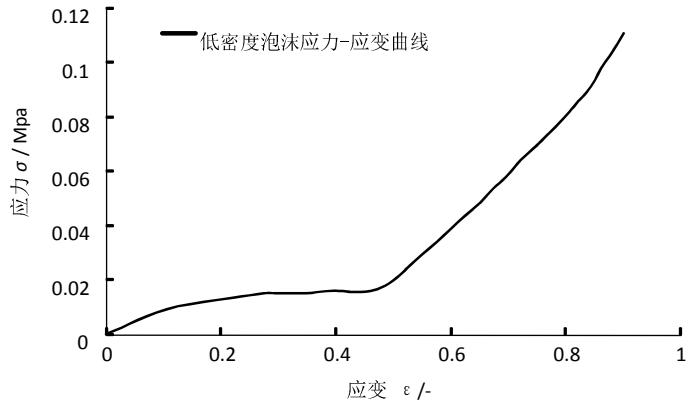

Figure 2.The stress-strain curves of seat foam material

图 2.座椅泡沫材料的应力应变曲线[5]

Table 1.The material properties of seat model

表 1.座椅模型材料属性

部件	节点数	单元数	单元类型	材料类型	密度（ρ/kg/m^3）	弹性系数 (*E* / MPa)	泊松比
织带	1092	879	一维安全带单元	安全带材料 SB_MAT	-	-	-
			二维安全带单元	安全带材料 Seatbelt	0.08	-	-
带扣	84	42	体单元	刚体材料	900	1050	0.3
骨架	6607	6274	壳单元	弹塑性材料	7850	210000	0.3

2.2 仿真模型的建立

根据学龄儿童的人体尺寸特点，本研究采用由第一技术公司（FTSS)开发和验证的的混III 6岁儿童假人有限元模型（第3.1版，如图1所示）[5] ，模型由日本名古屋大学水野幸治教授研究室提供。儿童模型包含头部、颈部、胸部、上肢和下肢，模型节点数为34844，单元数为40851。

本研究为了对比分析校车儿童安全约束系统对校车正面碰撞事故中的对儿童损伤的防护效率，分析儿童乘员在校车正面碰撞中的运力学和动力学响应，建立了6种不同的使用工况分析头部加速度、头部前倾位移量和胸部加速度等物理损伤参数，即①无安全带约束、② 2点式、③ 3点式和④ 5点式安全带约束及儿童使用3点式安全带的三种佩戴方式（③ 正确使用、⑤ 成人式安全带、⑥ 肩带侧滑），如图3所示。

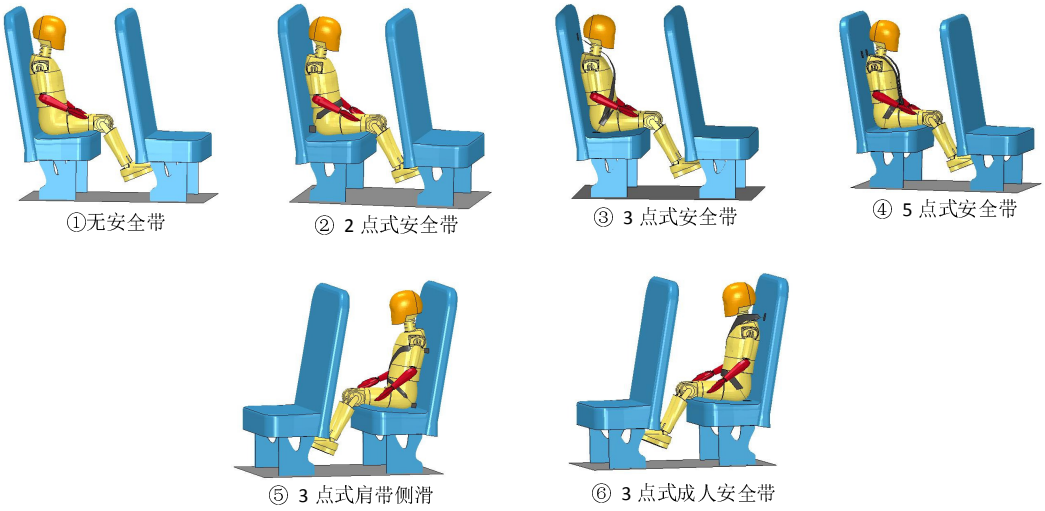

Figure 3.The finite element model

图 3.有限元模型

仿真碰撞条件为模拟校车前碰撞事故中的儿童座椅的台车试验（sled test)， 台车从静止开始启动，速度增加并产生前碰撞加速度波形。校车前碰撞事故中的加速度-时间曲线参考日本田中良知等人模拟校车在以30km/h速度前碰撞中给校车座椅加载的加速度曲线[7], 如图9所示。

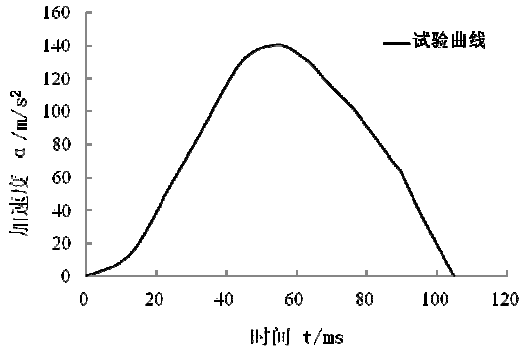

Figure 4.The acceleration - time curve of trolley

图 4 台车加速度-时间曲线

3 结果

3.1 座椅有限元模型的验证

根据中国国家标准《专用校车学生座椅系统及其车辆固定件的强度》（GB24406-2012）[6]的要求，分析对比抗后倾的静态试验和动态试验的仿真和试验结果进行验证。

3.1.1 抗后倾静态加载试验

根据国家标准和试验的设置要求对座椅靠背前部加载载荷，方向水平，加载高度在座椅 R 点以上 343mm 的水平面内。对装置设置一个 254mm 的边界条件。仿真模型如图 5 所示。

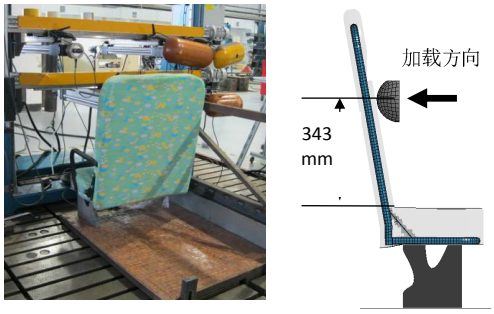

(1) 试验设置　　(2) 仿真设置

Figure 5.The static load test simulation model of seat

图 5.座椅静态加载试验模拟仿真模型

图 6 所示为抗后倾加载装置载荷-位移曲线，试验加载装置最大位移为 236mm，小于座椅靠背的位移法规值 254mm，仿真值为 210mm，与试验数据相差 11%；试验状态下最大载荷为 4380N，小于法规值 9786N，仿真值为 4333N，误差仅为 1.1%。由图 6 可知，仿真曲线与试验曲线拟合度较高，误差在合理的范围之内。变形后的座椅没有进入相距其他座椅原始安装位置 102mm 的范围内，座椅、连接件与配件在试验过程中未完全脱离。因此，该座椅模型符合静态加载试验的要求。

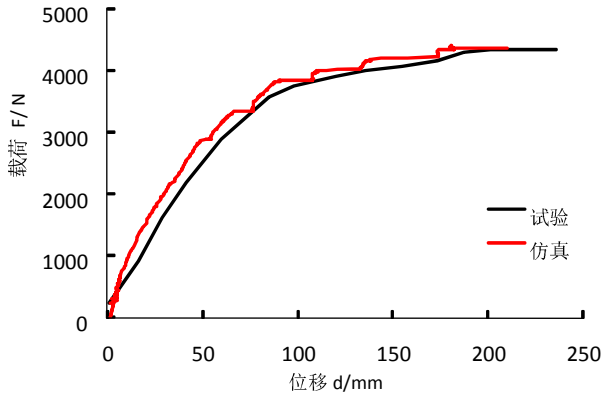

Figure 6.The force - displacement curve of the anti- backward loading device
图 6. 抗后倾加载装置力–位移曲线

3.1.2 动态试验验证

校车座椅的抗前倾的动态试验是根据国家标准 GB24406-2012 采用 P 系列 6 岁儿童假人并通过 2 点式安全带将其放置在减速台车上，模拟碰撞速度为 30km/h 的正面碰撞过程儿童假人的头部位移、头部 HIC 和胸部加速度等物理参数，仿真实验中，混III 6 岁儿童假人模型在 2 点式安全带约束下放置在校车座椅上，并对座椅加载试验中的台车减速度运动曲线（如图 7 所示）。

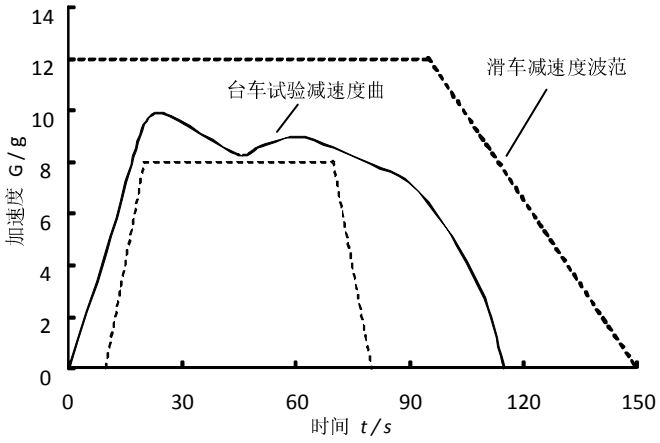

Figure 7.The comparison of the trolley acceleration waveform and the standard requirements
图 7.台车加速度波形与标准要求对比

图 8 所示为假人头部加速度-时间曲线的仿真与试验结果对比图，两者趋势较一致。仿真结果显示头部 HIC 值为 230（小于法规值 500）与 P6 儿童假人试验测得的头部 HIC 值（212）有较小误差（误差率 8%）。图 9 所示为胸部加速度-时间曲线对比曲线图，仿真结果显示指标（ThAC）23.5g，与试验结果为 26.5g 误差较小。由于仿真实验中采用的是混 III 6 岁儿童假人有限元模型，动力学方面的响应差异导致的误差在合理范围。仿真实验中儿童有限元模型的躯干和头部的向前位移未超过位于辅助座椅 G 点前 1.1m 的横向垂直面；座椅模型的骨架、支撑件及附件未产生失效现象。因此，可认为座椅模型是有效的，可用于儿童乘员损伤防护效率的研究。

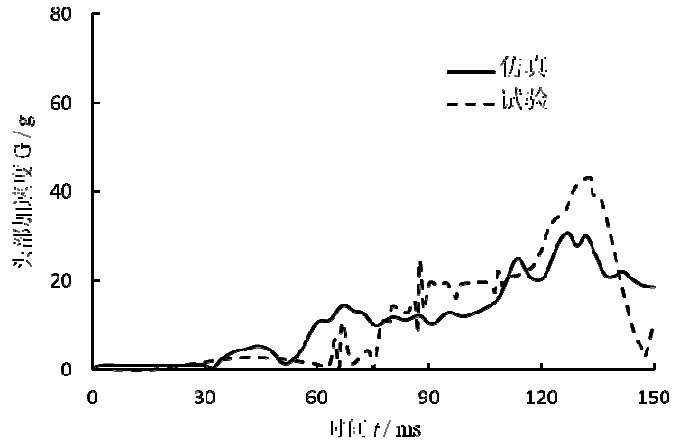

Figure 8.The head acceleration comparison of simulation with experimental results
图 8.头部加速度仿真与试验结果对比

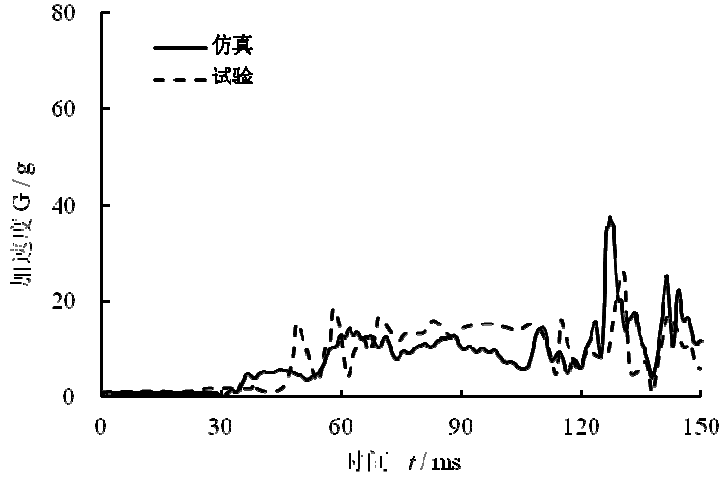

Figure 9. The chest injury indicators ThAC
图 9.胸部损伤指标 ThAC

3.2 儿童乘员动力学响应

3.2.1 运动学响应

在校车正面碰撞中，儿童乘员的头颈部、胸部、下肢等是常见的损伤部位[8]。儿童假人 90ms 和 110ms 时的运动学响应如图 10 和 11。在无安全带和使用 2 点式安全带工况中，儿童假人上体部没有约束，头部与前席座椅靠背碰撞（如图 10(a)、(b)和图 11(a)、(b)所示)。在正确使用 3 点式和 5 点安全带工况中，假人上体部受到了肩带的约束，头部未与前席座椅靠背发生接触（如图 10(c)、(d)和图 11(c)、 (d)所示)。

本文同时考查了正确使用 3 点式及 2 种误使用 3 点式安全带的工况下的儿童运动学响应。图如 10(c)、(e)、(f)所示，在 90ms，3 点式肩带侧滑时的假人前倾运动明显，使用 3 点成人安全带时对儿童假人的颈部约束过载，颈部受伤风险增加。在 110ms 时，肩带侧滑工况中，儿童上身部在无安全带约束的情况下，前倾运动显著，头部与前席座椅靠背碰撞，腹部受肩带的约束明显，受力增大。在使用成人安全带时，胸上部右侧和颈部受安全带作用受力增加，损伤风险增加。

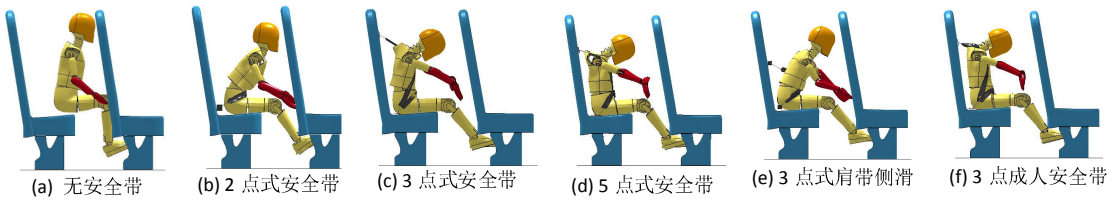

Figure 10.The movement of dummy at 90ms

图 10.90ms 时假人运动情况

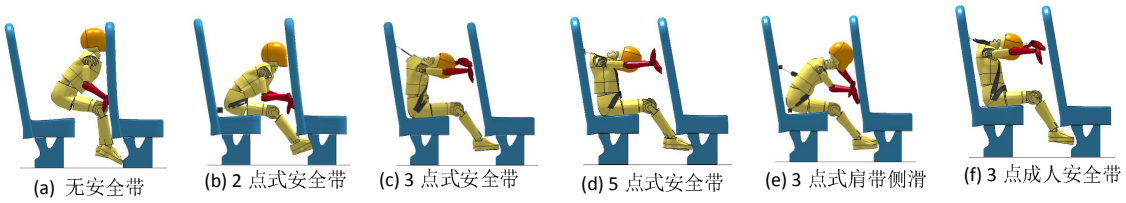

Figure 11.The movement of dummy at 110ms

图 11.110ms 时假人运动情况

3.2.2 头部加速度分析

四种工况下，假人头部的合成加速度如图 12 所示。从表格中可看出，无安全带工况下乘员的加速度在 95ms 时达到最大值 964m/s^2,两点式安全带工况下的假人头部加速度在 100ms 时达到峰值 1380m/s^2,明显高于三点式与五点式安全带工况的加速度。这是由于在这两种工况下，儿童假人的头部在惯性作用下撞击到前席座椅靠背，碰撞冲击力传递到头部导致的。两点式安全带工况下，由于安全带的约束，导致峰值出现的时刻滞后。FMVSS213 中头部合成加速度的规定值为 80g，除无安全带工况（98g）和两点式安全带工况（141g）,其他两种工况下的头部合成加速度峰值都小于 80g,符合标准。

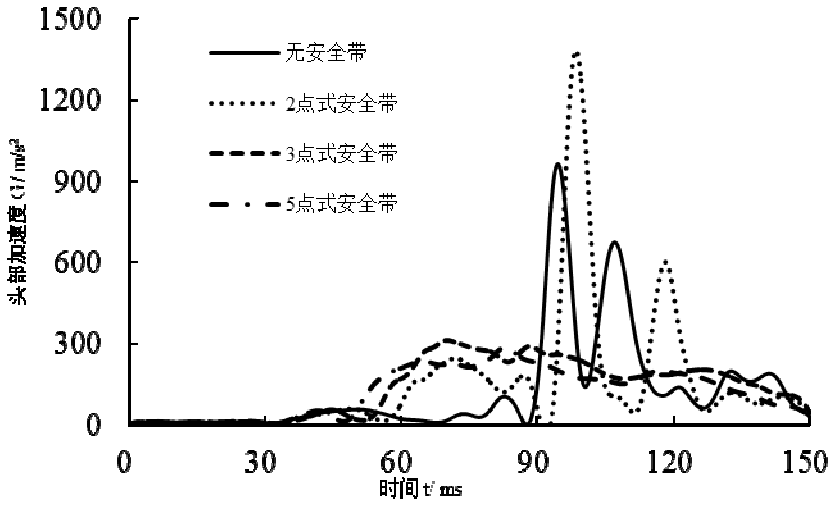

Figure 12.The head resultant acceleration comparison of four kinds condition

图 12.4 种工况头部合成加速度对比

3.2.3 胸部加速度分析

无安全带工况下，假人的胸部在前面 75ms 几乎没有受到约束，但在 95ms、115ms 和 125ms 达到峰值，结合仿真动画可知，这分别是由于假人头部和手碰撞到前排座椅靠背以及胸部在惯性作用下的前冲动作，产生的冲击力传递到胸部造成的。两点式安全带工况下，由于假人胯部受到约束，约束力传递到

胸部，所以在 70ms 时达到第一个峰值，也因此延迟了头部与前排座椅碰撞的时间，所以胸部加速度第二次峰值在 100ms 左右才达到。三点式和五点式工况下，假人胸部加速度峰值在 55ms 和 65ms 达到，这是安全带肩带直接作用的结果，并且由于五点式安全带的双肩带设计增大了接触面积，有效的约束了假人的运动，所以五点式安全带工况下的胸部加速度峰值小于三点式工况。

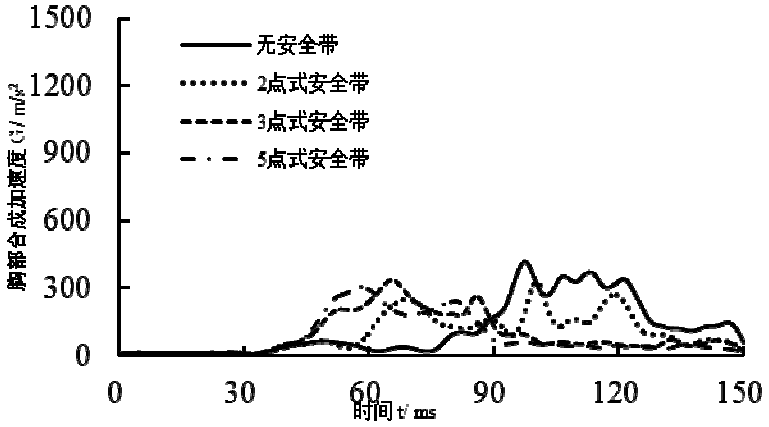

Figure 13.The resultant acceleration of chest
图 13.胸部合成加速度

3.2.4 头部最大位移量

由图可知，无安全带与两点式安全带工况下的头部最大前方移动量远大于三点式和五点式安全带工况。无安全带工况下，头部碰撞前排座椅后出现后仰回弹的情况，存在对颈部造成二次伤害的风险。两点式安全带工况下由于胯部受到安全带的约束，导致乘员上体部绕胯部旋转运动，故在竖直方向上的移动量更大。相比其他安全带，五点式安全带工况下，假人的头部最大位移量是最小的，对假人起到最好的约束效果。

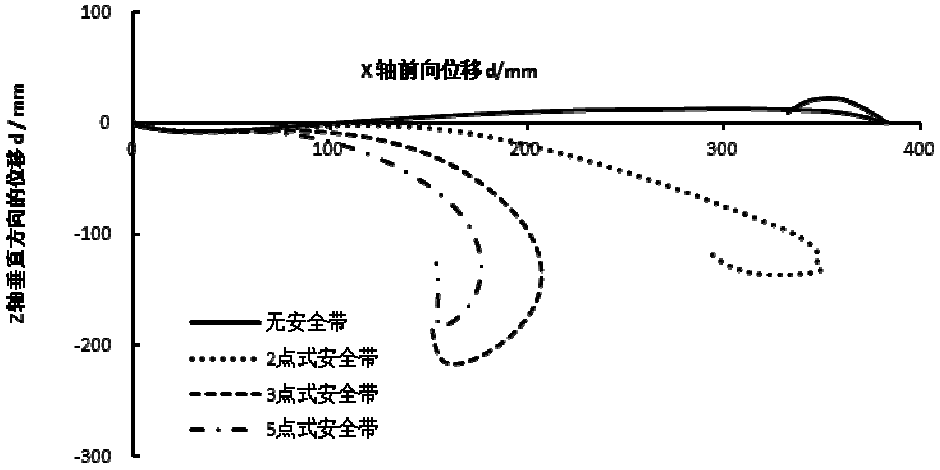

Figure 14.The maximum movement of the head
图 14.头部最大前方位移量

3.3 儿童约束系统误使用分析

在碰撞过程中，安全带的误使用常常导致对乘员的伤害，以下就三点式安全带肩带侧滑和使用成人三点式安全带这两种误使用方式与正确使用三点式安全带三种情况下儿童假人的运动学与动力学响应进行分析，对比儿童假人的损伤指标。

3.3.1 头部加速度分析

使用成人安全带的情况下，虽然头部合成加速度未超过规定值 80g，但是由于没有使用增高座椅，安

全带肩带通过儿童颈部位置，碰撞过程中肩带接触乘员的颈部，作用力传递到头部。加速度曲线出现多个波峰，说明肩带持续作用于颈部，容易引起窒息，伤害儿童安全。肩带侧滑的情况下，安全带对儿童的上躯干约束力较小，在 105ms 时乘员的头部在惯性力的作用下继续向前运动，撞击前排座椅靠背，从而出现加速度的最大值，因此，头部的加速度在这三种情况下是最大的，超过 FMVSS213 中头部合成加速度的规定值 80g。

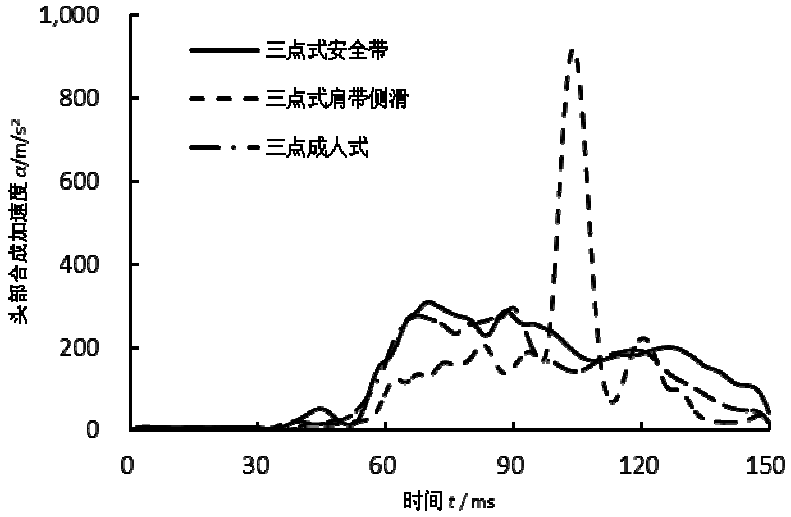

Figure 15.The head acceleration
图 15.头部加速度

3.3.2 胸部加速度分析

由图可知，使用成人式安全带的情况下，在最大值之后，仍旧出现了一次峰值，且峰值仍然大于肩带侧滑的最大值。这是乘员在身体前倾的时候，乘员身体随惯性继续向前，肩带继续勒紧胸部所致。这种情况是对乘员安全较大的威胁。

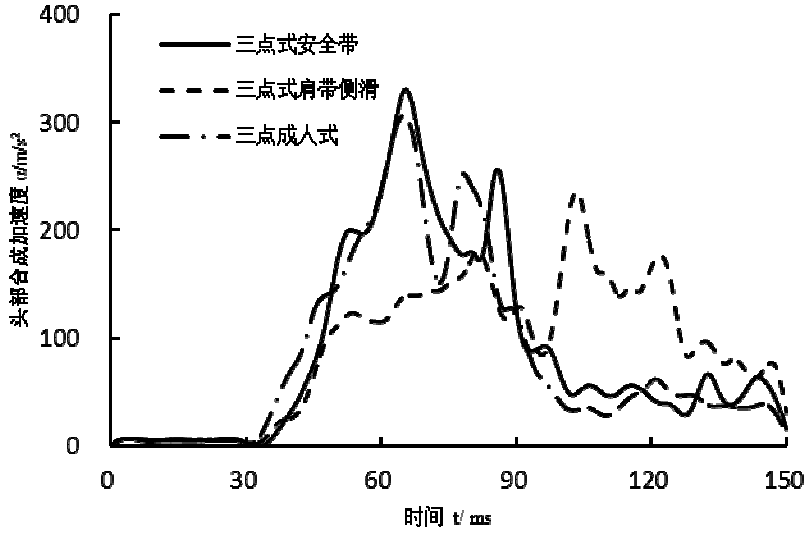

Figure 16.The chest acceleration
图 16.胸部加速度

3.3.3 头部最大前方位移量

肩带侧滑的情况下，乘员的上躯干并未被完全约束住，主要约束胸部以下部位，导致乘员身体向前侧倾，故头部最大前方移动量在这三种情况下是最大的。成人式安全带的情况下，随着运动的进行，肩带作用于颈部，约束住乘员的头颈部，因此，头部前方最大位移量小于三点式安全带工况。

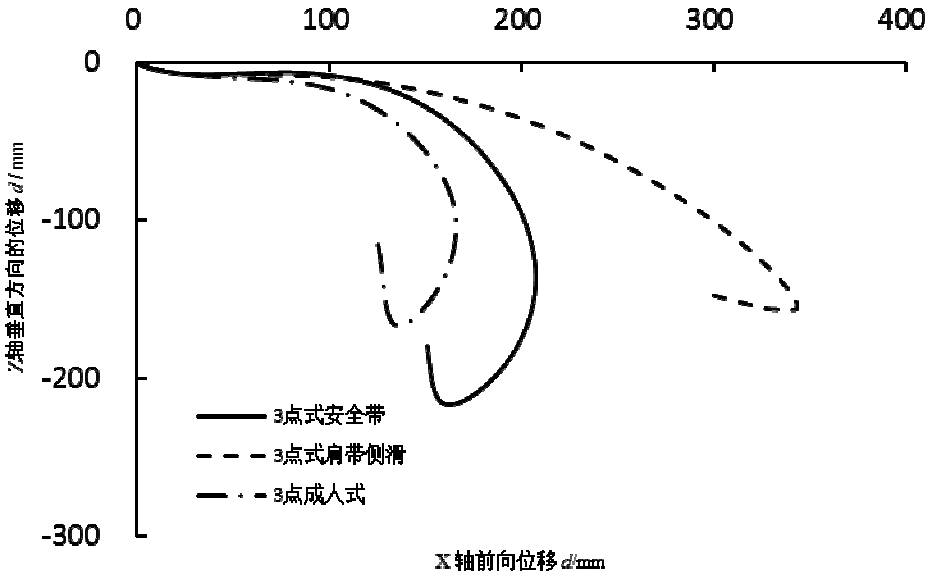

Figure 17. The maximum movement of the head

图 17.头部最大前方移动量

与正确使用儿童约束系统情况相比，误用降低了儿童约束系统的防护效果，使得儿童乘员损伤风险增加。仅使用三点式成人安全带情况下，安全带的肩带部分将勒住儿童的颈部，腰带部分将作用于脆弱的腹部，这将导致严重的颈部和腹部损伤[9]。肩带侧滑无法有效约束儿童的上躯干，在惯性作用下儿童头部易撞击前排座椅，造成损伤。

4 结论

在本次模拟的情况下，不戴安全带时，假人的头部与膝盖会碰撞到前座椅的背部。使用两点式安全带时，假人上身以腰部为中心旋转，头部在更低的位置碰撞前座椅背部。在儿童乘员受正面碰撞冲击时不能有效阻止儿童乘员在其惯性力的作用下向前方运动。三点式与五点式安全带能有效地约束假人，正确的使用能够有效降低伤害的程度。但三点式安全带工况下假人的胸部冲击力更大。综上所述，四种工况中，五点式安全带降低假人伤害的效果最好。乘员伤害主要在于头部与前座椅靠背的碰撞，因此增大前后排座椅之间的间隙，扩大乘员运动空间以及更换座椅材料增大座椅与乘员的摩擦力能有效降低伤害值。错误使用安全带会使安全带的保护作用大打折扣，肩带侧滑由于对儿童约束上半身约束不足，容易造成头部受伤。成人式安全带容易伤害儿童颈部。但相比不使用安全带仍有优势，建议增加儿童增高坐垫，这样使用成人安全带时，便可保护儿童的胸部和头颈部。

致谢

本研究获得了国家自然科学基金（编号：31300784）；福建省教育厅 A 类项目（项目编号：JA12250）和厦门理工学院对外科技合作项目的资助（项目编号：CP2012002)的资助；感谢厦门金旅客车公司技术中心提供校车儿童座椅。

参考文献（References）

[1] 中华人民共和国教育部.2011 年全国教育事业发展统计公报.2012

[2] 交通事故成为中国儿童第二杀手.人民日报海外版,2004-03-31 第四版

[3] 公安部交通管理局．中华人民共和国道路交通事故统计年报(2008 年度).2009

[4] Koji Mizuno, Tatsuya Namikiri. ANALYSIS OF CHILD RESPONSES IN CRS USING CHILD HUMAN FE MODEL. Nagoya University, Japan.

[5] FTSS. LS-DYNA Model of the Hybrid III 6-Year Old Child Dummy User Manual, April 2005

[6] 胡佳.基于试验和有限元仿真的儿童乘员正面和侧面碰撞安全研究[D].湖南大学博士论文，2008.10.

[7] GB 24406-2012，专用校车儿童座椅系统及其车辆固定件的强度[S].

[8] 田中良知.幼児専用車の安全に関する研究，日本，东京，交通安全环境研究所，2011.

[9] 杨杏梅,杨济匡,亓向翠.侧面安全气囊对儿童乘员的损伤防护效率.江苏大学学报,2011 年 7 月,第 32 卷,第 4 期.

[10] 杨杏梅.轿车碰撞事故中儿童乘员的损伤防护技术研究.湖南大学，2010.6

Proceedings of the 11th International Forum of Automotive Traffic Safety, 2014, pp 220- 227
No. ATS.2014.302

Research on the Factors of the Consistency of Child Restraint System Sled Test

YANG Lang[1], ZHU Xichan[1], DONG Liping[1], MA Zhixiong[1]，Zhang Shaowei[2]
[1]*School of Automotive Studies, Tongji University, Shanghai, China, 201804*
[2]*East Joylong Motor Airbag Co. Ltd, Shijiazhuang, China, 050000*
Email:yanglang200826001@163.com

Abstract: There are some differences between the child restraint system test results with the sled test parameters varying in different laboratories. This study includes establishing the Group I general simulation model of the child seat in Madymo and using the full factorial experimental design method in the parameter sensitivity analysis. The sled parameters are cushion stiffness, seat belt stiffness, acceleration waveform and the length of the belt pulled out from retractor. The conclusion is that the length of the belt pulled out from retractor is the main factor of the consistency of the child restraint system test.

Keywords: Automotive safety; Sled tests; Child restraint system; Consistency

儿童约束系统台车试验一致性影响因素研究

杨 浪[1]，朱西产[1]，董丽萍[1]，马志雄[1]，张绍卫[2]
[1]同济大学汽车学院, 上海，中国，201804
[2]东方久乐汽车安全气囊有限公司，石家庄，中国，050000
Email:yanglang200826001@163.com

摘　要：不同试验室中台车参数的差异使得同一款儿童约束系统的台车试验结果有一定的差异。在 Madymo 软件中建立了某款 I 组通用类安全带前向固定儿童座椅台车试验仿真模型，采用全因子试验设计方法研究了台车坐垫刚度、台车安全带刚度、台车加速度波形及台车安全带卷收器拉出量 4 个台车参数对试验结果一致性的灵敏度分析。研究得出台车安全带卷收器拉出量是造成儿童假人头部前移量一致性较差的主要因素。

关键词：汽车安全；台车试验；儿童约束系统；一致性

1 引言

儿童约束系统或称儿童安全座椅（Child Restraint System, CRS），是汽车里用来约束、限位身高体重在一定范围内儿童乘员的所有装置的总称[1]。虽然国家标准 GB27887-2011《机动车儿童乘员用约束系统》规定了关于儿童安全座椅试验以及儿童乘坐最低标准，但是我国目前并未出台有关儿童安全座椅的强制认证规定，而且国内各个试验室对法规中的试验方法的理解有所不同，导致目前存在同一款儿童座椅在不同的检测试验室或者厂家的试验室内进行动态测试时，试验的结果会有一定的差异[2]。解决儿童座椅动态试验中的一致性问题，是评价儿童约束系统是否能够有效保护儿童乘员急需解决的难点。

2 台车试验结果差异

对儿童座椅动态试验结果进行统计分析，发现同一款儿童座椅在不同试验室中进行的动态试验结果有差异，儿童假人头部前移量一致性较差[3]。以国内某款 I 组儿童座椅为例，在国内两大检测机构 A、B 以及厂家自己的试验室 C 进行动态试验，试验结果中头部位移量有很大的差异，结果如表 1 所示。在试验室 A 中进行的试验，使用该儿童座椅的假人头部位移量为 572 mm，已经超过法规规定的 550 mm 的位移限值；而在试验室 B 和 C 进行的试验结果却是截然相反，符合法规的要求。

Table 1 Test results of different laboratories

	头部水平最大位移/ mm
GB27887-2011 要求	< 550
检测机构试验室 A	572
检测机构试验室 B	545
厂家试验室 C	523

比较三个不同试验室中的试验条件，发现不同试验室中台车坐垫刚度、台车安全带刚度、台车卷收器安全带拉出量和台车冲击波形有差异。台车座椅的坐垫刚度会影响儿童座椅的运动姿态，进一步影响假人头部前移量；儿童座椅受到的约束力是通过成人安全带施加到座椅上，安全带刚度会影响儿童座椅的运动姿态，也会进一步影响假人头部前移量；卷收器设计为不同结构会导致在试验中台车安全带的拉出量不同，会影响假人头部前移量；整个动态试验是通过台车试验平台施加到儿童座椅上的，台车冲击波形也是影响儿童假人头部前移量的因素。

因此，本文从仿真中采用全因子试验分析方法研究了台车坐垫刚度、台车安全带刚度、台车加速度波形和台车安全带卷收器拉出量等 4 个因素对试验结果一致性的灵敏度分析。

3 儿童约束系统仿真模型的建立及验证

本文研究的原型座椅是国内某款 I 组通用类安全带前向固定的儿童座椅。在 MADYMO 软件中建立儿童约束系统仿真模型包括台车试验环境（包括试验用座椅、台车安全带等）、儿童假人模型、儿童约束系统模型等[4]。其中，台车座椅采用多刚体模型简化成四个平面，其固定方式、材料特性和外形尺寸按照国家标准要求建立；台车安全带采用多刚体模型建立；儿童假人模型按照该儿童约束系统的使用特点选取了 TNO P3 儿童假人[5]；儿童约束系统模型的结构和几何尺寸由实物测量确定，并建立其有限元模型，机械特性则是通过零部件的物理试验获取。建立的儿童约束系统仿真模型如图 1 所示。

进行仿真分析时，利用 HYGE 台车原理，直接对儿童假人和 CRS 所处的环境施加加速度场，从而不需要模拟台车台架结构也能获得相同的试验效果[6]。仿真模型中加速度脉冲如图 2 所示。

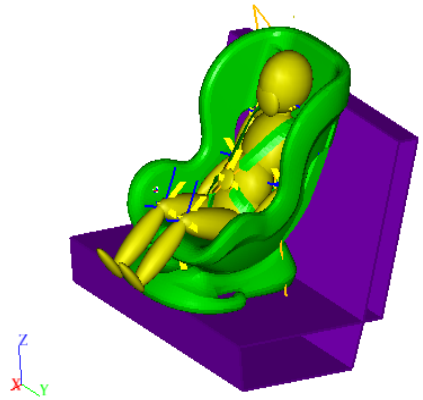

Figure 1. Simulation model of the child restraint system

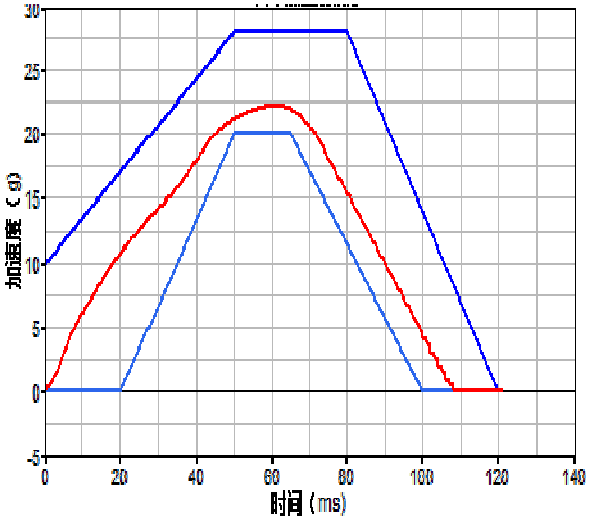

Figure 2. Curve: acceleration waveform of sled test

为了检验所建立模型的可靠性，必须利用台车试验结果进行验证[7]。儿童假人头部合成加速度曲线、胸部合成加速度曲线以及主要儿童假人伤害评价指标是验证仿真模型有效性的几个重点考察对象[8]。从儿童假人头部加速度对比（图 3）以及胸部加速度对比（图 4）可以看出，仿真的儿童假人头部加速度曲线和胸部加速度曲线与真实台车试验中的曲线在曲线趋势、峰值大小及范围、脉宽等方面都比较接近。仿真中的头部前移量和试验结果中的头部前移量分别为 538 mm 和 542 mm，误差为 7.4%，其他假人伤害评价指标对比如表 2 所示，仿真与试验的误差均不超过 15%。 由此可以得出：仿真模型可靠，可用于后续研发等相关工作。

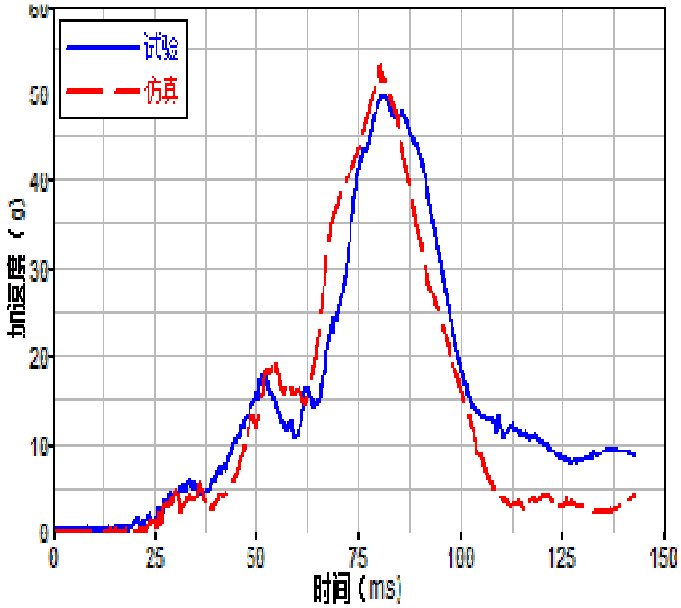

Figure 3. Curve: head acceleration of CAE mode and sled test

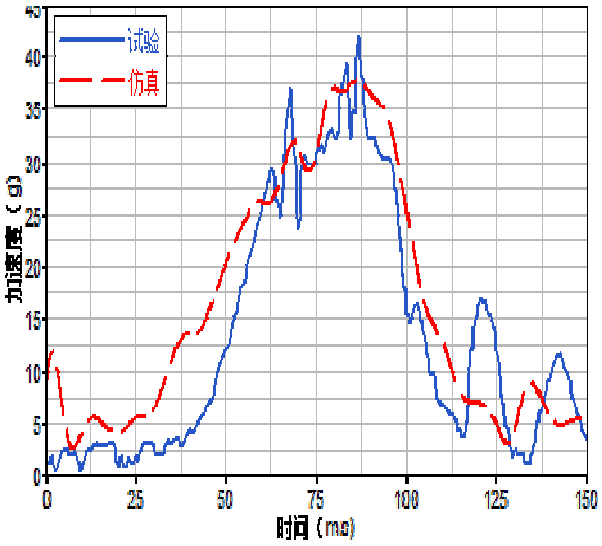

Figure 4. Curve: thorax acceleration of CAE mode and sled test

Table 2. Injury evaluation data of dummy

	试验结果	仿真结果	误差
胸部合成加速度峰值(3ms)（g）	42.09	37.96	-9.8%
胸部加速度（Z 方向）峰值（g）	20.99	19.12	-8.5%
头部水平方向最大位移（mm）	538	542	7.4%
头部垂直方向最大位移（mm）	704	720	2.3%

4 台车试验参数的选择

分析现有的儿童座椅台车试验方法，选择系统的输入参数即设计变量为：台车坐垫刚度、台车安全带刚度、台车加速度波形和台车安全带卷收器拉出量。各设计参数的分析及设置如下所述。

4.1 台车坐垫刚度

标准中对台车座椅的要求是座椅靠背和座椅都覆盖有聚氨酯泡沫，其抗压强度依据 ISO 2439B 为：压缩率为 25%时，抗压力为 125 N；压缩率为 40%时，抗压力为 155 N。并且要求定期对台车试验坐垫进行标定，标定结果与初始坐垫刚度误差在 15%以内为合格。由某检测机构提供的坐垫刚度每月标定结果可知，试验台车坐垫的刚度会随试验次数的增加而呈持续下降趋势。根据坐垫刚度标定结果选择坐垫刚度的取值范围如图 5 所示。

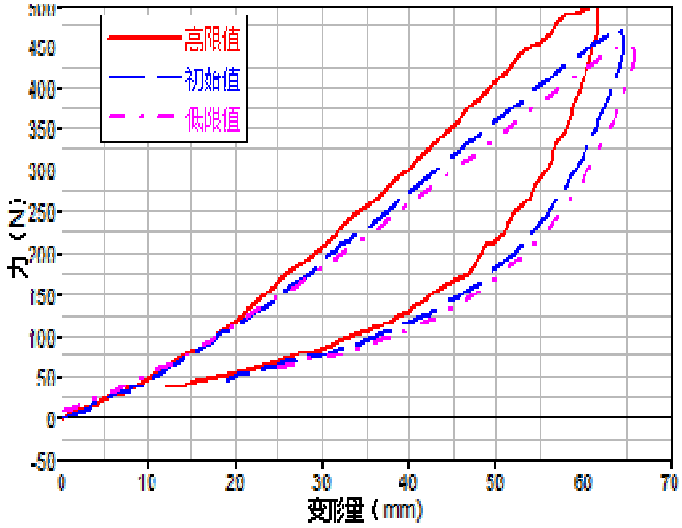

Figure 5. The range of cushion stiffness

4.2 台车安全带刚度

儿童座椅通过台车安全带安装在标准座椅上，受到的冲击惯性力也是通过台车安全带施加到标准座椅上。台车安全带刚度会影响儿童座椅的运动姿态，也会进一步影响假人头部前移量。GB27887—2011 对台车安全带刚度的要求是：安全带在拉力 10 kN 下，其延伸率为 6%~10%。台车安全带刚度取值曲线如图 6 所示。

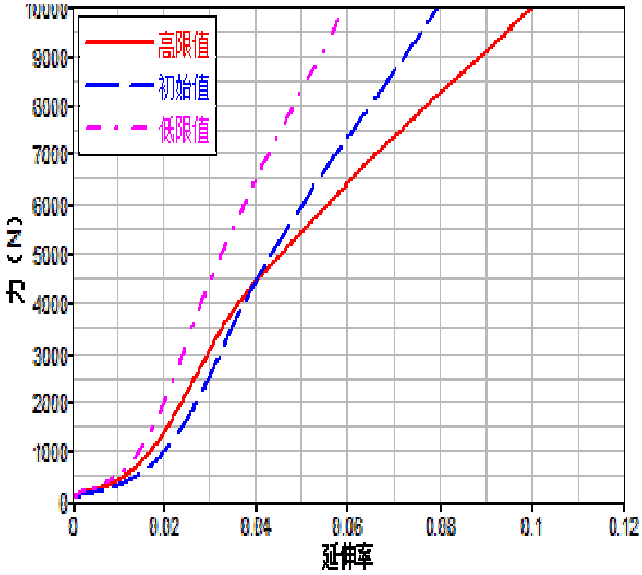

Figure 6. The range of sled belt stiffness

4.3 台车加速度波形

法规对台车加速度只有一个加速度上下限值和碰撞速度 48~50 km/h 的规定，并未规定台车加速装置，不同试验室的台车加速度波形存在一定差异。根据法规对台车波形上下限和碰撞速度的要求，选择的台车加速度波形的取值范围如图 7 所示。

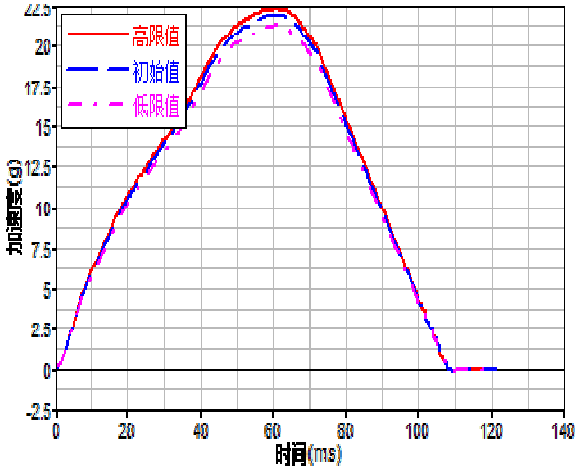

Figure 7. The range of acceleration waveform of sled test

4.4 台车加速度波形

台车安全带最终固定在一个通用卷收器中，卷收器设计为不同结构会导致在试验中台车安全带的拉出量不同。法规中对卷收器的要求是：卷收器和上导向环之间的织带张紧力为 1~7 N，松开 D 环，锁紧卷收器，使织带自由耦合。根据不同结构的台车安全带卷收器，选择台车卷收器拉出量的取值为：低限值为 0 mm、初始值为 0 mm、高限值为 40 mm。

本文研究的重点是儿童约束系统试验结果一致性问题，而试验结果差异性主要体现在儿童假人头部前移量不同。因此，试验设计的响应量为儿童假人头部前移量。正交试验系统参数如表 3 所示。

Table 3. Orthogonal design system parameters

	变量	初始值	参数范围	水平
设计变量	台车坐垫刚度		如图 5 所示	3
	卷收器拉出量	0mm	0mm、20mm、40mm	3
	台车安全带刚度		如图 6 所示	3
	台车加速度波形		如图 7 所示	3
响应量	儿童假人头部前移量			

5 全因子试验设计结果分析

采用全因子试验设计（Full Factorial）方法对台车试验参数灵敏度进行分析。根据上文选定的台车试验的四个设计参数及其变化范围对所选择的 4 个变量，每个变量设置 3 个水平，共进行 81 次仿真计算。

在全因子试验设计数据基础上，利用 Minitab 软件计算出儿童假人头部前移量的方差并得到各设计变量对响应量的贡献率和头部前移量主响应。台车加速度波形、卷收器拉出量和台车安全带刚度存在主响应，而台车坐垫刚度不存在主响应。同时，卷收器拉出量线陡峭，卷收器拉出量主响应量值最大，表明台车安全带卷收器拉出量对系统响应值影响最大。各设计变量对响应量的贡献率如图 8 所示，头部前移量主响应如图 9 所示。

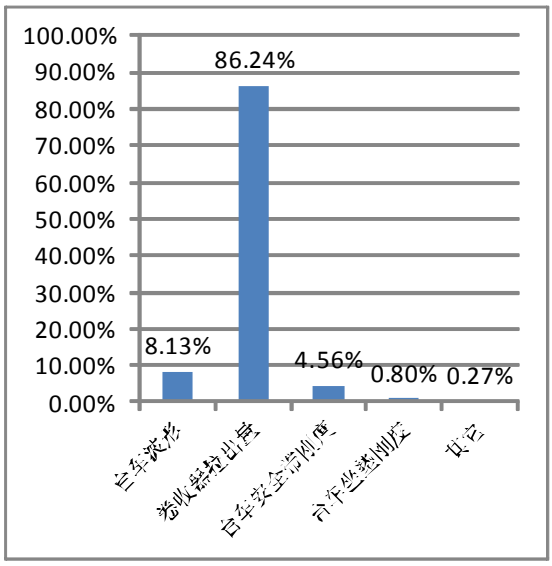

Figure 8. Contribution rate of design variables

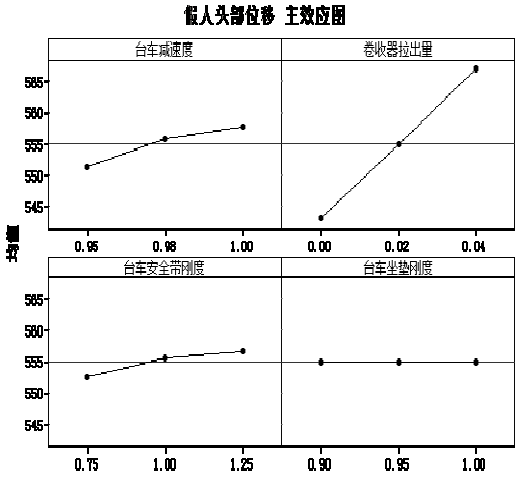

Figure9. Primary response plot of head forward distance

从设计变量的主效应图和对儿童假人头部前移量的贡献率图来看，可以得到的结论是卷收器拉出量对假人头部前移量影响最大，其次是台车加速度波形，第三是安全带刚度，坐垫刚度对假人头部前移量几乎无影响。

6 台车安全带卷收器拉出量影响分析

通过全因子试验设计方法对台车试验四个参数进行分析研究得出台车安全带卷收器拉出量对试验结果一致性影响最大。从理论分析来看，碰撞过程中随着台车上固定儿童座椅的安全带卷收器拉出量的增加，儿童座椅在惯性作用下向前运动的距离增加，而假人随着儿童座椅向前运动增加，使得头部前向位移量也随着增加。以卷收器拉出量0 mm为基础，当卷收器拉出量为20 mm和40 mm时，假人头部位移量分别增加了21 mm和35 mm。因此，碰撞过程中台车安全带卷收器拉出量的不同，会导致试验后儿童假人前移量的不同，试验结果一致性较差。

7 结论

目前国内各个实验室对国标 GB27887-2011《机动车儿童乘员用约束系统》中试验方法的理解有所不同，导致在不同的检测认证试验室或者厂家的试验室内进行试验的结果会有一定的差异，特别是在儿童座椅的动态试验中的一致性问题更加明显。本文建立 I 组通用类前向安全带固定的儿童座椅仿真模型，对影响儿童假人头部前移量的因素：台车加速度波形、台车安全带卷收器拉出量、台车坐垫刚度和台车安全带刚度等参数进行了参数灵敏度分析。分析得出，台车安全带卷收器拉出量对儿童假人头部前移量影响最大，是造成儿童假人头部前移量一致性较差的主要因素。国标 GB27887-2011 中的动态试验方法并未对卷收器的结构进行详细规定，故在我国下一步强制认证儿童约束系统时，在动态试验方法上需要对卷收器的结构进行详细规定，统一台车安全带拉出量，可以更好的确保儿童座椅动态试验的一致性。

参考文献 (References)

[1] GE Ruhai, MIAO Qiang. The summarize of child restraint system [J]. ***Chin Safety Sci J***, 2006, **16**(4): 42-47.

[2] ZHU Hang. Research on child occupant injury classification and preventive measure [D]. Shanghai: *Tongji University,* 2013.

[3] YU Yingcheng. Research on safety evaluation method of child occupant in passenger car [D]. Shanghai: *Tongji University*, 2013.

[4] Kendall R G, Sherwood C P, Crandall J R. A computational study of rear-facing and forward-facing child restraints [R]. **SAE** (Society of Automotive Engineers). 2008-01-1233.

[5] TNO MADYMO. Model Manual.Release7.4. The Netherlands:December 2013.

[6] HU Jia. Research on child occupant safety in frontal and side impact based on test and FE simulations [D].Changsha: *Hunan University,* 2008.

[7] YANG Xingmei, ZHANG Chaochen, YANG Jikuang. Parameter analysis and design optimization of child restraint system in vehicle frontal impacts [C]// *The 6th Int'l Forum of Automotive Traffic Safety* (INFATS), 2008-12.

[8] National Highway Traffic Safety Administration. Standardized child passenger safety training program participant manual [S]. Washington, DC: National Highway Traffic Safety Administration, 2000.

Proceedings of the 11th International Forum of Automotive Traffic Safety, 2014, pp 228-237
No. ATS.2014.303

Optimized Design of the Airbag Parameters for OOP Children Based on LS-OPT

Fei Jing[1] , Bai Zhonghao[2], Chen Keming[1]
[1] *China Automative Engineering Research Institute Co., Ltd., Chongqing , China,401122*
[2] *State Key Laboratory Of Advanced Design And Manufacturing For Vehicle Body, Hunan University, Changsha, ,410082*
Email: fj1234ff@163.com,baizhonghao@hnu.edu.cn,chenkeming@caeri.com.cn

Abstract: According to SAEJ1980-2008 regulation, The Multi-body and FE model is established for two OOP children aged 3 years old and 6 years old. The combined injury probability Pcomb is considered as the object function in reference to the US-NCAP regulation. The Response Surface Methodology is constructed with sampling points generated by Space Filling and dynamic Basis Function networks. The optimization tool is LS-OPT together with the explicit code of MADYMO. The hybrid adaptive simulated annealing algorithm including Genetic Algorithm and adaptive simulated annealing is used for metamodel optimization to minimum Pcomb. Meanwhile, dummy injury values of dual-stage inflator and single-stage inflator are compared in 25km/h and 54km/h frontal crash. The result indicates that the optimal object value meets the regulation requirement basically, protection effect of dual-stage inflator is better significantly than single-stage inflator.

Keywords: OOP children; airbag parameters;Pcomb; LS-OPT optimization

基于 LS-OPT 离位儿童乘员安全气囊参数优化

费敬 [1]，白中浩 [2]，陈可明 [1]
[1] 中国汽车工程研究院股份有限公司，重庆，中国，401122；
[2] 湖南大学汽车车身先进设计制造国家重点实验室，长沙，中国，410082
Email: fj1234ff@163.com,baizhonghao@hnu.edu.cn,chenkeming@caeri.com.cn

摘　要：根据 SAE J1980-2008 法规，建立了典型的 3 岁和 6 岁离位儿童乘员多刚体－有限元仿真模型。以乘员综合损伤评价指标 Pcomb 为目标函数，安全气囊参数为设计变量，采用 LS-OPT 集成 MADYMO 对选取的变量进行优化，选用空间填充试验设计采取样本点，以动态径向基函数（RBF）神经网络建立响应面模型，采用混合自适应模拟退火算法对响应面模型进行优化使 Pcomb 最小。此外，对比了双级和单级气体发生器气囊在低速和高速对假人损伤的影响。结果表明：对于 3 岁离位儿童，位置一和位置二气囊参数优化后的 Pcomb 值分别为 0.083 和 0.101；对于 6 岁离位儿童，位置一和位置二气囊参数优化后的 Pcomb 值分别为 0.063 和 0.076，基本满足 US-NCAP 法规的要求；同时双级气囊在高速时对假人的保护作用明显优于单级气囊。

关键词：离位儿童；安全气囊参数；Pcomb； LS-OPT 优化

1 引言

在各种道路使用者中，儿童是最脆弱的群体。据世界预防儿童伤害报告显示：2004 年 0-19 岁的儿童，道路交通伤占了大约有 262000 个，大约是所有伤亡儿童的 30%；同时，交通伤是 15-19 岁致死的最主要的原因[1]。根据美国的统计资料：2004 年，在美国共有 1859 个 15 岁以下的儿童在车辆碰撞事故中死亡，235912 个受伤，其中 52%的 5-9 岁和 63%10-15 岁死亡的孩子没有使用任何约束装置 [2]。因此，儿童安全问题已成为世界汽车交

通安全领域应优先考虑的问题。目前国内只有少许相关的研究机构或重点大学的学术团队对儿童乘员安全性法规、儿童约束系统的建模仿真及台车试验等进行初步的研究，研究成果相对较少。而现有的安全气囊通常是针对于正常体位的成年人设计的，对离位儿童的研究较少，本文从安全气囊的角度对离位儿童乘员进行研究，采用 LS-OPT 和 MADYMO 结合的方法对安全气囊的参数进行了优化。

2 正面碰撞仿真模型的建立

2.1 气囊有限元模型的建立

为了更好地模拟气囊与假人以及车体的接触，本气囊建立的是有限元模型，采用的是线性三节点三角形膜单元（ELEMENT.TRIADS）来模拟，共包含 14964 个单元和 7502 个节点。建立好的气囊模型的物理参数如表 1 所示。

Table 1. Physical parameters of the airbag
表 1. 安全气囊物理参数

织物密度 /(kg/m^3)	杨氏模量 /Mpa	泊松比	泄气孔直径/mm	厚度 /mm
620	200	0.3	45	0.25

在这里，气囊采用的是三根拉带平行布置的形式，其结构简单，不需要任何传感器，头部位置的两根拉带通过控制与头部接触的气袋的圆弧面的曲率从而改变头部与气袋的接触面积，进而控制乘员头部的接触力，从而有效降低头部加速度值进而减小对乘员头部的伤害；对胸部的保护与头部的保护是一个道理。气囊结构示意图如图 1 所示。

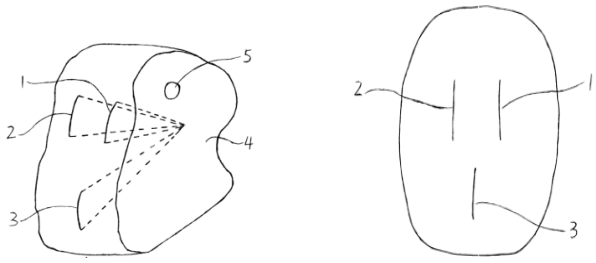

1-A 固定线　2-B 固定线　3-C 固定线　4-气袋　5-泄气孔

Figure 1. Curve:Schematic diagram of three parallel strap airbag
图 1. 三根拉带平行布置的气囊结构示意图

对气囊的折叠没有实际的气囊折叠方式的参考，参考了美国通用汽车公司研究与开发中心关于气囊折叠的方法。如图 2 所示，该方法在建立乘员侧安全气囊模型方面，较为简便、快捷。通过通用汽车公司研究与开发中心关于约束系统的相关优化研究，表明该折叠方法确实有效可行。具体的折叠方法是将气囊的参考模型导入到折叠软件 Primer 中，在参考模型的基础上，沿三维方向进行气囊单元和节点的比例缩放到合适的尺寸和状态。然后在折叠好的气囊模块下布以壳单元建立气囊的外壳模型，以便于模型的安装和角度的调整。

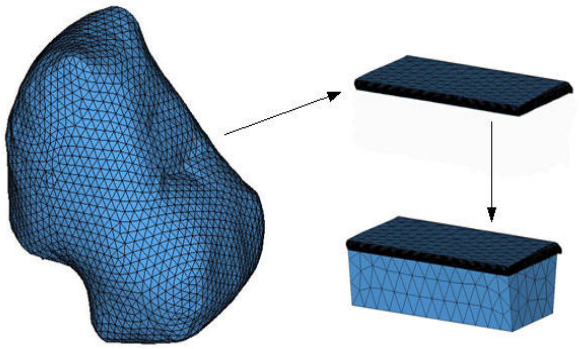

Figure 2. Curve:airbag fold process
图 2. 气囊的折叠过程

MADYMO 软件通过穿透量，定义的加载、卸载曲线以及迟滞模型来计算产生的非线性弹性力、粘滞阻尼及摩擦力。根据碰撞中可能发生的接触，模型中通过关键字 CONTACT.MB_FE 和 CONTACT.FE_FE 定义假人与车体及安全气囊的接触如表 2 所示。

Table 2. Contact between dummy and car and airbag
表 2. 假人与车体及安全气囊接触定义

接触对数	主面	从面
1	仪表板	头部、颈部、胸部
2	挡风玻璃	头部
3	膝部挡板	下肢
4	座垫	臀部、上肢、大腿
5	座椅靠背	肩部、背部、头部
6	假人	气囊

2.2 人-车仿真模型的建立与验证

SAEJ1980-2008 法规规定了儿童假人七个离位位置状态。本文选取了常见的两个离位位置进行了研究。位置一为假人坐在座椅的前边缘或站在地板上，下巴靠近仪表板的上表面，背部垂直于地板；位置二为假人的头部靠近仪表板的中部[3]。

利用 MADYMO 软件建立了 3 岁和 6 岁离位儿童乘员模型。如图 3 和图 4 所示。

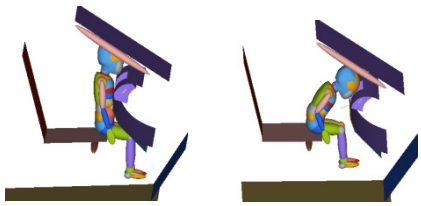

离位位置一　　离位位置二

Figure 3. Curve: OOP simulation models of 3 years old children
图 3. 3 岁离位儿童乘员模型

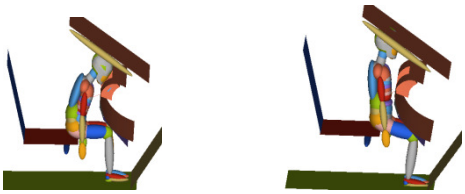

Figure 4. Curve: OOP simulation models of 3 years old children

图 4. 6 岁离位儿童乘员模型

对建立好的仿真模型需要进行试验以验证气囊展开效果的有效性。根据 SAEJ1980-2008 法规，对于离位儿童乘员可以进行两种试验，一种是气囊的静态起爆试验，另一种是以以初速度 25km/h，最大加速度 6.7G 进行动态试验。气囊模块的静态起爆试验主要用来进行气袋模块性能的考察并对仿真模型进行验证，从而为下一步的优化设计做准备。文献 4 和 5 对建立的模型进行了试验验证[4,5]。

3 目标函数和优化方法的确定

3.1 目标函数和设计变量的选取

通常我们所做的研究是以 HIC_{36}(或 HIC_{15})、胸部 3ms 准则、胸部压缩量、颈部 Nij 来衡量假人损伤的。但是这些损伤评价标准是以一定的容限水平来评价乘员约束系统设计的。为评价约束系统的整体性能，应该有一个包括单个伤害参数的完全伤害准则。基于这种考虑，我们参考了 US-NCAP 中关于 5 百分位女性假人的综合损伤指标 *Pcomb* 作为前碰撞中离位儿童乘员损伤的目标函数[6]，*Pcomb* 可综合反映头部、颈部、胸部的损伤。选取混合模拟退火算法进行优化，使 Pcomb 尽可能达到 US-NCAP 要求的五星级[7]，使 HIC_{15}、胸部压缩量、颈部 Nij 满足法规规定的范围，从而有效地保护离位儿童乘员。

目标函数 $Function = \min(Pcomb)$ （1）

$$Pcomb = 1-(1-P_{head})(1-P_{neck})(1-P_{chest}) \quad (2)$$

$$P_{head} = \Phi\left(\frac{\ln(HIC_{15}-7.45231)}{0.73998}\right) \quad (3)$$

$$P_{chest} = \frac{1}{1+e^{10.5456-1.7212*(ChestDefl)^{0.4612}}} \quad (4)$$

$$P_{neck} = \max imun(P_{neck_Nij}, P_{neck_Tens}, P_{neck_Comp}) \quad (5)$$

$$P_{neck_Nij} = \frac{1}{1+e^{3.2269-1.9688Nij}} \quad (6)$$

$$P_{neck_Tens} = \frac{1}{1+e^{10.958-3.770Neck_Tension}} \quad (7)$$

$$P_{neck_Comp} = \frac{1}{1+e^{10.958-3.770Neck_Compression}} \quad (8)$$

其中：P_{head} 为头部损伤评价分量，P_{chest} 为胸部损伤评价分量，P_{neck} 为颈部损伤评价分量。选取泄气孔面积缩放因子 *Vent_05Ffor*、不同气体发生器质量流率曲线 *InflatorDelay_05Ffor*、质量流率缩放系数 *InflatorScale*、气囊起爆时间 *VentOpenT_05Ffor*、气囊在仪表板上的安装角度 *RotationY*，以及拉带的长度 *Strap1_05Ffor* 作为约束变量；并初步确定变量的范围如下：

$$0.1 \leqslant Vent_05Ffor(A) \leqslant 3.6$$

$$0.18 \leqslant Strap1_05Ffor(B) \leqslant 1.38$$

$$1 \leqslant InflatorDelay_05Ffor(C) \leqslant 8$$

$$0.5 \leqslant InflatorScale(D) \leqslant 1.5$$

$$-1.05 \leqslant RotationY(E) \leqslant 1.05$$

$$0.005 \leqslant VentOpenT_05Ffor(F) \leqslant 0.03$$

3.2 优化方法的确定

本研究采用 LS-OPT 优化分析软件集成 MADYMO 对所确定的气囊参数进行优化分析。通过选取空间填充试验设计（Space Filling）作为样本点选取方法，在优化过程中不断更新采样空间，采用动态径向基函数(RBF)神经网络建立响应面模型，并通过混合自适应模拟退火算法对建立的响应面进行优化获得原优化问题的最优解[8]。在每一次迭代过程中采样空间被不断更新，响应面模型也不断更新以提高响应面模型的精度。本文优化循环的次数选为 15，每次循环计算 11 组，循环的次数选的越多计算的越精确，由于计算时间的原因选取了 15 次循环。

LS-OPT 是 LSTC 公司开发的优化工具软件，可以和所有的仿真软件连接，LS-OPT 为用户提供了结构化设计流程，可以根据特定的约束条件和目标参数进行设计和优化计算，也非常适用于解决系统识别问题和统计分析，可以用来解决复杂的非线性优化问题，用户可以在图形用户界面（GUI）中方便地设计优化输入参数，监控并控制仿真过程，还可以对优化数据作后处理分析，软件界面如图 5 所示。在用此界面操作之前，需要编写一个 LS-OPT 命令文件（Com.MadymoOpt）调用 MADYMO 里的.XML 文件，在此命令文件里包括你选用的优化方法、设计变量以及设计变量的范围、约束条件、响应以及响应表达式、目标函数以及目标函数表达式等。

本文所研究的目标函数和输入变量之间存在一个高度的非线性关系，很难用传统的数理方法建立数学模型。而径向基函数（RBF）神经网络具有较高的非线性映射能力，通过 RBF 网络的学习可以建立起两者之间的非线性关系。径向基函数神经网络作为一种性能良好的前馈式神经网络，是基于人脑的神经元细胞对外界的局部性而提出的。如图 6 所示，包括输入层、隐含层和输出层，隐含层的输出函数被定义为径向基函数，LS-OPT 提供两种径向基函数，分别为高斯函数（Gaussian）和多二次函数（Multi-Quadrics），默认的为多二次函数。径向基函数神经网络的优点是避免数据的分析和建模工作，能够从观测样本中发现隐含的复杂结构；具有较高的运算速度，能以任意精度全局逼近一个非线性函数。缺点是不能求出显示表达式。两种径向基函数的表达式如公式（9）和公式（10）所示。

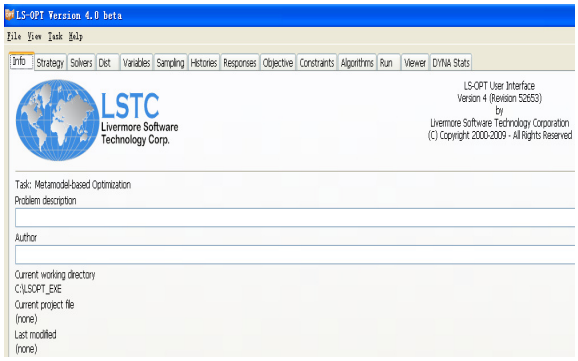

Figure 5. Curve: operator interface of LS-OPT

图 5. LS-OPT 操作界面

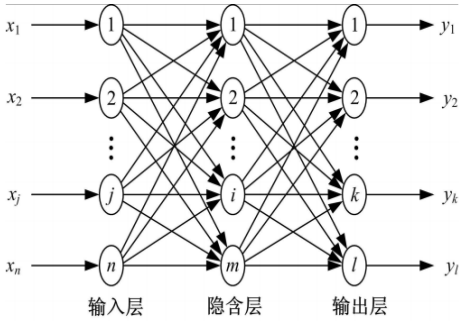

Figure 6. Curve: RBF neural network model

图 6. 径向基函数神经网络模型

$$Ri(x)=\sqrt{1+\left[\left\|X-Ci\right\|^2/\sigma_i^2\right]} \qquad i=1,2,\ldots,N_r \tag{9}$$

$$Ri(x)=\exp\left[-\left\|X-C_i\right\|^2/(2\sigma_i^2)\right] \tag{10}$$

式中，*Ri(x)*为隐层第 i 个单元的输入；*X* 为 *N* 维输入矢量，*X={Xp | Xp∈R*$_N$，*P*=1，2，…，*k*}；C_i为隐层第 *i* 个单元高斯函数的中心点，σ_i 为第 *i* 个隐节点的归一化参数，即该隐节点的宽度；*Nr* 为隐层的节点数；*P* 表示样本数。

模型中有未知的非线性关系，且这种关系没有一个可说服的参数回归模型来表示，并且约束不确定。在这种情况下，好的实验设计是让样本点均匀地分布在设计空间内，空间填充设计（Space Filling）没有给近似模型一个强加的假设，且允许单个变量有多个水平。因此，本研究选取空间填充设计选取样本点。

自适应模拟退火算法 ASA(Adaptive Simulated Annealing)是一种新的统计优化方法，其思想最早是由 N Metropolis 等人借鉴统计力学中物质退火方法而提出的。该算法的主要特性之一就是能以一定的概率接受目标函数值不太好的状态，即算法不但往好的方向走也可朝差的方向走。这使得算法即便落入局部最优的陷阱中，经过足够长的时间后也可跳出来从而收敛到全局最优解，是一种强大的随机搜索算法，能处理任意程度的非线性，不连续和随机的问题，具有对初始点的不依赖性，可以任意的选取出随机序列，可有效地避免陷入局部极小并最终趋于全局最优的串行结构的优化算法。但是趋于全局最优解的算法的时间要足够长。约束跳步优化算法 LFOPC(Leap-frog Optimizer for Constrained problems)将罚函数引入了无约束优化跳步算法，避免了后者求解效率对初始值的依赖性，能够快速准确的求解约束优化问题，较传统的共轭梯度算法有更快的收敛速度，且对梯度误差不敏感，具有较好的鲁棒性，但是是一种局部优化算法。混合自适应模拟退火算法将 ASA 和 LFOPC 有效地结合起来，使目标函数值收敛到全局最佳，这种算法被认为是一种有效和高效的全局优化算法[9-10]。因此本文采取此优化算法进行气囊参数优化研究。

4 基于 LS-OPT 的气囊参数优化

优化分析结果如图 7 及表 3 所示。根据 US-NCAP 要求，达到五星级级要求的 Pcomb<0.1，对应的 HIC_{15}≤250，chest deflation≤19mm，Nij≤0.3 [11]。由表 3 可直观地看到：对于 3 岁离位位置的儿童，位置一的目标函数值达到了五星级要求，位置二的目标函数值没有达到五星级标准，颈部损伤较严重。这可能是因为位置二的头部和胸部太靠近仪表板，气囊没有展开到最大就与假人接触，气囊没有起到一定的保护作用。对于 6 岁离位位置的儿童，位置一和位置二的目标函数值都达到了五星级要求。3 岁和 6 岁离位儿童的最优仿真结果如图 8-11 所示。

4.1 双级和单级气体发生器气囊对假人损伤影响对比

安全气囊展开时的速度和冲击力是很大的，由于儿童的骨骼比较脆弱且通常处于离位的状态，安全气囊一旦展开对儿童的伤害是很大的。研究表明：双级气囊模块对儿童的伤害相对于相同能量的单级气囊模块降低较明显，主要是因为把能量分为两个阶段，从而减小了对儿童的一次攻击性。双级气体发生器第一级和第二级气体发生量之比为60:40，两级起爆延迟时间为20ms。以3岁离位儿童位置一为研究对象，分别对比正面低速25km/h碰撞和正面高速54km/h碰撞双级气体发生器气囊和单级气体发生器气囊对儿童损伤的影响。25km/h和56km/h碰撞脉冲特性曲线如图12和图13所示，两速度下双级和单级气体发生器对假人损伤影响对假人损伤影响对比如图14和图15所示。需要说明的是，54km/h正面碰撞中头部损伤值很大，远大于胸部和颈部的损伤值，综合考虑将头部损伤值缩小100倍即图14和15中显示的数值。由图14和图15可知，正面低速25km/h碰撞，双级和单级气体发生器对假人损伤影响差不多；但是正面高速54km/h碰撞，双级气体发生器气囊对假人的保护作用明显高于单级气体发生器气囊，对头部和颈部的保护作用尤为明显，但是对假人的损伤依旧很大，主要是因为儿童处于离位状态，距离气囊较近，气囊的冲击力过大导致对儿童的损伤较大。

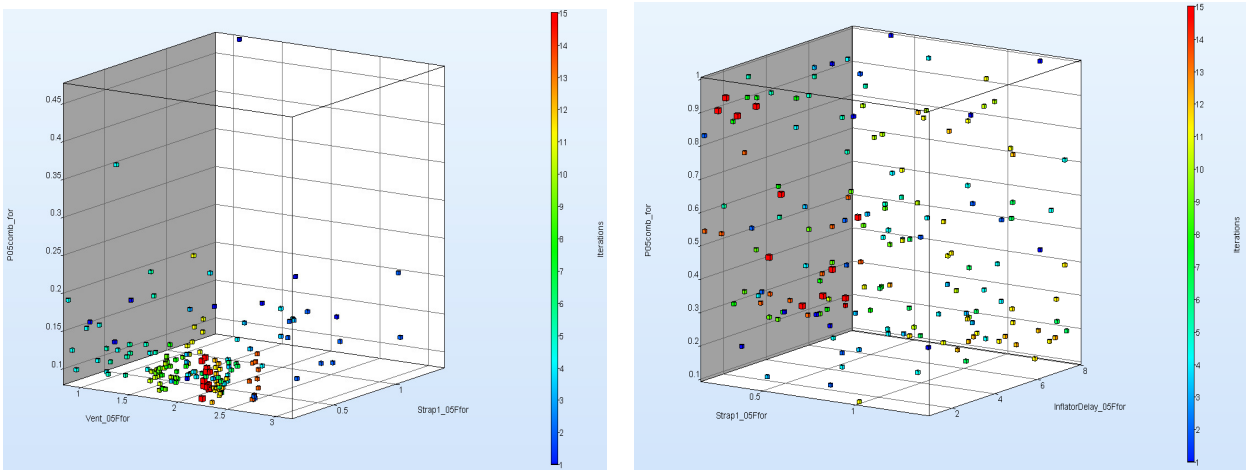

a）3岁离位位置一　　b）3岁离位位置二

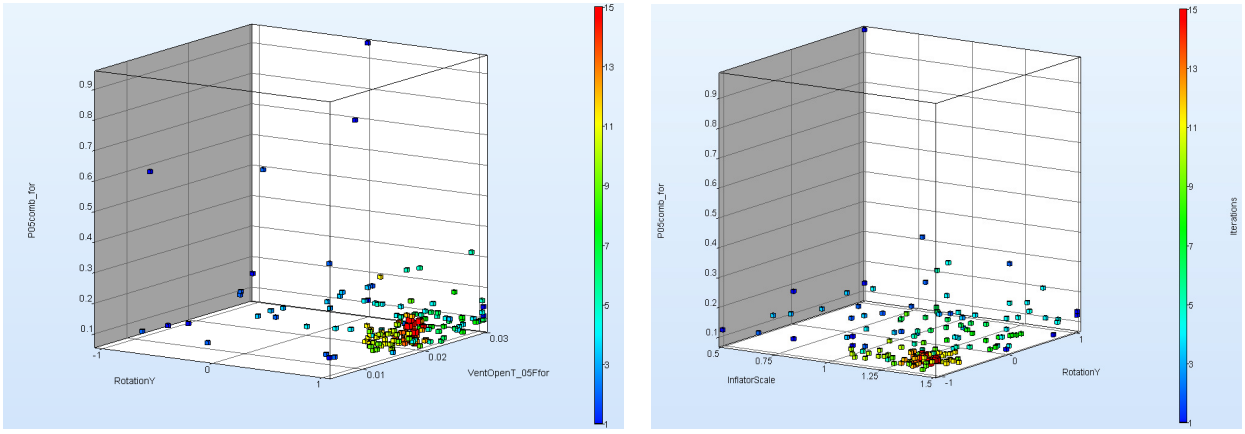

c）6岁离位位置一　　d）6岁离位位置二

Figure 7. Curve: distribution of sample points
图 7. 样本点分布图

Table 3. Summary of injury results for OOP children

表 3. 离位儿童损伤结果汇总

位置	变量						损伤值			综合损伤值
	A	B	C	D	E	F	HIC_{15}	D_{chest}	N_{ij}	Pcomb
OOP1(3 year)	0.09	2.31	7	1.13	-1.00	0.01	17.64	17.3	0.3	0.083
OOP2(3 year)	0.17	1.01	1	0.78	-0.05	0.006	8.02	3.14	0.5	0.101
OOP1(6 year)	1.96	1.11	6	1.48	1.03	0.024	10.97	12.30	0.21	0.063
OOP2(6 year)	1.49	0.61	4	1.41	0.16	0.025	29.73	13.3	0.31	0.076

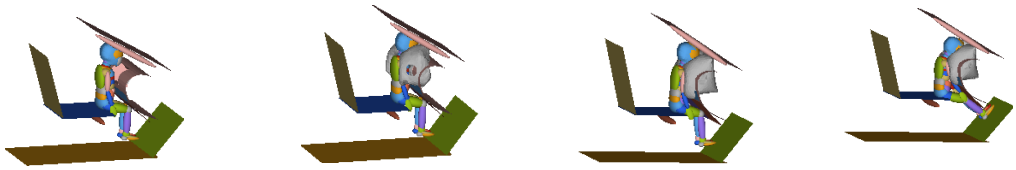

Figure 8. Curve: Optimal animation results of OOP 1 for 3 years old children

图 8. 3 岁离位儿童位置一仿真优化结果

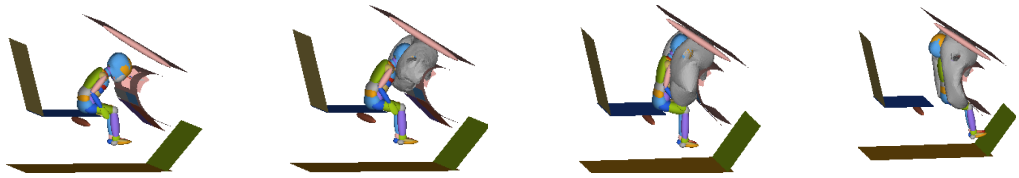

Figure 9. Curve: Optimal animation results of OOP 2 for 3 years old children

图 9. 3 岁离位儿童位置二仿真优化结果

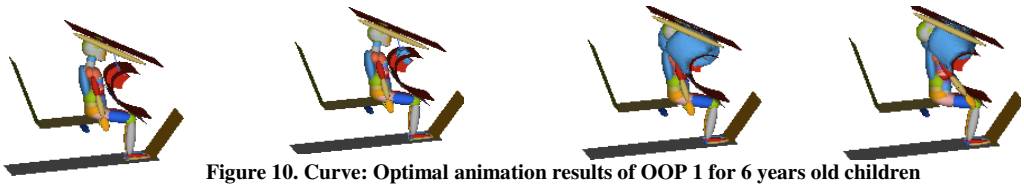

Figure 10. Curve: Optimal animation results of OOP 1 for 6 years old children

图 10. 6 岁离位儿童位置一仿真优化结果

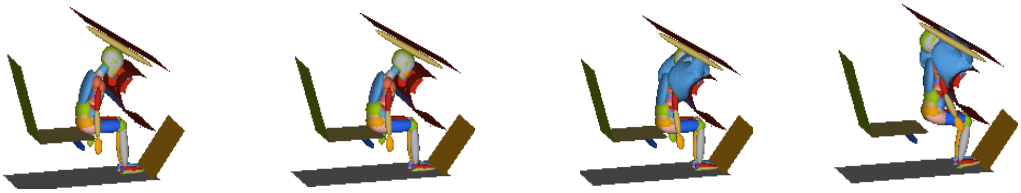

Figure 11. Curve: Optimal animation results of OOP 2for 6 years old children

图 11. 6 岁离位儿童位置二仿真优化结果

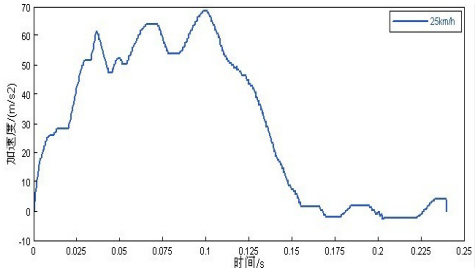

Figure 12. Curve: Crash pulse curve of 25km/h
图 12. 25km/h 碰撞脉冲特性曲线

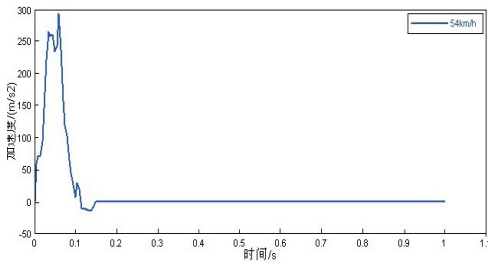

Figure 13. Curve: Crash pulse curve of 54km/h
图 13. 54km/h 碰撞脉冲特性曲线

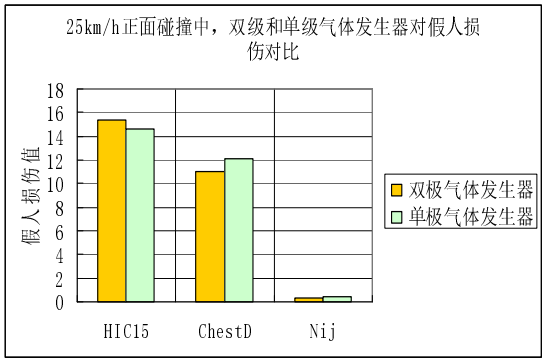

Figure14. Injuries of two inflators in 25km/h frontal crash
图14. 正面25km/h双级和单级气体发生器对假人损伤

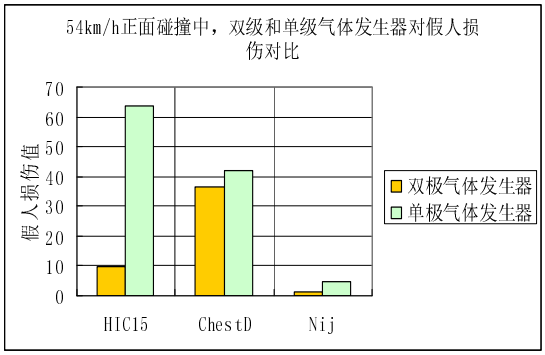

Figure15. Injuries of two inflators in54km/h frontal crash
图15. 正面54km/h双级和单级气体发生器对假人损伤

5 结论

本文参照SAEJ1980-2008法规和US-NCAP法规，对3岁和6岁儿童乘员进行了气囊参数优化，优化的结果基本上达到了法规的要求，为以后离位儿童乘员的研究做了基础性的工作。但在实际的车辆碰撞中，碰撞的程度远大于SAEJ1980-2008法规规定的值，儿童受伤害程度更大。这就需要花费更多的时间和经历来研究离位儿童的损伤，早日探索出一个如Pcomb 的综合损伤准则来评价离位儿童的伤害。同时，验证并优化此气囊对成年人及儿童共同的保护也是今后研究的重点。

参考文献 (References)

[1] Kate McMahon， Gururaj Gopalakrishna， Mark Stevenson。Word report on child injury prevention:31-51

[2] National Highway Traffic Safety Administration. 2004 Motor Vehicle Occupant Protection Facts:Children and Young Adults.[R]. DOT HS 810 654，2006

[3] SAEJ1980-2008，Guidelines for Evaluating Out-of-Position Vehicle Occupant Interaction with Deploying Frontal Airbags[S]

[4] 基于 6 岁儿童离位乘员安全气囊参数优化研究. 第十四届汽车安全技术学术会议，北京，中国，8,2011，p170-174.

[5] Zhonghao Bai，Jing Fei，Weijie Ma.Optimization of the OOP Children Restraint System，Applied Mechanics and Materials Vols.155-156 (2012).pp386-390

[6] DEPARTMENT OF TRANSPORTATION National Highway Traffic Safety Administration [Docket No. NHTSA-2006-26555]: Consumer Information - New Car Assessment Program. 2008

[7] Stander, N., Roux, W.J., Goel, T., Eggleston, T. and Craig, K.-J. LS-OPT User's Manual, Version 3.3,Livermore Software Technology Corporation, Livermore, CA, 2008.

[8] JIN R, CHEN W, SIMPSON T W. Comparative studies of metamodeling techniques under multiple modeling criteria[J].Struct Multidisc Optim,2001,23:1-13

[9] Tushar Goel,Nielen Stander, Adaptive Simulated Annealing for Global Optimization in LS-OPT. 7th European LS-DYNA Conference, Austria ，2009

[10] Nielen Stander, Tushar Goel, Willem Roux,New developments in LS-DYNA. LS-DYNA Anwenderforum, Bamberg 2008.

[11] Steffen Sohr, Axel Heym. Benefit of Adaptive Occupant Restraint System with Focus on the New US-NCAP Rating Requirements, The 21st International Technical Conference on the Enhanced Safety of Conference (ESV), International Congress Center Stuttgart，Germany June15-18，2009

Proceedings of the 11th International Forum of Automotive Traffic Safety, 2014, pp 238-250
No. ATS.2014.304

Optimization Research on Restraint System Development for Female Driver

Authors: Li Hongyun[1], Lu Shuang[1], Han Feifei[1], Li Guo[1], Cao Huan[1,2]
[1]*Cnina Automotive Technology & Research Center, Tianjin, China, 300300*
[2] *School of Mechanical Engineering , HeBei University of Technology, Tianjin, China，300130*
E-mail：lihongyun@catarc.ac.cn

Abstract: At present, the female driver gradually increased, but the development of restraint systems is mainly aimed at the male drivers, how to protect women drivers become a serious problem. In this paper, based on the existing driver restraint system configuration, combined with the simulation analysis method to calculate the effect of the restraint system to protect the female drivers, by contrastive analysis, it can identify the lack of current driver restraint system configuration and optimize, so that it can simultaneously satisfy the requirements of injury for male drivers and female drivers(E-NCAP version 2015), to improve compatibility with the driver restraint system.

Key words: Female Driver; Restraint System; Driver airbag;Optimization

女性驾驶员约束系统匹配与优化分析

李红运[1]，鲁爽[1]，韩菲菲[1]，曹欢[1,2]
[1]*中国汽车技术研究中心，天津，中国，300300*
[2]*河北工业大学机械工程学院，天津，中国, 300130*
E-mail：lihongyun@catarc.ac.cn

摘要:目前，女性驾驶员逐渐增多,但约束系统的开发多以男性驾驶员为基础，如何更好的保护女性驾驶员成为亟待解决的问题。本文根据现有的驾驶员约束系统配置，结合仿真分析手段，计算该约束系统对女性驾驶员的保护效果，通过对比分析，找出目前驾驶员约束系统配置的不足并进行改进优化，使其能够同时满足男性驾驶员和女性驾驶员的伤害值要求（2015版E-NCAP），提高驾驶员约束系统的兼容性。

关键词：女性驾驶员；约束系统；驾驶员气囊；优化分析

1 引言

随着我国经济的快速发展,女性驾驶员群体增长十分迅速。据不完全统计,目前全国女性驾驶员数量已超过1000 万。而目前车辆上匹配的乘员约束系统大多是以男性驾驶员为基础设计的，对身材矮小的女性驾驶员考虑较少，在一定程度上限制了驾驶员约束系统的性能。在美国，其碰撞法规 FMVSS208（2014）中都有驾驶员是女性的碰撞工况。欧洲 E-NCAP 将在 2015 年新增 50 公里正面碰撞工况，并且乘员（包括驾驶员、前排乘员和后排乘员）全部使用女性假人[1]。由此可见，碰撞工况中增加女性驾驶员是较为明显的国际趋势，国内相关法规和 C-NCAP 也将向此发展。因此，研究女性驾驶员约束系统的匹配和兼容性，具有较大的现实和法规意义。

本文根据现有的驾驶员约束系统配置，结合仿真分析手段，计算该约束系统对女性驾驶员的保护效果，通过与男性驾驶员保护效果对比分析，找出不足并进行改进优化，使其同时满足男性驾驶员和女性驾驶员的伤害值要求，提高驾驶员约束系统的匹配与兼容性。

2 男性驾驶员约束系统模型仿真分析

本文根据某车型的CAD数据和约束系统参数，建立该车型50公里正面碰撞驾驶员侧约束系统仿真模型，并以该车型在50km/h正面100%重叠刚性壁障碰撞试验获得的数据为基础，进行对标，保证模型的精度和准确度。

2.1 男性驾驶员仿真模型的建立

仿真模型包括座椅、地板、踏板、仪表板、安全带、方向盘、转向管柱、安全气囊等，在模型中放置Hybrid III第50百分位男性假人，并调整假人坐姿与试验状态相同，如图1所示。

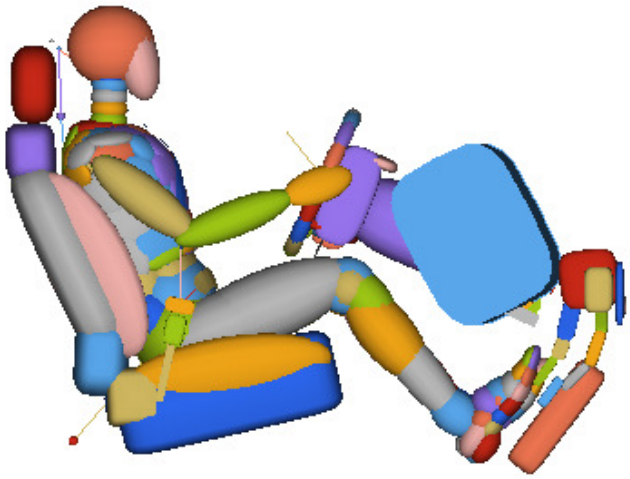

Figure 1. Model: male driver

图1. 男性驾驶员仿真模型

2.2 男性驾驶员仿真模型的对标

为保证仿真模型的准确度，需要将仿真结果与试验数据进行对标，关键伤害曲线对比结果如图2-图5所示。

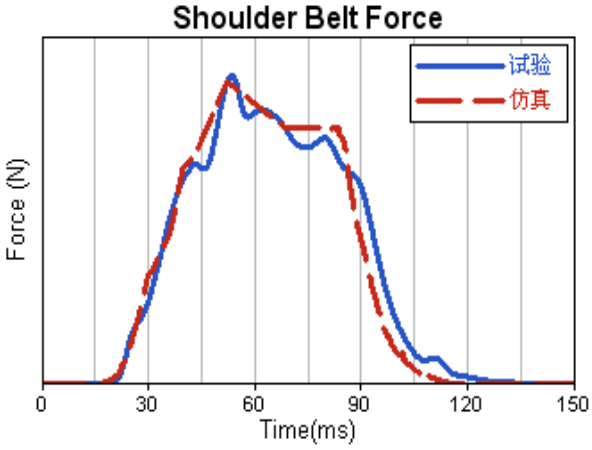

Figure 2. Contrast: shoulder belt force

图2. 肩带力对标结果

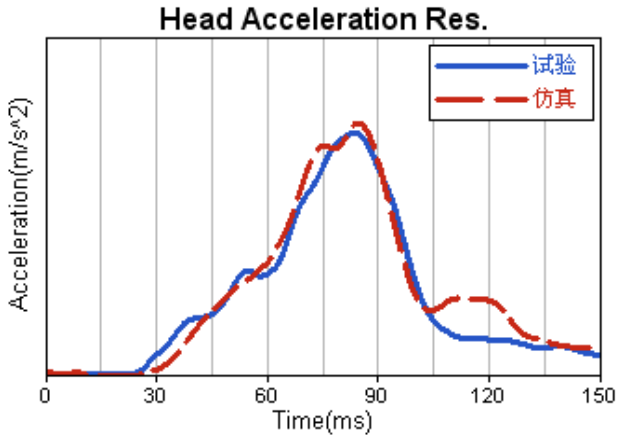

Figure 3. Contrast: head acceleration

图3. 头部加速度对标结果

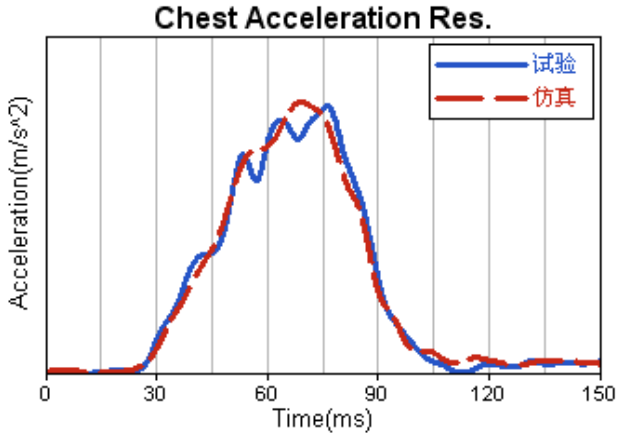

Figure 4. Contrast: chest acceleration

图4. 胸部加速度对标结果

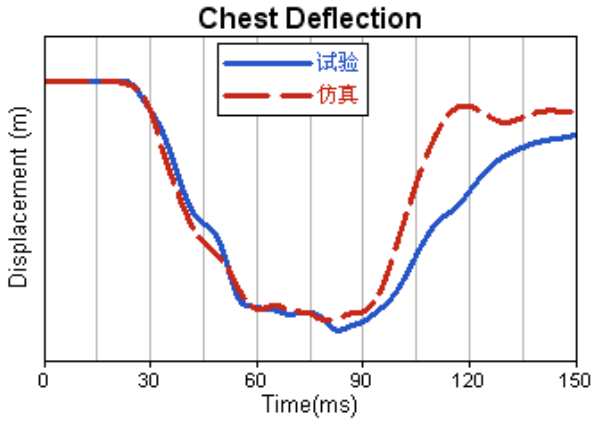

Figure 5. Contrast: chest deflection

图5. 胸部压缩量对标结果

综上所述，假人关键伤害曲线的吻合率均在 90%以上，满足对标要求，模型可用于后面的优化分析。

3 女性驾驶员约束系统模型仿真分析

将上述模型中 HybridIII第 50 百分位男性假人替换为 Hybrid III第 5 百分位女性假人，座椅由滑轨中间位置调整到最前端，转向管柱由中间位置调整到最下，调整 HybridIII第 5 百分位女性假人坐姿，重新拟合安全带，计算现有约束系统对女性驾驶员的保护效果。

使用相同的约束系统，HybridIII第 50 百分位男性假人和 HybridIII第 5 百分位女性假人的伤害曲线对比如下图 6-11。

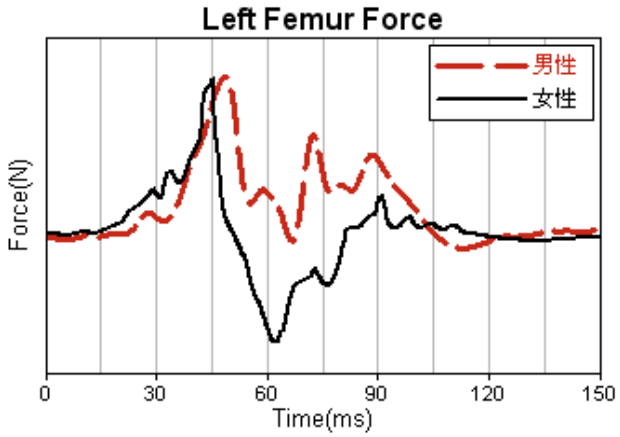

Figure 6. Left femur force(male VS. female)

图 6. 男驾驶员与女驾驶员左大腿力对比

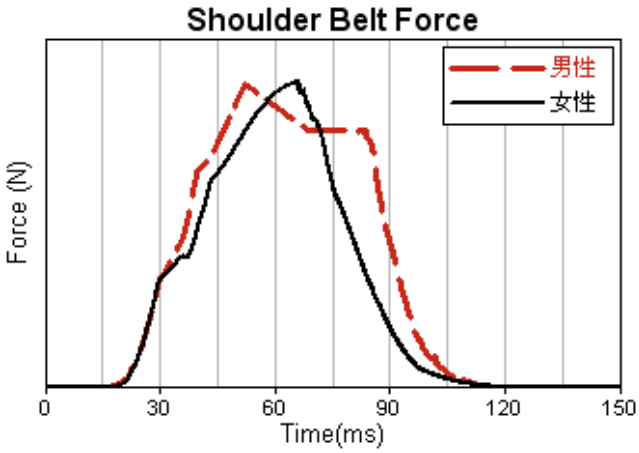

Figure 7. Shoulder belt force(male VS. female)

图 7. 男驾驶员与女驾驶员肩带力对比

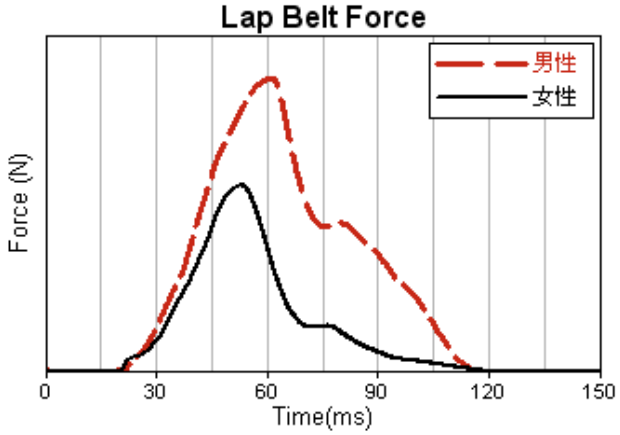

Figure 8. Lap belt force(male VS. female)

图8. 男驾驶员与女驾驶员腰带力对比

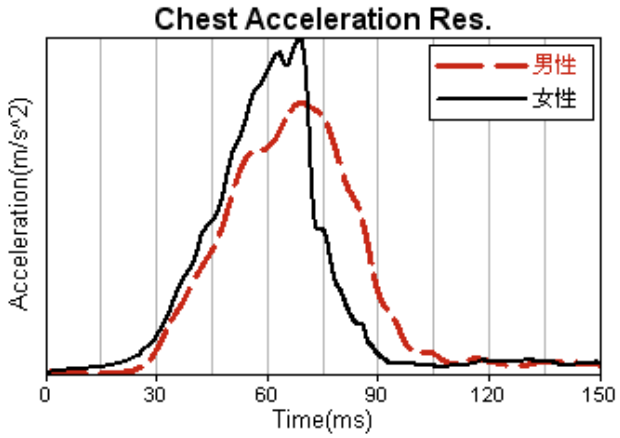

Figure 9. Chest acceleration(male VS. female)

图 9. 男驾驶员与女驾驶员胸部加速度对比

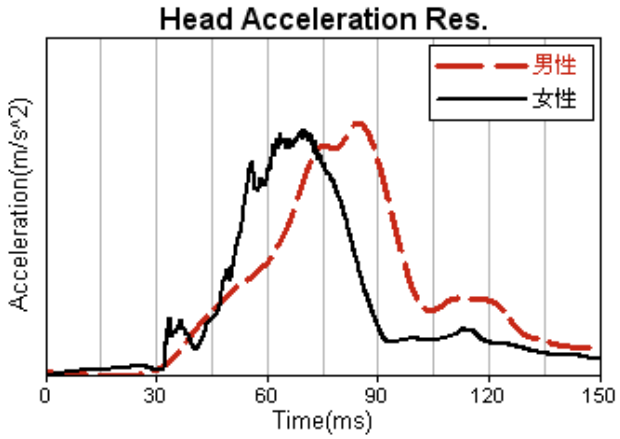

Figure 10. Head acceleration(male VS. female)

图 10. 男驾驶员与女驾驶员头部加速度对比

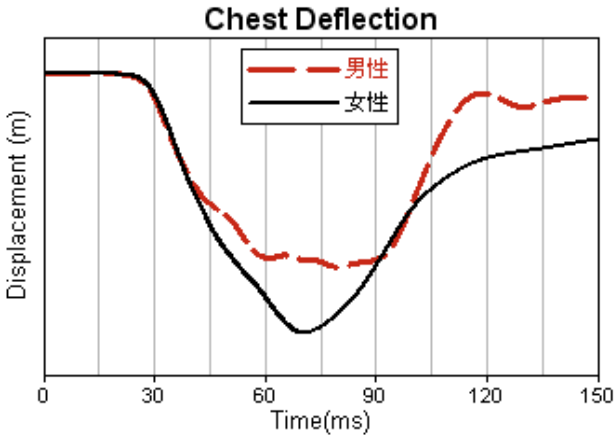

Figure 11. Chest deflection(male VS. female)

图 11. 男驾驶员与女驾驶员胸部压缩量对比

通过对比男性驾驶员和女性驾驶员的主要伤害值曲线和仿真录像可以发现：

(1) 由于女性假人形体矮小、座椅前移导致腿部与仪表板间距离变小，因此女性假人腿部和仪表板的接触时间提前。

(2)两者肩带力的峰值基本一致，但由于女性假人与气囊接触较早，气囊阻碍女性假人继续向前运动，因此女性假人的回弹时间比男性假人早；男性假人腰带力明显大于女性假人，这是因为男性假人骨盆的运动位移大于女性假人。

(3) 在相同预紧力和限力情况下，女性假人由于座椅靠前，与气囊接触提前，女性假人胸部加速度上升时间提前。

(4)女性假人位于座椅最前位置，与方向盘的距离比男性假人近，因此头部与气囊接触时间提前，从录像观察，女性假人头部在 45ms 开始与气囊接触，此时，男性头部距离气囊还有一定的空间。

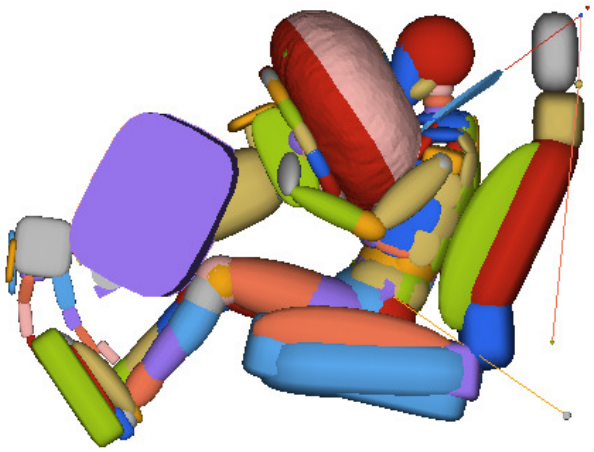

Figure 12. Female head contact with the airbag(45ms)

图 12. 45ms 时刻女性假人头部与气囊接触

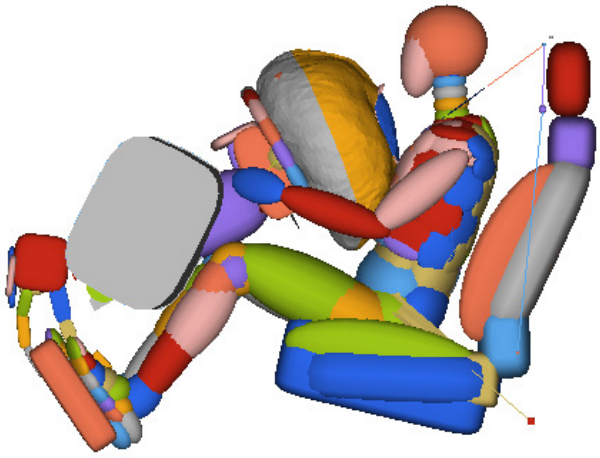

Figure 13. Male head not contact with the airbag(45ms)

图 13. 45ms 时刻男性假人头部未与气囊接触

使用相同的约束系统，HybridIII第 50 百分位男性假人和 HybridIII第 5 百分位女性假人的伤害值得分如表 1 和表 2。由于 C-NCAP 没有前排女性驾驶员工况，所以参考 Euro-NCAP（2015 版）50 公里正碰评分规则，女性假人伤害值得到 13.27 分（满分 16 分），失分项为胸部，如表 2 所示。由此可知，该车型满足男性驾驶员的约束系统不能较好地保护女性驾驶员，胸部伤害值需要优化。

Table 1. Male dummy injury value and point

表 1. 原约束系统配置男性假人伤害值得分

C-NCAP	性能指标	性能指标范围	基础模型	
			伤害值	得分
头部	HIC36	650-1000	569	5
	A3ms(g)	72-88	59	
颈部	弯矩(Nm)	42-57	13.77	2
	剪切力(kN)	1.9-3.1	0.75	
	拉伸力(kN)	2.7-3.3	1.17	
胸部	压缩量(mm)	22-50	26.7	4.16
	A3ms(g)	38-60	48.55	
大腿	左大腿载荷(kN)	3.8-9.07	0.138	2
	右大腿载荷(kN)		1.36	
	左膝滑移量(mm)	6.0-15.0	0.358	
	右膝滑移量(mm)		4.977	
小腿	左上 TI	0.4-1.3	0.38	1.66
	左下 TI		0.216	
	右上 TI		0.281	
	右下 TI		0.28	
	左小腿载荷(kN)	2.0-8.0	1.907	
	右小腿载荷(kN)		3.01	
合计			14.82	

Table 2. Female dummy injury value and point

表 2. 原约束系统配置女性假人伤害值得分

E-NCAP	性能指标	性能指标范围	基础模型	
			伤害值	得分
头部	HIC15	500-700	342.87	4
	头部 3ms（g）	72-80	56.69	
	合成加速度峰值(g)	<80	59.11	
颈部	弯矩 My(Nm)	36-49	9.14	4
	张力 Fz(kN)	1.7-2.62	1.14	
	剪切力 Fx(kN)	1.2-1.95	0.4	
胸部	压缩变形量(mm)	18-42	34.37	1.27
	VC(m/s)	0.5-1.0	0.11	
大腿	压力(kN)	2.6-6	1.67	4
总分			13.27	

4 约束系统优化

由于女性假人腿部的伤害值远小于性能指标范围，基本不会扣分。所以该车型的女性驾驶员和男性驾驶员约束系统匹配兼容性主要考虑头、颈、胸三个部位。

4.1 安全带限力优化

假人的胸部压缩量与安全带的作用密不可分，尤其是在假人胸部与气囊接触前，假人的胸部压缩量大小直接由安全带的力决定。因此，将安全带的限力等级由3500N分别降低到3000N、2500N，女性假人的伤害值如表3所示。

Table 3. Female injury value change by optimizing belt limiter level

表3. 安全带限力优化对女性驾驶员伤害值的影响

E-NCAP	性能指标	基础模型		限力 3000N		限力 2500N	
		伤害值	得分	伤害值	得分	伤害值	得分
头部	HIC15	342.87	4	311.7	4	273.9	4
	头部 3ms	56.69		54.72		51.47	
	合成加速度峰值	59.11		57.25		56.05	
颈部	弯矩 My	9.14	4	7.96	4	7.07	4
	张力 Fz	1.14		1.14		1.08	
	剪切力 Fx	0.4		0.44		0.51	
胸部	压缩变形量	34.37	1.27	31.82	1.7	27.9	2.35
	VC	0.11		0.1		0.09	
合计		9.27		9.7		10.35	

由表3可知，安全带限力等级降低，女性假人的胸部压缩量减小。从动画观察，女性假人头部距离方向盘最近的时刻如图14所示，女性假人的头部均未和方向盘接触。因此，降低安全带限力等级，有利于减小女性假人的胸部压缩量。

但同时也要考虑安全带限力等级降低对男性驾驶员伤害值的影响。由图15可知，安全带限力等级为3000N时，男性假人头部已经与方向盘发生接触，气囊被击穿。因此，单独降低安全带限力等级，不能同时兼顾男性

驾驶员和女性驾驶员。

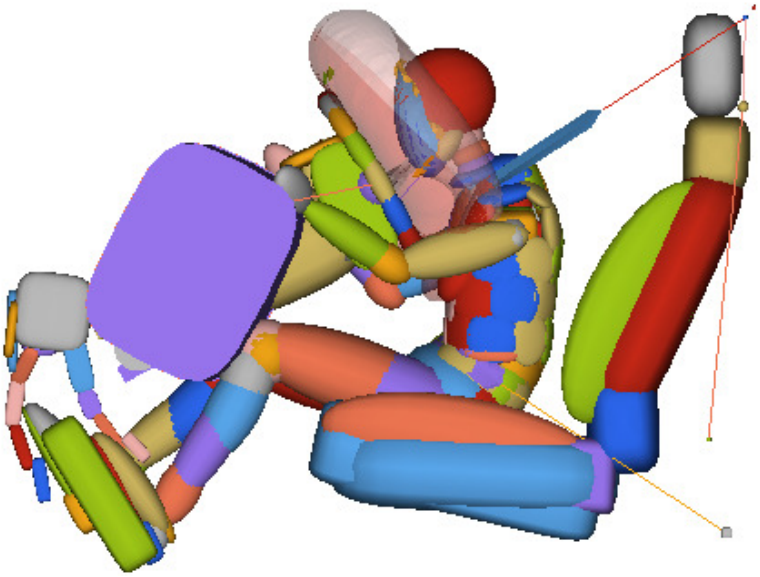

Figure 14. Closest distance between female and SW (belt LL2500)
图 14. 限力 2500N，女性假人头部与方向盘最近距离

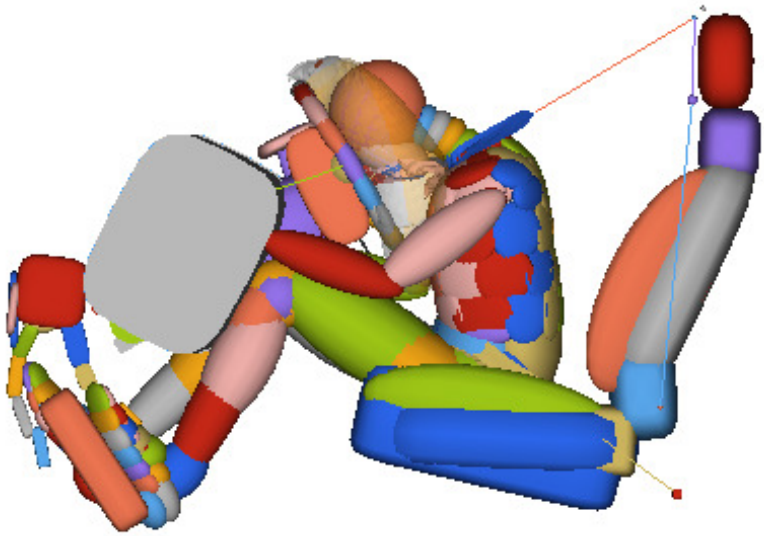

Figure 15. Closest distance between male and SW (belt LL3000)
图 15. 限力 3000N，男性假人头部与方向盘接触

4.2 安全气囊气孔优化

在降低安全带限力等级的基础上，减小气囊的气孔直径，将气孔直径由25mm减小到20mm，使气囊的泄气变慢，目的是女性假人胸压减小的同时，避免男性假人头部和方向盘发生接触。

对比优化后的男性驾驶员伤害值和女性驾驶员伤害值，如表4-5所示。

从仿真录像看，气囊未被击穿，男性假人头部与方向盘未发生接触，如图16所示。

采用安全带限力等级3000N，安全气囊气孔20mm的方案，男性驾驶员和女性驾驶员的伤害值均得到改善，男性驾驶员胸部得分提高0.61分，女性驾驶员胸部得分提高0.35分。

Table 4. Male driver injury value

表4. 男性驾驶员伤害值

C-NCAP	性能指标	基础模型		限力 3000N，孔 20	
		伤害值	得分	伤害值	得分
头部	HIC36	569	5	589	5
	A3ms(g)	59		61	
颈部	弯矩(Nm)	13.77	2	11.89	2
	剪切力(kN)	0.75		0.66	
	拉伸力(kN)	1.17		1.18	
胸部	压缩量(mm)	26.7	4.16	23.3	4.77
	A3ms(g)	48.55		46.4	
合计		11.16		11.77	

Table 5. Female driver injury value

表5. 女性驾驶员伤害值

E-NCAP	性能指标	基础模型		限力 3000N		限力 3000N_孔 20	
		伤害值	得分	伤害值	得分	伤害值	得分
头部	HIC15	342.87	4	311.7	4	353	4
	头部 3ms	56.69		54.72		56.36	
	合成加速度峰值	59.11		57.25		59.8	
颈部	弯矩 My	9.14	4	7.96	4	7.26	4
	张力 Fz	1.14		1.14		1.18	
	剪切力 Fx	0.4		0.44		0.49	
胸部	压缩变形量	34.37	1.27	31.82	1.7	32.3	1.62
	VC	0.11		0.1		0.1	
合计		9.27		9.7		9.62	

4.3 转向管柱优化

该车型的转向管柱压溃力约为3000N，压溃行程为20mm，将转向管柱的压溃力降低到2500N，分析转向管柱压溃力减小对假人伤害值的影响。分析结果如表6所示。

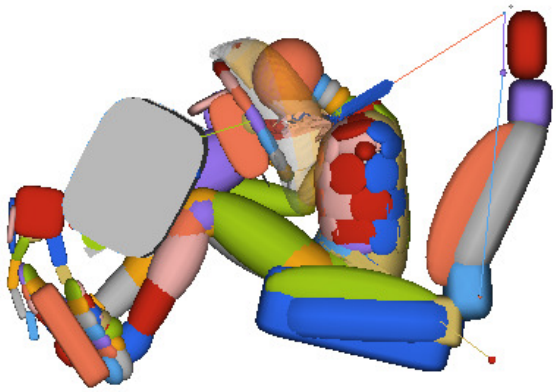

Figure 16. Closest distance between male and SW (belt LL3000, hole 20mm)
图16. 限力3000N，气孔20mm，男性假人头部与方向盘最近距离

Table 6. Male injury value change by optimizing SC
表6. 转向管柱优化对男性驾驶员伤害值的影响

C-NCAP	性能指标	基础模型		限力 3000N，孔 20		限力 3000N_孔 20_压溃力 2500N	
		伤害值	得分	伤害值	得分	伤害值	得分
头部	HIC36	569	5	589	5	444	5
	A3ms(g)	59		61		56.3	
颈部	弯矩(Nm)	13.77	2	11.89	2	16	2
	剪切力(kN)	0.75		0.66		0.67	
	拉伸力(kN)	1.17		1.18		1.41	
胸部	压缩量(mm)	26.7	4.16	23.3	4.77	23.7	4.7
	A3ms(g)	41.55		39.4		35.4	
合计		11.16		11.77		11.7	

由结果可知，减小转向管柱的压溃力，对于男性驾驶员和女性驾驶员的头部伤害值均有明显改善，但对胸部伤害值的改善不明显。从图17-18分析，转向管柱约在55ms开始压溃，75ms压溃过程结束，在该时间段内气囊对胸部的挤压作用减小，胸部压缩量减小，但从整个碰撞过程分析，假人胸部压缩量的峰值并未减小。

Table 7. Female injury value change by optimizing SC
表7. 转向管柱优化对女性驾驶员伤害值的影响

E-NCAP	性能指标	基础模型		限力 3000N_孔 20		限力 3000N_孔 20_压溃力 2500N	
		伤害值	得分	伤害值	得分	伤害值	得分
头部	HIC15	342.87	4	353	4	333	4
	头部 3ms	56.69		56.36		55.4	
	合成加速度峰值	59.11		59.8		57.5	
颈部	弯矩 My	9.14	4	7.26	4	7.48	4
	张力 Fz	1.14		1.18		1.16	
	剪切力 Fx	0.4		0.49		0.47	
胸部	压缩变形量	34.37	1.27	32.3	1.62	32.16	1.64
	VC	0.11		0.1		0.1	
合计		9.27		9.62		9.64	

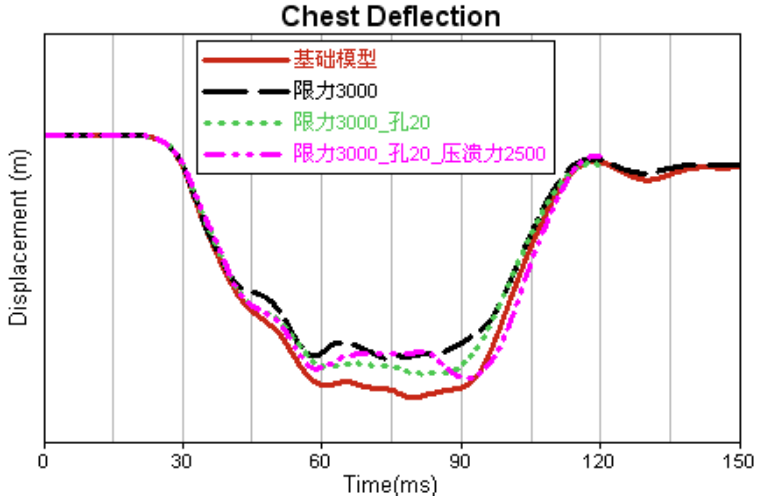

Figure 17. Male driver chest deflection

图17. 男性驾驶员胸部压缩量

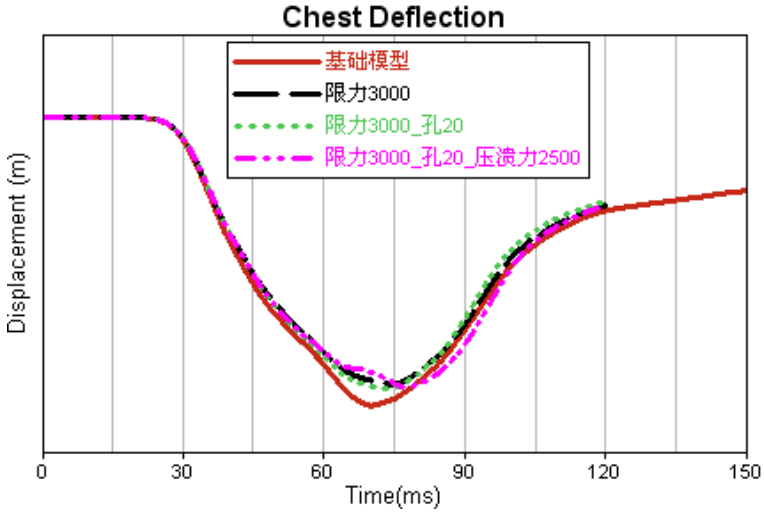

Figure 18. Female driver chest deflection

图18. 女性驾驶员胸部压缩量

5 结论

本文根据现有的驾驶员约束系统配置，结合仿真分析手段，对比分析了男性驾驶员和女性驾驶员在50km/h正面碰撞的保护效果，找出目前驾驶员约束系统配置的不足并进行改进优化。仿真分析表明，驾驶员通过优化安全带限力等级、安全气囊气孔、转向管柱压溃力等方式，能够同时满足男性驾驶员和女性驾驶员的伤害值要求（2015版E-NCAP），提高驾驶员约束系统的兼容性。从中可以得出以下结论：

（1）在保证男性驾驶员的头部不砸穿气囊的前提下，降低安全带限力等级，有利于同时降低男性驾驶员和女性驾驶员的胸部压缩量。

（2）只调整气囊的气孔，对胸部压缩量的改善作用不明显；但在降低安全带限力等级的基础上，适当减小气囊的气孔，保证头部和气囊不发生击穿，可以同时满足男性驾驶员和女性驾驶员的伤害值要求，实现驾驶员约束系统的兼容性。

（3）减小转向管柱的压溃力，压溃距离变大，对假人头部伤害值的改善比较明显。

致谢

本研究课题《前排女性乘员约束系统匹配与兼容性研究》的立项，得到中国汽车技术研究中心的资助，在此表示衷心的感谢。

参考文献 (References)

[1] Michiel van Ratingen, Euro NCAP Roadmap to Implementation 2013 to 2016, 2012 Annual General Meeting of the Automotive Safety Council, Scottsdale, March 2012.

[2] EUROPEAN NEW CAR ASSESSMENT PROGRAMME (Euro NCAP)-ASSESSMENT PROTOCOL–ADULT OCCUPANT PROTECTION, 2013

[3] C-NCAP（2012）中国汽车技术研究中心编. C-NCAP管理规则（2012版）

[4] Pan Ruyang, Wang Taoying, Guo Qingxiang. Analysis and Optimizing the Performance of Female Driver During the Frontal Crash潘如阳，王桃英，郭庆祥. 女性汽车驾驶员正面碰撞伤害分析及安全性能优化

Proceedings of the 11th International Forum of Automotive Traffic Safety, 2014, pp 251-257
No. ATS.2014.305

Research the effects of seat belt wearing position on HIII 5th female dummy's chest characteristics

Ma Weijie[1], Duan Bingxu[1], Bai Peng[1], Li Xiangrong[1]
[1]*China Automotive Technology and Research Center, Tianjin, China, 300300*
Email:maweijie@catarc.ac.cn

Abstract: China New Car Assessment programme(C-NCAP) version 2012 introduced HIII 5th dummy quantitative evaluation. In this paper, based on research the characteristics of female dummy's thorax response, to obtain a more accurate seat belt location. In this paper, low speed thorax impact tests were carried out, by improving the rigid cylinder and adjusting the pendulum impact location and Angle, to simulate the different thorax response characteristics when different seat belt load. The results show that the chest displacements decrease basically in linear, when the deviation of impact position is less than 60 mm upward from the 0 mm point at normal chest impact, and when the impact angle was 26°, the thorax displacement was the maximum. Which were very important for the design vehicle restraint systems and requirements of crash tests.

Keywords: vehicle passive safety; pendulum impact; seat belt wearing position; thorax characteristics; HIII 5th dummy

安全带佩戴位置对 HIII 5th 女性胸部特性影响的研究

马伟杰[1]，段丙旭[1]，白鹏[1]，李向荣[1]
[1]*中国汽车技术研究中心，天津，中国，300300*
Email:Maweijie@catarc.ac.cn

摘要：中国新车评价规程（C-NCAP）2012 版引入 HIII 5th 女性假人进行量化评价。本文通过对女性假人胸部特性响应的研究，从而获得较为准确的安全带佩戴位置。本文采用低速胸部标定试验，通过改进胸部标定摆锤，调整摆锤冲击位置和冲击角度，来模拟在碰撞过程中假人受到不同安全带载荷时胸部响应特征。结果表明，当偏离位置小于从正常胸部冲击的 0 点向上 60mm 时，胸位移基本为线性下降;摆锤冲击角度为 26°时，胸位移最大。对约束系统的设计和碰撞试验要求具有重要意义。

关键字：汽车被动安全；摆锤冲击；安全带佩戴位置；胸部特性；HIII 5th 假人

1 引言

在各国所实施新车评价规程(New Car Assessment Programme，NCAP)中，无论是正面 100%重叠刚性壁障碰撞试验，还是正面 40%重叠可变形壁障碰撞试验，Hybrid III 50th 假人胸部位移量都是作为胸部评价的主要依据之一。中国新车评价规程（C-NCAP）2012 版首次将 HIII 5th 女性假人引入到正面碰撞试验中，将假人放置于汽车第二排座椅左侧，进行量化分析。规程中规定在正碰、偏置碰和侧碰试验评价中分别给予最高 2 分。其中在正碰和偏置碰撞试验中，女性胸部压缩变形量为 1 分，占女性评分的 50%[1]。可见胸部评价指标对女性得分的重要性。

由于假人胸部损伤的主要原因之一是安全带的作用力，因此，作为汽车约束系统的一部分，正确佩戴安全带在汽车前碰撞试验中能够对假人起到较为有效的约束作用，从而对汽车乘员起到较好的保护作用。如果对假人胸部不同区域进行划分，胸部位移量对碰撞能量的敏感度是有较大差异的[2]。对于 Hybrid III 50th 假人来说，以正常胸部冲击位置的中心点为 0 点，沿 Z 向上 60mm 以内，假人的胸部位移量与正常位置安全带试验假人胸部位移量为线性关系[3]；将安全带靠近颈部放置比将安全带水平外移 50mm 所得的假人胸部位移量能够降低

34%[4]。Pereira 等在 2012 年所做的标定试验中，冲击 Hybrid Ⅲ 50th 假人第 6 根肋骨要比冲击第 3 根肋骨所得胸部位移量减少 33%，并给出胸部位移传感器正常位置在假人第 3 根肋骨处[5]。Yamasaki 等指出假人胸部加速度与安全带的佩带位置相关性较小[6]。

由于女性生理结构与男性不同，HIII 5th 女性假人的马夹与 Hybrid Ⅲ 50th 假人相比有所差异。主要多了两个乳房的仿真结构，这就造成了女性假人佩戴安全带的形式及力学响应与男性假人有所差异。本文通过改进冲击摆锤，模拟安全带的带状冲击载荷对胸部位移量的影响。以假人胸部低速（摆锤冲击速度为 3.0 m/s）摆锤冲击标定试验为基础，定义正常冲击位置为 0 点位置，加装冲击块与垂直方向夹角 α，通过改变 α 角度，来研究不同夹角时假人胸部变形量值影响。并选定 α，随后沿 Z 轴向上每隔 20mm 选取一个点，共选取 5 组进行标定试验对比分析。

2 假人胸部标定试验方法的研究

2.1 相关试验参数的确定

如下图 1 所示，本文将 0 点位置标记到马夹上，通过测量假人外廓尺寸可知，0 点位置距离肩部的 Z 向为 180mm，Y 向为 130mm，肩部外侧到颈部 Y 向距离为 80mm。

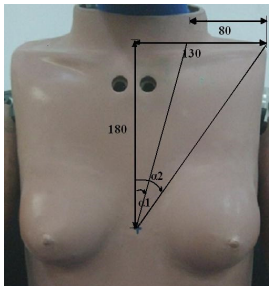

Figure 1. the size of HIII 5th female dummy jacket

图 1. HIII 5th 女性假人的马夹尺寸

由于安全带的佩带一般的通过肩部，且佩戴的角度范围如图 1 所示的 α_1 至 α_2，通过角度换算可得该角度的变化范围为 16-36°，因此将该角度范围做为本文研究的参数之一。另外，从 0 点位置起，沿 Z 轴向上偏移位置 P 做为另外一个试验参数。每隔 20mm 选取一个点，共选取 5 组进行分析研究。

2.2 标定摆锤的改进

由于女性假人标定所使用的摆锤冲击面较大，摆锤在与假人接触时为圆形载荷，先与假人的两侧乳房接触，而非直接冲击本文定义的 0 点位置。本文旨在模拟在正面碰撞过程中 Hybrid Ⅲ 5th 女性假人在受到安全带的带状载荷时，胸部变形量的相关特征。因此，通过在摆锤上安装一个冲击块来实现安全带的带状冲击效果。标定试验设置如下图 2 所示。

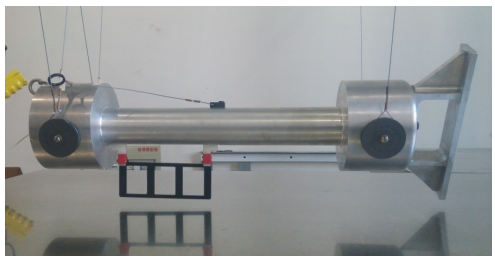

Figure 2. The improved calibration pendulum

图 2. 改进后的标定摆锤

在汽车约束系统的设计过程中，安全带的宽度一般规定为 46-50mm，本文通过对一系列车型的实际测量，最终确定冲击块的宽度为 48mm；冲击块长度为 260mm，以确保其与假人有足够的接触面积。冲击摆锤质量为 13.99kg，加装的冲击块质量为 0.79kg，改进后摆锤的总质量为 14.78kg。

2.3 标定方法的选择

对于 Hybrid Ⅲ 5th 女性假人胸部标定主要有两种方法，即美国国家公路交通安全管理局（National Highway Traffic Safety Administration，NHTSA）联邦法规（Code of Federal Regulations，CFR）Part 572 规定的胸部高速标定程序[7]和美国机动车工程师学会(Society of Automotive Engineers, SAE)SAE J2878 规定的胸部低速标定程序[8]。这两种摆锤冲击标定试验方法对环境温度的要求均为 20.6~22.2℃,对湿度的要求均为 10%~70%。高速标定的胸部变形量限值为 50-58mm，而低速标定的胸部变形量限值为 17.4-21.8mm。

目前 C-NCAP 摸底试验后排女性假人的胸部位移量一般在 35-55mm 之间。正常对女性假人进行标定时，采用高速标定方法。但是本文由于参数选择加多且位移量向 Z 向调整后在高速冲击时假人存在较大的损坏风险，因此，如图 3 所示，本文采用低速标定试验方法对 HIII 5th 女性假人胸部变形量进行定性的研究。

Figure 3. the set of Calibration test

图 3. 标定试验设置

3 假人胸部特性研究

3.1 标定摆锤改进前后结果对比分析

图 4 改进后冲击块角度 α 为 26°，由摆锤改进前后的对比曲线可知，胸部变形量在 5.3mm 到 18.4mm 之间时，改进后的获得的胸部刚度特性要高于改进前，这可能是由于改进后仿安全带的带状冲击载荷作用区域要比改进前小，由于乳房的缓冲作用的影响。胸部变形量峰值改进前为 22.2mm，改进后为 21.1mm，改进后的变形量峰值略有下降。

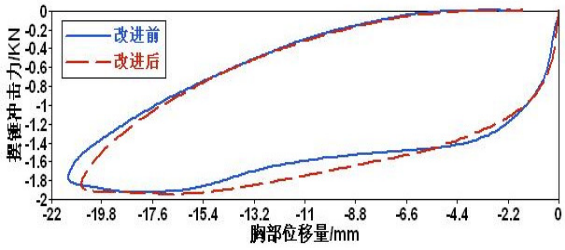

Figure 4. Curve: Comparison of the data before and after the pendulum improvement

图 4. 摆锤改进前后的数据对比

3.2 冲击块角度 α 与胸部变形量相关性研究

由于汽车车型的不同，后排安全带的上固定点的位置也不尽一致。本节标定试验主要是基于安全带都通过 HIII 5th 女性假人的胸位移传感器，但是由于后排座椅以汽车空间尺寸的不同所导致的安全带佩带角度对胸部变形量的影响。

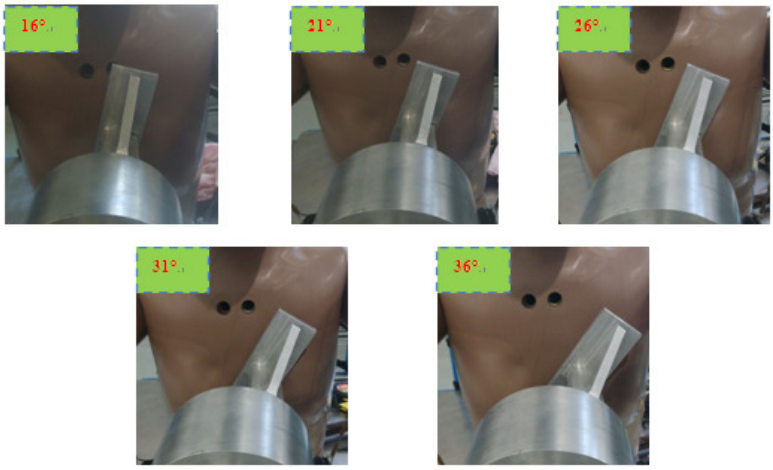

Figure 5. the diagram of impactor angles
图 5. 冲击块角度示意图

摆锤冲击块角度 α 的范围 16-36°，本文将该角度范围平均选取为 5 个特定角度进行冲击试验（如图 5 所示），试验结果如表 1 所示。

Table 1. Test data at different impactor angles
表 1. 冲击块不同角度的试验数据

组别	冲击块角度 /度	冲击力 /kN	摆锤速度 /m/s	胸位移 /mm
1	16	1.934	3.05	20.2
2	21	1.935	3.05	20.6
3	26	1.945	3.04	20.7
4	31	1.968	3.04	20.5
5	36	2.0	3.04	20.6

由试验结果可知，在摆锤冲击速率一定的情况下，随着冲击块角度的逐步增加，冲击力逐步增大；但是，胸部变形量在 16-26° 时，逐渐增大，随后的第 4 组试验假人胸部变形量有降低趋势，即冲击块角度为 31° 时比 26° 时减下。在所有 5 组试验中第 3 组试验的假人胸部变形量最大，为 20.7mm。

3.3 偏移量 P 与胸部变形量相关性研究

在试验过程中，还存在另外一个问题，后排 HIII 5th 女性假人在佩带安全带时，安全带常常向上偏移，从而避开胸位移传感器。在冲击试验研究过程中，可将摆锤的位置向上偏移的方法来实现。

在分析摆锤向上偏移量问题时，选定的冲击块偏转角度为 26° 。以正常胸部冲击位置的中心点为 0 点，沿 Z 轴向上偏移量 P，每隔 20mm 取一次试验样本，本文共取了包括 0 点在内的 5 组冲击试验，试验设置如下图 6 所示。

Figure 6. the diagram of impactor offset

图 6. 冲击块偏移量示意图

上图 6 选取了 0 位置 P0 和沿 Z 向向上偏移量为 80mm 的 P8 两张极限位置的图片。在冲击块角度不变的前提下，随着 P 值的增大带形冲击区域逐步向上偏移，P80 的位置为向上的极限位置，此时如果安全带佩戴在该位置，安全带已经勒到假人的颈部。冲击试验的结果如下表 2 所示。

Table 2. Test datas at different impactor offset position

表 2. 冲击块不同偏移位置的试验数据

组别	冲击块位置 /mm	冲击力 /kN	摆锤速度 /m/s	胸位移 /mm
P0	0	1.965	3.03	19.9
P20	20	1.892	2.96	19.4
P40	40	1.904	3.05	19.8
P60	60	1.89	3.05	19.5
P80	80	1.825	3.04	18.5

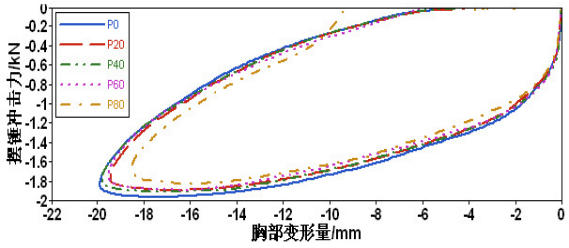

Figure 7. Curve: different impactor offset position

图 7. 冲击块不同偏移位置曲线

表 2 中的 P20 项试验在试验过程中可能存在一些干扰因素，冲击速度和冲击力都相比 P0 和 P40 小，且胸部变形量也相差较多。

而且从图 7 也可以看出 P20 组试验与其它组别试验差异较大。因此，在本次分析过程中将 P20 次试验视为无效试验，不予分析。

由 4 组试验结果可知，在摆锤冲击速率一定的前提下，随着摆锤从 0 点位置沿 Z 轴向上偏移量的增加，摆锤冲击力逐渐降低；而且，假人胸部变形量逐渐减小。

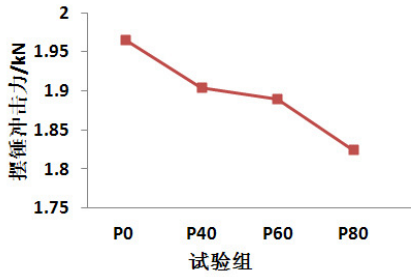

Figure 8. the chart of different tests pendulum impact force

图 8. 不同试验摆锤冲击力趋势图

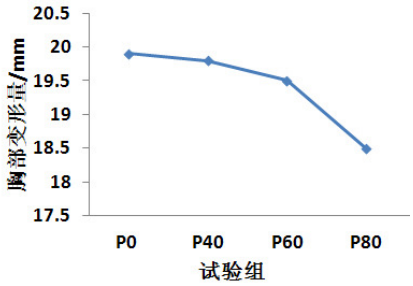

Figure 9. the chart of different tests dummy thorax displacement

图 9. 不同试验假人胸部变形量趋势图

如图 8、9 所示，值得注意的一点是：相比于 P0 与 P40 组试验、P40 与 P60 组试验数据降低程度较小，冲击力分别降低 0.061kN 和 0.014kN，胸部变形量分别减小 0.1mm 和 0.3mm。但是 P60 与 P80 组试验相比，在冲击力降低 0.065kN 的时候，胸部变形量减小 1mm，其变化速率较大。从图 7 同样可以看出 P0、P40 和 P60 组试验的力-位移曲线间隔相对平均。摆锤冲击位置在向上偏移 60mm 以内时，试验曲线间隔较为均匀，而当摆锤冲击位置向上偏移 80mm 时，其曲线间隔与前 3 个冲击位置所得曲线有明显区别。由此可知，摆锤冲击位置在上移 60mm 以内时，胸部位移量与外部冲击力基本为线性关系。而当摆锤冲击位置位置为 80 mm 时，开始呈非线性变化。

4 总结

本文通改进冲击摆锤，即在摆锤上加装冲击块进行 HIII 5th 女性假人的胸部冲击试验。并单独研究安全带不同佩戴角度和沿 Z 轴向上的不同偏移量两个变量。总结如下：

1.在佩戴安全带不同角度，且安全带均通过 HIII 5th 女性假人胸位移传感器时，偏转角 α 为 26° 所获得的胸部变形量最大，在此时，安全带通过 HIII 5th 假人肩部的中间位置；

2.对于 HIII 5th 女性假人来说，通过改进冲击摆锤，可知以 0 点位置为起点，沿 Z 向上偏移 60mm 以内时，假人的胸部位移量与正常位置安全带试验假人胸部位移量为线性关系。

试验结果表明该研究对实际汽车约束系统设计和汽车被动安全试验方法有重要意义。

参考文献

[1] 中国汽车技术研究中心.中国新车评价规程（C-NCAP）2012 版. 2012.http://www.c-ncap.org.
[2] 彭路,李筱磊,崔泰松,等.基于 Madymo 的前碰撞混合III型假人胸部位移量损伤分析[J].汽车工程, 2009: 1126-1128.
[3] 马伟杰,逯艳博,朱海涛.安全带非正常佩戴位置对假人胸部压缩变形量的影响[J].汽车安全与节能学报, 2014,1(5): 65-69.
[4] Horsch J, Melvin J, Viano D, et al. *Thoracic injury assessment of belt restraint systems based on Hybrid III chest compression*. 1991. USA.SAE Paper, 912895.
[5] Pereira R, Tank M. *Study of parameters influencing the chest deflection of HybridIII dummy in crash tests.* 2012. USA. SAE Paper,

2012-08-0002,2012.
[6] Takaaki YAMASAKI, Kouichi UESAKA. *Rear occupant protection JNCAP test-test results and findings.* he 22th international technical conference on the enhanced safety of vehicles (ESV). 2011. Washington, D.C. USA. Paper no. 11-0445.
[7] First Technology Safety System(FTSS). *User ' s manual for the 50th percentile male Hybrid ⅢⅢtest dummy[R].* SAE Paper, 2005-04-EA-23, 2005.
[8] The SAE Dummy Test Equipment Subcommittee. *Low speed thorax impact test procedure for the HⅠⅡ50 male dummy [R].* SAE Paper, 2010-01-2878, 2010.

Proceedings of the 11th International Forum of Automotive Traffic Safety, 2014, pp 258-268
No. ATS.2014.306

Effect of rotation of passenger compartment on occupant behavior in car impacts

Yiwei CHEN[1], Hiroki IWANAKA[1], Daisuke ITO[1], Koji MIZUNO[1,2] and Yong Han[2]

Nagoya University, Furo-cho, Chikusa-ku, Nagoya , Japan,4648603

Xiamen Technology of University, 600, Ligong Rd, Houxi, Jimei District, Xiamen, P.R.China,361024

E-mail: chen.yiwei@h.mbox.nagoya-u.ac.jp

Abstract: In vehicle collisions, vehicle accelerates and rotates during impacts, though three-dimensional rotation is generally not reflected in simulation analyses. The objective of this study is to understand the effects of car rotation on occupant kinematic behavior in vehicle impact with rotation. The method to provide the boundary condition for the occupants under car acceleration and rotation was formulated. The kinematics of occupant FE model was calculated under vehicle rotation conditions. Two crash cases with vehicle rotation were examined: small overlap frontal crash (yawing) and full-width crash tests (pitching). In the small overlap frontal test simulation, the head lateral displacement of occupant was almost the same in the conditions with and without vehicle yawing angle. The results of full frontal car simulation with pitching showed that the occupant acceleration was mitigated since the seatbelt anchor moved forward together with the occupant. Rotation angles of car influence the occupant kinematics, and it is necessary to include the car rotation to simulate the occupant kinematics in vehicle collisions.

Keywords: Occupant protection, Vehicle rotation, Finite element method

1 Introduction

In addition to translational acceleration, rotational motion can occur frequently during collisions. Especially stiff small cars have a relative large rotation angle in crash tests. In addition to vehicle linear acceleration, the occupant kinematics can be influenced by vehicle rotation. There are not many research studies that investigated the influence of vehicle rotation on occupant kinematics. Woitsch and Sinz (2013) showed the influence of yawing motion and pitching motion of vehicles on the injury measures of dummy with finite elements simulations. However, the systematic analysis were not conducted to understand the mechanisms of occupant kinematics with vehicle rotation. In this study, the condition to reproduce occupant kinematics under environment of passenger compartment rotation was formulated. The occupant kinematics under yaw and pitch rotation was compared to that without vehicle rotational behavior (only compartment deceleration was applied).

2 Theory of reproduction

The equations of motion in rotating coordinate system is derived with matrix. Stationary coordinate system O-xyz fixed at the inertial space and rotating coordinate system O-$x'y'z'$ share the origin point O. The components of column vector of the point P in O-xyz and O-$x'y'z'$ is expressed as $\{r\}=(x,y,z)^T$ and $\{r'\}=(x',y',z')^T$, respectively (Figure 1). Time derivative of the column vector is $\{\dot{r}'\}=(\dot{x}',\dot{y}',\dot{z}')^T$ and $\{\ddot{r}'\}=(\ddot{x}',\ddot{y}',\ddot{z}')^T$.

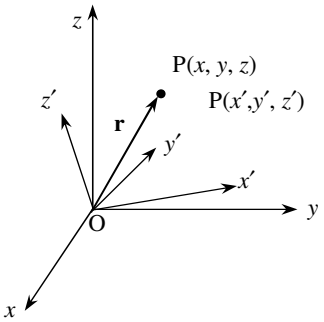

Figure 1. Coordinate system

By using the coordinate transformation matrix of rotation [*R*], the relationship between two vectors can be transferred as

$$\{r\} = [R]\{r'\} . \tag{1}$$

Since $[R]$ is an orthogonal matrix, the following equations hold:

$$[R][R]^T = [R]^T[R] = [I] \tag{2}$$

$$[R]^{-1} = [R]^T \tag{3}$$

$$\{r'\} = [R]^T\{r\} . \tag{4}$$

By substituting Eq. (4) into the first derivative of $\{r\}$ with respect to time $\{\dot{r}\} = [\dot{R}]\{r'\} + [R]\{\dot{r}'\}$, we can obtain

$$\{\dot{r}\} = [\dot{R}]([R]^T\{r\}) + [R]\{\dot{r}'\} . \tag{5}$$

Then, the matrix $[R]^T$ was multiplied to Eq. (5) from the left side to express in the component of the motion coordinate system, we obtain

$$[R]^T\{\dot{r}\} = [R]^T[\dot{R}]([R]^T\{r\}) + \{\dot{r}'\} \tag{6}$$

$$[R]^T\{\dot{r}\} = [\Omega]([R]^T\{r\}) + \{\dot{r}'\} \tag{7}$$

where $[R]^T[\dot{R}] = [\Omega]$ is an angular velocity matrix. This equation is a matrix expression of velocity vector, $\dot{\mathbf{r}} = \mathbf{v}' + \boldsymbol{\omega} \times \mathbf{r}'$ in the moving coordinate system.

The acceleration of the point P can be calculated from the time derivative of (5).

$$\{\ddot{r}\} = [\ddot{R}][R]^T\{r\} + [\dot{R}][\dot{R}]^T\{r\} + [\dot{R}][R]^T\{\dot{r}\} + [\dot{R}]\{\dot{r}'\} + [R]\{\ddot{r}'\} \tag{8}$$

We substitute (5) to (8), and then in order to express the components in O–$x'y'z'$, we multiply $[R]^T$ to equation from the left.

$$\begin{aligned}[R]^T\{\ddot{r}\} = {} & ([R]^T[\ddot{R}][R]^T + [R]^T[\dot{R}][\dot{R}]^T)\{r\} \\ & + [\Omega]^2[R]^T\{r\} + 2[\Omega]\{\dot{r}'\} + \{\ddot{r}'\}\end{aligned} \tag{9}$$

Since $[\Omega] = [R]^T[\dot{R}]$, we can obtain

$$[\dot{\Omega}] = [\dot{R}]^T[\dot{R}] + [R]^T[\ddot{R}] \tag{10}$$

$$[R]^T[\ddot{R}][R]^T + [\dot{R}]^T[\dot{R}][R]^T = [\dot{\Omega}][R]^T \tag{11}$$

Eq. (9) can be rewritten as:

$$\begin{aligned}[R]^T\{\ddot{r}\} &= [\dot{\Omega}]([R]^T\{r\}) + [\Omega]^2([R]^T\{r\}) \\ &\quad + 2[\Omega]\{\dot{r}'\} + \{\ddot{r}'\} \\ &= [\dot{\Omega}]\{r'\} + [\Omega]^2\{r'\} + 2[\Omega]\{\dot{r}'\} + \{\ddot{r}'\}\end{aligned} \tag{12}$$

The equation above means the vector expression:

$$\ddot{\mathbf{r}} = \mathbf{a}' + 2\boldsymbol{\omega} \times \mathbf{v}' + \boldsymbol{\omega} \times (\boldsymbol{\omega} \times \mathbf{r}') + \dot{\boldsymbol{\omega}} \times \mathbf{r}' \tag{13}$$

If we multiply $[R]^T$ from the left, the vector is projected in O–$x'y'z'$ system.

Let us consider the case that the origin point O′ is moving with translational acceleration, and O′-$x'y'z'$ is rotating with respect to the O-xyz system. The components of column vector of point P in O-xyz is $\{r\}=(x,y,z)^T$. In O-$x'y'z'$, it can be expressed as $\{r'\}=(x',y',z')^T$ (Figure 2). The position of point P in O′–$x'y'z'$ can be expressed as the superposition of the translational motion of O′ and the rotational motion of O-$x'y'z'$ system.

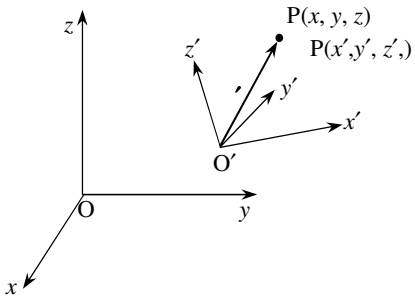

Figure 2. Coordinate system (origin moves)

$$\{r\}=\{r_{O'}\}+[R]\{r'\} \tag{14}$$

The position, velocity and acceleration of the point P in moving coordinate system can be expressed as:

$$[R]^T\{r\}=[R]^T\{r_{O'}\}+\{r'\} \tag{15}$$

$$[R]^T\{\dot{r}\}=[R]^T\{\dot{r}_{O'}\}+[\Omega]\{r'\}+\{\dot{r}'\} \tag{16}$$

$$\begin{aligned}[R]^T\{\ddot{r}\}=&[R]^T\{\ddot{r}_{O'}\}+[\dot{\Omega}]\{r'\}\\&+[\Omega]^2\{r'\}+2[\Omega]\{\dot{r}'\}+\{\ddot{r}'\}\end{aligned} \tag{17}$$

Force acting on the mass point can be expressed as

$$\{f'\}=[R]^T\{f\} \tag{18}$$

The gravity vector $\{g\}=(0\ \ 0-g)^T$ acts vertically downward. Therefore, the equations of motion in stationary coordinate system can be written as

$$m\{\ddot{r}\}=\{f\}+\{g\} \tag{19}$$

The component of equations of motion in moving coordinate system can be expressed in the moving coordinate system.

$$m([R]^T\{\ddot{r}\})=\{f'\}+[R]^T\{g\} \tag{20}$$

Substitute Eq. (16) (17) to (19), we can get

$$\begin{aligned}m\{\ddot{r}'\}=&\{f'\}+[R]^T\{g\}-m[R]^T\{\ddot{r}_{O'}\}\\&-m[\dot{\Omega}]\{r'\}-m[\Omega]^2\{r'\}-2m[\Omega]\{\dot{r}'\}\end{aligned} \tag{21}$$

To reproduce the equations of motion of O′–$x'y'z'$ in another system, such as sled, components of the external force acting on the mass point must be equal. Furthermore, considering that the direction of gravity is always acting vertically downward, it is necessary to reproduce the angle of O′–$x'y'z'$ w.r.t. the stationary coordinate system. Also, the acceleration of the origin O′ should be equal.

From the above discussion, we can conclude that in order to reproduce the motion of passengers in a sled test when the passenger compartment has a rotational motion, three conditions shown below should be satisfied:

1. The environment of the force applied to the dummy in passenger compartment (restraint system, seat, instrument panel, floor, etc.) should be identical with those of real test.

2. Acceleration at one arbitrary point in the passenger compartment should be identical with the acceleration at the same point in the passenger compartment in a crash test.

3. The time history of posture angle of the passenger compartment should be identical w.r.t. the stationary coordinate system.

3 Yawing Effect

3.1 The effect of yawing rotation on the compartment acceleration

The accelerations are different depending on the points at the passenger compartment when the vehicle rotates. At first step, the distributions of acceleration in the passenger compartment due to yawing were examined. As a crash with large yawing angle, a small overlap test was selected. A small overlap barrier crash test was conducted at 64.4 km/h and 25 percent overlap by IIHS (Insurance Institute for Highway Safety). The test car was Mazda 3. A Hybrid III dummy was seated in the driver seat on the impact side. Figure 3 shows the crash configuration. One vehicle accelerometer was fixed inside the vehicle (floor) and marked with photographic targets applied to the appropriate top surfaces of the vehicle.

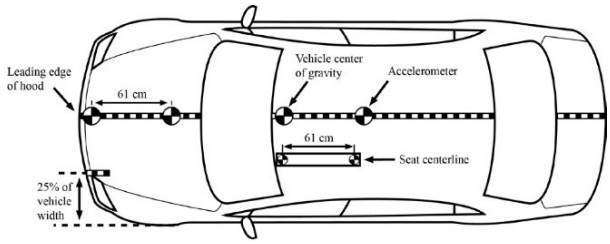

Figure 3. Crash configuration of Small overlap test

Figure 4 shows the translational accelerations of x' (longitudinal) and y' (lateral) directions. The time history of yaw angle was obtained by image analysis software from the movie of crash test (Figure 5).

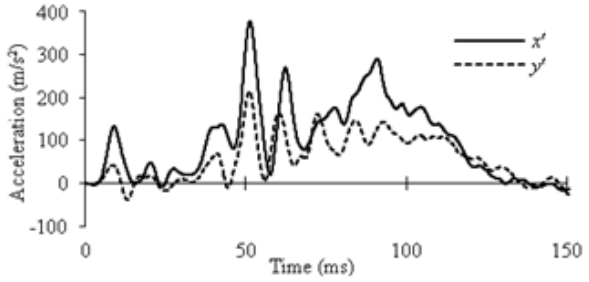

Figure 4. Acceleration of accelerometer (test result, car coordinate system)

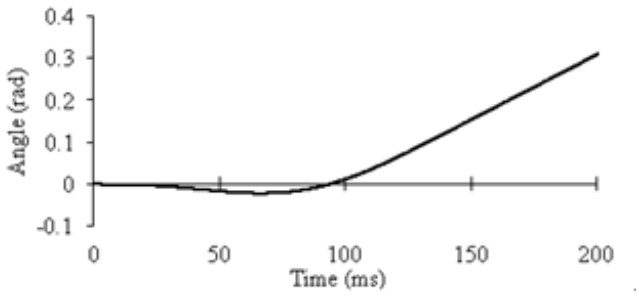

Figure 5. Yaw rotation of target car

Based on the test results, three types of acceleration field were exerted on the passenger compartment finite element (FE) model: only translational acceleration, only rotational acceleration and combination of translational and rotational accelerations were applied on the point of accelerometer attached point, and the effect of yawing rotation on the vehicle acceleration was examined. Accelerations of several points on the compartment model were measured. Figure 6 shows the locations of acceleration measured (A1 to A13).

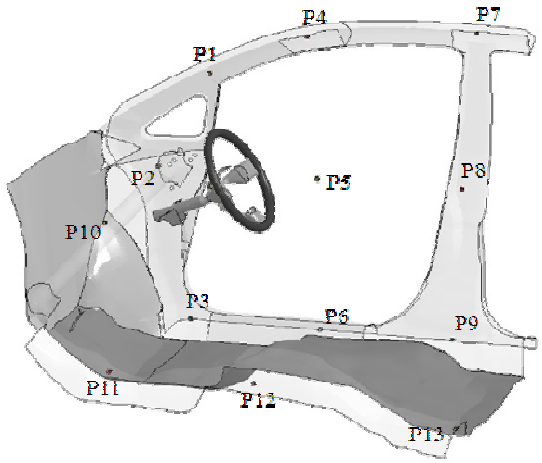

Figure 6. Locations of acceleration measured

When only translational acceleration was given, all points on the car have identical acceleration. In the case that only yawing angle with time was given, the result showed that the tendency of the vehicle acceleration curve was consistent with the curve of the yawing angular acceleration.

When both of the translational accelerations and angular acceleration were given, the accelerations of x-axis and y-axis divided into groups, respectively. The x accelerations of all the points on car separates into two groups. The points at tunnel side (P10, P11, P12, P13: same y' coordinate) have almost the same x' acceleration. And the points at door side (P1 to P9: same y' coordinate) also have almost same x' acceleration. Similarly, the y' accelerations of all the points on car divided into three groups (P1, P2, P3, P10, P11; P4, P5, P6, P12; P7, P8, P9, P13: same x' coordinate). Figure 7 shows the average acceleration curves of each location group. The results indicate that yawing angular acceleration can cause different acceleration of each point on the compartment according to its location.

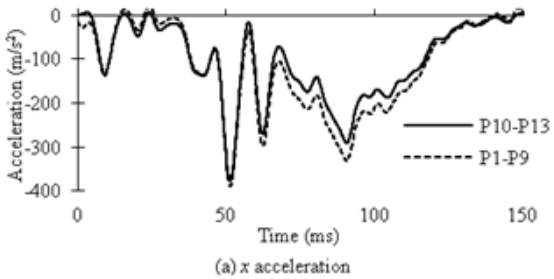

(a) x acceleration

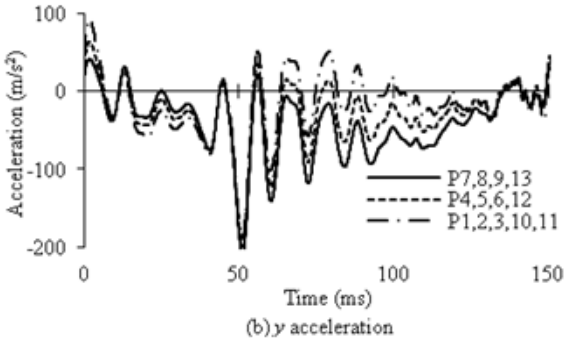

(b) y acceleration

Figure 7. Accelerations of points in the compartment

The acceleration of the point in the compartment can be obtained when substituting $\boldsymbol{v}'=0$ into eq. (13)

$$\ddot{\mathbf{r}} = \ddot{\mathbf{r}}_{O'} + \boldsymbol{\omega}\times(\boldsymbol{\omega}\times\mathbf{r}') + \dot{\boldsymbol{\omega}}\times\mathbf{r}' . \tag{22}$$

The above equation is also described by x and y component expression:

$$\begin{aligned} a_{x'} &= a_{Ox'} - \dot{\omega}y' - \omega^2 x' \\ a_{y'} &= a_{Oy'} + \dot{\omega}x' - \omega^2 y' \end{aligned} \tag{23}$$

Although both of x' and y' appears in the above equation, ω^2 is too small to affect the acceleration $a_{x'}$, $a_{y'}$. As a result, the x' component of the acceleration of the point relates with its y' coordinate and y' component relates with its x' coordinate.

3.2 Reproduction of small overlap crash test

In order to understand the kinematic behavior of frontal passenger affected by yawing rotation, a small over-lap crash test was reproduced by FE simulations. The crash test in section 3.1 was chosen as a basic case and the parameters of this test condition was used in the simulations.

A simplified FE model of passenger compartment was adopted in this simulation. The model consisted of passenger compartment which includes a front seat, steering, seatbelt and airbag. A Thums FE model was seated in the driver seat. According to the theory in section 1, we gave the x' and y' acceleration to the identical point on the accelerometer location of the tested car. At the same time, we gave a yawing angle with time around this point so that the motion occurred in crash test can be reproduced.

3.2.1 Relationship between head displacement of occupants and yawing motion

In order to make it clear that how yaw motion affects the kinematic behavior of occupant, we compared the yawing rotation case and no yawing rotation case by FE model simulations. The kinematic behavior of Thums is shown in Figure 8. The lateral displacement of the occupant head considering yawing motion was slightly smaller than that without yawing angle.

To understand the reason that the yaw motion has a little influence on the kinematic behavior of occupant, tension force of shoulder belt was analyzed (Figure 9). The shoulder belt outer and inner force $T_{\text{shoulder belt outter}}$, $T_{\text{shoulder belt inner}}$ were reflected in y direction (global coordinate system): $T_{y\ \text{outer}}$ and $T_{y\ \text{inner}}$. The results are shown as Figure 10. The components $T_{y\ \text{inner}}$ of both cases was almost equal while the $T_{y\ \text{outer}}$ of no yaw case was larger than that of yaw case. The difference, $T_{y\ \text{inner}} - T_{y\ \text{outer}}$ (the force that prevented Thums torso from moving toward the door) was larger for the yaw case. In yawing case, it was observed the shoulder belt anchor moved clockwise because of the yawing motion of vehicle, which made $T_{y\ \text{outer}}$ (with yaw) smaller than $T_{y\ \text{outer}}$ (without yaw). As a result, the lateral head displacement of Thums model was smaller in the yaw case.

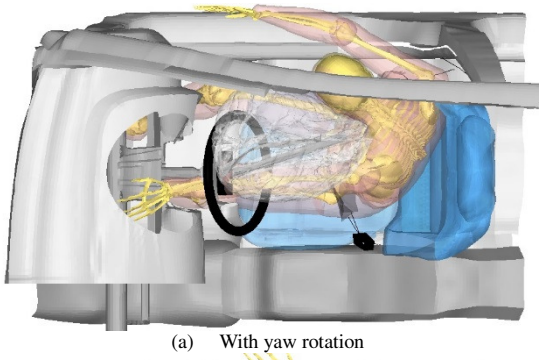

(a) With yaw rotation

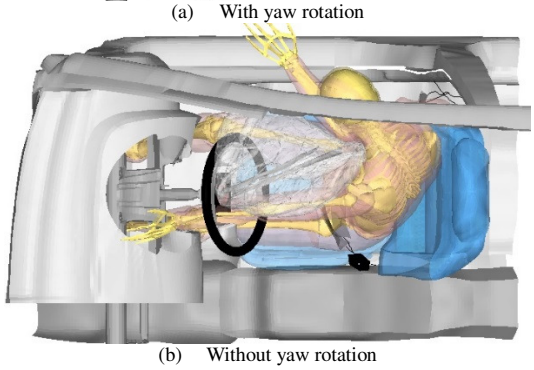

(b) Without yaw rotation

Figure 8. Maximal head lateral displacement of Thums model

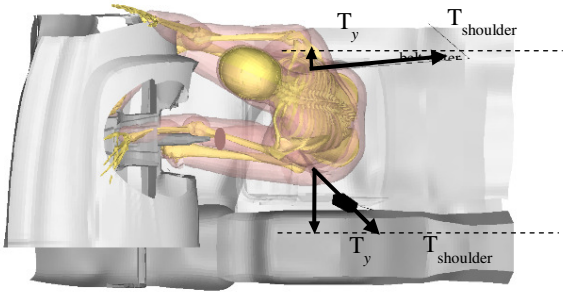

Figure 9. Shoulder belt force components

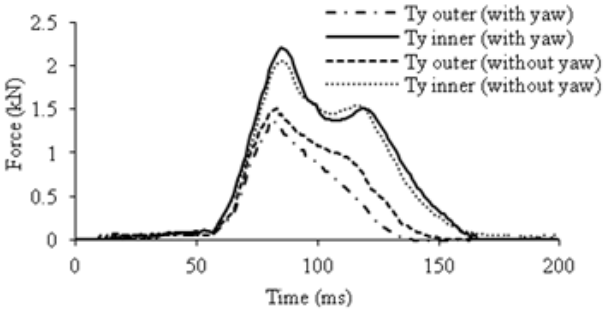

Figure 10. Shoulder belt tension in *y* direction

In addition, it was observed that the position of the seat belt anchor moved because of the yawing motion with respect to the human body, which changed the direction of resultant force applied on Thums body (Figure 11). Even though the seat belt anchor rotated, the seatbelt force was applied in the opposite direction of the Thums moving direction. As a result, it is likely that there was not a so large difference of the Thums torso motion. Another reason is that in the small

overlap crash test, during the period that shoulder belt applied force on the body of Thums seated, the angle of car rotation was still small (the car yaw angle was 8 degree at 150 ms). The anchor did not move a lot to change the lateral displacement of passenger. Therefore, the influence of yaw angle was not so large for occupant motion.

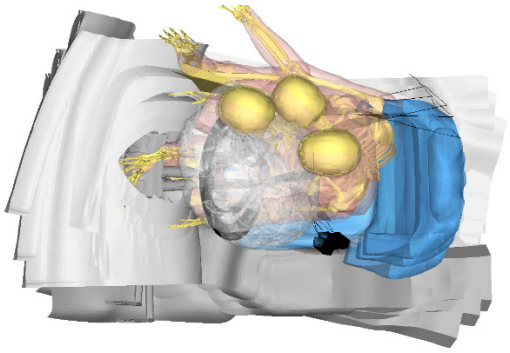

Figure 11. Track of belt anchor

4 Pitching Effect

4.1 Full frontal crash test

A full frontal crash test of a car with relatively large pitching motion was chosen to study the influence of pitching motion on occupants. The test car was minicar and impact speed was 55.6 km/h. The Hybrid III AM50th dummy was seated in the rear seat on the left hand. Several accelerometers were installed on the vehicle as shown as Figure 12.

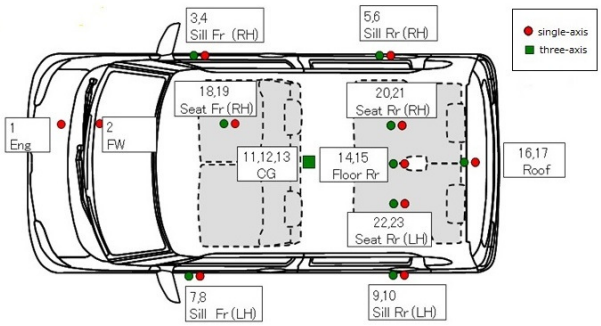

Figure 12. Location of accelerometers

4.2 Reproduction of Full Frontal crash test

The full frontal crash test was reproduced by FE simulations. We built a simplified rear seat FE model which only consisted of a rear seat and floor. The Hybrid III AM50th FE dummy model (Humanetics ver. 8.0) was seated in the seat with 3-point seatbelt. We chose the acceleration of rear side sill on the left hand to calculate the compartment rotational behavior in the crash test (Figure 13). The maximal value of longitudinal (x') acceleration reached 700 m/s^2. The pitching angle of the car was 0.175 rad at 150 ms (Figure 14).

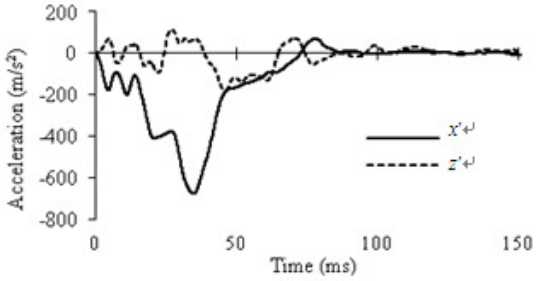

Figure 13. Acceleration of rear Side-sill on left-hand

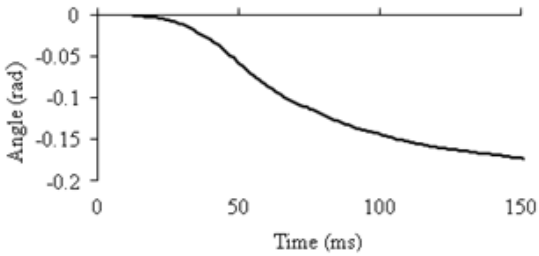

Figure 14. Pitch rotation of target car

4.2.1 The effect of pitch motion on the passengers

In order to examine the effect of pitching motion on rear seat occupant, two simulations were carried out. One was the case of full pitching angle given and the other was the case of no pitching angle given. Two cases were compared to understand how pitching rotational motion acts on the kinematic behavior of occupants.

The kinematic behavior of the dummy model was compared (Figure 15). When the vehicle pitch motion was reproduced, the forward displacement of the dummy with vehicle pitching was obviously smaller than that without vehicle pitching.

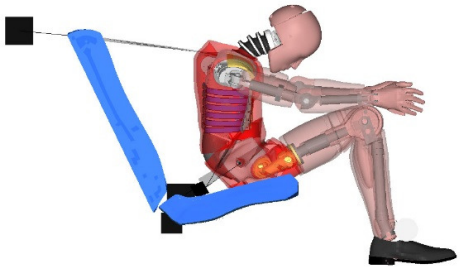

(a) With vehicle pitching rotation

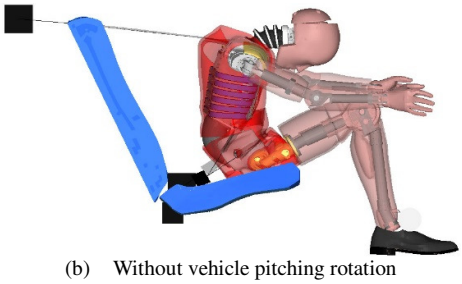

(b) Without vehicle pitching rotation

Figure 15. Kinematic behavior of dummy model with and without vehicle pitching

Shoulder belt tension force was compared. The results were shown as Figure 16. The maximal value of shoulder belt force showed up at about 60ms. When full pitch angle was given, the maximum of shoulder belt tension force was 12.8 kN. When no pitching angle given, the result showed that the maximum of shoulder belt tension force was 13.8 kN, which was 1 kN larger than the case of full pitching one. Similarly, the chest acceleration was also compared (Figure 17). When the pitching angle was given, the maximal value of chest acceleration became smaller. Therefore, according to the vehicle pitching behavior, the shoulder belt force was smaller and the occupant injury risk was lower.

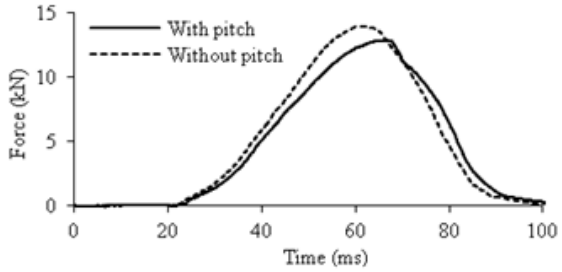

Figure 16. Shoulder belt tension force with and without vehicle pitching

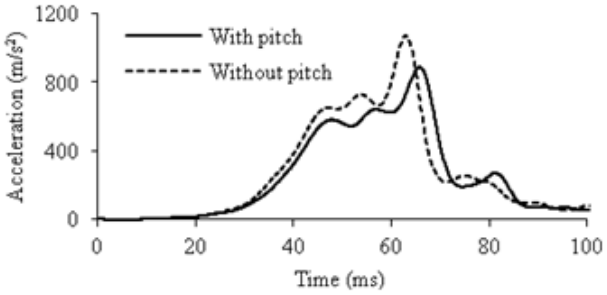

Figure 17. Chest acceleration with and without vehicle pitching

The reason for the reduction of shoulder belt tension force and chest acceleration in full pitching case can be explained from the movement of seat belt anchor. Figure 18 shows that the position of shoulder belt anchor moved forward due to the pitching motion. When the anchor moved forward, belt became longer, which resulted in the reduction of belt tension force.

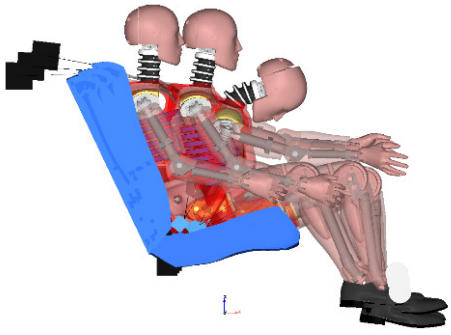

Figure 18. The seatbelt anchor movement during vehicle pitching motion

In summary, the pitching motion can reduce the force applied on chest by shoulder belts. Controlling vehicle pitch

properly can protect passengers from injury of chest. However, the part that pitching motion stops and the passenger compartment falls against ground was not researched in the paper. Large angle of pitching motion may result in a severe vertical deceleration to passenger when the rear part of the vehicle falls down to the ground. Therefore, it should be examined in the future study.

5 Conclusions

The effect of vehicle rotation on the occupant kinematics was examined by FE analysis. The results are summarized as follows:

1. The theory of providing boundary conditions to reproduce the occupant kinematics in vehicle rotation was formulated: giving the acceleration at one point in the passenger compartment and the rotation with time around this point.
2. The vehicle yawing motion in a small overlap test had a relatively small effect on the occupant kinematics.
3. The vehicle pitching motion was proved to have large effect on reducing loadings on passengers.

Acknowledgement

This research study was conducted under the grant of the High-End Foreign Experts Recruitment program of China (GDT20143600027).

References

[1] Gernot Woitsch and Wolfgang Sinz, Influence of pitching and yawing during frontal passenger vehicle crash tests on driver occupant's kinematics and injury. International Journal of Crashworthiness 2013. **18**(4): p.356–370.

Proceedings of the 11th International Forum of Automotive Traffic Safety, 2014, pp 269-277
No. ATS.2014.307

Development and Validation a Finite Element Model of the Thigh of a Chinese 50th Percentile Male

Authors: Guan-Jun Zhang[1], Long-Liang Wang[1], Xian-Ping Du[1], Yue-Qun Hu[2]
[1]*State Key Laboratory of Advanced Design and Manufacture for Vehicle Body, Hunan University, Changsha, China, 410082*
[2]*Department of Radiology, The Third Xiangya Hospital of Central South University, Changsha 410013*
E-mail: sdjywll@163.com

Abstract:

Background: Currently, crash dummies and mathematical model of human were mainly developed based on the European human statistical data. The prediction accuracy for Chinese was remained to be studied.

Objective: The current study aims to explore the modeling methods of Chinese 50th percentile human body.

Method and material: Geometry model based on the CT data from a Chinese male volunteer close to the anthropometry of 50th percentile was scaled to the 50th percentile male model according to Chinese human body statistics. The rate dependent and different property in compression and tension of cortical bone was simulated with Ls-Dyna material model. Trabecular of femoral head was divided into three parts with different material parameters to imitate the regional variations of it. The femoral head was also validated by compression loading.

Results: The result shows that the proposed model has higher accuracy and biological fidelity.

Conclusions: It is believed that the proposed method, modeling accuracy, geometry scaling and fully verified could be used to develop accurate 50th Chinese human body Finite Element (FE) model.

Keywords: Finite Element Model; Chinese 50th Percentile; Modeling Method; Thigh;

1 Introduction

Recently, with the rapid increase in economic and computational power, crash dummies and Finite Element Human Model are increasingly used in vehicle safety research [1]. Most of the dummy models are designed based on the human body of the Europe and other developed countries. However, a large number of simulation and experimental studies have shown that different regions have a different response. Only in human dimension, China 50th percentile body's physical size is about U.S. 10th percentile human body size [2]. If we used the foreign dummies and Finite Element Human Model to evaluate Chinese human injuries in crashing is clearly inaccurate, due to physical difference between Chinese and foreign body. The results can not effectively evaluate the degree injury of Chinese human body .What's more, it is not conductive to improve the capability of Chinese designing automotive safety.

The objective of this study is to explore the modeling method of Chinese 50th percentile human body. In this paper we mainly establish the thigh finite element model as an example. The geometry directly

reconstructed from the computed tomography (CT) scan data of a close to the anthropometry of 50th percentile male volunteer. The model includes accurate representations of the cortical and trabecular bone layers, flesh and skin. The material properties were rigorously defined based on the appropriate literature data [3][4].

2 Method

2.1 Geometry

The geometry reconstruction of the lower extremities was conducted by the Department of Radiology, The Third Xiangya Hospital of Central South University. A male volunteer with anthropometric characteristics (173.1 cm height and 69.7 kg weight) close to the 50th percentile male (170.8 cm/65 kg) was recruited. The geometries of the bony structures and soft tissues of the volunteer thigh region were reconstructed using the CT scanned images. Examples of these CT scans are shown in Figure 1 for thigh sections [4]. The scans obtained were manually processed using Mimics software so that the boundary of the structure could be easily recognized and three-dimensional surfaces were generated. Then the surface data was read into 3D structure design software for geometry repairing. The latest data was read into an ICEM CFD software (ICEM CFD 15.0, ANSYS Inc., USA) for mesh generation [5]. This software is efficient for meshing models with complex geometries by using the fine and high quality hex elements of the models.

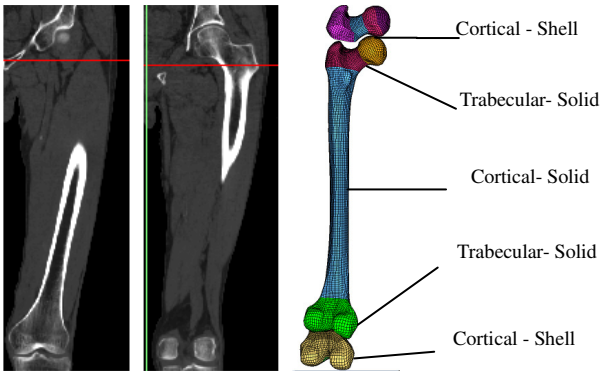

Figure 1. Example of thigh CT. Figure 2. Structure of bone models.

Two meshing approaches, structural and un-structural, were employed to achieve a good quality mesh. The structural mesh technique consists of filling the solid object with cubic blocks and projecting the outer and inner boundaries to the exterior and interior surfaces of the object ,while un-structural mesh technique were used to repair the poor quality elements by HyperMesh (Altair HyperWorks, Troy, MI). The bone models consist of the cortical and trabecular layers to represent the anatomical structure of the human bones as shown in Figure 2.

The trabecular layers in the epiphyses were modeled using solid elements surrounded by shell elements that represent the surface cortical layers (thickness of 1.0–3.0 mm) in order to keep the simulation time steps at reasonable values considering current computational power. Although the cavity inside the cortical tubular structure in diaphysis is filled with a yellow marrow, it is a fatty tissue and its contribution to high-energy impact response was deemed negligible. The cortical tubular structure was modeled using solid elements. The element size of the bony structures and most of the soft tissues (except flesh) generally ranges from 1.5 mm to 3 mm. The larger element size (~8 mm) was used for flesh, which is mostly responsible for impact energy absorption and transmission [6]. The quality of the FE model for computational reliability and stability was verified by checking the distribution of multiple element geometric parameters such as aspect ratio and element quality. The worst value of the mesh quality parameters was limited to values that would not cause model failure, taking aspect ratio ≤ 5 and the element quality≥ 0.3 for example.

Unfortunately, the CT data represents a close to the 50th percentile male so the resulting mesh needed to be scaled down to the Chinese 50th percentile based on China normal anthropometric measurements in Table 1 [7].Therefore, the

scale factor of femur was 0.978.

Table 1.Femoral parameters scaling

Paramters(mm)	FE model	Chinese 50th	scale factor
Femur length	445.41	433.01	0.972
Femur head diameter	47.10	46.17	0.980
Femoral neck diameter	24.00	23.40	0.975
Femoral shaft diameter	26.90	26.29	0.977
Femoral condyle width	81.20	79.90	0.983
Femoral condyle length	62.5	61.40	0.982

2.2Material Property

Bone is a non-linear, viscoelastic, anisotropic and inhomogeneous material [8]. It consists of two types of material: cortical and trabecular bone. Cortical bone is the external part, organized in cylindrical shaped elements called osteons composed of concentric lamellae. Variations in the mechanical properties of cortical bone can be influenced by the number, orientation and size of the osteons. Similarly, the structure of individual lamellae changes orientation in different regions of the bone. This variation gives the bone its orthotropic material properties and allows the bone to respond to optimising the usual load paths through the structure [8].

Trabecular bone is quite porous and is organized in trabecules oriented according to the direction of the physiological load. Trabecular bone is a highly anisotropic structure composed of a large number of interconnected rods, plates and beams. Moreover, the configuration of the trabecular structures is highly variable and depends on the anatomical site. The role of trabecular bone is to absorb and dissipate energy much like structural foam but it contributes relatively little to the overall strength of the bone [9].

A great deal of information can be found in the literature about mechanical and ultimate properties for cortical bones. Goldstein et al. (1993) [10] summarised many different research projects that were conducted to investigate femoral tensile, compressive and shear cortical properties according to differences in age, sex , dryness and direction of load. The values chosen are shown in Table 2.

The trabecular tissue for the femur bone has not been studied as intensely as the cortical so that the values of Young's moduli and ultimate strengths in different directions are not available.

Table 2. LSDYNA bone material properties used in the model

Bone	Density	Modulus of elasticity	Yield stress	References
Femoral head cortical 1	1800	13.5	115	
Femoral head cortical 2	1800	6	115	Yamada (1970)[15]
Femoral head cortical 3	1800	2	115	
Femoral condyle cortical	1800	13	115	Ehler et al (1970) [16][17]
Femur shaft 1	1900	17	115	
Femur head Trabecular 1	1500	0.7	9.3	
Femur head Trabecular 2	1500	0.4	9.3	Untaroiu [18]
Femur head Trabecular 3	1500	0.2	9.3	
Femoral condyle trabecular	1500	0.7	9.3	

According to literature data, the femoral head subchondral bone in the weight-bearing region has an elastic modulus

of approximately 1.5 GPa, which is lower than the corresponding value in the shaft region (6–21 GPa[12][13][14]). In addition, the elastic modulus of the cortical shell in the femoral neck region is 24% less than the shaft region. Based on these data reported in literature, the cortical bone layer of the proximal femur was divided into three small subcomponents: Femoral head cortical 1,2,3 with elastic moduli of 2, 6 and 13.5 GPa, respectively (Fig.3a). The yield stress of each respective component in the proximal femur region was scaled proportionally to its corresponding elastic modulus (13.5 GPa) and the assumed yield stress in the femoral shaft (115 MPa). Similar to the cortical bone, the stiffness and strength of femoral head trabecular bone decreases from the femoral head to the shaft region (Fig. 3b). Thus, the elastic modulus of femoral head trabecular bone was individually assigned to the Femur head Trabecular 1,2,3 with values of 0.7, 0.4, and 0.2GPa.

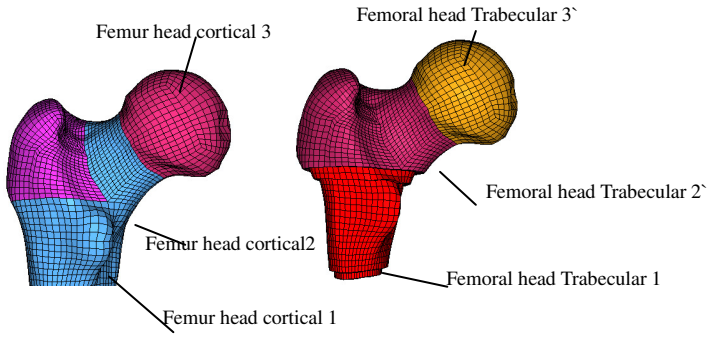

Figure 3. Proximal femur material properties of (a) cortical bone and (b) trabecular bone.

2.3 Model Validation

The thigh model was validated by comparing the FE results with quasi-static and dynamic tests in Table 3.

2.3.1 three-point bending Validation

The femur models were validated against dynamic 3-point bending tests and quasi-static for the femur in the lateral-medial direction.

Table 3. Model validations

FE model	Load type	velocity	Location/direction	References
Femur	Three-point bending (QS)	0.1m/s	Mid-shaft/AP	Yamada.（1970）[15]
Femoral shaft	Three-point bending (D)	1.2m/s	Mid-shaft/LM	Kerrigan et al.（2003）[18]
Femoral head	Compression (QS)	0.5mm/s	Head/ stance configurations	Keyaket al.[19][20]
Thigh	Three-point bending (D)	1.0m/s	Mid /LM	Kerrigan et al.（2003）[18]

AP: anterior-posterior; LM: lateral- medial; D: dynamic; QS: quasi-static.

Yamada (1970) [15]and Ehler et al（1970）[16][17]conducted three-point bending tests on wet femurs obtained from human cadavers of 20 to 39 years of age, as shown in Figure 4. To simulate this series of experiments, the

femur was along its posterior surface and the center of the anterior surface of the femoral shaft was gradually compressed at a constant velocity of 0.1 m/s to failure.

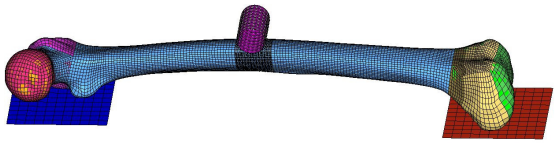

Figure 4: Simulation set-up for three-point bending test of the femur.

The femur was potted in potting cups with rollers at their distal and proximal ends. The roller part of the potting cup was placed on the support plate, and the support load was measured by a load cell placed underneath the plate. The ram had a circular tip and was rigidly attached to a servo-hydraulic test machine. The rigid ram was used for femur bending. The ram was displacement controlled at approximately 1.2 m/s, and displacement transducers were used to monitor the force-deflection response.

It is known that bones are strongest in compression, weaker in tension, and weakest in shear[21]. Therefore, long bones under bending loading usually break in tension and then, the fracture propagates in shear. While in several loading conditions femoral shaft fractures were observed in compression (due to the material model of cortical bone with similar tension and compression material properties) To avoid this situation, the element of the femur closeing to the impactor entity does not define failure.

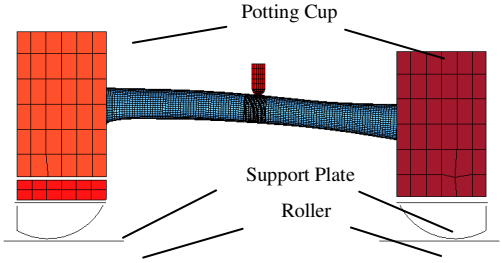

Figure 5.Schematic diagram of femur mid-shaft 3-point bending model.

2.3.2. Femoral head validation

The femoral head test was used to validate the material properties of the bone material model of the femur particularly in the area of the femoral head as well as the failure mechanism in the proximal femur. Since the physical experiments are tests to failure, the model should be able to correctly replicate the fracture locations and ultimate load experienced in the physical experiment at the initiation of fracture.

Keyak et al. (1998) conducted stance-like loading test on the femoral head and neck obtained from 10 female and eight male cadavers with an average age of 70.3 years and an age range of 52 to 92 years. One femur from each cadaver was randomly selected for investigation in a stance-like loading configuration. Force was applied to the femoral head and directed within the coronal plane at 20 degrees to the femoral shaft axis while the femoral shaft was fixed as shown in Figure 6(a). The femoral head and neck were compressed at a loading rate of 0.5 mm/s until failure. The simulation setup for the stance-like loading to the femoral head is shown in Figure 6(b). In the simulation, the femur posture was set to be the same as that used in the experiment.

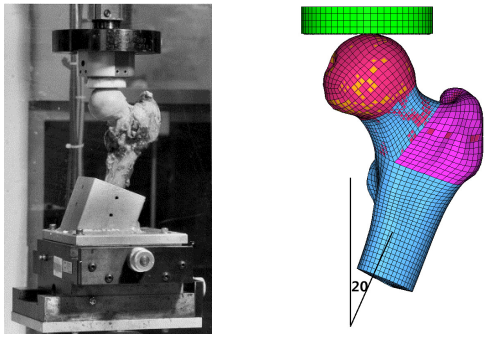

(a) Experimental setup (Keyak et al. 1998) (b) Simulation setup Figure 6: Stance-like loading to the femoral head

2.3.3 Thigh validation

Skin and muscle are viscoelastic material. In the collision, the skin and muscle mainly in compression. There was little information about muscle material, it was modelled using the viscoelastic material with solid element. The skin was used elastic-plastic material to simulate with thickness1mm, setting the modulus of elasticity of the skin 1 MPa , using the nodes overlap to connect the muscle and bone. The thigh model validation was same with femur shaft validation in Figure 7.

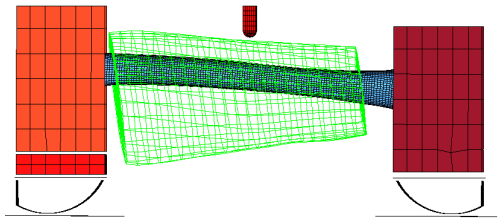

Figure 7. The FE model setup of thigh combined loading validation

3 Results

In quasi-static three-point bending test of the femur, the force–deflection response predicted by the femur model was compared with Yamada (1970) and Ehler et al（1970）. The response of the model was nearly linear and close to the corresponding test data (Figure 8) In the simulation, a bone fracture was predicted in the femoral mid-shaft at about a 3.82 kN, which was within the range of the experimental data (2.4–4.2 kN).

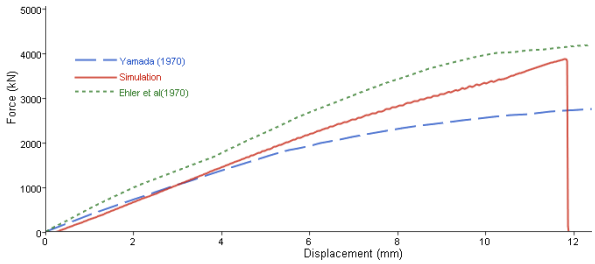

Figure 8: Force-displacement curves of quasi-static femur mid-shaft 3-point bending.

In dynamic three-point bending test of the femur, the force-deflection and moment-deflection response predicted by the femur model was compared with Kerrigan et al.（2003）The global response of the model close to the corresponding test data (Figure 9,10). The simulation results exhibited a good match with the experimental results, suggesting that the bone models can accurately reproduce the dynamic stiffness and failure properties of

the actual bones.

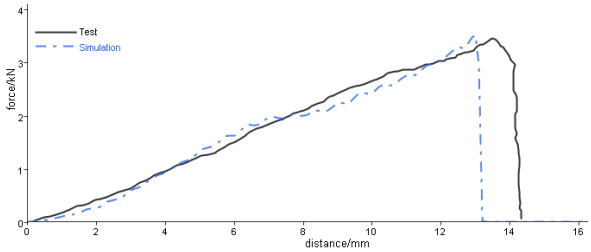

Figure 9: Force-displacement curves of dynamic femur mid-shaft 3-point bending.

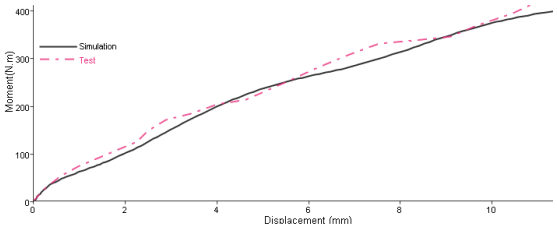

Figure 10: Moment-displacement curves of dynamic femur mid-shaft 3-point bending.

The fracture force of the femoral head and neck due to stance-like loading predicted by the model was 7.1 kN. On the other hand, the fracture force obtained experimentally from 18 specimens ranged from 3.1 to 15.0 kN with an average of 8.4±3.0 kN (Keyak et al. 1998) Figure 11.The fracture force predicted by the model was slightly lower than the average fracture force obtained experimentally but still within one standard deviation.

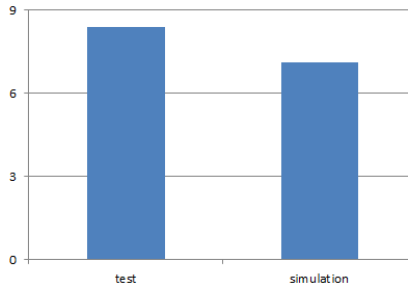

Figure 11: Fracture forces distribution in stance-like loading of the femoral head

In dynamic three-point bending test of the thigh, the force-deflection and moment-deflection response predicted by the thigh model was compared with Kerrigan et al.（2003） .The global response of the model close to the corresponding test data (Figure 12,13). The simulation results exhibited the force-deflection was slightly higher than the experiment at the beginning but still within one standard deviation. The moment-deflection had a good match with the experimental results.

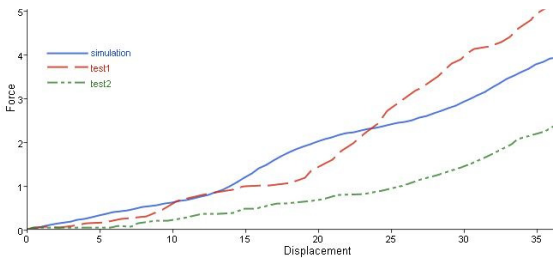

Figure 12: Force-displacement curves of dynamic thigh mid-shaft 3-point bending.

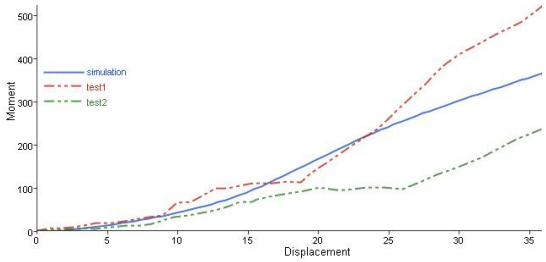

Figure 13: Moment-displacement curves of dynamic thigh mid-shaft 3-point bending.

4 Discussions

As shown in the previous sections, the FE model of the 50th percentile male replicates the forces and moment observed in the component-level tests. The FE simulation result was within the range of the physical test results although generally toward the high side of the test corridors.

As shown earlier in Figure 9,10,12 and 13, the simulation results showed that force-deflection and moment-deflection response of the femur and thigh in dynamic 3-point bending tests had a similar trending with the physical tests.

In Figure 11. The fracture force of the femur head predicted by the model was slightly lower than the average fracture force obtained experimentally but still within one standard deviation. This indicates that the FE model provides a reasonably good estimate of the location of initial fractures that will occur in crash loadings of the thigh.

As with any numerical model of a physical event there are improvements and refinements that could be made. For example, physical testing would help to provide more accurate orthotropic and rate sensitive properties of the bones. Also, the boundary conditions of the FE model should be accurated.

The most common numerical problem with the FE model involved element negative volume distortions of muscle. This often results in negative volume run terminations since elements made of the muscle material would experience very high distortions as the cortical bone failed.

In general, the FE model provides a good tool for exploring the forces and fracture mechanisms in the thigh since it accurately replicates the forces and failure patterns

5 Conclusions

An FE model of the 50th percentile male thigh was developed for use with the LS-DYNA non-linear dynamic FE software. The model features precise geometrical models of the bones including the actual cross-sectional geometry, non-linear failing material properties for the bones. The model results were compared to physical tests of femoral dynamic 3-point bending and quasi-static tests, femur head and thigh test. The comparisons showed that the FE model correctly replicates the peak forces and reactions for these component-level tests within the range of physical tests. The results of these validation experiments indicate to the authors that the FE model of the thigh will provide accurate and reliable results in exploring other types of thigh loadings that may be difficult to replicate with physical tests. The availability of a FE model provides a valuable analysis tool for understanding injuries to the thigh and designing vehicle interiors that minimise the number and severity of thigh injuries in the field. It is believed that the proposed method, modeling accuracy, geometry scaling, experiments scaling and fully verified, could be used to develop accurate 50th Chinese human body finite element (FE) model.

References

[1] Hao Ting , Wang Yong . *Application analysis of vehicle crash test and hybrid III dummy* [J] . Urban Vehicle,2003,1: 21-23 .

[2] Gordon, C. C., T. Churchill, C. E. Clauser, B. *Bradtmiller,J. T. McConville, I. Tebbetts, and R. A. Walker. 1988anthropometric survey of US army personnel: methods and summary statistics*. TR-89-044, 1989

[3] Takahashi Y, Kikuchi Y, Mori F, et al. *Advanced FE Lower Limb Model for Pedestrians* [C]. In: The 18th International Technical Conference on the Enhanced Safety of Vehicles (ESV). Nagoya, Japan: US Department of Transportation, National Highway Traffic Safety Administration, 2003, 1-14.

[4] Schuster P J, Chou C C, Prasad P, et al. *Development and Validation of A Pedestrian Lower Limb Non-linear 3-D Finite Element Model* [J]. Stapp Car Crash J, 2000. 44: 315-334.

[5] Gayzik, F. S., D. Moreno, C. Greer, S. Wuertzer, R.Martin, and J. D. Stitzel. *Development of a full body CADdataset for computational modeling:a multi-modalityapproach*.Ann. Biomed. Eng.39(10):2568–2583, 2011.

[6] Silvestri C, Ray MH. *Development of a finite element model of the kneethigh-hip of a 50th percentile male including ligaments and muscles.International Journal of Crashworthiness*, 2009, 14(2):215-229

[7] Snehalatha C, Viswanathan V, Ramachandran A. *Cutoff values for normal anthropometric variables in Asian Indian adults*[J]. Diabetes care, 2003, 26(5): 1380-1384.

[8] C.H. Turner and D.B. Burr,*Basic biomechanical measurement of bone: a tutorial.* Bone 14 (1993) pp. 595–608.C

[9] ICB Dent.[Internet],Mechanical properties of bone,2005. Available at http://www.feppd.org/ICB-Dent/campus/biomechanicsin dentistry/ldvdata/mech/basicbone.htm.

[10] S.A. Goldstein, E. Frankenburg, and J. Kuhn,*Biomechanics of bone,in Accidental Injury: Biomechanics and Prevention*,A.M. Nahum and J.W. Melvin, eds., Springer-Verlag, New York, NY, 1993, pp. 198–223.(accessed February 2008)

[11] T.M. Keaveny and W.C. Hayes, *Mechanical properties of cortical and trabecular bone*,in Bone Volume 7,B.K.Hall,ed., CRC Press, Boca Raton, FL, 1993, pp. 285–345.

[12] Keller, T. S., Z. Mao, and D. M. Spengler. *Young's modulus, bending strength, and tissue physical properties of human compact bone*.J. Orthop. Res.8:592–603, 1990.

[13] Untaroiu, C. D. *Development and Validation of a Finite Element Model of Human Lower Limb. PhD Dissertation*, University of Virginia, 2005.

[14] Untaroiu, C., K. Darvish, J. Crandall, B. Deng, and J. T.Wang. *A finite element model of the lower limb for simulating pedestrian impacts*. Stapp Car Crash J.49:157–181,2005.

[15] Yamada H. *Strength of Biological Materials*. Baltimore: The Williams & Wilkins Company. 1970, 19-280

[16] Ehler V E, Losche H. *Die Menschliche Tibia Unter Biegebelastung. Beitr*. Orthop. 1970. 17(5): 291-304

[17] Ehler V E, Losche H. *Biegeversuche am Menschlichen Femur. Beitr. Orthop.*, 1970. 17(5): 857-867

[18] Kerrigan J R, Bhalla K S, Madeley N J, et al. *Experiments for Establishing Pedestrian-Impact Lower Limb Injury Criteria. In: SAE Technical.* Paper 150 Number 2003-01-0895. Warrendale, PA: 2003

[19] Keyak, J. H., S. A. Rossi, K. A. Jones, C. M. Les, and H.B. Skinner. *Prediction of fracture location in the proximal femur using finite element models.*Med. Eng. Phys.23:657–664, 2001.

[20] Keyak, J. H., S. A. Rossi, K. A. Jones, and H. B. Skinner. *Prediction of femoral fracture load using automated finite element modeling.J. Biomech*.31:125–133, 1998.

[21] N. Olivetti, *Development of a Hill's model of the human knee-thigh-hip region for frontal car crash simulations* ,Master's thesis, Politecnico di Milano, Milano, Italy, 2006.

Proceedings of the 11th International Forum of Automotive Traffic Safety, 2014, pp 278-283
No. ATS.2014.308

Braking Effects on Occupant Kinematics and Injury during the Full Frontal Impact simulation using Human Model

Chengyue JIANG[1], Xi LIU[1], Yuanzhi HU[1],Shugang XIE[2], Hongyun LI[2]
[1] *Chongqing University of Technology, Chongqing, China, 400050*
[2] *China Automotive Technology and Research Center, Tianjin, China, 300300*
E-mail: Jiangchengyue@cqut.edu.cn

Abstract:

Background: Advanced Driver Assistance Systems (ADAS) in combination with the updated passive safety systems is the key to reduce future crash severity and improve the occupant protection performance. The autonomous braking system is able to reduce crash speeds and the crash severity levels significantly. Occupant kinematics would be changed due to certain pre-impact braking, which has not been considered in most in-lab crash tests.

Objective: This study aims to assess the effects of different pre-impact braking events on the occupant kinematics, as well as the injury possibility, by using full frontal impact simulation.

Method: MADYMO simulation and validation of a 50km/h frontal crash test were carried out for the following detailed investigation of dummy forward displacements due to pre-impact braking. The influences of different pre-impact scenarios (with the initial velocity of 80km/h, all leading to equal 50km/h before the crash phase), are considered in terms of vehicle accelerations. Occupant kinematics and potential injury possibility under different braking load cases were analyzed in the study by introducing the human body model. The evaluation is mainly concerning about dummy kinematics as well as contact risk between the dummy and vehicle interior. Besides, the study reviews the contribution of the human model in comparison with the dummy model and discusses the potential of using the human model for detailed simulation.

Results: The result shows that the occupant kinematics of the impact with pre-impact braking is different with that of the C-NCAP 50km/h frontal impact. This difference makes the dummy have high risk of airbag flapping, and the belt retractor has less efficiency in pretensioning (the maximum pull-in amount was reduced about 13mm).

Conclusions: This study recommends changes to occupant restraint systems to fit requirements of occupant forward displacement caused by pre-impact braking. The in-lab crash test considering emergency braking prior to the impact is highly recommended as well for detailed study, for further improvement of the occupant protection performance.

Keywords: Braking effect, Occupant kinematic, MADYMO simulation, Human model

1 Introduction

Pre-crash braking systems are being employed in vehicles on the market currently, and the performance of them is being improved with the availability of more accurate sensor technology and risk estimation algorithms[1]. Autonomous braking systems are able to reduce collision speeds, and therefore severity levels significantly. The Advanced Driver Assistance Systems (ADAS) in combination with the updated passive safety systems is the key to reduce future crash severity and improve the occupant protection performance[2]. The integrated safety is already implemented in the development of new cars, but so far the conventional crash tests do not take into consideration specific impacts of pre-crash braking. As a consequence, the influences of dipping of the vehicle front and possible pre-crash displacements of the

occupants have not yet been considered in these crash tests[1,3]. The posture of the occupants prior to the possibly unavoidable crash is known to have a large effect on the injury reducing performance of the restraint system [4]. Ejima et al. performed a series of tests with volunteer seated on rigid seats, restrained by a three-point belt system and subjected to a 600 ms 0.8 G constant deceleration. For a tensed volunteer, kinematic figures indicate that head forward displacement was in the order of 100 mm at 200 ms after impact, while T1 forward displacement was in the order of 25 mm and hip forward displacement around 10 mm. For a relaxed occupant restrained by a lap belt only, the head displacement was in the order of 600 mm at 600 ms after impact with T1 displacement around 400 mm[5].

Integrated vehicle safety is also a challenge for simulation models. Because the restraint systems are developed with different crash tests and simulations, which usually do not take into consideration the effect of the pre-crash braking [6]. Furthermore, a reproducible assessment of the additional benefit of vehicle safety systems, which prepare the occupants for the imminent impact, is not possible [3].

Additionally, most crash tests and simulations are evaluated with Hybrid III dummy models. Several studies have suggested that the Hybrid III dummy is not a good human surrogate in pre-crash maneuvers. Subsequently, the applicability of simulation models based on the Hybrid III dummy may be limited for studying pre-crash maneuvers [7].

Today, human models are frequently used for improvements in occupant and pedestrian protection[6]. In this study, a human model from the MADYMO database is introduced into a validated MADYMO simulation model, for the kinematics comparison and further detailed study. The difference between Hybrid III dummy and Human model was analyzed. To assess the effects of different pre-braking events on the occupant kinematics, as well as the injury possibility, different pre-crash scenarios with the initial speed at 80km/h, all leading to equal closing speeds (50km/h, as that of the C-NCAP full frontal impact), are introduced for the following occupant kinematics analysis and injury evaluation.

2 Method

For this study, a MADYMO model correlated with a 50km/h full frontal crash test was introduced. For further detailed analysis of the effects of different pre-braking events on the occupant kinematics and the injury possibility. The 50% Hybrid III dummy was replaced by the human model from the MADYMO dummy database, as shown in Figure 1.

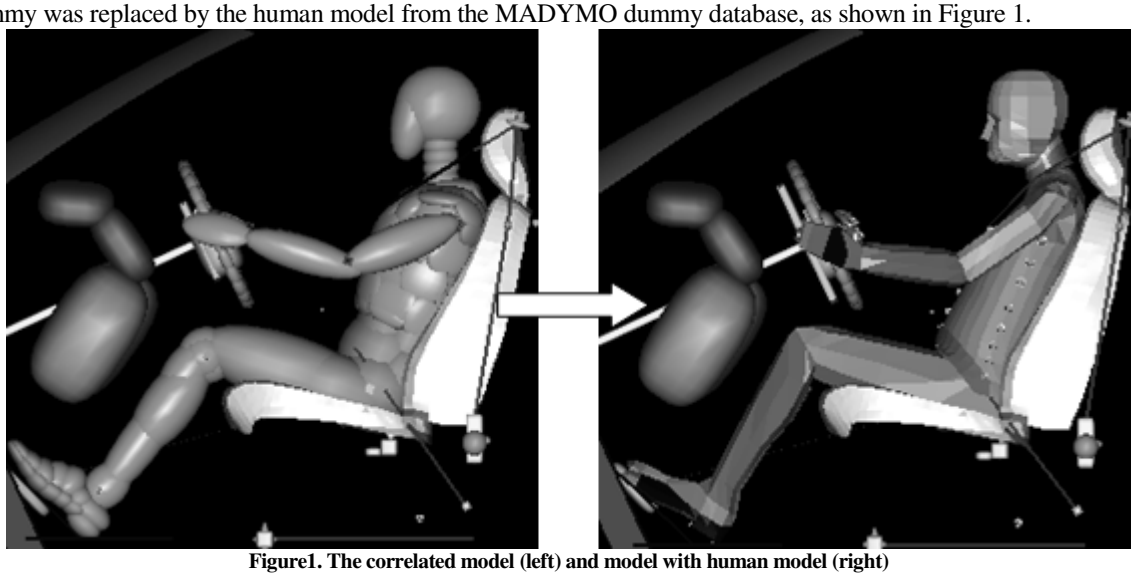

Figure1. The correlated model (left) and model with human model (right)

The shoulder belt forces output from the simulations indicate that the forces form both simulations correlate well with that of the test, while the peak lap belt force from the model with human model is less than that of the test, as shown in Figure 2 below. This is mainly due to the abdomen's deformation of the human model.

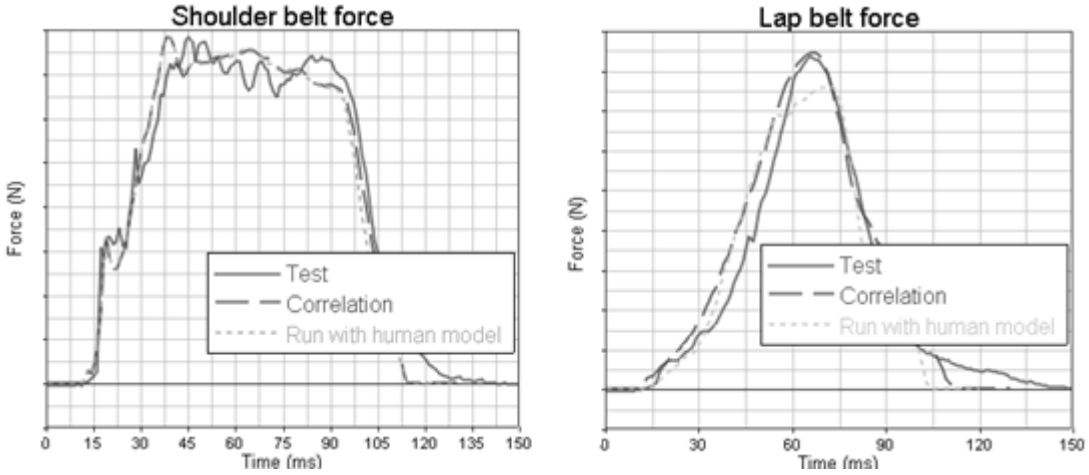

Figure2. Shoulder belt force comparison (left) and lap belt force comparison (right)

The dummy kinematics comparison is shown in Figure 3, which indicates that head displacement of the human model is larger than that of the Hybrid III dummy before the contact with the airbag. The simulations show that human dummy's spine and neck are more flexible than those of an Hybrid III dummy, which correlates well with the finding of the research [8].

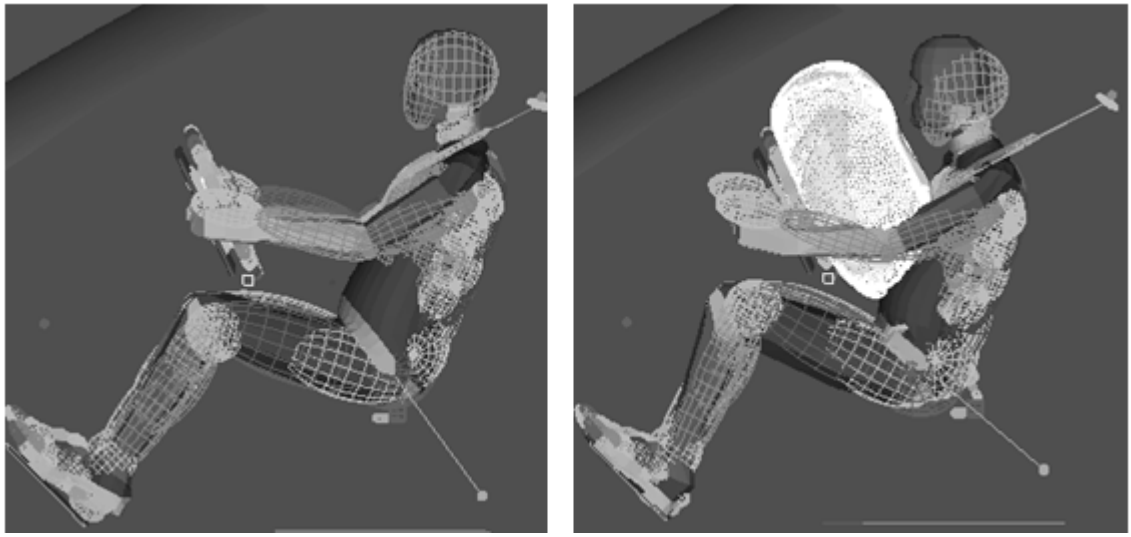

Figure3. Initial positions (left) and kinematics comparison (right)

The MADYMO model with the human model above will be used for the following detailed study on pre-crash braking effects on occupant kinematics.

Vehicle braking deceleration cannot exceed the road coefficient of friction and is accepted to be in the interval of 1.0"g" to 1.3"g" in very rare instances [8]. In this study, accelerations in X direction (without vehicle pitching), were applied on the occupant compartment model to evaluate vehicle braking effects. Two pulses （1: a brake assist system with

modulated braking (BAS) and 2: an autonomous braking system (AUT)) approximating possible responses from two types of pre-crash braking systems were introduced for following analysis as in the research of [1]. Both braking pulses assume decelerations from 80 km/h to 50km/h, the pre-impact braking pulses and the total velocity changes are shown in Figure 4.

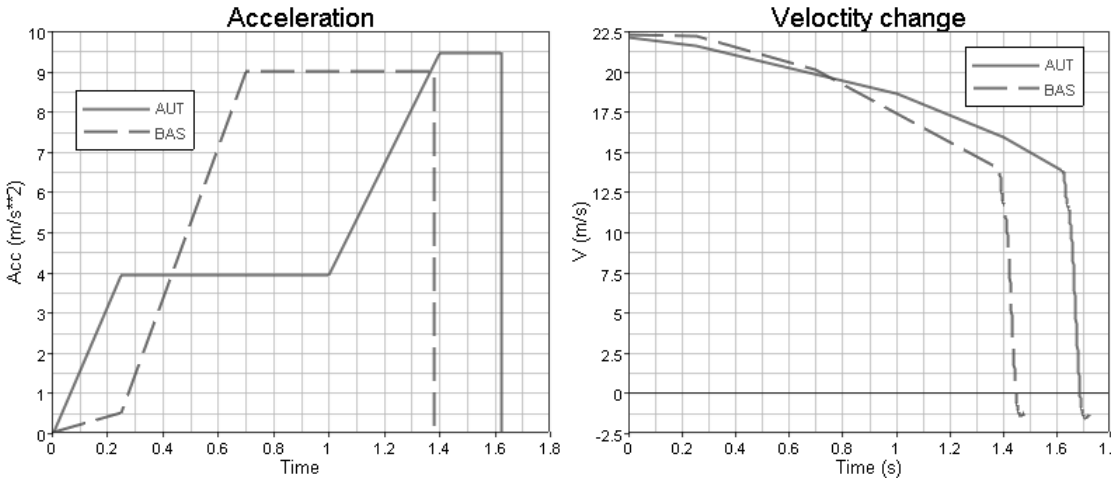

Figure4. Pre-impact braking pulses (left) the total velocity changes (right)

where BAS is the deceleration profile arising from a Brake Assist System in which the driver applied the brake while the system applies the amount of modulated braking necessary to prevent a collision with an object in front. AUT is the deceleration profile from an autonomous braking system that first applies partial braking at 4 m/s2, then full braking to assure collision avoidance.

3 Result s

The pre-impact braking pulses, together with the pulse of a C-NCAP 50FF test , were used as the input of the occupant compartment model. The occupant kinematics from the simulation show that there is a high risk of airbag flapping for the AUT simulation, in which the maximum head forward displacement due to the pre-impact braking was around 110mm, see Figure 5 left. The risk of airbag flapping is less for the BAS simulation, see Figure 5 right.

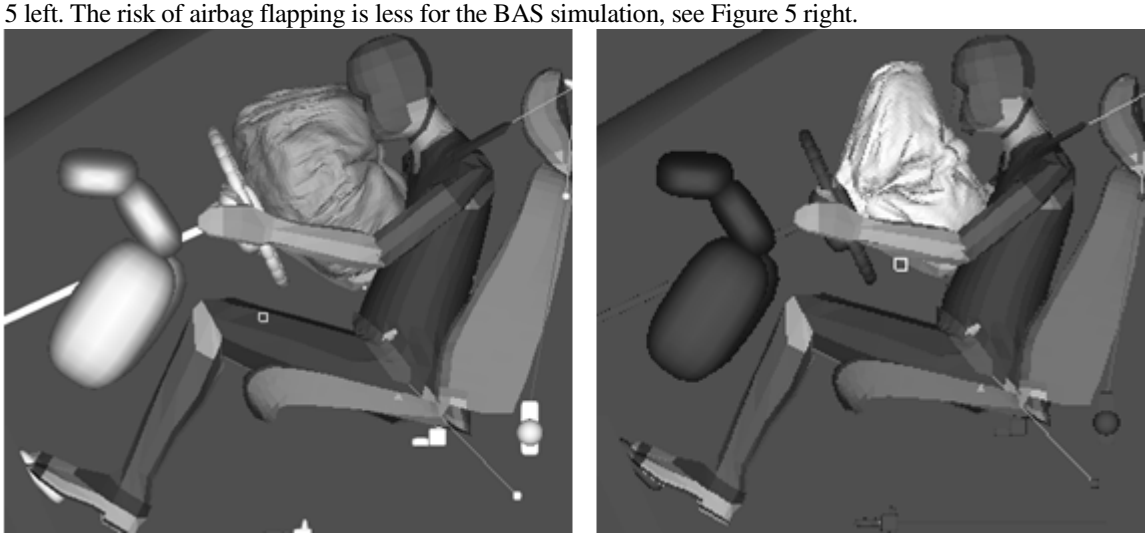

Figure5. dummy model kinematics of AUT simulation (left) and BAS simulation (right)

The pull-in length due to retractor's pretensioning of the original model is 68.7mm, while the length of the BAS model is 55.8mm and the length of the AUT model is 62.0mm, see figure below. The result indicate the pretensioner's efficiency of the impact with pre-impact braking is less than that of the original impact.

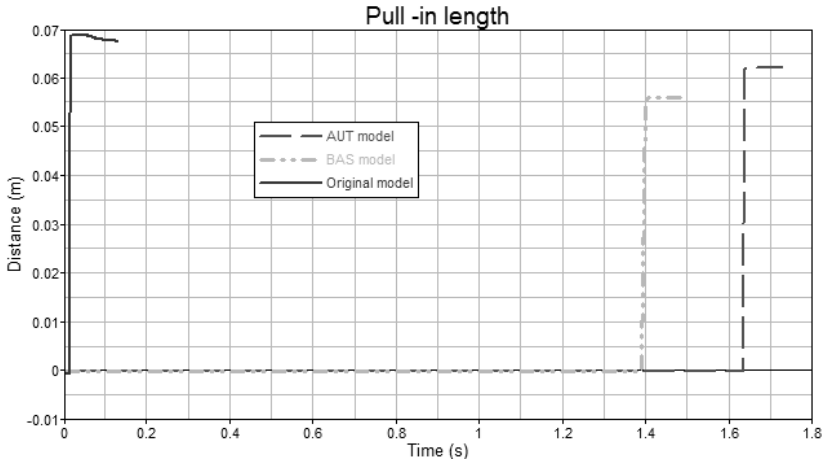

Figure6. Retractor's pull-in lengths of different models

The difference above is mainly caused by the occupant's forward displacements during the pre-impact braking phase. Comparing the should belt forces between AUT model and BAS model, it can be seen that both shoulder belt forces increase during the pre-impact phase, and the maximum force is under 200N, as shown in Figure 7.

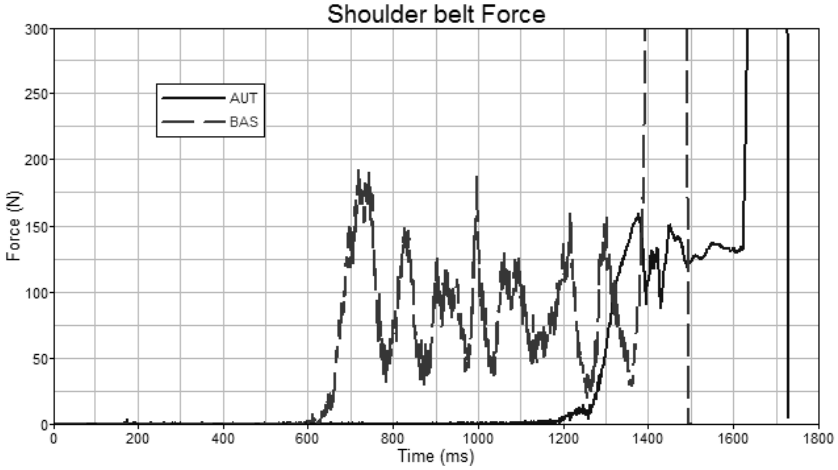

Figure7. Shoulder belt force during the pre-impact phase

The simulation result also indicates that there is little risk of hard contact between head and steering wheel, as shown in figure below.

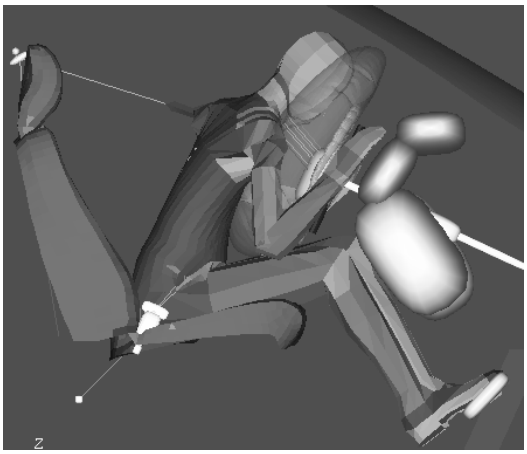

Figure8. No hard contact between head and steering wheel in the simulations

4 Conclusions

Based on the above study, the following conclusions are drawn:

1). Human dummy 's spine and neck are more flexible than those of the Hybrid III dummy model;

2). Pre-braking events have large effect on the occupant kinematics, especial for the head displacement;

3). Changes to occupant restraint systems to fit requirements of occupant forward displacement caused by pre-impact braking are highly recommended;

4). Further detailed research about in-lab crash test considering autonomous pre-impact braking prior to the impact is highly recommended as well;

Acknowledgement

This study is sponsored by Chongqing Science and Technology Expert Training Program (cstc2013kjrc-qnrc60002) and 2013 Program for Innovation Team Building at Institutions of Higher Education in Chongqing (KJTD201319). The authors would like to thank TNO China for offering the MADYMO education license as well.

References

[1] Lex, R. Effect of various pre-crash braking strategies on simulated human kinematic response with varying levels of driver attention. in Proc. 22nd ESV. 2011. Washington, USA.

[2] Gernot, W. and Wolfgang, S. Influences of pre-crash braking induced dummy – Forward displacements on dummy behaviour during EuroNCAP frontal crashtest, Accident Analysis & Prevention 2014. Volume 62, P.268–275.

[3] Ruecker, P. Crash Tests with Automatic Pre-Crash Braking Cars. SAE Technical Paper 2013-01-0200.

[4] Lex, R. and Jasper, P. Driver head displacement during (automatic) vehicle braking tests with varying levels of distraction. in Proc. 23rd ESV. 2013. Seoul, Republic of Korea.

[5] Ejima, S. Zama, Y. Ono, K. Kaneoka, K, Shiina, I. and Asada H. Prediction of pre-impact occupant kinematic behaviour based on the muscle activity during frontal collision, in Proc. 21st ESV. 2009. Stuttgart, Germany.

[6] Stefan, K . and Wolfgang, S. Detailed analysis of 3d occupant kinematics and muscle activity during the pre-crash phase as basis for human modeling based on sled tests. in Proc. 22nd ESV. 2011. Washington, USA.

[7] Craig, G. and David, V. Motorized shoulder belt tensioning: modeling and performance for a diverse occupant population, in Proc. of the 2008 SAE World Congress, SAE 2008-01-0516.

[8] Bastien, C. Investigation into injuries of Out- of-Position (OoP) posture occupants and their implications in active safety measures, in Proc. of ICRASH. 2010. Washington, USA.

Proceedings of the 11th International Forum of Automotive Traffic Safety, 2014, pp 284- 292
No. ATS.2014.309

Model Development of Grid Points Meshing in Pedestrian Headform Protection Simulation Based on HyperMesh

Zhao Rutao[1], Zhu Xichan[1], Dong Liping[1], Zheng Zudan[2], Wu Bin[2], Song Yalan[1], Ma Zhixiong[1]

[1]*School of Automotive Studies, Tongji University, Shanghai, China, 201804*

[2] *Shanghai Motor Vehicle Inspection Center, Shanghai, China, 201804*

Email:zrthit@163.com

Abstract

***Background*:** As the implementation of the pedestrian protection test procedures in Euro NCAP (V6.1), head collision grid point evaluation method has been adopted, which requires manufacturers to provide vehicle collision HIC. Considering the cost of real vehicle tests, car manufacturers usually adopt the method of computer simulation to get HIC of predictable grid point. So manufacturers should have effective means of simulation. Most existed pedestrian head simulation systems can finish pre-analysis simulation, but these are not applicative for Euro NCAP (V6.1). So developing new software based on the grid meshing evaluation method and realizing the automation of the head crash simulation calculation are of great importance for car manufacturers.

***Objective*:** The purpose of this paper is to study the automation of pre-treatment process such as head collision point meshing and post-treatment process like calculation using LS-Dyna to solve the automation, calculating HIC value and their scores, which can be used as simulation data for the Euro NCAP pedestrian protection evaluation provide head crash.

***Method and Material*:** Based on Euro NCAP (V6.1) pedestrian protection requirements, using Tcl/tk language to programme in HyperMesh10.0 for secondary development. Develop the automation method of vehicle front side reference line, WAD line and grid points meshing. After head positioning, export KEY file, which can be used for submitting the file to calculate and analyze the result using DOS batch program. Then, based on secondary development of HyperGraph, get HIC values and collision point scores.

***Results*:** The software mainly includes two major functional modules and three big functions. The preprocessing module is to realize the automatic pretreatment of pedestrian head collision finite element model, including generating side reference line, WAD line and the grid points. Computational analysis module has two functions, including automatic calculation of KEY documents and calculation of HIC value and the scores. Through the automation processing of the simulation analysis, the efficiency of the simulation is improved.

***Conclusions*:** The conclusion is that the length of the belt pulled out from retractor is the main factor of the consistency of the child restraint system test and we provide the foundation for compulsory certification regulation for child restraint system.

Compiled by Tcl\tk language, the interface is integraded into the Utility in HyperMesh option in the User panel, which highly improves the efficiency of the simulation.

Keywords: Pedestrain Headform Protection; Secondary Developemt of HyperMesh; Grid Meshing

基于HyperMesh的行人头部碰撞仿真网格划分模块开发

赵汝涛[1]，朱西产[1]，董丽萍[1]，郑祖丹[2]，吴斌[2]，宋亚蓝[1]，马志雄[1]

[1]*同济大学汽车学院，上海，中国，201804*

[2]*上海机动车检测中心，上海，中国，201804*

E-mail：zrthit@163.com

摘要

研究背景：随着 Euro NCAP(V6.1)行人保护试验规程的实施，头部碰撞网格点评价方法已被采用。行人头部网格点评价方法中要求制造商提供被测试车辆数十个目标网格点的碰撞 HIC 值。考虑到实车试验的成本问题，汽车制造商通常采用计算机仿真的方法来得到可预测 HIC 值网格点的 HIC 值，这要求制造商要具备高效的

上海市科学技术委员会科研计划项目（编号 12DZ2293901）资助

仿真手段。目前大多数行人头部仿真前处理软件或系统能完成碰撞区域划分，但这些软件或系统还是针对 Euro NCAP(V6.1)之前的评价规程，无法满足新的试验规程的需求。因此基于头部碰撞网格点新评价方法，开发行人头部保护软件，实现头部碰撞仿真的自动化计算对于汽车制造商具有重要的意义。

目的：本文旨在研究头部碰撞网格点划分等前处理过程和 LS-Dyna 计算求解后处理过程的自动化，实现 HIC 值及碰撞点得分计算，为 Euro NCAP 行人保护评价提供头部碰撞仿真数据。

方法和材料：基于 Euro NCAP(V6.1)中车辆行人头部保护性能的网格点评价方法，采用 Tcl\tk 语言对 HyperMesh10.0 进行二次开发，通过对车辆前端侧参考线、前端包络线、网格点划分的机理研究，提出车辆前端参考线、包络线和网格点的仿真自动划分方法。头部定位导出 KEY 文件后，利用 DOS 批处理程序，完成计算文件的自动提交计算及批量结果分析。再通过对 HyperGraph 的二次开发，实现 HIC 值和碰撞点得分的自动计算功能。

结果：该软件主要包含了两大功能模块，三大功能，即有限元前处理模块实现行人头部碰撞模型的自动前处理功能（自动生成侧参考线、WAD 线和网格点划分标记）、计算分析模块实现 KEY 文件的自动批量提交计算功能和自动计算仿真试验点的 HIC 值及分数的功能。通过将仿真分析流程中的三大模块都进行自动化处理，以提高仿真的效率。

结论：本文通过深入研究 Euro NCAP(V6.1)中的行人头部碰撞试验规程和评分原则，按照该规程的具体试验步骤及试验要求，研究并提出行人头部保护仿真的车辆前端侧参考线、车辆前端包络线、网格点划分自动化前处理机理和方法。通过 Tcl\tk 语言进行编译，将有限元前处理和批量后处理分析功能模块集成到 HyperMesh 中 Utility 选项中的 User 面板，实现行人头部保护碰撞仿真的自动化，极大地提高了仿真的效率。

关键词：行人头部保护；HyperMesh 二次开发；网格划分

1 引言

随着 Euro NCAP(V6.1)行人保护试验规程的实施，头部碰撞网格点评价方法已被采用。行人头部网格点评价方法中要求制造商提供被测试车辆数十个目标网格点的碰撞 HIC 值，这要求制造商要具备高效的仿真手段[1,2]。目前大多数行人头部仿真前处理软件或系统能完成碰撞区域划分，但这些软件或系统还是针对 Euro NCAP(V6.1)之前的评价规程，无法满足新的试验规程的需求[3]。

根据 Euro NCAP(V6.1)行人保护试验规程，头部碰撞仿真前处理的主要步骤包括：生成车辆前端侧参考线、前端包络线、网格点划分，后处理主要包括 LS-Dyna 计算。本文基于 HyperMesh 软件，采用 Tcl\tk 语言对其进行二次开发，研究并提出行人头部碰撞仿真中自动划分参考线、包络线和网格点划分及标记的前处理及与 LS-Dyna 相连接的批量后处理模块，设计流程图如下图 1 所示。

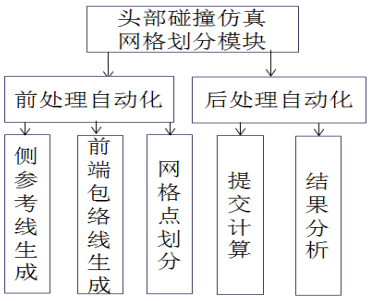

Figure 1. Flow chart of module design

图 1. 模组设计流程图

2 侧参考线生成

2.1 Euro NCAP 侧参考线要求

Euro NCAP 针对侧参考线的规定为：用长 700mm，在水平铅垂面内与水平方向成 45° 角的直尺沿着车辆

前部结构外表面移动，直尺与车辆前部结构接触的最高点形成的轨迹，即侧参考线[4]，如图 2。

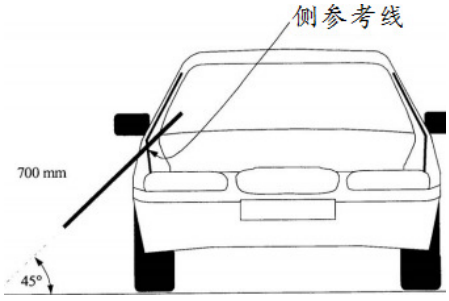

Figure 2. Euro NCAP side reference line diagram

图 2. 欧洲 NCAP 侧参考线

2.2 创建侧参考线过程

1）创建长度为 700mm 的几何切线：根据 Euro NCAP，在画车辆侧参考线时，主要经过的部件包括翼子板和 A 柱。通过 HyperMesh 中 HWAT 命令集合中的 BoundingBox 命令生成翼子板和 A 柱的包络矩形，即将集合中所有单元包含之内的最小矩形，得到侧参考线部件集合的边界坐标值，根据坐标值确定基点，在车辆的横向垂直平面内创建一个向内倾斜 45° 的线段，该线是创建侧面参考线所使用的几何切线。

2）生成切点：通过几何切线作横向垂直平面（yz 平面），切翼子板和 A 柱生成截面线。因为部件结构并非连续平面或者曲面，所以在生成截面线时，会出现多段线段。这需要在多条截面线段中筛选出距离几何切线最短的点。比较多段截面线与直线之间的最短距离值，找到最小值，继而锁定最短距离点。

3）平移几何切线：以一定偏移量沿 x 轴方向平移直线（保持直线始终在 yz），按同样的方法找到平移后的切点，直到切线超出前端结构集合的包络矩形的范围。

4）将所有的切点连接成线。以上步骤在 HyperMesh 中的显示如图 3 所示：

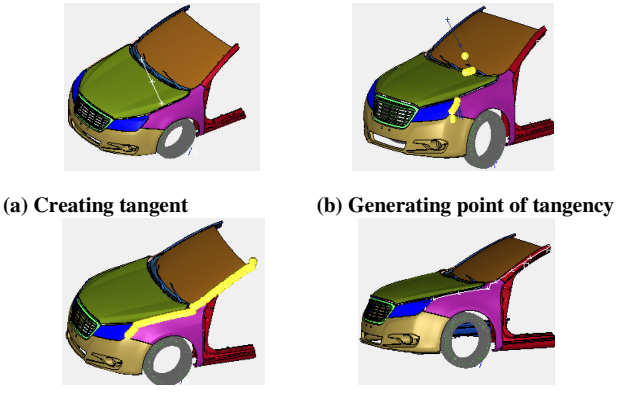

(a) Creating tangent **(b) Generating point of tangency**

(c) Moving tangent **(d) Creating line**

Figure 3. Process of creating side reference line

图 3. 创建侧参考线的过程

3 前端包络线生成

3.1 Euro NCAP 前端包络线要求

Euro NCAP 试验规程中，车辆前端包络线（ WAD 线）划分是采用柔性卷尺：用一条一定长度的柔性卷尺与 xz 平面保持平行并且将软绳绷紧紧贴车辆的车辆前端结构，保持柔性卷尺的下端垂直于水平面并且端部

与水平面相接触，柔性卷尺的上端与发动机罩表面相接触，从左到右扫掠车辆前端的部件，柔性卷尺上端与车辆前部结构上表面接触点的几何迹线则为相应的包络线，在新版的 Euro NCAP 试验规程中，主要的包络线包括 WAD1000mm，WAD1500mm，WAD1700mm 和 WAD2100mm[4]。如图 4 所示：

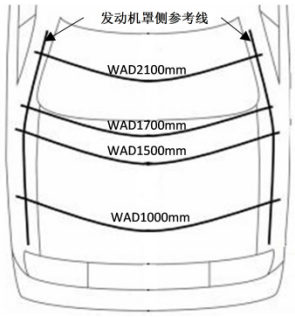

Figure 4. Euro NCAP wrap around distance line diagram

图 4. 欧洲 NCAP 包络线图

3.2 创建前端包络线过程

HyperMesh 中很难模拟柔性卷尺贴合车辆前端部件，只能采用近似的方法处理。其主体思想是通过一网格面与发动机罩前端部件曲面贴合生成切点来模拟柔性卷尺。

1）创建 WAD 线相关结构部件的集合：WAD 线相关的结构部件包括保险杠、前大灯、发动机罩、风挡玻璃和 A 柱。在进行 WAD 线划线程序前，需要创建这些结构的集合。

2）创建地面参考面：根据 Euro NCAP 规定划分 WAD 线时，柔性卷尺一段必须垂直于地面，且始终保持与地面接触。在自动划分 WAD 线时，利用 BoundingBox 获取模型的车辆尺寸（长、宽、高），根据车辆尺寸，在车辆最低处生成四个边角点，利用这四个点创建地面参考面。

3）创建标尺：标尺在自动划分 WAD 线过程中的作用类似于实际划分 WAD 线时的柔性卷尺，但是标尺最初状态并非一条弯曲的线段，而是由网格单元构成的单元面，同时赋予标尺厚度属性。

4）包络线算法：包络线算法是 WAD 线生成的关键。其核心是通过穿透检查确定标尺与车辆前端结构部件的近似切点。穿透检查保证了标尺可以较为准确地贴合车辆前端结构部件外部轮廓。

包络线算法主要包括两部分：平移算法和转动算法。

平移算法主要是因为标尺距离车辆前端还有一定的距离，不能直接求得两者之间的切点，因此建立平移部分循环，即判断两者之间是否存在穿透，如果没有，则将标尺向前移动 1mm；如果首次穿透，则记录下该点的 ID，并将穿透点以下的单元删除，以消除已穿透单元对后续穿透判断的影响。接下来将剩余的标尺单元沿着发生穿透单元的法向移动一段距离，移动的距离为穿透长度，该步操作的目的同样是保证本次穿透不影响下一次穿透判断。

转动算法主要是因为车辆前端结构的轮廓为曲线，无法直接用平移算法获得切点。先以平移算法找出的首个切点为基点，转动标尺，角度为 1°；再判断转动后的标尺是否与车辆的前端结构发生穿透，如果穿透，记录穿透点 ID，该点为新穿透节点，删除该点以下单元，再将标尺沿着穿透单元的法向移动一段距离，移动距离为穿透长度，直至穿透量为零；如果没有穿透，则继续转动标尺，直至穿透。在整个包络线算法中，需要一个循环控制判断，即节点位置判断。循环继续的条件是产生的节点位于发动机罩前缘点下方。

5）连接各节点，形成发动机罩前端各部件轮廓线。将轮廓线的最前端即包络线算法中求得的最前端切点投影到地面参考面上，并将最前端点与其投影点连接成线，最后将轮廓线与该线连接。

6）在投影线上求距离地面分别为 1000mm、1500mm、1700mm、2100mm 点。

7）移动标尺：WAD 线的生成，主要是通过柔性卷尺贴合车辆前端结构沿着 y 轴方向移动，柔性卷尺上端与车辆前部结构上表面接触点的几何迹线为相应的包络线，移动的距离应不小于 100mm。因此，在自动前处理仿真中，移动模拟柔性卷尺的标尺，每次移动距离为 100mm。

8）连点成线：将利用包络线算法生成对应 WAD 线的组成点按照顺序连接成线段，形成车辆一侧 WAD 线，将该线沿着纵向中心面对称，与原始一侧 WAD 线连接成一条完整的 WAD 线。

9）删除辅助的面和线：利用 WAD 线生成子模块，对模型进行 WAD 线自动生成，其实现的过程和结果如图 5 所示。

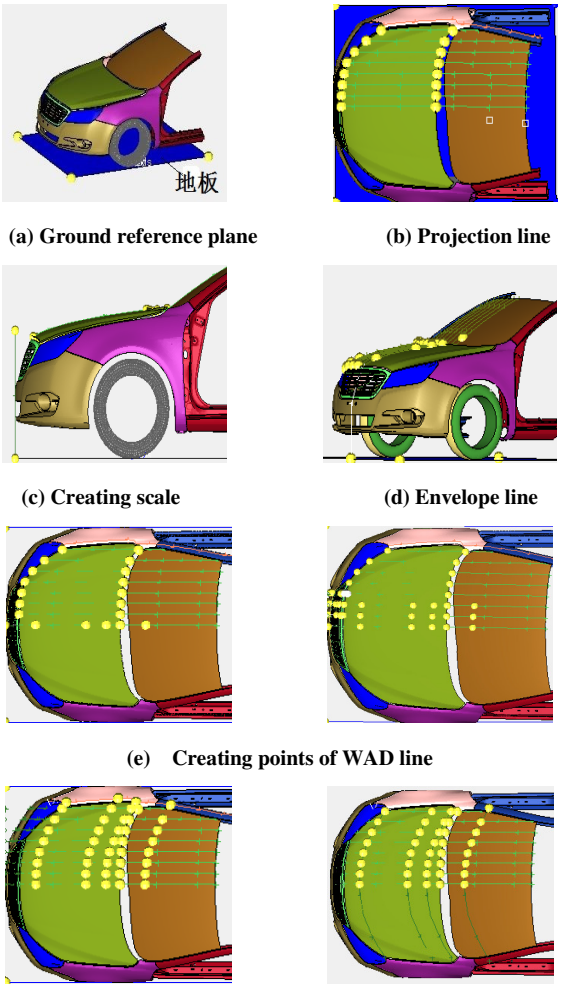

(a) Ground reference plane (b) Projection line

(c) Creating scale (d) Envelope line

(e) Creating points of WAD line

(f) Creating WAD line

Figure 5. Process of creating WAD line

图 5. 创建 WAD 线过程

4 网格点划分与标记

4.1 Euro NCAP 网格点划分要求

Euro NCAP 网格点标记规定：以原点为起点，以 100*100mm 矩阵在头部碰撞区域标记[4]。如图 6 所示：

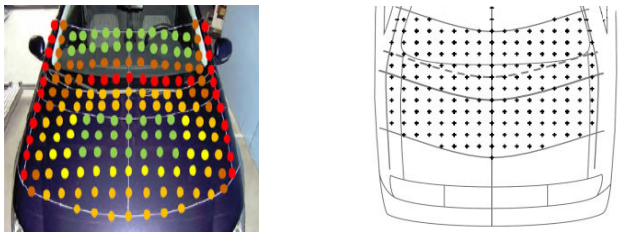

Figure 6. Euro NCAP grid points diagram

图 6. 欧洲 NCAP 网格点图

4.2 网格点标记过程

网格点标记实现的具体过程如下：

1） 生成网格点投影线：在生成 WAD 线时，已经生成了网格点投影线。

2） 确定网格点边界及起始点：网格点必须位于由 WAD 线所定义的头部碰撞区域范围内，因此，对于每一列网格点其前后边界点为 WAD1000mm 线和 WAD2100mm 线上的点，左右边界要求网格点到侧参考线的水平距离不超过 50mm。而网格点的起始点为 Euro NCAP 试验规程中定义的网格点原点，即 WAD1000mm 线与车辆纵向中心线的交点。在网格点标记子模块中，网格点边界通过求得对应 y 坐标下，WAD1000mm 线和 WAD2100mm 线上对应点的 x 坐标，如图 7 所示。而网格点原点通过求 WAD1000mm 线与车辆纵向中心线之间的最短距离点获得。

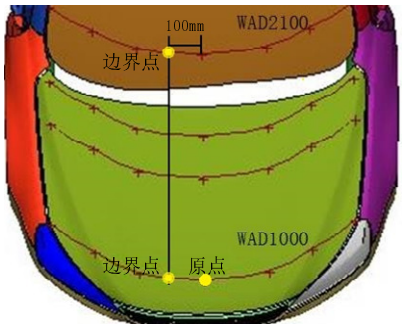

Figure 7. Boundary points and origin point

图 7. 边界点和原点

3）100*100 矩阵点标记算法：

在仿真的网格点标记子模块中，100*100 矩阵点标记算法主要包括网格点沿着 x 和 y 轴方向的平移、网格点位置判断、网格点投影和不合格网格点删除等部分。

首先，以网格点原点为起始点，沿着 y 轴水平移动，移动距离为 100mm。

其次，判断移动后的网格点是否在网格点边界范围内，网格点位置判断包含两部分：

当纵向中心线上的网格点在 WAD1000mm 和 WAD2100mm 线与纵向中心线的交点之间（包含交点）时，判断方法为将移动后的点坐标与该列上 WAD1000mm 和 WAD2100mm 线上点坐标对比。

如果移动后的网格点 x 坐标值在边界点坐标值之间（WAD1000mm 和 WAD2100mm 线上点 x 坐标值之间），且网格点距离侧参考线的水平距离大于 50mm，则生成网格点，再将网格点投影到对应的投影线上，并将沿着纵向中心平面对称，并将投影点和对称点存入点集之中。继续沿着 y 方向移动上一个网格点，移动距离为 100mm；如果移动后的网格点 x 坐标值不在边界点坐标值之间，则不生成网格点，并将纵向中心线上的上一个点网格点沿着 x 轴移动 100mm。

当纵向中心线上的网格点不在 WAD1000mm 和 WAD2100mm 线与纵向中心线的交点之间时，首先判断纵向中心线上的网格点是否超出 WAD2100mm 最末端边界点，如果未超出，则将纵向中心线上的网格点沿着 y 轴方向移动，直到网格点到相应侧发动机罩侧参考线的水平距离小于 50mm，判断生成的网格点是否在该列所对应边界点的范围内，如果在边界范围内，则将该点沿着 z 轴投影到对应的投影线上，并将投影后的点沿着纵向中心平面对称，将投影点与对称点存入点集合之中；如果不在边界范围内，则删除该点，并并将纵向中心线上的上一个点网格点沿着 x 轴方向移动 100mm，直至纵向中心线上的点超出了 WAD2100mm 最末端边界点。

4） 标记 A 柱上的网格点：A 柱上的网格点标记方法与发动机罩或者风挡玻璃上表面的网格点标记方法不同。Euro NCAP 试验规程中对 A 柱上网格点的定义是：水平铅垂平面与 A 柱上侧参考线的交点，每隔 100mm 取一个交点，100mm 为水平铅垂平面沿着 X 轴方向移动的距离。在网格点标记子模块中，标记 A 柱上的网格点的算法流程如图 8 所示。完成的网格点划分情况也如图 9 所示。

最终根据 Euro NCAP 规定，对网格点坐标进行标记。

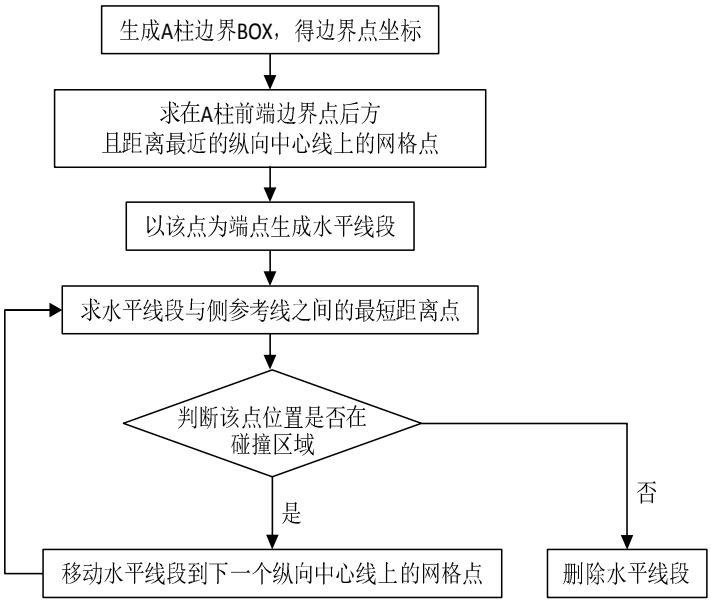

Figure 8. Flow chart of marking on A column

图 8. A 柱流标图

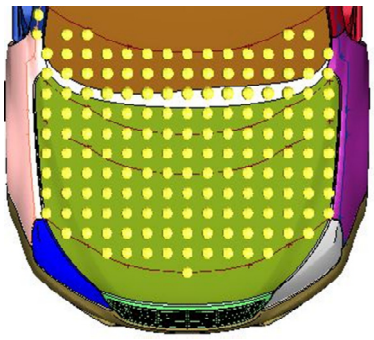

Figure 9. Diagram of grid meshing in HyperMesh

图 9. HyperMesh 网格的网格点图

5 HyperMesh 集成界面

在以上算法的基础上，通过 Tcl\tk 语言进行编译，将有限元功能模块集成到 HyperMesh 中 Utility 选项中的 User 面板中，如图 10 所示，红色标识为用户选项部分。其中前处理模块包含了侧参考线及前端包络线的划分及生成、网格点划分及标记，在前处理自动划分结束后，进行假人头部定位，选择碰撞网格点并导出 KEY 文件；后处理模块包含了自动提交计算和结果分析两部分：选择前处理生成的 KEY 文件，软件针对每次碰撞自动提交 Ls-Dyna 进行运算分析，最后生成碰撞仿真 HIC 值及对应的碰撞点得分情况。

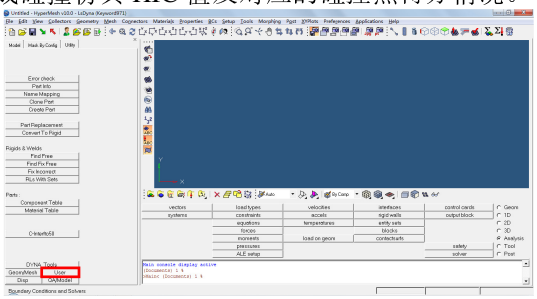

(a) Utility in HyperMesh

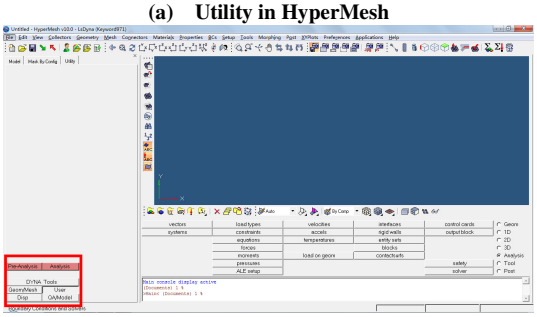

(b) User option in HyperMesh

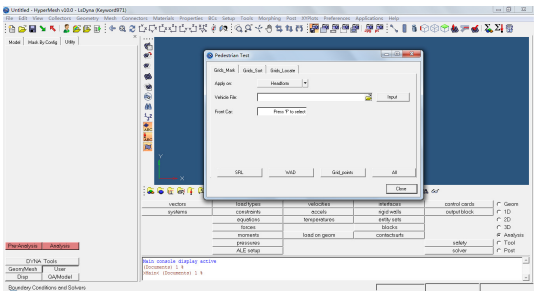

(c) Pre-analysis interface

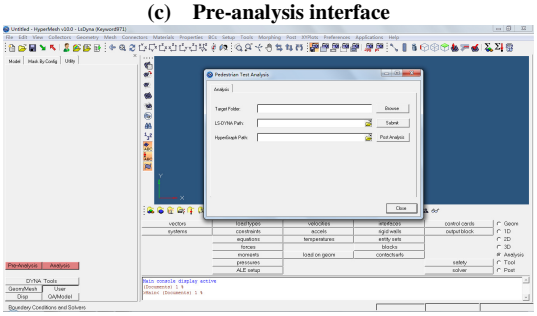

(d) Analysis interface

Figure 10. Interface in HyperMesh

图 10. HyperMesh 界面

6 结论

本文通过深入研究 Euro NCAP(V6.1)中的行人头部碰撞试验规程和评分原则，按照该规程的具体试验步骤及试验要求，研究并提出行人头部保护仿真的车辆前端侧参考线、车辆前端包络线、网格点划分自动化前处理机理和方法。通过 Tcl\tk 语言进行编译，将有限元前处理和批量后处理分析功能模块集成到 HyperMesh 中 Utility 选项中的 User 面板，实现行人头部保护碰撞仿真过程及结果计算的自动化，提高了仿真的效率。

致谢

感谢上海市科学技术委员会、同济大学及上海市机动车检测中心在整个研究中的指导和帮助。

References(参考文献)

[1] Richards D, Carroll J. Relationship between types of head injury and age of pedestrian[J]. Accident Analysis & Prevention, 2012, 47: 16-23.

[2] Arregui-Dalmases C, Lopez-Valdes F J, Segui-Gomez M. Pedestrian injuries in eight European countries: an analysis of hospital discharge data [J]. Accident Analysis & Prevention, 2010, 42(4): 1164-1171.

[3] 刘洋, 孙小光, 杨占军等. Euro NCAP 行人保护试验规程 (v5. 3.1 和 v6. 0)分析[J]. 汽车安全与节能学报, 2012,2:009.

[4] Euro NCAP-Pedestrian-Protocol-V6.1

Proceedings of the 11th International Forum of Automotive Traffic Safety, 2014, pp 293- 302
No. ATS.2014.310

Research on the Protective Effect of New Front Safety Seat in the Car Frontal Collision and Emergency Braking

Ge Ruhai, Hong Liang
Jiangsu University, School of Automobile and Traffic Enginering, Zhenjiang, China，212013
E-mail: 819996061@qq.com

Abstract：
Background：Rear-row occupants heads easily collide with front seat headrest or seatback in the frontal collision and emergency braking, because car rear row space is relatively small, causing occupants injury.
Objective：A assumption of new automotive front safety seat was putted forward, trying to reduce belted and unbelted rear-row female occupants injury in the car frontal collision and emergency braking respectively.
Method and material：Based on the geometry and feature parameters of one car model, MADYMO is used to establish the car rear-row restraint system simulation model, which was verified by the test.
Results：The simulation results show that compared to traditional front seats, when the rotational stiffness of the reed switches of new seats is 10 N·m /°, in the frontal collision, HIC15 (head injury criterion) and M_{yoc} (the peak extention torque of occipital bone) decreases 22.83% and 23.38%; in the emergency braking, HIC15, T3MS(the thorax injury value), F_{left} and F_{right} (the peak force of left and right femur) decreases 51.36%, 22.04%, 10.55% and 16.07% respectively.
Conclusions：That is to say, new front safety seats can effectively reduce rear-row female occupants injury, enhancing safety.

Keywords：Frontal collision, Emergency braking, New front safety seat, Rear-row female occupant, Protective effect

在轿车正面碰撞与紧急制动中新型前排安全座椅的保护效果研究

葛如海，洪亮
江苏大学 汽车与交通工程学院，镇江，中国，212013
E-mail: 819996061@qq.com

摘要
研究背景：由于轿车后排空间相对狭小，在正面碰撞或紧急制动中，后排乘员头部易与前排座椅头枕或靠背发生二次碰撞，造成后排乘员伤害。
目的：提出了一种新型汽车前排安全座椅的设想，拟在轿车正面碰撞与紧急制动中，分别减轻佩戴三点式安全带与未佩戴安全带的后排女性乘员受到的伤害。
方法和材料：以某型轿车相关尺寸与性能参数为依据，采用碰撞仿真软件 MADYMO 建立了后排乘员约束系统仿真模型，并经试验验证。
结果：仿真结果表明，相比于传统前排座椅，当新型座椅的转簧转动刚度为 10 N·m /°时，在正面碰撞中，女性乘员的头部伤害指标 HIC15 与枕骨伸张弯矩峰值 M_{yoc} 分别降低了 22.83%、23.38%；在紧急制动中，HIC15、胸部伤害值 T3MS 以及左、右大腿力峰值 F_{left}、F_{right} 分别降低了 51.36%、22.04%、10.55%与 16.07%。
结论：因此，新型前排安全座椅能够有效降低后排女性乘员伤害，提高后排乘员安全性。

关键字： 正面碰撞　紧急制动　新型前排安全座椅　后排女性乘员　保护效果

1 引言

汽车座椅是汽车内室系统的必要组成部分，同时也是汽车乘员约束系统最主要的部件之一。座椅主要由座垫、靠背、头枕、靠背倾角调节器以及座椅连接件构成，如图 1 所示。其坐垫约束了乘员的向下运动，靠背约束了乘员的向后运动，头枕约束了乘员头部的向后运动，靠背倾角调节器用于调节靠背倾角，座椅连接件用于连接汽车地板[1]。

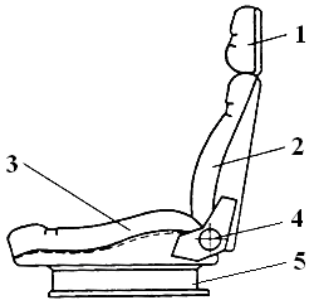

1、头枕；2、靠背；3、坐垫；4、靠背倾角调节器；5、座椅连接件

Figure 1. The composition of automobile seat

图 1. 汽车座椅的构成

座椅安全性分为被动安全性与主动安全性。被动安全性是指在发生事故时，座椅能够最大限度地减轻乘员伤害的能力。

2 正面碰撞中轿车座椅被动安全性的研究现状

文献[2]提出了移动式安全座椅的概念。在正面碰撞中，该座椅可发生相应的变形，起到防止乘员“下潜”、消除安全带与乘员间初始间隙以及降低胸部加速度的作用。仿真结果显示：相比于传统座椅，移动式座椅能够使乘员的头部伤害值降低 37.5%，上颈部伸展弯矩、剪切力与拉伸力分别降低 24.0%、25.8%及 35.0%。

文献[3]利用碰撞仿真软件 MADYMO，研究了轿车发生正面碰撞或紧急制动时，增大驾驶员座椅坐垫与地板间的夹角对驾驶员伤害的影响。仿真分析获得：在正面碰撞中将坐垫与地板间的夹角由 10°增大至 25°，可使驾驶员头部伤害指标 HIC36 下降 21.4%，胸部 3ms 合成加速度 T3MS 下降 16.6%,而髋部合成加速度仅仅增加 8.2%。

文献[4]收集了有关驾乘人员最常使用的前排座椅的前后位置信息，并且分析了在正面碰撞事故中前排座椅前后位置与女性乘员、男性乘员伤害的关系。研究显示：座椅位置偏后的女性乘员与座椅位置靠前的男性乘员在碰撞中受到伤害的几率较大。

文献[5]利用死尸假人研究了在正面碰撞中，整体向后倾斜的座椅对乘员伤害的影响，如图 1.14 所示。研究表明：相比于普通座椅，倾斜的座椅承受了绝大部分的碰撞能量，并将能量传递给人体不易受伤的髋部。此外倾斜的座椅能够避免乘员的“下潜”现象，减少颈部的向前弯曲，最终有效降低乘员伤害。

文献[6]研究指出在高速正面碰撞中，若前排座椅靠背的屈服强度不足，则未佩戴安全带的后排乘员会击溃前排靠背，导致后排乘员与靠背一起撞击受安全带与安全气囊约束的前排乘员，使前排乘员的伤害率与死亡率大幅增加。

戴姆勒-克莱斯勒、宝马汽车公司等研制出智能座椅[7-8]。当正面碰撞不可避免时，该座椅会在碰撞发生前向后纵向移动，使驾驶员远离仪表板与转向系统，有效减轻驾驶员头部、颈部与胸部的伤害。

上述研究表明：当前正面碰撞中轿车座椅被动安全性的研究主要集中在座椅对自身乘员的保护上，并未涉及对非自身乘员的保护。但轿车座椅会对非自身乘员造成伤害，如因轿车后排空间相对狭小，在正面碰撞中，

后排乘员头部易撞击到前排座椅头枕或靠背上，导致后排乘员伤害。为此，本文提出了新型前排安全座椅的设想（专利号：201410044747.7）。

3 新型前排安全座椅的组成与工作原理

新型前排安全座椅主要由座椅头枕、头枕导杆、靠背骨架、U 形头枕导套、纵板、转簧、横杆等组成，如图 2 所示。最上端为头枕，头枕下方为头枕导杆、U 型导套；U 型导套包括两端的竖直杆和中间的水平杆；头枕导杆可插入两端的竖直杆中，用于调节头枕高度；U 型导套的水平杆下方固定有两纵板；靠背骨架中的一横杆间隙穿过纵板中的圆孔，从而纵板与横杆形成转动链接，纵板可绕横杆转动；纵板间设有一转簧，转簧过盈套装于横杆上，转簧两端分别卡在纵板的小孔中。

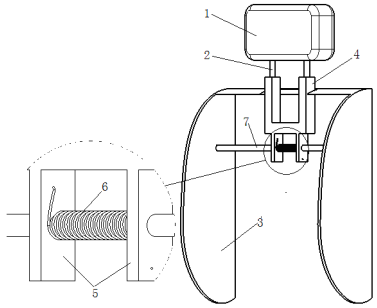

1、头枕；2、头枕导杆；3、靠背骨架；4、U 形导套；5、纵板；6、转簧；7、横杆

Figure 2. The composition of new front safety seat

图 2. 新型前排安全座椅的组成

新型前排安全座椅的工作原理是：在轿车正面碰撞中，后排乘员头部在惯性力的作用下撞击该座椅头枕时，转簧的两端在纵板的压力作用下发生扭转弹性变形，这样纵板就绕靠背骨架中的横杆向前转动一定角度，同时 U 型导套、导杆与头枕向前转动一定角度，从而吸收碰撞能量，有效减轻后排乘员受到的伤害。当碰撞结束后，后排乘员在安全带的拉力作用下向后位移，纵板失去后排乘员头部撞击力的作用，不再给转簧施加压力；此时转簧的两端恢复原有形状，反作用于纵板，使其绕横杆恢复原始状态，同时 U 型导套、导杆与头枕恢复原来位置，正常保护前排乘员头、颈部安全。

4 仿真分析模型的建立及验证

为分析新型前排安全座椅对正面碰撞中后排女性乘员的保护效果，以某型轿车乘员区域相关尺寸及性能参数为依据，采用碰撞仿真软件 MADYMO 建立了后排乘员约束系统仿真模型。具体步骤为：

①建立乘员车内环境模型，主要包括地板刚体模型、前排与后排座椅有限元模型。此时两前排座椅靠背与头枕导杆，导杆与头枕间的链接方式均为固定链接。

②根据 2012 版 C-NCAP 中正面 100%重叠刚性壁障碰撞（正面碰撞）试验的相关规定，调入 MADYMO 软件中自带的 Hybrid Ⅲ第 5 百分位女性椭球假人模型，并将其定位在后排左侧座椅上；

③建立三点式安全带混合模型，主要包括安全带卷收器、高度调节器、固定锚点以及带扣点；并对女性假人模型进行安全带预定位；在安全带混合模型中，与假人身体相接触的部分为有限元模型，不接触的部分为刚体模型。

④定义假人肩部、盆骨与后排座椅靠背的接触，盆骨、大腿与后排座椅坐垫的接触，头部与前排座椅头枕、靠背的接触，膝盖、小腿、双脚与前排座椅靠背的接触，双脚与地板的接触，胸部、肩部与安全带肩带的接触以及腹部、盆骨与腰带的接触；

⑤基于试验测得的数据，定义座椅模型各部件的刚度以及各运动铰的刚度；

⑥由于碰撞试验中，B 柱的变形量较小，B 柱加速度能够真实反映出作用于假人身上的加速度，因此将实际 50km/h 正面碰撞试验中车体左侧 B 柱减加速度反向施加至女性假人模型，进行仿真计算。

至此仿真模型已建立完成，如图 3 所示。

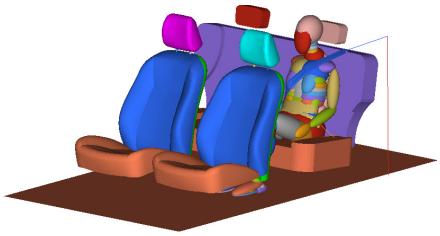

Figure 3. The simulation model of rear occupant restraint system

图 3. 后排乘员约束系统仿真模型

正面碰撞试验中假人伤害响应曲线与仿真模型中假人伤害响应曲线的对比见图 4 所示。

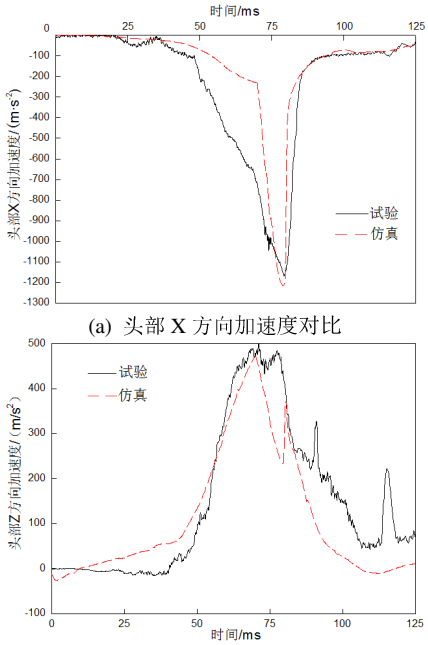

(a) 头部 X 方向加速度对比

(b) 头部 Z 方向加速度对比

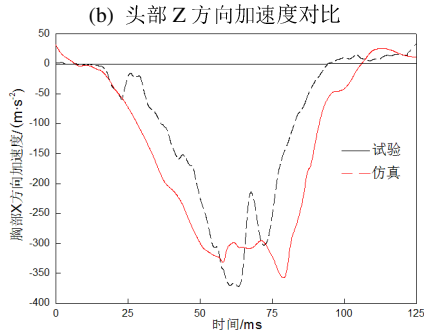

(c) 胸部 X 方向加速度对比

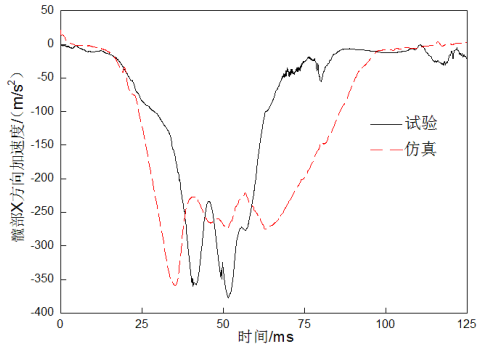

(d) 髋部 X 方向加速度对比

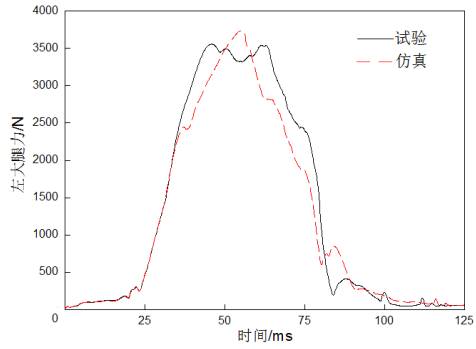

（e） 左大腿力对比

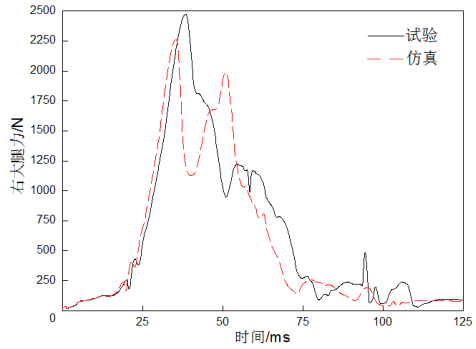

(f) 右大腿力对比

Figure 4. The comparison of rear dummy injury response curves in test and simulation

图 4. 后排假人试验伤害响应曲线与仿真曲线的对比

图 4 显示仿真得到的假人各伤害响应曲线与试验曲线拟合度较好，因此可将此仿真模型作为基本模型进行深入研究，仿真值可信度较高。

5 正面碰撞中新型前排安全座椅对后排女性乘员的保护效果分析

基于新型前排安全座椅的工作原理，将上述模型中左侧前排座椅靠背与头枕导杆间的固定链接改为转动铰链接，转动铰位于图 2 中转簧的位置，以模拟新型安全座椅中转簧的作用。并分析 4 种转簧（转动铰）转动刚度对后排女性乘员的保护效果，结果如表 1 及图 5 所示。

Table 1. The influence of four rotational stiffness of reed switch on rear female ocupant injury in the frontal collision

表 1. 在正面碰撞中 4 种转簧转动刚度对后排女性乘员的保护效果

伤害指标	固定链接	新型前排安全座椅中转簧的转动刚度			
		40N·m/°	20 N·m /°	10 N·m /°	5 N·m /°
头部伤害指标 HIC15	948.07	910.28	806.32	716.71	707.39
胸部 3ms 合成加速度 T3MS/（m/s^2）	376.20	362.73	355.72	350.59	349.82
胸部压缩量峰值 Thpc/mm	30.66	30.63	30.45	30.51	30.54
颈部枕骨伸张弯矩峰值 M_{yoc}/(N·m)	36.78	35.57	32.42	28.55	28.05
髋部合成加速度峰值 a/（m/s^2）	373.93	384.13	385.32	377.81	374.73
组合伤害概率 $P_{combine}$	15.68%	13.85%	10.32%	8.11%	7.93%

由表 1 分析可知，依次减小转簧的转动刚度，可以降低乘员头部、颈部与胸部的损伤值，且胸部压缩量与髋部合成加速度变化不大。当转动刚度为 10 N•m /°时，继续减小转动刚度已不能显著改善头部、颈部与胸部损伤值，并且太小的刚度值容易引起汽车正常行驶中头枕误动，不利于其自身乘员的乘坐舒适性。因此确定前排安全座椅转簧的最佳转动刚度为 10 N•m /°，此时相比于原座椅，后排女性乘员的 HIC15，M_{yoc}，T3MS 及组合损伤概率 $P_{combine}$ 分别由 948.07 降至 716.71，36.78 N•m 降至 28.55 N•m，376.20 m/s^2 降至 350.59 m/s^2，15.68% 降至 8.11%，各自的下降幅度为 24.4%，22.38%，6.8%及 48.28%。$P_{combine}$ 表示乘员受 AIS（简略损伤等级） 4 级以上重伤（危及生命）的概率[9]，其计算公式为：

$$P_{combine}=\left(1+e^{(5.02-0.00351\times HIC15)}\right)^{-1}+\left(1+e^{(5.55-0.0693\times T3MS/9.81)}\right)^{-1}$$
$$-\left(1+e^{(5.02-0.00351\times HIC15)}\right)^{-1}\times\left(1+e^{(5.55-0.0693\times T3MS/9.81)}\right)^{-1}$$

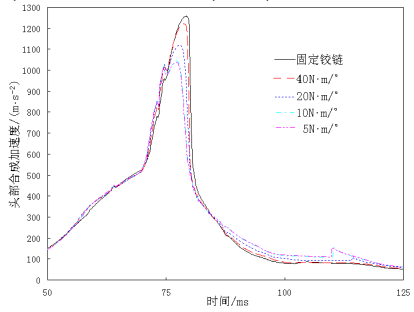

（a） 对头部合成加速度的影响

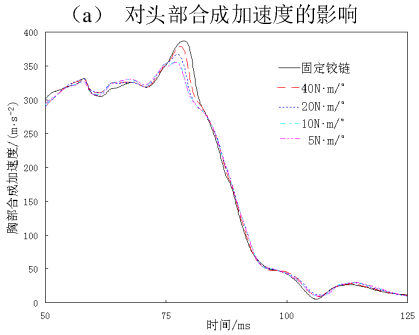

（b） 对胸部合成加速度的影响

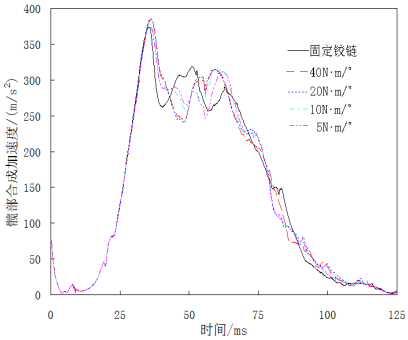

（c） 对髋部合成加速度的影响

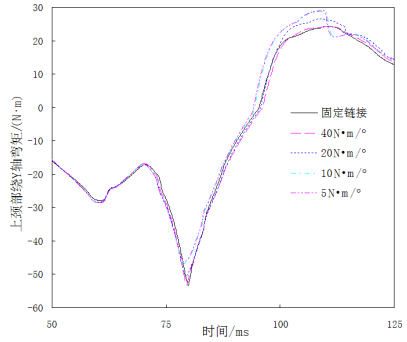

（d） 对上颈部绕 Y 轴弯矩的影响

Figure 5. The influence of new front safety seat on rear female occupant injury

图 5. 新型前排安全座椅对后排女性乘员伤害的影响

采用该机构时女性乘员的运动姿态如图 6 所示，当女性乘员头部撞击前排头枕时，头枕导杆绕转动铰向前转动一定角度，头枕随之向前转动，靠背相对静止。之后头枕导杆、头枕恢复原来位置，正常保护前排乘员头、颈部。

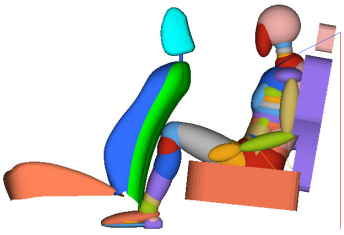

（a） 0ms

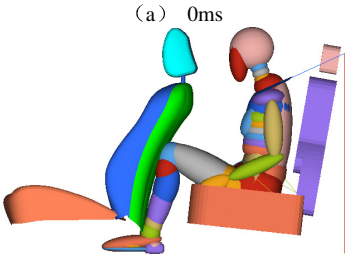

（b） 50 ms

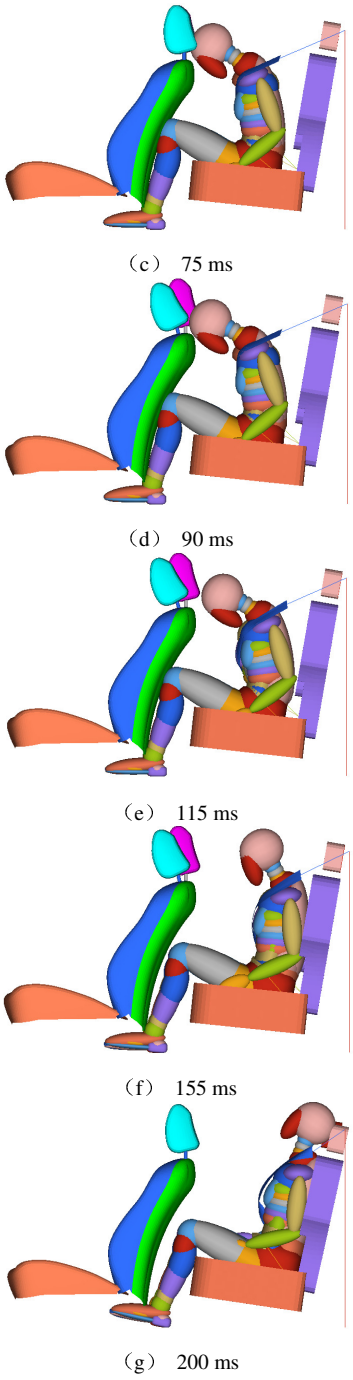

Figure 6. Movement state of female occupant and headrest

图 6. 女性乘员及头枕的运动姿态

6 紧急制动中新型前排安全座椅对后排女性乘员的保护效果分析

在我国，后排乘员安全带佩戴率相当低，因此在轿车紧急制动过程中，未佩戴安全带的后排乘员头部易与前排座椅发生二次碰撞，造成伤害。以下分析在紧急制动中，新型前排安全座椅对未佩戴安全带的后排女性乘员的保护效果。

正面碰撞工况与紧急制动工况存在相似性，因此本文在原有正面碰撞后排约束系统仿真模型的基础上，建立了紧急制动后排约束系统仿真模型。两者最大的区别在于反向施加在后排假人身上的减速度波形不同，因此需用紧急制动的减速度波形代替正面碰撞中 B 柱减速度波形。由于未能得到研究车型的紧急制动减速度波形，所以使用吉林工业大学田万仓得到的某轻型越野车的紧急制动减速度波形（制动初速度为 45km/h）代替，如图 7 所示。将该紧急制动减速度波形通过 LOAD.SYSTEM_ACC 命令反向施加到后排女性假人身上，以模拟紧急制动中后排乘员的运动。

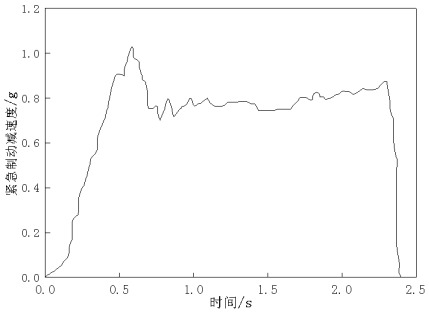

Figure7. The accelation-time curve of emergency brake

图 7. 紧急制动减速度曲线

新型前排安全座椅的 4 种转簧（转动铰）转动刚度对后排女性乘员的保护效果见表 2 所示。

Table21. The influence of four rotational stiffness of reed switch on rear female ocupant injury in the emergency braking

表 2. 在紧急制动中 4 种转簧转动刚度对后排女性乘员的保护效果

伤害指标	固定链接	新型前排安全座椅中转簧的转动刚度			
		40N·m /°	20 N·m /°	10 N·m /°	5 N·m /°
HIC15	46.67	41.31	29.54	22.70	22.26
T3MS/（m/s^2）	130.08	111.10	109.59	101.41	100.74
胸部压缩量 Thpc/mm	2.09	2.00	2.05	1.87	1.95
髋部合成加速度峰值 a/（m/s^2）	77.33	77.52	77.87	75.86	75.86
颈部枕骨伸张弯矩峰值 M_{yoc}/（N·m）	0.55	0.16	2.31	2.76	1.71
左大腿力峰值 F_{left}/N	1101.67	1088.24	1055.74	985.47	980.51
右大腿力峰值 F_{right}/N	1117.40	1101.18	1054.69	937.83	929.64

有表 2 可知，随着新型安全座椅中转簧转动刚度的减少，女性乘员头部伤害值 HIC15，胸部 3ms 合成加速度 T3MS，以及左、右大腿力峰值呈明显下降趋势，此外其他伤害值变化不大。同上，当转簧的转动刚度为 10 N·m /°时，继续减小转动刚度已不能显著改善女性乘员的损伤值。此时，相比于原座椅， HIC15 由 46.67 降至 22.70，降低了 51.36%，T3MS 由 130.08 m/s^2 降至 101.41 m/s^2，降低了 22.04%，左、右大腿力峰值分别由 1101.67N 降至 985.47N，由 1117.40N 降至 937.83N，下降幅度各为 10.55%、16.07%。

7 结论

（1）本研究表明相比于普通座椅，在轿车正面碰撞或紧急制动中，新型前排安全座椅能够显著减少后排女性乘员的伤害。

（2）在正面碰撞中，随着新型前排安全座椅转簧转动刚度的减小，后排女性乘员头部、胸部与颈部伤害值逐渐降低，其它部位伤害值变化不大；在紧急制动中，头部、颈部、胸部以及腿部伤害值逐渐降低。

（3）综合考虑，最终确定新型前排安全座椅转簧的最佳转动刚度为 10 N·m /°。

参考文献（References）

[1] Ge Ruhai, Liu Zhiqiang, Chen Xiaodong. Automobile Safety Engineering[M]. Beijing: Chemical industry press, 2005.

葛如海, 刘志强, 陈晓东. 汽车安全工程[M]. 北京: 化学工业出版社, 2005.

[2] Xiao Z, Jac Wismans, Jiang X Q, et al. A Study on the Occupant Protection Performance of Moving Safety Seats[J]. Automotive Engineering, 2011,33(7): 603–607.

肖志, Wismans J, 蒋小晴, 等. 移动式安全座椅的乘员保护性能的研究[J]. 汽车工程, 2011,33(7): 603–607.

[3] Ge R H, Zang L and Wang H T, et al. Analysis on the influence for the protection on frontal impact by vehicle seat cushion obliquity[J]. Journal of Mechanical Engieering, 2009, 45(11): 230-234.

葛如海，臧绫，王浩涛，等. 汽车座椅坐垫倾角对正面碰撞乘员保护影响分析[J]. 机械工程学报，2009，45(11)：230-234.

[4] Hill J D, Boyle L N. The safety implications of vehicle seat adjustments[J]. Journal of Safety Research, 2006, 37: 187–193.

[5] Wiechel J, Bolte J. Response of reclined post mortem human subjects to frontal impact[C]. SAE, Paper Number: 2006–01–0674.

[6] Mayrose J, Blatt A, Roberts D, et al. The effect of unrestrained rear-seat passengers on driver mortality[J]. Journal of Trauma-Injury Infection & Critical Care, 2006, 61(5): pp 1249-1254.

[7] Schöneburg R, Baumann K H. PRE-SAFE - The next step in the enhancement of vehicle safety[C]. The 18th International Technical Conference on the Enhanced Safety of Vehicles, May 19-22, 2003, Nagoya, Japan: Paper Number 03-0410.

[8] Pack R, Koopmann J and Yu H, et al. Pre-crash sensing countermeasures and benefits[C]. SAE, Paper Number: 2005–02–02.

[9] Newstead S, Cameron M. Correlation of results from the new car assessment program with real crash data[R]. Victoria, Aust ralia: MUARC, 1997.

[10] Tian W C, Sha W P and Liu W. Vehicle Response Analysis under Ernergency Braking[J]. Automotive Engineering, 1996, 18(1): 60-64.

田万仓，沙伟平，刘伟. 汽车紧急制动响应的分析[J]. 汽车工程，1996，18(1): 60-64.

Proceedings of the 11th International Forum of Automotive Traffic Safety, 2014, pp 303- 310
No. ATS.2014.311

Abdominal Impact Study on Pediatric Cadaveric Subjects

Jun Ouyang[1], Qingan Zhu[2], Zeyu Li[1], Chang Liu[1], Shizhen Zhong[1]

[1]*Department of Anatomy, Guangdong Provincial Medical Biomechanical Key Laboratory, Southern Medical University, Guangzhou, China 510515*

[1]*Shenzhen Digital Orthopedic Engineering Laboratory, Shenzhen, Guangdong, China 510515*

[2]*Department of Orthopedics, Nanfang Hospital, Southern Medical University*

Email : jouyang@smu.edu.cn

Abstract:

Background: The purpose of this study was to provide structural response of front abdominal impact in children.

Methods: Nine unembalmed cadavers were divided into 2 groups. A young cohort aged 2-4 years (4 cadavers) and an older cohort aged 5-12 years (5 cadavers) were impacted. An autopsy was performed after the impact.

Results: The average velocity of the cadaveric tests was 6.3 m/s (±0.25 m/s). Mean peak V*C values were 2.53±0.59 m/s and 1.98±0.41 m/s in old cadaveric cohort and young cadaveric cohort respectively (P>0.05). The maximum deformation and mean peak forces were 9.27±0.21 cm, 530.30±102.62N and 9.88 ±1.50 cm, 929.16±133.24N in young cohort and old cohort separately (P<0.05). Eight cadavers were found various injuries.

Conclusions: Good force-deformation data may be derived from the cadaveric response data, and force/deformation corridors have been derived for both subject populations.

Keywords: Children, abdomen, impact, injury, biomechanics

1 Instruction

In order to protect children in car crashes, the use of child restraint systems is recommended by American Academy of Pediatrics (AAP) and the National Highway Traffic Safety Administration (NHTSA) [1], including the use of child restraint systems with harnesses for children from birth to at least 4 years of age, followed by the use of belt-positioning booster (BPB) seats until their height reach 1.45 m. But only very few children use car seat in China and many children begin using the vehicle belt prematurely around the world, which puts them at an increased risk for serious injuries in a crash. The lap belt should fit low and snug on the hips and upper thighs, but due to the height of children various; inappropriate use of the lap belt would across the belly and cause viscera injuries during the car crash.

In 2004, Arbogast et al. investigate 243,540 automobile crash involved 19,125 children under age of sixteen, and found out children 4-8 years of age were at highest risk of abdominal injury: they were 24.5 times and 2.6 times more likely to sustain an Abbreviated Injury Scale 2+ abdominal injury than those 0-3 years and 9-15 years, respectively. The other important finding is that no reduction in abdominal injury risk was seen with rear seating [2]. In order to find out the relationship between the position of seat belt and the injury, Stacey et al. designed a porcine model to simulate 6-year-old human abdomen, and showed us that the injury frequency distributions from upper and lower abdominal belt loading were found to be significantly different ($p<0.01$). Upper position seat-belt resulted primarily spleen broken and rib fractures, whereas lower position loading produced the large and small intestines injuries [3].

Generally speaking, most of previous researches focused on the pediatric abdominal injury patterns and mechanisms by using dummy, animal surrogates and retrospective assessments [2-7]. All these results provided useful information somehow to help prevent the pediatric injury during crashes. But as far as we know, there are few biomechanical data from the pediatric impact test reported. The purpose of this study was to provide structural response of front abdominal impact in children.

2 Methods

The pediatric cadavers used in the present study were donated after family consent. The ethical guidelines for cadaver testing recommended by the National Highway Traffic Safety Administration (NHTSA) and the National Academy of Science were adopted. Prior to the study, an independent review board approved the test protocol.

2.1 Specimens' preparation

Nine unembalmed cadavers ranging in age from two to twelve years were obtained. Age, anthropometric data, and cause of death for each of the nine subjects are listed in Table 1. Specimens were prepared as described before [4]. In brief, following transverse CT scanning of the subjects (10 mm contiguous slices), they were individually sealed in plastic bags and stored in a freezer at -20℃. On the day of testing, the subject was removed from the freezer and thawed in a warm water bath (the subjects were thawed in the bag to prevent excessive water perfusion). When thawed, pre-test x-ray images (anterior and lateral views) were taken of the head, neck, thorax, abdomen and pelvis to ensure that there were no pre-existing abnormalities or injuries. All specimens were not intubated and lungs were collapsed and not expanded during the impact tests. Also no arterial pressurization was done in the subjects.

Table 1. Anthropometry and cause of death for the pediatric specimens

Subject	**Age** (yr)	Sex	Weight (kg)	Stature (cm)	Cause of Death
1	2	F	13	97.0	Fluoracetamide poisoning
2	2.5	M	10.5	87.5	Cerebral edema
3	3	M	13.5	93.0	Brain tumor
4	3	F	10.5	85.0	Heart disease
5	5	M	13	101.0	Cerebritis
6	6	M	16.5	108.0	Leukemia
7	6	M	20	109.0	Mediterranean anemia
8	7.5	F	17	117.0	Acute urinaemia
9	12	F	29	142.5	Leukemia

2.2 Test apparatus-pneumatic impactor

A free mass pneumatic impactor device was developed for impact testing. The pneumatic impactor is driven by using a pre-set air pressure through a powered entrance region to a specified velocity. The fully retracted piston is fired by manually opening a stop-cock valve between the piston and the air tank. The free travel velocity of the impactor is controlled by regulating the initial pressure within the tank. The initial drive tank pressure was set using a pressure transducer (MSI Measurement Spec. Model MSP-300-250-P-3-N) with an accuracy of 0.05 psi. The pressure tank was allowed to equilibrate with the ambient temperature to ensure repeatable results. This allowed the specification of impact velocity to better than 2%. When this velocity is reached, the device dumps the drive pressure and enters an un-powered free flight region where the impact occurs. This allows the piston and impactor to travel freely at nearly constant velocity for approximately 110 mm.

This device has several advantages as compared with a pendulum impact device. These include higher impact velocities in smaller experimental space, a well-controlled horizontal impulse imparted to the subject, and an enhanced ability to use load cell instrumentation to investigate the impact event.

2.3 Abdominal testing

The cadavers were supported in a seated position facing the impactor, with the head and spine erect, and the arms extended horizontally in the anterior direction. Teflon sheeting was placed beneath the cadaver to reduce friction at the support platform surface. The head was supported in an upright position using a cervical collar and frangible tape. Phototargets were placed on the hip (greater trochanter), shoulder (center of rotation), head (Frankfort plane), mid-chest, mid-abdomen, spinal accelerometer, and lumbar accelerometer. The impact location was selected as the position one third the distance from the umbilicus to the bottom of the sternum. However, if the impact location resulted in impactor contact closer than 1 cm from the bottom of the rib cage, the impact location was moved downward until there was a 1 cm distance from the bottom of the rib cage to the impactor. Cadaveric positioning criteria were (in order of importance):

- Impact location between umbilicus and lower sternum
- Impact head parallel to impact site (mid sternum)
- Spine vertical
- Head upright

The cadaver was positioned to limit the free stroke of the piston to 65% of the measured abdominal depth at the umbilicus (est. spine dimension 2 y.o.=2 cm, 4 y.o.=4 cm). This step was taken to limit the potential for spinal injuries from high velocity contact with the impactor.

Two impactors were used in the testing. All of the pneumatic impacts were at a nominal 6 m/s velocity. Impact tests with the 2-4 years cadavers used the 5 cm diameter, 2.5 kg mass impactor, while tests for the 5-12 years cadavers used the 7.5 cm diameter, 3.5 kg mass impactor.

Data of impact forces and accelerations were acquired using the IDDAS portable data acquisition system (R.A. Denton Inc.) with a sample rate of 10 kHz. Also, high-speed video was taken of all tests using a Kodak Ektapro 1000 at 1000 frames per second. Instrumentation of the cadavers included a lumbar spinal accelerometer opposite the abdominal impact point on the L-3 vertebra, and a 5-axis load cell, which is used to record the impact force at the impact site. A power failure to the data acquisition system in specimen 4 prevented the collection of transducer data.

2.4 Post-test procedures

Although the current manuscript only deals with the abdominal testing, these cadaveric subjects were used in several series of tests, including abdominal impact, thoracic impact and pelvic impact in order [4,5]. Each serial test of a subject was finished in one day, and there were no refrozen and thaw between the test series. Immediately following a test post-test x-ray images (anterior and lateral views) were produced of the head, neck, thorax, abdomen and pelvis. An autopsy was performed concentrating on the abdomen to document both soft and hard tissue injuries after the serial impact.

3 Statistical analysis

All data were analyzed using the SPSS 10.0 software package (SPSS Inc. USA). T-test were used to determine whether there is a significant difference ($P<0.05$) between two specimen groups.

4 Results

A test matrix for the abdomen testing is shown inTable 2. The average velocity of the cadaveric tests was 6.3 m/s (±0.25 m/s). No significant head motion occurs during this period. Motion is predominantly abdominal deformation. During this time, there is high-speed video evidence that the impactor contacted hard structure at approximately 9 ms

from the initial impact. This coincides with a substantial increase in force seen in the load cell and indicates the bottoming of available abdominal deformation.

Table 2: Cadaver Abdomen Test Matrix

Subjec t	Impactor Mass (kg)	Impactor Diameter (cm)	Impact Velocity (m/s)
1	2.5	5.0	6.2
2	2.5	5.0	6.4
3	2.5	5.0	6.1
4	2.5	5.0	N/A
5	3.5	7.5	6.1
6	3.5	7.5	6.3
7	3.5	7.5	6.9
8	3.5	7.5	6.3
9	3.5	7.5	6.2

The cadaveric V*C time histories for the young cadaveric cohort (ages 2-4 years) are shown in Figure 1 A. V*C time histories for the old cadaveric cohort (ages 5-12 years) are shown in Figure 1 B. The time histories show qualitatively and quantitatively similar behavior in both cadaveric groups. Peak V*C values with timing are tabulated and the mean peaks were 2.53±0.59 m/s and 1.98±0.41 m/s in old cadaveric cohort and young cadaveric cohort respectively. There is no statistically significant difference between the peak V*C of the two groups.

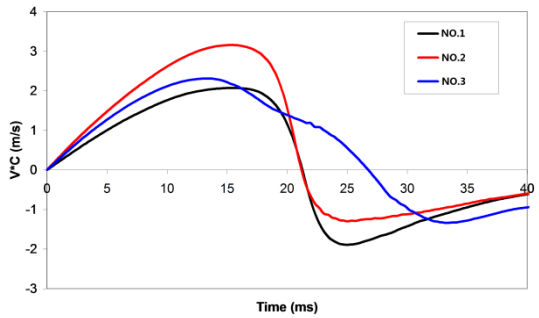

A.Cadaver Young Cohort (2-4 Years)

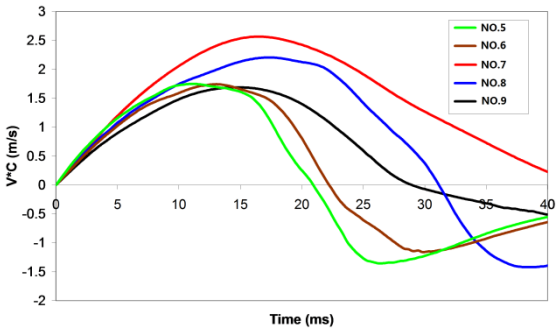

B. Cadaver Old Cohort (5 - 12 years)

Figure 1: Abdomen Impact – V*C vs. Time – 6.0 m/s Nominal Impact Velocity

Cadaver force-deformation profiles for the young cadaveric cohort (ages 2-4 years) are shown in Figure 2 A, and force-deformation profiles for the old cadaveric cohort (ages 5-12 years) are shown in Figure 2 B. The profiles for the young cohort show qualitatively and quantitatively similar behavior among the tests. For the old cohort, there is evidence of possible rib contact with the impactor in specimen No.7. The maximum deformation are 9.27±0.21 cm and 9.88 ±1.50 cm in young cohort and old cohort separately. There is statistic significance difference between the two cohort (P<0.05). But there is no statistic difference in the maximum abdominal compression between the two cohorts, which is 72.67%±12.34% in young cohort and 62.60±8.65% in older cohort.

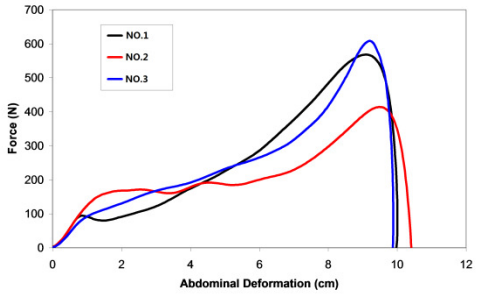

A. Cadaver Young Cohort (2-4 Years)

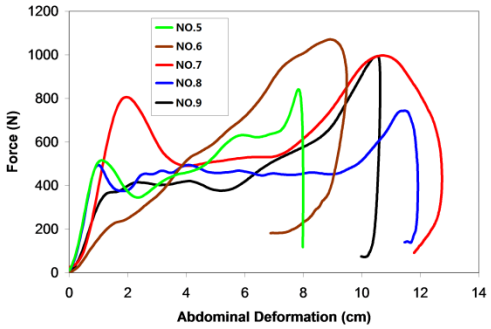

B. Cadaver Old Cohort (5 - 12 years)

Figure 2: Abdomen Impact – Force vs. Deformation – 6.0 m/s Nominal Impact Velocity

Peak force with timing is tabulated in Table 3, and the mean peaks were 530.30±102.62N and 929.16±133.24N in young cadaveric cohort and old cadaveric cohort respectively. There is a statistically significant difference between mean peak force levels of the two groups (P<0.05).

Average force deformation contours, including ±1 standard deviation corridors, for the young cohort is shown in Figure 3 A and for the old cohort are shown in Figure 3 B. The average body mass of the older cohort was 19.3 kg ± 5.4 kg, and the average body mass of the younger cohort was 11.9 kg ± 1.8 kg. As the result of the relatively homogeneous sample population, the force/deformation corridors were not scaled for subject mass. The corridors are qualitatively similar. Initiation of contact produces a relatively smooth increase in force as the abdomen deforms. Generally, no initial inertial force peak is seen owing to the compliance of the abdominal viscera. The deformation increases until a force peak is reached upon compression contact of the impactor with the subject spine.

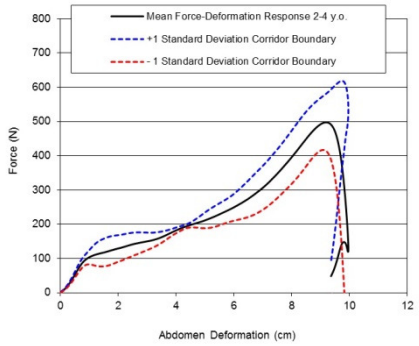

A.Cadaver Young Cohort (2-4 Years)

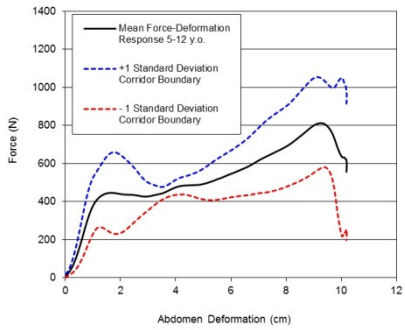

B. Cadaver Old Cohort (5 - 12 years)

Figure 3: Abdomen Impact– Force vs. Deformation, Mean and ± 1 Standard Deviation Corridors –7.5 m/s Nominal Impact Velocity

Autopsy after the impact shows various injuries in all specimens as described in Table 3 except No. 7. Hemorrhage and fistulae perforation were the most common injuries.

5 Discussion

Seat belt syndrome was first described as an injury pattern seen in lap-belted adult trauma patients in early 1960's [6]. This pattern of injuries involves soft tissue trauma to the abdominal wall and injury to intra-abdominal organs and the lumbar spine. In 1980's, children's seat-belt syndrome was reported [7]. American Academy of Pediatrics and the National Highway Traffic Safety Administration advises parents to let children ride in a belt-positioning booster seat until they have reached 4 feet 9 inches tall and are between 8 and 12 years of age. Although booster seat could provide better belt fit when children us e adult seat belts in the vehicle, abdominal injury associated with seat belt restraint is still the highest risk for children between 4-15 years of age in developed countries. This increased injury risk occurs because children are transitioning from child seats into adult seat belts. To protect children at these ages from injuries from safety restraint systems is a unique change.

There are many factors that influence the increased risk of children abdominal injuries by seat belt. These factors could be divided into anatomical characteristics and design features of standard seat belt system. Compared with adults, children have smaller body size, especially small underdeveloped pelvis. Children's head is heavier and larger in relation to body height, this would resulting in increased deceleration forces. The abdominal muscles in children are

thinner, weaker and less developed, and there is less fat tissue to protect internal abdominal organs [8,9].

The other important factors are the design of vehicle restraint system and misuse of the seatbelt. The ill-fitting shoulder belt often cross the child's face or neck, and some parents try to put the shoulder belt behind the back for child's comfort, which lead the upper torso to be unrestrained. Also the lap belt designed for adult body frame makes it hard to tight fit across child's pelvis[10-13].

Most researchers agreed that the deceleration following the collision is the common mechanism for seat belt mediated injuries in children. The deceleration caused the child's body moves forward rapidly and the belt overrides the anterior superior iliac spines could slip up over the soft abdomen. At the same time the child's upper torso hyper-flexes over the lap belt and compressed the anterior abdominal wall and internal organs against the spine. This kind of sudden compression increases the intestinal pressure and leaves the bowel perforations as one of the most common injuries found in clinic [13, 14]. In this study, we use impactor with free travel velocity to simulate the lap belt force, although the impact speed is fairly low (6.31m/s±0.26m/s) in the experiment, we still found 6 specimens out of 9 had the hollow organ perforation injuries, include stomach, small intestine and colon perforations. Since the intestines were fixed by various ligaments and mesenteric structures, shearing force formed by the seatbelt during a crash could leave these kind of structures injured [11].

Spine injuries are another common trauma. As the abdominal wall and the internal organs directly compressed on the spine by the seatbelt, the hyperflexion of the spine led to a special spine fracture-chance fracture, which is caused the compression of anterior vertebral elements and distraction of posterior vertebral elements [15, 16]. This kind of fracture often found in a high speed crash, the impact speed in this study was far less to cause this kind of injury.

As we demonstrated in previous research [4] , the stature and weight of individual subjects with age are compared to the reference population of Chinese children [7, 8] . For both stature and weight, the cadaveric subject populations are comparable to reference population. But most subjects we collected were below the average Chinese population at the same ages due to the long time suffering from the disease and undernourishment.

Due to the lack of first hand biomechanical response from postmortem pediatric subject, development of the current generation of child dummies has been driven by scaling of the biomechanical response requirements of the existing adult test dummies. The comparison research showed there are some significant difference between the dummies and postmortem subjects [17]. This study is, of course, limited by the use of pediatric subjects with a fairly large range of ages, but the results would provide unique blunt abdominal impact response data to evaluate the efficacy of those scaling methodologies.

The peak viscous criterion (V*C) values and maximum abdominal compression for two groups are not statistically different, but the peak force values and the maximum deformation values are statistically different. Good force-deformation data may be derived from the cadaveric response data, and force/deformation corridors have been derived for both subject populations. In the cadaver children, the force response was much less stiff as the abdominal viscera compressed into the spinal region. In addition, abdominal injuries suffered by the subjects in the testing do not correlate well with the standard injury criteria.

References

[1] http://www.safercar.gov/parents/RightSeat.htm

[2] Arbogast, K.B., et al., *Predictors of pediatric abdominal injury risk.* Stapp Car Crash J, 2004. **48**: p. 479-94.

[3] Stacey, S., et al., *Pediatric Abdominal Injury Patterns Generated by Lap Belt Loading.* The Journal of Trauma: Injury, Infection, and Critical Care, 2009. **67**(6): p. 1278-1283.

[4] Ouyang, J., et al., *Thoracic impact testing of pediatric cadaveric subjects.* J Trauma, 2006. **61**(6): p. 1492-500.

[5] Ouyang J, et al., Experimental cadaveric study of lateral impact of the pelvis in children. J First Mil Med Univ. 2003(05): p. 397-401

[6] Garrett, J.W. and P.W. Braunstein, *The seat belt syndrome.* J Trauma, 1962. **2**: p. 220-38.

[7] Vandersluis, R. and H.M. O'Connor, *The seat-belt syndrome.* CMAJ, 1987. **137**(11): p. 1023-4.

[8] Rothrock, S.G., S.M. Green, and R. Morgan, *Abdominal trauma in infants and children: prompt identification and early management of serious and life-threatening injuries. Part II: Specific injuries and ED management.* Pediatr Emerg Care, 2000. **16**(3): p. 189-95.

[9] Franklyn, M., et al., *Pediatric material properties: a review of human child and animal surrogates.* Crit Rev Biomed Eng, 2007.**35**(3-4): p. 197-342.

[10] Agran, P.F., D.E. Dunkle, and D.G. Winn, *Injuries to a sample of seatbelted children evaluated and treated in a hospital emergency room.* J Trauma, 1987. **27**(1): p. 58-64.

[11] Smith, M.D., 2nd, et al., *Pediatric seat belt injuries.* Am Surg, 1997. **63**(3): p. 294-8.

[12] Tso, E.L., B.L. Beaver, and J.A. Haller, Jr., *Abdominal injuries in restrained pediatric passengers.* J Pediatr Surg, 1993. **28**(7): p. 915-9.

[13] Jordan, B., *Lap belt complex. Recognition & assessment of seatbelt injuries in pediatric trauma patients.* JEMS, 2001. **26**(5): p. 36-43.

[14] Durbin, D.R., K.B. Arbogast, and E.K. Moll, *Seat belt syndrome in children: a case report and review of the literature.* Pediatr Emerg Care, 2001. **17**(6): p. 474-7.

[15] Arkader, A., et al., *Pediatric Chance fractures: a multicenter perspective.* J Pediatr Orthop, 2011. **31**(7): p. 741-4.

[16] Loumangardiner, K., et al., *Pediatric lumbar Chance fractures in British Columbia: Chart review and analysis of the use of shoulder restraints in MVAs.* Accident Analysis & Prevention, 2008. **40**(4): p. 1424-1429.

[17] Parent, D.P., et al., *Comparison of Hybrid III child test dummies to pediatric PMHS in blunt thoracic impact response.* Traffic Inj Prev, 2010. **11**(4): p. 399-410.

Proceedings of the 11th International Forum of Automotive Traffic Safety, 2014, pp 311-318
No. ATS.2014.312

Evaluation of Mass-based Scaling Law for Brain Injury Criteria: A Preliminary Study

Lihai REN[1], Daniel BAUMGARTNER[2], Jikuang YANG[1], [3], Narayan YOGANANDAN[4],Brain D STEMPER[4]

[1] *State Key Laboratory of Advanced Design and Manufacture for Vehicle Body, Hunan University, Changsha, China, 410082*

[2] *ICube Laboratory, University of Strasbourg, Strasbourg 67000, France*

[3] *Department of Applied Mechanics, Chalmers University of Technology SE-412 96 Gothenburg, Sweden*

[4] *Department of Neurosurgery, Medical College of Wisconsin, Milwaukee, USA*

Email: lihai.ren@hotmail.com, daniel.baumgartner@unistra.fr, jikuangyang@hnu.edu.cn, jikuang.yang@chalmers.se

Abstract:

Numerous in vivo impacts tests have been conducted on animal heads for the investigation of the traumatic brain injuries results from real-world impact accidents. The mass-based scaling law has long been used as a principal method for the scaling of input loadings as well injury thresholds between surrogate animal brains and human brain in those animal impact tests. The purpose of this study was to evaluate the performance of the mass-based scaling law for brain injury criteria.

Coronal plane rotational impacts were simulated using a rat head FE model and a human head FE model. Amplitudes and durations of rotational accelerations were defined based on prior in vivo experimental tests on rats. In total, 18 simulations, including 9 simulations using the rat brain model and 9 simulations using the human brain model, were conducted. Strain responses were extracted from four anatomical regions of interest (ROIs): parietal cortex, hippocampus, thalamus, and hypothalamus.

From the comparisons of peak strains of those ROIs, different strain patterns could be observed between those two head FE models. Meanwhile, the effects of the rotational acceleration durations on the peak strains of those ROIs were weaker in the human head FE model than the corresponding effects in the rat head FE model. Similar effects of the rotational acceleration amplitudes on the peak strains of those ROIs were observed between those two head FE models.

The simulations demonstrated that, the mass-based scaling law could be used for the scaling of the amplitude of inputted rotational accelerations, but it has limits for the scaling of the acceleration durations. Moreover, region-specific characteristics should be considered in scaling procedures of brain injuries between animals and human.

Keywords: traumatic brain injury; scaling law; finite element simulation; brain injury criteria

1 Introduction

Traumatic brain injury (TBI) is a serious public health problem in our modern society. A summary of 23 European reports showed that, for every 100,000 population in Europe, there were about 235 people suffered a TBI [1]. In the United States, 1.7 million people sustained TBI annually, and 52,000 civilians died from TBI-related injuries every year on average between 1997 and 2007 [2]. It has been revealed that approximately 60 percent of TBI cases are a result of road traffic injuries while the percentage of motor-vehicle-related TBI will grow continuously in the next decade along with the development of motorization in the developing countries [3]. Clearly understood injury mechanisms and reliable injury criteria for TBI could be helpful for the measurement of the brain injury risks in traffic accidents as well as the development of relative protection device.

Considering the similar anatomical structures of the brains between human and other mammals, in vivo animal impacts have been used as an effective tool to investigate the TBI. Not only the pathology of specific TBI, but also the tolerance of mechanical loadings as well the intracranial dynamical responses could be studied via those in vivo animal

impacts. How to scale the mechanical loadings that sustained by human head from traffic accidents to those animal head and how to apply those animal experiments to human brain protection are two essential issues that should be clearly understood. A mass-based scaling law (or Holbourn's law) for the brain injuries caused by rotational accelerations was proposed by Ommya et al. [4] and further improved by Margulies et al. [5] and Gutierrez et al. [6]. The injury scaling model was base on scaling angular head acceleration by a ratio of brain mass to the power of -2/3. By applying this mass-scaling law, diffuse brain injuries were produced in the rabbit brain while the rabbit head sustained to a sagittal plane rotational acceleration [6]. Similarly, Davisson et al. [7] investigated the diffuse axonal brain injuries in the rat brain in which study sagittal plane rotational accelerations were scaled from the corresponding accelerations for human brain injuries. Inversely, Fijalkowski et al. [8] proposed a tolerance for the concussion of the human brain based on the investigations of diffuse brain injuries in the rat brain. Moreover, a rotational injury criterion was proposed by Margulies and Thibault [9] using this scaling procedure based on the results of a primate injury model [10]. However, this scaling law was proposed based on assumptions that the brain tissue was elastic and there was no geometry difference between the human head and surrogate-animal heads [4]. In spite of the assumptions, this scaling law has not been exactly validated, especially when small mammals were used, like the rabbit and rat.

Thus, the purpose of the current study was to evaluate the performance of the mass-based scaling law for brain injury via the finite element (FE) simulations. Intracranial strain responses were calculated and compared between FE head models of the rat and human. The simulations could be helpful for the future studies on the application of the head impacts from animal experiments to human.

2 Materials and Methods

2.1 Finite element models

2.1.1 Rat head FE model

The rat head FE model (Figure 1) was developed by Baumgartner et al. [11] and previously improved and validated by Lamy et al. [12] and Ren et al. [13]. The model consisted of 150,390 nodes, 143,776 Hexahedral elements and 1 shell elements with an average edge size of 0.25 mm. the rat brain model was organized into 25 parts to present most of those essential anatomical feature of the rat brain, containing the skull, skull-brain interface (MCSF), cerebellum, olfactory bulbs, brainstem and 20 parts of the cerebrum.

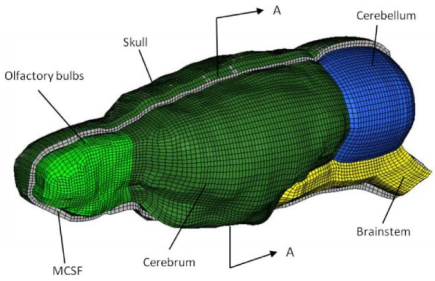

(a) Global view

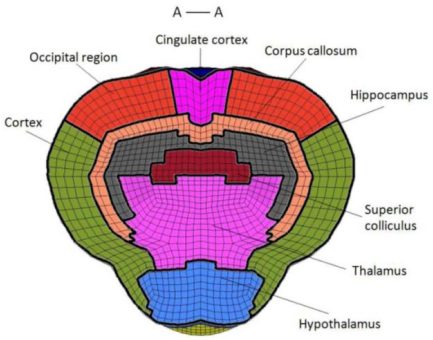

(b) Middle coronal cection view of the cerebrum

Figure 1. The rat head FE model

2.1.2 Human head FE model

A 3D human head FE model that developed by Yang et al. [14] was used in this study (Figure 2). The human head FE model consisted of 38 components, 57,043 nodes and 80,627 elements, with an effect mass of 4.4 kg. The model presented all essential anatomical features of a 50th percentile male head, including scalp, skull – with outer table, diploe, and inner table – dura, falx cerebri, tentorium, falx cerebelli, pia, cerebrospinal fluid (CSF), cerebrum, cerebellum, brain stem, and ventricles.

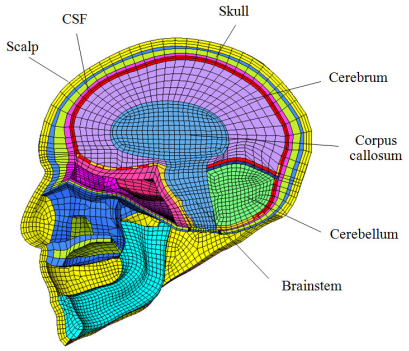

Figure 2 Middle sagittal plane view of the human FE head model

To eliminate the effect of the difference of material model/properties between these two head FE models, in the current study, same material model (LS-DYNA 971 Material Type 6) with the material properties of the rat brain were assigned to the brain tissue of the rat and human head models.

2.2 Scaling law for brain injury criteria and FE simulations

2.2.1 Scaling law for brain injury criteria

The mass based scaling law, which was suggested by Ommaya et al. [4] and further improved by Margulies et al. [5] and Gutierrez et al. [6] provides a relationship between rotational acceleration (α) and mass (m) of human and rat brains as:

$$\alpha_H = \alpha_R \left(\frac{m_R}{m_H}\right)^{2/3} \tag{1}$$

where the subscripts H and R are human brain and rat brain respectively. Provided that the human and rat brains have similar density and geometrics and are incompressible, elastic, homogeneous, and isotropic, the mass in Eq. (1) can be

substituted with the cube of the length ratio between the human and rat:

$$\alpha_H = \alpha_R (\frac{r_R}{r_H})^2 \tag{2}$$

where rH represents the radius of the human, and rR represents the radius of the rat. And for the duration (t) of the acceleration pulse:

$$t_H = t_R (\frac{r_H}{r_R}) \tag{3}$$

2.2.2 Simulations of coronal plane rotational impacts

Coronal plane rotational impacts were applied to evaluate performance of the mass based scaling method on mild traumatic brain injury. Typical shapes of the applied rotational acceleration curve included a half sine-wave acceleration pulse and a half sine-wave deceleration pulse (Figure 3). Amplitudes of the acceleration pulses were defined as 295 krad/s2 for low case (M1), 425 krad/s2 for medium case (M2), and 535 krad/s2 for high case (M3). Durations of the acceleration pulses were defined as 1 ms for low case (D1), 2 ms for medium case (D2), and 3 ms for high case (D3). Additionally, hese amplitudes/durations of rotational accelerations have been applied for the production of mild brain injuries (concussions) in the rat brain [8]. To stop the rotational motion mildly, amplitudes of deceleration pulses were defined as quarter as amplitudes of corresponding acceleration pulse, while durations of deceleration pulses were defined four times as durations of corresponding accelerations. Amplitudes and durations of acceleration curves for human head were scaled from corresponding values for rat head according to mass based scaling law (where the measured rH and rR were approximately 70 mm and 8.5 mm at the middle coronal plane of those two head FE models, respectively): M1 was 4.35 krad/s2, M2 was 6.19 krad/s2, and M3 was 7.89 krad/s2;. D1 was 8.24 ms, D2 was 16.5 ms , and D3 was 24.7 ms.

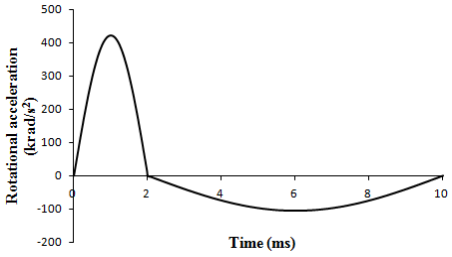

(a) Rotational acceleration for the rat head model

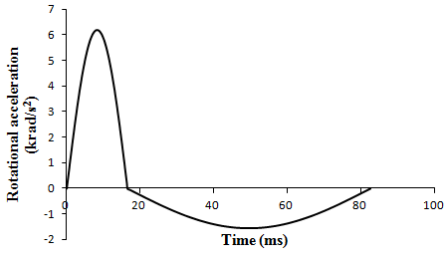

(b) Rotatiaon acceleration for the human head model

Figure 3. Sample of Rotational acceleration pulses: half sine-wave acceleration pulses followed by half sine-wave deceleration pulses (M2D2).

Intracranial strain responses (maximum principal strain) were calculated for the rat head model and the human head model, respectively. Peak strains were extracted from four anatomical regions of interest (the parietal cortex, hippocampus, thalamus, and hypothalamus) and compared between those two head models.

3 Results

Totally, 18 simulations were conducted: 9 simulations using the rat brain FE model and 9 simulations using the human head FE model, respectively. Intracranial strain responses were calculated and the maximum strains were extracted from these four anatomical regions of interest (ROIs), respectively.

3.1 Intracranial strain responses of the rat head FE model

A typical strain contour in the middle coronal plane section of the rat head FE model (sustained the acceleration with medium amplitude and medium duration-M2D2) is illustrated in Figure 4. High strain responses can be observed at up, middle and low areas in the coronal section, where the parietal cortex, hippocampus/thalamus, and hypothalamus are located, respectively. As a sample, the elemental time historical strain responses in the parietal cortex with medium amplitude and medium duration acceleration are illustrated in Figure 5.

Peak strain responses of the parietal cortex, hippocampus, thalamus and hypothalamus are illustrated below. As shown in Figure 6, peak strain responses are increased with the increase of the amplitudes of impact accelerations, but reduced slightly with the increase of the acceleration durations. This trend was consistent in all these four ROIs.

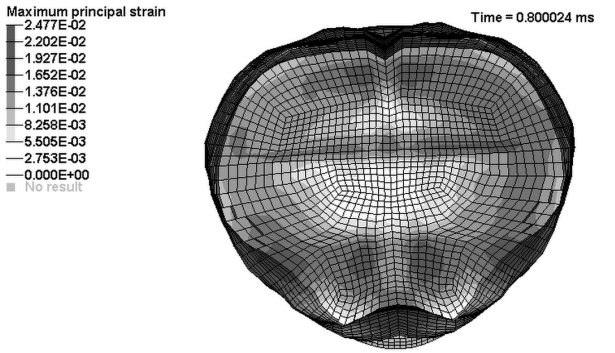

Figure 4. Strain responses in the middle coronal plane section of the rat head FE model (M2D2).

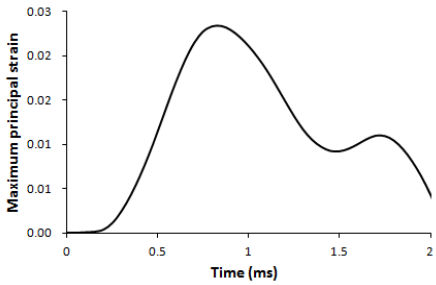

Figure 5. Sample of the elemental time history curve of the maximum principal strain in the parietal cortex of the rat head FE model (M2D2).

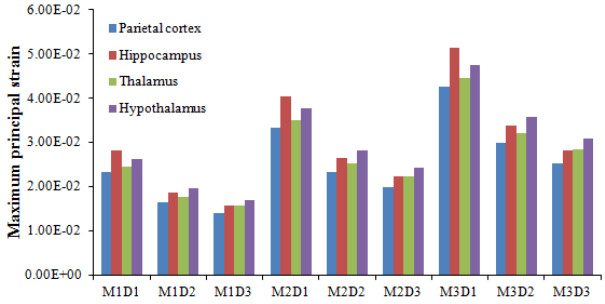

Figure 6. Peak strains in the parietal cortex, hippocampus, thalamus, and hypothalamus of the rat head model.

3.2 Intracranial strain responses of the human head FE model

A typical strain contour in the middle coronal plane section of the human head FE model is illustrated in Figure 7. High strain responses can be observed in cortex, middle area of corpus callosum, and especially basis areas. A typical time history curve of the elemental maximum principal strain is illustrated in Figure 5.

Peak strains of the parietal cortex, hippocampus, thalamus and hypothalamus calculated. As shown in Figure 9, peak strains are increased with the acceleration amplitudes, but decreased with the acceleration durations. And also, this trend was consistent in all these four regions.

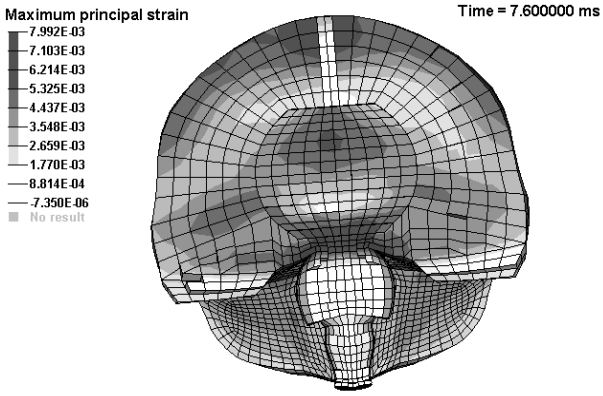

Figure 7. Strain responses in coronal plane section of the human head FE model (M2D2).

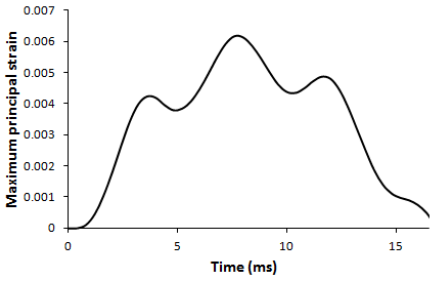

Figure 8. Sample of the elemental time history curve of the maximum principal strain in the parietal cortex of the human head FE model (M2D2).

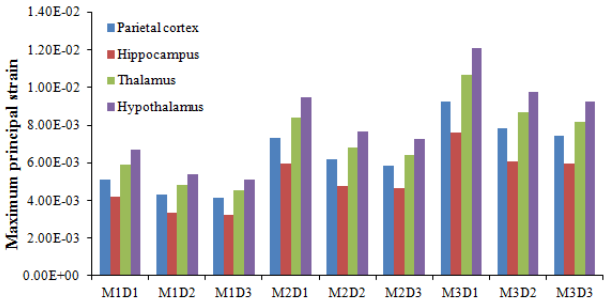

Fiugre 9. Peak strains in the parietal cortex, hippocampus, thalamus, and hypothalamus of the human head model.

4 Discussions

The objective of this study was to evaluate the mass-based scaling law for brain injuries caused by rotational accelerations. In spite of the amplitude of the rotational acceleration, the acceleration duration also has significant effect on the severity of the brain injuries while larger durations could induce longer unconsciousness [15]. Thus, angular acceleration pulses with three levels of the amplitude and three levels of the duration were imposed on the head FE models.

Generally, calculated peak strains of those four selected regions in the human head FE model were lower than those corresponding values in the rat brain model. In these four ROIs of the human head FE model, the highest peak strains were observed at the hypothalamus, followed by the peak strains of the thalamus, parietal cortex and hippocampus. In the rat head FE model, higher peak strains were located at the hippocampus and hypothalamus, followed by the peak strains of the thalamus and parietal cortex. The observed difference of the intracranial strain patterns (of those ROIs) between the rat and human head FE models could result different brain injury patterns in the rat brain and human brain, respectively. This difference also reflected one of the limitations of the mass-based scaling law that region-specific responses as well region-specific injury mechanisms/tolerances were not considered.

Effect of the durations of the rotational accelerations: The peak strains of those ROIs decreased with the durations of the imposed rotational acceleration pulses in both the rat and human head FE models. With the durations increased from D1 to D2, the percentage changes of the peak strains were -29.8%, -34.3%, -27.7 and -24.9% of the parietal cortex, hippocampus, thalamus and hypothalamus in the rat head FE model, respectively. The corresponding percentage changes were lower in the human head FE model with the corresponding values ranged from -15% to -20% of those ROIs. With the durations increased from D2 to D3, the percentage changes of the peak strains ranged from -11.6% to -16.0% of those ROIs in the rat head FE model, while the corresponding values of the human head FE model ranged from -2.3% to -5.9%. The difference of the effect of the durations of the rotational accelerations on the peak strains between the rat and human head FE models demonstrated that, the mass-based scaling law (Eq. 3) has limits for the scaling of the durations of rotational acceleration pulses.

Effect of the amplitudes of the rotational accelerations: The peak strain values of those ROIs increased with the amplitudes of the rotational acceleration in both the rat brain model and the human brain model. Meanwhile, the percentage increases of the peak strains in all ROIs were close to each other as the amplitude of the rotational acceleration increased (in both the rat brain model and the human head model). Moreover, the percentage changes of the peak strains associated with the acceleration amplitudes in the rat head model were similar as the corresponding percentage changes in the human head FE model. With the amplitudes increased from M1 to M2, the peak strain in these ROIs increased approximately 42%. With the amplitudes increased from M2 to M3, the percentage increase of those peak strain values were approximately 27%. In spite of the difference of the calculated peak strain values between

those two head models, the similar trends of the peak strains associated the amplitudes of the rotational accelerations demonstrated that mass-based scaling law (Eq. 2) were partly effective for the scaling of the amplitudes of rotational acceleration pulses.

Considering the different modeling strategies between the rat and human head FE models, additional errors could be induced into the simulations. For example, the falx cerebri was not represented in the current rat head FE model which could reduce the strains of the brain tissue adjacent to the falx cerebri [10]. Additionally, the generally lower strain responses of the human head FE model (compared with the corresponding strains of the rat head FE model) may also caused by different modeling strategies between the rat and human head FE models (figures 6 and 9).

In summary, the mass-based scaling method could be used for the scaling of the amplitudes of inputted rotational accelerations, but it has limits for the scaling of the duration of such accelerations. Meanwhile, region-specific characteristics of different anatomical regions should also be considered future studies.

References

[1] Tagliaferri F., Compagnone C., Korsic M., Servadei F., and Kraus J. A systematic review of brain injury epidemiology in Europe. Acta Neurochirurgica. 2005; 148(3):255-268

[2] Coronado V.G., Xu L., Basavaraju S.V., et al. Surveillance for traumatic brain injury-related deaths: United States, 1997-2007. Atlanta: US Department of Health and Human Services, Centers for Disease Control and Prevention, 2011.

[3] Puvanachandra P., and Hyder A.A. The burden of traumatic brain injury in Asia: a call for research. Pakistan Journal of Neurological Sciences. 2009; 4 (1): pp. 27-32.

[4] Ommaya, A.K., Yarnell, P., Hirsch, A.E., and Harris, E.H. Scaling of experimental data on cerebral concussion in sub-human primates to concussion threshold for man. SAE Technical Papers. 1967.

[5] Margullies S.S., Thibault L.E., and Gennarelli T.A. A study of scaling and head injury criteria using physical model experiments. In Proceedings of the IRCOBI Conference. 1985.

[6] Gutierrez E., Huang Y., Haglid K., and et al. A new model for diffuse brain injury by rotational acceleration: I model, gross appearance, and astrocytosis. Journal of Neurotrauma. 2001; 18(3):247-257.

[7] Davidsson J., Angeria M., and Risling M. Injury threshold for sagittal plane rotational induced diffuse axonal injuries. In Proceedings of IRCOBI Conference. 2009. York, UK.

[8] Fijalkowski R.J., Stemper B.D., Pintar F.A., Yoganandan N., and Crowe M.J. New rat model for diffuse brain injury using coronal plane angular acceleration. Journal of Neurotrauma. 2007; 24(8):1387-1398.

[9] Margulies S.S., and Thibault L.E. A proposed tolerance criterion for diffuse axonal injury in man. Journal of Biomechanics. 1992; 25(8): 917-923.

[10] Margulies S.S., Thibault L.E., and Gennarelli T.A. Physical model simulations of brain injury in the primate. Journal of Biomechanics. 1990;23(8):823-836.

[11] Baumgartner D., Lamy M., and Willinger R. Finite element analysis of traumatic brain Injuries mechanisms in the rat. In Proceedings of IRCOBI conference. 2009. York UK.

[12] Lamy M., Baumgartner D., Yoganandan N., Stemper B.D., and Willinger R.. Medical & Biological Engineering & Coputing. 2013; 51(3):353-365.

[13] Ren L., Baumgartner D., Davidsson J., Yang J., and Willinger R. Effect of the Inhomogeneous Brain Mechanical Characteristic on Dynamic Responses of Head under Trauma. In Proceedings of IRCOBI conference. 2014. Berlin, Germany.

[14] Yang J., Xu W., and Otte D. Brain injury biomechanics in real world vehicle accident using mathematical models. Chinese Journal of Mechanical Engineering (English Edition). 2008; 21(4): 81-86.

[15] Fijalkowshi R.J. Roational acceleration pulse characteristics affect midl diffuse brain injury severity. Marquette, Milwaukee

Proceedings of the 11th International Forum of Automotive Traffic Safety, 2014, pp 319- 25
No. ATS.2014.313

Simulation Analysis of Impact to Occupant Head Based on Head Impact Regulation FMVSS 201U

Du Tianya[1], Chen Jiqing [2], Huang Wei, Ma Zhengwei
[1] *School of Mechanical and Automotive Engineering, South China University of Technology, Guangzhou, China ,510640,*
[2] *Guangdong Provincial Key Laboratory of Automotive Engineering, South China University of Technology, Guangzhou, China, 510640*
Email: dty_525@163.com

Abstract: The technical requirements and test method of Federal Regulation FMVSS 201U for head impact are introduced in this paper. The head finite element model developed based on 50th percentile Chinese male adult is outlined. The traditional hybrid III free motion head(FMH) finite element model has been substituted by the developed 50th head model, which is applied to the simulation of impact on A pillar according to FMVSS 201U; the dynamics response and injury of head are shed light on based on different impact velocities.
Keywords: FMVSS 201U; Head FEM; Impact; Dynamic response

1 Introduction

On account of great complexity of road construction and car parc increasing in China, road traffic safty need more attention. Over 100000 persons died in traffic accidents every year. The number of injured people even reached 1000000[1]. The head injury always leads to the disability and death, along with tremendous financial loss and psychological trauma in society. In order to improve the vehicle crashworthiness, many European developed countries and America legislated the corresponding rules and brought them into force successively. These regulations promotes the automobile manufacturers for safety effectively. The Federal Motor Vehicle Safety Standard(FMVSS) established and implemented by the National Highway Traffic Safety Administration(NHTSA) is one of the most significant regulations, which is mainly referred to due to the shorter period of studying passive safety in other countries. In 1998, the United States government enforced the FMVSS 201U regulation to decrease injury caused by automobile to occupant head. The free motion headform[2] (FMH) model applied to FMVSS 201U is part of Hybrid III dummy[3] at present. However, the FMH size accorded with American 50th male adult, equivalent to Chinese 95th male adult. It's quite different from Chinese 50th male adult. Hence formulation of the automobile safety regulation based on Chinese human figure demands prompt solution.

The technical requirements and test methods of FMVSS 201U- Occupant Protection in Interior Impact are introduced in the paper, followed by the brief description of Chinese 50th male adult head finite element model developed by South China University of Technology. The model used in simulation is the second script, which has been modified and verified to make sure that it has high biofidelity to be used for simulation analysis of head injury and biomechanical response.

The traditional hybrid III free motion head(FMH) finite element model has been substituted by the modified 50th head model developed by SCUT(South China University of Technology), which is applied to the simulation of different velocities' impact on A pillar according to FMVSS 201U.

2 FMVSS 201U Gordian Technical Requirement Introduction

The vehicle crashworthiness could be classified as primary collision and secondary collision. The security of vehicle external structure is mainly investigated in primary collision while the protection to occupants of restraint system and interior trim parts in secondary collision [4]. The location of impact targets inside vehicle has been defined precisely. The targets distribute in two areas: the upper interior components such as seat belt anchorages, door frame, brace, pillar, sunroof, and the lower interior components. The seat backs, instrument panels, armrests and sun visors are included, as shown in figure 1. The left A-pillar was chosen as impact target part in the simulation.

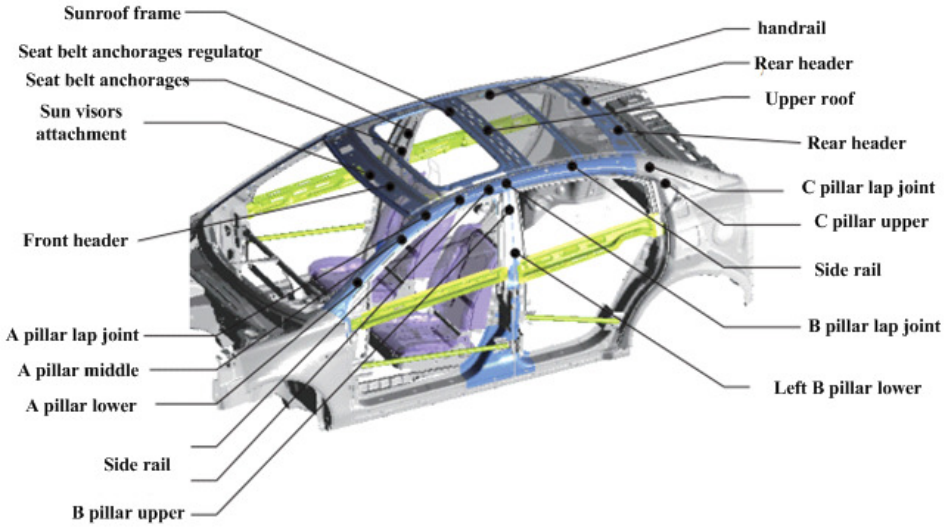

Figure 1. Impact points in vehicle upper part

2.1 AP2 Targets

In accordance with FMVSS 201U, define a vertical transverse plane (Plane 1) at the rearmost point of the windshield trim. The intersection of Plane 1 and the vehicle exterior surface is Line 1. With the vehicle side door open, set a vertical plane tangent to the outboardmost point on Line 1.there is a point (Point 1) on line 1,which is at the location of 125mm inboard of the intersection of Line 1 and the vertical plane. Locate Point 2 along the vehicle exterior surface in a longitudinal vertical plane (Plane2) passing through Point 1, 50mm rearward of Point 1. Locating a line perpendicular to the vehicle exterior surface at Point2. Set the intersection of the line and the interior roof surface as A pillar reference point. Locate the horizontal plane (Plane 3) which intersects point APR. Define the horizontal plane (Plane 4) which is 88 mm below Plane 3. Target AP2 is the point in Plane 4 and on the A-pillar which is closest to CG–F2 for the nearest seating position. CG–F2 is located at the place where the seat is in its rearmost normal design driving or riding position.

As shown in Figure [5] 2.

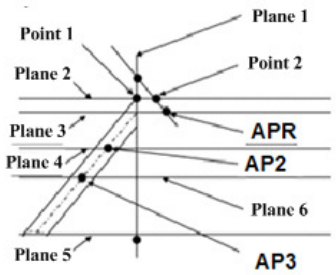

Figure 2. A pillar impact targets

2.2 Configure in Impact Tests

2.2.1 Approach Angle

The FMH attitude is described with approach angle, which is devided into horizontal angle and vertical angle. The horizontal angle of targets is the angle formed by the launched velocity vector of the FMH and the X-axial of vehicle, projecting on the horizontal surface. The vertical angle of target is the angle formed by the launched velocity vector on the midsagittal plane of FMH and horizontal surface.

The headform launching angle is within the range specified in Table 1

Table 1.A pillar approach angle limits

Interior compartment	Horizontal （°）	Vertical （°）
Left A pillar	195~255	-5~50

2.2.2 Impact Velocity

The average velocity of head impact in accidents is 24km/h, therefore NHTSA decided the velocity of head impact test as 19.2km/h or 24km/h, depending on if there is side airbag equipped or not.

When equipped with a dynamically deployed upper interior head protection system, any speed up to and including 19 km/h is required.

Any speed up to and including 24 km/ h is required for vehicles that don't meet the occupant crash protection requirements by means of inflatable restraint systems.

2.2.3 Forehead Impact Zone

The forehead impact zone of the headform is determined according to the procedure. The impacted targets must be in the zone.

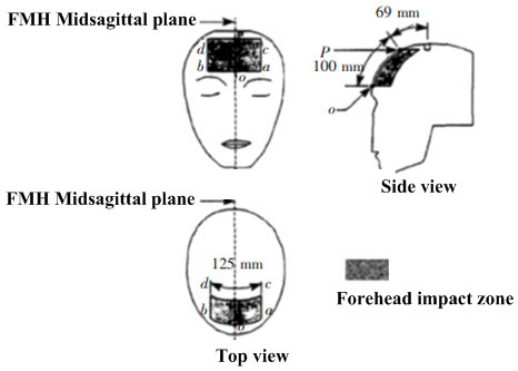

Figure 3. Forehead impact zone

2.3 Performance Criterion

The HIC(d) shall not exceed 1000 when calculated in accordance with the following formula:

$$HIC = \left[\frac{1}{(t_2 - t_1)} \int_{t_1}^{t_2} a dt \right]^{2.5} (t_2 - t_1)$$

Where the term a is the resultant head acceleration expressed as a multiple of g (the acceleration of gravity), and t_1 and t_2 are any two points in time during the impact which are separated by not more than a 36 millisecond time interval.

For the free motion headform:

$$HIC(\mathrm{d}) = 0.75446 * HIC + 166.4$$

3 Chinese 50th Male Adult Head Finite Element Model

The Chinese 50th male adult head finite element model has been modified based on the old script developed by Cai Zhihua[6,7] from South China University of Technology. The altered parts include brain tissue, skull, skin, etc. The material characteristics of model have also been revised. Moreover, for the sake of improving the computational accuracy, the mesh quality was enhanced in later modification. The modified model is shown in figure 4. The model mass is 4.52kg, measuring up the regulation.

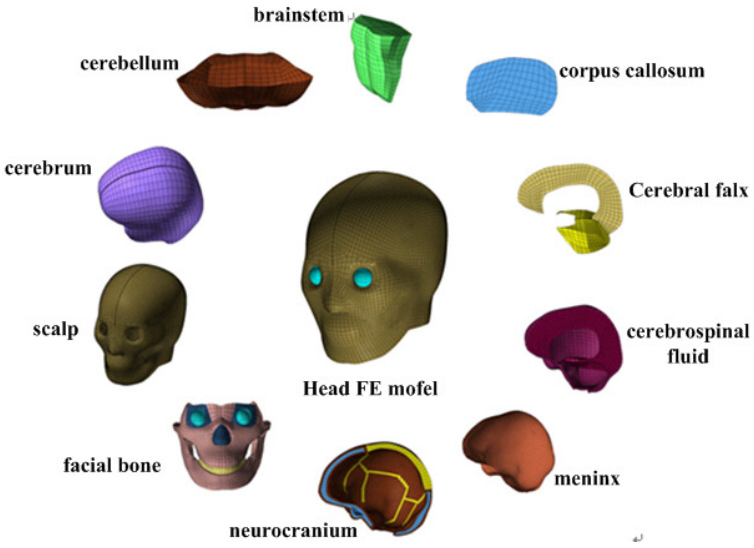

Figure 4. Modified head finite element model

The modified head model has been verified by an experiment executed by Nahum [8] for closed head impact injury, revealed that it has high biofidelity to be used for simulation analysis of head injury and biomechanical response.

Table 2.Model parameters

Part	Material type	density（g/cm[3]）	elasticity modulus (Mpa)	Poisson's ratio	G_0（Kpa）	G_∞（Kpa）	β（s$^{-[1]}$）
Scalp	elasticity	1.20	16.7	0.42			
cerebral dura mater	elasticity	1.14	31.5	0.45			
pia mater	elasticity	1.14	11.5	0.45			
cerebrospinal fluid	viscoelasticity	1.04	2 190		1	0.9	80
cerebrum	viscoelasticity	1.14	2 190		10	2	80
cerebellum	viscoelasticity	1.14	2 190		12.5	2.5	80
brainstem	viscoelasticity	1.14	2 190		22.5	4.5	80
cerebral falx	elasticity	1.14	31.5	0.45			
tentorium	elasticity	1.14	31.5	0.45			
tissue	Material type	density（g/cm[3]）	elasticity modulus (Mpa)	Poisson's ratio	yield stress(Mpa)	failure strain	
Cortical bone	elastic-plastic	2	15000	0.25	32	1.5%	
cancellous bone	elastic-plastic	1.3	4600	0.3	28	1%	

4 Head Impact Simulation Based on FMVSS 201U

4.1 Procedure conditions

According to FMVSS 201U regulation, the simulation analysis of A pillar-head impact was simulated with three different velocities (18km/h, 24km/h, 30km/h), keeping the approach angle constant, to analyze the effect of impact velocity on head injury and dynamic response. The model was set as free boundary condition because of the short computation time. AP2 was chosen as impact target. The simulation period was 15 seconds.

Table 3. simulation parameters

target	impact velocity	horizontal	vertical
AP2	18km/h	20°	230°
AP2	24km/h	20°	230°
AP2	30km/h	20°	230°

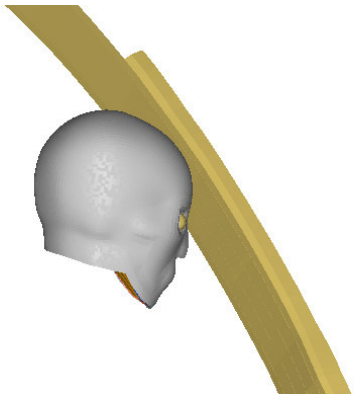

Figure 5. A-piilar impact simulation

4.2 Result Analysis

The simulation was processed in LS-DYNA, obtaining the impact force-time curve, the acceleration-time curve and the stress contour.

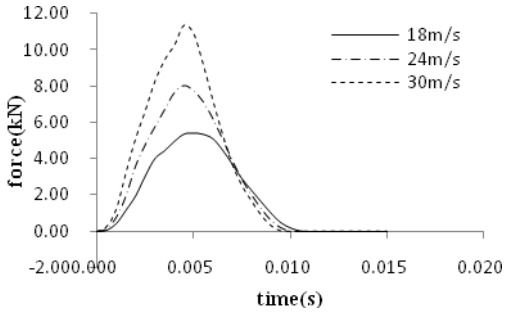

Figure 6. Force-time curve

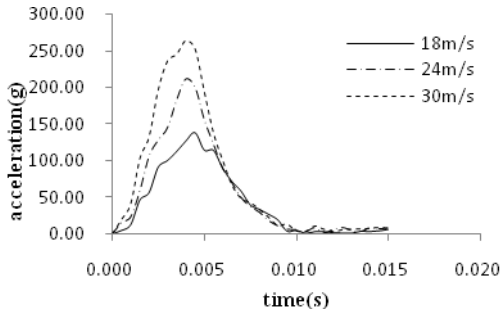

Figure 7. Acceleration-time curve

It reveals that different velocities don't affect the impact duration, maintaining 10 ms. The peak value of impact force is reached at 5ms while acceleration peak value reached earlier. However, both the curves run the same trend. Value increased as time passed, decreasing after reaching the peak. With the impact velocity raising, the force and acceleration increases faster and the peak values get greater.

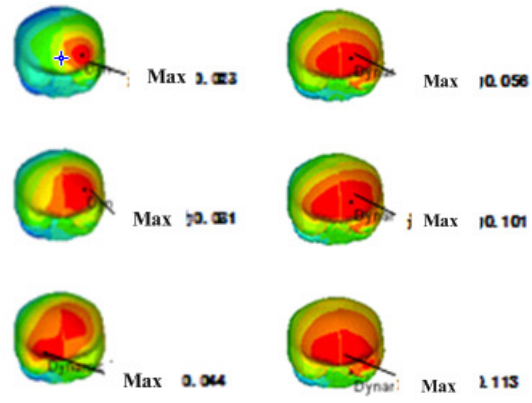

(a) 1ms **(b) 2ms**

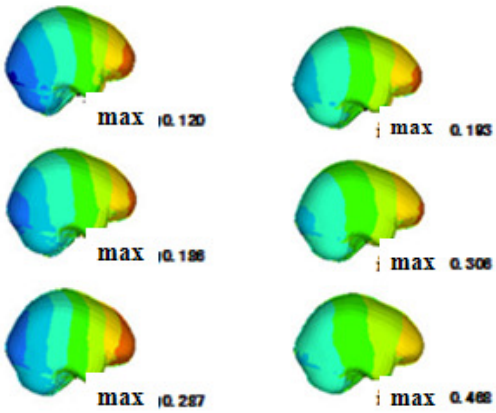

(c) 3ms **(d) 4ms**

Figure 8. Brain tissue stress contour

The brain tissue stress contours at 1ms, 2ms, 3ms, and 4ms are shown in figure above. The stress distribution pattern at different moment is in accordance. Stress concentrated in impact area at beginning. The stress contour shed light on typical impact/contrecoup distribution pattern. In fore impact zone, stress produced by compression is positive. In contralateral occipital bone zone, stress produced by tension is negative. Brain tissue suffered higher stress in the wake of higher impact velocities, following the increasing peak stress in impact zone as well as the contralateral zone.

Table 4. Brain tissue impact results

Velocity(km/h)	HIC	HIC_d	Forehead peak stress （MPa）	Back nest peak stress （MPa）
18	518.628	557.684	0.193	-0.110
24	1212.99	1081.55	0.306	-0.158
30	2451.52	2015.97	0.468	-0.211

The result of head-Apillar impact simulation reveals that HIDd value was becoming greater while impact velocity rose. The HIDd was 518.628 at velocity of 18km/h, which indicated the head injury was slight and in the reasonable range. When velocity was set as 24km/h, HIDd climbed over 1000, even reaching 2015.97 when 30km/h. it signified the brain tissue would get seriously injured and the probability of getting AIS3+ damage will greatly increase.

5 Conclusions

Under the frame work of FMVSS 201U regulation, the simulation analysis of A pillar-head impact was studied with different velocities, the traditional FMH model substituted by modified 50th Chinese male adult head finite element model. AP2 was chosen as impact point. The result indicates that the head injury risk becomes higher as impact velocities increasing, which can be basis data of automobile safety regulation formulation.

References

[1] Carsten O and Day J. Injury priority analysis task a.USA: Department of Transportation National Highway Traffic Safety Administration (NHTSA) 1988 2-30.

[2] Finite Element Model of FMH[G]. First Technology Safety Systems (FTSS), 1998.

[3] National Highway Traffic Safety Administration,Dept. of Transportation Standard No.201: Occupant Protection in Interior Impact, 49 CFR, Ch. V, Parts 571. 201[s]. Federal Motor Vehicle Safety Standards, October 1998.

[4] Wang Yajun, Chen Chaozhuo, Wu Shenrong. Application of FMVSS201 in vehicle collision interior impact to occupant head Injury [J].J Automotive Safety and Energy, 2010, 1(2):127-131.

[5] Xu Baining, Yao Chunge. Simulation on Head Impact of Interior Trim Based on Generator[J].Auto Engineer, 2013(9):30-32.

[6] Cai Zhihua, Lan Fengchong, Chen Jiqing, Shi Lei. Construction and Validation of the Assessment Model for Human Head Injury in Vehicle Traffic Accident[J].Automotive Engineering, 2012, 34(9):782-786.

[7] Shi Lei. Study on Human Head Biomechanical Response and Simulation in Vehicle Collisions[D]. Guangzhou: South China University of Technology, 2011.

[8] Nahum A,Simth M D.An experimental model for closed head impact injury. In:Proc of 20th Stapp Car Crash Conference. Dearborn: Society of Automotive Engineers,1976,785-814

Proceedings of the 11th International Forum of Automotive Traffic Safety, 2014, pp 326- 333
No. ATS.2014.314

Development and Validation of a Human Neck Muscles FE Model in Low-speed Vehicle Collisions

Cao Yingchun，Li Fan，Hu Wei，Su Sicheng

State Key Laboratory of Advanced Design and Manufacturing for Vehicle Body，Hunan University，Changsha，China，410082

Email:caoyingyoyo@163.com

Abstract：Base on the human head-neck FEM developed in Hunan University, this paper presented a neck-muscles 3D finite element model, which evaluated modeling of cervical muscle using a combination of passive viscoelastic solid elements and active spring Hill elements. The whole model was validated through the volunteer tests in frontal impact tests. Simulation results showed that the active muscle response had a great effect on head-neck dynamic responses; furthermore, the head-neck model had a good biofidelity, which will contribute to the numerical research.

Keywords: FE model; active muscle response; frontal impact; kinematics response

汽车低速碰撞中乘员颈部肌肉有限元模型的建立和验证

曹迎春，李凡，胡伟，粟思橙

湖南大学汽车车身先进设计制造国家重点实验室，长沙，中国，410082

Email:caoyingyoyo@163.com

摘　要：在已有的由湖南大学开发和验证的人体头颈部有限元模型的基础上，建立了一个人体颈部肌肉三维有限元模型。该模型包括肌肉被动与主动响应，用六面体实体单元和梁单元进行模拟，其材料分别定义为粘弹性和弹性。头颈整体模型用前碰撞志愿者实验数据进行了验证。验证结果表明颈部肌肉主动响应对头颈动力学响应的影响较大，该头颈有限元模型具有较好的生物逼真度，可应用于前碰撞环境中的数值研究。

关键词：有限元模型；肌肉主动力；前碰撞；动力学响应

1　引言

颈部损伤是交通事故中最为常见的一种乘员损伤形式，往往会给伤者带来严重的伤害或者长期性的痛苦，给社会与个人造成巨大的经济负担和精神损失。多年来研究者们进行了大量的实验与数值研究，但由于其复杂的解剖学结构和生物力学特性，人们仍然无法深入地认识颈部的损伤机理。

随着数值计算技术的发展，数值模型得到了广泛应用。近年来国内外建立了多个用于动力学分析的颈部有限元模型，Pontius 与 Liu 等人采用头颈部多体模型研究了肌肉主动响应对后碰撞环境中乘员动力学响应的影响[1]；De Jager、Van der Horst 与 Wittek 等人相继建立了以 Hill 骨骼肌本构模型为基础的头颈多体及有限元模型[2,3,4]；Frechede 与 Meyer 分别以实体单元建立了头颈部模型[5,6]；Ejima 建立了颈部主要肌肉的详细几何模型，首次在有限元模型中考虑颈部肌肉的几何外形与解剖学位置对头颈响应的影响[7]；Hedenstierna 建立了具有真实肌肉几何特征以及肌肉主动响应的头颈有限元模型[8]。

本文是在已有的湖南大学头颈部有限元模型的基础上，建立了一个基于人体解剖学结构的颈部肌肉三维有限元模型，并将其进行匹配。经过前碰撞验证的模型具有较高的生物逼真度，能够满足头颈部动力学响应研究

和损伤机理研究。

2 方法和材料

建立了一个 50 百分位成年男性的颈部肌肉的三维有限元模型，然后与头颈基础模型进行匹配[9]，并对头颈基础模型进行适当的调整。完整的头颈有限元模型应用美国海军生物力学实验室的前碰撞志愿者实验结果进行了验证。

2.1 基础模型

本研究中采用的基础模型包含两部分，头颈部和胸部有限元模型。头颈有限元模型是由杨济匡等人基于 LS-DYNA 有限元软件开发的 HBM-Head-Neck FE Model II 50 百分位头颈部模型[9-11]，该模型应用美国海军生物力学实验室前碰撞志愿者实验[12]及查尔摩斯大学后碰撞滑车实验[13]数据进行了验证；胸部模型采用王方[14,15]等人建立、验证的与头颈基础模型匹配的胸部有限元模型的胸腔骨骼部分，作为颈部肌肉下端连接与固定的基础，该模型按照若干实验数据[16-19]进行了模拟验证。除去以梁单元模拟的肌肉之后，基础模型如图 1 所示。

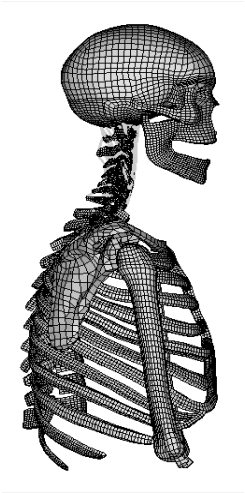

Figure 1. HBM-Head-Neck FE Model
图1. HBM头颈基础有限元模型

2.2 颈部肌肉建模

颈部主要肌肉的几何模型是基于志愿者颈部的 MRI 影像资料建立的，并利用克里格插值方法将该几何模型匹配至已有的头颈基础模型上，然后建立了相应的颈部肌肉有限元模型。

根据解剖学等效原则，志愿者颈部所有肌肉被划分为以下 12 对分别进行重建：舌骨下肌群、颈前肌、肩胛提肌、头最长肌、颈最长肌、小棱形肌、胸锁乳突肌、横突棘肌、头半棘肌、头夹肌、斜角肌以及斜方肌。其中，斜方肌仅重建了 T5 到颅底的部分；多裂肌、回旋肌、颈半棘肌整体重建为横突棘肌；前、中、后斜角肌整体重建为斜角肌；颈长肌和头长肌共同重建为颈前肌。头直肌和头斜肌由于尺寸较小，形状简单，并没有重建，而是直接以一维梁单元模拟。

在建模过程中，首先使用 8 节点和 6 节点的实体单元来描述颈部肌肉的肌腹部分。然后采用梁单元代替肌腱部分以简化连接并且肌腹实体单元两端覆有壳单元以分散载荷。此外肌肉网格外表面还覆有一层壳单元用于

基金项目：国家自然科学基金项目（51205117）；湖南省科技计划项目（2014SK3213）

定义接触。如图 2 所示，在肌肉的实体单元内部分布有串联的梁单元以模拟肌肉的主动响应，两者以共节点方式连接。

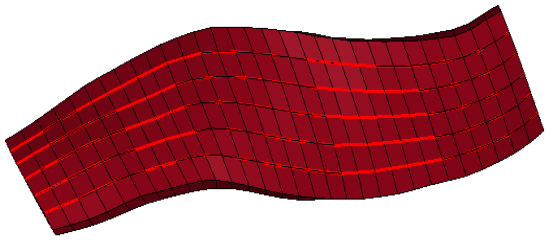

Figure 2. Neck-muscles element:a combination of viscoelastic solid elements and spring Hill elements attached at coincident nodes

图 2. 实体单元肌肉组织以及内附的梁单元

2.3 材料参数

在头颈模型中，颈部肌肉的被动响应由实体单元构造，采用 Ogden 超弹性橡胶模型进行模拟，模型的材料参数是在 Matlab 软件中基于最小二乘法对 Myers 测定的工程应力曲线拟合获得，确定的模型参数如表 1 所示。

Table 1. The Ogden constitutive model

表 1. Ogden 本构模型参数

本构关系	密度/(kg/m³)	泊松比	弹性响应	粘性响应
Ogden模型（MAT_77_O)	1.06	0.495	μ_i(Mpa)=0.01148 α_i=12.32	G_i(Mpa)=0.001;0.575;0.288;0.137 $\beta_i(s^{-1})$=73.4;50.3;42.7;0.255

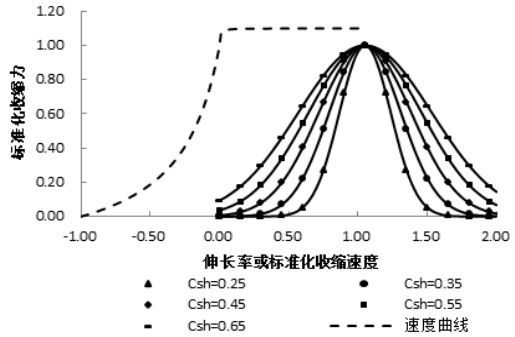

Figure 3. Curve: length and velocity of Hill element

图 3. Hill 模型的长度曲线与速度曲线

颈部肌肉的主动响应采用 LS-DYNA 中的 Hill 本构模型 MAT_156 实现，模型中所用长度曲线与速度曲线如图 3 所示，其中 Csh 为长度曲线的形状参数，针对 Myers 实验数据拟合而得 Csh 为 0.45[20-21]。

由于不同肌肉之间长度与 PCSA 等几何特征并不相同，因此最大等长收缩力 F_{max} 与最大收缩速度 V_{max} 需要针对各肌肉分别定义。F_{max} 与 V_{max} 分别由公式(1)与(2)定义：

$$F_{max}=\sigma_{max}\cdot PCSA \qquad (1)$$

$$V_{max}=10l_{opt} \qquad (2)$$

其中 σ_{max} 是最大等长收缩应力，PCSA 是肌肉的等效生理横截面积，l_{opt} 是肌肉产生最大等长收缩力的长度。相关研究中，σ_{max} 的平均估计值在 0.2~1Mpa 之间，本文采用 Winters 与 Stark 建议的 0.5Mpa[22-23]。l_{opt} 在不同研究中取值在 0.9~1.4 之间，文中采用 Zajac 建议的 1.05[24]。公式(1)中 PCSA 使用的是头颈模型中各肌肉的实测值。公式(2)则是 Zajac 对骨骼肌所对应的 V_{max} 的一个平均估计。同时，单个肌肉中主动响应是由多个相互并联

的 Hill 梁单元串联实现的，所以公式(1)确定的 F_{max} 应该平均分配至每个 Hill 梁单元串上，头颈有限元模型中各肌肉的 F_{max} 由表 2 给出。

Table 2. The cervical muscles;number of Hill element in serial and peak isometric force F_{max}

表 2　颈部肌肉模型中 Hill 梁单元串个数以及最大收缩力 F_{max}

肌肉名称	PCSA(mm^2)	F_{max}(N)	Hill 单元个数	V_{max}(m/s)	F_{max}/M(N)
舌骨下肌群	133.6	66.8	6	0.99	11.1
颈前肌	184.9	92.4	4	1.68	23.1
肩胛提肌	308.8	154.4	8	1.27	19.3
头最长肌	73.9	36.9	4	0.98	9.2
颈最长肌	63.4	31.7	1	1.76	31.7
胸锁乳突肌	558.4	279.2	10	1.71	27.9
横突棘肌	1281.1	640.5	6	0.95	106.8
头半棘肌	246.9	123.4	10	0.94	12.3
头夹肌	252.0	126.0	8	1.23	15.8
斜角肌	281.0	140.5	16	1.10	8.8
斜方肌	1236.5	618.3	40	1.62	15.5

肌肉模型两端的肌腱部分以杨氏模量 1.2Gpa，泊松比为 0.3 的线弹性材料模型进行模拟[25]。

匹配完成的颈部肌肉网格模型参考相关解剖学文献，以并联的梁单元连接到头颈基础模型的相关位置上。由于基础模型中没有舌骨结构，舌骨下肌群上端肌腱的末端刚性连接至 C3 椎体上。同时，模型中没有肌膜、筋膜等包裹肌肉的致密结蹄组织，因而以刚度较低的弹性梁单元连接肌肉与颈椎以稳定肌肉在冲击环境中的位置，完整的头颈有限元模型如图 4 所示。

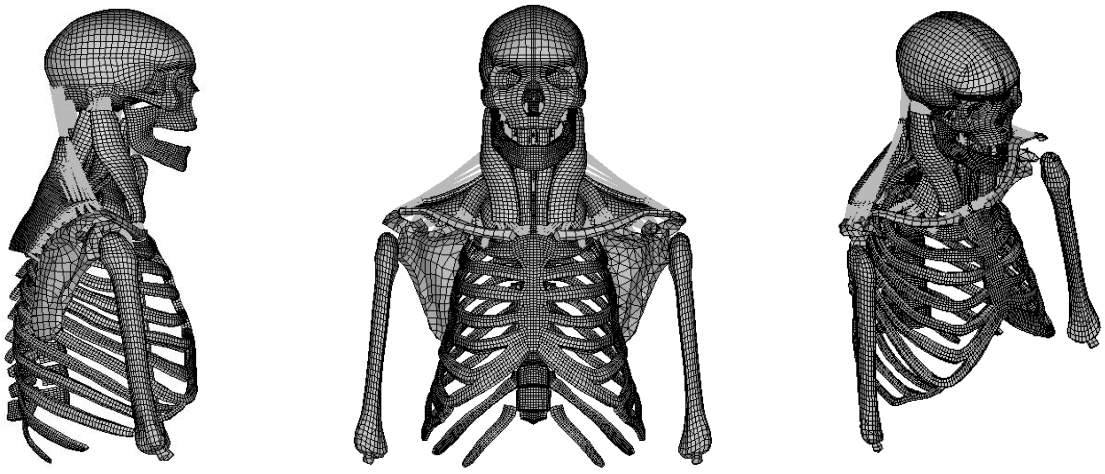

(a) 头颈模型侧面图　　(b) 头颈模型正面图　　(c) 头颈模型轴测图

Figure 4. The new head-neck FE model

图 4 完整的头颈有限元模型

2.4 载荷及边界条件

模型使用 Ewing 等人[12]给出的实验数据进行了验证，该实验是 Ewing 等人于 1978 年在美国海军生物力学实验室进行的，强度为 15g 的前碰撞志愿者实验。实验记录了碰撞过程中头部相对于 T1 胸椎的动力学响应参数。图 5 所示为碰撞过程中记录的 T1 水平加速度曲线以及转动曲线。

在仿真模拟时将头部与胸部按照动力学等效的原则转换为刚体，对颈部肌肉的主动收缩单元定义适当的激

活曲线并按照满足动力学响应的原则进行调整。将 T1 胸椎的水平加速度曲线与角位移曲线作为输入载荷条件施加于 T1 椎体最前最上端点。头颈模型定义在常规重力场中。约束胸部除水平方向平动以及矢状面内转动以外的所有自由度。其他所有结构为自由边界条件，定义肌肉之间、肌肉与骨骼之间、骨骼相互之间的接触作用。仿真时间历程 250ms。

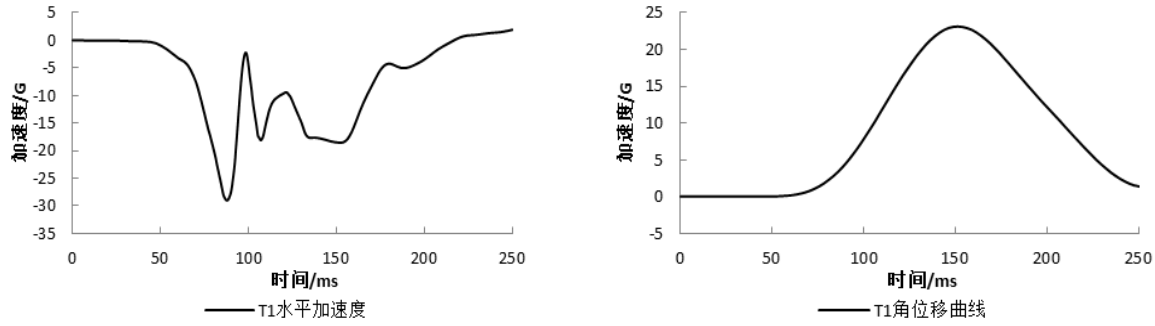

(a) T1 水平加速度曲线　　(b) T1 转动曲线

Figure 5. Kinematics of Ewing's frontal-impact experiments

图 5 前碰撞验证运动输入曲线

3 结果

图 6 为前碰撞验证仿真时头颈部的运动响应过程。

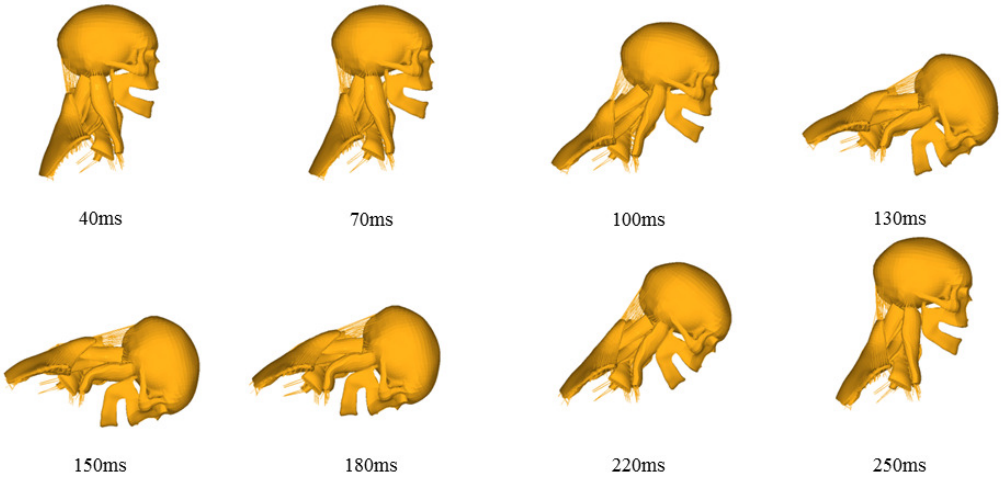

Figure 6. Movement of head-neck during frontal impact

图 6 前碰撞验证仿真中头颈运动响应

观察仿真动画可知，0 至 60ms 之间整个模型几乎处于静平衡状态，从 60ms 时刻开始 T1 产生明显的水平运动，并带动 C2~C7 颈椎以及肌肉下端向后移动，头部由于惯性作用直到 75ms 都几乎没有运动，因而 C2~C7 颈椎发生了相对于 C1 及头部枕髁的向后转动。75ms 至 100ms 之间，T1 加速向后运动，并逐渐产生了明显的转动，头部在颈椎以及肌肉的牵引下加速向下并向后运动，但其转动并不明显。此时颈椎呈 S 形状，上端椎体略微伸展转动，下端椎体产生较明显的弯曲转动。100ms 至 120ms 期间头部加速发生转动。颈椎的 S 形状运动逐渐转变为全段的弯曲转动。120ms 之后头部继续向下转动，直到 175ms 运动到其最大转动角度，此时在重力与肌肉收缩力作用下，颈椎处于压缩-弯曲-剪切的复合载荷状态中。175ms 至 250ms 期间头颈在肌肉的拉伸作用下逐渐回弹，并在 250ms 时基本恢复正常坐姿时头颈的姿态。

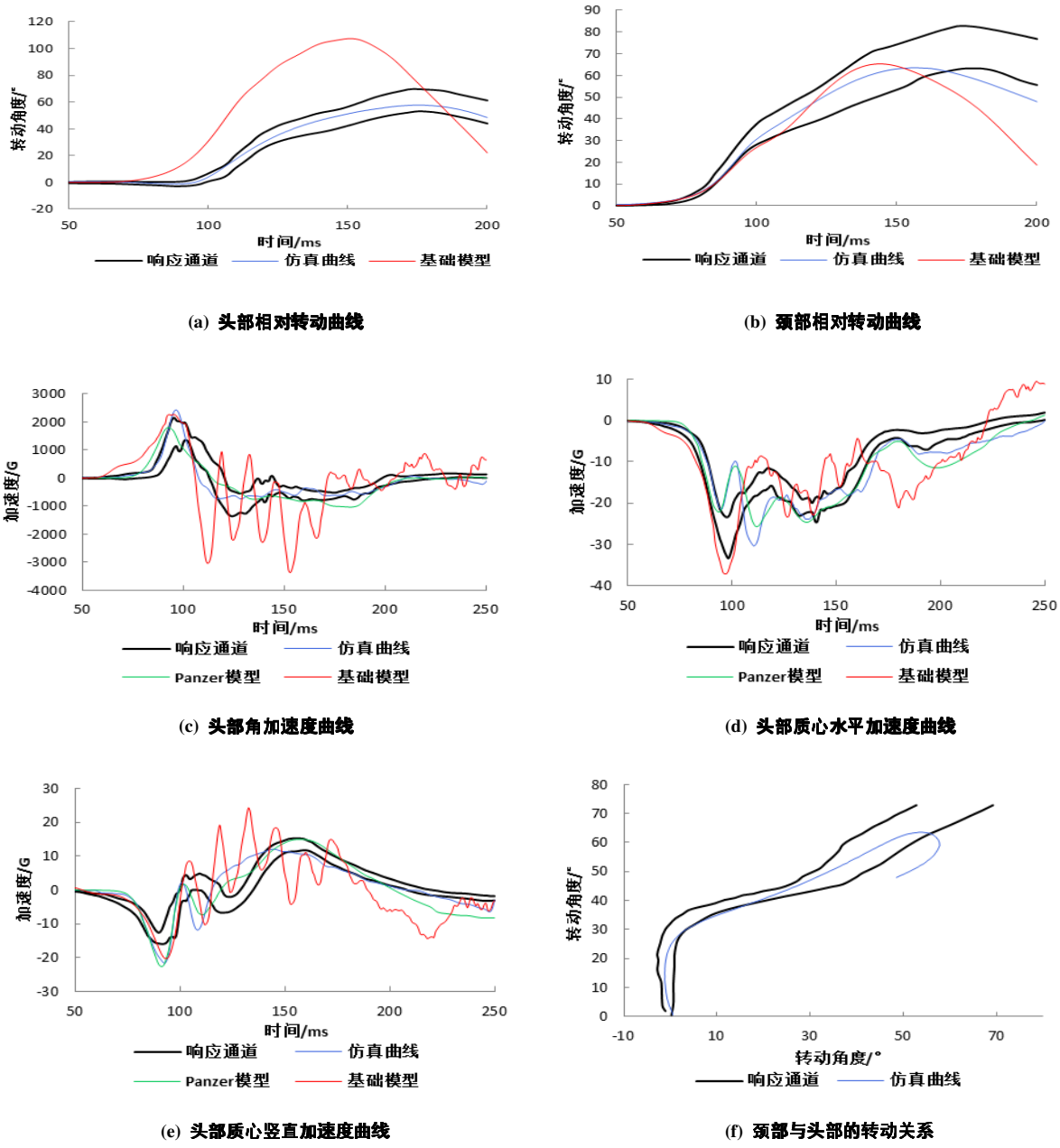

Figure 7. The validation curve of front impact

图 7 前碰撞动力学响应验证曲线

验证曲线如图 7 所示，图中分别补充了头颈基础模型[9]以及 Panzer[26]建立的以离散单元描述肌肉主动响应的头颈模型在相同载荷条件下的动力学参数曲线。

图 7(a)中头部转动角度曲线的趋势与响应通道一致程度较高，转角峰值以及峰值时刻也准确对应。(b)颈部转动角度曲线在 150ms 之前与响应通道符合程度较好，而峰值相对较低，峰值时刻为 155ms，较志愿者响应提前了 15ms，过早的回弹导致颈部转动在回弹过程中低于响应通道的范围。(c)头部角加速度曲线与志愿者响应的符合程度较好，基本落在响应通道内。第一个波峰出现的时刻与响应通道重合较好，峰值高出通道峰值 273rad/s2，约 12%。95ms 至 120ms 之间头部角加速度下降较快，略微超出了通道范围。(d)头部质心水平加速度曲线并没有准确的预测志愿者响者响应中98ms时刻的第一个峰值，而是在该时刻前后(94ms与110ms)分别得

到了两个加速度波峰。(e)头部质心竖直加速度曲线的前两个波峰皆高出响应通道约 5G，同时第二个波峰到达时刻相对于志愿者提前了 10ms。(f)给出了志愿者头颈转动的相对关系，从图中可以观察到在颈部转动达到峰值之前，模型头颈转动的相对关系与志愿者响应通道符合程度较高。模型准确预测了志愿者实验中所观察到的头部运动滞后的特征以及头部转动锁止效应。

4 讨论

本文的目的在于建立一个基于人体解剖学结构的颈部肌肉有限元模型，并与头颈基础模型进行匹配，在 15G 前碰撞环境中对头颈模型的有效性进行了验证，结果表明建立的头颈模型在前碰撞环境中的动力学响应与志愿者一致。

建立的头颈模型与 Panzer[26]模型一致程度较高，如图 7 所示，头部质心水平加速度曲线、头部质心竖直加速度曲线以及头部角加速度曲线的趋势与 Panzer 模型基本一致，仅在部分区域存在微小的差异，而且头部角加速度曲线的整体趋势比 Panzer 模型的还要好。相较于杨济匡等人[9]建立的头颈基础模型，本文建立的头颈模型扩大了验证参数集合，提高了头颈模型的生物逼真度。如图 7 所示，头颈基础模型的验证曲线都出现了较明显的波动，与响应通道的一致程度较差，而且还存在过度回弹的现象，得到不真实的运动响应。以上缺陷限制了头颈基础模型的研究应用范围，使其有效性仅局限于前 150ms 之内。本文建立的头颈模型在一定程度上避免了头颈基础模型的缺陷，在整个前碰撞过程中与志愿者响应的一致程度较好，不存在大幅的振动。与 Hedenstierna 的头颈部有限元模型[8]相比，其肌肉模型更加的细化和规整，通过实体单元来模拟颈部韧带并建立了气管的有限元模型。此外，该头颈模型建立了相应的舌骨结构，使得模型更加的精细，生物逼真度更高，这也是我们下一步要开展的工作。

通过与头颈基础模型以及 Panzer 的研究对比可知，建立的头颈模型的有效性相对于头颈基础模型有较大的改善，达到同类研究的基本水平。然而出于模型结构以及参数等因素，模型的生物逼真度仍存在一定的局限性。模型与志愿者响应的主要差异在于头部质心水平加速度曲线的双波峰，头部质心竖直加速度曲线第二个波峰的提前与幅值偏高，以及颈部转动峰值时刻的提前与幅值的偏低三个方面。前两个差异可能是由椎间盘模拟的简化、颈部结构间的空隙与软组织预张紧力的缺乏等因素引起的，第三个差异表明颈部转动的频率偏高，刚度偏大。经观察，额外的刚度可能是由颈部肌肉引入的。调试激活曲线的过程中发现，增加颈部肌肉力中主动部分的比例有利于延迟转动峰值时刻。所以颈部转动曲线的结果表明模型中肌肉被动响应的比例偏高。所有的颈部肌肉都参照 Myers[17-18]测定的兔子 TA 的被动力学性能定义参数可能不合适，需要更多地参照相关研究对颈部肌肉的被动响应进行适当的调整。

前碰撞验证仿真表明肌肉的主动响应对头颈动力学过程存在显著的影响。由于缺乏 15G 前碰撞过程中志愿者颈部肌肉活动的数据，本验证过程中采用的激活曲线是按照满足动力学响应要求的原则调整获得的，即基于建立的模型根据动力学响应对激活曲线进行反推。所以本验证仿真中肌肉的主动响应并不能准确地反映志愿者的真实响应，仅仅是一个粗略的估计。为了提高模型的生物逼真度并加深对人体在碰撞环境中真实响应的理解，应该针对肌肉的活动特征开展相关研究。

总的来说，建立的头颈有限元模型在前碰撞条件下具有较高的生物逼真度，能够满足头颈动力学响应与损伤分析研究的需求。

参考文献 (References)

[1] Pontius U R, Liu Y K. Neuromuscular cervical spine model for whiplash. In: Proc of Offshore Technology Conference. 1976 (SAE Spec Pub SP-412).

[2] De Jager M K J. Mathematical head-neck models for acceleration impacts. Eindhoven Technische Universiteit Eindhoven 1996.

[3] Wittek A. Mathematical modeling of the muscle effects on the human body responses under transient loads example of the head-neck complex: [Dissertation]. Chalmers University of Technology, 2000.

[4] Vander Horst M J. Human head neck response in frontal, lateral and rear end impact loading: modeling and validation. Technische Universiteit

Eindhoven, 2002.

[5] Frechede B, Bertholon N, Saillant G, et al. Finite element model of the human neck during Omni-directional impacts. Part II: relation between cervical curvature and risk of injury. Computer methods in Biomechanics and Biomedical engineering, 2006, 9(6): 379-386.

[6] Meyer F, Bourdet N, Deck C, et al. Human Neck Finite Element Model Development and Validation against Original Experimental Data. Stapp car crash journal, 2004, 48: 177-206.

[7] Ejima S, Ono K, Kaneoka K, et al. Development and validation of the human neck muscle model under impact loading. In: Proc of the 2005 International IRCOBI Conference on the Biomechanics of Impact, Held in Prague, Czech Republic, September 21-23 2005 IV-Biomechanics of Neck Injuries. 2005.

[8] Spitzer W O. Scientific monograph of the Quebec task force on whiplash- associated disorders: redefining 'whiplash' and its management. Spine, 1995, 20: 1-73.

[9] Xu Wei. Finite Element Modeling of Head-Neck Biomechanical Responses of Occupant in Vehicle Crashes. Master Thesis, Hunan University, 2004.

许伟. 汽车碰撞事故中乘员头颈部生物力学响应的有限元分析和研究[湖南大学硕士学位论文]. 长沙: 湖南大学, 2004.

[10] Yang Jikuang and Yao Jianfeng. *Development and Validation of a Human Neck FE Model in Impact Loading Condition*. Journal of Hunan University (Natural Science), 2003, 30(4): 40-46.

[11] Yang Jikuang, Xu Wei and Otte Dietmar. *Brain Injury Biomechanics in Real World Vehicle Accident Using Mathematical Models*. Chin J Mech Eng-En, 2008, 32 (4): 81-86.

[12] Thunnissen J, Wismans J, Ewing C L, et al. Human volunteer head-neck response in frontal flexion: a new analysis. In: Proc of Stapp Car Crash Conference. Society of Automotive Engineers SAE, 1995, 39: 439-460.

[13] DAVIDSSON J，DEUTSCHER C，HELL W ，et al. Human volunteer kinematics in rear-end sled collisions [A].International Research Council on the Biomechanics of Impact[C].1998.289-301.

[14] Wang Fang, Yang Jikuang, Li Guibing. Finite Element Analysis on Human Thorax Responses under Quasi-static and Dynamic Loading [J]. Automotive Engineering, 2014, 36(2):189-194.

王方, 杨济匡, 李桂兵. 准静态和动态载荷下的人体胸部响应有限元分析.汽车工程, 2014, 36(2):189-194.

[15] Wang Fang, Yang Jikuang, Li Guibing. Finite Element Analysis of Human Rib Fracture under Various Impact Loading Conditions, Chinese Journal of Theoretical and Applied Mechanics, 2014, 46(2): 300-307.

王方, 杨济匡, 李桂兵. 多种冲击载荷条件下的人体肋骨骨折有限元分析, 力学学报, 2014, 46(2): 300-307.

[16] Kemper Andrew R, McNally Craig, Kennedy Eric A, et al. Material Properties of Human Rib Cortical Bone from Dynamic Tension Coupon Testing [J]. 49th Stapp Car Crash Journal, 2005, 49:199-230.

[17] Kallieris D, Schonpflug M, Yang J, et al. Injury Mechanisms Database [R]. Official Deliverable of HUMOS - 2. Report No.3ESI-030901-E1-DB, 2004.

[18] Li Zuoping, Kindig Matthew W, Kerrigan Jason R, et al. Rib Fractures Under Anterior-posterior Dynamic Loads: Experimental and Finite Element Study [J]. Journal of Biomechanics, 2010, 43(2): 228-324.

[19] Patrick Lawrence M. Impact Force-Deflection of the Human Thorax [J]. 25th Stapp Car Crash Journal, 1981, 811014: 471-496.

[20] Myers B S, Van Ee C A, Camacho D L, et al. On the structural and material properties of mammalian skeletal muscle and its relevance to human cervical impact dynamics. In: Proc of Stapp Car Crash Conference. Society of Automotive Engineers SAE, 1995, 39: 203-214.

[21] Myers B S, Woolley C T, Slotter T L, et al. The influence of strain rate on the passive and stimulated engineering stress--large strain behavior of the rabbit tibialis anterior muscle. Journal of biomechanical engineering, 1998, 120(1): 126-132.

[22] Winters J M, Stark L. Analysis of fundamental human movement patterns through the use of in-depth antagonistic muscle models. Biomedical Engineering, IEEE Transactions on, 1985 (10): 826-839.

[23] Winters J M, Stark L. Estimated mechanical properties of synergistic muscles involved in movements of a variety of human joints. Journal of biomechanics, 1988, 21(12): 1027-1041.

[24] Zajac F E. Muscle and tendon: properties, models, scaling, and application to biomechanics and motor control. Critical Reviews in Biomedical Engineering, 1988, 17(4): 359-411.

[25] Maganaris C N, Paul J P. In vivo human tendon mechanical properties. The Journal of Physiology, 1999, 521(1): 307-313.

[26] Panzer M. Numerical modeling of the human cervical spine in frontal impact. 2006.

Proceedings of the 11th International Forum of Automotive Traffic Safety, 2014, pp 334- 342
No. ATS.2014.315

Study of anatomical differences between six-year-old child and adult based on CT images

LV Wen-le[1], RUAN Shi-jie[1], LI Hai-yan[1], WANG Chun-xiang[2], CUI Shi-hai[1]

[1]Center for Injury Biomechanics and Vehicle Safety Engineering, Tianjin University of Science and Technology, Tianjin, China,300222, [2]Department of Radiology, Tianjin Children's Hospital, Tianjin, China, 300222

Email:lvwenle_86@126.com

Abstract:

Background: In recent years, many intact finite element models of different percentile adults have been successfully constructed by many domestic and foreign researchers, while the development of finite element models for children was restricted by ethical and other factors, CT data, material parameters and verification data used for modeling were difficult to obtain, which was a major obstacle for the development of children's finite element models.

Objective: This paper is aimed to illustrate and study quantitatively the anatomical differences between a six-year-old child and adult, which provided new data reference and basis for model construction and children injury studies.

***Method and Material*:** The anatomical features of head, chest, hip and knee were observed and measured by using medical software MIMICS based on CT images of a six-year-old child and adult. The relevant structural data of the main bones and soft tissues was measured and compared.

***Results*:** The area ratios between the six-year-old child and adult were 86.79% for the skull and 79.90% for the brain, respectively. For the child head, differences existed in anatomical dimension; degree of body development, in the anterior-posterior direction was more developed than in superior-inferior direction. The occipital lobes were more mature than the frontal lobes. The joints of the six-year-old child exhibited with thicker cartilages, indicating the ossification process was not yet completed as adult bones.

***Conclusions*:** The differences in development of various tissues sizes and directions between six-year-old children and adults indicated that children are not simply smaller versions of adults, so the finite element models of children obtained by scaling adult model had limitations. The present paper provides new reference and evidence for model construction and children injury studies.

Keywords: Six-year-old child; Adult; CT images; Anatomical differences

基于 CT 图像的六岁儿童与成人解剖学结构差异的量化对比研究

吕文乐[1]，阮世捷[1]，李海岩[1]，王春祥[2]，崔世海[1]

[1] 天津科技大学损伤生物力学与车辆安全工程中心 300222，天津，中国

[2] 天津市儿童医院影像科，300222，天津，中国

Email:lvwenle_86@126.com

摘 要：

研究背景：近年来，国内外研究人员已成功构建出不同百分位的完整成人有限元模型，而儿童有限元模型的开发则受到伦理道德等因素的限制，用于建模的 CT 数据、材料参数及验证数据难以获取，使得儿童模型的开发存在很大的困难。

目的：本文旨在研究六岁儿童与成人之间的解剖学结构的量化差异程度，为儿童损伤建模研究提供了新的数据参考和依据。

方法与材料：基于 1 例六岁儿童和成人的 CT 图像，应用医学软件 MIMICS 观察头部、胸部、臀部及膝关节的解剖学特点，对主要的骨骼及软组织的相关结构数据进行测量对比。

结果：六岁儿童与成人的脑颅轮廓面积比和大脑轮廓面积比分别为 86.79%和 79.90%，两者在解剖学几何上存在着差异性；六岁儿童头部前后方向发育比竖直方向相对成熟，大脑的枕叶发育比额叶成熟，其组织在不同方向的发育程度存在差异性；六岁儿童骨骼不同部位存在着较厚软骨，成人时这些软骨已部分骨化成骨。

结论：六岁儿童与成人各个组织的尺寸和不同方向的发育程度都存在差异性，说明儿童不是成人的简单缩小，所以通过缩放成人有限元模型获得的儿童有限元模型具有局限性。本研究为儿童损伤建模研究提供了新的数据参考和依据。

关键字：六岁儿童；成人；CT 图像；解剖学差异

1 引言

儿童在日常生活中属于弱势群体，容易遭受各种不同类型的伤害，其中儿童的跌伤发生率在伤害发生类型中占首位[1]，交通事故对儿童的致死率处于各种死因的第二位[2]。为了更好地研究伤害发生过程中儿童损伤情况，更为有效地保护儿童，研究儿童各组织结构的解剖学特点显得尤为重要。国内外学者对于成人解剖学结构的研究已日趋成熟，而儿童解剖学的相关研究显得相对匮乏。其中具有代表性的有 Ogden 及廖亚平的儿童解剖学研究著作，Ogden[3]著作中简要地描述了儿童骨骼的发育过程及解剖学结构，并借助 患者的 CT 图像进行儿童骨折方面的研究。廖亚平[4]著作中对成人解剖学结构进行了简单的概述，并阐述 了儿童各组织器官的生长发育过程。另外随着医学影像技术的发展，CT 图像已广泛应用于人体解剖学结构方面的研究[5-6]。

本文基于六岁儿童和成人的 CT 图像，应用 MIMICS 对主要的骨骼和软组织结构数据进行测量及对比分析，研究二者之间的解剖学结构差异程度，为儿童有限元模型的构建及损伤机理研究提供科学的数据参考。

2 材料与方法

2.1 材料

本文采用的 CT 图像来源于 1 名健康六岁儿童和成人。应用 CT 机以 1mm 层厚对六岁儿童进行扫描并重构图像，最终以 DICOM 格式保存。

2.2 方法

将 CT 图像导入到 MIMICS 软件中，应用阈值分割方法并适当调整对比度，使得各组织之间的边界更加清晰，以便于骨骼及软组织结构数据的测量。本文所需观察测量的对象为：头部尺寸、颅骨、大脑、胸骨、肋骨、髋骨、髌骨和股骨。

2.2.1 头部尺寸

六岁头部所需测量的尺寸数据共有 4 个，如图 1 所示，分别为头围（a）、头高（b）、头长（c）和头宽（d）。其中头高、头宽和头长在 MIMICS 中可直接测量获得，而头围的获得则需将待测位置的外轮廓应用曲线命令提取，并导入到三维软件中，应用其强大的测量功能测得。根据所测的儿童头部尺寸数据，在国家标准 GB/T 26158《中国未成人人体尺寸》中选取尽可能近似的百分位头部尺寸数据[7]，并参考国家标准 GB/T 10000《中国成年

人人体尺寸》，选取相应百分位的成人头部数据[8]。

2.2.2 颅骨与大脑

颅骨分为后上部的脑颅和前下部的面颅，二者以眶上缘和外耳门上缘连线为分界线[9]。脑颅和面颅所支持的器官不同，而有着各自不同的发展过程。脑颅骨的发育与脑的发育相适应，从胚胎开始脑颅骨得到快速的发育，出生以后反而减慢[4]，六岁时的脑颅发育已比较接近成人脑颅。应用 MIMICS 软件提取六岁儿童和成人颅骨的中矢状面外轮廓线（如图 2 所示），并将所得轮廓线导入到三维软件中，调整颅骨使其处于竖直方向且鼻骨尖端位于同一水平线上。

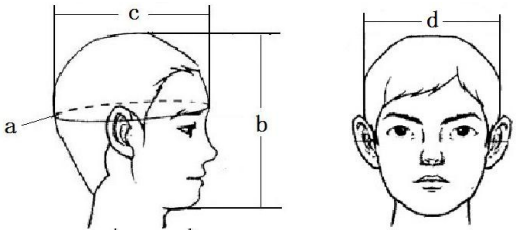

Figure 1. Schematic diagram of the head measurement

图 1.头部测量项目示意图

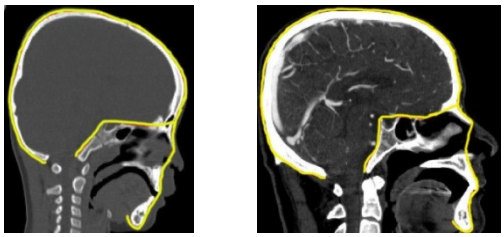

(a) **(b)**

Figure 2. Skull contour (a) skull contour of six-year-old-child (b) skull contour of adult

图 2.颅骨轮廓线 (a)六岁儿童颅骨轮廓线；(b)成人颅骨轮廓线

应用上述方法提取六岁儿童和成人大脑的轮廓线，如图 3 所示，并用大脑轮廓所围面积表示其发育程度，并计算获得两者间的比值。

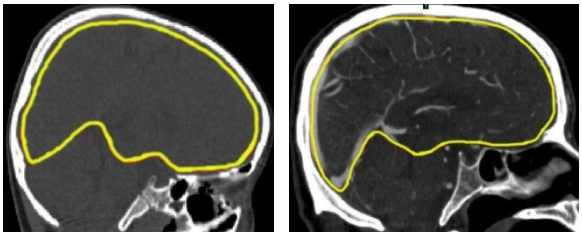

(a) **(b)**

Figure 3. Brain contour (a) brain contour of six-year-old-child (b) brain contour of adult

图 3. 大脑轮廓线 (a)六岁儿童大脑轮廓线; (b)成人大脑轮廓线

2.2.3 胸骨与肋骨

胸骨是由胸骨柄、胸骨体和剑突三部分构成。图 4（a）所示 CT 图像为六岁儿童胸骨中矢状面，胸骨柄与胸骨体间由软骨连接，图 4（b）为通过阈值分割方法提取的胸骨几何模型。

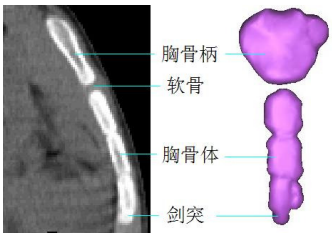

(a) (b)

Figure 4. Sternum of six-year-old child (a) CT image of sternum (b) geometrical model of sternum

图 4. 六岁儿童胸骨 (a)胸骨 CT 图像; (b)胸骨几何模型

肋骨是弓形的带状扁骨。儿童八岁之前，肋骨后端的肋头和肋结节是由软骨组成，随后各出现一个次级骨化中心，逐渐实现肋头和肋结节关节面的骨化[4]。图 5 所示为六岁儿童和成人胸椎、肋骨的 CT 图像，观察可以发现：成人肋头、肋结节处完全骨化，而六岁儿童的肋头、肋结节处存在不同厚度的软骨，并应用 MIMICS 测量其厚度。

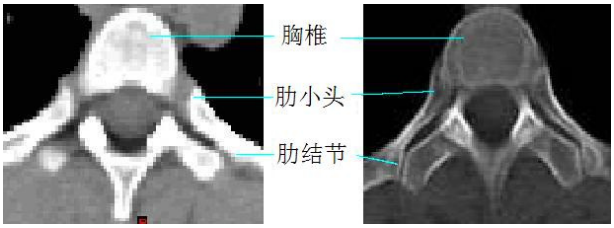

(a) (b)

Figure 5. Thoracic vertebrae and ribs CT image of six-year-old child and adult (a) Thoracic vertebrae and ribs CT image of six-year-old child (b)Adult CT image of thoracic vertebrae and ribs

图 5. 六岁儿童和成人胸椎、肋骨 CT 图像 (a)六岁儿童胸椎和肋骨 CT 图像 (b)成人胸椎和肋骨 CT 图像

2.2.4 髋骨

成人髋骨是一块完整的不规则形状的扁骨，而儿童的髋骨由独立的髂骨、坐骨和耻骨组成，它们之间通过“Y”型的软骨连接[4]。图 6（a）为六岁儿童髋骨 CT 图像，其中曲线所围区域为软骨。图 6（b）为 MIMICS 中提取的髋骨几何模型，其中 3 块独立骨块间的“Y”型间隙为软骨部分，并分别测量出软骨 3 个端部的宽度、厚度以及 3 个分支的面积。

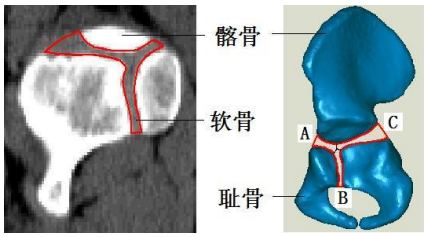

(a) (b)

Figure 6. Hip of six-year-old child (a) CT image of hip
(b) geometrical model of hip

图 6. 六岁儿童髋骨 (a)髋骨 CT 图像; (b)髋骨几何模型

2.2.5 髌骨和股骨

新生儿的髌骨完全是软骨，且髌骨属于软骨内成骨。随着年龄的增长，软骨由内向外进行骨化，直到青春期才完成骨化过程[4]。图 7 为六岁儿童和成人髌骨 CT 图像，图 8 为六岁儿童和成人髌骨几何模型的剖视图。

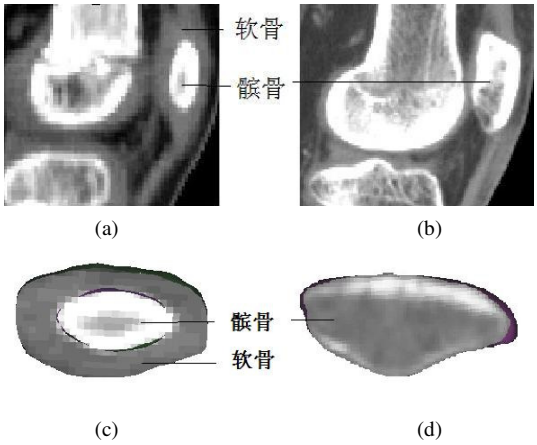

Figure 7. Patella (a) CT image of a six-year-old child's patella (b) CT image of adult patella (c) sectional view of the patellar geometrical model of six-year-old child (d) sectional view of the patellar geometrical model of adult

图 7. 髌骨 (a)六岁儿童髌骨 CT 图像;(b)成人髌骨 CT 图像;
(c)六岁儿童髌骨几何模型剖视图;(d)成人几何模型剖视图

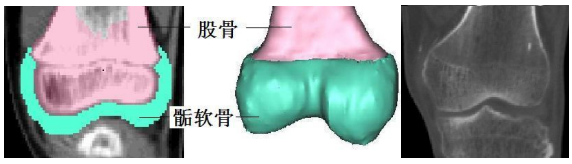

Figure 8. Femur (a)CT image of six-year-old child's femur

(b)geometrical model of six-year-old child's femur

(c) CT image of adult femur

图 8. 股骨 (a)六岁儿童股骨 CT 图像；(b)六岁儿童股骨几何模型;

(c)成人股骨 CT 图像

六岁儿童胫骨上端、股骨下端均有一层髌软骨，其随着年龄的增长逐渐钙化变薄，直至完全钙化。本文以股骨为例，图 8（a）为六岁儿童股骨 CT 图像，通过手动描绘的方法区分股骨与髌软骨，图 8（b）为 MIMICS 应用阈值分割方法提取的股骨几何模型，图 8（c）为成人股骨 CT 图像。

3 结果与讨论

3.1 头部尺寸

表 1 为所测六岁儿童头部数据及国标中相应百分位的儿童与成人头部数据，其中的成人头部尺寸参考了国家标准 GB/T 10000《中国成年人人体尺寸》，其给出了第 50 百分位和第 90 百分位头高尺寸分别为 223mm 和 237mm[8]，未能给出第 75 百分位成人头高， 则应用线性插值方法获得其值为 231.75mm。从表格数据可知，六岁儿童头长占成人的 94.05%，头高占成人的 91.91%，说明儿童与成人的头长差异小于头高差异，即六岁儿童头部沿前后方向发育比竖直方向相对成熟。总体上看，六岁儿童头部尺寸占成人的比例都达到了 91%以上，其发育程度比较接近成人。表 1 中 Pn 表示第 n 百分位，百分位表示具有某一人体尺寸和小于该尺寸的人占统计对象总人数的百分比，Pn 表示有 n%人某尺寸等于或小于该尺寸。

3.2 颅骨与大脑

六岁儿童和成人中矢状面颅轮廓对比（见图 9），分别用虚线和实线来表示（颅轮廓分为脑颅和面颅轮廓），

可以看出儿童的颅轮廓小于成人的颅轮廓，为了准确地表达六岁儿童与成人间的差异，本文用颅轮廓所围面积表示其发育程度，并计算出相应颅轮廓面积间的比值。如表 2 所示，六岁儿童与成人的脑颅轮廓面积比与面颅轮廓面积比分别为 86.79%和 83.05%，且比值越大表示六岁儿童与成人颅骨发育程度的差异越小，由此可知脑颅间的差异小于面颅间的差异。脑颅轮廓面积比大于面颅轮廓面积比，也说明了六岁儿童的脑颅骨发育较面颅骨相对成熟，较为接近成人的发育程度。

Table 1. Head dimensions of six-year-old child and adults

表 1. 六岁儿童和成人头部尺寸

	头围/mm	头长/mm	头宽/mm	头高/mm
6 岁儿童 CT	539.44	174.91	165.12	215.28
GB/T 26158	511.00(P50)	174.00(P50)	152.00(P50)	206.00(P50)
4-6 岁儿童	536.00(P90)		167.00(P99)	213.00(P75)
GB10000	560.00(P50)	185.00(P50)	153.00(P50)	223.00(P50)
成人 36-60 岁	580.00(P90)		167.00(P99)	231.75(P75)
6 岁儿童尺寸/成人	96.33%(P50)	94.05%(P50)	107.92%(P50)	96.54%(P50)
尺寸(Pn)	92.41%(P90)		98.87%(P99)	91.91%(P75)

Table 2. Cranial contour area and brain contour area of six-year-old child and adult

表 2. 六岁儿童和成人的颅轮廓面积及大脑轮廓面积

	脑颅轮廓面积/mm^2	面颅轮廓面积/mm^2	颅轮廓面积/mm^2	大脑轮廓面积/mm^2
6 岁儿童	17361.37	5907.10	23268.47	10461.44
成人	20003.35	7112.82	27116.17	13092.89
6 岁儿童/成人	86.79%	83.05%	85.81%	79.90%

六岁儿童和成人大脑的矢状面轮廓线分别用虚线和实线表示（见图 10），可以看出大脑发育程度差异最小和最大分别出现在枕叶和额叶，说明大脑不同部位的发育程度存在着差异，且这种差异与年龄增长呈非线性变化[10]。由表 2 可知六岁儿童和成人大脑轮廓面积间的比值为 79.90%，小于二者间的脑颅轮廓面积比值 86.79%，说明脑颅骨发育较大脑发育相对成熟，颅骨发育为大脑发育提供了更为广阔的发展空间。

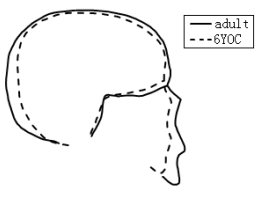

Figure 9. Cranial contours of six-year-old child and adult

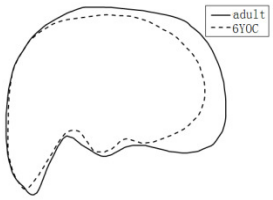

Figure 10. Brain sagittal contours of six-year-old child and adult

图 9.六岁儿童颅和成人颅轮廓　图 10. 六岁儿童与成人大脑矢状面轮廓

3.3 肋骨

应用 MIMICS 测得的六岁儿童的肋头、肋结节处软骨厚度（见表 3），其中第 11、12 肋骨没有肋结节，所以没有给出肋结节软骨厚度。图 11 为不同肋骨肋头、肋结节的软骨厚度曲线对比情况, 可以看出第 1-12 肋骨的肋头软骨厚度总体上呈减小趋势，左肋肋头软度厚度比相应右肋肋头软骨厚度大，且在第 4、5 肋骨处二者间的

差异最小；左右肋肋结节软骨厚度值交替变化，第 4、6 肋骨处二者间的差异最大；肋头处软骨厚度比肋结节处软骨厚度大。肋骨不同部位软骨的厚度差异，说明了这些软骨间骨化程度和骨化速度的差异性。

Table 3. Cartilage thickness of costal head and costal tubercle

表 3. 肋头、肋结节处软骨厚度

肋骨	肋头处软骨厚度/mm		肋结节处软骨厚度/mm		肋骨	肋头处软骨厚度/mm		肋结节处软骨厚度/mm	
	左肋	右肋	左肋	右肋		左肋	右肋	左肋	右肋
Rib1	2.85	1.98	1.65	1.75	Rib7	1.98	1.70	1.28	1.16
Rib2	2.24	1.90	1.47	1.27	Rib8	1.96	1.71	1.67	1.51
Rib3	2.42	2.23	1.10	1.05	Rib9	1.95	1.76	1.51	1.52
Rib4	2.35	2.27	1.67	1.22	Rib10	2.07	1.67	2.04	1.64
Rib5	1.81	1.76	1.07	1.01	Rib11	1.96	1.48	—	—
Rib6	2.53	1.99	0.97	1.41	Rib12	1.49	1.21	—	—

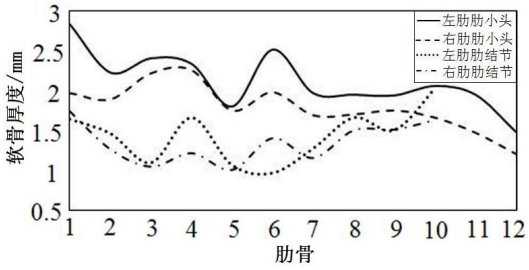

Figure 11. Cartilage thickness of costal head and costal tubercle of different ribs

图 11. 不同肋骨肋头、肋结节软骨厚度

3.4 胸骨与髋骨

胸骨柄与胸骨体之间是通过软骨连接的（见图 4），且胸骨是软骨内成骨。随着年龄的增长，胸骨软骨的骨化使得骨化中心逐渐接近，最终实现胸骨柄和胸骨体之间的骨化愈合。髋骨的发育过程与胸骨相似，六岁儿童的髋骨通过“Y”形软骨连接为一体。随着儿童的生长发育，软骨的骨化使得髋骨各部分的骨化中心相互靠近，成年时“Y”形软骨完全骨化成骨，最终连结形成一块完整的髋骨。由表 4 可以看出，软骨 A 端和 C 端的宽度相近，约为 B 端宽度的 2 倍；软骨 A 端和 B 端的厚度相近，约为 C 端厚度的一半；A 分支和 B 分支的面积相近，约为 C 分支面积的 2/3。

Table 4. Relevant data of hip cartilage of six-year-old child

表 4. 六岁儿童髋骨软骨的相关数据

	宽度/mm	厚度/mm		面积/mm2
A 端	12.41	4.20	A 分支	148.06
B 端	6.09	5.03	B 分支	162.62
C 端	12.52	14.12	C 分支	260.40

3.5 髌骨与股骨

六岁儿童髌骨的外围包裹着一层髌骨软骨（见图 7（a）），结合其几何模型的剖视图，可以看出骨化髌骨与软骨的位置关系类似于鸡蛋的蛋黄与蛋清。成人骨已完全骨化，其表面不存在软骨（见图 7（b））。

为了准确地表达六岁儿童与成人髌骨的发育程度差异，应用 MIMICS 对其进行尺寸测量，包括竖直方向、前后方向和水平方向的最大尺寸（见表 5）。

由表 5 中可以看出，六岁儿童髌骨在各个方向的骨化程度有差异，前后方向上髌骨骨化程度最低（49.56%），竖直方向和水平方向骨化程度几乎相等（59.99%和 59.56%）；从六岁儿童髌骨软骨尺寸与成人髌骨尺寸比值可知，儿童髌骨在前后方向上的发育程度最高（70.83%），水平方向上的发育程度最低（55.17%）。

图 8（a）中红色区域表示股骨，蓝色区域表示骺软骨，股骨内侧髁、髁间窝和外侧髁处的骺软骨厚度分别为 4.97mm，4.78mm 和 5.64mm。图 8（b）中的股骨几何模型可以直观形象地表达股骨与髁软骨的相互关系，髁软骨紧密地包裹着股骨下端。骺软骨随着儿童的生长发育不断骨化，成人时完全骨化成骨（见图 8（c））。

Table 5. Patellar dimension of six-year-old child and adult

表 5. 六岁儿童髌骨与成人髌骨尺寸

	竖直方向 /mm	前后方向 /mm	水平方向 /mm
6 岁儿童骨化髌骨(a)	16.82	7.87	15.66
6 岁儿童髌骨软骨(b)	28.04	15.88	26.27
成人髌骨(A)	46.78	22.42	47.62
a/b	59.99%	49.56%	59.61%
b/A	59.94%	70.83%	55.17%

4 结论

本研究基于 1 例六岁儿童和成人的 CT 图像，应用医学软件 MIMICS 观察主要骨骼及大脑的解剖结构特点，对其进行相关结构数据的测量及对比分析，直观地说明了两者之间的解剖结构差异，且文中的六岁儿童仅表示此例儿童，并不是代表全部的六岁儿童。通过以上研究，本研究得到以下结论：

（1）六岁儿童的骨骼和大脑的尺寸都小于成人，但整体上已比较接近成人尺寸；六岁儿童的各个组织发育程度存在着差异性，例如脑颅骨发育较面颅骨相对成熟，脑颅骨发育较大脑发育相对成熟。

（2）六岁儿童各个组织在不同方向的发育程度存在差异性，如六岁儿童头部沿前后方向发育比竖直方向相对成熟，大脑的枕叶发育比额叶成熟，髌骨的水平、竖直方向发育比前后方向发育成熟。

（3）六岁儿童骨骼不同部位存在着软骨，随着儿童的生长发育软骨不断的骨化，成人时这些软骨已部分骨化成骨。如胸骨柄与胸骨体间的软骨连接，髋骨通过“Y”形软骨连接成为一个整体，肋骨肋头和肋结节处覆盖一层软骨，髌骨和股骨下端表层都包裹着一层软骨。

六岁儿童与成人各个组织的尺寸和不同方向的发育程度都存在差异性，说明儿童不是成人的简单缩小，所以通过缩放成人有限元模型获得的儿童有限元模型具有局限性，与真实儿童解剖学结构存在着较大差异。本研究为儿童有限元模型的构建及损伤机理研究提供了数据参考和理论依据。

致　谢

衷心感谢天津科技大学损伤生物力学与车辆安全工程中心的各位老师和同学在文章编写过程中提出的宝贵建议。

参考文献

[1] 李丽萍，黄革，马小红，等. 2553 名 7-16 岁儿童伤害的现状分析[J]. 中国流行病学杂志，1999，20(1): 27-30.

[2] 张晓霞. 大陆交通安全社会行动：12 岁以下儿童必须坐在汽车后[EB/OL].http://www.cheyoo.com/active/report/200512/266.html, 05-12-27.

[3] JOHN A. OGDEN. Skeletal Injury in the Child[M]. Lea and Febiger: Philadelphia, 1982:128-130.

[4] 廖亚平. 儿童解剖学[M]. 上海：上海科学技术出版社 1987:69-85.

[5] 段春岳, 吕红斌, 胡建中. 基于影像学及计算机图像处理方法研究活体腰椎小关节结构三维分布[J].医用生物力学, 2012,27(2):159-165.

[6] 龚伟华, 曾一鸣, 唐坚, 等. 髋部骨折的发生与股骨近端三维几何解剖形态的相关性研究[J]. 医用生物力学, 2013,28(1):109-114.

[7] B/T 26158-2010, 中国未成年人人体尺寸[S]. 2011.

[8] GB 10000-88, 中国成年人人体尺寸[S]. 1988.

[9] 柏树令，应大君. 系统解剖学[M]. 北京：人民卫生出版社，2007:19-20.

[10] ROTH, S., RAUL, J.S., RUAN, J. and WILLINGER, R., Limitation of scaling methods in child head finite element modelling. J. Vehicle Saf.2007, 2(4): 404-421.

Proceedings of the 11th International Forum of Automotive Traffic Safety, 2014, pp 343-351
No. ATS.2014.316

Development of a FE Model of Lower Extremity for Chinese Pedestrians

Lan Fengchong, Huang Wei, Chen Jiqing, Wu Kai
South China University of Technology, Guang Zhou, China, 510640
E-mail: scuthuangwei0504@163.com

Abstract:

Pedestrian protection is a research focus in the field of automotive safety. In order to improve the study of injure biomechanics and pedestrian protection, many investigators both at home and abroad have developed FE models for pedestrians according to foreign data. But most of them are not suitable to Chinese pedestrians because of the difference between Chinese and foreigners. Based on the CT scans of 50th percentile Chinese male volunteer, this paper developed a finite element model of lower extremity with good biomechanical properties. The FE model contained major anatomical structures of human lower limb, such as femur, tibia, fibula, patella, hip and knee-joint. Especially, the knee-joint model included important soft tissues such as ligaments, meniscus and capsule. The bones were modeled with hexahedral solid elements, included cortical and trabecular layers; the ligaments were modeled with quadrilateral shell elements. Both the bone models and ligament models were defined failure to model the fracture of bones and the tear of ligaments. The model developed in this study was compared with other models developed by Untaroiu(2004), Takahashi(2000), etc. As with other models, this model has high biofidelity. The FE Model of lower extremity can be used in the research of injure biomechanics for Chinese pedestrians in traffic accidents.

Keywords: Car crash safety; Pedestrian Protection; Injury Biomechanics; Finite Element Method of Lower Extremity

1 Introduction

China is one of the countries with the largest number of casualties in traffic accident. According to official data, in 2009 the automobile population of China only accounts for 3% of the world, but the road deaths account for 16%. Compared with passengers, pedestrians are the vulnerable group of road users. Statistically, Pedestrian deaths as a percentage of total traffic fatalities approach 26% in China, however, it's only 11% in the US and 14% in Germany. [1-2] In the field of pedestrian protection, China drops behind developed countries.

In road accidents, head and lower extremity are the most common injury parts of pedestrians, accounts for 31.3% and 32.4% respectively of casualties in traffic accidents. Head injuries are the major cause of pedestrian deaths. Though lower extremity injuries are generally not fatal, it is the major factor that makes pedestrians disability. The finite element model of human lower extremity is developed to study the injury mechanisms and predict the risk of injury of pedestrians' lower extremity in road accidents. It can provide technical basis for safety design of vehicles, which has vast importance to pedestrian protection.

Many investigators both at home and abroad have developed FE models of lower extremity. For instance, Yang J K et al. developed a FE model of the human lower extremity skeleton in 1996, which was highly simplified in structures.[3] In the model reported by Costin Untaroiu et al.(2005), major anatomical structures were included and the model was validate against several PMHS tests.[4] Most of the models were developed according to foreign data, such as Visible Human Male Project(VHMP) developed by The National Library of Medicine. Obviously, there are many differences

between Chinese and foreigners in human body size. For example, the average heights of Chinese and American males are 168mm and 177mm respectively. Therefore those models are not suitable to Chinese pedestrians. This Paper aims to develop a FE model of lower extremity of 50th percentile Chinese male. The model is developed to understand the injury mechanisms of lower extremity during car to pedestrian impacts.

2 Development of lower extremity model

According to the anatomical structures, human lower extremity includes thigh, knee joint, leg and foot. During vehicle-pedestrian collision Accident, bone fracture and ligament tear are the most severe injuries of lower extremity with an Abbreviated Injury Scale (AIS) rating about 3.[5] In view of this, the study has an emphasis on the development of skeleton models and ligament models in knee joint, especially long bones of lower extremity such as femur, tibia and fibula.

2.1 Modeling method

The modeling flow diagram of lower extremity is shown in Figure 1. The geometry model was based on the CT scans collected from a volunteer close to the 50th percentile Chinese male. To reconstruct the geometry of lower extremity, points cloud was derived from the CT scans using medical software Mimics. The figure 2 shows the points cloud extraction of hard bones in lower extremity. The geometric models of lower extremity bones were reconstructed based on the points cloud through reverse modeling method. Appropriate geometric simplification was taken for finite element pre-processing. The FE mesh was generated using special pre-processor software ICEM, which has special function of plotting hexahedron gridding through mapping technology. Soft tissues such as ligaments can't be extracted from CT scans, therefore they were built according to anatomical structures using hypermesh without geometry models. The material properties were selected from references published before. The geometry of the bones in this study is shown in Figure 3.

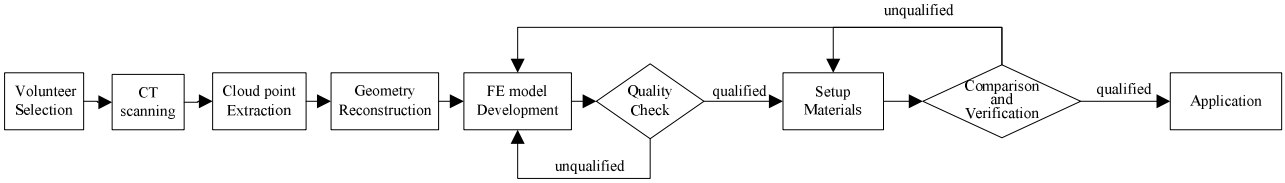

Figure 1. The modeling flow diagram of lower extremity

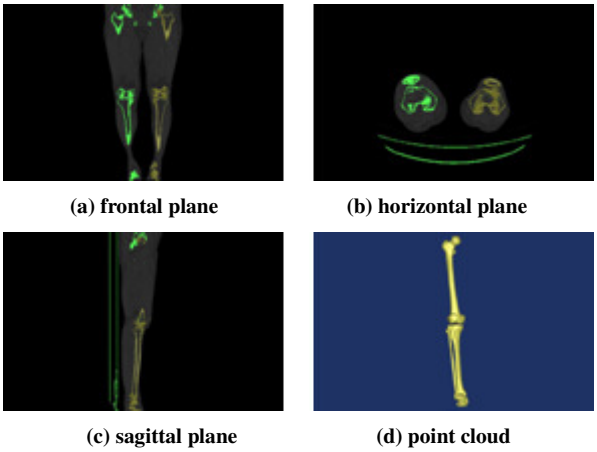

(a) frontal plane **(b) horizontal plane**

(c) sagittal plane **(d) point cloud**

Figure 2. Point cloud extraction of hard bones in lower extremity

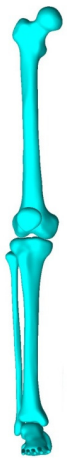

Figure 3. Geometry of bones in lower extremity

The comparison of physical characteristics is shown in table 1. The subject in this study is very close to the 50th percentile Chinese male(GB 10000-88) in physical characteristics. Besides, the difference between 50th percentile Chinese male and VHMP subject is obvious enough. Therefore, compared to those models which were based on VHMP subject, the model developed in this study is more suitable for Chinese pedestrians.

Table 1. The comparison of physical characteristics

	Height	Weight	Length(mm)	
	(mm)	(Kg)	thigh	leg
subject in this study	1680	59	470	366
50^{th} percentile Chinese male	1678	59	465	369
VHMP subject	1800	90.5	-	-
Hybrid III (50^{th} percentile)	1755	77.7	-	-

2.2 Model introduction

The FE model of lower extremity is constituted by bones and soft tissues. Bone models include hip, femur, tibia, fibula, patella and foot bone. Soft tissues concentrate in knee joint, contains ligaments, meniscus and capsule. The bones and meniscus were modeled with hexahedral solid elements. Cortical and trabecular bones were distinguished by different material properties. Soft tissues such as ligaments and capsule were meshed with quadrilateral shell elements. The interface between ligament and bone was modeled using shared nodes. The FE model of lower extremity is shown Figure 4.

Femur, tibia and fibula are all long tubular bones with marrow cavity inside. The diaphyseal of femur and tibia were modeled with three-layer hexahedral solid elements, all the three layers were considered as cortical bone. The thickness of the cavity wall was controlled in a range of 3-6 mm according to statistics. The epiphyseal cortical bone was modeled with only one outer layer solid elements, because compact bone in epiphyseal is much thinner than it in diaphyseal. To avoid the element size to be too small, the marrow cavity of fibula was ignored. Just like femur and tibia, the diaphyseal region of fibula model was considered as cortical bone. And the epiphyseal cortical bone was modeled with only the outer layer of epiphyseal solid elements, where the interior region is filled with trabecular bone elements. The FE models of hip, patella and foot bone were also meshed with hexahedral solid elements, and cortical and

trabecular layers were included. Bone models were connected by ligaments with nodes shared. The Figure 5 shows the FE model of tibia.

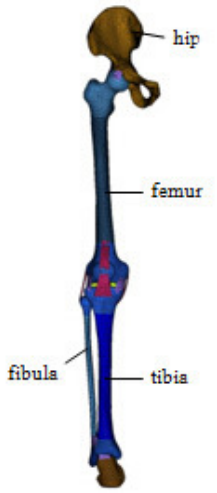

Figure 4. The FE model of lower extremity

Knee joint is not only the biggest but also the most complicated joint in the human body. It plays an important role in biomechanical responses of lower extremity in pedestrian-vehicle collision. Besides, knee joint injury is a common injury type for pedestrians in road accidents. Therefore the knee joint model was an emphasis object in this study. The knee joint model contained major soft tissues such as ligaments, meniscus and capsule, which contribute to joint kinematics and stability. Ligament models included medial collateral ligament (MCL), lateral collateral ligament (LCL), anterior cruciate ligament (ACL), posterior cruciate ligament (PCL) as well as patellar tendon. They were meshed with quadrilateral shell elements. To avoid hourglass deformation, the ligaments were modeled with fully integrated shell element. Since lack of reliable data in related literatures, the thicknesses of ligament models were assumed to be the same, with constant shell thickness of 3.5mm. Knee capsule was also modeled with shell elements with thickness of 0.5 mm, which covered the knee joint and connected the distal femur to the proximal tibia. Meniscus was a major anatomical component in knee joint between distal femur and proximal tibia. It was meshed with hexahedral solid elements. Ligaments and capsule connected bones by using shared nodes. The interface between menisci and tibial plateau was modeled by tied contact. Figure 6 shows the FE model of the knee joint.

The whole model consists of 51897 hexahedral solid elements and 2783 quadrilateral shell elements. The quality of the FE mesh was verified, such as jacobian. The minimum jacobian of the solid elements was 0.31. Only 2 % of the total solid elements were less than 0.55. Besides, the jacobian of shell elements were above 0.7. The quality of the entire model is acceptable.

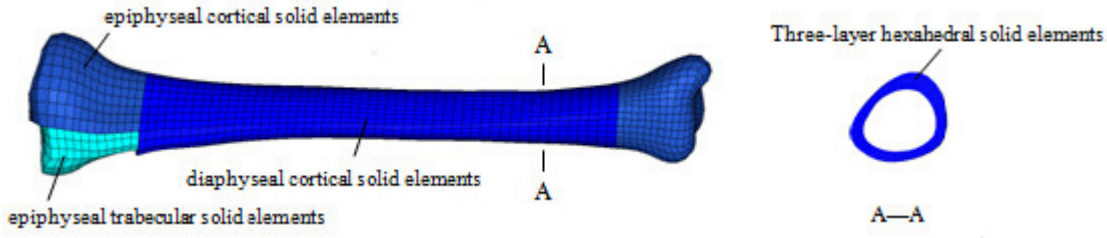

Figure 5. The FE model of tibia

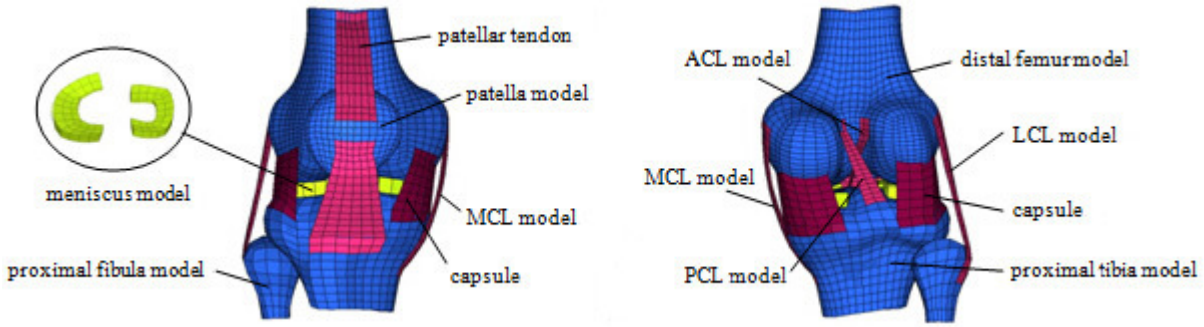

(a) front view (b) rear view

Figure 6. The FE model of knee joint

2.3 Material for the FE model

LS-DYNA was chosen as the FE solver in this paper. All the material models were selected from the existing LS-DYNA material library. Material properties of biological tissues such as bones and ligaments are always nonlinear and viscoelastic. In this study, as the limitation of the material library and the lack of correlative studies, isotropic elastic-plastic material was chosen for bones and ligaments models(*MAT_PLASTIC_KINEMATIC). The failure can be defined in the material model to simulate bone fracture and the ligament tear. The other tissues such as meniscus, capsule and patellar tendon were considered as elastic materials(*MAT_ELASTIC). The damages of them were ignored in this study. Material parameters were selected according to the researches from Untaroiu, Takahashi, Zhang, etc. The difference between Chinese and foreigners in material parameter was neglected .The material parameters used in this model are summarized in Table 2 and Table 3.

Table 2. Mechanical Properties of Bones used in the Model[4,6-7]

Bones		Density（kg/m^3）	Elastic Modulus (GPa)	Poisson's Ratio	Yield Stress(MPa)	Failure Strain(%)
Femur	diaphyseal cortical bone	1850	13.5	0.315	129	3.7
	epiphyseal cortical bone	1850	14.1	0.315	120	2.0
	epiphyseal trabecular bone	1100	0.295	0.315	9.3	13.4
Tibia	diaphyseal cortical bone	1850	17.1	0.315	125	1.8
	epiphyseal cortical bone	1850	17.5	0.315	129	2.8
	epiphyseal trabecular bone	1100	0.30	0.315	5.3	13.4
Fibula	diaphyseal cortical bone	1850	17.5	0.315	105	1.0
	epiphyseal cortical bone	1850	17.9	0.315	120	3
	epiphyseal trabecular bone	1100	0.445	0.315	7.2	13.4
Hip Patella	cortical bone	2000	17.3	0.315	100	-
	trabecular bone	1000	0.25	0.315	10	-

Table 3. Mechanical Properties of Soft tissues used in the Model[8]

Soft tissues	Density（kg/m^3）	Elastic Modulus (GPa)	Poisson's Ratio	Yield Stress(MPa)	Failure Strain(%)
MCL	1100	0.190	0.40	36	2
LCL	1100	0.170	0.40	29	1
ACL	1100	0.200	0.40	58	4
PCL	1100	0.160	0.40	35	2
Patellar tendon	1000	0.225	0.40	-	-
Capsule	1000	0.100	0.40	-	-
Meniscus	1000	0.250	0.40	-	-

3 Comparisons

As the FE model of lower extremity developed in this study was based on 50th percentile Chinese male, it was different from other models developed by foreign researchers. Typical models developed by Takahashi, Untaroiu and Kikuchi respectively were selected to compare with the model developed in this study.

Long bongs such as femur, tibia, and fibula are the most important structures in lower extremity. Long bong models developed in this study were compared with other models by modeling the quasi-static 3-point bending test, which was conducted in 1970 by Yamada[9], etc. The simulation process of femur model is shown in figure 7. The femur model was positioned horizontally on its posterior sides. Friction coefficient was defined between the femur model and the support plate to avoid the femur model slipping during loading. The femur model was loaded at the mid-shaft by a cylindrical impactor with a diameter of 25mm. The impactor was constrained to move against the femur model with a constant velocity of 0.01m/s until the fracture of femur model happened. The cylindrical impactor and support plates were meshed with solid elements, and all of them were considered as rigid. The simulation condition in this study should keep consistent with it in related literatures. Force-deflection curves were obtained and compared with the results published by Untaroiu(2004)[10] and Takahashi(2000)[6]. The simulation processes of tibia and fibula model were the same as femur.

MCL is one of the most important ligaments. It is also the most vulnerable ligaments for pedestrians in road accidents. MCL model developed in this study was compared with other models by modeling ligament tensile test, which was conducted by van Dommelen [11] in 2005. The simulation process of MCL model is shown in figure 8. The proximal tibia model was fixed. The distal femur model moved straight up in a constant velocity of 1600mm/s until the ligament was torn. In the procedure of simulation, force-deflection curve of MCL model was obtained and compared with the results published by Untaroiu(2005)[4] and Kikuchi(2006)[12].

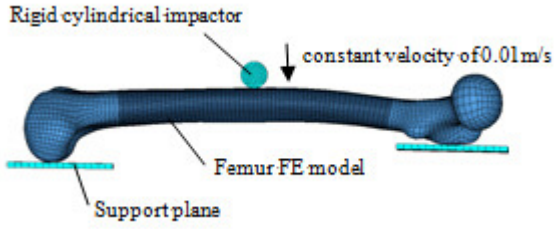

Figure 7. Simulation process of femur model

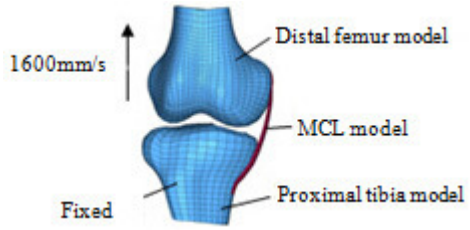

Figure 8. Simulation process of MCL model

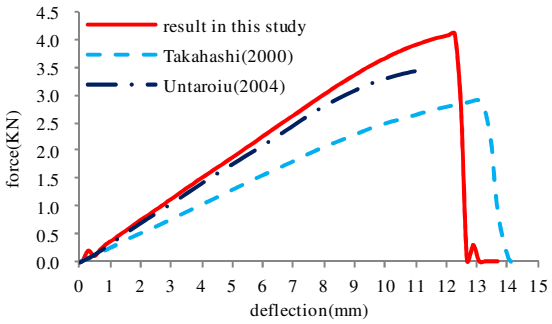

Figure 9. Comparison of different femur models

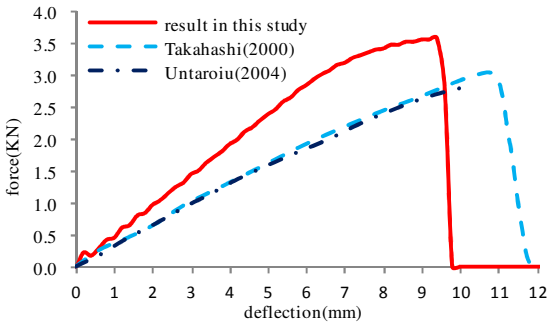

Figure 10. Comparison of different tibia models

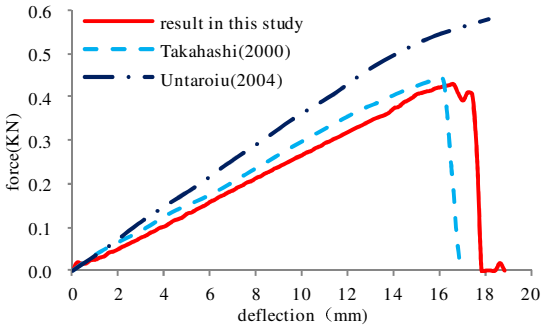

Figure 11. Comparison of different fibula models

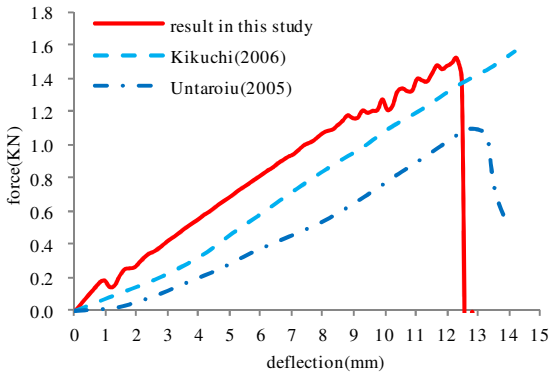

Figure 12. Comparison of different MCL models

The comparisons of quasi-static 3-point bending simulation results for long bone models are shown in figure 9-11. It can be found that the curvilinear trend of three different models is identical. The ultimate forces of femur, tibia, and fibula model in this study were 4.08KN, 3.58KN and 0.43KN respectively. The results of femur and tibia model were obviously higher than the results of Takahashi, but the fibula models showed good agreement. In the study of Takahashi, the diaphyseal cortical bone of femur and tibia were modeled by only one-layer solid element, in contrast, diaphyseal cortical models in this paper were meshed with three-layer solid element. The mechanical properties of which modeled by only one-layer elements should be worse than those meshed with multilayer elements. On the other hand, considering the individual difference, the difference among those three models is acceptable. In other words, the models of femur, tibia, and fibula in this study have high biofidelity just as the models developed by Untaroiu and Takahashi.

In addition, the simulation results show that long bones have good linear relation between deflection and loading force under static load in the middle range. The linear relation can be shown to be:

$$f=ax.$$

where x is the deflection of long bones in mid-shaft and f is the loading force. The parameter a, ultimate forces and deflections for femur, tibia and fibula model in this study are shown in the table 4. With this formula, deflection or load can be calculated when the other one is known.

Table 4. Parameters in the linear formula

$f=ax$	femur	tibia	fibula
a (KN/mm)	0.33	0.38	0.03
ultimate force (KN)	4.08	3.58	0.43
ultimate deflection (mm)	12.3	9.4	16.6

The comparison of simulation results for different MCL models is shown in figure 12. The ultimate force of the MCL model developed in this study was 1.61KN. The simulation result showed good agreement with the result of Kikuchi. In the study of Untaroiu, the MCL model was stretched in quasi-static condition, so the ultimate force was much smaller than the result of 1.61KN. As with the models developed by Kikuchi and Untaroiu, the MCL model developed in this study is reliable.

4 Conclusions

This study developed a finite element model of lower extremity with good biomechanical properties to research injure biomechanics and pedestrian protection. Specially, the model was based on 50th percentile Chinese male. It can

represent Chinese human body characteristics.

The model included major anatomical structures of human lower limb such as such as femur, tibia, fibula, patella, hip and knee-joint. The knee-joint included important soft tissues such as ligaments, meniscus and capsule. Cortical and trabecular bones were distinguished by different material properties. Both the bone models and the ligaments models were defined failure to model bone fracture and ligament tear.

The model was compared with other models developed by foreign researches. As with those models, the model developed in this study has high biofidelity. It can be used in the research of injure biomechanics for Chinese pedestrians in road accidents.

References

[1] ERSO. Statistical Report 2006[6]. European Commission: European Road Safety Observatory, 2006.

[2] NHTSA. Traffic Safety Facts 2006[R]. USA: Department of Transportation National Highway Traffic Safety Administration, 2007.

[3] Yang J K, Wittek A, Kajzer J. Finite Element Model of the Human Lower Extremity Skeleton in a Lateral Impact, 1996.

[4] Costin Untaroiu, Kurosh Darvish and Jeff Crandall. A Finite Element Model of the Lower Limb for Simulating Pedestrian Impacts[J]. Stapp Car Crash Journal, 2005(49), 157-181.

[5] Kai-Uwe Schmitt, Peter F.Niederer, Markus H.Muser, et al. Trauma Biomechanics: Accidental injury in traffic and sports [M]. Beijing: China Machine Press, 2012, pp. 123-124.

[6] Takahashi Y, Kikuchi Y, Konosu A, et al. Development and validation of the finite element model for the human lower limb of pedestrians[J]. Stapp Car Crash J, 2000(44): 335-55

[7] Zhang Guanjun.A Study on Characteristics of Lower Extremity and Related Parameters in Vehicle-Pedestrian Crashes[D]:Hunan University, 2006.

[8] Kennedy J C, Hawkins R J, Willis R B, et al. Tension Studies of Human Knee Ligaments: Yield Point, Ultimate Failure, and Disruption of the Cruciate and Tibial Collateral Ligaments[J]. Journal of Bone and Joint Surgery, 1976,58(3): 350-355.

[9] Yamada H. Strength of biological materials: The Williams & Wilkins Company, 1970: 19-280.

[10] Costin Untaroiu, Kurosh Darvish, Jeff Crandalf, et al. Development and Validation of a Finite Element Model of the Lower Limb[C] // 2004 ASME International Mechanical Engineering Congress and Exposition, 2004 : 53-62.

[11] van Dommelen J.A.W, Ivarsson B.J, Jolandan M, et al. Characterization of the Rate-Dependent Mechanical Properties and Failure of Human Knee Ligaments [C] // SAE Technical, Paper Number 2005-01-0293, Warrendale, 2005: 1-11.

[12] Yuji Kikuchi, Yukou Takahashi and Fumie Mori. Development of a Finite Element Model for a Pedestrian Pelvis and Lower Limb[C] // 2006 SAE International, Paper Number 2006-01-0663, 2006.

Proceedings of the 11th International Forum of Automotive Traffic Safety, 2014, pp 352- 356
No. ATS.2014.317

Impact Simulation of a Child Head and the Engine Hood

CUI Shi-hai LI Xiang-nan LI Hai-Yan ZHAO Wei RUAN Shi-jie
College of Mechanical Engineering,Tianjin University of Science &Technology,Tianjin,China,300222
Email: shihaicui@tust.edu.cn

Abstract: The finite element head model of a child with detailed anatomical structure was established based on CT images of a 6-year-old healthy child head. According to national standard GB/T 24550-2009, impact simulation experiments between the child head model and the simple engine hood were done. And the HIC value and the stress distribution of brain tissues were analyzed when different head parts impacted the engine hook. The results showed that brain injury mainly occurred in brainstem, parietal-occipital lobe and et al. The brain injury would be worst when the temporal part of the brain impacted the engine hood.
Keywords: six-year-old child head; finite element model; engine hood; impact simulation; brain injury

儿童头部与发动机罩的碰撞仿真研究

崔世海 李向楠 李海岩 赵玮 阮世捷
天津科技大学机械工程学院，天津，中国 300222
Email：shihaicui@tust.edu.cn

摘 要：本研究基于已构建的 6 岁儿童头部有限元模型，根据国标 GB/T 24550-2009 分析了儿童头部不同位置与简化的发动机罩碰撞时的 HIC 值以及对应的脑组织应力分布，结果表明，碰撞时脑组织损伤可能发生在脑干、大脑顶枕叶等位置，尤其是颞部与发动机罩碰撞时的脑组织损伤最严重。

关键词：六岁儿童头部；有限元模型；发动机罩；碰撞仿真；脑损伤

1 前言

据国外流行病学研究称，大脑外伤是引起少年儿童死亡及致残的主要原因[1]。车祸和坠落是引起少年儿童大脑外伤的主要诱因。研究儿童头部损伤准则及耐受限度，对于研究损伤机理及致伤原因，以及开发头部保护装置有重要意义。

但是由于涉及伦理道德，儿童尸体实验匮乏，限制了儿童颅脑损伤研究。近年来，有限元方法为儿童颅脑损伤研究提供新途径。2007 年 Roth 等 [2]建立了包括脑、大脑镰、小脑幕、卤门、脑膜、颅骨和面骨等组织在内的 6 个月儿童头部的有限元模型，并将其用于剧烈摇晃和外部碰撞两种不同载荷情况下儿童颅内响应的研究。但 Roth 等所建立的有限元模型并没有区分大脑、小脑、脑干等软组织，因而无法评估局部脑组织的应力应变分布。2012 年阮世捷等[3]建立了包括大脑、小脑、脑干等软硬组织结构在内的 6 岁儿童头部有限元模型，验证了模型的有效性。

本研究在阮等[3]模型的基础上，基于实际 CT 图像进一步细分脑白质、灰质、间脑以及软硬脑膜、窦等脑组织结构，构建具有详细颅脑结构的儿童头部有限元模型，根据国标 GB/T 24550-2009 利用该模型初步研究了儿

童头部与简化的发动机罩碰撞时的头部损伤情况。

2 儿童头部有限元模型的构建

本研究基于一名健康 6 岁儿童头部 CT 扫描图像，构建了图 1 所示的包括软硬组织在内的具有详细解剖学结构的儿童头部有限元模型，颅骨包括额骨、顶骨、颞骨、枕骨的内外骨板和未发育成熟的板障，软组织包括大脑、小脑、间脑、脑干、脑室、胼胝体、窦沟、大脑镰、小脑幕、软脑膜、硬脑膜、脑脊液等结构，其他还包括如面骨、上颌骨、下颌骨、头皮等，其中大脑镰、小脑幕、脑膜等软组织采用壳单元，其余结构均采用八节点六面体单元。整个模型包括六面体单元 96128 个，壳单元 17346 个，共有 103716 个节点。本模型除眼睛和嘴巴采用固联接触外，其余都通过共节点方法将不同部位的软硬组织连接起来。

儿童头部各组织的材料参数主要根据参考文献[4-8]进行选取，具体参数如表 1 所示。根据输入的头部各组织的材料参数，计算出该儿童头部的质量约为 3.4kg。

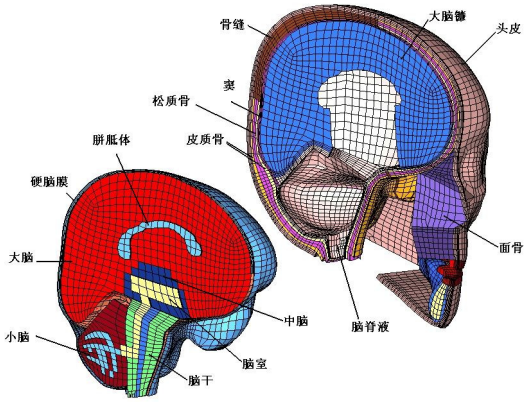

图 1 具有详细解剖学结构的儿童头部有限元模型

表 1 头部模型材料参数

头部组织	密度 ρ/kg • m^{-3}	泊松比	杨氏模量 E/MPa
脑膜	1140	0.45	31.5
脑脊液	1040	0.49	0.012
头皮	1200	0.42	16.7
颅骨皮质骨	2150	0.22	9870
颅骨松质骨	2150	0.22	3690
颅骨骨缝	2150	0.22	1100
脑组织	1040	G_0=49KPa,G_∞=16.2KPa, β=145s^{-1}	K=1125MPa

3 儿童头部有限元模型与发动机罩的碰撞试验仿真

国内于 2009 年发布了国标 GB/T 24550-2009“汽车对行人的碰撞保护”[9]，在国标中规定了儿童头锤试验所要求的头锤撞击器总质量 3.5kg,直径 165mm**Error! Reference source not found.**。本研究所建立的 6 岁儿童头部模型质量为 3.4kg，头宽为 157mm，与国标中头部冲击器的质量和尺寸近似，可用于头锤仿真试验。

3.1 儿童头部有限元模型跌落标定仿真

GB/T 24550-2009 中规定儿童头锤在进行试验前需标定。采用头部有限元模型参照头锤标定步骤进行仿真，

即头部模型从 376mm 高度坠落至刚性平面，碰撞过程中，头部前额与刚性平面接触。

仿真试验结果表明儿童头部有限元模型的合成加速度峰值为 279.16g，满足 GB/T 24550-2009 中要求加速度值大于 245g 小于 300g 的要求。

3.2 儿童头部有限元模型撞击发动机罩试验仿真

3.2.1 发动机罩碰撞位置的选取

仿真试验中将发动机罩尺寸简化为矩形厚壳单元，厚度为 0.75mm，尺寸长 1300mm，宽 700mm，发动机罩材料为 DP200 钢。仿真试验中将发动机罩后端两侧及前端中间位置进行全约束，前端两侧位置的 Z 轴方向进行约束 [10]。儿童头锤仿真试验中不考虑风挡玻璃，把车辆发动机罩的儿童头锤测试区域划分为如 2 所示的 12 个区域，并选取图 2 中的 2AB 区域（靠近风窗玻璃位置）作为仿真碰撞区域。仿真时，根据 GB/T 24550-2009 要求，头部有限元模型的不同部位以 35km/h 的速度冲击发动机罩顶面，过头部模型质心的速度与水平面成 50 度角，头部的前额与发动机罩碰撞。

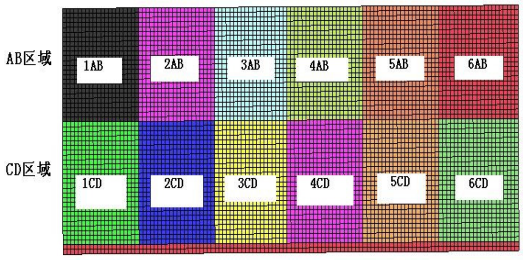

图 2 发动机罩碰撞测试区域

图 3 所示为头部不同位置与发动机罩碰撞时的加速度-时间历程曲线，其中颞部碰撞的加速度峰值最大，达到 154g，顶部碰撞的加速度峰值最小，达到 148g，可见不同碰撞位置的头部峰值加速度存在一定的差距，但仿真试验的峰值加速度基本与头锤试验数据相吻合[10]。根据国标中 HIC_{15} 值计算公式得到前额碰撞的 HIC_{15} 值为 348.48，顶部碰撞的 HIC_{15} 值为 362.73，颞部碰撞的 HIC_{15} 值为 363.68，枕部碰撞的 HIC_{15} 值为 348.48。

虽然仿真试验中的峰值加速度与头锤试验数据基本吻合，但 HIC_{15} 明显小于头锤试验结果[10]。可能的原因是由于仿真没有考虑发动机罩下硬点，而硬点的存在会减小发动机罩的变形，减少吸能，引起加速度和 HIC 值的增加；同时头锤试验的加速度-时间历程曲线较仿真曲线更宽，导致相同的峰值加速度下，头锤试验中的 HIC 值较大。头锤试验的加速度-时间历程曲线较仿真曲线宽度主要与头锤结构有关，仿真试验中有限元模型的皮肤厚度只有 2.85mm，撞击过程几乎没有缓冲作用，而头锤试验中儿童头锤外部包裹的合成皮肤厚度达到 14mm 左右，且撞击侧曲率较有限元模型大，使得撞击过程中缓冲明显，加速持续时间较长。

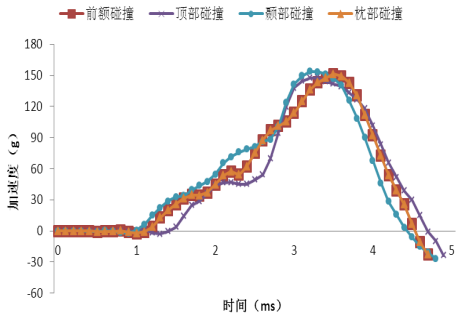

图 3 头部不同位置与发动机罩碰撞时加速度曲线

无论是峰值加速度，还是 HIC 值，头部不同位置与发动机罩碰撞，都呈现出一定差距。这与头部的实际解

剖学结构有关。以颞部与发动机罩碰撞为例，由于颞部曲率较大，使颞部与发动机罩接触面较大；同时儿童颞部骨缝的存在，会起到一定的缓冲作用。因此，其峰值加速度及 HIC 值较其他碰撞位置高。而头型冲击器由于其自身结构的原因，无法模拟出头部不同位置与发动机罩碰撞时产生的加速度及 HIC 值的不同。

虽然可以通过头部冲击器测算 HIC 值来评估头部损伤，但其无法对颅内组织，特别是脑组织的应力或应变进行评价。由于应力或应变才是与生物体组织损伤直接相关的重要参数[11]，而头部有限元模型的最大优势在于可以研究碰撞过程中脑组织的应力应变分布。Willinger[2]提出应力可作为评价儿童脑组织损伤的指标，认为当 von mises 应力达到 0.011MPa 时，脑组织损伤的概率为 50%。图 4 和图 5 所示为头部不同部位与发动机罩发生碰撞 von mises 应力达到最大值时脑组织的应力分布，可见当头部不同部位与发动机罩碰撞时，脑组织的应力峰值和高应力集中区域有所不同，具体见表 2。

以颞部与发动机罩碰撞为例，该试验仿真中脑组织应力峰值及高应力区域即损伤风险区域均较其他碰撞位置更大，这与颞部碰撞时的 HIC 值最大相对应。同时在大脑顶枕叶及中脑位置都出现了损伤风险，且两个风险区域的应力值均超过 0.015MPa，损伤风险较大。尤其是大脑顶枕叶处，不仅皮质出现损伤风险，还累及大脑白质，导致轴索损伤。这与 Gennarelli[12]和 Maxwell[13]对成人脑组织损伤的研究结果相一致。

表 2 脑组织损伤风险区域及应力峰值

碰撞位置	损伤风险区域	Von mises 峰值（出现位置）
前额碰撞	脑干、胼胝体、对冲处	0.013MPa（脑干）
顶部碰撞	脑干、胼胝体	0.032MPa（脑干）
颞部碰撞	脑干、对冲处、中脑、顶枕叶皮质及白质	0.038MPa（脑干）
枕部碰撞	脑干、对冲处	0.032MPa（脑干）

头部不同部位与发动机罩碰撞时最大应力均出现在脑干处，表明儿童脑干在碰撞中的损伤风险比较大，这与 Edburg 关于成人的脑组织损伤研究结果类似[14]。由于脑干外部分布着大量神经纤维，内部包含重要的神经核，如一般躯体运动核、一般内脏运动核等。一旦承受较大的载荷，必然导致神经调节障碍，对身体产生影响甚至危及生命。

头部不同部位与发动机罩碰撞的结果表明，无论碰撞发生在何种位置，都会导致脑组织发生损伤风险，所以必须加强对儿童行人头部的防护。

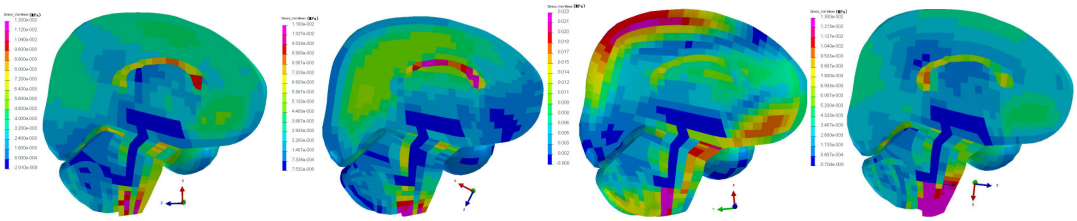

(a)前额碰撞　(b)顶部碰撞　(c)颞部碰撞　(d)枕部碰撞

图 4 von mises 应力达到最大值时矢状面内脑组织的应力分布

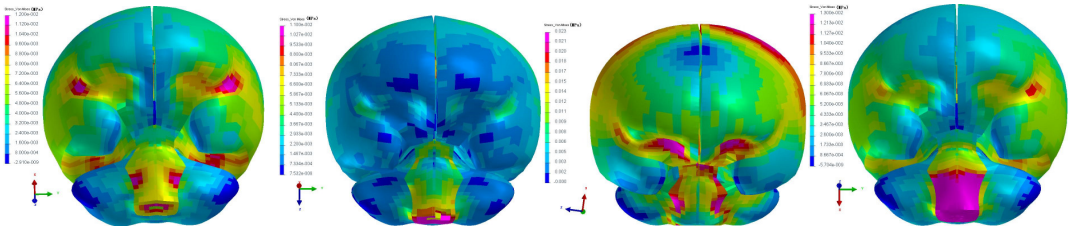

(a)前额碰撞　(b)顶部碰撞　(c)颞部碰撞　(d)枕部碰撞

图 5　von mises 应力达到最大值时冠状面内脑组织的应力分布

4　结论

本研究构建了一个包括脑白质、灰质、间脑等细分脑组织及软硬脑膜、窦等在内的具有完整颅脑结构的儿童头部有限元模型；利用该模型，根据国标 GB/T 24550-2009 要求，研究了头部与简化的发动机罩在不同位置碰撞时的 HIC 值，结果表明靠近风窗玻璃前缘的发动机罩 2AB 区域的 HIC 值较大。在该区域进一步进行的头部不同位置的碰撞仿真试验结果表明，脑干较脑组织其他部分更容易出现损伤风险，颞部碰撞的脑组织损伤风险区域最大且应力峰值最高。研究结果还表明，在 HIC 值较小的情况下，儿童脑组织可能已经出现损伤，因此儿童颅脑损伤评估必须考虑脑组织的应力情况。

参考文献

[1] D Viano, H VonHolst, E Gordon. Serious brain injury from traffic related causes: priorities for primary intervention[J]. Accid. Anal.1997, Prev29:811-816

[2] Sébastien Roth , Jean-Sébastien Raul, Rémy Willinger, et al. Finite element analysis of impact and shaking inflicted to a child[J]. Int J LegalMed, 2006,121(3):223–228

[3] 阮世捷,李盼东等. 6 岁儿童头部有限元模型的构建与验证[J]. 中国生物医学工程学报,2012,8(31):502-506

[4] C Zhou, T.B.Kahlil, L.J.Dragovic. Head injury assessment of a real world crash by finite element modeling[J].Proceedings of the AGARD Conference,1996.

[5] R.willingre, L.Tableb. Modal temporal analysis of head mathematical models[J].J.Neurotrauma,1995(4):743-754

[6] Matthew T.Davis, Andre M.Loyd, et al. The mechanical and morphological properties of 6 year-old cranial bone[J]. Journal of Biomechanics,2012(45): 2493–2498

[7] K.L.Thibault,S.S.Margulies, Age dependent material properties of the porcine cerebrum:effect on paediatric inertial head injury criteria[J].J.Biomech.,1998,31(12):1119–1126

[8] Michael T.Prange, Jason F.Luck, et al. Mechanical Properties and Anthropometry of the Human Infant Head[J].Stapp Car Crash Journal,2004,10(48):1-21

[9] GB/T 24550-2009.汽车对行人的碰撞保护，2009

[10] 李向荣,王凯等.汽车发动机罩儿童行人保护安全性仿真研究[J].汽车工程,2010,1(32):56-59

[11] Fung Y.C.. The application of biomechanics to the understanding of injury and healing. Accidental Injury-Biomechanics and prevention[M].2nd Edition,Ed.A.M.Nahum and J.W.Melvin.Springer-Verlag New York Inc.2002:1-11

[12] Gennarelli, T.A.,Thibault,L., Adams, J., Graham, D.,Thompson, C., and Marcincin, R.. Diffusd degeneration of the cerebral white matter in severe dementia following head injury[J].Ann. Neurol.,1982,12(6):564-574

[13] Maxwell, W. L., Watt, C., Graham, D. I., and Gennarelli, T. A.. Ultra-structural evidence of axonal shearing as a result of lateral acceleration of the head in non-human primates[J]. Acta Neuropathol., 1993,86(2):136 –144

[14] Edbery, S., Rieker, J.,Angrist, A., Study of impact pressure and acceleration in plastic skull model[J].Lab. invest., 1963,12(12):1305-1311

Proceedings of the 11th International Forum of Automotive Traffic Safety, 2014, pp 357- 362
No. ATS.2014.318

Numerical analysis of compressive neck injuries due to vertical loading applied through the head

Haibin CHEN[1], Liying ZHANG[2], Jing ZHANG[1,3], Shuo TANG[1], Li HE[1], Jihong ZHOU[1]

[1]*State Key Laboratory of Trauma, Burns, and Combined Injuries, Institute of Surgery Research, Daping Hospital, Third Military Medical University, Chongqing 400042, China;*

[2]*Bioengineering Center, Wayne State University, 818 W. Hancock, Detroit, MI 48201, USA;*

[3]*College of Optoelectronic Engineering, Chongqing University, Chongqing 400044, China*

Email: chenhb1996@vip.163.com

Abstract:

Background: The vehicle injury priority rating data indicated that neck injuries became the fifth most important injury category (after head, face, chest and abdomen). During rollovers the centrifugal force tends to maintain a belted occupant erect with his/her head upward and outboard, and an impact to the occupant's head would come from the upper and lateral sides of the vehicle. Up to now, knowledge on the mechanism causing this kind neck injury is still rather limited.

Objective: The purpose of this paper is to summarize a numerical analysis of compressive neck injuries due to vertical loading applied through the head.

Method and Material: Our own validated, custom-made head-neck complex FE model was used to simulate those cadaver compression tests, which was integrated 50th percentile human head-neck model with various ligaments, joint capsule and muscles connecting the head and the neck.

Results: Comparing all the cases, in general C2-C3 facets were compressed most in both local x-axis (along the facet joint surface) and z-axis (normal to the facet joint surface) more than other facets, and severe disc compression can be seen in C5-C6 and C7-T1 discs.

Conclusion: The role of compression force with more sliding in cervical facet surface may be an important causal mechanism leading to facet failure in compressive neck injuries.

Keywords: Neck injury, Facet capsule, Rollover crashes, Numerical analysis

1 Introduction

The vehicle injury priority rating data indicated that neck injuries became the fifth most important injury category (after head, face, chest and abdomen). Previous experimental (Bahling et al, 1990) and numerical (Hu, 2008) studies have shown that during rollovers the centrifugal force tends to maintain a belted occupant erect with his/her head upward and outboard, and an impact to the occupant's head would come from the upper and lateral sides of the vehicle. Therefore, a combined lateral bending, compression, and flexion/extension could be a very common neck loading mode during rollovers. Up to now, knowledge on the mechanism causing this kind neck injury is still rather limited.

For this reason, this paper summarizes a numerical analysis of compressive neck injuries due to vertical loading applied through the head.

2 Method and Material

2.1 Cervical compression test simulations

Pintar et al in 1995 performed dynamic compression tests on a total of 20 human cadaver head-neck complexes (Figure 1). Our own validated, custom-made head-neck complex FE model was used to simulate those cadaver compression tests, which was integrated 50th percentile human head-neck model with various ligaments, joint capsule

and muscles connecting the head and the neck.

To mimic the test condition, the FE neck model was fixed at the T1 inferior surface using the casting model as shown in Figure 2. The integrated neck-head model developed in neural position was rearranged to the stiff axis (Figure 2) by leveling vertebrae axis in alignment with the location of the occipital condyle. To simulate flexion and extension positions of the neck axis as described in experimental setup, the FE model was modified by moving the head 5 mm in the positive and negative x directions. The muscles were removed from the FE model. The casting was fixed in all directions at the inferior surface. A constant velocity loading was given to the impactor coated with a layer of ensolite. Only the average velocity of 5.25 m/s was used because the paper by Pintar et al. did not report exact velocities for each case. The additional velocities of 3.25 m/s and 7.25 m/s were simulated as well. The impactor was given at above velocities to a distance of 24 mm from the point of contact.

2.2 Facet capsule strain

Having validate force-deflection responses of the FE neck model against results from cervical axial compression tests performed by Pintar et al. 1995, the compression and facet strain from all three loading conditions (straight/compression, flexion and extension) were calculated for three impact velocities (3.25 m/s, 5.25 m/s, 7.25 m/s). To calculate facet stretch, the local co-ordinate system (body fixed frame) within each adjacent vertebra next to facet surfaces was defined and any movement in the +X and +Z axes was assumed to be tension and in -X and -Z axes to be compression. The facet stretch under cervical axial compression was calculated by measuring the movement of the n^{th} inferior facet cartilage surface with respect to $n+1^{th}$ superior facet cartilage surface in both local x-axis (along the facet joint surface) and z-axis (normal to the facet joint surface)

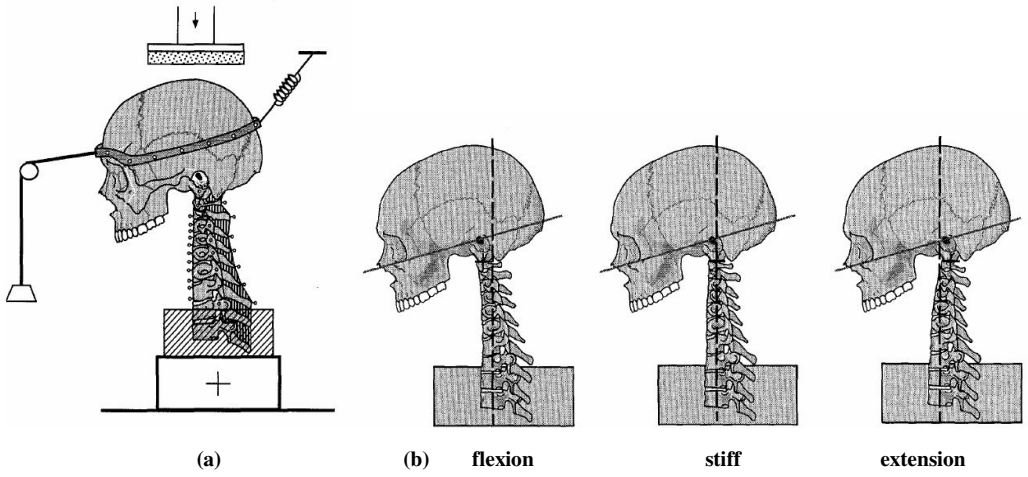

Figure 1. (a) Experimental setup showing the positioning of the cadaver and loading applied

(b) Experimental positions (flexion, stiff and extension) inducing flexion, compression and extension type injuries.

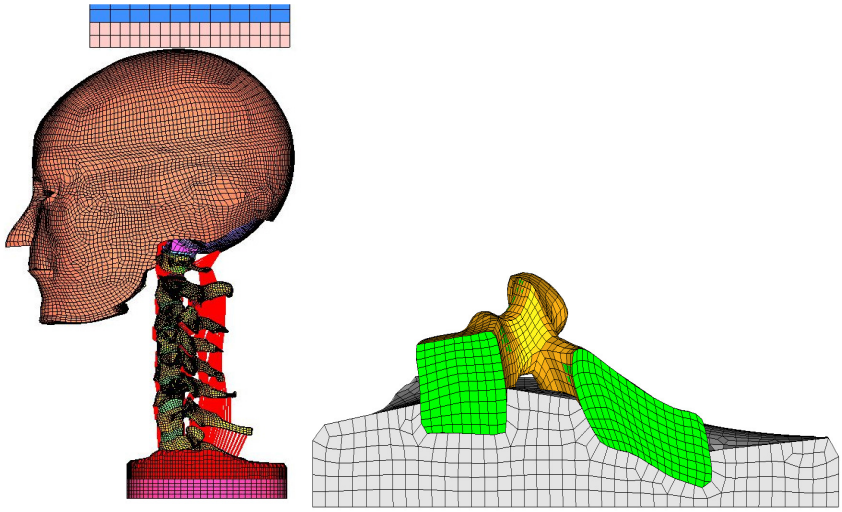

Figure 2. (a) FE model setup (b) T1 fixed to the casting

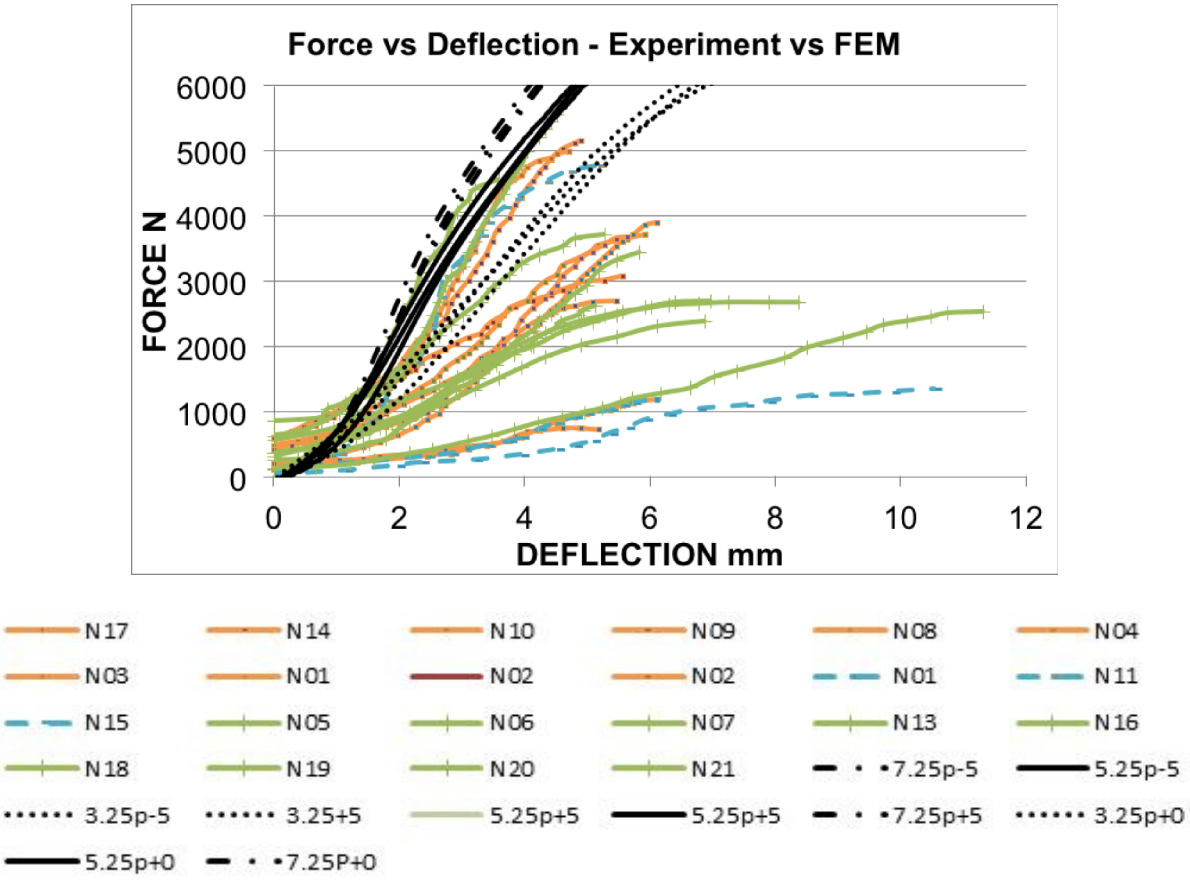

Figure 3. Model predicted neck force-deflection vs experiment results by Pintar et al. 1995

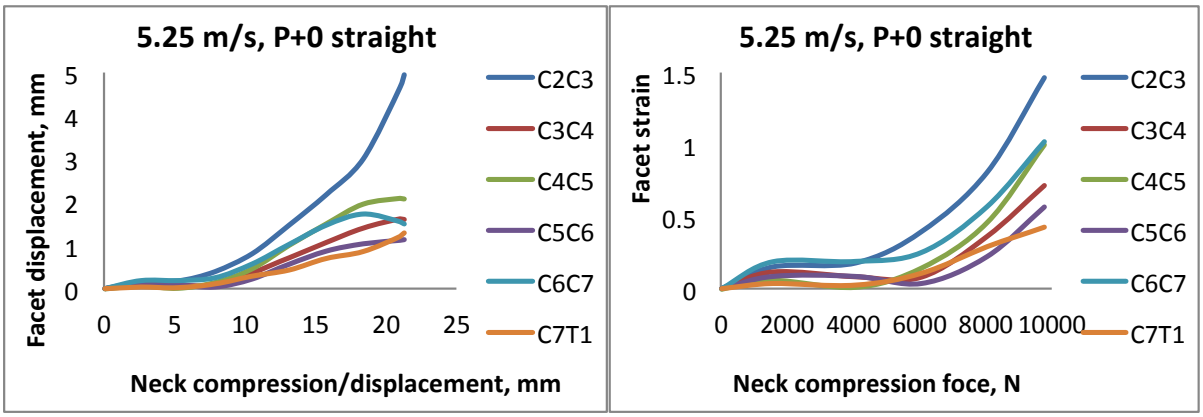

(a) (b)

Figure 4. Facet resultant displacement/strain as functions of neck compression

(a) and compression force (b) with more sliding occurs in C2-C3 facet in straight neck position from 5.25 m/s impact (Pintar et al. 1995).

3 Results and Discussion

3.1 Compression force vs compression deflection

The cervical axial compression experiments done by The Medical College of Wisconsin are very different from the drop test. Here the impactor is maintained at a constant velocity and the axis of the spine is straightened or a "stiff axis" is maintained by removing the cervical lordosis. It produces a direct loading to the spine and gives very little space for the viscoelastic components to dissipate energy during the loading.

The FE model was rearranged to the stiff axis by bringing the vertebrae to the stiff axis by leveling it to the location of the occipital condyle. The intervertebral discs and facet capsules were created again for this loading. The muscles were removed from the FE model. A constant velocity of 5.25 m/s was used because the paper did not report exact velocities for each case. To add information for model sensitivity additional velocities of 3.25 m/s and 7.25 m/s were simulated. The head was moved 5 mm in the anterior and posterior direction to simulate flexion and extension injuries as reported in the paper.

The FE model was simulated to make the impactor move down to a distance of 24 mm from the point of impact to ensure the stability of the FE model (Figure 3). The FE model force response for 3.25 m/s and 5.25 m/s was in the range of force versus deformation plots provided by the researchers. The higher velocity impact gave a high force response as the impactor travelled down.

Since there is not much information given about the velocity of impact, we cannot give a proper conclusion about the reasons behind a higher force peak at a distance close to 12 mm from the point of impact.

All the FE simulations resulted in a compression type injury for 7.25 m/s cases. The 5.25 m/s cases had a buckling response at the C2-C3 level for the flexion and extension cases. The 3.25 m/s case had a similar injury pattern. No further study was made regarding the model sensitivity in this validation due to lack of information from the paper.

Vertebral body compression was noted at the C7 vertebra in all the cases and very small deformation was observed in the C5 and C6 level. Mid column fractures reported by Pintar et al. can be seen in the simulation. These experiments did not report any facet joint injury. The major areas of injury were vertebrae, ALL and PL. In the FE model, no vertebral body compression was seen except for 7.25 m/s case were a minor C7 vertebral body compression occurred. At higher velocities, the skull fractured and was still able to contribute a higher force on the C7 vertebral body. This makes the C6-C7 and C7-T1 region a potential injury site.

Comparing all the cases, severe disc compression can be seen in C5-C6 and C7-T1 discs. In the case of flexion setup where the head was moved 5 mm from the stiff axis, the lowest velocity case produced bending in the cervical spine whereas the other two cases produced a compression type injury with minor bending at the C4-C5 level. The C4-C5 disc experiences a partial shear loading due to the shape of the C5 vertebral body. So this becomes a typical rotation center during the flexion setup. This bending produced a severe posterior C2-C3 disc compression. In the extension type setup C2-C3 disc compressed more than the other discs. In all the cases the C3-C4 and C4-C5 disc was less vulnerable to injury. There was no evidence of spinous process fractures in all the cases.

3.2 Axial compression vs Facet strain

At 5.25 m/s impact for example, in case while the neck was in straight position, the compressive force was over 7000 N. The C3-C4 and C4-C5 facets experienced high compression in the X axis. C7-T1 facet experienced tension along X axis. The facetssustained compression in both X and Z axes. The C7-T1 facets experienced a negligible facet movement in both the axes. Same trend was observed in the flexion position case except C2-C3 facetswhich showed higher facet compression in Z close to 1.5 mm.For extension position case, C7-T1 facets tensed in X axis and the C4-C5 facets sustained a greater facet compression of 1.5 mm in the X axis than others. The facet movement in Z axis was mostly compression with C6-C7 facet compressed more than the previous facets. For flexion and extension cases, the compression force reached over 7800 N.

For all the six cases, in general C2-C3 facets were compressed most in both axes more than other facets. The compression of the vertebral body transformed the force to the C2-C3 facets which were in an oblique angle and therefore were forced to move along the face surface in X and Z. This indicated that increases in compression may lead to increases in facet strain subjected to vertical loadings (Figure 4). The C7-T1 facets experienced a compression in the earlier stage of the loading followed by extension as the force dropped down due to the relative movement of the C7-T1 vertebrae occurred at the end of the simulation.

4 Conclusions

The numerical analysis which was based on cadaveric cervical axial compression studies by Medical College of Wisconsin can be classified as severe impacts to the spine occurring during rollover car crashes. In that test, the spine stiffens out before impact and when the roof contacts the skull, the loading is directly applied to the spine. Pintar et al. have brought the “stiff axis” position to directly load the cervical spine components.

Comparing all the cases, in general C2-C3 facets were compressed most in both local x-axis (along the facet joint surface) and z-axis (normal to the facet joint surface) more than other facets, and severe disc compression can be seen in C5 C6 and C7 T1 discs. Of note, the positive correlation between compression and cervical facet capsule strain suggested important mechanisms occurred during this crown impact. The role of compression force with more sliding in cervical facet surface may be an important causal mechanism leading to facet failure in compressive neck injuries. More simulations of facet strain from cadaver tests are needed to confirm the hypothesis.

Acknowledgements

This work was supported by grants from the National Natural Science Foundation of China (No. 30928005), the Third Military Medical University Research Foundation (No. 2009XHG16), and the Military Medical Research Foundation of China (No. AWS11J008).

References

[1] Chen HB, Zhang LY, Wang ZG, et al. Biomechanics of the Neck [M]. Rijeka, Croatia: InTech Publish, 2011: 835-402..

[2] Bahling GS, Bundorf RT, Kaspzyk GS. Rollover and drop tests - The influence o*f roof strength on injury mechanics using belted dummies*. Proc. 34th Stapp Car Crash Conference, 1990. 34: 101-112.

[3] Hu JW, Yang KH, Chou CC, et al. *A numerical investigation of factors affecting cervical spine injuries during rollover crashes*. Spine, 2008. 33(23): 2529-2535.

[4] Zhang LY, Yang KH, Dwarampudi R, et al. *Recent advances in brain injury research: a new human head model development and validation*. Stapp Car Crash J, 2001: 45: 369-394.

[5] Chen HB, Zhang LY, Tan LW, et al. *Comparative Geometrical Dimensions of Chinese and Western Cervical Vertebrae*. TELKOMNIKA Indonesian Journal of Electrical Engineering, 2012. 10(8): 2320-2329.

[6] Pintar FA, Yoganandan N, Voo L, et al. *Dynamic characteristics of the human cervical spine*. Proc. 39th Stapp Car Crash Conference, 1995. 39: 195-202.

[7] Yoganandan N, Kumaresan S, Pintar FA. *Biomechanics of the cervical spine Part 2: Cervical spine soft tissue responses and biomechanical modeling*. Clinical Biomechanics, 2001. 16(1): 1-27.

[8] Nighitingale RW, McElhaney JH, Camacho DL, et al. *The dynamic responses of the cervical spine: Buckling, End conditions and tolerance in compressive impacts*. Proceedings of the 41st Stapp Car Crash Conference, 1997: 451-471.

Proceedings of the 11th International Forum of Automotive Traffic Safety, 2014, pp 363-369
No. ATS.2014.319

Finite element analysis of human thoracic injury criteria in side impact

Fang WANG [1], Jikuang YANG [2, 3], Yong HAN [1], Guibing LI [4], Xiaoqing JIANG [2]
[1]*School of Mechanical and Automotive Engineering, Xiamen University of Technology, Xiamen, China*
[2]*VTS, State Key Laboratory of Advanced Design and Manufacturing for Vehicle Body, Hunan University, Changsha, China*
[3]*Department of Applied Mechanics, Chalmers University of Technology, Gothenburg, Sweden*
[4]*Trinity Centre for Bioengineering, Department of Mechanical and Manufacturing Engineering, Trinity College Dublin, Dublin 2, Ireland*
E-mail: wangfang83715@163.com

Abstract

This study aimed at analyzing the correlation between injury responses of human thorax and the injury criteria of human thoracic injury under side impact, by using a previously developed and validated human thorax FE model. For this purpose, the human thorax model was used to simulate human thorax impactor tests at a range of certain angles in side impact. The normalized number of rib fracture (NRF) were calculated and analyzed for comparing with normalized simulated injury parameters based on various human thoracic injury criteria. The evaluation analysis with the human thorax FE model suggested that the Thorax Trauma Index (TTI) criterion correlated with the NRF better than the other criteria.

Keywords: human thorax; finite element model; side impact; injury criteria

1 Introduction

It was reported that the ratio of side impact accidents to the frontal impacts shows a downward trend in the period of 1997 to 2007 by using data from the FARS and NASS databases [1], while the ratio for fatal crashes caused by side impact and frontal impact accidents exhibits a generally increasing trend. The fact indicated that the effect of occupant injury prevention in side impact is not as significant as that in frontal impact. Actually the state of knowledge of injury biomechanics research on human body, especially human thorax in side impact is less advanced than that in frontal impact.

The experiments with PMHS were widely carried out for the early research on human thoracic injury in passenger vehicle crash events, including frontal and side impacts. The results from human thorax impactor experiments by Stalnaker et al. [2] suggested that side thorax deflection could be used for assessment of thoracic injury severity.

Four side impactor PMHS experiments were recorded in the research of Eppinger et al. [3] in 1984, and the experiment data was used for the development of injury index, mechanical response corridors and the NHTSA's Side Impact Dummy (SID). In 1998, a series of side impactor experiments were carried out by Talantikite et al. [4] with the aim of investigating the sensitivity of the injury criteria to loading mass and velocity variation. The impactor masses used were 12 and 16 kg and the velocities were 6 to 8.5 m/s. The impact surface was flat, rigid and of 150 mm diameter. It was concluded that the V*C and the deflection criteria are sensitive to the variations of the impact masses and velocities. The purpose of Chung et al's research [5] is to get more understanding of the thoracic response and injury mechanisms in side impact to the human chest wall. A series of cadaver tests were conducted to measure biomechanical response and injury data, which were used to correlate injury criteria for side impact to the number of rib fractures (NRF). It was suggested that chest deflection or the energy generated in a side impact correlated better with NRF than

acceleration or the viscous response.

With more and more attention was paid to the research of human thoracic injury in side impact, the achievement has been made mainly by means of PMHS experiments. But as the most popular and intelligent approach in research field of vehicle safety and human injury biomechanics, the FE (Finite Element) method was not widely used yet in side impact.

Objective of the current study was to determine the correlation of the number of rib fractures (NRF) with the thoracic injury criteria under side impact by using a previously developed human thorax FE model.

2 Methods and materials

2.1 Model description

The current human thorax FE model was developed in a research project on human body model (HBM) of Hunan University [6, 7, 8, 9], as shown in Figure 1. The model has been validated against PMHS experiments [6].

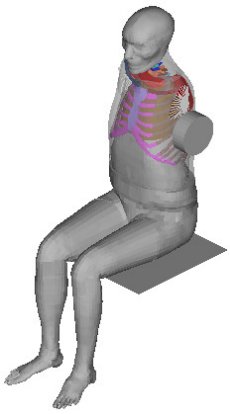

Figure 1. ISO view of current thorax FE model in impactor loading conditions

2.2 Definition of the boundary and loading conditions in side impacts

In research of human thoracic injury, impactor test is a quite useful and efficient experimental method, not only in frontal impact but also in side impacts. This method was also employed in current study, with the rigid impactor of 152mm diameter surface, 16kg mass, and impact velocity of 6m/s, referring to the research of Talantikite et al [4].

The principal direction of force (PDOF) has been introduced, which were categorized for side impact-induced injuries [10, 11, 12]. The loadings were defined in a clockwise sequence with impact directions varied from PDOF of 90° to PDOF of 35° (Figure 2). Total of 12 impact simulations was conducted. In the simulations, the center of the impactor was aligned at the same vertical height as that in research of Shaw et al. [13] and with the axis of force through the center of gravity of the torso, as described in Figure 2.

Rib fractures are the most frequent type of thoracic serious injuries [14], so in the research of human thoracic injury, NRF is treated as the assessment index of human thoracic injury severity [5, 15]. In the current study, NRF was obtained through simulating the thorax response in 12 different directions of side impact loadings with an impactor. The results were analyzed for comparing with simulated injury parameters based on various human thoracic injury criteria in side impact.

2.3 Analysis of impact responses using thorax injury criteria

The validated model was utilized in simulations of thorax impact responses for obtaining the NRF in total 12 impact directions. Output of injury parameters was analyzed for rib fracture based on existing human thoracic injury criteria in side impact [5, 14, 16], including contact force, chest deflection, compression, Viscous Criteria (VC), upper spine acceleration and Thoracic Trauma Index (TTI). For analyzing the rib fracture in side impact, by correlating the various injury criteria and NRF, all of the injury parameters were normalized in terms of injury criteria, as well as NRF, with the following normalization Equation 1.

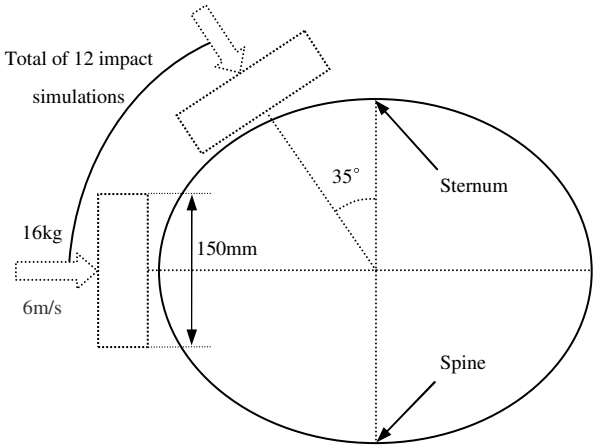

Figure 2. Distribution of impact directions in side impacts

$$N_i^C = \frac{X_i^C - X_{\min}^C}{X_{\max}^C - X_{\min}^C} \quad (1)$$

Where:N is the normalized value;i=12;C means the injury parameters including NRF and the six different injury criteria; X_i, X_{max}, and X_{min} represent the non-normalized value of sample number i, maximum value, and minimum value for each injury parameter.

The correlation of normalized NRF with the six normalized injury parameters can be described by the evaluation function f which is given in Equation 2:

$$f(X_i^R, Y_i^R) = \sum_{i=1}^{N} \sqrt{(X_i^R - X_i^B)^2 + (Y_i^R - Y_i^B)^2} \quad (2)$$

Where:N=12;Xi and Yi represent abscissa and ordinate of data-point of sample number i, R and B mean predicted parameter data and baseline y=x.

3 Results

The model was used for simulation of thorax impact responses and calculation of injury parameters. The peak values of corresponding injury parameters are presented in Table 1, including NRF, impact force, deflection, compression, deflection velocity, T1 (the 1st thoracic vertebra) acceleration, and TTI. The maximum of rib fractures is 11 at impact angle of 70 degrees. All of the normalized results were as shown in Table 2.

Table 1. Simulated values of injury parameters

Impact angle	NRF	Peak Force (kN)	Peak Deflection (mm)	Peak Compression (%)	Peak Deflection velocity (m/s)	Peak T1 Acceleration (g)	TTI
90	7	4.77	61.3	22.7	5.4	182.3	179.9
85	9	4.62	61.1	22.8	6.0	222.5	182.3
80	10	4.46	64.9	24.2	6.7	186.0	177.9
75	10	4.31	66.5	24.4	6.7	159.8	155.7
70	11	4.15	68.4	25.1	6.2	146.5	180.9
65	9	4.08	70.5	25.8	9.4	132.9	178.1
60	7	4.01	69.2	25.1	6.8	162.7	178.5
55	6	3.88	69.0	25.0	6.0	173.7	166.1
50	4	3.85	70.6	25.4	7.2	194.8	162.3
45	2	3.89	69.4	24.8	8.2	164.1	164.0
40	1	3.83	72.4	26.0	8.8	159.7	156.5
35	1	3.78	74.9	27.1	9.1	156.8	150.9

Table 2. Normalized values of injury parameters

Impact angle	NRF	Peak Force	Peak Deflection	Peak Compression	Peak Deflection velocity	Peak T1 Acceleration	TTI
90	0.6	1.00	0.01	0.00	0.00	0.55	0.93
85	0.8	0.84	0.00	0.01	0.16	1.00	1.00
80	0.9	0.68	0.27	0.34	0.32	0.59	0.86
75	0.9	0.53	0.39	0.38	0.33	0.30	0.15
70	1.0	0.37	0.53	0.56	0.21	0.15	0.96
65	0.8	0.30	0.67	0.70	1.00	0.00	0.87
60	0.6	0.23	0.58	0.54	0.35	0.33	0.88
55	0.5	0.10	0.57	0.51	0.15	0.46	0.49
50	0.3	0.07	0.69	0.61	0.44	0.69	0.36
45	0.1	0.11	0.60	0.49	0.70	0.35	0.42
40	0.0	0.05	0.81	0.75	0.85	0.30	0.18
35	0.0	0.00	1.00	1.00	0.94	0.27	0.00

The correlation of normalized NRF with the six normalized injury parameters can be identified in Figure 3. According to the Equation 2, the lower *f* means the higher correlation. The function *f* was calculated for all the six injury criteria as showed in Table 3. Obviously the function values for TTI was the lowest and that for impact force, deflection, compression, deflection velocity were higher, so it was indicated that the TTI criterion well correlated with the NRF. The correlations of the other injury parameters are not relevant, including contact force, the upper spine acceleration, chest deflection, compression, and Viscous Criteria (VC).

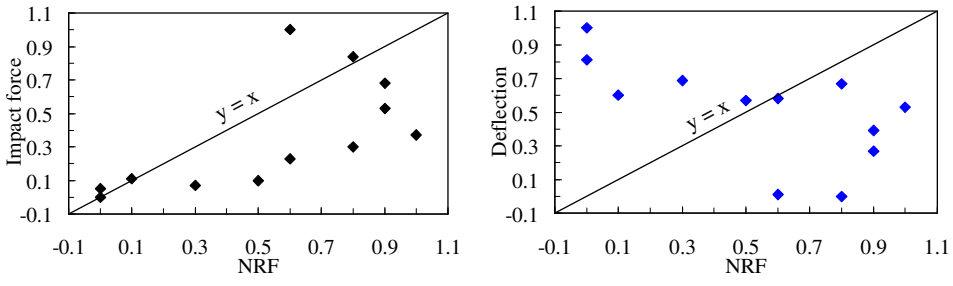

(a) Contact force **(b) Deflection**

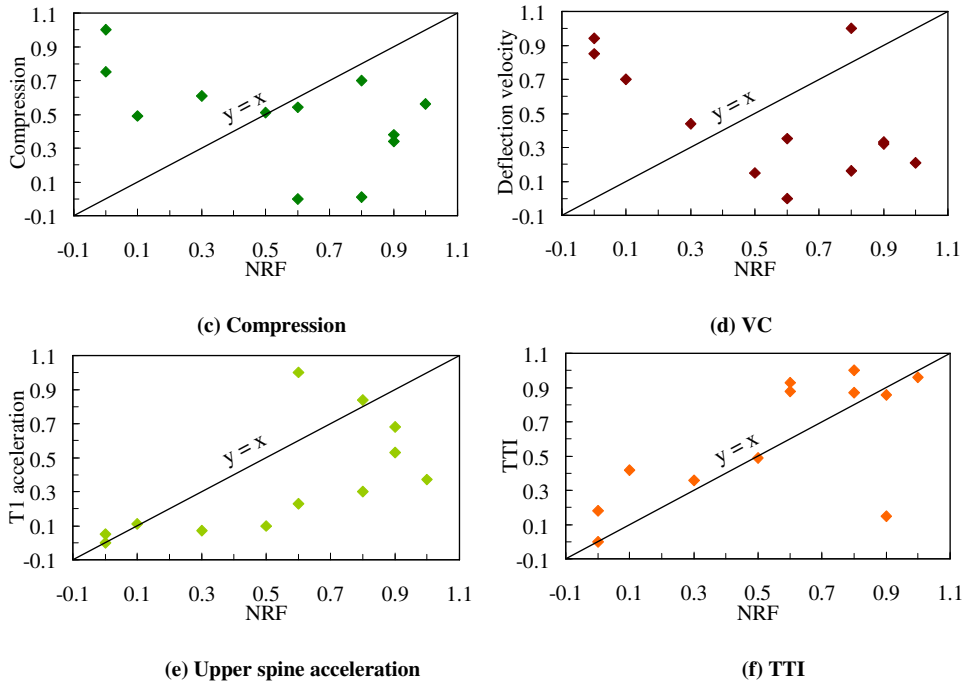

(c) Compression **(d) VC**

(e) Upper spine acceleration **(f) TTI**

Figure 6. Normalized NRF as functions of the various injury criteria

Table 3. Calculated values from correlation Equation 2 for various injury criteria

	Contact force	Deflection	Compression	VC	Upper spine accelaration	TTI
$f(X_i^R, Y_i^R)$	2.28	4.19	3.91	4.60	3.06	1.61

4 Discussions

It was indicated in the current paper that the TTI criterion in side impact correlated with the number of rib fractures best. However, it was suggested from the research of Viano [17] that the VC criterion had the best correlation with injury risk for chest. With the PMHS experiments in different impact directions, Kent et al. [18] thought that the chest deflection was the most appropriate injury criterion because it was the most related to injuries independent of the loading conditions.

Several different thoracic injury criteria were involved in the current research. The criterion of acceleration was the product of early attempts to quantify thoracic loading and injury, and it was a basic injury criterion for assessment of thorax injury in impact loadings. The criterion of contact force is similar to acceleration criterion, and directly relates to acceleration criterion. Afterwards, there were more thoracic injury criteria with the development of research on thoracic injury in vehicle safety, which originated from human even animal experiments in various loading conditions. TTI was developed using data from series of side impact cadaver sled tests [18]; the criteria of deflection and compression were both based on data from frontal impactor cadaver experiments [19, 20, 21]; and VC was proposed by analyzing data from 123 frontal impacts to rabbits [22]. Generally all of the criteria were developed based on macro level injury responses such as impact force, deflection, acceleration and so on. However, considering the variations from subject to subject in terms of age, gender, body size even health situation, the occurrences of all the thoracic injuries, whether skeleton injuries or soft tissue injuries, must have something to do with the micro level biomechanical parameters including stress and strain etc, which should be focused on in the future work with the basis of the current study.

5 Conclusions

The correlation of different criteria for thorax injuries could be determined by using an evaluation function based on calculated injury parameters from FE modeling of the thorax impact. It indicated that among all the injury criteria, the TTI criterion well correlated the NRF. Other injury criteria have a weak connection to the NRF, including the contact force criterion, thorax deflection criterion, compression criterion, VC and upper spine acceleration criterion.

Acknowledgments

This work was supported by the National Hi-tech Research and Development Program of China (863 Program) under Grant No. 2006AA110101; the National Natural Science Foundation of China under Grant No. 31300784.

References

[1] Damin Subit, Sonia Duprey, Lau Sabrina et al. *Response of the Human Torso to Lateral and Oblique Constant-Velocity Impacts*. Ann Adv Automot Med. 2010 (54): 27-40.

[2] Stalnaker, R. L., Roberts, V. L. and McElhaney, J. H. *Side Impact Tolerance to Blunt Trauma*. 17th Stapp Car Crash Conference Oklahoma City, US: SAE, 1973, 17: 377-408.

[3] Eppinger, Rolf H., Marcus, Jeffrey H. and Morgan, Richard M. *Development of Dummy and Injury Index for NHTSA's Thoracic Side Impact Protection Research Program*. 28th Stapp Car Crash Conference Warrendale, US: SAE, 1984, 28: 983-1011.

[4] Talantikite Youcef, Bouquet Robert, Ramet Michelle et al. *Human Thorax Behaviour for Side Impact. Influence of Impact Masses and Velocities*. Proceedings of the 16th International Technical Conference on the Enhanced Safety of Vehicles, Proceedings. Volume II. Washington, D.C., NHTSA, 1998, p. 1542-1549.

[5] Chung Jaekoo, Cavanaugh, John M., King, Albert I. King et al. *Thoracic Injury Mechanisms and Biomechanical Responses in Lateral Velocity Pulse Impacts*. 43nd Stapp Car Crash Conference Warrendale, US: SAE, 1999, 43: 39-54.

[6] Wang Fang, Yang Jikuang, Li Guibing. Finite Element Analysis of Human Rib Fracture under Various Impact Loading Conditions, Chinese Journal of Theoretical and Applied Mechanics, 2014, 46(2): 300-307.

[7] Yang Jikuang and Yao Jianfeng. *Development and Validation of a Human Neck FE Model in Impact Loading Condition*. Journal of Hunan University (Natural Science), 2003, 30(4): 40-46.

[8] Yang Jikuang, Xu Wei and Otte Dietmar. *Brain Injury Biomechanics in Real World Vehicle Accident Using Mathematical Models*. Chin J Mech Eng-En, 2008, 32 (4): 81-86.

[9] Han Yong, Yang Jikuang, and Mizuno Koji. *Virtual Reconstruction of Long Bone Fracture in Car-to-pedestrian Collisions Using Multi-body System and Finite Element Method*. Chin J Mech Eng-En, 2011, 24 (6): 1045-1055.

[10] Yoganandan Narayan, Pintar, Frank A., Gennarelli, Thomas A. et al. *Chest Deflections and Injuries in Oblique Lateral Impacts*. Traffic Inj Prev, 2008, 9(2): 162-167.

[11] Yoganandan Narayan and Pintar, Frank A. *Deflections from two types of Human Surrogates in Oblique Side Impacts*. Proceeding of 52nd Annual Conference Annals of Advances in Automotive Medicine Boston, US: AAAM, 2008; 52: 301–314.

[12] Yoganandan Narayan, Pintar, Frank A., Humm, John R. et al. *Analytical and Experimental Data of Chest Deflections and Injuries in Side Impacts*. Proceedings of the 22nd International Technical Conference on the Enhanced Safety of Vehicles Washington, D.C, US: ESV, 2011: Paper No. 11-0256.

[13] Shaw, Joshua M., Herriott, Rodney G., McFadden, Joseph D. et al. *Oblique and Lateral Impact Response of the PMHS Thorax*. 50th Stapp Car Crash Conference Dearborn, US: SAE, 2006, 50: 147-167.

[14] Trosseille Xavier, Baudrit Pascal, Leport Tiphaine et al. *Rib Cage Strain Pattern as a Function of Chest Loading Configuration*. 52nd Stapp Car Crash Conference San Antonio, US: SAE, 2008, 52: 205–231.

[15] Shimamura Munemasa, Ohhashi Hideyuki, and Yamazaki Minoru. *The Effects of Occupant Age on Patterns of Rib Fractures to Belt-Restrained Drivers and Front Passengers in Frontal Crashes in Japan*. 47th Stapp Car Crash Conference San Diego, US: SAE, 2003, 47: 349-365.

[16] Kuppa Shashi, Eppinger, Rolf H., McKoy Felicia et al. *Development of Side Impact Thoracic Injury Criteria and Their Application to the Modified ES-2 Dummy with Rib Extensions (ES-2re)*. 47th Stapp Car Crash Conference San Diego, US: SAE, 2003, 47: 189-210.

[17] Viano, David C. *Biomechanical Responses and Injuries in Blunt Lateral Impact*. 33rd Stapp Car Crash Conference Washington, D.C, US: SAE, 1989, 26: 113-142.

[18] Kent R. W., Crandall J. R., Bolton J. et al. *The Influence of Superficial Soft Tissues and Restraint Condition on Thoracic Skeletal Injury Prediction*. 45th Stapp Car Crash Conference San Antonio, US: SAE, 2001, 45: 183-204.

[19] Tarriere C., Walfisch G., Fayon A. et al. *Synthesis of Human Tolerances Obtained From Side Impact Simulation*. Proceedings of the 7th International Technical Conference on the Enhanced Safety of Vehicles Paris, France: ESV, 1979: 359-373.

[20] Kroell C. K., Schneider D. C. and Nahum A. M. *Impact Tolerance and Response of the Human Thorax*. 15th Stapp Car Crash Conference Warrendale, US: SAE, 1971, 15: 84-134.

[21] Kroell C. K., Schneider D. C. and Nahum A. M. *Impact Tolerance and Response of the Human Thorax □*.18th Stapp Car Crash Conference Ann Arbor, US: SAE, 1974, 18: 383-457.

[22] Lau, Ian V. and Viano, David C. *The Viscous Criterion – Bases and Applications of an Injury Severity Index for Soft Tissues*. 30th Stapp Car Crash Conference Warrendale, US: SAE, 1986, 30: 123-142.

Proceedings of the 11th International Forum of Automotive Traffic Safety, 2014, pp 370-378
No. ATS.2014.401

Control Strategy of Regenerative/Electro-Mechanical Hybrid Braking System for Hybrid Electric Vehicle Based on Urban Driving Cycle

Zhen WEI[1], John XU[2], Dunant HALIM[3]
[1,2]*Department of Electrical and Electronics Engineering*
[3]*Department of Mechanical, Materials and Manufacturing Engineering,*
The University of Nottingham Ningbo , China 315100
[1]*E-mail: Zhen.Wei@nottingham.edu.cn*

Abstract: This paper aims to investigate the braking control strategy for an Electro-Mechanical Hybrid Braking system, and compare different control strategies for improving the braking performance and regenerative braking efficiency for Hybrid Electric Vehicles (HEVs) in urban driving conditions. In this paper, the urban driving cycle was analyzed from the point of view of braking process. Different braking control strategies for the hybrid braking system, which was composed of the regenerative braking system and Electric-mechanical Braking system (EMB), were compared and a control strategy that based on a typical urban driving cycle, was proposed. Comparative simulations were carried out to validate the performance of the proposed hybrid braking system. The simulation results indicate that by adopting the proposed control strategy, both the braking performance and regeneration efficiency of the hybrid braking system can be significantly improved, in comparison with the conventional control strategy.

Keywords: Driving cycle, Braking control, Electro-mechanical brake, Regenerative braking

1 Introduction

A driving cycle is a series of data points representing the speed of a vehicle versus time, it is widely used to determine the fuel consumption, pollution emissions and development of new automotive technologies [1,2]. Research has shown that, in urban driving conditions, nearly one half of the total vehicle traction energy is wasted during braking [3-5]. In contrast to cars with conventional internal combustion engines, A Hybrid Electric Vehicle (HEV) can achieve a better fuel efficiency in busy urban road conditions. The regenerative braking system is seen as the core technology of hybrid electric vehicles, which is an energy recovery mechanism to slow a vehicle down by converting kinetic energy into another energy form, such as electrical energy. The performance of energy recovery mechanism is strongly influenced by the local driving condition Therefore, in order to maximize the regenerative braking energy, the driving cycle should be considered in developing the regenerative braking control strategy.

Due to the restriction of maximum power of regenerative braking system, a mechanical braking system is still required to ensure the safety of vehicle. Therefore, the hybrid braking system of HEV should be well coordinated to achieve a good braking performance and a high regenerative braking efficiency [3,5]. The Electro-Mechanical Braking system (EMB), which eliminates the use of a conventional hydraulic mechanism, is powered by the electric power from a battery and controlled by the electric signals from the Brake Control Unit (BCU). The vacuum booster and hydraulic pipelines in conventional hydraulic systems are replaced by torque motor and EMB actuator. Compared to the conventional hydraulic braking system, EMB system has several advantages such as lighter weight, more compact in size, rapid signal transmission and fast actuation response, high transmission efficiency, powerful electronic control functions and eco-friendly. All of these advantages make the system very suitable for electrified vehicles (HEV/EV/FCEV) [6,7]. The EMB system is considered to be the future direction of braking system as a representative of Brake-By-Wire technology (BBW). Automobile component manufacturers have developed different types of EMB

systems, especially Germany, BOSCH, CONTINENTAL TEVES, and SIEMENS, who have their own patents for EMB systems [8]. Researchers worldwide also have carried out studies in this area. However, present research in EMB systems is mainly focused on the control algorithm and control strategy [9-12].

It is noted that for diverse driving conditions, each regenerative braking system will have varying performances, especially for the hybrid braking systems. Thus, in order to further improve the regenerative braking efficiency and braking performance, the investigation into the driving cycle is introduced in this work.

2 Driving Cycle Analysis

Driving cycles are produced by different countries and organizations to assess the performance of vehicles in various ways, among them ECE driving cycle (Europe), FTP75 (US), 10.15 (Japan) are the three most widely used ones [4,5]. In this paper work, the ECE driving cycle is introduced as an example, with the cycle is shown in Figure 1. The actual result can be optimized if the used driving cycle that been used is as close to the real driving as possible.

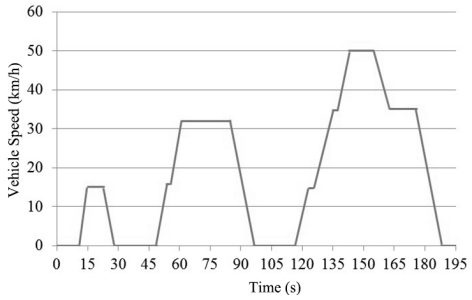

Figure 1. The ECE Driving Cycle

When driving on a flat road, the vehicle driving power can be expressed as [4]:

$$P = \frac{V}{1000}(Mgf_r + \frac{1}{2}\rho_a C_D A V^2 + M\delta\frac{dV}{dt}) \qquad (1)$$

Where M is the vehicle weight; g is the gravitational acceleration; is the rolling resistance coefficient; is the air density; C_D is the air resistance coefficient; A is the vehicle windward area; V is the vehicle speed; and δ is the rotational inertia factor.

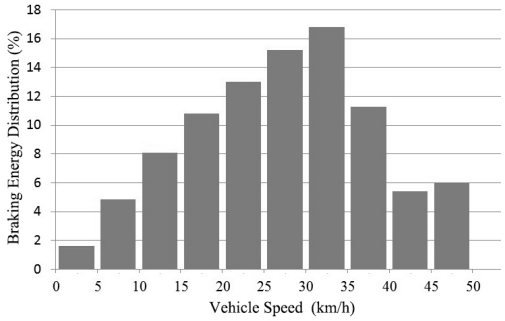

Figure 2. Braking Energy Distribution of ECE Driving Cycle

Under the given ECE driving cycle, integrating equation (1) over the driving time can give both the traction energy and braking energy, the vehicle braking energy distribution for the varying in the whole speed range is shown in Figure 2, and Figure 3 illustrates the percentage of braking energy under certain speed. The vehicle parameters are shown in Table 1.

Table 1. Vehicle Parameters

Item	Symbol	Value
vehicle weight (kg)	M	1600
rolling resistance coefficient	f_r	0.015
air resistance coefficient	C_n	0.25
vehicle windward area (m^2)	A	2.4
wheelbase (m)	L	2.7
distance between gravity center and front wheels (m)	La	1.1
height gravity center (m)	hg	0.6
tires	-	195/60R15

Figure 2 indicates that in the urban driving conditions the vehicle braking energy is mostly consumed in the middle vehicle speed range (20~40km/h), and Figure 3 further indicates that in the low vehicle speed range (0~15km/h), 20% of the total braking energy is dissipated and under 10km/h the percentage is only 10%. Furthermore, electric motor/generator suffers from low efficiency at low speed, and the regenerative braking system cannot provide enough braking torque at low speed. Therefore, the regenerative braking should be applied beyond a threshold speed, and when the vehicle is within the threshold speed, all the braking force is provided by the mechanical braking system. In the design for braking strategy off HEV/EV, the threshold of low vehicle speed needs to be set, which is closely related to the local driving conditions. For the ECE cycle, the speed is recommended to be between 10km/h to 15km/h.

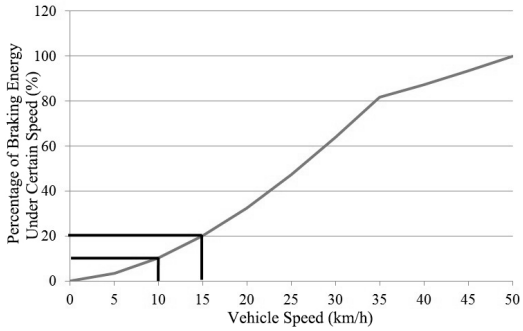

Figure 3. Percentage of Braking Energy under Certain Speed

For HEVs, electric motors are only used during low speed driving and regenerative braking. The electric motors adopted in HEVs are not as powerful as that for pure electric vehicles (EVs). Therefore, from the point view of braking, selecting a suitable motor power capacity can help to improve the fuel efficiency and performance of HEV without oversized design, thus reducing the overall cost.

The simulation results of braking energy based on the ECE cycle is shown in Figure 4, with the vehicle parameters are listed in Table 1. The simulation results indicates that most of the braking energy is consumed in mid-power braking, while a small amount of power is dissipated in the power range beyond 17kw. Therefore, theoretically a 17kw electric motor is able to recover over 90% of braking energy.

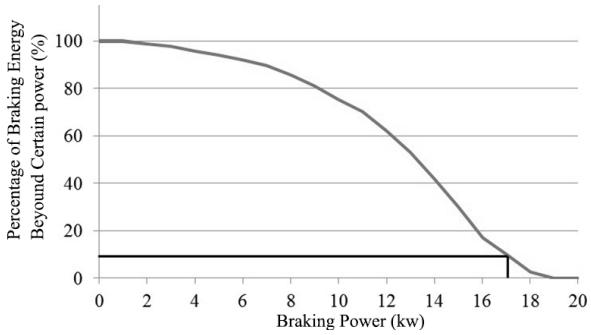

Figure 4. Percentage of Braking Energy beyond Certain Power

In HEV, the electric motor is linked with the front wheels with a fixed gear ratio, and the motor power is proportional to the motor speed before reaching the base speed. Therefore, the motor power is also related to the vehicle speed. The bar chart in Figure 5 shows the braking power distribution of the ECE cycle vehicle speed range. It can be seen that the maximum braking power profile naturally matches the motor power–speed characteristics, as shown in Figure 5. It is observed that a 17kw electric motor can cover most area of vehicle braking power-speed range of the ECE cycle.

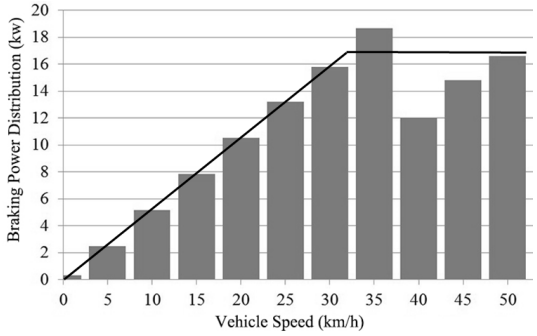

Figure 5. Braking Power Distribution of Vehicle Speed Range

3 Electro-mechanical Braking System

The EMB system is mainly comprised of an electronic brake pedal, a brake control unit, and EMB actuators, as shown in Figure 6. In contrast to the hydraulic braking system, the brake signals are transferred through wire in the EMB system to realize the idea of Brake-By-Wire. With the benefits from the high performance of electric motor and rapid signal transmission speed, the EMB braking system can greatly improve the vehicle brake performance.

Based on the signal obtained from the electronic brake pedal, BCU controls the angular direction and speed of the EMB motor. The EMB actuator has a gear reduction mechanism, which increases the output torque. Moreover, the EMB actuator transforms the rotating motion from the motor into the linear motion for generating the necessary clamping force on the brake. In order to achieve the brake force close to the target value, the feedback information of the motor current, torque and wheel speed are sent back to BCU to continuously adjust the brake signal output.

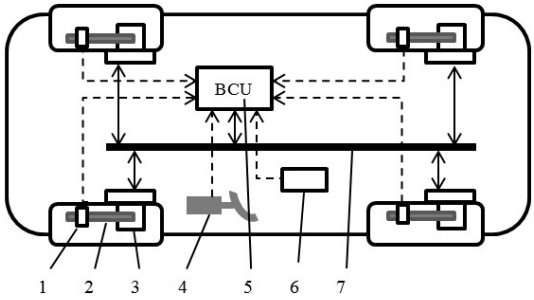

1.Wheel speed sensor 2.Brake disc 3.EMB actuator 4.Electronic brake pedal 5.Brake control unit 6.Vehicle sensors 7.Communication network

Figure 6. EMB System Structure

4 Braking Force Control Strategy

The ideal braking force distribution curve (I curve), as shown in Figure 7, is an ideal braking strategy for both front and rear wheels to obtain the maximum brake force while achieving the best brake performance. However, since it is a nonlinear hyperbolic curve, a precise control system is needed to track the ideal curve, which is very hard to achieve for conventional braking systems. In conventional vehicles, the hydraulic brake pedal is mechanically connected to the hydraulic brake circuits, and the brake force distribution on front/rear wheels is set as a fixed value β, which is determined by the design parameters of the braking system as shown by the β line in Figure 7.

Hybrid electric vehicles usually adopt the front-wheel drive configuration, so the electric motor can only recover braking energy from the front wheels. In order to maximize the regenerative braking efficiency, the brake force needs to be distributed on the front wheel as much as possible. However, to ensure a better braking performance, part of the brake force needs to be distributed on rear wheel. The ECE regulation dictates the minimum braking force on rear wheels, as shown by the ECE curve in Figure 7, and the equation can be expressed by [13]

$$z \geq 0.1 + 0.85(\mu - 0.2)$$
$$z = \frac{du}{dt} \cdot \frac{1}{g} \qquad (2)$$

Where z is the brake intensity; μ is the adhesion coefficient of the road; and u is the vehicle velocity.

At present, hydraulic braking systems are still widely adopted in HEV, the hybrid braking system of HEV can be simply regarded as the combination of a conventional hydraulic braking system and a regenerative braking system. In most cases, all the braking force is produced by regenerative braking system on the front wheels. When the desired deceleration is larger than a certain value; the hydraulic braking system provides the extra brake force to guarantee the braking performance as shown in Figure 7. However, the major disadvantage of the conventional HEV braking strategy is that the braking energy on front wheel is not fully utilized. Since the β_{hy} line is far from the ideal curve in medium brake intensity, the vehicle may suffer from a poor braking performance in some extreme road conditions, such as in gravel road, wet road and dirt road with a low road adhesion.

With benefits from the advancement of electronics and control technologies, EMB system is being developed, and makes it possible to control the braking force on each wheel independently. This configuration can greatly improve the braking performance by completely track the ideal braking curve. However, there is a contradiction between the braking performance and regenerative braking efficiency. It is observed that a large amount of brake energy is consumed on the rear wheels if the ideal braking curve is to be followed, especially in the small deceleration range.

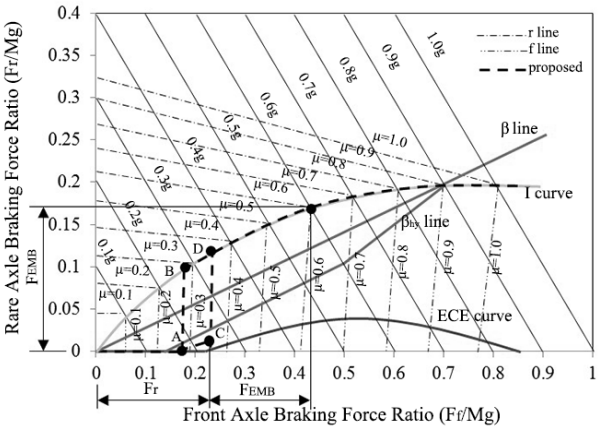

Figure 7. Brake Force Distribution

In order to improve the regeneration efficiency of the fully controllable hybrid brake system, a modified braking force distribution (BFD) strategy for regenerative/electro-mechanical hybrid braking system is proposed in this work, as shown in Figure 7. The details of proposed braking strategy are described as follows:

As mentioned in the previous Section, the regenerative braking system suffers from a poor efficiency in the low speed range. Therefore, the braking force is produced completely by the EMB system under the low vehicle speed.

Under the low brake intensity, the regenerative braking system is able to produce enough braking force, so only the regenerative braking system is used to slow down the vehicle, and all the braking force is distributed on the front wheels (Point A). For some HEVs that adopt high powered motors, the BFD curve needs meet the requirement of the ECE regulation, the extra brake force on rear wheel is provided by the EMB system before reaching the limitation of ECE regulation (Point A to point C).

When the required front wheel brake power is beyond the power capacity of the motor (Point B), the designed BFD directly gets close to the ideal curve (Point A to point B or point C to point D);

From point B, the vehicle is under medium to high intensity braking, as the brake performance is the key consideration. The BFD follows the ideal curve; the brake force distributed on each wheel is regulated by the EMB system to ensure the accuracy of brake force control. In addition, when under high brake intensity, the regenerative braking force needs to be reduced to zero, for the mechanical braking to be more reliable.

The designed BFD combines the advantages of the existing BFD strategies, achieving high regenerative braking efficiency under normal deceleration, and optimal brake performance in emergency braking situations.

5 Simulations and Results Analysis

Figure 9 illustrates the configuration of Simulink /AMESim Co-Simulation system for hybrid braking system simulation. The entire system is comprised of Simulink control model, AMESim to Simulink Interface and AMESim HEV Model. The control algorithm model and EMB model are established in Simulink environment. A 15 degree-of-freedom vehicle model in the AMESim is used, which includes the regenerative braking system model, data collection module, vehicle aerodynamic model and other models of vehicle components such as suspension, tire and electric motor. To validate the braking performance of the proposed braking control strategy, the conventional braking strategies are also simulated for comparison.

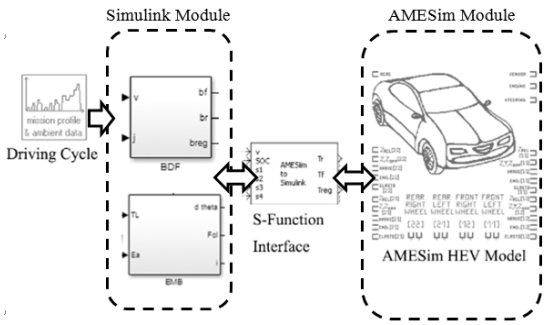

Figure 9. Simulink/AMESim Co-Simulation

In the simulation of braking distance, the HEV braking strategy and the proposed braking strategy are simulated in three types of road surface conditions with different road adhesion coefficient [14]. The initial braking speed is set at 50km/h, while the ABS function is introduced in the braking system to ensure the wheel slip rate within the safe range. The simulation results as shown in Table 2, indicate that the proposed braking control strategy can significantly decrease the braking distance compared with the conventional HEV. Thus, the proposed braking strategy improves the braking performance of the vehicle, especially in difficult road conditions with a low adhesion coefficient.

Table 2. Braking Distance Simulation

Road	Road Adhesion Coefficient μ	Conventional HEV	Proposed	Improvement
Wet Concrete	0.8	27.63m	24.90m	9.88%
Gravel	0.6	41.86m	34.53m	17.51%
Dirt	0.68	34.82m	30.47m	12.49%

The simulations of the regeneration efficiency are carried out based on the ECE driving cycle. Basic vehicle parameters are shown in Table 1. A 17kw electric motor is adopted in the regenerative braking system, and the threshold speed is set at 15km/h according to the analysis results of the driving cycle. The road is assumed to have high adhesion coefficient of 0.95. The simulation results are shown in Figures 10 and 11.

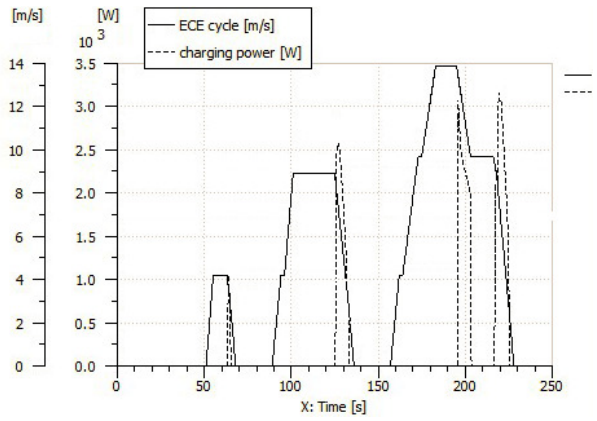

Figure 10. Simulation of Conventional Strategy

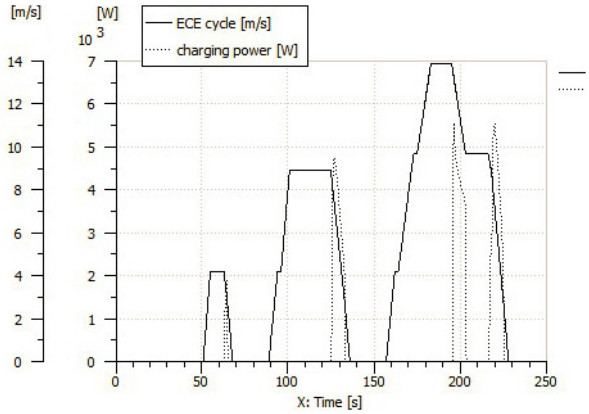

Figure 11. Simulation of Proposed Strategy

To evaluate the energy regeneration performance of the proposed braking strategy, the regeneration efficiency η_{reg} is expressed as:

$$\eta_{\text{reg}} = \frac{E_{reg}}{E_b} \times 100\% \qquad (3)$$

Where E_{reg} regenerative energy; and E_b is the total braking energy. The simulation results are shown in Table 3.
For the original EMB braking control strategy, since the BFD is on the ideal curve, part of the braking energy is dissipated on the rear wheels, which cannot be recovered by the regenerative braking system. The regeneration efficiency of the original EMB strategy is only 25.73% compared with 44.55% of the proposed strategy. Therefore, the regeneration efficiency improvement is nearly 20% under the ECE driving cycle.

Table 3. Regeneration Efficiency Simulation

Strategy	Total Kinetic Energy	Regenerative Energy	Efficiency	Improvement
Original EMB	23.14kJ	5.955kJ	25.73%	-
Proposed	23.14kJ	10.31kJ	44.55%	18.82%

6 Conclusions

In order to design the optimal HEV braking system for urban driving, the urban driving cycle was analyzed in the point view of braking, and a regenerative braking control strategy based on EMB system was proposed. The braking performance and regeneration efficiency of the proposed control strategy were simulated in Simulink/AMESim Co-simulation and compared with other strategies.

The simulation results indicated that by adopting the proposed regenerative braking control strategy, both the braking performance of hybrid braking system and the braking efficiency in urban driving were significantly improved. In future research, more complex urban driving cycles will be introduced, and experiments based on a real EMB system will be carried out to further validate the performance of proposed braking control strategy.

References

[1] Jacobson, B., "*On Vehicle Driving Cycle Simulation*," SAE Technical Paper 950031, 1995, doi:10.4271/950031.

[2] Richter, H., Korte, V., and van Beckhoven, L., "*Actual Driving Conditions in Europe and the Proposed EEC Extra Urban*

Driving Cycle," SAE Technical Paper 890585, 1989, doi:10.4271/890585.

[3] S. R. Cikanek and K. E. Bailey, Energy Recovery Comparison Between Series and Parallel Braking System for Electric Vehicles Using Various Drive Cycles, Advanced Automotive Technologies, American Society of Mechanical Engineers (ASME),New York, DSC vol. 56/DE Vol. 86, pp. 17–31, 1995.

[4] Y. Gao, L. Chu, and M. Ehsani, "*Design and control principle of hybrid braking system for EV, HEV and FCV*," 2007 IEEE VPPC.

[5] Y. Gao, L. Chen, and M. Ehsani, "*Investigation of the effectiveness of regenerative braking for EV and HEV," Society of Automotive Engineers (SAE) Journal*, SP-1466, Paper No. 1999-01-2901, 1999.

[6] Elizabeth A. Bretz. By-Wire Cars Turn the Corner [J]. IEEE 2001.3: 54 [2]Richter, H., Korte, V., and van Beckhoven, L., *"Actual Driving Conditions in Europe and the Proposed EEC Extra Urban Driving Cycle,"* SAE Technical Paper 890585, 1989, doi:10.4271/890585. [22] M. Bertoluzzo, P. Bolognesi, O. Bruno, et al, Drive-by-Wire Systems for Ground Vehicles [J].IEEE 2004: 61.

[7] Ko, J., Lee, G., Ko, S., Ahn, S. et al., "*Co-operative Control of Regenerative Braking using a Front Electronic Wedge Brake and a Rear Electronic Mechanical Brake Considering the Road Friction Characteristic*," SAE Technical Paper 2012-01-1798, 2012, doi:10.4271/2012-01-1798.

[8] Zhou, Z., Mi, C., Zhang, G., "*Integrated control of electromechanical braking and regenerative braking in plug-in hybrid electric vehicles*," International Journal of Vehicle Design 2012; 58(2): 223-239.

[9] http://www.european-patent-office.org/index.en.php.

[10] Tadashi Tamasho, Masahiro Kubota, Masahiro Tsukamoto. Electromechanical Brake System[P]. US, 6397981 B1. 2002-6-4.

[11] Johannes Ante, Stephan Heinrich, Andreas Ott. Measuring Device For An Electromechanical Brake[P]. US, 2005/0140205 A1. 2005-6-30.

[12] Yasuhiko Fujita, Toshiaki Arai, Masami Ogura, et al. Motor Disc Brake System[P]. US,5107967. 1992-4-28.

[13] Gao, Y. and Ehsani, M., *"Electronic Braking System of EV And HEV---Integration of Regenerative Braking, Automatic Braking Force Control and ABS,"* SAE Technical Paper 2001-01-2478, 2001, doi:10.4271/2001-01-2478.

[14] Bosch, *Automotive Handbook*, Robert Bosch GmbH, Karlsruhe, Germany, 2000

Proceedings of the 11th International Forum of Automotive Traffic Safety, 2014, pp 379- 386
No. ATS.2014.402

A Safety Impact Benefit Assessment of Autonomous Emergency Braking Systems Based on Real Traffic Scenarios

He Jun[1], Guo Sasa[2], Miao Qiang[2], Wang Dayong[2], Wang Dazhi[2]
[1]*School of Automotive Studies in Tongji University, Shanghai, 201800,*
[2]*Technology Center of SAIC Motor, Shanghai, 201800*
Email:hejun.tj@foxmail.com

Abstract: In this paper, a safety impact benefit assessment of Autonomous Emergency Braking Systems (AEB) based on real traffic scenarios in Shanghai is presented. Real driving scenarios in Shanghai were collected by video drive records (VDR) and analyzed to build AEB test scenarios. With traffic accident data, connections between the relative velocities of two cars in rear-end collisions and the risk of passengers to suffer certain kinds of injuries can be built. By comparing the relative velocities of cars in AEB test scenarios when the collision happened with and without AEB system, the injury reduction of a test owing to the AEB system was estimated. As with different weights of four test scenarios and different relative velocities in real-end collisions, a total safety impact benefit of this AEB system was estimated as a total reduction of relevant injuries.

Keywords: Autonomous Emergency Braking Systems; Real traffic Scenarios; Safety impact; Test scenarios; rear-end collision

基于真实交通工况的自动紧急制动系统安全收益分析

何鋆[1]，郭飒飒[2]、苗强[2]、王大勇[2]、王大志[2]
[1]*同济大学汽车学院，上海，201800*
[2]*上海汽车集团股份有限公司技术中心，上海，201800*
Email:hejun.tj@foxmail.com

摘　要：基于上海地区的真实交通工况，建立了一种自动紧急制动系统（Autonomous Emergency Braking System, AEB）的安全收益评价方法。首先对上海地区真实交通中存在的追尾工况进行了采集和分析，得到了符合上海地区道路交通特征的 AEB 测试场景。同时根据交通事故数据，建立了追尾碰撞时两车相对速度与乘员相对受伤风险的关系。对四个 AEB 测试场景的多个试验进行建模，分别计算车辆有无 AEB 系统的情况下，发生追尾事故时的两车相对速度，从而得到在该试验中 AEB 系统能够减少的受伤人数比例。最后根据不同相对碰撞速度以及场景出现的频率，综合加权得到该 AEB 产品能够减少的对应伤害的受伤人数，即为其总体安全收益。

关键词：自动紧急制动系统；真实交通工况；安全收益；测试场景；追尾

6.11　引言

AEB 是一种先进辅助驾驶系统（Advanced Driver Assistance System, ADAS），属于汽车主动安全技术。AEB 系统采用雷达、摄像头等一个或多个传感器探测前方障碍物、实时获取交通环境信息，并通过分析模块估计当前环境危险程度。当检测到危险时，系统对驾驶员发出警告并提醒驾驶员采取回避措施，当驾驶员没有及时对警告信息做出正确反应而情况变得危急时，系统会通过自动制动的方式来主动介入以回避碰撞或是减轻碰撞程度[1]。

Andras 等[2]通过 GIDAS 等交通数据建立起相对碰撞速度与受伤人数的关系，以 AEB 系统能够减少的相应伤害的受伤人数比例来评价其收益，这种方法能够直观地得到 AEB 系统的安全收益。但是一来我国缺乏类似

的详尽的交通事故数据库，二来不同国家地区的交通环境不同、驾驶员的驾驶习惯也有所差异，不能直接应用其他国家的测试场景。本文首先对上海地区行驶工况进行采集和统计分析，并据此提出符合上海地区真实交通特征的 AEB 测试场景[3]。根据交通事故数据，得到车辆碰撞速度与碰撞中两车乘员受伤风险的关系。再对测试场景进行建模，在测试车辆上加入 AEB 控制策略对其进行仿真计算，得到该 AEB 系统能够减少的 MAIS（Max Abbreviated Injury Scale, 最大简明伤害等级）2 级以上的重伤和长期挥鞭伤的受伤人数，即为其安全收益。

6.2 2　建立测试场景

2.1 真实交通工况的采集

本文通过装载在出租车和警车上的 Horiba 行车记录仪（Video Drive Record，VDR）来采集上海市嘉定区的真实交通工况（图 1）。VDR 将通过内置摄像头记录车辆前方的交通状况，同时也会记录车辆速度、纵向加速度、侧向加速度等信息。当车辆的纵向加速度或侧向加速度大于 0.4g 时将触发 VDR 的记录功能，只保留触发前 15s 到出发后 5s 的数据。

Figure 1. Collecting real driving scenarios with VDRs

图 1. 通过 VDR 采集工况

2.2 AEB 测试场景的提出

总计采集了约 4000 例触发工况，通过人工筛选，剔除没有发生危险的工况后将剩余工况分为四个危险等级：0-危险预兆、1-轻微危险、2-一般危险、3-紧急危险。本文选取了危险等级为 2 与 3 的危险工况，总计 430 例。

按照 NHTSA 提出的 37 类预碰撞（Pre-Crash）场景分类方法[4]对这 430 例危险工况进行分类，最典型的 6 类工况有 329 例（表 1），其中排名第二的“由于前车减速导致的危险工况”即为追尾工况，也就是 AEB 系统适用的工况，共有 87 例。

Table1.the first 6 dangerous situation in Shanghai

表 1. 上海地区前 6 类危险工况

分类	工况数量	百分比	排名
无预先车辆行为的二轮车冲突	91	21.2%	1
前车减速	87	20.2%	2
有预先车辆行为的二轮车冲突	61	14.2%	3
车辆在路口右转	38	8.8%	4
车辆同向变道	29	6.7%	5
前车偏离车道	23	5.3%	6

根据这 87 组危险工况，利用驾驶员反应时间来确定危险开始点，分析危险开始点的数据得到 AEB 测试场景的基本参数（本车速度、目标车速度、目标车加速度和测试开始时的两车距离等）。将得到的 AEB 测试场景

参数组合，按照目标车运动状态分类，提出了符合上海地区道路状况的四种测试场景（目标车静止、目标车匀速、目标车轻微制动和目标车紧急制动）。

Table2. Acquired AEB testing scene according to dangerous situation
表 2. 根据危险工况得到的 AEB 测试场景

工况类型	v(SV) [km/h]	v(TV) [km/h]	a(TV) [m/s^2]	D [m]
TV 静止	10	0	0	14
	20	0	0	28
TV 匀速	20	10	0	14
	30	10/20	0	28/14
	40	20/30	0	28/14
TV 轻微制动	10	10	-2	5
	20	10/20	-2	9/14
	30	10/20/30	-2	28/14/13
	40	20/30/40	-2	28/14/17
TV 紧急制动	10	10	-6	5
	20	10/20	-6	9/14
	30	10/20/30	-6	28/14/13
	40	20/30/40	-6	28/14/17

注：TV（Target Vehicle）：目标车、SV（Subject Vehicle）：本车、v：速度、a：加速度、D：初始距离。

通过聚类分析得到四个场景出现的比例关系（表 3）。

Table3.The rate of testing scenes
表 3. 各个测试场景的出现比例

工况类型	所占比例
TV 静止	30%
TV 匀速	10%
TV 轻微制动	50%
TV 紧急制动	10%

2.3 AEB 控制策略

本文中测试的 AEB 触发时刻如下，减速度大小为 1g，速度单位为 km/h：

$$\begin{cases} TTC=(V_0-V_1)/72, & V_0-V_1<30km/h \\ TTC=0.833-12.5/(V_0-V_1), & V_0-V_1\geq 30km/h \end{cases} \quad (1)$$

其中 V_0 为本车速度，V_1 为目标车速度。

6.3 3 安全收益标准

AEB 系统的设计出发点就是为了减轻碰撞时乘员受到的伤害或是直接避免碰撞[5]，因而本文将一个 AEB 系统能够减少的两车中的受伤人数的能力作为其安全收益水平。

追尾事故中乘客容易受到两类严重伤害：MAIS 2+的重伤（包括死亡），以及 AIS 虽为 1 级，却会对受伤者生活带来严重不便的超过一个月伤害症状的挥鞭伤。本文将分别评估追尾工况中，AEB 系统分别能够减少的两类伤害的受伤人数比例。

6.4 4　安全收益分析

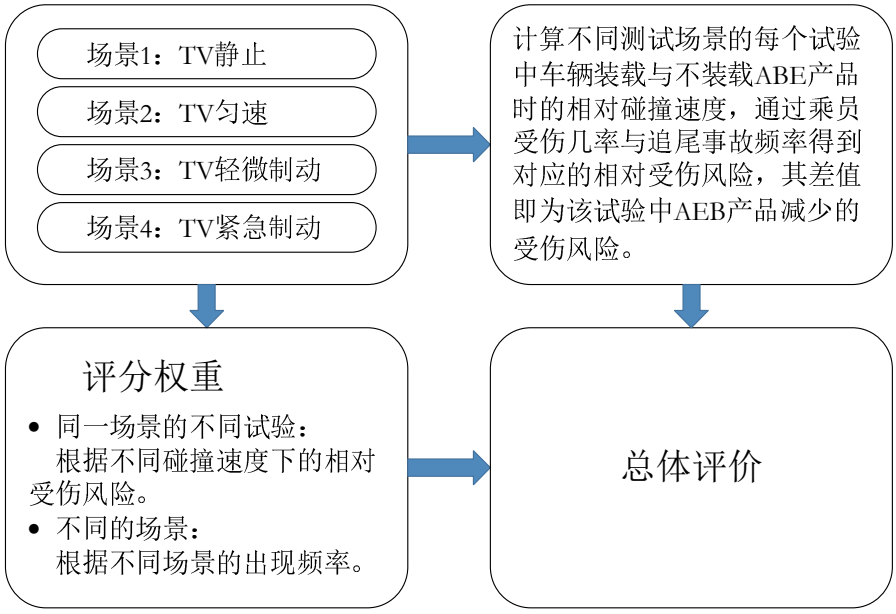

Figure 2. The analysis structure of the safety impact oncertain injury
图 2.对于某种特定伤害的安全收益的评价方法结构

如图 2 所示，本文中评价 AEB 系统对于某种特定伤害的安全收益主要分为三个步骤：首先，根据交通事故数据得到乘员在不同相对碰撞速度区间下的相对受伤风险；其次，分别计算有无 AEB 系统的车辆在四个测试场景的多个试验中发生碰撞时的两车速度，并依据第一步的结果可以计算出有无 AEB 系统时乘员的相对受伤风险的差值，得到不同试验下 AEB 系统减少的受伤人数比例；最后，根据同一测试场景下不同试验中无 AEB 系统时的相对受伤风险作为权重，加权得到四个测试场景中 AEB 系统分别能够减少的受伤人数比例，再根据不同测试场景的出现频率作为权重，加权得到 AEB 系统总体能够减少的受伤人数比例。

下面将详细说明整个分析过程。

4.1 交通事故数据

4.1.1 单次碰撞中乘员受伤几率

单次碰撞中乘员的受伤几率实际上是受到多种因素影响的（例如：乘员年龄、身高体重、车辆使用年数以及具体车辆的被动安全水平等等），但在统计上，可以只考虑一个变量——碰撞时车辆的速度变化量，本文中将用 Delta-V 来表示。Delta-V 的大小代表了碰撞时乘员所受的冲击力大小，一般 Delta-V 越大，乘员的受伤几率越大。

由于缺乏国内详尽的交通事故数据库，只能采用国外的数据。图 3a 为追尾事故中乘员受到长期挥鞭伤的几率随 Delta-V 的分布，数据取自于 Folksam 保险公司的碰撞数据[6]。其中本车中乘员受伤几率并非随 Delta-V 单挑递增的原因可以部分得由安全气囊的触发条件（Delta-V 约等于 25km/h 时）解释。图 3b 为追尾事故中乘员受 MAIS 2+的伤害的几率随 Delta-V 的分布，数据取自于 NASS/CDS（National Automotive Sampling System/Crashworthiness Data System）[7]。

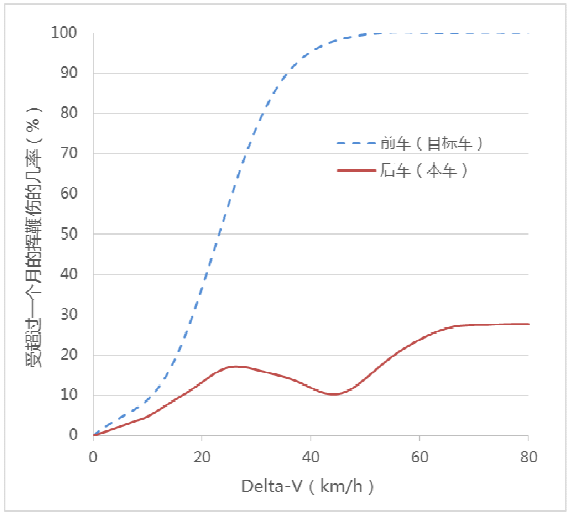

Figure 3a. Risk of injuries with long-term whiplash symptoms in rear-end crashes

图 3a. 追尾事故中乘员受长期挥鞭伤的几率

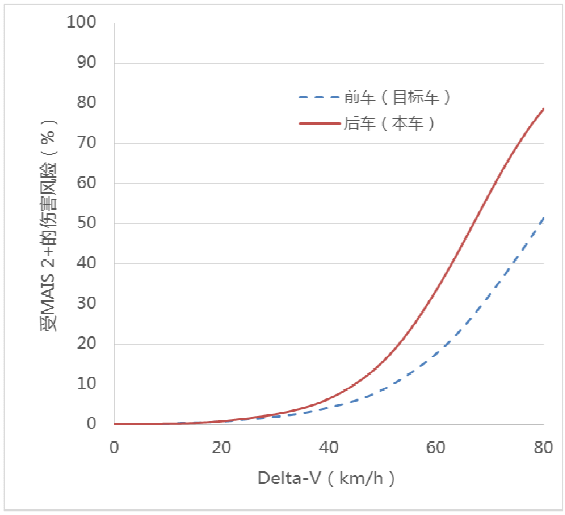

Figure 3b. Rish of MAIS 2+ injuries in rear-end crashes

图 3b. 追尾事故中乘员受 MAIS 2+伤害的几率

4.1.2 事故频率

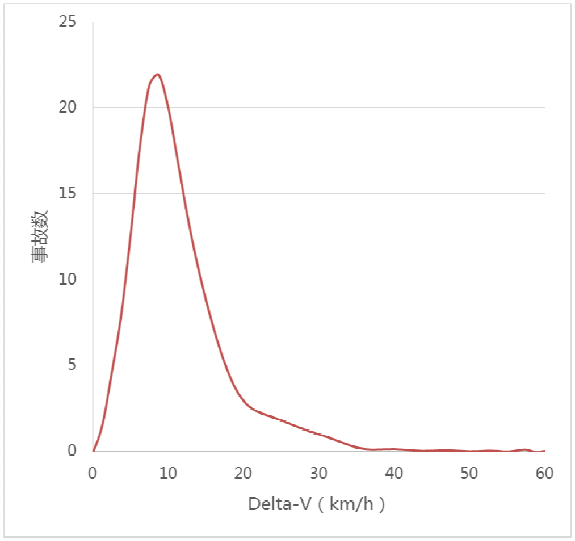

Figure 4. Crash frequency in rear-end crashes, derived from Folksam crash data

图 4. 追尾事故发生频率，取自 Folksam 保险公司数据

同样由于缺乏国内交通事故详尽数据，事故频率数据同样分别采用 Folksam 保险公司（图 5）与 NASS/CDS（图 6、图 7）的碰撞事故统计数据。

其中 Folksam 保险公司数据用于评价对于长期挥鞭伤的安全收益，NASS/CDS 的碰撞数据则用于评价对于 MAIS 2+伤害的安全收益。

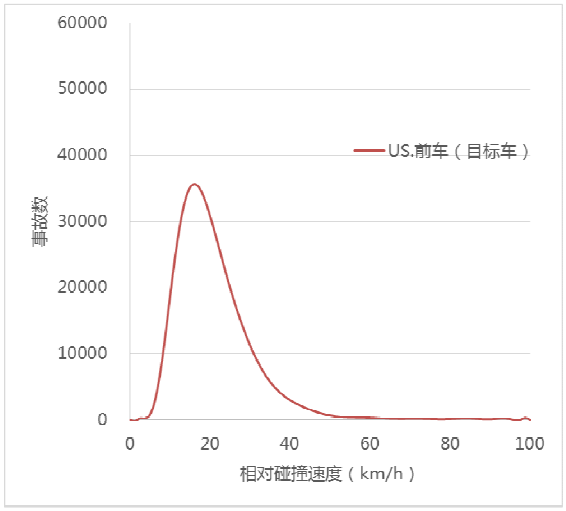

Figure 5a. Crash frequencies for target vehicle in rear-end crashes in the US, from NASS/CDS

图 5a 美国追尾事故目标车碰撞频率，取自 NASS/CDS

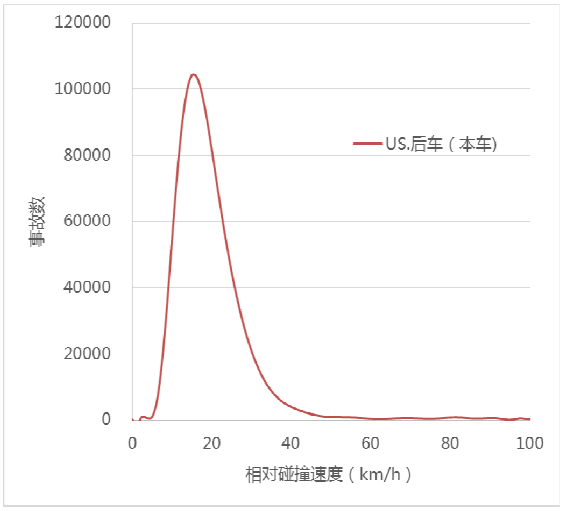

Figure 5b. Crash frequencies for subject vehicle in rear-end crashes in the US, from NASS/CDS

图 5b 美国追尾事故本车碰撞频率，取自 NASS/CDS

4.2 乘员相对受伤频率

为简化起见，本文假设两车质量相等，发生的碰撞为 100%重叠，恢复系数为 0 的追尾碰撞。在这种条件下，两车的 Delta-V 都等于二分之一碰撞前刻的两车相对速度。

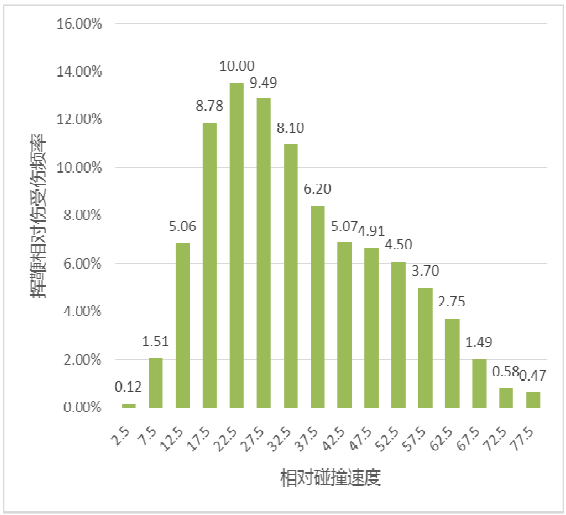

Figure 6a. The relative frequency of injuries with long-term whiplash symptoms

图 6a 长期挥鞭伤的相对受伤频率

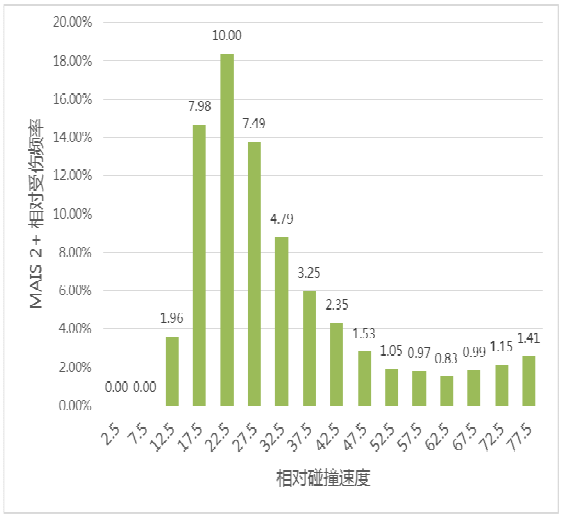

Figure 6b. The relative frequency of MAIS 2+ injuries

图 6b MAIS 2+伤害的相对受伤频率

设 C(ΔV)为车辆的碰撞频率，I(ΔV)为单次碰撞中乘员的受伤几率，其中ΔV 为两车相对碰撞速度。将相对碰撞速度从 0 到 80km/h 划分为 16 个大小为 5km/h 区间。对于(m,m+5]速度区间来说，取：

$$C((\mathrm{m},\mathrm{m}+5]) = C\left(\frac{2\mathrm{m}+5}{2}\right) \qquad (2)$$

$$I\left((\mathrm{m},\mathrm{m}+5]\right)=I\left(\frac{2\mathrm{m}+5}{2}\right) \tag{3}$$

那么该速度区间内的相对受伤频率为：

$$RI\left((\mathrm{m},\mathrm{m}+5]\right)=C\left((\mathrm{m},\mathrm{m}+5]\right)*I\left((\mathrm{m},\mathrm{m}+5]\right) \tag{4}$$

图 6a 和图 6b 则分别为乘员在不同相对碰撞速度下受到长期挥鞭伤与受到 MAIS 2+伤害的相对受伤频率。相对受伤频率越高则说明该区间内可能被减少的受伤人数就越多，对于 AEB 系统来说能够产生的安全收益就越大。因此我们将相对受伤频率最高的区间的安全收益权重设置为 10，其他区间的安全收益权重则为该区间的相对受伤频率比上最大相对受伤频率乘以 10，具体数值可见于图 6a 与图 6b。

4.3 单次试验中 AEB 系统减少的受伤人数

对于表 2 中的 AEB 测试场景的单项试验，通过运动学方程计算得到碰撞前刻两车的相对速度。同样，加入 AEB 控制策略后，计算得到此时碰撞前的两车相对速度。

该试验中目标车的预计受伤人数为：

$$T_{\mathrm{wo}}=\sum_{\Delta V_1} C_T\left(\Delta V_1\right) I_T\left(\Delta V_1\right) \tag{5}$$

其中，为目标车碰撞频率、为目标车单次碰撞中乘员的受伤几率。

装载了 AEB 系统后的目标车受伤人数为：

$$T_{\mathrm{w}}=\sum_{\Delta V_2} C_T\left(\Delta V_2\right) I_T\left(\Delta V_2\right) \tag{6}$$

同理，可得到该试验中对应的本车没有 AEB 系统时的预计受伤人数与装载了 AEB 系统后的受伤人数。

该试验下，AEB 系统减少的受伤人数比例为：

$$R=1-\frac{T_w+S_w}{T_{wo}+S_{wo}} \tag{7}$$

4.4 单个场景中 AEB 系统减少的受伤人数

得到测试场景中每个试验中能够减少的受伤人数比例后，根据 4.2 中不同相对碰撞速度时所具有的安全收益权重，加权得到该测试场景下 AEB 系统能够减少的受伤人数比例，如表 4 所示。

Table 4. The ability of 3 AEB systems to reduce injured person rate

表 4　3 种 AEB 系统能够减少的受伤人数比例

	测试速度		相对碰撞速度		挥鞭伤		MAIS 2+伤害	
测试编号	本车	前车	无 AEB	有 AEB	权重	减少比例	权重	减少比例
030101	10	10	10.00	0.00	5.06	100%	1.96	100%
030201	20	10	20.00	0.00	10.00	100%	10.00	100%
030202	20	20	20.00	4.36	10.00	89%	10.00	100%
030301	30	10	30.00	0.00	8.10	100%	4.79	100%
030302	30	20	28.74	12.30	9.49	65%	7.49	89%
030303	30	30	25.96	11.12	9.49	65%	7.49	89%
030401	40	20	40.00	12.76	5.07	85%	2.35	97%
030402	40	30	28.74	18.61	9.49	50%	7.49	59%
030403	40	40	29.69	19.23	9.49	50%	7.49	59%
				总计	76.21	77%	59.04	87%

4.5 总体安全收益

如表 3 所示，对应四个测试场景在真实危险工况中的出现比例，加权得到该 AEB 系统分别能够减少 84%的长期挥鞭伤伤害与 93%的 MAIS 2+伤害，即为其总体安全收益。

Table 5. The AEB system total safety earnings
表 5. 该 AEB 系统总体安全收益

测试场景	长期挥鞭伤	MAIS 2+伤害	场景比例
01TV 静止	86%	100%	30%
02TV 匀速	100%	100%	10%
03TV 轻微制动	77%	87%	50%
04TV 紧急制动	98%	99%	10%
总体	84%	93%	100%

6.5 5 总结

本文通过获取真实驾驶场景，根据其中的追尾危险工况总结出了 AEB 测试场景。分别计算了在测试场景中，车辆装载 AEB 系统与不装载 AEB 系统时的相对碰撞速度。根据交通事故统计中的单次碰撞乘员受伤几率与事故发生频率将追尾事故中的相对碰撞速度与乘员相对受伤风险联系起来。将得到的单次试验减少的受伤人数比例按照其相对碰撞速度下的相对受伤风险不同而加以不同的权重，得到单个测试场景中 AEB 系统能够减少的受伤人数比例。最后根据四个测试场景在真实工况下的出现比例，加权平均得到该 AEB 系统能够减少 84%的长期挥鞭伤伤害与 93%的 MAIS 2+伤害。

本文提出的 AEB 系统安全收益评估方法是根据我国上海地区危险工况中提取的 AEB 测试场景建立的，与我国城市道路工况相对应，对在中国上市的 AEB 系统的评估具有重要意义。同时本方法只需计算在测试场景中碰撞时的两车相对速度，对于具体的 AEB 控制策略并无要求，可适用于不同的 AEB 系统，具有普遍价值。

目前只能采用国外的交通事故数据库，未来需要更为详尽的上海地区交通事故统计以获得更为精确的结果。同时本文也没有考虑误报与漏报的影响，未来也需要加入相关系数，以对 AEB 系统进行更为全面的评价。

6.6 参考文献

[1] Euro-NCAP, http://www.euroncap.com/testsexplained/aeb.aspx

[2] András Bálint, Fagerlind H. *A test-based method for the assessment of pre-crash warning and braking systems*[J]. Accident Analysis and Prevention , 2013(59):192-199.

[3] Jiang Junli,He Jingpeng,Liu weiguo .etc, *Research on the test scene automatic emergency brake system*[J].vehicle technology,2014,(1):39-43.

[4] 江丽君,贺锦鹏,刘卫国等.*自动紧急制动系统测试场景研究*[J].汽车技术,2014,(1):39-43.

[5] NHTSA,*Pre-Crash Scenario Typology for Crash Avoidance Research*, April 2007.

[6] Kusano, K.D.; Gabler, H.C., "Injury mitigation in the collision partners of pre-collision system equipped vehicles in rear-end collisions,"*Intelligent Transportation Systems* (ITSC), 2011 14th International IEEE Conference on , vol., no., pp.1846,1851, 5-7 Oct. 2011

[7] Kullgren, A., Stigson, H., 2011. *Whiplash Injury Report 2011*. Internal Report or Folksam.

[8] Kusano, K.D.; Gabler, H.C., "Injury mitigation in the collision partners of pre-collision system equipped vehicles in rear-end collisions,"*Intelligent Transportation Systems* (ITSC), 2011 14th International IEEE Conference on , vol., no., pp.1846,1851, 5-7 Oct. 2011

[9] Yizhen Zhang; Antonsson, E.K.; Grote, K., "A new threat assessment measure for collision avoidance systems,"*Intelligent Transportation Systems Conference*, 2006. ITSC '06. IEEE , vol., no., pp.968,975, 17-20 Sept. 2006

[10] Searson, DJ, Anderson, etal. *Integrated assessment of pedestrian head impact protection in testing secondary safety and autonomous emergency braking*[J]. Accident Analysis and Prevention, 2014(63):1-8.

Proceedings of the 11th International Forum of Automotive Traffic Safety, 2014, pp 387- 393
No. ATS.2014.403

Summarization of Typical Scenarios of AdaptiveCruise Control Based on Natural Drive Condition

Gu Rongrong, Zhu Xichan
College of Vehicle Engineering, Tongji University, 201804, Shanghai ,China
E-mail:grrong1990@163.com

Abstract：Recently, the topic of autonomous drive is hot. The development of different kinds of advanced driver assistant systems are necessary to realize the autonomous drive. To some degree, ACC realizes the longitudinal autonomous drive. Nowadays, the development of ACC emphasizes on the realization of function while ignoring the research of driver behavior.This article summarizes the ACC typical scenarios based on the natural drive conditions collected by drive video record. The ACC typical scenarios can be the important basis of the research of the driver behavior.The laboratory collects the natural drive videos of the drivers in Shanghai in 2013.This article summarizes the types of ACC typical scenarios by referring to the definition of ACC test scenarios in ISO15622 and the features extracted from the natural drive videos.According to the features such as the shapes of the road, the relative movement of the subject vehicle and the target vehicle, summarize the typical ACC scenarios. Use PreScan to draw the typical ACC scenarios.The summarization of typical ACC scenarios provides a detailed and actual reference for the research of driver behavior in typical scenarios. The further analysis of performance parameters such as the velocity of the subject car and THW(Time headway) of the typical ACC scenarios can improve the ACC control strategy to increase the comfort of ACC product.

Keywords：Adaptive Cruise Control; Natural Drive Condition; ACC typical scenarios

基于自然驾驶工况的自适应巡航控制典型工况类型总结

顾荣荣，朱西产
同济大学汽车学院，上海，中国, 201804
E-mail:grrong1990@163.com

摘要：自动驾驶的话题如今愈演愈热,各种辅助系统的开发完善是自动驾驶的必要条件。自适应巡航控制 ACC（Adaptive Cruise Control）系统一定程度上实现了车辆纵向自动驾驶，是实现自动驾驶的重要条件。目前，自适应巡航控制的控制策略着重于功能实现，缺乏对于驾驶员行为的研究，ACC产品舒适性有待提高。本文旨在从行车记录仪所采集的大量自然驾驶工况中总结出 ACC 典型工况，为 ACC 典型工况中驾驶员行为的研究提供基础。参考 ISO15622（自适应巡航控制的性能要求和测试流程）中 ACC 的测试场景的要求，研究 TWIN 行车记录仪采集到的 2013 年上海市私家车自然驾驶工况，总结出 ACC 典型工况的类型。研究 ISO15622 中 ACC 测试场景以及行车记录仪记录的自然驾驶工况，提取出道路形状、两车相对运动状态以及前车运动状态这些ACC典型工况基本特征，进而总结出ACC典型的工况类型，并且利用PreScan画出对应的场景示意图。ACC典型工况的总结为进一步研究典型工况下驾驶员的行为奠定了基础，驾驶员行为的研究能够为 ACC 控制策略的改善提供重要的参考，最终能够实现提高 ACC 产品的舒适性以及用户满意度的目的。

关键词：自适应巡航系统 ACC；自然驾驶工况；ACC 典型工况类型

1 前言

自动驾驶的话题如今愈演愈热。各种辅助系统的开发完善是自动驾驶的必要条件。自适应巡航控制一定程度上实现了车辆纵向的自动驾驶。

自适应巡航控制系统从传统定速巡航控制系统发展而来，不仅具有定速功能，又具有车载雷达传感器信息自动调整行驶速度，保持本车与前车安全距离的功能[1]。由自适应巡航控制系统进一步发展而来的全速自适应巡航系统能够在低速工况下实现对车辆速度的控制，减轻驾驶员负担。

任何一款产品的开发都是为了解决驾驶员在行车过程中实际遇到的问题。任何一款汽车辅助功能产品的开发都是为了辅助驾驶员实际行驶工况中所遇到的问题。定速巡航起初正是为了解决高速公路上车速较为恒定的时候驾驶员双脚必须一直踩着油门的问题。定速巡航系统解放了驾驶员长期放在油门踏板上的双脚，属于驾驶辅助系统中重要的组成部分。由之发展而来的自适应巡航系统除了定速功能，还具备跟车功能，进一步提高了自动化程度。

目前，ACC 在中高档车上已经成熟应用，但是用户对于 ACC 的抱怨声却非常大。原因之一是在开发 ACC 控制策略的过程中过多地考虑到功能实现，缺乏了对于驾驶员行为的研究分析，使得开发出来的产品的舒适性水平不高。

本文基于国际标准以及行车记录仪采集到的大量实际驾驶工况，提取出 ACC 典型工况，为驾驶员行为分析提供基础，进而为 ACC 控制策略的改善提供现实依据。

目前对于 ACC 工况的分类主要是基于功能实现分为车辆切入、跟车、车辆切出、定速这四种工况。该工况分类比较笼统，只考虑到了车辆与车辆之间的相对运动关系，忽略了道路环境、天气情况等因素的考虑。

本文结合 ISO15622 中对于 ACC 测试场景的定义以及大量自然驾驶工况，提取出 ACC 典型工况特征，并总结出典型的 ACC 驾驶工况。再通过 PreScan 软件对这些工况进行场景复现。

2 ACC 分类方法

2.1 ACC 国际标准相关总结：

ISO15622 是 2002 年颁布的关于自适应巡航控制系统的国际标准[2]。ISO15622 描述了自适应巡航控制系统的基本控制策略、最低功能要求、基本的人机交互界面、故障诊断及处理的最低要求以及性能检测规程。着重参考性能检测规程。

ACC 的性能检测主要分为探测距离测试、目标识别测试和弯道适应能力测试。

探测距离测试主要是保证一定距离的车辆参考平面内并且具有一定的横向位置偏移的反射体被检测到。

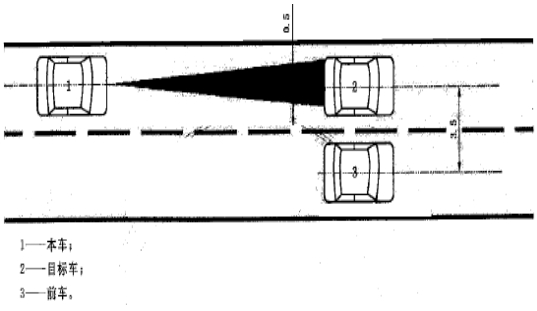

Figure1. the original condition of the target distinguish test

图 1 目标识别试验初始状态

目标识别能力是在直道上测试装载有 ACC 的本车是否能够排除相邻车道车辆的干扰，识别出本车道在探测距离之内的前车。图 1 是初始状态，1 是本车，2 是目标车，3 是另一车道上的前车，目标车与另一车道上的前车纵轴线之间的横向距离是 3.5m。本车与目标车纵轴线之间的横向距离不大于 0.5m。当本车行驶超过相邻车道的前车时，实验结束，成功完成目标识别能力测试。如图 2 所示[4]。

而弯道适应能力测试主要是判断车辆在弯道上能否在一定时间内做出跟随前车的正确反应。ISO15622 根据弯道行驶能力对 ACC 进行了如下分类。如表 1 所示。所定义的弯道最小半径是 125m。

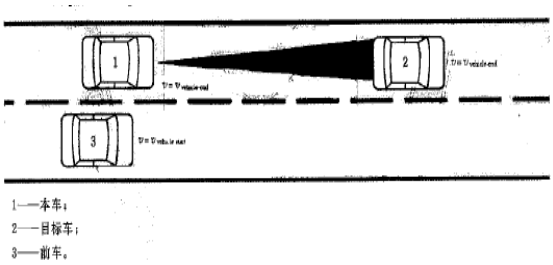

Figure 2. the end of the target distinguish test

图 2 目标识别实验结束状态

图 3 中 1 是初始位置，2 位置是试验结束位置。在位置 2 处，本车开始减速或者车头时距降至 2/3(THW)时实验结束。跟车时距 THW 定义为本车车头到前车车尾的距离除以本车的速度。该参数表征了自车前部边缘行驶到前车后部边缘的当前位置所需的时间[3]。ACC 控制依据：定速工况下对于车速的控制，跟车工况下对于车头时距的控制。

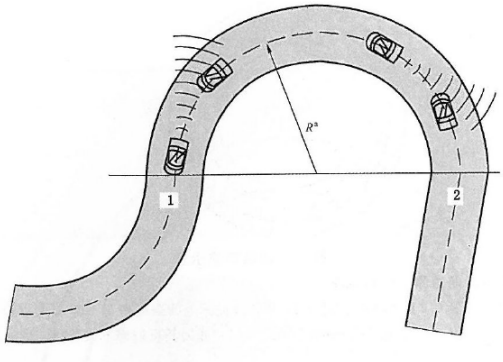

Figure3. bend road test

图 3 弯道适应能力试验

探测距离测试针对 ACC 上所用探测传感器雷达的测试。目标识别能力测试主要是针对 ACC 直道工况的测试。弯道适应能力测试主要是针对 ACC 弯道工况的测试。从 ISO 标准中总结得到道路形状这一特征参数。

Table1. The Types of ACC Based on the Ability onBend Road

表 1 基于弯道行驶能力的 ACC 系统分类

类型	对弯道半径的适应能力
ACC Ⅰ	没有要求
ACCⅡ	R≥500m
ACCⅢ	R≥250m
ACCⅣ	R≥125m

2.2 TWIN 行车记录仪采集的上海市私家车数据

实验室利用 TWIN 行车记录仪采集了 2013 年上海市私家车驾驶数据。将 TWIN 行车记录仪装在前挡风玻璃内侧，摄像头视角朝外，探测本车前方的行驶工况。通过大量的工况总结，从这些数据可以找到 ISO15622 中没有提到的典型场景，进而完整 ACC 典型工况的分类。

3 ACC 典型工况总结

3.1 ACC 典型工况定义

将自然驾驶工况中符合 ACC 应用场合的工况定义为 ACC 工况，将这些 ACC 工况分类，总结出代表性的工况即为 ACC 典型工况。

Figure 4.the window of drive recorder TWIN

图 4 TWIN 行车记录仪界面截图

3.2 ACC 典型工况类型

通过参考 ISO15622 以及对大量行车工况的观察，得到以下结论：ACC 工况主要地理位置为高速公路和高架桥，因为在这两种道路上车流量相对较小，稳定跟车阶段比较多。并且提炼出 ACC 典型工况的三个主要特征参数：道路形状、本车与前车相对运动状态以及前车运动状态。针对三个特征参数分别讨论：道路形状主要分为直道、弯道、直道与弯道交汇处。本车与前车运动状态主要是针对车道而言，根据标准 ISO15622 定义，雷达只能检测本车道上的车辆，两者纵轴线横向距离在 0.5m 的范围内。两车相对运动状态即前车切入本车车道，本车跟随前车行驶以及前车切出本车车道这三种运动状态。在稳定跟车过程中，前车的运动状态又影响着本车的运动状态。当前车加速时，本车加速；前车匀速时本车匀速；前车减速时本车减速。总共有十五种具体类型，如表格 2 所示。

Table 2. Summarization of the typical ACC scenarios

表 2 ACC 典型工况类型总结

特征参数 类型种类	道路类型	两车相对运动状态	前车运动状态	本车运动状态
1	直道	前车切入		
2			前车加速	本车加速
3		稳定跟车	前车匀速	本车匀速
4			前车减速	本车减速
5		前车切出		
6	弯道	前车切入		
7			前车加速	本车加速
8		稳定跟车	前车匀速	本车匀速
9			前车减速	本车减速
10		前车切出		
11	直道弯道交汇处	前车切入		
12			前车加速	本车加速
13		稳定跟车	前车匀速	本车匀速
14			前车减速	本车减速
15		前车切出		

3.3 ACC 典型工况 PreScan 场景建立

PreScan 是荷兰 TNO 公司开发的一款为汽车智能系统提供设计、验证和评价环境的仿真软件。PreScan 中可以快速建立场景(自然环境，交通环境)、添加传感器、定义车辆运动学和动力学模型等，并与 Matlab/Simulink 交互使用，也可以在 Simulink 模型中添加自定义的控制算法。

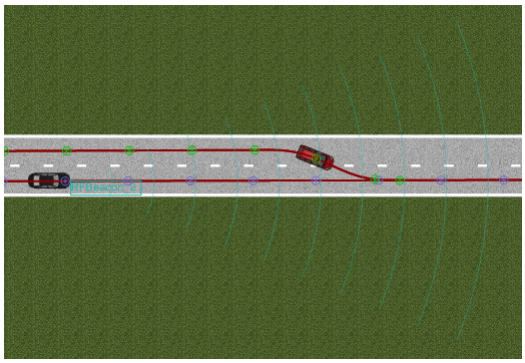

Figure 5. straight road cut in

图 5 直道切入

为了更加直观地表示这些场景，利用 PreScan 建立场景示意图，如图 5-11。图中黑色车辆是本车，红色车辆是前车。两车行驶方向相同，均为向右行驶。红色直线表示两车行驶路线。图 5 中，道路为两车道或三车道，每条车道的宽度均为 3.5m。蓝色曲线为雷达信号。

当前车变换车道进入到本车同一车道时，本车探测到前车，并将前车确定为目标车辆。图 5 表示直道切入工况。红色车辆变道到本车车道，并且被本车探测到，识别成目标车辆。该工况为直道切入工况。

当目标车辆稳定行驶于本车前方时，处于直道稳定跟车阶段。根据设定的车间时距值，本车跟随前车运动状态的改变来改变自身的运动状态，如图 6 所示。此工况为直道稳定跟车工况。

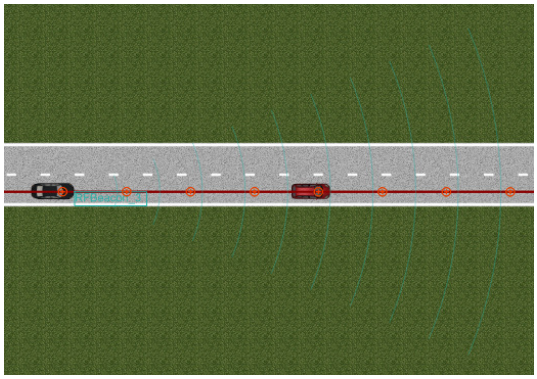

Figure 6.straight road follow up

图 6 直道稳定跟车

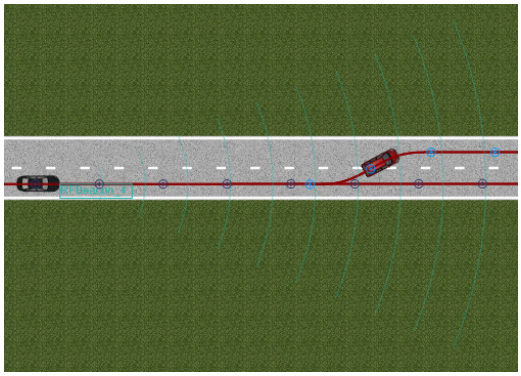

Figure7. straight road out

图 7 直道切出

当前车变道，驶出本车道时。本车不再将前车当做目标车辆。如图 7 所示，该工况为直道切出工况。

弯道时，同样有这样三种工况，前车切入、本车跟车以及前车切出工况，如下图 9-11 所示。在本车稳定跟车情况下根据前车的运动状态又分为前车加速、匀速、减速三种工况。ISO15622 中定义的弯道半径很大，所以示意图弯道半径也很大。

图 8 表示弯道切入工况，前车变道到本车道。成为本车目标车辆。图 9 表示弯道跟车工况，本车稳定跟随前车在同一车道上行驶。图 10 表示弯道切出工况。

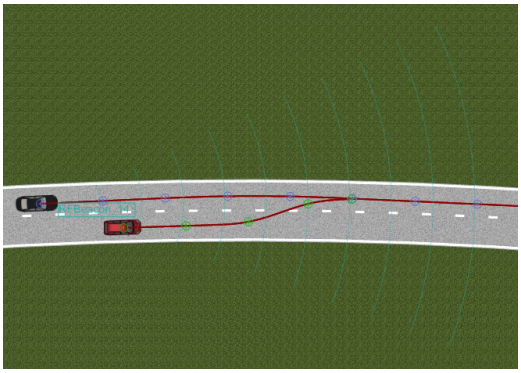

Figure 8. bend road cut in

图 8 弯道切入

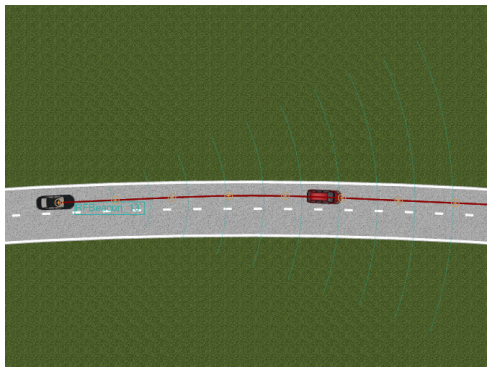

Figure 9. bend road follow up

图 9 弯道跟车

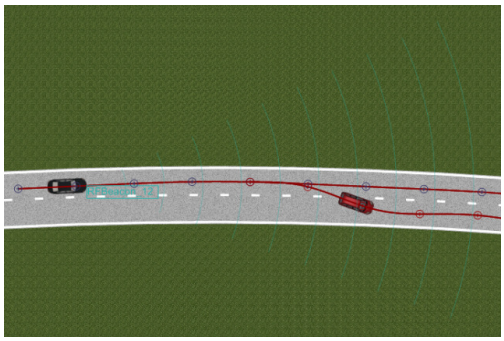

Figure10.bend road out

图 10 弯道切出图

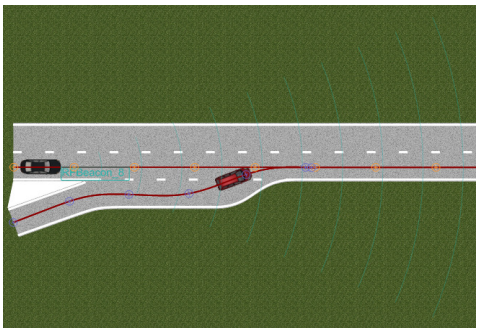

Figure 11. straight and bend road cut in

11 直道弯道交汇处切入

除了弯道和直道这两种典型路面，在高速道路或者高架桥路上，一旦分方向的时候，出现直道与弯道交汇的道路形状。图 11-13 为直道与弯道交汇处的三种工况。图 11 为前车从弯道驶出切入直道。

图 12 表示本车跟随目标车，两车同时改变直行方向，驶入弯道。此为直道弯道交汇处跟车工况。

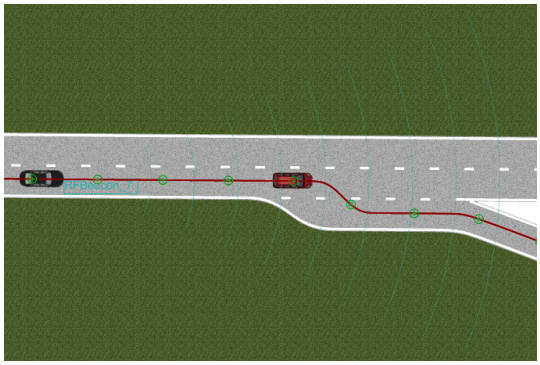

Figure12.straight and bend road follow up

图 12 直道弯道交汇处跟车

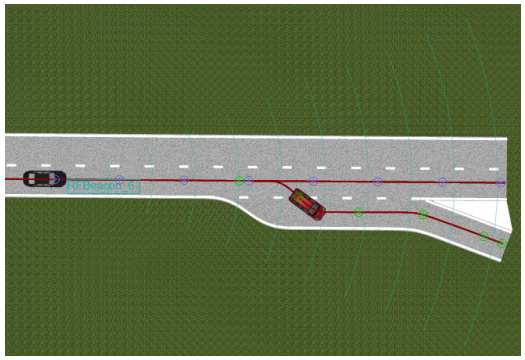

Figure 13. straight and bend road follow up

图 13 直道弯道交汇处切出

前车离开直道改变行驶方向，本车维持直道行驶时。如图 13 所示，此为直道弯道交汇处切出工况。

在所有的工况中，如果考虑环境天气。又分为白天和黑夜两种大环境。环境感知传感器对于环境较为敏感，在白天和夜晚，传感器的性能也会有所不同白天和黑夜能见度差别较大，对车载传感器的要求不一样。

4 结论

本文参考 ISO15622 中对于 ACC 性能试验场景的定义以及 TWIN 行车记录仪所采集的 2013 年自然驾驶工况，提炼出道路基本形状，两车相对运动状态，前车运动状态者三个特征参数，将 ACC 工况总结成如表 2 所示的 15 类。除了这 15 类工况，本车定速行驶也是一个最基本的工况。

在基本工况确定的基础上，可以进一步分析这些自然驾驶工况的速度信息，车间时距信息。通过这些信息的分析可以了解自然驾驶工况下驾驶员行为。从而改进现有 ACC 控制策略的开发，提高 ACC 产品的舒适性。

5 致谢

感谢导师朱西产老师为本文撰写提供的指导。

参考文献

[1] Zhang Nanfeng, Chen Junhui, Chen Shuguan.*The Research and development of Adaptive Cruise and Control*[J]. A collection of Papers from the Twentieth Annual Conference of the teaching of basic courses in Higher School in electronic and electrical appliances of the ministry of education. 2010/07

张南峰，黄军辉，陈述官. *汽车自适应巡航控制系统应用研究与发展*[J]. 教育部中南地区高等学校电子电器基础课教学研究会第二十届学术年会论文集，2010 年 7 月

[2] Bosch Company. Translated by Wei Chunyuan and so on. *Comfort and Convenience Systems. Beijing: The Press of Beijing Insititute of Technology*.2007

德国 BOSCH 公司编，魏春源等译. *汽车安全性与舒适性系统*//Safety, Comfort and Convenience Systems. 北京：北京 理工大学出版社，2007

[3] ISO15622. *Transport information and control system – Adaptive Cruise Control systems- Performance requirements and test Procedures* .2002

[4] GB/T20608.*Intelligent transportation information systems – Adaptive Cruise Control systems- Performance requirements and test Procedures*.2006

[5] GB/T 20608. *智能运输系统-自适应巡航系统-性能要求和检测方法*. 2006

Proceedings of the 11th International Forum of Automotive Traffic Safety, 2014, pp 394- 403
No. ATS.2014.404

Study on the Influence of the Driving Behavior When Vehicle Collision Avoidance

Huang Jiang，Li Hong
Hunan University，ChangSha，China，410082
Email：huangjiang7903@126.com

Abstract: Vehicle active collision avoidance is a research hit in automotive active safety area, while most other researches mainly restrict the vehicle trajectory by steering control, and braking or accelerating in this procedure is rarely considered. This paper proposes an offset distance within a certain station to define the ability of the vehicle's emergency obstacle avoidance. It reveals the relationship between the vehicle handling behavior and obstacle avoidance ability by the dynamical analysis on vehicle particle and 2DOF vehicle model respectively. The research shows that it benefits the vehicle's obstacle avoidance ability with a suitable brake when the vehicle takes a steering maneuver simultaneously. The cause and its influence factors are further studied. This study affords a theoretical foundation for vehicle handling control when the vehicle takes an active obstacle collision avoidance maneuver.

Keywords: Vehicle active safety; active collision avoidance; driving behavior; obstacle avoidance ability

车辆紧急避障时的操纵行为研究

黄江，李红
湖南大学，长沙，中国，410082
Email：huangjiang7903@126.com

摘　要：车辆主动避障是车辆主动安全领域的一个研究热点，多数研究在实现车辆避障时，都是利用转向控制来约束车辆轨迹，极少涉及制动或加速的控制。本文采用一定行程内的车辆偏移距离来定义车辆避障能力，通过车辆质点和二自由度车辆模型的动力学分析，揭示了紧急避障时车辆操纵行为与避障能力之间的关系，证明了车辆在转向的同时进行一定强度的制动，对提高车辆的避障能力是有利的，并对其原因和影响因素进行了进一步的说明，为完善主动避障时车辆的操纵控制研究提供基础和依据。

关键字：汽车主动安全，主动避障，操纵行为，避障能力

1　引言

车辆主动避障和智能辅助避障是智能汽车研究的一个关键问题，也是车辆主动安全领域的一个研究热点，其关键问题主要是两个：一是车辆避障路径规划；二是车辆避障行为的控制实现。目前，车辆避障的研究主要都集中在这两个问题上，或通过各种算法规划合适的路径，使车辆跟随道路、躲避障碍[1][2]；或利用转向控制实现车辆轨迹约束，使车辆避开障碍[3][4][5]。在进行这些研究时，对象车辆一般车速都不太高，车辆的附着条件使车辆有能力进行障碍规避；在进行车辆轨迹控制时，一般也只进行转向控制，极少涉及制动或加速的控制。

基金项目：
国家自然科学基金青年基金项目（51105136），湖南省科技支撑计划项目（2012GK3154）

当高速车辆遇到突发状况而进行紧急避障时，通常进行的操纵行为就是转向和制动。由于附着条件的限制，车辆有可能不易完成规避动作，这时就需要对操纵行为与车辆避障能力的关系进行分析。一般认为，车辆在纯转向情况下的避障能力是最强的，即轮胎没有受到纵向力的情况下所能提供的侧向附着力是最大的。但另一方面，如果转向的同时进行制动，制动可以降低车速，从而减小车辆转向所需的向心力。可见，转向和制动都会影响车辆的规避动作，从而对车辆的避障能力产生影响。

本文就是通过对操纵行为与车辆避障能力的关系进行研究，进一步探讨提高车辆避障能力的方法。

2　车辆避障过程中的操纵行为分析

车辆紧急避障过程中，车辆通常需要进行比较激烈的转向动作，产生较大的轮胎侧偏角，从而使轮胎受到较大的侧偏力。对于高速车辆，车辆在紧急避障过程中，很容易产生以下两种危险情况：

（1）由于车辆转向系统和轮胎附着力的限制，无法产生足够的侧向力使车辆完成小半径转向，导致车辆无法完成避障。

（2）车辆在转向过程中，轮胎附着力超过其附着极限，使车轮产生较大的滑移，而导致车辆失稳。

对于第二种状况，通过对轮胎纵向滑移率和侧偏角的控制，可以最大程度的避免危险发生；对于第一种状况，由于转向机构和轮胎附着力的限制，主要是后者的限制，当障碍物足够近，足够宽时，车辆是无法完全避开的。因此，在一定车速下，一定距离内，车辆转向时所能达到的最大侧向位移，比较直观的反映了车辆的避障能力。

车辆的避障能力是与驾驶者对车辆的操纵行为密切相关的。第一，在轮胎附着力允许的前提下，转向角越大，转弯半径越小，车辆的避障能力越强；第二，制动力越大，车辆减速度越大，车速的降低可以减小转向时所需的侧向力，但由于轮胎附着力的限制，制动力增加又会减小轮胎的侧向附着能力，使车辆容易发生侧滑。

由此可见，转向和制动都会对车辆的避障能力产生影响，而转向和制动同时进行时，又会对车辆的避障能力参数什么样的影响？接下来文章就通过避障车辆的动力学分析，对这个问题进行深入的探讨。

2.1 质点运动方程

为了简化分析，可以将汽车看作一个质点，不考虑车辆的横摆运动和质心侧偏角，此时，车辆受到的纵向力方向和车辆速度方向一致，侧向力方向与车辆速度方向垂直，如图 1。

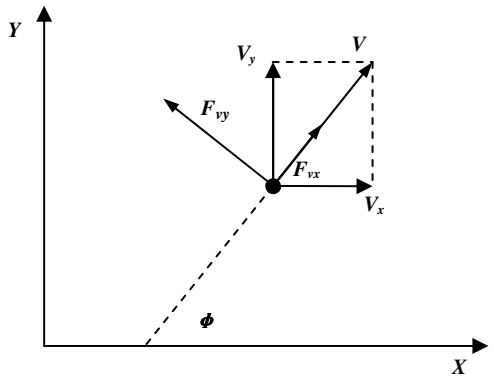

Figure1.the motion model of vehicle centroid

图 1. 车辆质点运动模型

2.1.1 模型建立

令车辆速度 V 与大地坐标系 x 轴的夹角为Φ，车辆沿 x 轴受力为 F_x，沿 y 轴受力为 F_y，则有：

$$F_x = F_{vx}\cos\phi - F_{vy}\sin\phi \qquad (1)$$

$$F_x = F_{vx}\cos\phi - F_{vy}\sin\phi \qquad (2)$$

其中，

$$\cos\phi=\frac{v_x}{v}，\quad \sin\phi=\frac{v_y}{v} \tag{3}$$

于是有：

$$\begin{cases}\dot{v}_x=\dfrac{F_{vx}}{m}\cdot\dfrac{v_x}{v}-\dfrac{F_{vy}}{m}\cdot\dfrac{v_y}{v}\\ \dot{v}_y=\dfrac{F_{vx}}{m}\cdot\dfrac{v_y}{v}+\dfrac{F_{vy}}{m}\cdot\dfrac{v_x}{v}\\ \dot{v}=\dfrac{F_{vx}}{m}\end{cases} \tag{4}$$

考虑到轮胎附着力的限制，附着极限可用摩擦椭圆近似表示，于是有：

$$\frac{F_{vx}^2}{F_{x\max}^2}+\frac{F_{vy}^2}{F_{y\max}^2}=1 \tag{5}$$

令地面附着系数为 μ，轮胎各向异性系数为 ζ，车辆的纵向加速度为 a_{vx}，侧向加速度为 a_{vy}，则有：

$$\frac{a_{vx}^2}{(\mu g)^2}+\frac{a_{vy}^2}{(\zeta\mu g)^2}=1 \tag{6}$$

式中，g 为重力加速度。

假设车辆沿大地坐标系 x 轴、y 轴的位移分别为 l_x、l_y。

令 $x_1=v_x$，$x_2=v_y$，$x_3=v$，$x_4=l_x$，$x_5=l_y$，则质点运动状态方程可表示为：

$$\begin{cases}\dot{x}_1=\dfrac{1}{x_3}\left(x_1a_{xv}-x_2a_{vy}\right)\\ \dot{x}_2=\dfrac{1}{x_3}\left(x_1a_{vy}+x_2a_{vx}\right)\\ \dot{x}_3=a_{vx}\\ \dot{x}_4=x_1\\ \dot{x}_5=x_2\end{cases} \tag{7}$$

令 $X=\begin{bmatrix}x_1 & x_2 & x_3 & x_4 & x_5\end{bmatrix}^T$，当 $X\big|_{t=0}$ 和 a_{vx} 已知时，根据式（6）（7）可以求出车辆的运动轨迹。

2.1.2 实例计算

设汽车初速度为 100km/h，障碍物在车辆前方 40m 处，地面附着系数为 0.8，轮胎各向异性系数为 0.85。当汽车以确定的减速度进行制动，并同时转向，利用式（6）（7）可得车辆的运动轨迹。

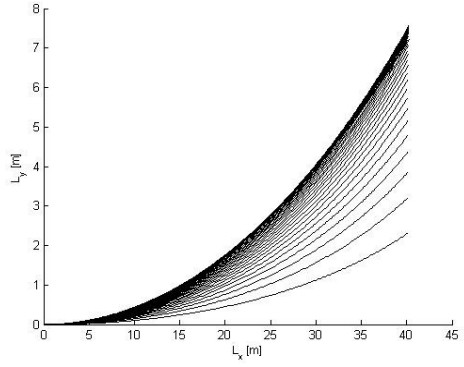

Figure2.vehicle collision avoidance Trajectory of centroid in Different braking intensity

图 2. 不同制动强度下车辆质点避障轨迹

由图 2 可知，在保证车辆稳定性的前提下，制动强度不同，车辆的避障能力不同。

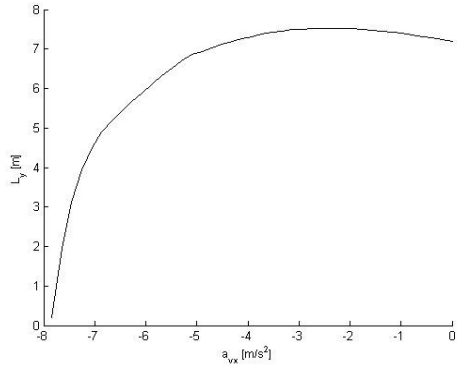

Figure3.the funtion of the vehicle centroid-velocity decrease in braking

图 3. 车辆质点侧向位移与制动减速度的关系

由图 3 可以看到，随着制动强度的增加，车辆质点的侧向位移先增加后减少，当 $a_{vx}=-2.352m/s^2$ 时，质点侧向位移最大，即车辆的避障能力最强。

为了分析车辆的避障能力，定义车辆的避障效率为 η_b：

$$\eta_b = l_y / l_x \qquad (8)$$

设车速分别为 100km/h、110km/h、120km/h，可以得到不同车速下的最大避障效率。

$$\eta_{\max}=\begin{cases}0.165 & v=100km/h, a_{vx}=-2.35m/s^2\\ 0.133 & v=110km/h, a_{vx}=-1.86m/s^2\\ 0.11 & v=120km/h, a_{vx}=-1.76m/s^2\end{cases} \qquad (9)$$

不同车速下，车辆避障效率和制动减速度的关系如图 4 所示。可以看到，车速越高，制动强度对避障效率的影响越小，利用合理的制动提高避障效率的效果越不明显。

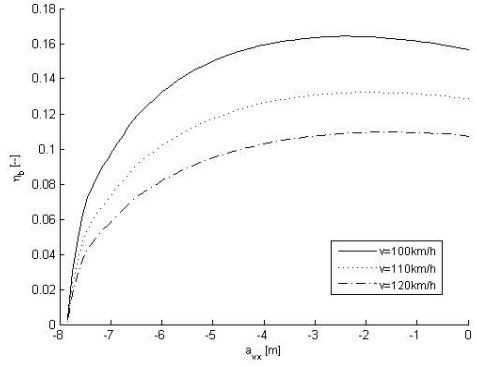

Figure4.the funtion of efficiency of vehicle collision avoidance -vehicle centroid-braking velocity

图 4. 车辆质点避障效率与制动减速度的关系

由式（6）可得：

$$\frac{da_{vy}}{da_{vx}}=-\zeta^2\cdot\frac{a_{vx}}{a_{vy}}=-\zeta^2\cdot\frac{a_{vx}R}{v^2} \qquad (10)$$

式中，R 为转弯半径，于是有：

$$|R|=\left|\frac{da_{vy}}{da_{vx}}\right|\cdot\frac{\zeta^2v^2}{|a_{vx}|} \qquad (11)$$

由式（11）可知，当$|a_{vx}|$较小时，$\left|\frac{da_{vy}}{da_{vx}}\right|$接近于 0，同时$|a_{vx}|$的存在又可有效降低$v$，因而车辆的转弯半径较小，避障能力增加；随着$|a_{vx}|$增加，$\left|\frac{da_{vy}}{da_{vx}}\right|$迅速增大，而$v$降低较慢，导致转弯半径迅速增加，避障能力明显下降。另一方面，车速越高，v^2影响越大，导致$|R|$明显增加，同时避障时间减小，会使利用$|a_{vx}|$减小转弯半径的效果下降。

2.2 二自由度车辆动力学模型

通过对质点运动方程的分析，可以说明制动和转向对车辆避障能力的影响，并对产生影响的原因作出较合理的解释。但质点运动模型没有考虑车辆的横摆和侧偏，与车辆实际运动状况差异较大，因此，有必要建立更精确的模型来对避障运动进行分析。

为了考虑车辆横摆与侧偏的影响，同时又不至于使求解过于复杂，本文建立二自由度车辆动力学模型来分析避障过程。

2.2.1 模型建立

文献[6]给出了线性二自由度车辆的转向特性。如图 5 所示，汽车质量为m，前进速度为V，质心侧偏角为β，前轮转角为δ，质心到前、后轴的距离分别为a、b，汽车横摆角速度为$\omega=\dot{\psi}$，前、后轴等效侧偏刚度为K_f、K_r，汽车绕z轴的转动惯量为I_z。

根据几何关系有：

$$\alpha_1=\beta+\frac{a}{V_x}\cdot r-\delta,\quad \alpha_2=\beta-\frac{b}{V_x}\cdot r \tag{12}$$

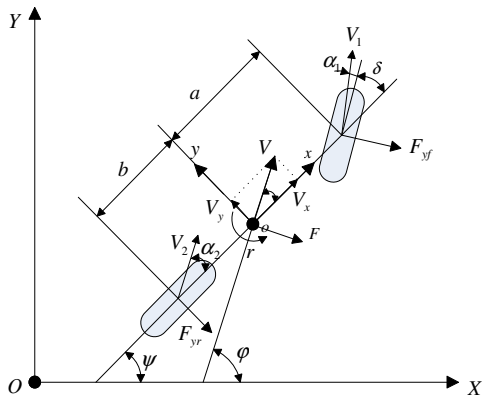

Figure5.two free degree vehicle model

图 5. 二自由度车辆模型

不考虑空气动力影响，可得车辆模型的平衡方程：

$$\begin{cases} m\left(\dot{V}_y+V_x\omega\right)=-\left(K_f\alpha_1+K_r\alpha_2\right) \\ I_z\dot{\omega}=aK_f\alpha_1+bK_r\alpha_r \end{cases} \tag{13}$$

将式（12）代入式（13）可得：

$$\begin{cases} \dot{V}_y=\dfrac{K_f+K_r}{mV_x}V_y+\left(\dfrac{aK_f-bK_r}{mV_x}-V_x\right)\omega-\dfrac{K_f}{m}\delta \\ \dot{\omega}=\dfrac{a^2K_f+b^2K_r}{I_zV_x}\cdot\omega+\left(aK_f-bK_r\right)\dfrac{V_y}{V_x}-\dfrac{aK_f}{I_z}\delta \end{cases} \tag{14}$$

行令 $x_1=V_x$、$x_2=V_y$、$x_3=\omega$、$x_4=\psi$、$x_5=l_x$、$x_6=l_y$，当汽车以加速度 a_x 进制动时，有：

$$\begin{cases} \dot{x}_1=a_x \\ \dot{x}_2=\dfrac{K_f+K_r}{mx_1}x_2+\left(\dfrac{aK_f-bK_r}{mx_1}-x_1\right)x_3-\dfrac{K_f}{m}\delta \\ \dot{x}_3=\left(aK_f-bK_r\right)\dfrac{x_2}{x_1}+\dfrac{a^2K_f+b^2K_r}{I_zx_1}\cdot x_3-\dfrac{aK_f}{I_z}\delta \\ \dot{x}_4=x_x \\ \dot{x}_5=\sqrt{x_1^2+x_2^2}\cdot\cos\left(x_4+\dfrac{x_2}{x_1}\right) \\ \dot{x}_6=\sqrt{x_1^2+x_2^2}\cdot\sin\left(x_4+\dfrac{x_2}{x_1}\right) \end{cases} \tag{15}$$

当车辆以 a_x 制动减速时，前轮受到的纵向力为：

$$\begin{cases} F_{xf} = mg \cdot \dfrac{b + a_x h_g / g}{a+b} \\ F_{xr} = mg \cdot \dfrac{a - a_x h_g / g}{a+b} \end{cases} \tag{16}$$

式中，h_g 为质心高度。

为了在避障过程中保持车辆的稳定性，需要对车轮的侧偏角进行判断。前轮的侧偏角大于后轮侧偏角时，前轮轮胎力先达到附着极限；前轮的侧偏角小于后轮侧偏角时，后轮轮胎力先达到附着极限。因此，控制侧偏角较大的车辆的纵滑和侧偏，使其轮胎力不超过附着极限，则能保证前、后轮轮胎力都处于其稳定区间。

当 $\alpha_1 \geq \alpha_2$ 时：

$$\alpha_1 = F_{fy} / K_f \tag{17}$$

当 $\alpha_1 < \alpha_2$ 时：

$$\alpha_2 = F_{ry} / K_r \tag{18}$$

$$\alpha_1 = \frac{x_3}{x_1}(a+b) - \delta^* - \alpha_2 \tag{19}$$

式中 δ^* 为前一时刻的前轮转角，当前时刻的前轮转角则由下式计算：

$$\delta = \frac{x_2}{x_1} + a \cdot \frac{x_3}{x_1} - \alpha_1 \tag{20}$$

某轮胎侧偏角为 5°，地面附着系数为 1.0，垂直载荷为 4500N 时，轮胎侧向力和纵向力关系如图 6 所示。

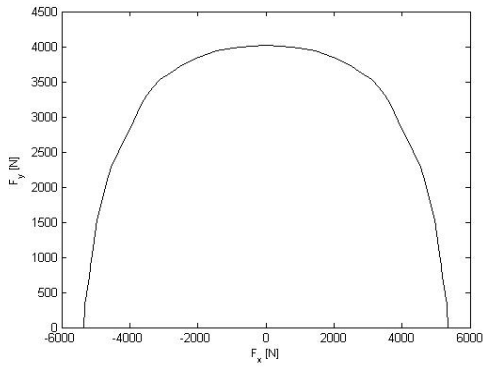

Figure6.the funtion of lateral force-longitudinal force

图 6. 轮胎侧向力与纵向力的关系

图 6 近似表达了轮胎的附着极限。若考虑充分利用轮胎附着力，根据式（16）计算出轮胎纵向力后，再按照实验得到的纵向力和侧向力的关系，求得轮胎的侧向力，从而利用式（17）-（20）计算前轮转角。

2.2.2 实例计算

某车参数如表 1 所示。

Table1.vehicle parameters of a vehicle

表 1. 某车的车辆参数

参数	数据	单位	参数	数据	单位
m	1529.98	kg	I_z	607.67	kg·m^2
a	1.139	m	b	1.637	m
K_f	-72230	N/rad	K_r	-76815	N/rad
h_g	0.606	m			

汽车初速度为 100km/h，障碍物在车辆前方 40m 处，地面附着系数为 0.8。

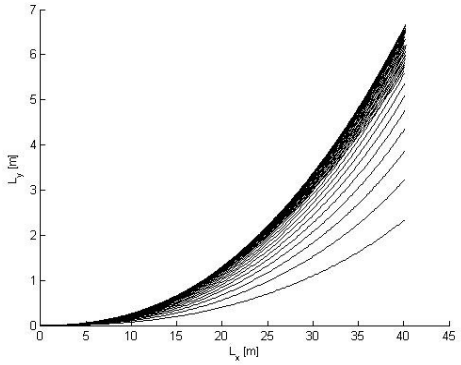

Fig7.vehicle collision avoidance Trajectory in different braking intensity

图 7. 不同制动强度下车辆避障轨迹

当汽车以确定的减速度进行制动，并同时转向，利用式（15）可得车辆的运动轨迹。

由图 7 可见，考虑车辆的横摆和侧偏，制动强度同样会影响车辆的避障能力，但为了保证车辆运动状态的稳定，当一个车轮达到附着极限时，另一个车轮的附着力未被完全利用，车辆的避障能力相对于质点模型有所下降。

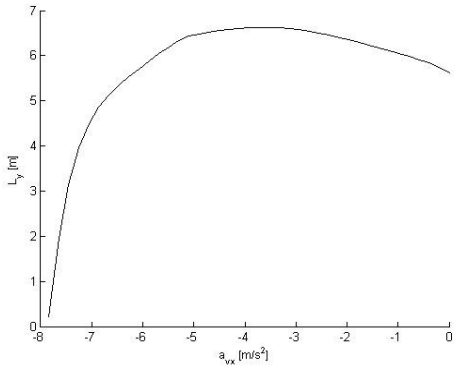

Figure8.the lateral displacement-braking velocity funtion

图 8. 车辆侧向位移与制动减速度的关系

如图 8 所示，随着制动强度的增加，车辆质点的侧向位移先增加后减少，当 $a_{vx}=-3.724m/s^2$ 时，车辆的避障能力最强。相对于质点模型，制动减速度提高车辆避障能力的作用更加明显，这是由于一般车辆都具有不足转向特性，进行制动时，车辆载荷前移，车辆的不足转向度会逐渐减小，从而进一步提高了车辆的避障能力。

当初始车速不同时，不同车速下的最大避障效率为：

$$\eta_{\max}=\begin{cases}0.166 & v=100km/h, a_{vx}=-3.72m/s^2\\ 0.131 & v=110km/h, a_{vx}=-3.43m/s^2\\ 0.107 & v=120km/h, a_{vx}=-2.94m/s^2\end{cases} \quad (18)$$

不同车速下，车辆避障效率和制动减速度的关系如图 9 所示。可以看到，紧急避障时，制动操作能够显著地提高车辆的避障效率；随着车速的提高，特别是车速达到 120km/h 后，利用制动提高避障效率的效果会明显下降。

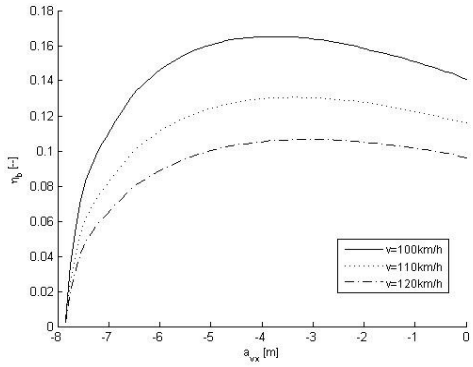

Fig9.the efficiency of vehicle collision avoidance-braking velocity funtion

图 9. 车辆避障效率与制动减速度的关系

3 结论与展望

3.1 结论

论文通过对车辆质点模型和二自由度车辆模型的分析，阐明了制动和转向对车辆避障运动的影响。

（1）低强度的制动在降低车速的同时，并不会过多的降低车辆的侧向附着能力，还可以在保证车辆稳定性的前提下减小不足转向，因此，低强度的制动对提高车辆的避障能力是有利的。车速较低时，制动对提高车辆避障效率的作用尤为明显。

（2）当车速较高时，制动对提高车辆避障能力的作用有所下降，但低强度的制动在稍稍提高车辆避障能力的同时，还能降低车辆的速度，总体来说，对车辆应对紧急状况是有利的。

（3）为了保证紧急避障时车辆的稳定性，在制动的同时，还需要根据轮胎的附着情况实时调整转向，其转向控制方法对避障时的方向控制策略有一定的借鉴意义。

3.2 展望

在论文涉及的研究过程中，也发现了一些问题与不足，希望在后续的研究中近一步解决。

（1）论文所采用的分析模型进行了大量的简化，与实车结果会有一定出入。为了得到更精确的分析结果，需要建立更复杂的四轮车辆模型，考虑载荷变化、轮胎特性变化和悬架特性的影响。

（2）论文在计算避障路径时，为了使避障能力最大化，未对车辆的方位角进行限制。考虑到环境因素和车辆避障后的姿态调整，在车辆避障路径末端进行一定的方位控制是有必要的，需要在后续研究中予以解决。

参考文献

[1] Keonyup Chu, Minchae Lee, Myoungho Sunwoo. *Local Path Planning for Off-Road Autonomous Driving With Avoidance of Static Obstacles. IEEE Trans*. Control Syst. Technol., December 2012, Vol.13, No.4:1599-1616.

[2] Junsoo Kim, Kichun Jo, Keonyup Chu, et al. *Road-model -based and graph-structure-based hierarchical path-planning approach for autonomous vehicles*. Proceedings of the Institution of Mechanical Engineers, Part D: Journal of Automobile Engineering 2014; 228: 909-928.

[3] David Fernández Llorca, Vicente Milanés, Ignacio Parra Alonso, et al. *Autonomous Pedestrian Collision Avoidance Using a Fuzzy Steering Controller. IEEE Trans*. Control Syst. Technol., June 2011, Vol.12, No.2:390-401.

[4] Yongsoon Yoon, Jongho Shin, H. Jin Ki m, et al. *Model-predictive active steering and obstacle avoidance for autonomous round vehicles*. Control Engineering Practice 2009; Vol.17:741-750.

[5] Taehyun Shim, Ganesh Adireddy and Hongliang Yuan. *Autonomous vehicle collision voidance system using path planning and model-predictive-control-based active front steering and wheel torque control*. Proceedings of the Institution of Mechanical Engineers, Part D: Journal of Automobile Engineering 2012; 226(6) 767-778.

[6] Guo Konghui. *Vehicle handling dynamics. Changchun*: Jilin Science and Technology Press, 1991

[7] 郭孔辉. *汽车操纵动力学*. 长春：吉林科学技术出版社，1991

Proceedings of the 11th International Forum of Automotive Traffic Safety, 2014, pp 404- 411
No. ATS.2014.501

Comparative Study between the WorldSID and the EuroSID II in Static Impact Tests

Maria de ODRIOZOLA[1], Adrià FERRER [1], Ignacio LÁZARO[1]
[1]Applus+ IDIADA L'Albornar, PO Box 20, 43710 Santa Oliva, Tarragona (SPAIN)
Email: maria.odriozola@idiada.com, adria.ferrer@idiada.com, ilazaro@idiada.com

Abstract: In the past decade, most side impact protocols have been based on the results obtained from the EuroSID II. However, with the arrival of the new Euro NCAP 2015 protocol, the Passive Safety society will have to face a new challenge: to develop vehicles according to the results obtained using WorldSID. For this reason, an in-depth analysis of the WorldSID together with a comparison between both dummies has been done. Furthermore, a series of impact tests were defined, making a special effort to obtain test results from dummies in very similar configurations.This study will make it possible to reach conclusions in order to detect the differences obtained from the two dummies. By comparing the impact that side impact crashes can have on the two studied dummies, it will be possible to discern if there are any necessary changes to be done on future vehicle developments.

Keywords: WorldSID, EuroSID II, Comparison

1 Introduction

Global accident statistics show that approximately 30% of all impacts and 35% of total road fatalities are due to side impact crashes [1].

It is for this reason that it is so important to develop advanced safety systems to reduce vehicle occupant injuries and fatalities caused by side impacts. Because of this, all vehicle safety regulations include strict requirements that must be accomplished by means of side impact crash testing. These regulations and protocols intend to enhance the safety of new vehicles by obliging manufacturers to develop restraint systems based on the vehicle's behaviour to side impact. In this way, the vehicle occupants have a major protection in case of lateral accident.

However, although the main protocols to be tested have always been very restrictive in order to ensure vehicle integrity and passenger safety; they used to use a wide range of side impact dummies, with low biofidelity rank values, in their assessments [2,3]. Until the arrival of the WorldSID, all of the side impact dummies that were being used throughout the world obtained ISO Biofidelity Classification rates from Unacceptable to Fair, reaching a maximum Biofidelity ranking of 5.7 (out of ten).

The noticeable improvement found with the WorldSID in comparison to its predecessing side dummies has eladed to the incorporation of this new generation dummy to the new Euro NCAP Protocol that will be in force from year 2015, onwards.

Although most Euro NCAP test procedures suffered major changes in their main settings, the greatest challenge that OEMs will have to overcome when testing their vehicles according to the new Euro NCAP protocol is the use of the WorldSID (WS) instead of the EuroSID II (ES-2) in the Adult Occupant Protection (AOP) side impact assessment.

As it will be demonstrated further on in this paper, WS shows a clearly higher sensitivity to external stimulus than ES-2. This leads to a high probability of the vehicle being downgraded when assessed using WorldSID instead of its predecessor.

2 Methodology

2.1 Objectives

So as to understand the methodology and main testing decisions that were made, it is important to comprehend which were the most important aspects to be considered in this project. These were:

1. The high repeatability of the tests
2. Controlled boundary conditions
3. Similar level of impact as that of a Full Scale Crash test

For this preliminary testing, the interaction between the dummy and the vehicle was not studied, as the aim of the project was to carry out a direct comparison between both dummies under the same external stimulus. The main idea was to fulfill an in-depth analysis of both dummies and to correlate them before they were studied separately under crash impact conditions.

The tests to be carried out in this first phase of the project had to be as standardized as possible. These tests would become a useful analysis of the effect of performing Oblique Side Pole Impact tests instead of fully perpendicular impacts.

2.2 Test setup explanation

After considering the test objectives shown above, it was decided that the best option was to carry out tests with a similar setup as the calibration testing that is used to certify dummies for crash testing. These tests consist in using a 23.4 kg Standard Pendulum Rig to impact the dummies to be studied in a desired Impact Point. The impact points that were chosen were the shoulder bolt and the mid thoracic rib bolt. These areas were chosen due to their importance when studying side impact crashes and their common use as main impact areas against Side Airbags and/or door panels..

On the other hand, due to the fact that the WorldSID may not sit free without a backrest it was decided to carry out all of the tests with the dummy seated on the Standard WorldSID Calibration Bench. By doing all of the tests with the dummies seated in the same bench, the sitting position was kept fairly constant throughout the entire test matrix.

It was decided to carry out all of the tests with a target impact speed of 3 m/s. This decision was taken due to its similarity with the normal calibration and crash impact test speeds. Simulation carried out by the vehicle manufacturer showed that this speed corresponded to the actual intrusion speed that could be of interest in their vehicle development.

Furthermore, as the main objective of these tests is to assess the impact of Oblique Impacts on both the EuroSID II and the WorldSID, for this reason the tests were done using 5 different impact angles.

The test setup for the tests that have been carried out may be observed in the test matrix (Table 1) shown below:

3 Analysis – Summary of Results

In this section, some of the results that were obtained from the previously described component tests may be found.

Note that, the author would like to highlight the fact that most of the sensor results that are shown in the following graphs have been pre-processed before being graphically represented. In order to do this, the signals have been filtered (according to the same filtering criteria that are used for Euro NCAP Protocol tests) and, if necessary, an offset has been applied to ensure that all signals started at 0. The only signals that have not been pre-processed have been those that correspond to the rib rotation in the WorldSID.

Table 1. Dummy Static Test Matrix – First Phase

Test Settings	Impact Point	Impact	Tests
WorldSID Calibration Bench, 23.4 kg Standard (Male Dummy) Calibration Pendulum Rig, Target Speed: 3 m/s, Arm Positioning according to Euro NCAP Crash Test Protocol	Shoulder Bolt	0º (*)	2 x EuroSID II 2 x WorldSID
		10º	2 x EuroSID II 2 x WorldSID
		20º	2 x EuroSID II 2 x WorldSID
		30º	2 x EuroSID II 2 x WorldSID
		45º	2 x EuroSID II 2 x WorldSID
	Middle Thoracic Rib Bolt	0º	2 x EuroSID II 2 x WorldSID
		10º	2 x EuroSID II 2 x WorldSID
		20º	2 x EuroSID II 2 x WorldSID
		30º	2 x EuroSID II 2 x WorldSID
		45º	2 x EuroSID II 2 x WorldSID
Extra Tests (for repeatability analysis			
Same Tests Settings as (*)			1 x WorldSID 1 x WorldSID

3.1 Shoulder Impact Tests

To start with, the data corresponding to the Shoulder Impact Tests has been studied. In this case, only the upper thoracic rib displacement and acceleration have been analyzed. It has been chosen to study these channels because in all of the shoulder impact tests, the upper thoracic rib is the most critical one during side impacts (specially pole tests). Also, it is important to bear in mind that the upper thoracic rib is the closest rib to the impact point and that is present in both dummies. Of course, in the case of the WorldSID, studying the Shoulder rib displacement and acceleration is of vital importance too but as it is not present in the EuroSID II it has not been studied in this paper. Furthermore, the shoulder force has also been analyzed to see the different behaviors of the shoulder assembly from both dummies.

In Figure 1, it is possible to see that the Upper Thoracic Rib Displacement curves show a clear trend where, as it was expected, the values of the registered displacement in the purely lateral direction increase as the impact angle decreases. This effect is one of the main reasons why it is considered that the EuroSID II has shortages. As the ES-2 is only capable of measuring purely lateral displacements, and not resultant rib deflections, the EuroSID II will always read remarkably lower chest deflections when tested under oblique conditions. This fact may derive in an underestimation of the injury that an occupant may suffer during a vehicle collision in an oblique impact direction.

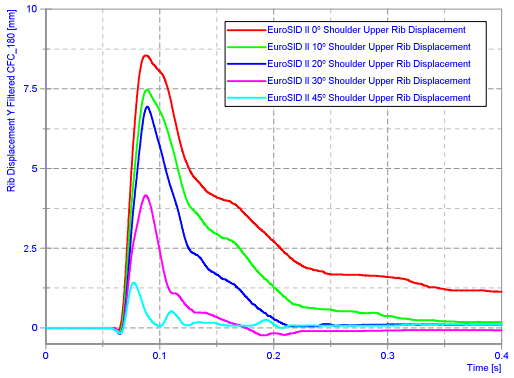

Figure 1. EuroSID II Upper Thoracic Rib Displacement in Y. Comparison by Impact Angle.

The previously mentioned effect of oblique testing can also be seen in Figure 2, shown below. It can be seen that, in the WorldSID Shoulder Impact results, again, the rib intrusion values show a trend by which the rib intrusion values decrease when the impact angle increases.

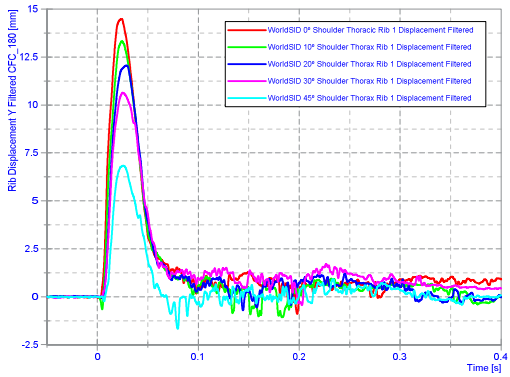

Figure 2. WorldSID Upper Thoracic Rib Displacement in Y. Comparison by Impact Angle.

Nevertheless, in the case of the WorldSID the differences found between each of the studied curves (one for each impact angle) are remarkably smaller than the ones that were perceived in Figure 1.

Moreover, the fact that the rib rotation varies depending on the impact angle will also have a non-equal effect on the calculation of the Rib Resultant Displacement, making the evaluation of the oblique tests much more trustworthy than in the case of EuroSID II. This phenomenon may be observed in Figure 3, found in the next page.

On the other hand, when analyzing the previous graph, an unexpected result was obtained. In the case of the 0º Shoulder Impact very high positive rotation is obtained. A certain positive rotation was expected, as the WorldSID has a clear tendency towards forward movement but, this rotation was expected to be minor than 2º-2.5º (negligible). In this case, a maximum positive rotation of 6.46º was observed. This absolute value is close to the one that was obtained in the 30º test (-6.96º) with the opposite sign.

The results that have been previously highlighted were surprising and lead to two different considerations. On one hand, one of the options that was considered was the presence of a human error during testing. This option would justify the obtained results and would be the easiest solution. For this reason, the 0º Shoulder Impact test configuration was repeated once again, obtaining almost identical results to those that were gained in the first two repetitions.

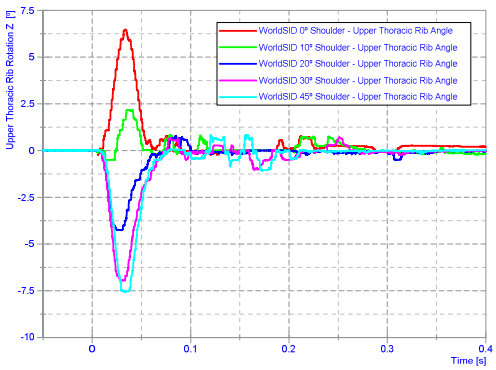

Figure 3. WorldSID Upper Thoracic Rib Angle in Z. Comparison by Impact Angle

Subsequently, the human error option was discarded. Therefore, it was deduced that this dummy has a clearer tendency towards positive rotation than other side impact dummies and, although the trend that may be seen when increasing the impact angle can seem logical, the starting point is not as neutral as it would be expected. In other words, when the WorldSID is tested under non-oblique conditions, the resulting rotation is highly positive, and not neutral.

Furthermore, the positive rotation of the upper rib has also been justified with the movement that the rib must do when it is pressed by the dummy's arm during the impact. This phenomenon will be studied in the Thorax Impact Test Result Analysis.

In addition, it has been observed that, in general, in shoulder impact tests the chest intrusion values that have been obtained when testing with the WorldSID are clearly higher than those that derive from testing the ES-2 in the same configuration.

By analyzing the dummy signal graphs and the videos that were recorded during the testing it has been deduced that, the differences found between the WS and ES-2 rib displacement values occur due to the fact that the WorldSID has a greater sensitivity and because the dummy's arm presses on the ribs during the impact. This effect can be seen in the general results for the upper rib displacement where the WorldSID upper rib values are always approximately 6 mm higher than for the EuroSID II.

It has also been observed that, in all Shoulder Impact tests, the peak values for the Shoulder Force in Y are very close in all cases (approximately -1 kN). However, there is a noticeable difference in the trends found with one dummy and with the other. In Figures 4 and 5, it is possible see the differences in the behaviors of both dummies' shoulders (Shoulder Force in Y).

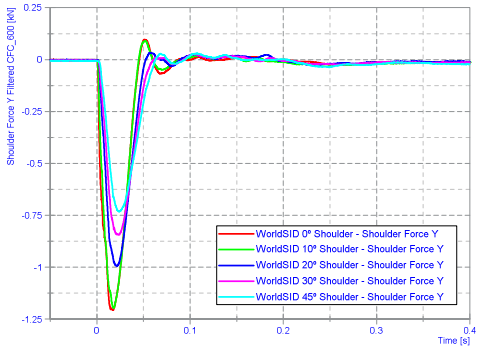

Figure 4. WorldSID Shoulder Force in Y. Comparison by impact angle (Shoulder impact tests)

In the case of the EuroSID Iogical trend that may be found in the results from the WorldSID is not present. When using the ES-2, the values of the Shoulder Force do not show clear signs of increasing or decreasing depending on the impact angle. This fact highlights the scarce development of the EuroSID II shoulder in comparison with that of the WorldSID together with its low reliability when tested under oblique loading conditions.

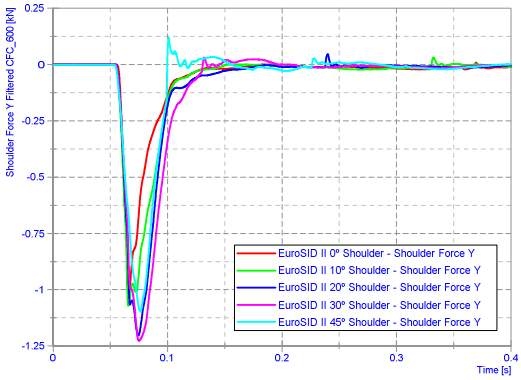

Figure 5. EuroSID II Shoulder Force in Y. Comparison by impact angle (Shoulder impact tests)

3.2 Thorax Impact Test Results

In the case of thorax impact test results, the same three comparative test graphs have been done, in order to show the impact that the impact angle has on the studied rib. In this case, the analyzed channel has been the Middle Thoracic Rib displacement and, in the case of WorldSID, its rotation. In this way, the direct impact point behavior has been studied.

In the following graphs it may be observed that the maximum rib displacement diminishes when the impact angle increases, in both dummies. However the EuroSID II Rib Displacement graph (Figure 6) does not follow a well-defined trend, as many of its curves count with more than one peak. Nevertheless, it may be seen that in remarkably oblique test conditions, the ES-2 rib displacement values are minor than 7.5 mm, which is considered to be a very low rib displacement value.

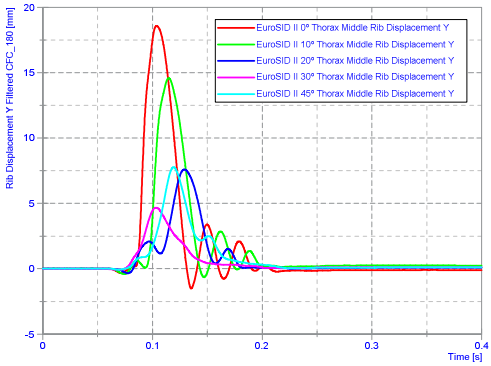

Figure 6. EuroSID II Middle Rib Displacement in Y Comparison (by Impact Angle) in Thorax Impact Tests

In the case of WorldSID (See Figure 7); however, the same trend as in the Shoulder Impact Tests has been followed, where the rib displacement values gradually decrease when the impact angle increases.

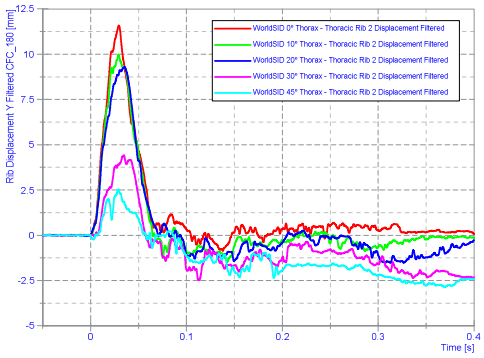

Figure 7. WorldSID Middle Rib Displacement in Y Comparison (by Impact Angle) in Thorax Impact Tests

Note that, in this case, the graph showing the differences in the rib rotation depending on the impact angle (Figure 8) shows a very clear trend. In the thorax impact phase, there are no unexpected results as the only positive rib displacement values that were obtained were in the 0º Impact Test and they were negligible (+2.4º). This suggests that, if the resultant rib displacement were calculated, the gap between the resultant displacement curves would be greatly reduced.

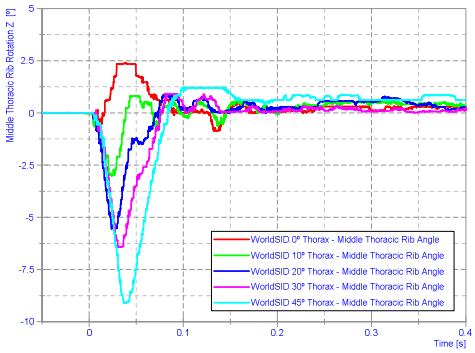

Figure 8. WorldSID Middle Rib Rotation in Z Comparison (by Impact Angle) in Thorax Impact Tests

On the other hand, the following results from the middle rib rotation in Z show that when the thoracic rib behavior is studied, lower initial positive rotations are found. This leads to the conclusion that part of the positive rotation that was achieved in the Upper Thoracic Rib (Shoulder Impact) was due to the arm rotation.

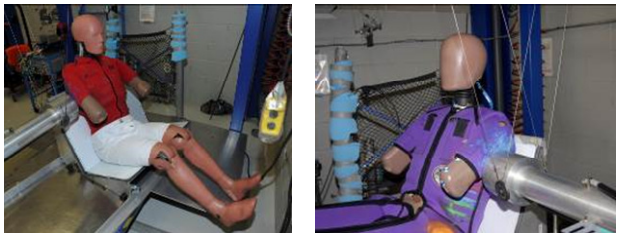

Figure 1. Comparison between both dummies' middle rib impact points in the 10º Thorax Impact Test

Furthermore, it has been observed that in thorax impacts using the WS, part of the pendulum energy was dissipated by moving the arm away from the impact direction. When using the EuroSID II, this does not happen as the dummy's seating position and the shape of its arm force the pendulum to impact directly upon the ribcage, underneath the arm.

Consequently, the energy absorption occurs only by means of rib deflection. Figure 9 shows the differences between the pendulum impact points when using both dummies in the same test setup.

4 Summary/Conclusions

The ES-2 and the WS are two advanced side impact dummies that count with remarkable differences between them. To start with, their anthropometry and construction characteristics force the two dummies to have variable responses to the same external impacts. This occurs due to the inequality in the interaction between the pendulum that has been used for the testing, and the dummy; as well as the influence of the rotation in Z on both dummies.

On the other hand, clear variances have been found between the shoulder and thorax tests. In the first case, the WS showed major values in all rib intrusion results due to the pressure of the dummy's arm against the ribcage. Nevertheless, in thorax impact tests, the ES-2 showed higher intrusion values than the WS. These results were obtained due to the fact that in the ES-2 tests, the pendulum impacted directly on the ribcage instead of impacting on the arm of the dummy and moving it away (dissipating in this way, part of the energy from the impact).

To conclude, the author would like to highlight that this study represents the first phase of a long-term WorldSID study that is to be carried out in the near future. Further testing and analysis of this particular dummy will be accomplished in the near future.

5 Definitions/Abbreviations

EuroSID II / ES-2	European Side-Impact Dummy II
WorldSID / WS	Worldwide Side Impact Dummy
Euro NCAP	European New Car Assessment Programme
AOP	Adult Occupant Protection

Acknowledgement

The authors of this paper would like to show their gratitude to all of the members of the IDIADA Passive Safety team that have made this project possible as well as those customers that have helped with their implication and collaboration in this work.

Special mention would like to be given to Paul Lemmen and Arie Schmidt, from Humanetics, for their continuous help and support in the study of the WorldSID.

References

[1] McNeill, A., Haberl, J., Holzner, M., Schoeneburg, R. et al., *"Current Wordwide Side Impact Activities – Divergence versus harmonisation and the possible effect on future car design."* Proceedings of the 19th International Technical Conference on the Enhanced Safety of Vehicles (ESV). Paper Number 05-0077

[2] Liu, Y., Zhu, F., Wang, Z., van Ratingen, M. *"Side Impact Injury Prediction with FE Simulations of the New Advanced World SID FE Dummy Models."* Proceedings of the 20th International Technical Conference on the Enhanced Safety of Vehicles (ESV). Paper Number 07-0372

[3] Scherer, R., Bortenschlager, K., Akiyama, A., Tylko, S., *"WorldSID Production Dummy Biomechanical Responses"*. Proceedings of the 21st International Technical Conference on the Enhanced Safety of Vehicles (ESV). Paper Number 09-050. Pages 1 and 8

Proceedings of the 11th International Forum of Automotive Traffic Safety, 2014, pp 412- 416
No. ATS.2014.502

Comparison of Current ATDs with China's Adult Population in Anthropometry

Kai ZHANG, Lingbo YAN, Xin LV, Libo CAO
State Key Laboratory of Advanced Design and Manufacture for Vehicle Body, Hunan University, Changsha, China,410082
E-mail: milanylb@hotmail.com

Abstract: Crash test dummies are full-scale anthropomorphic test devices (ATDs) that simulate the dimensions, weight proportions and articulation of the human body, and are used to measure human injury potential in vehicle crashes. The Hybrid-III dummy familywhich is widely used currently refers to selection of the respective percentiles of U.S. adult males and females as design targets. Based on the Chinese National Physical Fitness Surveillance for the year 2000, 2005, 2010 and Chinese standard GB/T 10000-1988, a series of anthropometric parameters for Chinese adults were obtained, and data analysis was conducted between the populationsof China and of ATDs design targets. The results show that there are obvious distinctions between the current ATDs and the recent China population in anthropometry. For 50th-percentiles female, the stature is about 2.6% shorter than the ATDs design targets and the body weight is about 8.03% lighter. For 50th-percentiles male, the stature is about 3.59% shorter and the body weight is about 10.52% lighter, despite there is a tendency that Chinese adults are becoming higher and heavier with time goes on. The implications of these differences will provide an important reference for designing and optimizing vehicle restraint system for Chinese passengers.

Keywords: anthropomorphic test devices, anthropometry, China's adult population, ATDs design targets

1 Introduction

In order to evaluate the vehicles' ability to protect occupants in motor-vehicle crashes, anthropomorphic test devices (ATDs) of different titular percentile values are used in crash tests. For example, the Hybrid-III family is involved in crash tests of FMVSS, NCAP and other standards or regulations all over the world. Likewise, the Hybrid-III 50th-percentile male dummy is the most widely used ATD for frontal collision testing in China, which simulates the dimensions, weight proportions and articulation of the midsize American male body[1]. There is no doubt that human dimensions of Chinese adults are different from those of American adults, but the quantitative analysis of the difference between current ATDs with china's adult population in anthropometry has not been presented.

The anthropomorphic test devices (ATDs) are usually developed in a 4-step process [2]. First, the reference population is selected. For the Hybrid-III adult dummy family, the general American adult population was used, both males and females. Second, among these reference dimensions, stature and body weight are chosen. Third, target percentiles are selected based on the desired size of the ATD [3]. The Hybrid-III adult dummy family was designed to target the 5th, 50th, 95th percentiles of U.S. population, separately, for stature and body weight. Forth, besides stature and body weight, other dimensions of the ATD are obtained from detailed anthropometric data from individuals similar in size to the reference dimensions.

Although the reference dimensions of the Hybrid-III adult dummy family are based on the anthropometric parameters of American adult population, there are still some disparity between the dimensions of the ATDs and the reference dimensions for manufacturing technique reasons. For example, the weight of the 50th-percentile male design target is 77.0 kg, but for that reasons the hybrid-III 50th-percentile male is 77.65±1.18kg. In order to eliminate this influence, the data of the hybrid dummy family design target were used rather than the real dummies' parameters in comparisons.

In this article, general trends of stature and body weight for Chinese adults are presented using data from surveys

in 1988, 2000, 2005, 2010 (current). The current Chinese adults' anthropometric parameters are compared with the reference values for the Hybrid-III family of ATDs.

2 Materials and Methods

The data which were used to design the Hybrid-III dummy family were obtained in 1974 by collecting the dimensions of U.S. adult population, and the corresponding data of China's adult population were obtained from the Chinese National Physical Fitness Surveillance (CNPFS) and Chinese standard GB/T 10000-1988 (Human Dimensions of Chinese Adults).

The Chinese National Physical Fitness Surveillance (CNPFS)is a continuing probability of China's population that gathers several anthropometric dimensions among hundreds of health-relate variables, such as stature, body weight and so on. The CNPFS release data every 5 years, beginning in 2000.

In this article, the CNPFS data of 2000 were got from *Report on National Physical Fitness Surveillance (2000)*, number of samples is 25,687. The CNPFS data of 2005 were got from *Report on the second National Physical Fitness Surveillance*, number of samples is 163,448, which were published by PEOPLE'S SPORTS PUBLISHING HOUSE OF CHINA.The CNPFS data of 2010 were obtained from *Bulletin on National Physical Fitness Surveillance (2010)*, which presented on the website of the General Administration of Sport of China, number of samples is 155,054.

To assess the trends of China population anthropometry over time, the stature and body weight of 50^{th} percentile male and female were selected from Chinese standard GB 10000-1988 for year of 1988, and CNPFS reports for year of 2000, 2005, and 2010 (current). In order to compare the stature and body weight of the Hybrid-III adult dummy family with the dimensions of China's adult population, the statures and body weights of dummy design targets were obtained from published tables for the 1974 National Health and Nutrition Examination Survey II (Abraham et al. 1978).

The reference stature and body weight for each Hybrid-III adult ATD were the dummy design targets size of 1974. CNPFS reports have only stature and body weight of 50^{th} percentile male and female, so that this article only compare these data of the Chinese with the U.S. population's data of 1974. Although 50^{th} percentile female Hybrid-III ATD is not available currently, midsize female is also an important part in evaluation the injury risks for the female in the frontal collision, so 50^{th} percentile male and female are all included in comparison.

3 Results

Table 1 lists the 50th percentile male and female values of stature and body weight for Chinese adults of year 1988, 2000, 2005, and 2010. For 50th-percentile female, stature raises only 0.4% (6mm) during 22 years. But for male, stature raises 0.7% (12mm). For the change of body weight, the 50th-percentile male and female increased 16.78% (9.9kg) and 10.19% (5.3kg) respectively. Comparatively speaking, the 50th-percentile population's body weight values increased markedly; especially from year 1988 to 2000.The fact that the dimensions of Chinese adults are changed rapidly during the past two decades provides a huge influence on the automotive safety system design.

Table 1. Stature and body weight of Chinese adults

	50^{th}-percentile female		50^{th}-percentile male	
Year	Stature*	Body weight**	Stature*	Body weight**
1988	1570	52.0	1678	59.0
2000	1574	56.1	1685	65.5
2005	1574	55.8	1687	66.4
2010	1576	57.3	1690	68.9

* The unit of stature is millimeter.** The unit of body weight is kilogram.

Table 2 lists the stature and body weight for the Hybrid-III adult dummy design targets. Table 3 describes the ratios which show the distinction of stature and body weight values between Chinese adult population with the target stature

and body weight for the Hybrid-III ATDs.

Table 2. Reference stature and body weight for the Hybrid-III adult ATDs (U.S. population data)

	50th-percentile female		50th-percentile male	
Year	Stature*	Body weight**	Stature*	Body weight**
1974	1618	62.3	1753	77.0

* The unit of stature is millimeter.** The unit of body weight is kilogram.

Table 3. Comparison of reference stature and body weight for the Hybrid-III adult ATDs with Chinese 50th adults

Year	50th-percentile female		50th-percentile male	
	Stature variance*	Body weight variance**	Stature variance*	Body weight variance**
1988	2.97%	16.53%	4.28%	23.38%
2000	2.72%	9.95%	3.88%	14.94%
2005	2.71%	10.43%	3.76%	13.77%
2010	2.60%	8.03%	3.59%	10.52%

*The formula of stature variance is.**The formula of body weightvariance is.

Analyzing these data listed above,the current stature percentile values for Chinese adults are slightly lower than the reference values. For example, the reference stature for the midsize male ATD is 1753mm, and Chinese male midsize stature is 1690mm in 2010, the variance of stature is only 3.59%. Same to the midsize male stature, the midsize female stature also maintains about 3% shorter than the reference midsize women stature. Even though the diversity of stature is small, the difference is lager for the body weight. The U.S. 50th-percentile male body weight is 77.0kg in 1974, compared with the Chinese value for the midsize male of 68.9kg in 2010. The variance is 10.52%, the body weight of U.S. midsize men is much heavier than that of same percentile Chinese men and same to the 50th-percentile women. Even though with time going, Chinese population is become heavier and taller, and the anthropometric values are closer to the reference values of current Hybrid-III ATDs, but is still lighter and shorter than the Hybrid-III adult ATD.

Table 4. Comparison of stature and body weight for the Chinese 50th males with the U.S. 50th males

Year	Stature*			Body weight**		
	Chinese 50th males	U.S.50th males***	variance****	Chinese 50th males	U.S.50th males***	variance****
1990s	1678	1755	4.4%	59.0	79.8	26.1%
2010s	1690	1761	4.0%	68.9	85.4	19.3%

* The unit of stature is millimeter.** The unit of body weight is kilogram.*** The values from .Reed et al. (2013)**** The formula of variance is.

Table 5. Comparison of stature and body weight for the Chinese 50th females with the U.S. 50th females

Year	Stature*			Body weight**		
	Chinese 50thfemales	U.S.50thfemales***	variance****	Chinese 50thfemales	U.S.50thfemales***	variance****
1990s	1570	1618	3.0%	52.0	65.5	20.6%
2010s	1576	1622	2.8%	57.3	71.0	19.3%

* The unit of stature is millimeter.** The unit of body weight is kilogram.*** The values from .Reed et al. (2013)**** The formula of variance is.

Table 4 and Table 5 list the comparisons of Chinese 50th males and Chinese 50th females with U.S. 50th males and U.S. 50th females, respectively. The main difference lies in body weight the same as what is discovered above. Although as time goes on, the difference decreases, there is still an obvious divergence (about 19%) in body weight

between Chinese 50th adults and U.S. 50th adults.

4 Discussion

Different percentile ATDs used in the vehicles or restraint systems testing must in some way represents the whole population of vehicle drivers and passengers. Superficially, ATDs can only accurately represent the individuals whose dimensions are similar to those of ATDs.Currently the most widely used ATDs for frontal collision in China is the Hybrid-III adult dummy family. According to analysis in this article, the anthropometry parameters for which the Hybrid-III adult dummies were designed have significant difference with the dimensions of Chinese population, which suggests that these ATDs may not be sufficiently representative of the Chinese population.

Discovering the difference of anthropometry parameters between the currently used ATDs and the Chinese adult population has a positive influence on the vehicle design and testing efforts. If a certain percentile ATD is considered to represent some individuals during design efforts, the optimal design could be fit these people well. That is to say, if engineersare clear about the difference between the current ATDs and the Chinese population, the designs of vehicles and restraint systems can focus on fitting Chinese population, the real users in China roads.

The difference in body weight between the China population and the ATDs design targets over the past 20 years have become smaller and smaller, but also maintain 10% disparity, and the main difference is lay on the body weight. For a particular crash scenario, the ATD's body weight is associated with the passive safety device, such as energy dissipation of power-absorbing, complianceof the car seat, belt restraints, air bag, and other vehicle components. If the passive safety device designed for a heavier ATD, they may not fit the lighter passenger. The air bag inflators may become higher-output, and the pre-tightening load of belt system may become bigger.From this perspective, vehicle safety performance engineers should not underestimate the difference of body weight when design vehicles for markets in China.

Chinese adults are about 3%~4% shorter than the ATDs design targets for different percentile. Different statures between Chinese adults and ATDs design targets leads to different dimensions of upper limbs, lower limbs and other parts. All of these dimensions determine the locations of the body regions that are targeted by the restraint systems, particularly the head, knees, and torso[3]. Even though the difference in body dimension between Chinese adults and the Hybrid-III dummy design targets is small, the difference of somatotype is obvious, particularly in the pelvis and chest regions. The current ATD shapes represent people who are more obese than Chinese adults, with wider shoulder and longer torso.

The futureresearch for occupant protection in China should focus on reducing injury risks by optimizing currently used ATDs to meet Chinese population dimensions, and protections for obese occupants should be pay more attention because there is a prominentincrease for Chinese adults body weight in past two decades.

Acknowledgements

This study was sponsored by the National High Technology Research and Development Program of China "863 Program" No. 2012AA111802 and Independent Research Topic of State Key Laboratory of Advanced Design and Manufacture for Vehicle Body, Hunan University No. 51275001.

References

[1] Backaitis Stanley H., and Harold J. Mertz. *Hybrid III: The first human-like crash test dummy*. Warrendale, PA: Society of Automotive Engineers, 1993. 830 (1993).

[2] Schneider L W, Robbins DH, et al. *Development of anthropometrically based design specifications for an advanced adult anthropomorphic dummy family, volume 1.*Washington DC: US Department of transportation, NHTSA; 1983. Final report DOT-HS-806-715.

[3] Reed Matthew P., and Jonathan D. Rupp. *An anthropometric comparison of current ATDs with the US adult population.* Traffic

injury prevention 14.7 (2013): 703-705.

[4] Mertz Harold J., et al. *The Hybrid III 10-year-old dummy.* No. 2001-22-0014. SAE Technical Paper, 2001.

[5] GB 10000-1988, *human dimensions of Chinese adults.*

[6] General Administration of Sport of China. *Report on National Physical Fitness Surveillance (2000)* [M]. Beijing: People's Sports Publishing House of China, 2002.

[7] General Administration of Sport of China. *Report on the Second National Physical Fitness Surveillance* [M]. Beijing: People's Sports Publishing House of China, 2007

[8] General Administration of Sport of China. *Report on National Physical Fitness Surveillance (2010)* [M]. Beijing: People's Sports Publishing House of China, 2011.

[9] Abraham, S., Johnson, C. L., & Najjar, M. F. (1979). Weight and height of adults 18-74 years of age. United States, 1971-74. Vital and health statistics. Series 11, Data from the national health survey, (211), 1.

Proceedings of the 11th International Forum of Automotive Traffic Safety, 2014, pp 417- 424
No. ATS.2014.503

Comparative Analysis of the Biological Simulation of Pedestrian FLEX-PLI and TRL-LFI

Wang Kun，Li Haibin，Wang Yang
China Automobile Technology & Research Center, Tianjin, China, 300300
E-mail: wangkun@catarc.ac.cn, lihaibin@catarc.ac.cn, wangyang@catarc.ac.cn

Abstract: At present, the TRL legform impactor and FLEX legform impactor are widely accepted by pedestrian protection test standards to evaluate pedestrian lower leg protection performance. However, the performance of TRL legform is questioned because it cannot simulate bending of leg bones. In this paper, the structure and characteristic of FLEX legform impactor and TRL legform impactor are analyzed; the mechanics tests are conducted, the biological simulation performance are compared based on the research achievements of corpse tests achieved by previous researchers. Foreground of application of FLEX legform impactor is put forward.

Keywords: vehicle, safety, pedestrian protection, FLEX legform, biological simulation

行人腿型冲击器 FLEX-PLI 与 TRL-LFI 生物仿真性对比分析

王坤，李海斌，王阳
中国汽车技术研究中心,天津，中国，300162
E-mail: wangkun@catarc.ac.cn, lihaibin@catarc.ac.cn, wangyang@catarc.ac.cn

摘　要：当前,行人保护试验标准普遍采用 TRL 腿型冲击器和 FLEX 腿型冲击器评价车辆对行人下腿的碰撞保护性能，但由于无法模拟腿骨的弯曲，TRL 腿型冲击器的性能受到质疑。本文分析了两种冲击器结构和特性，对 TRL 腿型冲击器和 FLEX 腿型冲击器进行力学特性试验，得到其力学响应，并基于前人尸体试验的研究成果，对比两种冲击器的生物仿真性。指出 FLEX 腿型冲击器在行人保护测试方面的应用前景。

关键词：汽车，安全，行人保护，FLEX 腿型，生物仿真性

1 引言

2003 年，欧盟率先将行人碰撞保护写入法规，即 2003/102 号指令，该指令所采用的试验方法基于 EEVC (the European Experimental Vehicles Committee，欧洲试验车辆委员会)提出的试验议案，采用了 TRL 公司生产的具有可变性膝部韧带关节的 TRL-LFI（TRL Leg Form Impactor，TRL 腿型冲击器）作为行人下腿冲击器，由于其采用了刚性管柱模拟人体腿部骨骼，也被称为刚性腿型冲击器。2002 年，JARI 和 JAMA 开始共同研究与人体生物力学特性更为接近的柔性腿型冲击器（FLEX-PLI，FLEX Pedestrian Legform Impactor），经多次讨论与改进，FLEX-PLI 最终定型。2013 年开始，日本法规和 JNCAP 均采用了 FLEX-PLI 作为行人腿型冲击器。EuroNCAP 行人保碰撞护评价也于 2014 年起使用 FLEX-PLI 替代 TRL-LFI 作为行人腿型冲击器。同时，行人碰撞保护全球法规、ECE 标准以及美国联邦机动车法规均在讨论将 FLEX-PLI 列入实施计划，并逐步取代 TRL-LFI。

我国汽车生产商在行人碰撞保护方面的研究落后于西方国家，车辆行人保护设计也处于起步阶段，行人腿部保护也多针对 TRL-LFI 进行设计。经验表明，使用 TRL-LFI 获得较高评价的车辆，不能确保在 FLEX-PLI 试

验中获得高分。为此，需要了解两种冲击器之间的差异，并对车辆设计方法进行有针对性的改进，才能适应行人保护法规的发展趋势。

2 行人腿部结构及伤害机理

行人腿部结构中，股骨、胫骨和膝部是最容易受伤的重要部位。股骨和胫骨是下肢支撑结构的主要构成，而膝关节内部结构复杂，多条韧带交织于关节腔内，连接骨骼和肌肉，上述部位功能的丧失会严重影响人的站立和行走功能。图 1 所示为膝关节的主要结构示意，前十字韧带、后十字韧带、内侧副韧带和外侧副韧带是膝部主要的韧带，也是较易受伤的膝关节软组织。

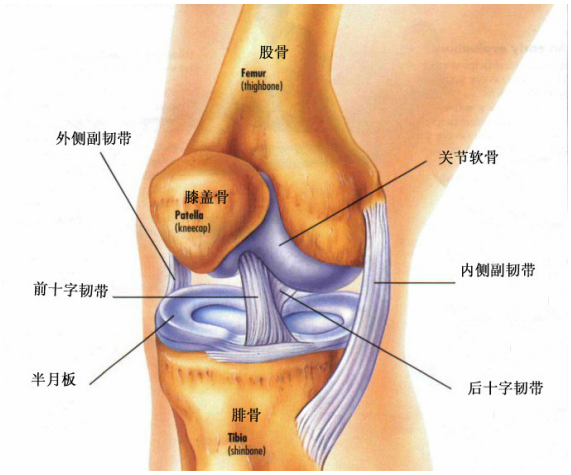

Figure1. structure of knee
图 1 膝关节结构示意图
图 1 膝关节结构示意图

行人碰撞事故中，碰撞产生的力作用在皮肤、肌肉、韧带、骨骼等部位。一旦相应部位的受力超过限值，就会造成骨折、韧带断裂、肌肉损伤等伤害。

股骨和胫骨骨折的原因是碰撞产生的弯矩导致腿骨所受应力超出其强度极限。因此，行人碰撞器需充分考虑腿部的弯曲变形，并且能够测量碰撞过程中腿部的弯曲应力或所受到的弯矩，才能更为有效地评价行人腿部的受伤程度。

碰撞事故中，行人上下腿先后接触车辆，从而导致膝关节受到较大的剪切作用力，进而拉伸韧带；另外，行人与车辆发生正面碰撞后，膝关节的弯曲方向与其自由运动方向相反，导致韧带承受巨大的拉力。当韧带的拉伸应力超过其强度时就会导致韧带断裂。因此，对行人碰撞器的膝部应有特殊设计，以测定碰撞过程中，膝关节的弯曲角度、剪切位移，进而依据生物力学特性，评价行人膝部的受伤程度。

3 FLEX-PLI 与 TRL-LFI 结构对比

行人腿型冲击器的性能直接影响测试结果的有效性和可重复性。为保证这一点，需要对人体腿部结构进行模块划分，依照每个模块的生物力学特性来设计冲击器。FLEX-PLI 与 TRL-LFI 均由大腿模块、膝部模块和小腿模块构成，但设计方式上 FLEX-PLI 整体采用了可变性的弹性体而 TRL-LFI 则采用了部分可变形的刚性体。图 2 所示两种腿型冲击器与人体腿部结构的对比。可见，FLEX-PLI 具有更多的柔性可变形关节，且具有更多的骨骼测量通道和膝部韧带测量通道。

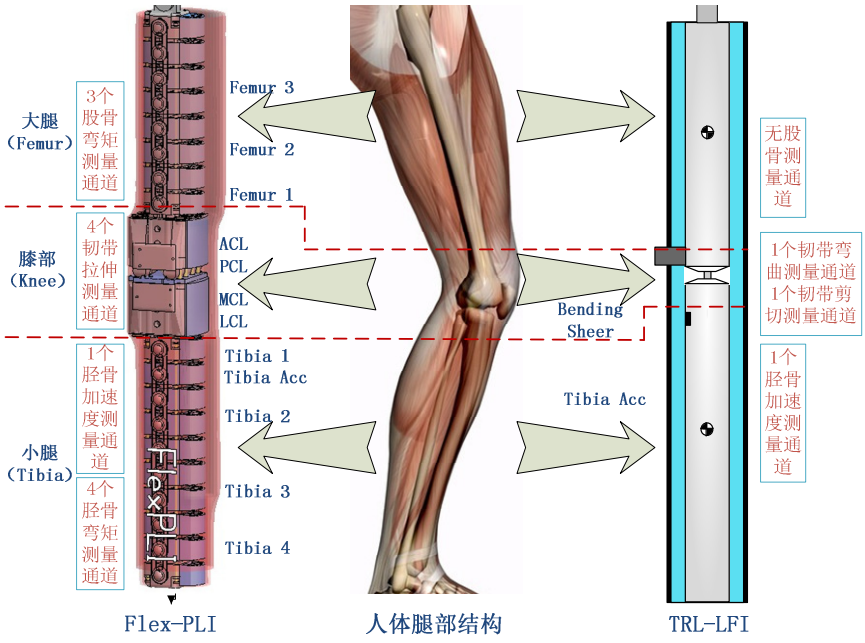

Figure 2. Structure of FLEX-PLI & TRL-LFI
图 2　FLEX-PLI、TRL-LFI 结构示意图

图 3 所示为 FLEX-PLI 的模拟骨骼结构。FLEX-PLI 的股骨与胫骨骨骼使用工程塑料制成，能够模拟腿部的弯曲变形状况，通过骨骼上的 7 组应变测量装置 Tibia-1、Tibia-2、Tibia-3、Femur-1、Femur-2、Femur-3、Femur-4 测量腿骨所受的弯曲载荷。另外，胫骨还装有加速度传感器，测试碰撞时胫骨上端的减速度。

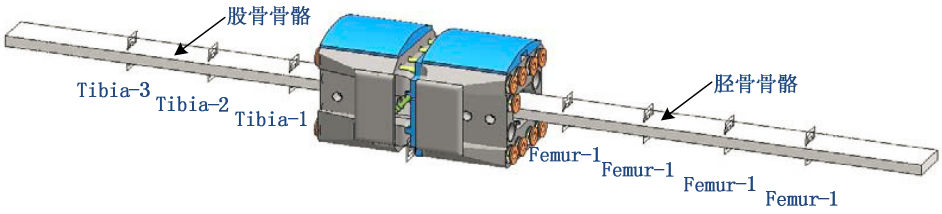

Figure 3. Simulant bone structure of FLEX-PLI
图 3　FLEX-PLI 的模拟骨骼结构

图 4 所示为 FLEX-PLI 的模拟膝部结构。其内部安装 24 根弹簧构成一个弹性系统，模拟人体腿部关节的力学特性。同时，膝部模块模拟人体膝关节的韧带结构布置了四个位移传感器，用于测量 ACL（Anterior Cruciate Ligament，前十字韧带）、PCL（Posterior Cruciate Ligament，后交叉韧带）、LCL（Lateral Collateral Ligament，外侧副韧带）、MCL（Medial Collateral Ligament，内侧副韧带）的拉伸量。

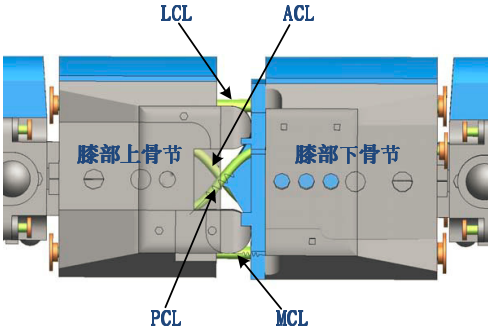

Figure 4. Simulant knee structure of FLEX-PLI

图 4　FLEX-PLI 的模拟膝部结

图 5 所示为 TRL-LFI 的结构。该冲击器上安装了三个传感器，一个加速度传感器和两个角位移传感器，分别用于测量胫骨加速度、膝关节弯曲角及膝关节剪切位移。其中，角位移传感器采集到数据后，经过一定的换算关系得到弯曲角度和剪切位移信息。

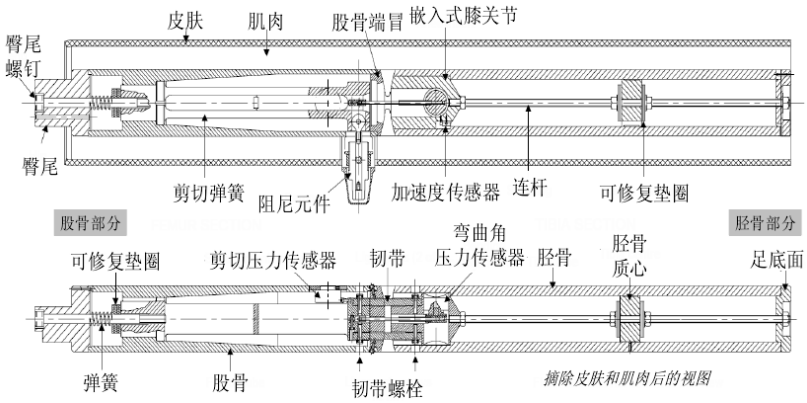

Figure 5. Structure of TRL-LFI

图 5　TRL-LFI 结构图

TRL-LFI 采用了刚性金属管模拟胫骨和股骨，骨骼内部拥有调节腿部质心的机械结构，由于金属管的强度较高，很难有效地模拟人体腿部的变形，因此，TRL-LFI 不能模拟腿骨各个部位的骨折，仅能通过安装在下腿的加速度传感器评价腿部骨折的风险。

图 6 所示为 TRL-LFI 的膝部结构，它是一个可塑形变形的关节，股骨与胫骨之间通过一对金属韧带片相连，该韧带片经过精细的计算与设计以确保与人体膝部韧带的生物力学性能相近。但是，由于发生塑性变形后，膝部金属韧带片的特性有较大改变，其试验的重复性并不理想。同时，TRL-LFI 简化的设计结构与人体膝关节的实际构造有较大差别，因而，其无法模拟膝关节各条韧带的受损情况。

综合以上论述可知，设计方式的不同决定了 FLEX-PLI 在结构上比 TRL-LFI 更接近人体腿部构造，因此，能够针对人体腿部的特定部位放置测量单元，只要腿部模型的力学特性设计能够与人体生物力学性能吻合，其必然能获得更为客观的评价结果。

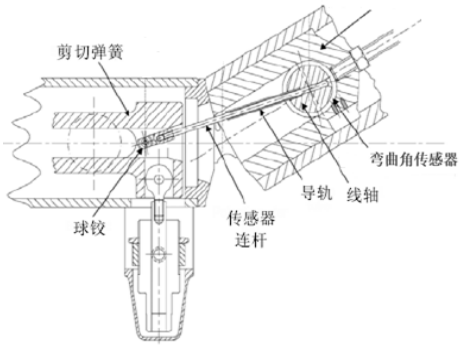

Figure 6.Knee structure of TRL-LFI

图 6　TRL-LFI 膝部结构

4 FLEX-PLI 与 TRL-LFI 性能对比

尸体试验是获取人体的生物力学特性的有效手段，对大腿、小腿、膝关节等新鲜尸体施加一定的载荷，直至骨骼折断或膝关节韧带断裂，通过传感器记录试验过程中的力矩、变形量、弯曲角度、剪切位移等数值即可确定大腿、小腿和膝部的生物力学响应。Kerrigan et al 等研究者通过对试验得到的结果如图 7~图 11 所示。

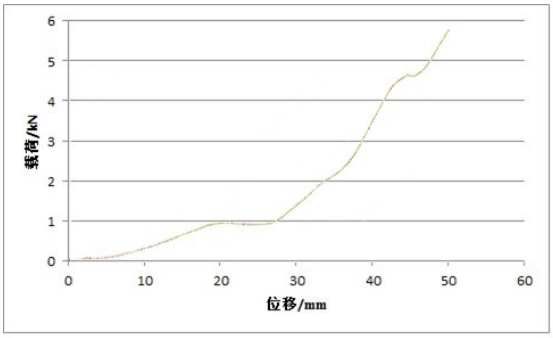

Figure 7.Bending moment-displacement of femur

图 7　大腿中部弯矩与位移关系

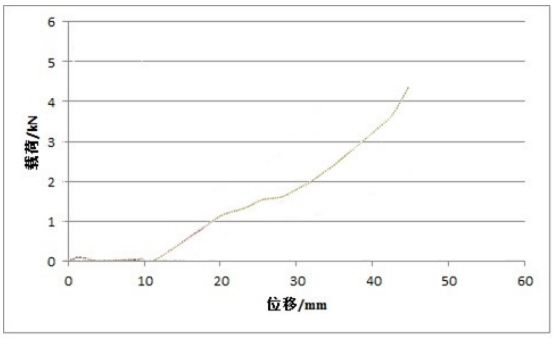

Figure 8.Bending moment-displacement of tibia

图 8　小腿中部弯矩与位移关系

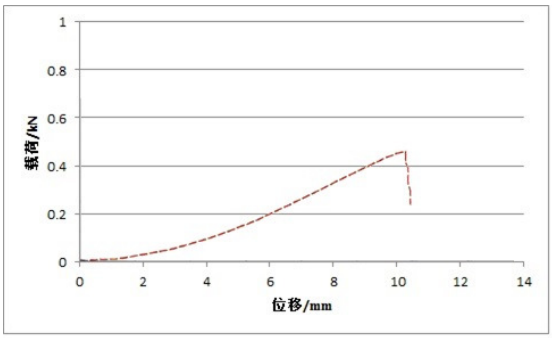

Figure 9. Tensile force-displacement of MCL

图 9　膝部 MCL 准静态拉伸力与位移关系

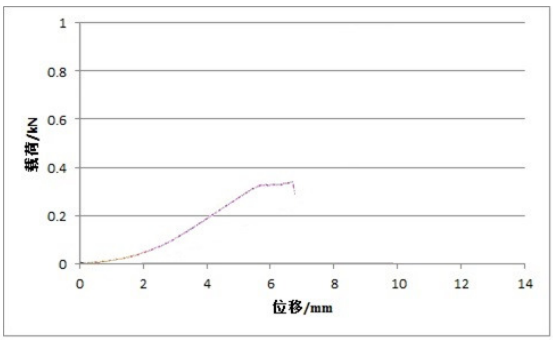

Figure 10. Tensile force-displacement of LCL

图 10　膝部 LCL 准静态拉伸力与位移关系

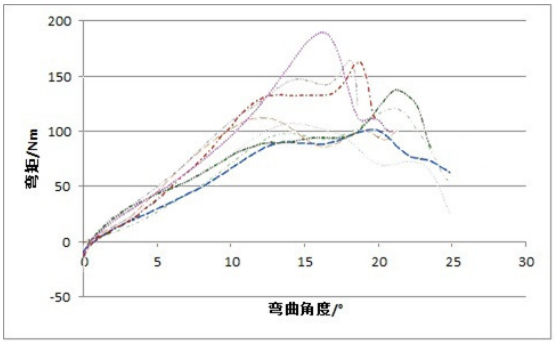

Figure 11. Bending angle-bending moment of knee
图 11 膝关节弯曲角度与膝关节弯矩关系

为了进行力学特性对比，对 FLEX-PLI 的大腿、小腿和膝部进行静力加载测试，图 12 所示为大腿和膝部的静力加载试验，通过记录试验中腿部模块受到的载荷、弯矩、变形及其相互关系，即可获得其力学特性。图 13、图 14 所示为 FLEX-PLI 大腿、小腿和膝部弯曲载荷与变形之间的关系，对比其受力变形特性与腿部的生物力学特性可以看出，FLEX-PLI 具有较高的生物仿真度。

图 15 所示为 TRL-LFI 的静力加载测试，对腿部施加弯矩，对膝部附近施加剪切力，得到 TRL-LFI 的膝部弯角、膝部剪切位移与载荷之间的关系，如图 16 所示。可以看出，TRL-LFI 膝部弯角对载荷的响应整体上与膝部的生物力学特性接近，但有所差别。

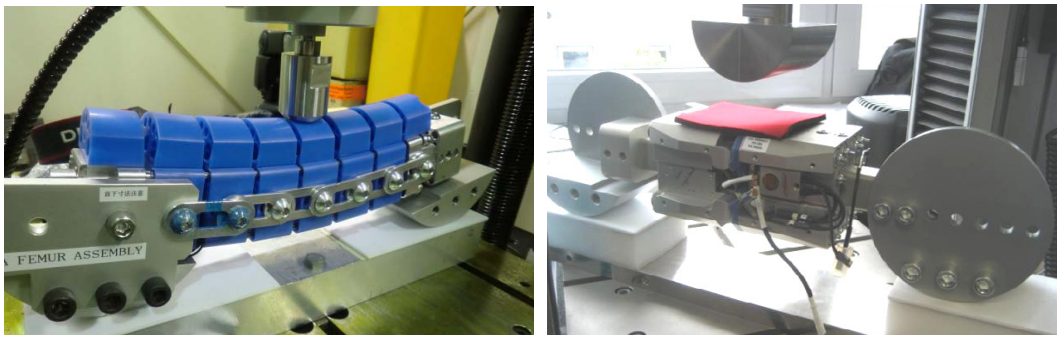

Figure 12. Static load test of femur and knee of FLEX-PLI
图 12 FLEX-PLI 大腿、膝部静力加载测试

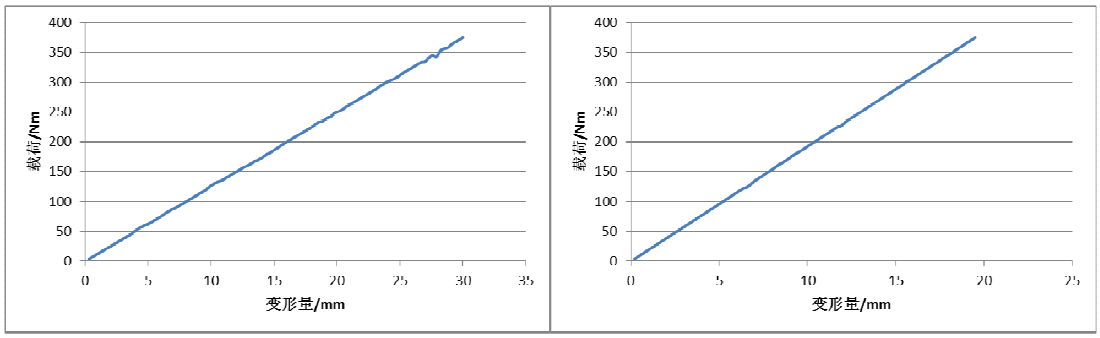

大腿 **小腿**

Figure 13. Bending Moment-displacement of femur and tibia of FLEX-PLI
图 13 FLEX-PLI 大腿、小腿弯矩与变形的关系

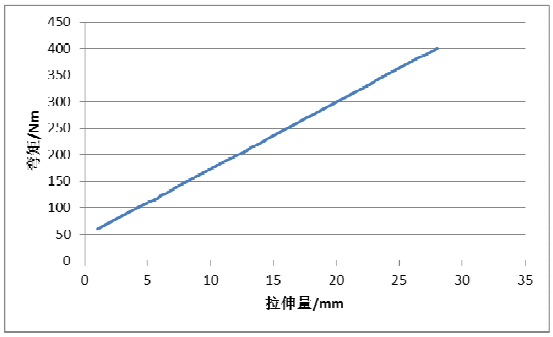

Figure 14. Bending moment-tensile displacement of knee of FLEX-PLI
图 14　FLEX-PLI 膝部拉伸量与弯矩的关系

Figure 15. Static load test of TRL-LFI
图 15　TRL-LFI 的静力加载测试

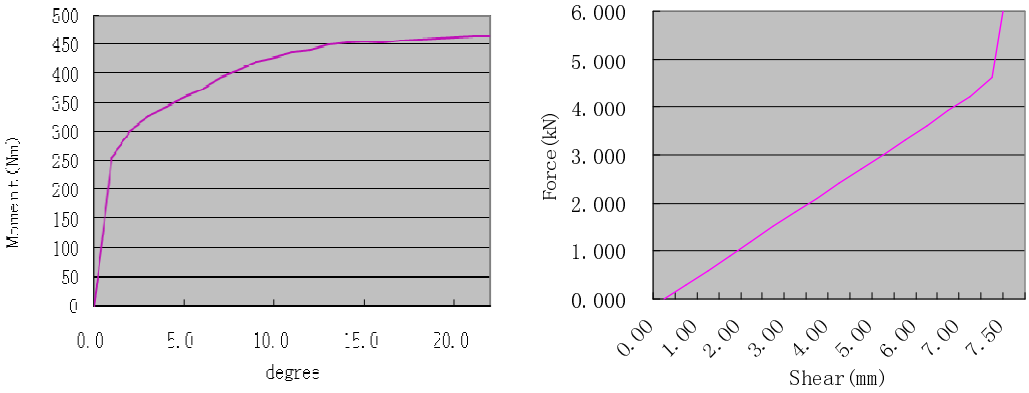

Figure 16. Load-bending angle & load-sheering displacement of knee of TRL-LFI
图 16　TRL-LFI 膝部弯角、膝部剪切位移与载荷的关系

5 总结与展望

综合本文以上论述可知，在结构上，FLEX-PLI 较 TRL-FLI，增加了对大腿、小腿骨胳的模拟，增加了对前、后、内侧及外侧韧带的模拟，评价指标更加具有针对性、更加全面，更为接近人体腿部构造；同时，在生物力学性能方面，FLEX-PLI 更加接近人体的生物力学特性，具有更高的生物仿真度。尽管将 FLEX-PLI 应用于行人

保护试验评价中的重复性和可靠性仍待进一步验证，但 FLEX-PLI 相较 TRL-FLI 来讲，技术上无疑是更加先进的。

目前，除日本外，TRL-FLI 仍是各国法规所采用的行人下腿冲击器，但多年的研究证实，FLEX-PLI 具有更好的生物力学特性，因此，部分国家和地区的 NCAP 率先引入了 FLEX-PLI，并制定了未来将 FLEX-PLI 引入法规的时间表。尽管如此，FLEX-PLI 也存在结构复杂、部件寿命较低等缺点，但相信通过应用过程中发现并解决所存在的问题，FLEX-PLI 会更加完善，并最终被行人保护法规所接受。

参考文献

[1] European Union. REGULATION (EC) No 78/2009 OF THE EUROPEAN PARLIAMENT AND OF THE COUNCIL of 14 January 2009 on the type-approval of motor vehicles with regard to the protection of pedestrians and other vulnerable road users, amending Directive 2007/46/EC and repealing Directives 2003/102/EC and 2005/66/EC. Europe: Official Journal of the European Union，2009.4.2.

[2] European Union. COMMISSION REGULATION (EC) No 631/2009 of 22 July 2009 laying down detailed rules for the implementation of Annex I to Regulation (EC) No 78/2009 of the European Parliament and of the Council on the type-approval of motor vehicles with regard to the protection of pedestrians and other vulnerable road users, amending Directive 2007/46/EC and repealing Directives 2003/102/EC and 2005/66/EC. Europe: Official Journal of the European Union，2009.7.25.

[3] Euro NCAP. *Pedestrian Testing Protocol Version 7.0*.Europe: Euro NCAP, March 201.

[4] UNITED NATIONS. *Global Technical Regulation No. 9 Pedestrian Safety*. Geneva: ECE/TRANS, 26 January 2009.

[5] Du Tianqiang, Zhu Qiwen. *Pedestrian protection legform impactor modularized analysis*[J], vehicle engineer,2009, (09):43-48

[6] 杜天强，朱其文. *行人保护下腿碰撞器模块分析*[J]. 汽车工程师，2009，(09):43-48.

[7] Shinya Hayashi, Masahiro Awano, Isamu Nishimura, etc. *Development of a Flex-PLI LS-DYNA Model*[C/CD]// 7th European LS-DYNA Conference, May 14-15 2009, Salzburg Austria.

[8] Shui Y. *The FE analysis of pedestrian protection legform impactor test*[J]. Journal of vehicle engineer,2011, 1(4):385-391

[9] 水野幸治.*针对行人下肢保护的腿型冲击试验有限元分析*[J].汽车工程学报，2011，1(4):385-391.

[10] Han Yong.*Lower limb dynamics respond and Injury biomechanics analysis during Vehicle pedestrian collision*[D].Hunan University, 2009

[11] 韩勇. *车辆与行人碰撞中下肢动力学响应和损伤生物力学分析*[D].湖南大学，2009.

[12] Zhang Guanjun. *Study on the impact injury characteristics of pedestrian lower leg and its related parameters*[D].Hunan University, 2009.

[13] 张冠军.*行人下肢的碰撞损伤特性及相关参数研究*[D].湖南大学，2009.

[14] Li Yuan. *Reseach on the design elements of motor vehicles with regard to the protection of pedestrians*[D].Jilin University,2009.

[15] 李源. *乘用车与行人碰撞腿部保护设计要素研究*[D].吉林大学，2009.

[16] Humanetics Innovative Solutions. *Flex PLI GTR User Manual*.2013.

[17] Chen Jie, Liu Junyong,Liu Qi .etc. *Application and research of pedestrians flexible lower leg base on EuroNCAP*[A].The sixteenth international forum of automotive traffic safety 2013[C]:2013

[18] 陈杰，刘军勇，刘奇等.*基于EuroNCAP 的行人柔性小腿应用与研究*[A].2013 年第十六届汽车安全国际研讨会[C]：2013

Proceedings of the 11th International Forum of Automotive Traffic Safety, 2014, pp 425- 430
No. ATS.2014.504

Research on Lumbar Calibration of 50th Crash Dummy

Li XIANGRONG[1], Wang KAI[1], Duan BINGXU[1],Xie MINGHAO[1]
[1]China Automotive Technology and Research Center, Tianjin, China, 300300
Email:lixiangrong@catarc.ac.cn

Abstract: By doing H-III 50thdummy lumbar calibration tests, this paper research on the lumbar calibration method, and discusses the lumbar hardness. It is valuable to the dummy performance research and vehicle crash test assessment system.

Keywords: Dummy, Lumbar, Chest Calibration, Hardness

Introduction

The vehicle safety is always an important aspect in consideration of the vehicle design，The vehicle crash test is an important method in vehicle safety research. In crash test, different load cells are installed in the dummy, which used for the measurement of the head acceleration, neck bending force, chest displacement and acceleration, femur load, tibia load etc. After analysis of the test data, the vehicle safe of the passenger protection can be acquired. Therefore, dummy is the vital equipment in crash test. Currently, there are various kinds of dummies in crash test and H-III 50th male dummy is most widely used in frontal impact test. With the improvement of the vehicle safety assessment system, the performances of dummy's parts will directly influence the evaluation result in car assessment. Therefore, dummy calibration test is an important method to identify the dummy property. For the H-III 50th dummy, the dummy company has laid down the calibration procedures for head, neck, chest, leg and so on. However, there is no clear requirement for lumbar calibration. Furthermore, there are few studies on lumbar performances. This paper will discuss the relationship between the lumbar hardness and calibration results through the research on H-III 50th male dummy lumbar calibration test procedure.

5 Lumbar hardness of the H-III 50th dummy

2.1 Hardness measurement

Hardness is the resistance capacity of other hard objects pressed into its surface. Magnitude of hardness is the conditional quantitative reaction which indicates the hardness and softness degree of the material. It is a kind of integrated index which is composed of a series of mechanical properties such as resilience; plasticity and toughness while not a simple physical quantity. And it is determined by material property, measurement condition and method.

Measurements of hardness are various and Shore hardness test is mainly used for rubber materials. After inserting the Shore durometer into the tested material, connect the indicator of the dial plate to a pin by mechanical spring, and stab the surface of the tested material, the figures shown on the dial plate is hardness value. The unit of Shore hardness is degree and described by Shore A and Shore D, which showing the different hardness range, Shore A is for 0～90 degree and Shore D is for 90 degree and above.

2.2 Lumbar hardness

The lumbar of the H-III 50th male dummy is shown in Figure 1. The normal hardness of the rubber part is 75 to 85(Shore A)[1]. The hardness of the lumbar will influence on the dummy condition in a certain extent. As a result of the soft lumbar, the upper torso will tend to lean forward and shift easily in the impact [2].

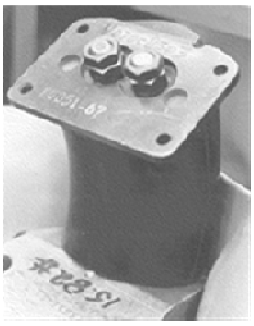

Figure.1 Lumbar of the H-III 50th dummy

6 Lumbar Calibration method research

3.1 Test method

Based on the calibration procedure of female dummy upper torso test, the similar method will be taken on male lumbar calibration (Figure.3). In order to get a deeper research and reduce the interference factors, only the dummy spine will be kept which is connected with lumbar. This is different with female dummy calibration which is installing the whole upper torso. The interference factors such as rib, chest skin, and rubber abdomen will be removed in bending process. In the test, fix the pelvis part, pull the upper spine with a wire rope, install the force transducer in the rope for measuring the loading process of the tension force, and install the angle transducer on the top of the spine for measuring the bending angle changes of the lumbar [3].

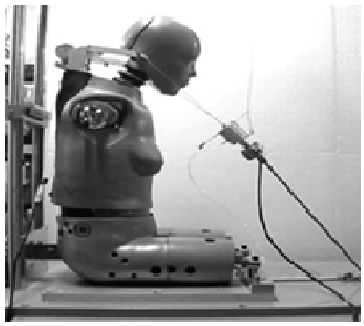

Figure.2 Upper torso calibration of the H-III 5th female dummy

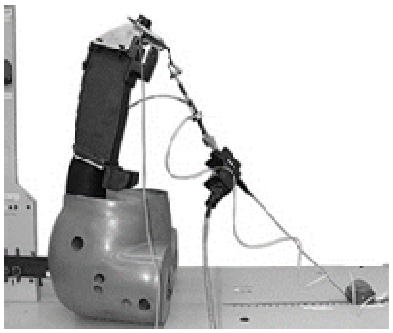

Figure.3 Lumbar calibration of the H-III 50th male dummy

To ensure the calibration consistency, the tightening torque of the lumbar tight wire is set to 1.25Nm. The original angle of the lumbar is set to 13 degree based on multiple measurements. During the loading process, record the tension force respectively at 10 degree, 20 degree and 30 degree. These three figures will be references for the judgment of the lumbar property conformity.

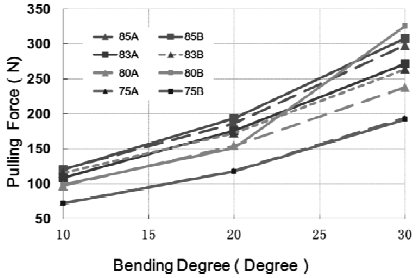

Figure.4 The result of different hardness of the lumbar spine

3.2 Problems during the test

The method shown in Figure 3 is used in lumbar calibration of the H-III 50th male dummy via multiple measurements, recording the tension force at 10 degree, 20 degree and 30 degree. The calibration test used different hardness of lumbar such as Shore hardness 75/80/83/85. Some unusual tension force came out in the test when the blending angle is near 30 degree (Figure 4). The tension force changes a lot. After analysis, we can figure out that the shelf of the chest displacement transducer touch the rubber surface of the lumbar, which is possible infects the test result when the bending angle changes to around 29 degree(differs from the original angle).

The deeper study on this show some potential factors such as structure weight and torso blending installation difference may influence the result of the calibration test. Through the study, it shows that some condition parameters should be required in calibration test (original angle and standardized tension force loading installment which can replace lumbar). Because good test repeatability can be achieved at the 10 and 20 degree bend angles (Sheet 1), the test result of 30 degree will not be used in the lumbar calibration as a suggestion. It's another reason that the H-III 50th dummy will unlikely bend to the extreme 30 degree with safe belt and air bag in normal crash test.

3.3 Confirmation on test condition and measurement parameters

Based on the analysis on the above result and to ensure the consistency of the calibration, the initial parameters are set as following: the tightening torque of the lumbar tight wire is 1.25 Nm; the original angle of the spine is 13 degree; record the tension force at 10 degree and 20 degree during bending. These two figures of tension force will be the reference in judging the lumbar property.

7 Hardness effect on lumbar property

4.1 Relations between bending angle and tension force

The Sheet 1 shows the comparison result of the different lumbar. Considering the instability of the figure in 30 degree, we only analyze the figures at 10 degree and 20 degree.

From the result we can see that the rubber hardness of the lumbar influence a lot on the lumbar calibration result. Lumbar hardness are 75, 80, 83 and 85, the tension force will grow with the rubber hardness at same bending angle.

Table 1. The result of different hardness of the lumbar spine

Test number	Force at 10º (N)	Force at 20º (N)	Lumbar hardness(Shore A)	Sample Number
1	120.6	186.5	85	A
2	120.3	193.5	85	A
3	108.6	175.8	83	B
4	115.3	172.4	83	B
5	97.1	154.3	80	C
6	98.9	151.2	80	C
7	72.1	118.7	75	D
8	71.8	117.8	75	D

4.2 Lumbar hardness effect on chest calibration result

Sheet 2 shows the chest calibration result which used different hardness as 75, 80 and 85. In order to eliminate the interference factors, the same dummy was used in the tests and only lumbar part with different hardness ware changed.

Table 2. Chest calibration results of different hardness

Sample Number	Largest chest compression (mm)	Chest hysteresis	Pendulum force(N)	Lumbar hardness
A	71.3	71.2	563.3	85
A	71.6	71.4	564.8	85
B	71.9	71	557.4	80
B	70.5	71.3	554.9	80
C	68.5	72.6	541.6	75
C	69.7	72	553.5	75

Test condition is shown as Figure 5. The quantity of the impact pendulum including measurement system is 23.4 kg, its' shape is a cylinder with 152mm diameter. The data collection system meet the requirement of SAEJ211. During the calibration test, the temperature is 20.5～22.2 degree, the humidity is around 10% to 70%, the pendulum speed is between 6.5m/s and 6.9m/s[4]. To ensure the consistency of the rib property, the interval of each two tests is 30 minutes to recover the rib state.

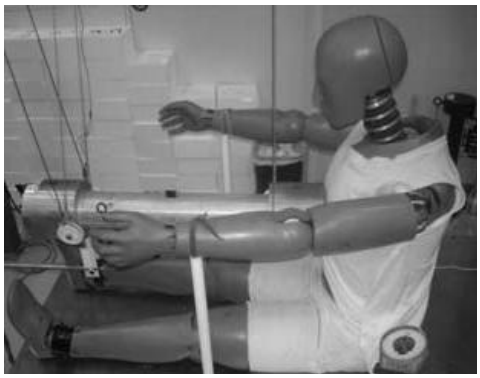

Figure.5 Chest calibration of the H-III 50th dummy

4.2.1 Lumbar hardness VS chest compression

Sheet 3 shows the results of the chest compression with different hardness lumbar, taking the average value of two tests. With the increasing of the lumbar hardness, the chest deflection increase accordingly.

Table 3.Chestdeflectionof different hardness lumbar

Test number	Hardness 75A Def.（mm）	Hardness 80A Def.（mm）	Hardness 85A Def.（mm）
1	68.5	71.9	71.3
2	69.7	70.5	71.6
Average	69.1	71.2	71.45

The average figure increases from 69.1mm to 71.45mm, increases by 3.4%. The linear fitting result is shown as Figure 6.

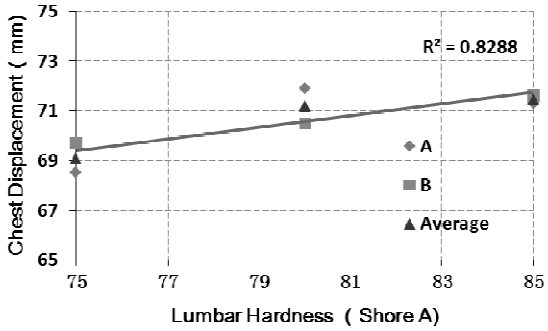

Figure.6 Hardness of the lumbar spine VS Chest displacement

4.2.2 Lumbar hardness and pendulum force

Sheet 4 shows the result of pendulum force used different hardness lumbar, take the average value of two tests. With the increasing of the lumbar hardness, the pendulum force increase accordingly.

Table 4.Resistive force of different hardness of the lumbar spine

Test number	Hardness 75A Force（N）	Hardness 80A Force（N）	Hardness 85A Force（N）
1	541.6	557.4	563.3
2	553.5	554.9	564.8
Average	547.6	556.2	564.1

The average figure increase form 547.5N to 564.1N, increased by 3.0%. The linear fitting result is shown as Figure 7.

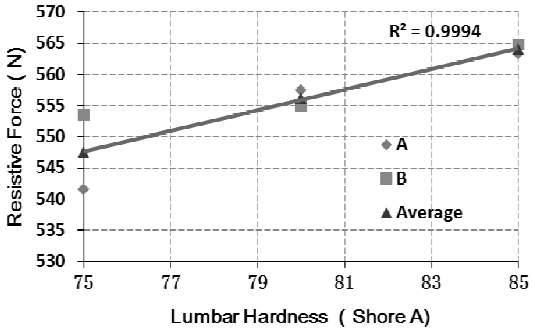

Figure.7 Hardness of the lumbar spine VS pendulum force

4.2.3 Lumbar hardness VS chest hysteresis

Table 5.Chest hysteresis of different hardness lumbar

Test number	Hardness 75A	Hardness 80A	Hardness 85A
1	72.6	71	71.2
2	72	71.3	71.4
Average	72.3	71.15	71.3

Sheet 5 shows the result of the chest hysteresis used different hardness lumbar, take the average value of two tests. With the increase of the lumbar hardness, the chest hysteresis decrease. The chest hysteresis mainly reflects the nature of the rib, so the test result changes a little.

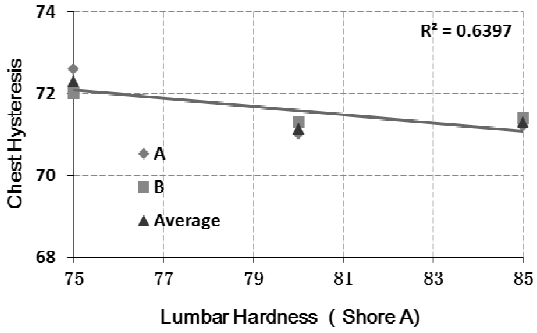

Figure.8 Hardness of the lumbar VS Chesthysteresis

8 Conclusion

1. Different kinds of influencing factors should be in consideration in lumbar calibration of H-III 50th maledummy.

2. Repeatability is good when bending angle is at 10 degree and 20 degree in lumbar calibration of H-III 50th male dummy.

3. Chest compression increase with the increasing of the lumbar hardness.

4. The changes of lumbar hardness will affect the chest property in the vehicle crash test. A deeper research is required.

References

[1] FTSS (First Technology Safely Systems). H-III 50th Lumbar Bend Test. http//www.humaneticsatd.com/.2013

[2] Zhang long,*The research of the finite element model of thoracolumbar section of Hybrid III 50th dummy:[Master Dissertation of Hunan University]*.ChangSha: Hunan University,2011

[3] FTSS (First Technology Safely Systems). Hybrid III 5th Percentile Female User Manual.2008

[4] Wang Kai,Li Xiangrong,Zhu Haitao & Zhang Xianglei, *A Research on the Calibration of Low Speed Impact on the Thorax of Hybrid 50th Percentile Dummy,* Automotive Engineering, 2009(Vo.l 31) No. 1

Proceedings of the 11th International Forum of Automotive Traffic Safety, 2014, pp 431- 434
No. ATS.2014.505

Optimization of Two-dimensional Measurement Equipment in Vehicle Crash Test

Zhu Cuiping, Zhao Youmei, Ma Deren
Chery Automobile Co.,LTD ,WuHu,China,241009
Email:zhucuiping1105@126.com

Abstract: In vehicle crash test, two-dimensional measurement is used to measure the 3-D H machine, dummy location, and seat position. The common method is the parallel measurement. In this paper a unique method is introduced by found the vehicle angle and rotating the 2-D laser mechanism the same angle to conduct the measurement. In this case, the 2-D laser mechanism is in the same coordinate system as the vehicle, the measurement accuracy is improved.

Keywords: Two-dimensional laser, angle, length, parallel

汽车碰撞试验中二维测量设备优化的研究

朱翠平 ，赵友梅 ，马德仁
奇瑞汽车股份有限公司，芜湖, 中国，241009
Email:zhucuiping1105@126.com

摘　要：在汽车碰撞安全试验中，二维尺寸的测量较为频繁，主要应用在三维 H 点装置、试验假人的摆放和汽车座椅的调节；在汽车安全试验中的二维测量方面，目前主要是采用等距平行的原理进行测量。本文着重介绍一种利用带有分度尺的回转工作台结构，将不能直接测量的平行关系转化为可以精确控制的角度关系，通过角度确定二维测量激光装置和车辆平行，使二者在同一座标系里进行测量，以提高测量精度的方法和装置。

关键词：二维激光; 角度; 长度; 平行

1 引言

随着消费者对汽车安全的越来越重视，国内汽车安全的标准也逐渐提高，这也对我们试验中使用的试验方法和设备精度提出了更高的要求。

由于缺乏相关标准，目前国内各大试验室在座椅调节和三维 H 点摆放中使用的标记方式较为粗放，主要是采用等距平行的原理进行测量，即在车身上寻找两个点[1]与测量装置等距，从而确定二者的平行关系。以下简称“长度二维激光”。

在实际的测量过程中，首先车身上与车辆中心线平行的点难以确定，其次利用钢直尺等测量设备确定等距关系也存在较大的测量误差，总体的测量原理不尽合理；目前的标记装置主要由直线滑轨和铝托等组成，整体刚度不够，底盘缺乏灵活性，导致平行调节的不便利。

2 测量原理

本方案主要优化在座椅调节和 3D-H 假人摆放过程中的测距和标记问题。它的测量原理是通过带有分度尺的回转工作台结构，将不能直接测量的平行关系转化为可以精确控制的角度关系，利用角度确定和车辆平行，使

二维测量激光装置和车辆在同一座标系里进行测量，以提高测量精度[2]。以下简称“角度二维激光”。在设备方面，主要提高了整体刚度，同时增强底部调节的灵活性。

3 基本机构

它的结构是：如图 1 所示，整套装置主要有两套回转激光测量仪组成，分别布置在车辆正前方和车辆一侧。如图 2 所示的是车头二维激光装置。这个装置主要由 Y 方向导轨（1）、底座（2）、Z 方向导轨（3）、十字激光发射器（4）、精确转盘（5）、转盘角度调节件（6）、和滑块（7）等组成。如图 3 所示，车侧二维激光装置主要由 X 方向导轨（9）、精确转盘（5）、底座（2）、Z 方向导轨（3）、十字激光发射器（4）、滑块（7）、支撑枕板（10）和定位顶丝（11）等组成[3]。

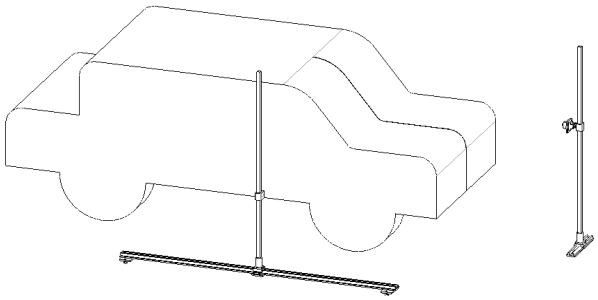

Figure 1. Angle 2D laser layout
图 1 角度二维激光布置图

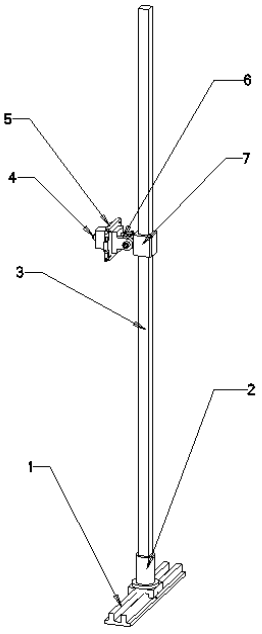

Figure 2. Angle 2D laser head laser device
图 2 角度二维激光车头激光装置

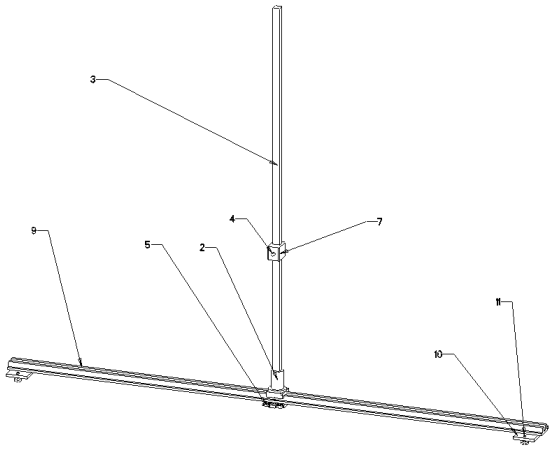

Figure 3. Angle 2D laser car side laser device
图 3 角度二维激光车侧激光装置

通过本方案提供的技术我们可以实现：在碰撞试验中，利用本方案可以提高座椅调节和三维 H 点装置摆放过程中的测距和标记的精度，同时提高工作的效率。

4 试验对比

4.1 长度二维激光的操作步骤

如图 4 所示：1 为二维激光装置，2 为待测车辆。

a、将车辆推进测量间，利用举升机将其顶升起来；

b、利用卷尺等工具测量激光仪横梁到车身前部固定点的距离 L1；

c、重复步骤 2，测量激光仪横梁到车身后部固定点的距离 L2，并使之于步骤 2 中的距离相等；

d、利用平行线原理，得到车身与测量仪之前的平行关系，用十字激光发射器测量距离、标记 R 点、H 点等。

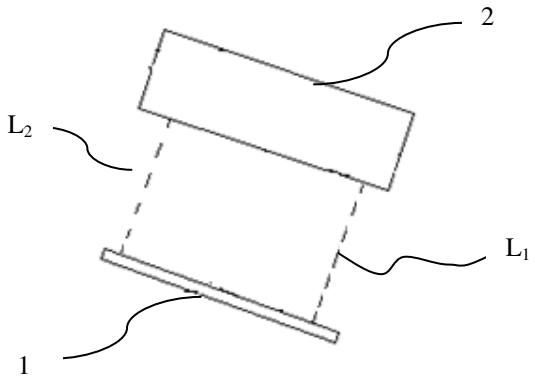

Figure 4. Schematic diagram of 2D laser length measurement

图 4 长度二维激光测量示意图

4.2 角度二维激光的操作步骤

如图 5 所示：测量前准备工作标记车辆的中心线，在测量间的地面沿车辆前进方向标记三条间距为 2m 的平行线；确定车辆一侧的二维激光装置与地面最边上的平行线重合，车头的二维激光装置与地面平行线垂直[4]。

a、将车辆推进测量间，尽量平行于地面直线，通过转动车头二维激光装置的精确转盘（5），使得十字激光的竖直光束与车辆中心线重合，读出车头二维激光转动的角度 α 。

b、调节车侧二维激光装置的精确转盘（5），使得 X 方向导轨（9）和地面平行线的角度 β = α 。

c、通过几何关系可以得知，车辆的转角 γ = β = α ，车辆中心线和车侧二维激光装置测量仪平行[5]。车侧二维激光装置的测量工作可以在和车辆同一坐标系里在 X 方向和 Z 方向导轨上滑动，用十字激光发射器测量距离、标记 R 点、H 点等。测量的精确性得到保证[6]。

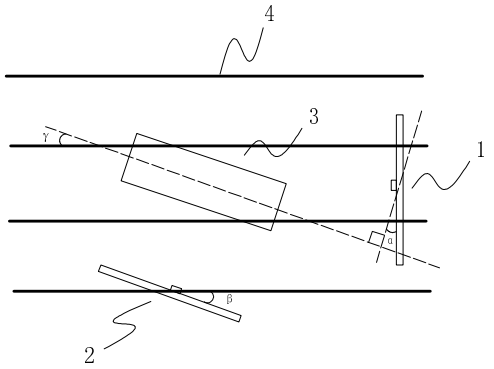

Figure 5. Schematic diagram of 2D laser angle measurement

图 5 角度二维激光测量示意图

5 试验结果分析

5.1 试验结果

实验结果如表 1 所示，其中，两个设备测量的标准长度为 M=267mm，设备 A 为角度二维激光测量仪，设备 B 为长度二维激光测量仪。

Table 1. Test data of two kinds of 2Daser measuring instrument
表 1. 两种二维激光测量仪的试验数据

	1	2	3	4	5	6	7	8
A	270	271	269	270	272	264	272	269
B	272	261	275	276	279	278	282	277

5.2 结果分析

Table 2. Performance data of 2D laser measuring instrument
表 2. 两种二维激光测量仪的性能数据

类别	相对误差	标准差
角度二维激光	0.98%	2.56
长度二维激光	2.99%	6.37

5.2.1 考察数据的准确性

由表 1，可知两组数据的平均值分别是 M_A= 269.63mm ，M_B=275.00 mm。

两组数据平均值和它们标准值的绝对误差是$\triangle_A$= M_A-M=269.63-267=2.63，同理 $\triangle_B$=8.00 ，两组数据平均值和它们标准值的相对误差是σ_A= 0.98% ， σ_B=2.99%，σ_A＜σ_B，故 A 组数据较 B 组数据更接近真实值。

5.2.2 考察数据的稳定性

标准差

$$S=\sqrt{\frac{1}{n}[(x_1-\bar{x})^2+(x_2-\bar{x})^2+\cdots+(x_n-\bar{x})^2]}=\frac{1}{n}[x_1^2+x_2^2+\cdots+x_n^2)-n\bar{x}^2]$$

S_A =2.56，S_B=6.37,S_A＜S_B ，故 A 组数据较 B 组数据的离散程度小，更具稳定性。

6 结论

综上所述，角度二维激光测量仪较长度二维激光测量仪所测数据更接近真实值，更具有稳定性。角度二维激光测量仪的测量原理更合理，在实际操作过程中，更加方便、精确、稳定。

参考文献

[1] 周炳琨, *激光原理*, 国防工业出版社 2009.1
[2] Zhou Bingkun, *laser principle National defence industry press* ,2009.1
[3] 陈家瑞, *汽车构造*, 机械工业出版社 2009.6
[4] Chen Jiarui, *Vehicle Construction* Machine industry Press 2009.6
[5] ECE R94，*Uniform Provisions Concerning the Approval of Vehicles with Regard to the Protection of the Occupants in the Event of a Frontal Collision* .
[6] 唐振民;赵春霞;孙怀江;陆建峰;杨静宇;;*地面自主移动平台信息融合与路径规划系统*[J];南京理工大学学报(自然科学版);2003 年 01 期
[7] [7] Ming-Hong Chiu,Der-Chin Su.*Angle Measurement Using Total-internal-reflection Heterodyne Interferometry OpticalEngineering* . 1997
[8] Liu Dequan, Li Yinzhang.*Error production of angular surveying and reduction method*[J]. Shuili Tiand.2007(12)
[9] 刘德平,张银瑞.*角度测量的误差来源及消减方法*[J]. 水利天地. 2007(12)

Proceedings of the 11th International Forum of Automotive Traffic Safety, 2014, pp 435- 443
No. ATS.2014.506

A Study on the Effect of Changes in Side Impact Protocol of 2015 Euro NCAP

Liu Xilong[1], Dong Liping[1], Zhu Xichan[1], Ye Wentao [2], Huang Xuan [2]
[1] *School of Automotive Studies, Tongji University, Shanghai, China, 201804*
[2] *FAW-Volkswagen Automotive Company Ltd, Changchun, 130011*
Email: tj_liuxilong@hotmail.com

Abstract: In 2015 Euro NCAP will be updating its side impact test procedure and assessment parameters. These updates will be centred on the adoption of the WorldSID (World side impact dummy) anthropometric test device and a new barrier face for the mobile deformable barrier (MDB)-Advanced. In this article, based on one tested car, using PAM-SAFE the simulation tests in side impact were designed. It studied the effects of the new MDB and the new dummy WorldSID on the design of vehicle, especially on the damage of the dummy.

Keywords: Euro NCAP, Side impact, Simulation, WorldSID, AE-MDB

2015 年 Euro NCAP 侧碰规程变化的影响研究

刘喜龙 [1]，董丽萍 [1]，朱西产 [1]，叶文涛 [2]，黄　炫 [2]
[1] *同济大学汽车学院，上海，中国，201804*
[2] *一汽-大众汽车有限公司，长春，中国，130011*
Email: tj_liuxilong@hotmail.com

摘　要：2015 年 Euro NCAP 规划计划对侧面碰撞的评价规程进行更新，主要更新内容是将原壁障 MDB 更换为新的壁障 AE-MDB，将原来的 ES-2 假人更换为 WorldSID 假人。本文基于有限元软件 PAM-SAFE 设计针对某车型的侧面碰撞模拟计算试验，分析更新后的壁障和假人对于整车设计的影响，主要考虑假人伤害情况。

关键词：Euro NCAP，侧面碰撞，仿真，WorldSID，AE-MDB

1 引言

Euro NCAP 于 1997 年由 7 个欧洲国家（法国、德国、瑞典、荷兰、英国、卢森堡及西班牙）牵头，与国际汽车运动联合会、国际消费者研究及测试机构（ICRT）、欧洲汽车俱乐部以及车辆保险修复研究中心共同发起推出。通过十余年的发展，Euro NCAP 已经成为世界上很有影响力的汽车安全评价体系。

2013 年之后，Euro NCAP 制定新的规划，计划在 2015 年 Euro NCAP 更新侧面碰撞的评价规程，其中较为重要的变化就是前排的驾驶员侧的碰撞假人由原来的 ES-2 假人更换为 WorldSID 假人，侧面碰撞的移动壁障由原来的 MDB 更换为 AE-MDB，同时壁障与碰撞车辆的碰撞点也向后移 250mm。

2 WorldSId 假人与 AE-MDB 壁障介绍

2.1 WorldSID 假人介绍

目前国际上有至少三种侧碰的成人假人。一个是由美国的 NHTSA（National Highway Traffic Safety Administration）开发研制的 SID 假人，这个假人在美国的 FMVSS214（Federal Motor Vehicle Safety Standards）

侧面碰撞法规中使用，还有一个是由欧洲开发研制的 EuroSID 假人，在欧洲的法规要求中，必须使用这个假人。而 WorldSID 假人的开发使得在全世界，不同的法规标准要求下，都可以使用一个共同标准的假人。

研究开发的 WorldSID 五十百分位男性假人，具有更好的生物学仿真度，这对于提高整个侧面碰撞规程的国际化有很大的帮助，同时可以提升车辆使用者的安全性，并且降低客户和厂商的成本。

Figure 1. WorldSID dummy model
图 1. WorldSID 假人模型

ES-2 假人从头部、胸部、腹部、骨盆四个方面对假人在侧面碰撞中的伤害情况进行评价的，而 WorldSID 假人则是从头部、肩部、胸部、腹部、骨盆五个方面进行评价的。其中，头部的评价基本保持不变；WorldSID 假人增加了对于肩部的评价，肩部增加了扣分项，当肩部的侧向力大于 3kN 时，进行扣分；胸部、腹部、骨盆的评价指标也重新做了调整。

2.2 AE-MDB 壁障介绍

自从欧洲的 R95 侧面碰撞壁障被应用以来，欧洲汽车车型逐步得到改进，因此，目前使用的侧面碰撞壁障不能再真实的反应目前市场上的乘用车型，尤其是在事故情况下的乘用车型。2011 年 Euro NCAP 同意将 AE-MDB 引入到未来的侧面碰撞测试中，其侧碰小组（SIWG）成立了新的特别工作组来进行新的壁障模型和细节的设计。

AE-MDB 在材料、质量、几何形状、刚度、强度等方面都有一定的变化。相比于目前正在使用的 MDB R95（UN-ECE Regulation 95），AE-MDB 重量由 950kg 增加到 1300kg；如图 2 所示，AE-MDB 在左右两侧增加了长宽为 300mm 的 45° 倒角；同时在宽度上，AE-MDB 由原来 MDB 的 1500mm 增加了 200mm；相较于 MDB，AE-MDB 将原来底部蜂窝铝块突出于上部蜂窝铝块的部分设计为刚度不同的一个缓冲块。

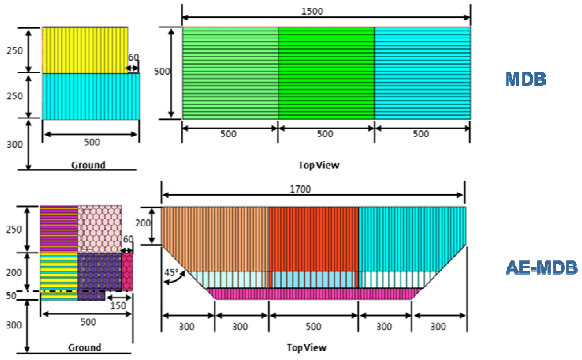

Figure 2. Comparison of MDB and AE-MDB model
图 2. MDB 与 AE-MDB 模型对比

欧洲汽车安全委员会和国际标准化研究中心共同研究并开发的这个新侧面碰撞的可变形移动壁障，满足现有车型的前端结构刚度趋势。其与目前市场上面现有的车型的形状相似。在图 3 中可以看出，现在使用的 MDB 和即将使用的 AE-MDB 与不同类型车辆前端的对比研究。AE-MDB 更符合这些车型的前端特征。

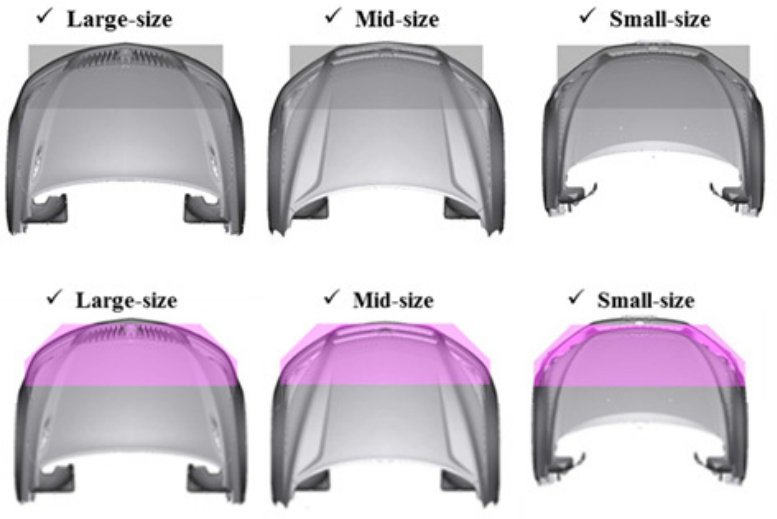

Figure 3. Comparison of MDB and AE-MDB model
图 3. MDB 与 AE-MDB 模型对比

3 实验设计方案

本文中所用的车辆车体模型是经过产品验证的模型。由于目前没有实体模型，也没有进行过对 WorldSID 假人和 AE-MDB 侧碰壁障的实车试验，所以在本文中，主要进行的是有限元模型的仿真试验。

根据前排侧碰假人的变化和侧面碰撞壁障的变化设计了如下的四组侧碰试验，研究分析其变化对于整车侧面碰撞安全系统开发的影响：

Table 1. Table of experiment
表 1. 实验设计表

试验组	1	2	3	4
假人	ES-2	ES-2	WorldSID	WorldSID
壁障	MDB	AE-MDB	MDB	AE-MDB

根据上述实验设计，进行四组侧面碰撞模拟仿真试验，分析试验中假人的伤害情况，进行研究。

4 实验结果与分析

4.1 试验 1 与试验 2 对比分析

试验 1（ES-2 假人、MDB R95）与试验 2（ES-2 假人、AE-MDB）对比，主要是研究分析全新壁障 AE-MDB 对目前的整车侧面碰撞安全系统开发的影响。

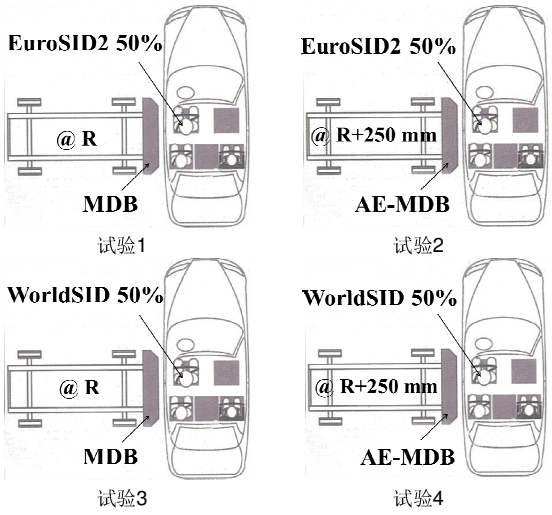

Figure 4. Schematic diagram of experiment design

图 4. 实验设计示意图

本文中蓝色虚线为试验 1（ES-2 假人、MDB R95）结果，红色实线为试验 2（ES-2 假人、AE-MDB）结果。

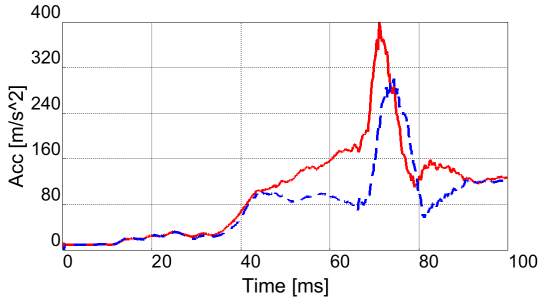

Figure 5. Curve：Head acceleration of driver

图 5. 驾驶员头部加速度曲线图

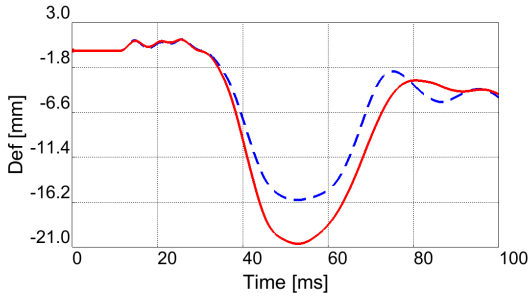

Figure 6. Curve: Upper chest rib lateral compression of driver

6. 驾驶员胸部上肋骨变形量曲线

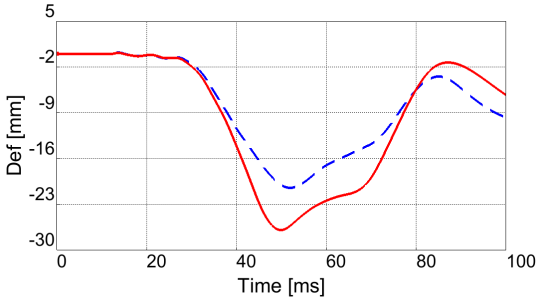

Figure 7. Curve: Middle chest rib lateral compression of driver

图 7. 驾驶员胸部中肋骨变形量曲线

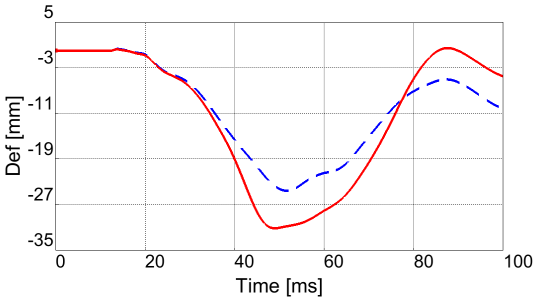

Figure 8. Curve: Low chest rib lateral compression of driver

图 8. 驾驶员胸部下肋骨变形量曲线

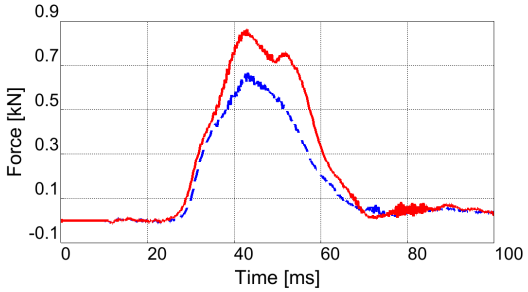

Figure 9. Curve: Abdominal force of driver

图 9. 驾驶员腹部力曲线

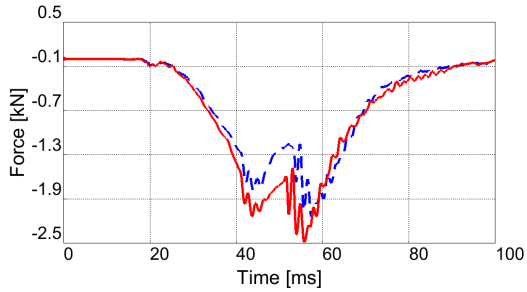

Figure 10. Curve: pubic symphysis lateral force of driver

图 10. 驾驶员耻骨力曲线

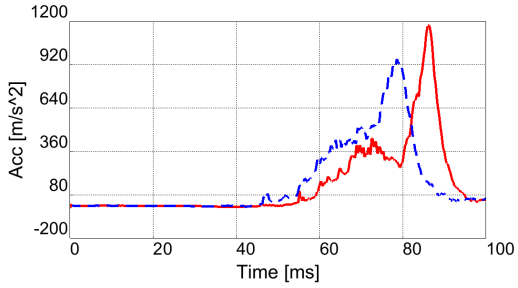

Figure 11. Curve：Head acceleration of rear passenger

图 11. 后排乘员头部加速度曲线

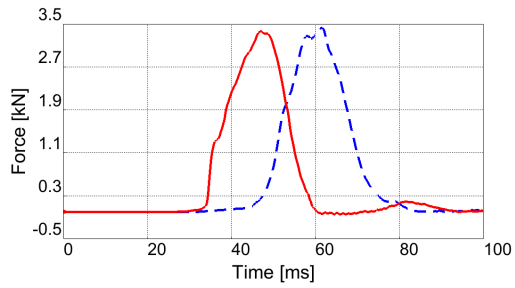

Figure 12. Curve：Pelvis force of rear passenger

图 12. 后排乘员骨盆合力曲线

Table 2. Resulting data of test1 and test2

表 2. 试验 1 与试验 2 结果数据

测量参数	试验 1	试验 2	变化百分比
HIC36	26.73	55.58	107.9%
3ms 合成加速度	27.32	33.66	23.2%
肋骨变形量	24.59	31.16	26.7%
VC 值	0.15	0.34	126.7%
背板力	0.31	0.75	141.9%
T12 Fy	0.50	0.62	24.0%
T12 My	66.65	106.55	59.9%
腹部力	0.66	0.86	30.3%
耻骨力	2.14	2.49	16.4%
HIC15	495.63	526.30	6.2%
骨盆合力	3.46	3.40	-1.8%

在假人响应方面：

1) 相较于 MDB 的碰撞试验，AE-MDB 碰撞试验中，ES-2 假人在头部、胸部、腹部、骨盆四个部位的伤害值都相应的增大，其中头部的 HIC36 值，胸部的粘性系数，背板力的增幅变化较大。

2) AE-MDB 质量的大幅增加，前端的碰撞块的强度增强使得 B 柱车门的侵入量和侵入速度增加，同时也使得假人的伤害情况变得更为恶劣。从图 13 中可以看出，试验 2 中的假人的侧向移动大于试验 1 的假人，同时头部的运动情况更为剧烈。

后排假人 SID-IIs 的头部加速度曲线峰值降低，但是其加速度高值出现比较集中，使得头部伤害值也有小幅增加，骨盆合力基本保持不变。从曲线出现峰值的时间看，试验 2 更早一些，这是由于 AE-MDB 的碰撞点相较于原来的 R 点向后移动了 250mm，使得碰撞时对后门的侵入量、侵入速度变得较大，从而使得假人与车门接触的时间变短，更早的出现峰值。

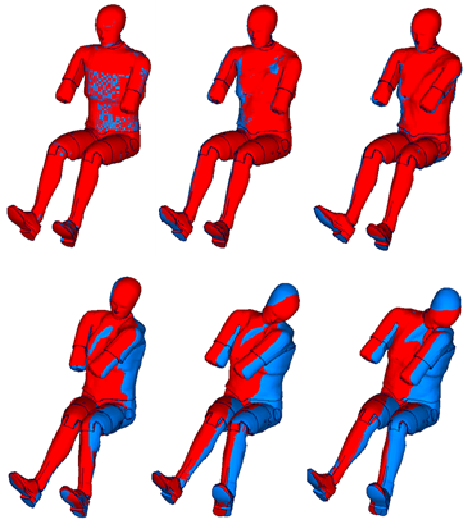

Figure 13. Reaction of ES-2 dummy in test1(blue)and test2(red)
图 13. 试验 1（蓝）与试验 2（红）中 ES-2 不同响应

4.2 试验 1 与试验 3 对比分析

试验 1（ES-2 假人、MDB R95）与试验 3（WorldSID 假人、MDB R95）对比，主要是研究分析全新假人 WorldSID 假人对目前的整车侧面碰撞安全系统开发的影响。

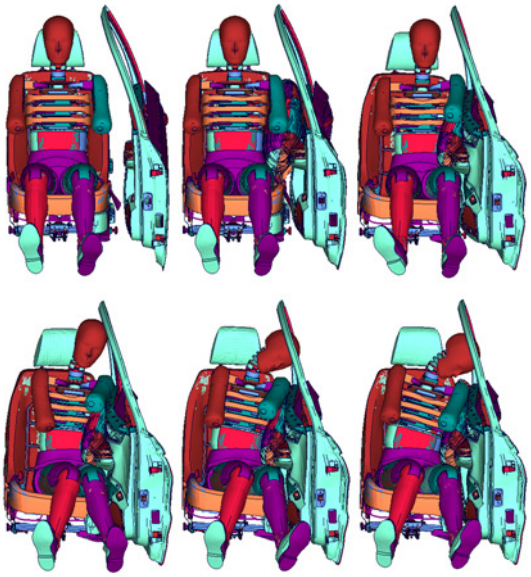

Figure 14. Reaction of ES-2 dummy in test1
图 14. 试验 1 中 ES-2 假人侧面碰撞响应

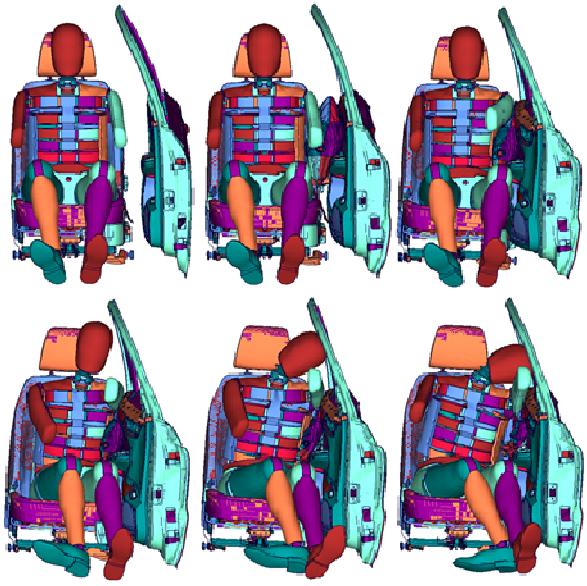

Figure 15. Reaction of WorldSID dummy in test3
图 15. 试验 3 中 WorldSID 假人侧面碰撞响应

本文中蓝色虚线为试验 1（ES-2 假人、MDB R95）结果，黑色实线为试验 3（WorldSID 假人、MDB R95）结果。

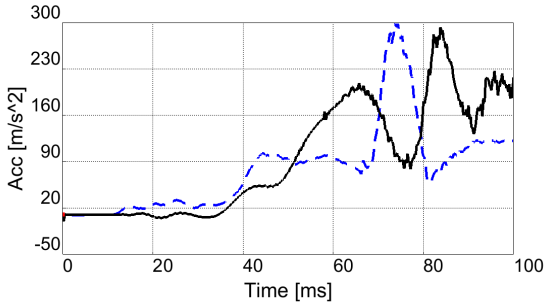

Figure 16. Curve：Head acceleration of driver

图 16. 驾驶员头部加速度曲线

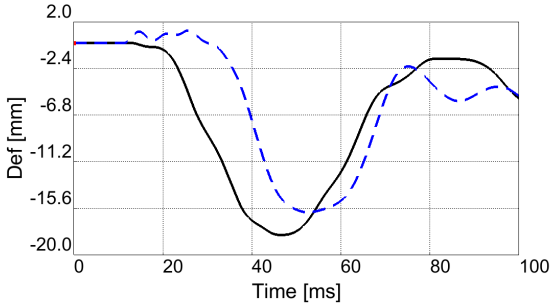

Figure 17. Curve: Upper chest rib lateral compression of driver

图 17. 驾驶员胸部上肋骨变形量曲线

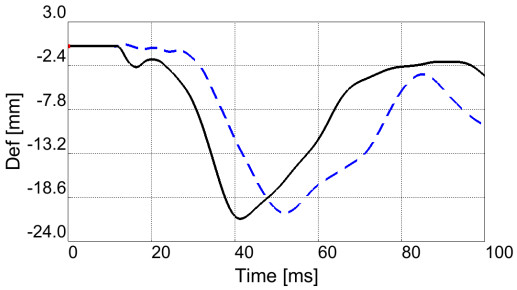

Figure 18. Curve: Middle chest rib lateral compression of driver

图 18. 驾驶员胸部中肋骨变形量曲线图

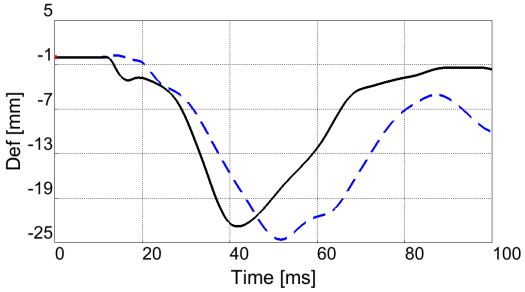

Figure 19. Curve: Low chest rib lateral compression of driver

19. 驾驶员胸部下肋骨变形量曲线

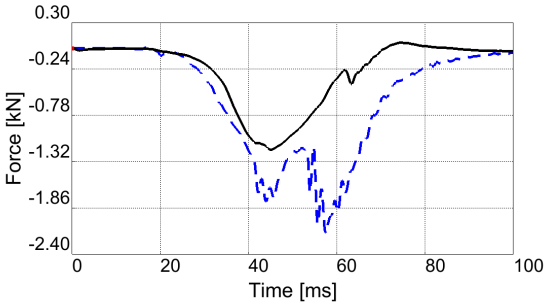

Figure 20. Curve: pubic symphysis lateral force of driver

图 21. 驾驶员耻骨力曲线

Table 3. Resulting data of test1 and test3

表 3. 试验 1 与试验 3 结果数据

测量参数	试验 1	低限值	试验 3	低限值
HIC36	26.73	4.1%	31.96	4.9%
3ms 合成加速	27.32	37.9%	23.41	32.5%
肋骨变形量	24.59	111.8%	21.75	77.7%
VC 值	0.15	46.9%	0.16	50.0%
腹部	0.66kN	66.0%	19.78mm	42.1%
耻骨力	2.14	71.3%	1.36	80.0%

在假人响应方面：

1) 由于两种假人的评价标准不同，不能直接进行比较，因此采用假人的测量参数占其对应标准中的低性能限值的百分比来表示，其中头部伤害值上面没有明显的变化，腹部的伤害值情况 WorldSID 假人略好于 ES-2

假人，这可能与 WorldSID 假人在腹部的结构上面的巨大变化相关，WorldSID 假人能够更好的对侧面碰撞中模拟乘员响应。骨盆的伤害值情况 WorldSID 假人的略高于 ES-2 假人，但是变化不是很明显。

2) WorldSID 假人在肋骨变形量上低于 ES-2 假人，从结构和动画可以看出 WorldSID 假人的肋骨设计更为灵活，每根肋骨部分可以独立的运动，同时能够有转动的动作，ES-2 假人的胸部结构为一个整体，不能灵活运动，这样的设计使得 WorldSID 假人是用于±30°的侧面碰撞，这可能是其伤害值变小的原因之一。

3) ES-2 假人的手臂可以随着锁骨转动至假人的前部，使得胸部的肋骨与车门直接接触，原本肩部受到的部分载荷也会由胸部承担；WorldSID 假人手臂不能向前转动，这也可能是胸部伤害情况降低的原因之一。

4.3 试验 3 与试验 4 对比分析

从表 4 分析结果可以看出，相较于 MDB 的碰撞试验，AE-MDB 碰撞试验中，WorldSID 假人在头部、肩部、胸部、腹部、骨盆五个部位的伤害值都相应的增大，其中头部的 HIC36 值变化最大，胸部变形量次之，这与试验 1 与试验 2 的对比结果接近；后排假人 SID-IIs 的头部加速度曲线峰值降低，头部伤害值也有小幅增加，基本保持不变，与试验 1 和试验 2 对比结果相同，验证了试验 1 与试验 2 对 AE-MDB 影响分析的正确性。

Table 4. Resulting data of test3 and test4
表 4. 试验 3 与试验 4 结果数据

测量参数	试验 3	试验 4	变化百分比
HIC36	31.96	109.5	237.6%
3ms 合成加速度	23.41	36.96	57.9%
肩部力	1.38	2.09	51.4%
胸部肋骨变形量	21.75	26.54	22.0%
VC 值	0.16	0.23	43.8%
腹部肋骨变形量	19.78	23.89	20.8%
耻骨力	1.36	1.57	15.4%
HIC15	504.73	537.79	6.6%
骨盆合力	3.49	3.51	0.6%

4.4 试验 2 与试验 4 对比分析

从表 5 分析结果可以看出，在同样用 AE-MDB 进行侧碰试验时，WorldSID 假人和 ES-2 假人头部伤害值上面变化不大，WorldSID 假人在肋骨变形量上低于 ES-2 假人，腹部的伤害值情况 WorldSID 假人略好于 ES-2 假人，骨盆的伤害值情况 WorldSID 假人的略高于 ES-2 假人，但是变化不是很明显。与试验 1 和试验 3 对比结果相同，验证了试验 1 与试验 3 对 WorldSID 假人影响分析的正确性。

Table 5. Resulting data of test2 and test4
表 5. 试验 2 与试验 4 结果数据

测量参数	试验 2	低限值百分比	试验 4	低限值百分比
HIC36	55.58	8.6%	109.5	16.8%
3ms 合成加速度	33.66	46.8%	36.96	51.3%
肋骨变形量	31.16	141.6%	26.54	94.8%
VC 值	0.34	106.25%	0.23	71.9%
腹部	0.86kN	86.0%	23.89mm	50.8%
耻骨力	2.49	83.0%	1.57	92.4%

5 结论

5.1 AE-MDB 对侧面碰撞安全系统开发的影响

1) AE-MDB 质量的大幅增加，前端的碰撞块的强度增强也使得假人的伤害情况变得更为恶劣，假人

在头部、肩部、胸部、腹部、骨盆部位的伤害值都相应的增大，其中头部的 HIC36 值变化最大。

2) AE-MDB 的碰撞点相较于原来的 R 点向后移动了 250mm，使得碰撞时对后门的侵入量、侵入速度变得较大，从而使得假人与车门接触的时间变短，后排假人的头部加速度曲线及骨盆合力曲线更早的出现峰值。

5.2 WorldSID 假人对侧面碰撞安全系统开发的影响

1) 相较于 ES-2 假人，WorldSID 假人头部伤害值上面没有明显的变化，腹部的伤害值情况 WorldSID 假人略好于 ES-2 假人，这可能与 WorldSID 假人在腹部的结构上面的巨大变化相关，WorldSID 假人能够更好的对侧面碰撞中模拟乘员相应。骨盆的伤害值情况 WorldSID 假人的略高于 ES-2 假人，但是变化不是很明显。

2) WorldSID 假人在肋骨变形量上低于 ES-2 假人，从结构和动画可以看出 WorldSID 假人的肋骨设计更为灵活，每根肋骨部分可以独立的运动，同时能够有转动的动作，ES-2 假人的胸部结构为一个整体，不能灵活运动，这样的设计使得 WorldSID 假人是用于±30°的侧面碰撞，这可能是其伤害值变小的原因之一。

3) ES-2 假人的手臂可以随着锁骨转动至假人的前部，使得胸部的肋骨与车门直接接触，原本肩部受到的部分载荷也会由胸部承担；WorldSID 假人手臂不能向前转动，这也可能是胸部伤害情况降低的原因之一。

由于没有 AE-MDB 和 WorldSID 假人的真实模型，目前没有做过相应的真实试验，仅限于模拟仿真，所以对于 AE-MDB 和 WorldSID 假人对侧面碰撞安全系统开发的影响还需要进一步调查研究。

致 谢

感谢刘静岩工程师对我在实际工程上的指导和帮助！

参考文献

[1] Ellway J D. *The development of an advanced European mobile deformable barrier face (AE-MDB)*[C]//Proceedings of the 19th Conference on Enhanced Safety of Vehicles (ESV), Washington DC, USA. 2005

[2] Youn Y, Lee E D, Kim D. *A COMPARISON STUDY OF TWO SIDE IMPACT DUMMIES BASED ON THE PROBABILITY OF INJURY RSIK CURVES*[J].

[3] Iwata K, Tatsu K, Saeki H, et al. *Comparison of Dummy Kinematics and Injury Response between WorldSID and ES-2 in Side Impact*[J]. SAE International Journal of Transportation Safety, 2013, 1(1): 192-199.

Proceedings of the 11th International Forum of Automotive Traffic Safety, 2014, pp 444- 451
No. ATS.2014.507

Research on Validation Metrics for Multiple Dynamic Responses Comparison

Zhenfei ZHAN[1], Junqi YANG [1], Ling ZHENG[1], Yajing SHU[1], Yan FU [2], Ren-Jye YANG [2], Saeed Barbat [2]
[1]*College of Automotive Engineering, Chongqing University, Chong Qing, China, 400000*
[2] *Ford Research and Advanced Engineering, 2101 Village Rd, Dearborn, Michigan, USA, 48121*
Email:zhenfeizhan@cqu.edu.cn

Abstract:

***Background*:**Increasing computer programs and models are developed to simulate vehicle crashworthiness, dynamic, and fuel efficiency. To maximize the effectiveness of these models, the validity and predictive capabilities of these models need to be assessed quantitatively.

***Objective*:**This paper is aimed to develop objective validation metrics that has the desirable metric properties to quantify the discrepancy between multiple tests and simulation results in the form of time histories.

***Method and Material*:** This study is carried out by utilizing principal components analysis (PCA) to address multivariate correlation. Then Area Metric is applied to calculate the disagreement between two data sets presented in the type of time histories to obtain the discrepancy of the overall distribution of data. Then, time histories are translated into frequency domain for the purpose of getting the features of errors in phase, topology and magnitude.

***Results*:** The study results show thatthe values of measurements in magnitude, phase and topology are consistent with intuitive judgment based on graphics, which approves good performance of proposed metrics.

***Conclusions*:**The proposed metrics satisfy the necessary properties of ideal metric in model validation and the investigated method is capable for automotive safety applications.

Keywords: Model validation, Multivariate dynamic responses, Principal component analysis, Frequency analysis

1 Introduction

With the ever shortening speed to market, computer aided engineering (CAE) has become a crucial tool for product development in automobile industry. Various computer programs and models are developed to simulate dynamic systems. Before using these models, their validity and predictive capabilities need to be assessed quantitatively. Model validation is the process of comparing CAE model outputs with test data in order to assess the validity or predictive capabilities of the CAE model for its intended usage. One of the critical tasks to achieve model validation is to select a validation metric that has the desirable metric properties for model assessment of a dynamic system with multiple functional responses[1, 2].

Developing quantitative model validation methods has attracted considerable researchers' interest in recent years[3]. They were applied to various model validation problems and showed significant potential. Statistical hypothesis testing is one approach to provide quantitative model validation. Fu et al. [4]and Zhan et al. [5]further exploited the Bayesian based validation methods for multivariate dynamic systems. However, these methods considered the whole distribution of interested time history, the agreements of the important features were not addressed. Error Assessment of Response Time Histories (EARTH) provides independent errors of phase, magnitude and slope but without an intuitive quantity to present the validity of a model. To tackle this problem, Zhan and Fu[6] investigated such method and proposed an enhanced version called Enhanced Error Assessment of Response Time Histories (EEARTH), which translates the three kinds of errors into a score between 0 and 100%. So it is convenience for engineers to conduct

decision making. However, those two methods for time histories conduct the process of model validation only in the time domain. Since frequency domain contains more intuitive information about phase, magnitude and shape, this paper investigates an innovative method for model validation of dynamic systems, which integrates both the analysis in time domain and frequency domain.

In this paper, a quantitative multivariate validation method and common process is proposed to quantitatively assess the agreements of important features of multiple dynamic responses simultaneously. It exploits several techniques such as principal component analysis (PCA)[7] and proposed validation method. The PCA approach is used to address multivariate correlation. To the validation metrics, in time domain, Area Metric is applied to calculate the disagreement between two data set presented in the type of time histories to obtain the discrepancy of the overall distribution of data. Then time histories are translated into frequency domain for the purpose of getting the features of errors in phase, topology and magnitude.

2 Multivariate Validation for Time Histories

2.1 PCA based dimension reduction

In multivariate data analysis, one major target to deal with highly correlated multivariate data is to remove the dependence amongst variables and reduce the dimension of variables. Amongst all techniques, PCA[8] is a well-established statistical method for dimensionality reduction and has been widely applied in data compression, image processing, exploratory data analysis, pattern recognition, and time series prediction. PCA involves a matrix analysis technique called eigenvalue decomposition. The eigenvalues and eigenvectors from decomposition represent the amounts of variation accounted for by each principal component and the weights for the original variables, respectively. Its main objective is to transform a set of correlated high dimensional variables to a set of uncorrelated lower dimensional variables (principal components). The important property of PCA is that the principal component projection minimizes the squared reconstruction error in dimensionality reduction. The PCA is not based on a probabilistic model, so no data distribution assumption is involved in a PCA transform process. In automotive safety applications, the output multiple responses are generated from the same crash event, hence, some of the responses are highly correlated. PCA could transform highly correlated original responses into uncorrelated lower dimensional responses. The judgment based on reduced principal components can be efficient and minimize the squared reconstruction error in dimension reduction.

To determine the proper number of principal components that should be retained is an important issue in PCA implementation. The first p eigenvalues are typically high, implying that most information is accounted for in the corresponding principal components. Thus, the intrinsic dimensionality p is obtained by calculating the cumulative percentage of the p eigenvalues (i.e., the total variability by the first p principal components) that is higher than a threshold value, say 95%, as is presented in expression 1. This implies that the retained p principal components account for 95% information of the original data.

$$\sum_{i=1}^{p} \lambda_i \Big/ \sum_{i=1}^{m} \lambda_i \geq 95\% \quad (1)$$

2.2 Error assessments of dynamic responses

To the model validation of data represented in the form of time histories, in time domain the features of time curves, such as phase and frequency, cannot be obtained intuitively. So In this study, analysis in both time domain and frequency domain are associated to provide a comprehensive consideration of the magnitude error, phase error and shape error.

In the time domain, there exists a well-established metric called Area Metric. The Area Metric is firstly proposed by Ferson [3]to investigate the disagreements of repeated tests and simulations in the statistical features. In this study, the normalized and dimension-reduced data are utilized to construct the distribution of samples. They are represented as non-decreasing step function with a steady step. For the data are in the type of discrete points, the distribution of data in a time curve is expressed as

$$S_n(x) = \frac{\sum_{i=1}^{n} I(x_i, x)}{n} \qquad (2)$$

Where

$$I(x_i, x) = \begin{cases} 1 & x_i \leq x \\ 0 & x_i > x \end{cases}$$

It is implied that the $S_n(x)$ has the function of presenting the number of points below a specific quantity x. After plotting the $S_n(x)$ of two data sets that needed to be compared, the area between the two distributions can be calculated as the measure of discrepancy, as is denoted in Equation 3.

$$d(S_n, S_n') = \int_{-\infty}^{\infty} |S_n(x) - S_n'(x)| dx \qquad (3)$$

For the analysis in frequency domain includes the error assessment of magnitude, if the normalized data are used to be transformed, the maximum and minimum quantities of two curves are all normalized into 1 and 0, which leads to losing the information of minimum and maximum values. Thus only test data for the analysis in frequency domain are under pretreatment of normalization while CAE data are just the dimension-reduced version with relative discrepancy to test data.

In this step, multiple methods aiming at transforming data into frequency domain exist, such as Laplace Transform (LT) and Fast Fourier Transform (FFT). In the process of transformation, original time histories are decomposed into plenty of signals of sine or cosine. By choosing the signals with big values in magnitude, the principal signals are determined.

Since the results in both time and frequency domain are obtained, metrics for errors of magnitude, phase and shape are introduced respectively. Analysis in frequency domain provides information of frequency and corresponding amplitude and phase, based on which the error in magnitude and phase for a certain response can be calculated with Equation 4 and Equation 5.

$$\varepsilon_{magnitude} = \sum_{i=1}^{q} \left(\frac{M_{Test_i}}{\sum_{i=1}^{q} M_{Test_i}} \left| \frac{M_{CAE_i} - M_{Test_i}}{M_{Test_i}} \right| \times 100\% \right) \quad (4)$$

$$\varepsilon_{phase} = \sum_{i=1}^{q} \left(\frac{M_{Test_i}}{\sum_{i=1}^{q} M_{Test_i}} |P_{CAE_i} - P_{Test_i}| / 2\pi \times 100\% \right) \quad (5)$$

where q denotes number of frequency components, M_{CAE} and M_{Test} are the arrays of magnitudes while P_{CAE} and P_{Test} present phases for each frequency. With the computed ε_{phase}, error in shape can be obtained in Equation 6.

$$\varepsilon_{shape} = Area \times \varepsilon_{phase} \qquad (6)$$

3 Case Study

In this section, the proposed approach is demonstrated with a rear seat child restraint system with a hybrid III 3-year dummy model[9]. Figure 1 shows the CAE model and the rigid seat test set-up corresponding to the Evenflo Vanguard-5, respectively. Sixteen tests were conducted with different configurations, including different setting of seat

cushion positions, top tether routing configurations and input crash pulses. Correspondingly, 16 sets of computer outputs were generated from the model.

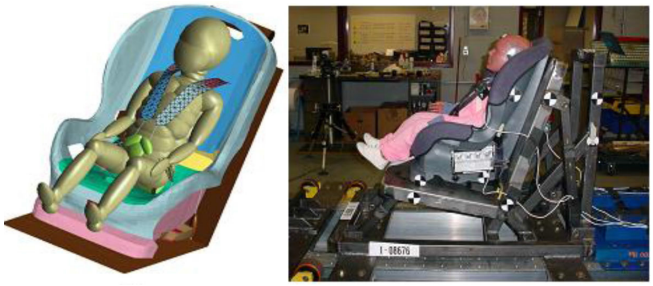

(a) (b)

Figure 1 Rear seat child restraint system: (a) CAE model and (b) rigid seat test set-up

In the study, 8 responses (e.g., acceleration, deflection, force, etc.) in the form of histories are measured at a variety of locations of dummy and each contains 203 sampling points. Table 1 provides the meanings of those responses and Figure 2 plots the 8 responses and the simulation outputs in the same condition respectively. To demonstrate the proposed validation metrics, a pair of test and CAE data is selected.

Table 1. Reponses and corresponding descriptions

Variables	Description	Variables	Description
Response1	Head acceleration at x-direction	**Response5**	Chest acceleration at z-direction
Response2	Head acceleration at z-direction	**Response6**	Upper neck shear (Fx)
Response3	Pelvis resultant acceleration	**Response7**	Upper neck tension (Fz)
Response4	Chest acceleration at x-direction	**Response8**	Upper neck moment (My)

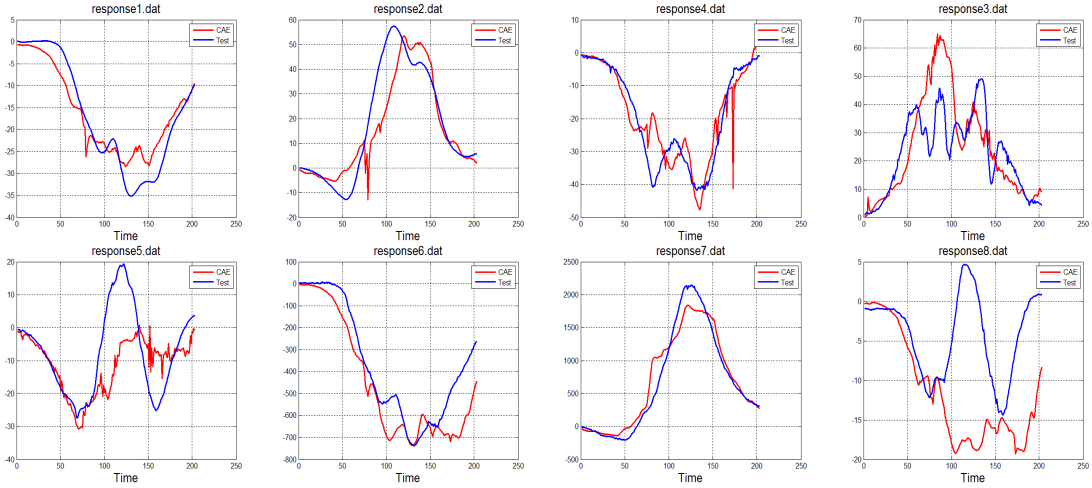

Figure 2. CAE and Test outputs for 8 responses

The original test matrix can be constructed in the size of. The technique of PCA is utilized to reduce the dimensions and address the correlation among responses. After the eigenvalues and corresponding eigenvectors are computed, principal components can be decided with eigenvalues. The eigenvalues are regarded as the measurements of the contributions of principal components. If 95% information of original data are required after projected on the new

coordinates, the eigenvalues of chosen principal components should contribute at least 95% to the sum of eigenvalues. Figure 7 presents the contributions of each component to the whole.

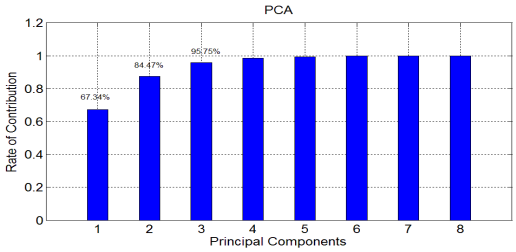

Figure 3. Rate of contribution for each principal component

Based on Figure 3, the first 3 components contain more than 95% information of the original data. Thus, the three corresponding eigenvectors are utilized as the updated projecting directions. After conducting the process of dimension reduction, 8 responses are transformed into test data matrix T* with 3 responses reserving information of data as much as possible. Similarly， outputs of CAE are projected onto the same axes to obtain the matrix C*.

After the process of pretreatment completed, model validation in time domain and frequency domain is conducted. Firstly, Area Metric is utilized to computing the degree of mismatch of CAE and Test. Secondly, data are transformed into frequency domain to reveal the features of phase and magnitude. Figure 4 presents the 'area' between CAE and Test in graphic way and quantitative way respectively.

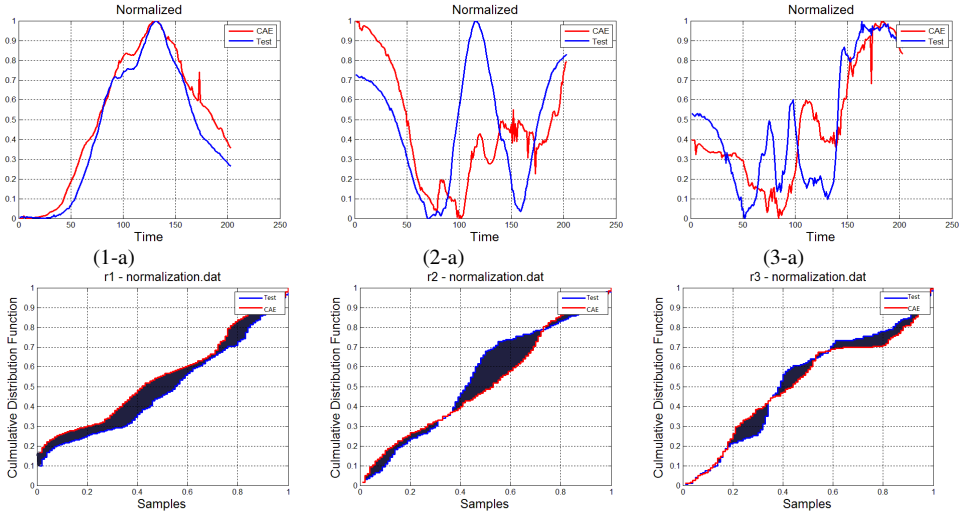

Figure 4 Area Metric measurements for each principal component, graphically

The measurements of Area Metric offer the reference for the density distribution of samples in a certain response. Though the shape of curves can be recognized in some special conditions, but for complex waves the metric need to be combined with features in frequency domain. For instance, in Figure 9 (1-b), the CDF of Test is always lager than that of CAE, which presented as that the two curves never intersect with each other and are in similar tendency graphically. It is consistent with Figure 9 (1-a). Thus conclusion can be made that the CAE and Test outputs of principal response 1 share the similar shape. However, figures of response 2 and response 3 are with more complexity so that it is not easy and proper to conclude their similarity in topology. Therefore, further study are required in frequency domain.

Fast Fourier Transformation (FFT) is utilized to transform the time histories into frequency domain. The original curves are decomposed as multiple sine waves with the features of magnitude, frequency and phase. The transformed responses are depicted in Figure 5.

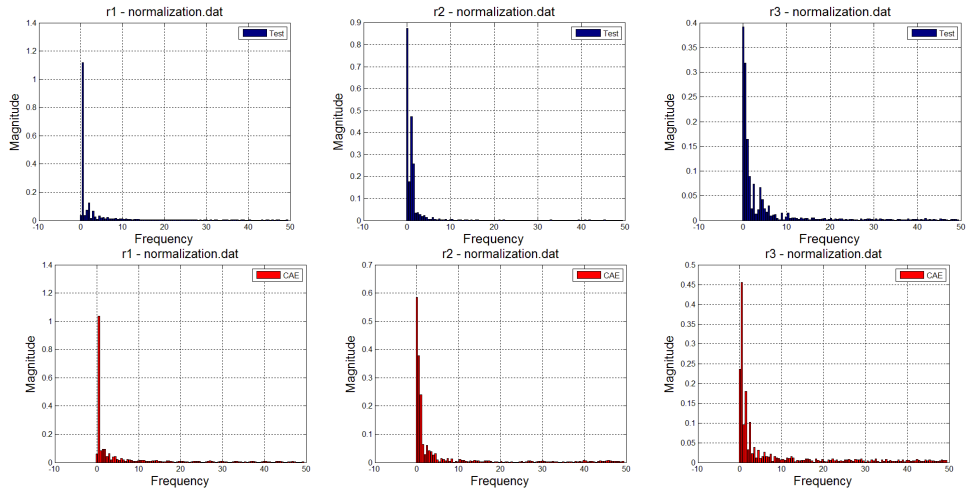

Figure 5. Frequency characteristics of principal components

100 frequency components are generated in each Test and CAE, but only the components with significant amplitude need to be taken into consideration for others effect trivially on the results. Computing based on dominate frequency is time saving and with high validity. Due to space limitations, only 3 frequency components are provided in Table 2 for each responses. The quantities are calculated according to the aforementioned Equation 4, Equation 5 and Equation 6.

Table 2. Error analysis in frequency domain

Test-r1		CAE-r1		Test-r2		CAE-r2		Test-r3		CAE-r3	
Magnitud e	**Phase**	**Magnitud e**	**Phase**	**Magnitud e**	**Phase**	**Magnitud e**	**Phase**	**Magnitud e**	**Phase**	**Magnitud e**	**Phas e**
1.12	135.92	1.03	133.87	0.87	0	0.58	0	0.39	180	0.23	180
0.12	113.06	0.09	102.56	0.47	-42.13	0.24	-84.15	0.31	46.15	0.45	55.06
0.74	-11.31	0.09	67.764	0.25	98.44	0.063	-77.64	0.16	81.75	0.09	79.19
$\varepsilon_{magnitude}$	37.84 %	ε_{phase}	2.99 °	$\varepsilon_{magnitude}$	75.41 %	ε_{phase}	-37.71 °	$\varepsilon_{magnitude}$	70.89 %	ε_{phase}	8.03 °

As is presented in Table 2, total relative error in amplitude and mismatch in phase are computed based on the information in frequency domain. They act as the measurements of magnitude and phase shift directly. As is stated before, Area Metric provides reference of how samples distributed, and the phases of dominate frequencies reflect where the peak and valley appearance. Therefore, multiplying the quantities obtained in Area Metric in Figure 4 and Phase Mismatch in Table 2 offers the measurement for topology. Above all, the errors in magnitude, phase and shape are presented independently in Table 3.

Table 3. Analysis in frequency domain for sine curves

Error	Magnitud e	Phase	Shape
r1	37.84%	2.99°	0.19
r2	75.41%	-37.71°	2.42
r3	70.89%	8.03°	0.34

The whole process of model validation based on the investigated method (metrics specifically) for the validation problem in engineering is completed. If the metrics really work, the quantitative measurements should be consistent with the intuitive judgments on original responses. So comparison is required between the quantities in Table 3 and the graphics in Figure 4. The curves of response 1 show that CAE and Test are consistent with each other in shape, magnitude and phase in a good condition graphically. And values of three types of errors in Table 3 reveal high validity of the simulation, which agrees with the curves in Figure 4. With respect to figures of r2 and r3, r2 has the largest discrepancy in the magnitude while CAE of r3 is in the same tendency of Test with fewer mismatches than r3. As can be seen in Figure 4, those characteristics are reflected in Magnitude and Shape in Table 3 intuitively too. Moreover, in terms of r2, the positions of peaks in Test and CAE differ a lot, which leads to that there exists a major error in phase shifting. So in summary, the investigated method for model validation is capable for such kind of problem.

Conclusions

In the problem of model validation, for the purpose of obtaining results successfully, it is of great importance to select or even develop proper metrics for specific applications. Appropriate metrics are required to be applicable on the deterministic system. In terms of dynamic system, the outputs of CAE and test are frequently in the form of time histories. However, it is not enough to analyze the discrepancy in just the values in time histories for such type of data. More features must be recognized to conduct overall analysis and make the decision whether to reject or accept the model, such as errors in magnitude, phase and topology. In this paper, methods for better representation of errors of magnitude, phase and topology are developed and investigated. Two main steps are included the proposed methodology. Firstly, a novel tool aiming at selecting principal components is proposed. Secondly, the proposed metrics are adopted to recognize the features in errors both in time domain and frequency domain. For the purpose of illustration, a practical engineering case of children restraint system is introduced and the whole process of validation is applied to it. The values of measurements in magnitude, phase and topology are consistent with intuitive judgment based on graphics, which approves good performance of proposed metrics.

However, the study in this paper only concentrate on how to present and quantify the errors in the three features. Therefore, to avoid obtaining a confusing result, the method to integrate several errors into a score quantity calls for further study.

References

[1] Oberkampf, W.L., Barone, M.F. *Measures of agreement between computation and experiment: validation metrics*. in Journal of Computational Physics. 2006. Changsha, China. 217(1):5-36. doi:10.1016/j.jcp.2006.03.037

[2] Oberkampf, W.L., Trucano, T.G. *Design of and Comparison with Verification and Validation Benchmarks*. Technical Report Sand No. 2006-5376C, Sandia National Laboratories, Albuquerque, New Mexico, USA.

[3] Ferson, S., Oberkampf, W.L., Ginzburg, L. *Model validation and predictive capability for the thermal challenge problem*. Computer Methods. In Applied Mechanics and Engineering, 2008. 197(29-32):2408-2430. doi:10.1016/ j.cma.2007.07.030

[4] Fu, Y., Zhan, Z., Yang, R.J., 2010. *A Study of Model Validation Method for Dynamic Systems*. In SAE World Congress, Detroit, USA, SAE 2010-01-0419.

[5] Zhan, Z., Fu, Y., Yang, R.J., Peng, Y. *An enhanced Bayesian based model validation method for dynamic systems*. In Journal of Mechanical Design, 2011a 133(4):041005. doi:10.1115/1.4003820.

[6] Zhan, Z., Fu, Y., Yang, R.J. *Enhanced Error Assessment of Response Time Histories (EEARTH) Metric and Calibration Process*. In SAE World Congress, Detroit, USA, 2011b. SAE 2011-01-0245.

[7] Joliffe, I.T. *Principal Component Analysis.* In *Springer*. 2002. New York, USA.

[8] Hotelling, H. *Analysis of a complex of statistical variables into principal components*. In *Journal of Educational Psychology*. 1933.24(6):417-441. doi:10.1037/h0070888.

[9] Zhan, Z., Fu, Y., Yang, R. J., Peng, Y., *Development and Application of a Reliability-Based Multivariate Model Validation Method*, International Journal of Vehicle Design, 60(3/4): 194-205, 2012.

Proceedings of the 11th International Forum of Automotive Traffic Safety, 2014, pp 451- 456
No. ATS.2014.508

Research on the AE-MDB and Vehicle Front Stiffness

Li Xiangrong[1], Ma Weiji[1], Zhu Haitao[1]
[1]*China Automotive Technology and Research Center, Tianjin, China, 300300*
Email:lixiangrong@catarc.ac.cn

Abstract：With the innovation of auto technology, the front stiffness and curb weight of the automobiles which are saling in the China market have great changes. Through one vehicle frontal crash test ,using load cell wall(LCW) got the vehicle stiffness in frontal impact test, this paper discussed the properties of aluminum honeycomb for new side impact test (AE-MDB) and the actual vehicle front end stiffness , and the methods of automobiles' front stiffness. The results show that the method could be more really reflecting this vehicle front stiffness characteristics, and the AE-MDB was more conform to this vehicle front stiffness. this paper is important for the study of vehicle side impact test methods.

Keywords: Side Impact, AE-MDB, stiffness, LCW

AE-MDB 侧碰可变形壁障性能与车辆前端刚度关系的研究

李向荣[1]，马伟杰[1],朱海涛[1]
[1]*中国汽车技术研究中心，天津，中国，300300*
Email:lixiangrong@catarc.ac.cn

摘要：随着汽车技术的革新，中国市场上销售的汽车正面刚度与整备质量有较大变化。本文通过某款车型的正面碰撞试验，运用测力墙采集车辆前端撞击力数据，重点研究车辆前部刚度情况，进而讨论新型侧面碰撞试验用可变形壁障(AE-MDB)的性能与实际车辆前端刚度的关系，以及汽车前部刚度的研究方法。结果表明，该研究方法能够较为真实的体现汽车前部刚度特性，并且，新型可变形壁障（AE-MDB）更为符合该车型的前部刚度特性。本文对于车辆侧面碰撞试验方法的研究具有重要意义。

关键词：侧面碰撞，AE-MDB，刚度，测力墙

1 引言

可移动变形壁障（MDB）是实车侧面碰撞试验中的重要工具，进行侧面碰撞试验时，用 MDB 代替实车来撞击试验汽车，故其结构和性能要尽量反映真实汽车相关特性。MDB 主要由两部分构成：移动台车和前端的可变形吸能块。由于所产车型的不同，不同国家和地区采用的 MDB 的型号规格和质量也会有所不同，概括起来主要分为美国和欧洲两个体系。在美国体系中不同的测试机构采取的规格也不尽相同，主要分为两个规格:一是美国 US-NCAP 及 FMVSS214 采用的 MDB，由两个单元构成，其总体质量为 1361±4.5kg,壁障前端的离地高度为 279mm，壁障的宽度为 1750mm[1]；另外是美国 IIHS-NCAP 使用的 MDB，其规格代表大型 SUV 和小型卡车，它的总体质量为 1500±5kg,壁障前端的离地高度为 379mm，壁障本体高度为 759mm，宽度为 1676mm[2]；欧洲现阶段 EURO-NCAP 及 ECE R95 使用的 MDB 质量为 950kg,离地高度为 300mm，壁障本体高度为 500mm，宽度为 1500mm，该型号规格的壁障应用也最为广泛，J-NCAP，C-NCAP，K-NCAP，A-NCAP 也都采用了该规格的 MDB。

但是，欧洲相关机构通过研究发现，ECER 95 法规中使用的 MDB 并不能完全代表当前欧洲车型的前部特性，也不能同时模拟前后排座椅上乘员的真实响应。因此 EEVC WG13 工作组于 2001 年着手新壁障的研究，并称之为 AE-MDB，并于 2003 年在 18 届 ESV 国际会议上公布了第一次使用 AE-MDB 壁障的测试效果，2005 年又公布了第二版 AE-MDB V2 的测试情况[3]。在 V2 版本的基础上又进行一系列性能考核，包括法规认证试验、高速平面墙

碰撞试验、柱碰撞试验、边缘加载刚性墙碰撞试验、栏板加载刚性墙试验、柔性墙碰撞试验等，确定了该壁障的最终性能 AE-MDB V3.9[4][5]。AE-MDB 已经被 EURO-NCAP 和 K-NCAP 新规则采用，计划于 2015 年进行正式应用。本文希望通过车辆正面碰撞试验，研究车辆前部刚度情况，进而讨论新型侧面碰撞试验用蜂窝铝(AE-MDB)的性能参数与实际车辆前端刚度的一致性关系。

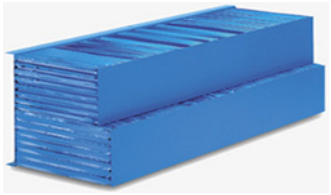

Figure.1EVC Advanced-2000
图 1EVC Advanced-2000 型蜂窝铝

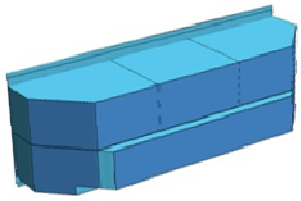

Figure.2 AE-MDB
图 2AE-MDB 蜂窝铝

2 AE-MDB 性能研究

2.1 侧碰可变形壁障（EEVC Advanced-2000）

欧洲现阶段 EURO-NCAP 及 ECE R95 使用的 MDB 前端安装的是 EEVC 2000 可变形壁障，它由 6 个单元构成，其技术参数在 ECE R95(修订 3 版）及 EC96/27 中有具体的规定。

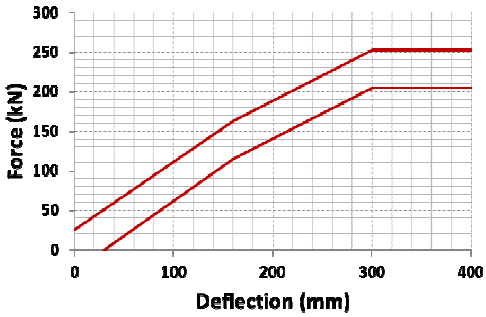

Figure.3 EEVC-2000 Force-Deflection
图 3EEVC-2000 压溃性能要求

冲击阻力性能在 Multi-2000 型可变形壁障基础上得到全面改善。该型可变形壁障于 1999 年由 Cellbond 进行了原形设计，2002 年得到 EuroNCAP 应用，之后 ANCAP,C-NCAP 均采用。

EEVC 2000 可变形壁障动态冲击试验压溃总的性能要求如图 3 所示。160mm 变形时压溃力在 115～163KN 之间；300mm 变形时压溃力在 205～253KN 之间。另外对应可变形壁障 6 个不同的单元，每一单元也分别规定了变形量与压溃力的限值通道，以规范变形壁障的性能。

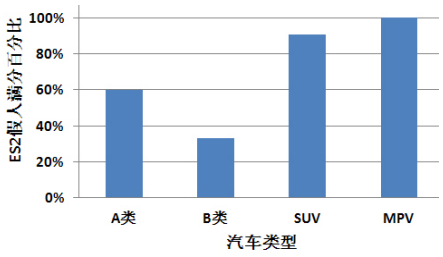

Figure.4ES2 score
图 4ES2 假人得分

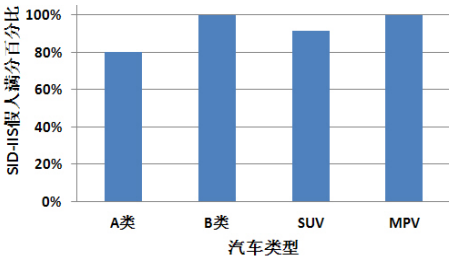

Figure.5SID-IIS score
图 5 SID-IIS 假人得分

本文统计了 37 个基于 2012 版 C-NCAP 进行评价侧碰试验结果，得分情况如上图 4、5 所示。图 4 表明，在侧碰试验中 ES2 假人获得满分率为 67.6%，得分 15 分以上为 89.2%，SUV 满分率为 90.9%，MPV 满分率为 100%，A 级车满分率为 60%，B 级车满分率为 33.3%。图 5 中 SID-IIS 假人满分率为 86.5%，出现后来扣分的车型为小型车、A 级车和小型 SUV。由此可知，在侧碰试验中获得前、后排假人高分的比例都很高；且 SID-IIS 假人要比 ES2 假人更容易获得满分。2012 版 C-NCAP 碰面碰撞试验对汽车侧面被动安全性优略的区分度较小。

2.2 AE-MDB 动态测试性能指标

Cellbond 于 2001 年，在欧洲各工作小组和机构合作进行开发新的侧面碰撞用可变形壁障，V3.9 版本将在 2015 年的 Euro-NCAP 上得到应用(官方型号规格于 2013 年 2 月份正式发布)。AE-MDB 可变形壁障宽度为 1700mm，高度 500mm，净重 25kg。

AE-MDB 可变形壁障同样分为 6 个单元，每一单元也分别规定了变形量与压溃力的限值通道，以规范变形壁障的性能。总的变形量与压溃力要求如图 7 所示。10mm 变形时压溃力在 9～65KN 之间；135mm 变形时压溃力在 179～195KN 之间；165mm 变形时压溃力在 150～160KN 之间；300mm 变形时压溃力在 262～05KN 之间。通过限值通道曲线可以看出，AE-MDB 可变形壁障与 EEVC-2000 可变形壁障相比，同样变形量的情况下压溃力有所提升。

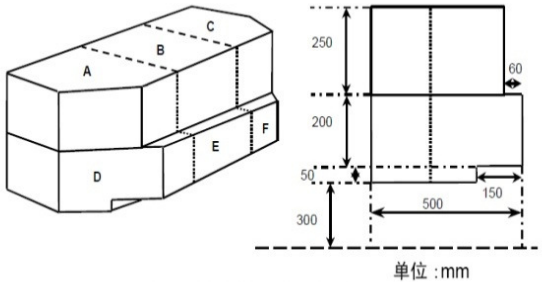

Figure.6AE-MDB
图 6AE-MDB

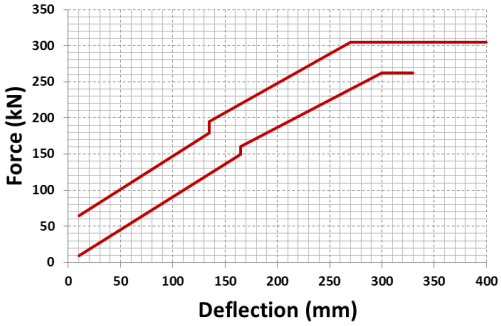

Figure.7AE-MDB Force-Deflection
图 7AE-MDB 压溃性能要求

3. 车身前端刚度测量

3.1 正面碰撞试验中测力墙（LCW）的应用

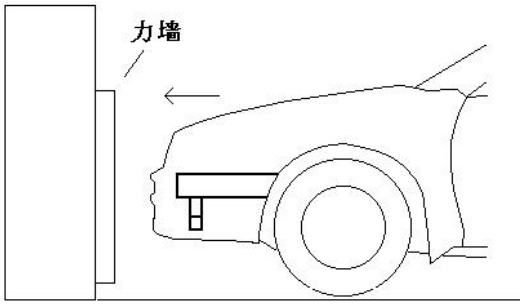

Figure.8Full-Frontal Impact Test
图 8 正面碰撞试验

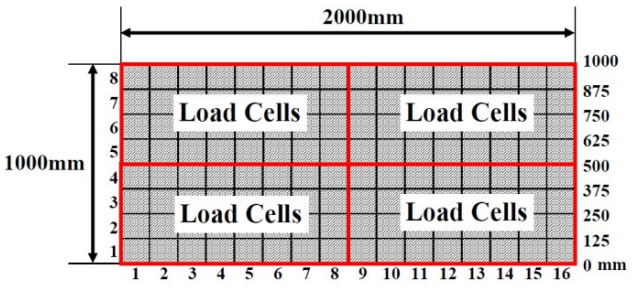

Figure.9 LCW
图 9LCW 力传感器分布

车身刚度测量运用测力墙（LCW）采集车身前端的撞击力，具体试验形式如图 8 所示，试验为百分之百正面碰撞，车辆速度 50km/h，车身 B 柱部位安装加速度传感器以测量车辆整体加速数据。测量墙（LCW）载荷传感器的分布如图 9 所示。共有 128 块载荷传感器，分析中主要运用 X 方向的数据，即车辆运动方向的载荷值。

3.2 测力墙载荷

图 10 中分析显示了 20ms～60ms 的载荷云图。从云图中可以很清楚的看到车辆前端与刚性壁障撞击时产生的力值大小及分布情况。

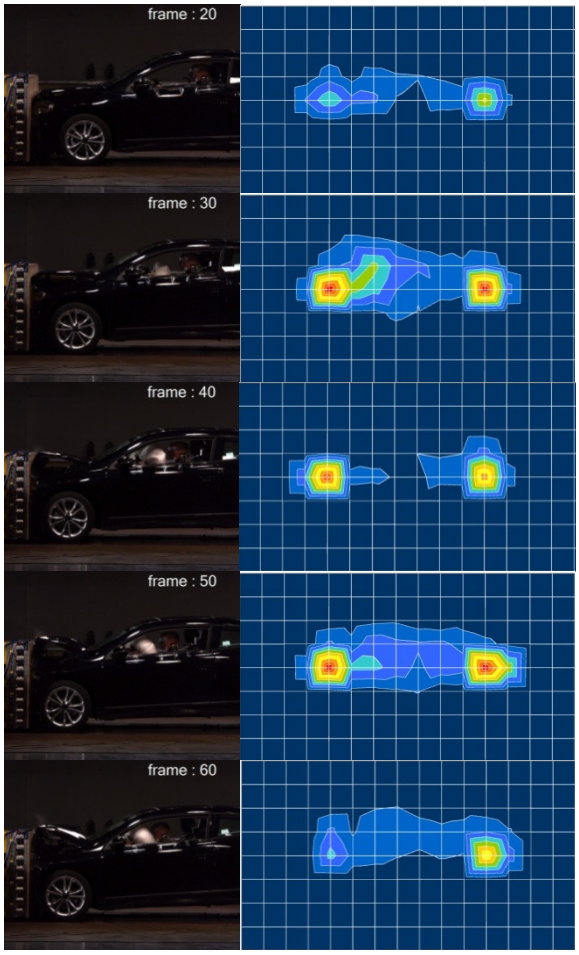

Figure.10 LCW Force
图 10 LCW X 向载荷图

测力墙采集的 X 方向整体载荷曲线如图 11 所示，在 30ms 及 50ms 左右，分别出现两个波峰，撞击力达到最大值。

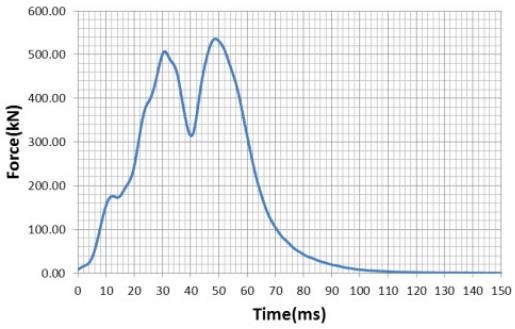

Figure.11 LCW Total Force Load
图 11 LCW X 向整体载荷曲线

3.3 车辆前端刚度与 AE-MDB 性能

车辆前端的刚度特性通常是用前端变形量对应碰撞力载荷曲线来进行表达。因此在进行分析之前，需要得到车身前端在碰撞过程中的形变数据。在前面已经提到试验时在车辆 B 柱位置安装有加速度传感器，对加速度进行两次积分即可得到车辆的位移量，即碰撞过程中车身前端的形变过程。本文研究的试验中，初始速度为 50km/h，加速度通道采用 CFE180 进行低通滤波，滤波后的曲线一次积分得到车辆整体速度变化曲线，二次积分得到车辆整体位移曲线（如图 12 所示）。

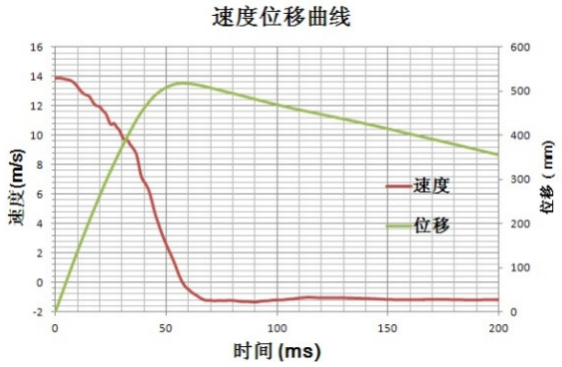

Figure.12 Vehicle Velocity and Displacement

图 12 车辆速度计位移量曲线

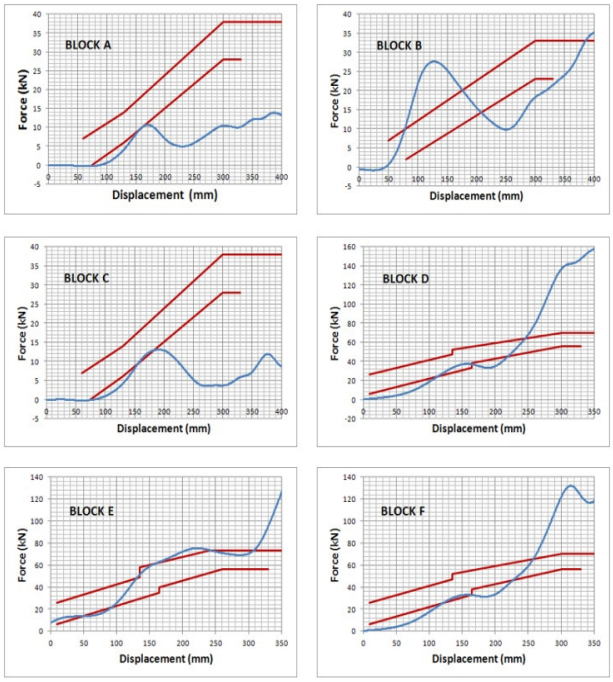

Figure.13 Different regions of Vehicle Force and Displacement

图 13 车辆不同区域的变形量对应载荷

将测力墙按照 AE-MDB 的 6 个单元分布设置成由左到右，由上到下对应的 6 块区域（A、B、C、D、E、F 六块）。每块区域将载荷力合成，得到如图 13 所示的载荷曲线。载荷曲线与 AE-MDB 动态冲击性能参数要求的限

值通道进行对比。A、C 区域在压溃量为 150mm 之前基本与 A-EMB 的限值范围较为吻合；B 区域载荷力的变化超出限值范围较多；D、E、F 区域载荷力合成曲线基本符合 AE-MDB 的限值范围。

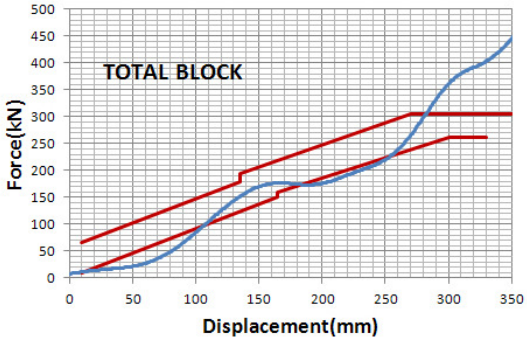

Figure.14 Vehicle Force and Displacement

图 14 车辆变形量对应载荷

由图 14 可知，整车的力-位移曲线较为符合 AE-MDB 的限制要求。说明此车型的前部刚度与 AE-MDB 的刚度特性较为符合。

4 结论

1. AE-MDB 动态冲击性能特性相比 EEVC-2000 型可变形壁障而言要更硬一些。
2. 采用测力墙(LCW)可以有效的获取车身前端在正面碰撞试验过程中的载荷变化情况，进而得到车辆前端刚度。
3. 用车身前端压溃量与载荷关系表示的车身刚度曲线，在 300mm 压溃量之前，与 AE-MDB 性能限值通道范围比较吻合。
4. AE-MDB 的性能特性改善比较成功，与现在车辆的前端刚度性能较为匹配。

参考文献

[1] National Highway Traffic Safety Administration. *Laboratory test procedure for the new car assessment program-side impact moving deformable barrier test.* Rev.09/19/2012. US.

[2] Insurance Institute for Highway Safety. *Side impact crashworthiness evaluation crash test protocol.* Version VI. 2012. US.

[3] Roberts,A.K, Van Ratingen,M.R, (on behalf of EEVC WG13). *Progress on the development of the advanced european mobile deformable barrier face (AE-MDB).*The 18th international technical conference on the enhanced safety of vehicles (ESV). 2003. Nagoya, Japan. Paper no. 126.

[4] Ellway,J.D, van Ratingen,M.R, Versmissen,T, etc. *The advanced european mobile deformable barrier specification for use in euro NCAP side impact testing.* The 23th international technical conference on the enhanced safety of vehicles (ESV). 2013. Seoul, Korea. Paper no. 13-0069.

[5] Marie-Laure Roussaire, Richhard Zeitouni, Céline Adalian. *Enhancement of side impact protection using an improved test procedure.*The 20th international technical conference on the enhanced safety of vehicles (ESV). 2007. Lyon, France. Paper no. 07-0245.